UNIVERSITÀ
DEGLI STUDI
DI PADOVA

Head Office: Università degli Studi di Padova

Department of Management and Engineering, DTG

Ph.D. COURSE IN MECHATRONICS AND PRODUCT INNOVATION ENGINEERING

CURRICULUM: MECHANICS OF MATERIALS

DOCTORAL CYCLE: XXXIV

DESIGN TOOLS AND METHODS FOR ADDITIVE MANUFACTURING

Thesis written with the financial contribution of
Fondazione Cassa di Risparmio di Padova e Rovigo (CARIPARO)

Coordinator: Prof. Daria Battini

Supervisor: Prof. Gianpaolo Savio

Co-Supervisor: Ch.mo Prof. Gianmaria Concheri

Ph.D. student: Stefano Rosso

Index

Abstract ... 4

1 Introduction ... 6

2 Background ... 11

- 2.1 Additive Manufacturing ... 11
  - 2.1.1 AM technologies ... 12
  - 2.1.2 Workflow ... 19
  - 2.1.3 AM related international standards ... 20
- 2.2 Design and modeling for AM ... 22
  - 2.2.1 Design for Additive Manufacturing ... 23
  - 2.2.2 Geometric modeling and representation schemes ... 27
  - 2.2.3 Cellular solids ... 30
    - 2.2.3.1 Lattice structures classification ... 32
    - 2.2.3.2 Geometric modeling of lattice structures ... 38
    - 2.2.3.3 Lattice structure optimization ... 41
    - 2.2.3.4 Numerical analysis and mechanical testing of lattice structures ... 45
  - 2.2.4 Functionally graded AM (FGAM) parts ... 49
  - 2.2.5 File formats for AM ... 51
- 2.3 Limitations and issues ... 53

3 Design and optimization of lattice structures ... 56

- 3.1 Conformal wireframe generation ... 56
  - 3.1.1 Tween curves division method ... 57
  - 3.1.2 Arc division method ... 57
  - 3.1.3 Curvature division method ... 58
  - 3.1.4 NURBS free-form deformation method ... 59
- 3.2 Optimization of lattice structures ... 61
  - 3.2.1 Size optimization of lattice structures ... 61
  - 3.2.2 Multi-objective optimization of lattice structures ... 65
- 3.3 Geometric modeling of conformal lattice structures ... 70
  - 3.3.1 Geometric modeling of lattice structures with beam elements ... 70
    - 3.3.1.1 Subdivision surface schemes ... 71
  - 3.3.2 Internal walls and external skin integration ... 74
- 3.4 Optimization workflow in design for AM ... 87

4 Test cases 91
4.1 Piston rod 91
4.2 Aerospace propellant tank 102
5 Numerical and experimental tests 113
5.1 Numerical validations of the subdivision surface modeling method 113
5.1.1 Geometrical deviation 113
5.1.2 Curvature analysis 116
5.2 Material and mechanical characterization of AM parts 122
5.2.1 Test campaign on stainless steel 316L samples manufactured by SLM 122
5.2.2 Comparison between polyamide 12 parts manufactured by SLS and MJF 131
6 Conclusions 159
References 164
Appendix A – Internal walls implementation code 184
Appendix B – Materials data sheets 188
Appendix C – Related publications 195

Abstract

The additive manufacturing (AM) technologies allow producing components layer upon layer in a completely different way with respect to the traditional techniques. This new approach in building the parts enables unprecedented design freedom; indeed, objects with complex shapes, cellular solids, internal features, and multiple materials can be easily produced. However, even though the manufacturing technologies are ready for producing such components, the literature emphasized that the available design tools are not appropriate and do not allow taking full advantage of the AM capabilities. For instance, the geometric modeling of structures with a lot of elements requires high computational resources, Boolean operations often fail, and the methods are not robust; the modeling of multi-material parts require new approaches able to describe the model at each point of the volume, and not only on the external surface.

This research project aims to overcome some of the highlighted limitations by developing new geometric modeling methods suitable for exploiting the capabilities offered by AM. To reach the objective, several research topics have been addressed. Methods for the geometric modeling and optimization were proposed; approaches for the generation of conformal wireframes and for the size and multi-objective optimization of lattice structures were presented. A geometric modeling method based on meshes and subdivision surface algorithms that allows obtaining smooth surfaces without sharp edges was developed; more, the possibility of introducing internal walls and external skins to lattice structures was implemented. These approaches were then introduced in a more comprehensive optimization workflow for AM, dealing with the embodiment design phase and including the possibility of performing size and topology optimization. The proposed geometric mesh modeling method was then numerically validated, and experimental campaigns on both bulk samples and lattice structures produced by several powder bed fusion AM technologies were conducted.

The results showed that the proposed mesh modeling method, together with the subdivision surface algorithm, is suitable to design lattice structures efficiently, requiring low computational resources and, at the same time, offering a good dimensional accuracy with respect to reference models. The C2 curvature continuity of the model allows reducing the stress concentration at the nodal points of the lattice if compared to similar

structures obtained by traditional CAD software. Furthermore, the possibility of introducing internal walls makes it possible to create optimized ducts and paths and can locally modify the properties of the component.

Due to the versatility of AM, the outcomes of the research can be adopted in different fields, as shown by the presented test cases: in the automotive field where lightweight and energy absorption components are used for reducing the fuel consumption and increasing the performance and safety of the vehicles; in the aerospace field, where lightweight components are required; in high-performance heat exchangers, microfluidic applications, and biomedical scaffolds where fluid dynamics plays a key role; and in consumer goods such as sports apparel and equipment.

1 Introduction

Since the studies of Charles W. Hull and the introduction of the first commercial system in 1987 by 3D Systems Inc., additive manufacturing (AM) technologies have received increasing attention up to the present day, where they are considered on par with traditional manufacturing technologies. As defined by international standards, the distinctive feature that characterizes AM technologies is the possibility "to make parts from 3D model data, usually layer upon layer, as opposed to subtractive manufacturing and formative manufacturing methodologies" [1]. This layer-wise approach opens a completely new way of designing components since an unprecedented level of complexity is reached and innovative parts that were impossible to produce by the conventional technologies can now be manufactured. The complexity of an additively manufactured object can be declined in different ways [2,3]. Organic and complex shapes such as structurally optimized models (Figure 1a), lattice structures (Figure 1b), and internal ducts can be easily produced, and custom textures or finishes can be obtained on the surface of the object; material complexity allows producing parts presenting different materials (Figure 1c) or different material blends in different zones of the same part resulting in tailored properties, and different process parameters can result in different material microstructures, acting in a scale way smaller that the macroscale of the part; more, functionally integrated design such as embedded electronics or information (Figure 1d) can be manufactured in one single step and assemblies can be redesigned to present a lower number of components. Other than the complexity factor, AM brings other benefits [4]: the production ramp-up time and the cost are reduced since no tooling is needed, supply chains become simpler, lead times shorter, and inventories lower, small production batches become feasible and economical and it is possible to change the design of the part without introducing delays in the production.

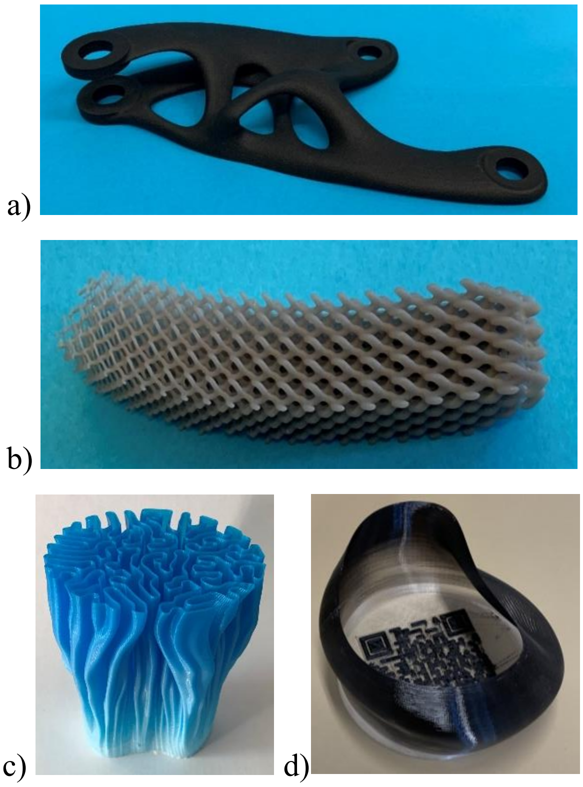

Figure 1. Examples of parts obtained by AM: a) topology optimized shape b) lattice structure with graded beams, c) complex shape printed with multi-material, d) multi-material jar with an embedded QR code.

All these benefits and opportunities have been noted by both the industry and the research community. Concentrating on the industry market, from 2009 to 2019 the AM market grew on average by 27.4 % per year. Even with the COVID-19 pandemic, in 2020 the market was able to expand, even if with a reduced rate of 7.5 %, to nearly $12.8 billion [5]. The pie chart in Figure 2 shows the market subdivided by the industrial sectors as in 2018 [6].

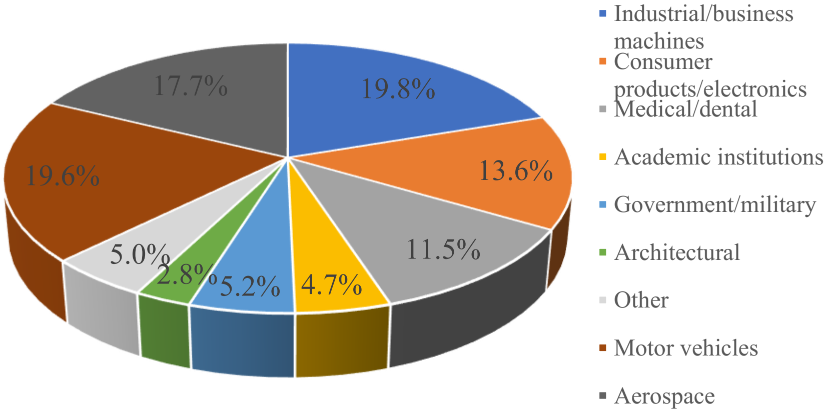

Figure 2. AM market shares by industrial sectors in 2018 [6].

As can be noted, the versatility of the AM engages several industrial sectors, even different from each other. The industrial/business machine was the leading industrial sector, including office equipment and industrial automation equipment such as CNC machines and robots, owning 19.8 % of the market; right after (19.6 %), the motor vehicle industry, where the AM is mostly used to produce concept designs, prototypes, and the race department. The aerospace industry too holds a high quote of the market (17.7 %), indeed lightweight complex parts are often adopted in this field. Then, consumer products and electronics (13.6 %) can take advantage of the limitless possibility of customization of goods and the embedding of electrical devices. Finally, the biomedical industry (11.5 %) exploits the possibility of customizing products such as prostheses, earing devices, and dental aligners designed exactly for the single patient, and porous structures are produced for customized scaffolds.

Moving on to the research community, the number of documents indexed in the Scopus database [7] containing "additive manufacturing", "3D printing", or "rapid prototyping", i.e., all different names used to address AM, in their title, abstract, or keywords has exponentially grown (Figure 3), reflecting the increasing importance of the topic.

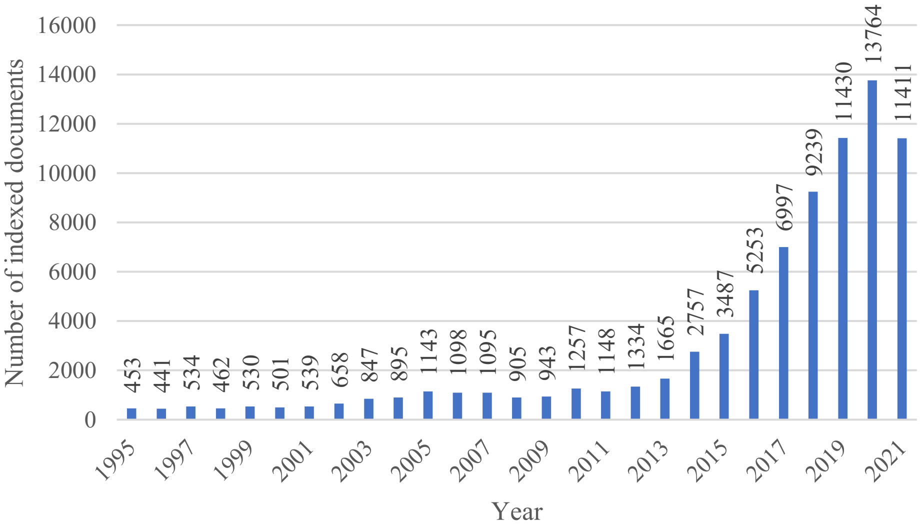

Figure 3. Number of indexed articles in Scopus database containing the words "additive manufacturing", "3D printing" or "rapid prototyping" in their title, abstract, or keywords (updated 24/09/2021).

With their studies, researchers promoted the improvement of AM. New AM technologies were presented [8,9] and studies on the existing ones were done to obtain optimized components [10,11]; the production of parts with different types of materials, i.e., metals

[12], polymers [13], and ceramics [14] was considerably improved; innovative geometric modeling methods were proposed for the design of lattice structures [15,16], structurally optimized parts [17,18], and multi-material components [19,20].

At the same time, on different occasions, it was remarked that limitations in AM remain and improvements are still needed [3,21]. International standards dealing with AM are being developed but, right now, they do not give guidelines in all the AM process phases [22]; AM technologies are not suitable yet for large-scale production [23]; the mechanical behavior of AM materials need to be investigated, especially considering the complex shapes of the manufactured parts [24]. Furthermore, a big issue that hinders to fully exploit the manufacturing freedom of AM is the lack of suitable and reliable approaches for the geometric modeling of complex components; the geometrical kernels of the most diffused software are based on boundary representations [25] and present limitations when trying to model parts with a lot of elements, such as lattice structures [26], where, for instance, Boolean and filleting operations are needed but they require a lot of computational resources and often fail. More, multi-material parts require modeling approaches able to describe the component point-by-point and not only on the surface [27]. Finally, the need for a better workflow that covers all the phases of the design process was emphasized [28].

In this context, this research aims to develop design and geometric modeling methods to overcome some of the limits highlighted and to exploit the geometrical complexity possibilities offered by AM technologies. For reaching the objective, research topics involving geometric approaches for the modeling of lattice structures were proposed. In particular, methods for the generation of conformal wireframes were presented and compared; workflows and approaches for the structural size optimization and the multi-objective optimization of beams-likes structures were conceived; two mesh-based geometric modeling methods lattice structure were proposed and implemented: one deals with the modeling of conformal truss-like lattice structures, whereas the second provides for the integration of internal walls and external skins; both the approaches initially create a coarse mesh model with a low number of polygons and easy to handle since it does not require high computational resources, and then a subdivision surface algorithm is applied to refine the mesh and obtaining smooth surfaces, without the need of further filleting operations. These methods were then introduced in a more comprehensive workflow that covers the entire embodiment design phase, together with the possibility of performing the topology optimization. Case studies, numerical validations, and experimental campaigns were then performed to validate the proposed methods. The experimental tests executed on different AM technologies allowed also to investigate the properties of polyamide 12 and stainless steel 316L materials.

The present manuscript is organized as follows. In Chapter 2 a literature review is performed to present the state of the art and give a solid background about AM to the reader; both general AM topics and other more focused on the design approaches for AM components are addressed. Chapter 3 describes the proposed methodologies for the design and the geometric modeling of lattice structures, together with the developed optimization approaches. In Chapter 4 the methods are implemented in two test cases: the re-design of a piston rod exploiting both the size and topology optimization following the proposed optimization workflow for the embodiment design phase for AM, and the multi-objective optimization of an aerospace propellant tank for small satellites with an internal conformal lattice structure, where the optimization objectives are the mass minimization and the first natural frequency maximization. Chapter 5 deals with the numerical and experimental validation of the mesh-based geometric modeling method that exploits the subdivision surface algorithm. Numerical analyses are performed for determining the geometrical deviation of the method when modeling shell-like lattice structures described by implicit equations and for analyzing the curvature of the surfaces of the resulting meshes. Experimental tests are then performed on both standardized bulk and lattice structures specimens to investigate the fatigue life behavior of the lattice structures modeled adopting the proposed method. Samples produced in stainless steel 316L by the selective laser melting technology and in polyamide 12 by the selective laser sintering and the Multi-Jet Fusion technologies are tested; contextually, a comparison between the selective laser sintering and the Multi-Jet Fusion technologies is performed. In Chapter 6 the work is summed up and the conclusions are drawn. Finally, a part of the implemented code, the used material datasheets, and the published papers related to the research project are reported in Appendix A, B, and C, respectively.

2 Background

This chapter presents background about AM, from the manufacturing technologies to the modeling approaches, from the complex types of objects that can be produced to the current open issues in this field. The identification of the issues motivates the present research; in particular, the analysis of the limits of the existing software allows identifying and synthesizing the research objectives and the presented topics.

2.1 Additive Manufacturing

According to ISO/ASTM 52900 standard [1], additive manufacturing is defined as the "process of joining materials to make parts from 3D model data, usually layer upon layer, as opposed to subtractive manufacturing and formative manufacturing methodologies". Before being firstly standardized in 2009 in the ASTM F2792 standard [29], several names were used to refer to this type of process such as 3D printing, rapid prototyping, rapid manufacturing, and solid freeform fabrication.

As pointed out by Beaman et al. [30], the layer-by-layer approach has been used at least since the construction of the pyramids. In more recent years, the ancestors of AM are identified in the photosculpture and the topography. Photosculpture was patented by Francois Willeme in 1864 as a method to generate 3D replicas [31]. It consisted in placing an object or a subject in a circular room and taking photographs of him from 24 cameras placed in a uniform circular pattern; these photographs were then projected on a screen, the outlines were traced on sheets, the sheets were cut following the traces and were finally stacked together to recreate the object. In 1892 Joseph Blanther patented a method for obtaining 3D relief maps [32]. Wax sheets were cut along topographic lines of constant elevation and pressed one on another to form a three-dimensional representation of the map. A fundamental lack in these patents, as opposed to what happens in AM technologies – and of course justifiable due to the time the patents were submitted – was that they did not use a computer model. In 1971, Swainson proposed a method similar to the photosculpture in which a computer was able to receive the information of the laser beams to obtain a mathematical description of the object [33]. In the same year, Ciraud filed a patent describing a technique able to create parts by spraying powders into an energy beam [34] using a control device and a programmer. The first AM commercial systems were developed between the 1980s and the 1990s. In 1987, 3D Systems Inc.

commercialized a system based on a liquid photopolymer contained in a vat and an ultraviolet laser source able to solidify a thin layer of the liquid; the part was manufactured layer after layer by lowering the platform, allowing the uncured resin to flow over the top of the part. The process was initially developed by Charles W. Hull [35] and was called Stereolithography. In 1991, Stratasys introduced a technology called fused deposition modeling (FDM) developed by Scott Crump [36]. It consisted in extruding a filament made of a thermoplastic polymer through a heated nozzle and depositing material on a baseplate or previously extruded material. In the same year, Helisys Corporation introduced a sheet lamination system, initially developed by Feygin [37]. A laser or a knife was used to cut paper or plastic layers glued to the previous ones. Later on, in 1992, DTM Corporation proposed a manufacturing system that selectively fused a layer of leveled powder with a laser, only in the region of the cross-section of the part; this technology was previously studied by Deckard [38]. In the following years several other technologies were introduced both in the research and the industrial field, with different manufacturing approaches but all pooled by the layer-by-layer idea.

2.1.1 AM technologies

As previously stated, the layer-by-layer approach for producing parts can be obtained by different techniques. According to ASTM F2792 and ISO/ASTM 52900 standards [1,29], these technologies can be subdivided into seven categories, depending on the type of the machine architecture and the physics of the material transformation as first proposed in 2007 in the Materials Processing Handbook [39]. The seven categories are:

1. Binder jetting,
2. Directed energy deposition,
3. Material extrusion,
4. Material jetting,
5. Powder bed fusion,
6. Sheet lamination,
7. Vat photopolymerization.

In the binder jetting (BJ) process, powder particles lay in the build platform and are joined together by a liquid binder that is ejected from the print heads, in a line-wise patterning process. The binder is selectively released only on the cross-section of the part, the platform is lowered, a new layer of powder is spread by a coater mechanism, and the procedure is repeated until the entire part is built. The process can be economically scaled by increasing the number of nozzles and a high deposition speed can be reached at a relatively low cost since no high-powered energy sources are used. No supports are needed thanks to the surrounding powder that acts as support itself. Usually, the parts need to undergo post-process operations such as curing, de-powdering, sintering, infiltration, annealing, and finishing, depending on the material and the desired properties [40]. Several materials can be used: ceramics, metals such as 316 stainless steel, Cobalt-chrome, and Inconel 718, biomaterials such as calcium silicate and Hydroxyapatite, and polymers like polylactic acid (PLA) and Polymethyl methacrylate (PMMA) [41].

Directed energy deposition (DED) melts material as it is being deposited. A laser or an electron beam is used as a focused heat source to heat the substrate, melt the substrate, and melt the material that is being deposited into the melt pool of the substrate. In this way, entire near-net-shape parts with complex geometries can be built, or repair and additional features can be added to existing components. Almost exclusively metals are used with DED and the material can be provided as powder or as wire feedstock; powder-based DED is the most used approach since metals powders are readily available, whereas wire feedstock techniques provide lower resolution but have a higher deposition rate and can build larger structures [42].

Material extrusion (MEX) is probably the most known and diffused AM technology thanks to the possibility of buying inexpensive machines starting from a few hundred Euros and thanks to the fact that they are easy to operate. In the MEX process a filament of material is pushed in a hot chamber by a set of pinch rollers, the filament melts and it can flow out through a nozzle on the baseplate or the previous layer of the part. The machine can control the in-plane position of the nozzle with respect to the baseplate to extrude a single layer; then, the nozzle is raised, or the baseplate is lowered, and the next layer is extruded. Depending on the shape of the part, material support could be necessary if the next layer overhangs with respect to the previous one or if a suspended part like a bridge is created; supports can be produced using the same material as the part or with a different one, usually soluble, if the machine is equipped with a second nozzle. MEX machines mostly work with amorphous thermoplastic polymer since they can be extruded in a viscous paste and the most common ones are PLA, acrylonitrile butadiene styrene

(ABS), and polycarbonate (PC) [43]. If high performance is needed, ULTEM 9085 material offers a high strength-to-weight ratio and good fire-, smoke-, and toxicity properties making it suitable for use in aircraft, marine, and ground vehicles [44]. Fiber-reinforced filaments can be used to enhance the mechanical properties of the products: the literature shows the possibility to include carbon fibers, fiberglass, and Kevlar [45]. More, in the biomedical field biocompatible and biodegradable components are obtained by extruding hydrogels in a jellylike form and porous scaffolds can be produced [46].

As in BJ, the material jetting (MJ) process uses print heads to dispense material on a baseplate or the previous layer; the difference between BJ and MJ is that in the MJ process all of the part material is dispensed from the print heads, without the need of a powder bed. Depending on the material, it could be necessary to UV-cure the photopolymers ejected from the nozzles. Again, high speed and scalability can be easily obtained by using print heads with hundreds or thousands of nozzles and by adding print heads to the machine. Multiple print heads can be also used to obtain multi-material components or to use soluble support material in addition to the material of the part. Most of the commercial MJ systems work with photopolymers and waxes; the former allow obtaining realistic prototypes and functional parts, the latter allow obtaining investment casting patterns [47]. In the research field, efforts have been made for printing ceramics [48] and metals [12]. MJ process presents some drawbacks and challenges too: part accuracy for large size parts is not so good due to the need to use large droplets and droplets formation from a continuum volume of liquid and droplets flight path need a perfectly tuned hardware and depend on the material [2].

The powder bed fusion (PBF) is a process in which thermal energy selectively fuses regions of a bed of a powder. A layer of powders is evenly distributed on the baseplate using a coating mechanism and the 2D slice of the part geometry is fused by selectively sintering or melting the powders that lay on the plate; then, the base plate is lowered to a height equal to the layer thickness and the operations are repeated until the component is built. The process takes place in a chamber filled with a low percentage of Oxygen for minimizing oxidation, degradation of the powdered material, and undesired reactions. Even though all the materials that can be melted and resolidified can be used in the PBF process, metals and polymers are the most widespread, whereas composites and ceramics are less adopted [49]. When dealing with polymers, different technologies are available, and they differ by the way the thermal energy is provided and the way the sintering of the surrounding powders is prevented; laser sintering (LS) is the most common approach, where a laser selectively sinters the powder only in the space defined by a 3D model [50]; high-speed sintering (HSS) aims at sintering 2D profiles of powder layers by adding carbon black that absorbs infrared radiations and increases the rate of sintering, and using an infrared lamp to sinter without the need for a laser [8]; selective inhibition sintering (SIS) is characterized by the deposition of a sintering-inhibitor liquid along the layer profiles to prevent the sintering of selected areas and the uninhibited powder is sintered by a heated nichrome filament, again, without using a laser [51]; the multi-jet fusion (MJF) technology is a hybrid between HSS and SIS since it uses a so-called "fusing agent" inside the model boundaries to promote the sintering of the powder, and a "detailing agent" on the edges of the model to inhibit the sintering and create fine details and smooth surfaces [52]. Polyamides, especially polyamide 12, are widely used in polymers PBF [53–55], but also thermoplastic polyurethane (TPU) [56], polypropylene (PP) [57], and polyether ether ketone (PEEK) [58] parts can be manufactured. PBF of polymers does not require supports since the surrounding powder acts as support itself. Moving on to metal PBF technologies, the two main energy sources are a laser beam or an electron beam. The laser beam is adopted in the selective laser melting (SLM) technology, where, similarly to the LS, the laser selectively melts the powders that lay in the powder bed layer after layer [59]. The electron beam replaces the laser in the electron beam melting (EBM) [60]. SLM is cheaper and allows obtaining better surface finish and finer feature details than EBM. EBM is faster and produces less residual stress and distortion in the final part, so it requires fewer support structures; at the same time, EBM works at high temperature, up to 750 °C for titanium and stainless steels [61]: some of the powder particles that surrounds the part could partially sinter and it could be difficult to perform the de-powdering of the part or the cleaning of the internal channels. A wide range of metals can be produced by PBF and the most common are stainless steels [62], aluminum alloys [63], titanium alloys [64], and cobalt-chrome [65]. Since parts produced by metal PBF are prone to distortion, the process planning phase in which the part orientation in the chamber and the supports geometry are optimized is fundamental; furthermore, post-processing operation such as support removal, sandblasting for enhancing the surface finish and removing partially molten powders, and hot isostatic press for reducing the porosity of the final part are required. Regardless the material, the powders must be handled with care, both for the safety of the operators and for the success of the print job.

In the sheet lamination (SL) process sheets of materials are cut, stacked, and bonded to form a part. SL is cheap, easy to handle, and can be used for building very large objects. Depending on the order of the operations done to obtain the part, two approaches can be identified: the "bond-then-form" method and the "form-then-bond" method; in the former, the sheet is bonded to the substrate and then is formed into the cross-sectional shape, whereas in the latter the laminate is first cut and then bonded to the substrate [2]. More, different methodologies can be used to achieve the bonding between the layers. Adhesive bonding uses a polymer-based adhesive that can be activated by a heated roller that passes after each sheet is placed [66]; thermal bonding is especially used for metal SL where the temperature is increased to promote the bonding between the sheets [67]; a quicker and less expensive option could be the sheet metal clamping, where the clamping, or bolting, itself can act as a reference point to position each laminate with respect to the others. Also, ultrasonic metal seam welding has been applied, where a rotating sonotrode moves along the metal foil applying a force and oscillates at a high frequency transversely to the direction of motion [68].

Vat photopolymerization (VP) is a process in which a liquid polymer that reacts to radiation, i.e., a photopolymer, is contained in a vat, is hit by radiation usually in the ultraviolet wavelength range, and chemically reacts solidifying. As previously said, VP was the first patented and commercialized AM process with the original name of Stereolithography [35]. During the process, the light radiation hits a thin layer of liquid polymer that lays between the part that is attached to a baseplate and a transparent film placed between the optics and the plate following the cross-sectional area of the object; the baseplate is then lowered, and the following layer is photopolymerized. Among the AM processes, VP allows achieving a fine layer resolution, usually 10 µm, at a reasonable cost. Different configurations can be adopted for the photopolymerization processes. The "vector scan" approach uses a laser, focusing and adjustment optics, and two galvanometers to scan point-by-point each layer of the part, allowing to obtain good accuracy and surface finish; the "mask projection" approach uses a dynamic mask to project the bitmap of the cross-section onto the resin surface and can cure an entire layer at a time, resulting in a speed-enhanced process; the “two-photon” approach uses polymers that require two photons to strike the photoinitator before the polymerization can start and this leads to a great increase in the resolution of the obtained part [69]. Talking about materials used in the VP process, the photopolymers resins were first prepared from acrylates but the parts were characterized by geometrical inaccuracy due to shrinkage and curling; so they were substituted by epoxy resins that led to better accuracy, with shrinkage of 1-2% with respect to 5-20% [70]; at the same time, epoxy resins have a slow photospeed and the final parts are brittle. As a compromise, modern resins are epoxy ones with the addition of some acrylate content.

Figure 4 shows a recap of the presented categories, together with the most diffused commercial names of the technologies and the related vendors [71].

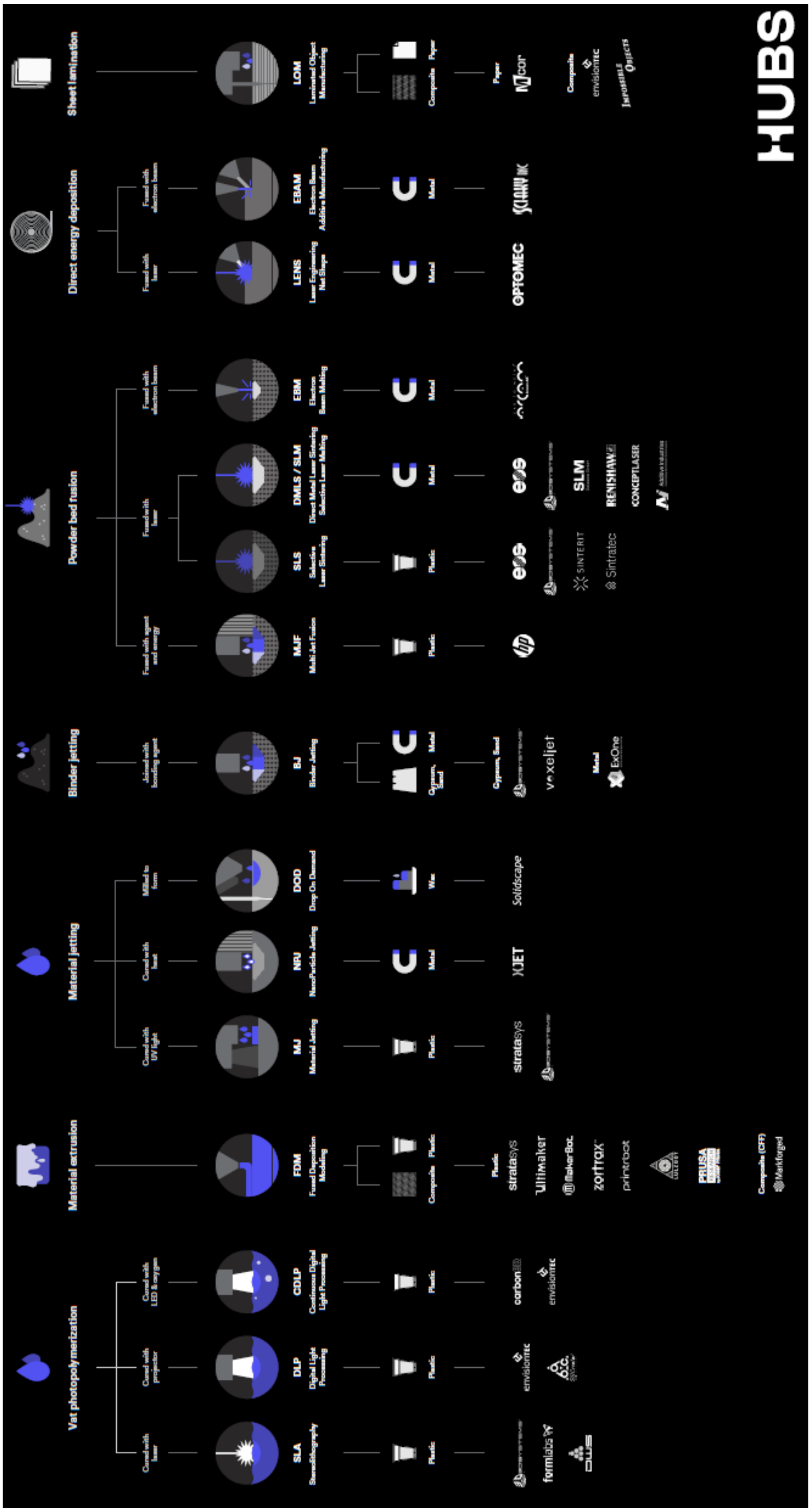
Vat photopolymerization
Cured with laser
Cured with projector
Cured with LED & oxygen
SLA
Stereolithography
DLP
Digital Light Processing
CDLP
Continuous Digital Light Processing
Plastic
formlabs
DWS
envisiontec
carbon
Material extrusion
FDM
Fused Deposition Modeling
Composite
Plastic
stratasys
Ultimaker
MakerBot
zortrax
printrbot
PRUSA
Composite (CFF)
Markforged
Material jetting
Cured with UV light
Cured with heat
Milled to form
MJ
Material Jetting
NPJ
NanoParticle Jetting
DOD
Drop On Demand
Metal
Wax
XJET
Solidscape
Binder jetting
Joined with bonding agent
BJ
Binder Jetting
Gypsum, Sand
voxeljet
ExOne
Powder bed fusion
Fused with agent and energy
Fused with laser
Fused with electron beam
MJF
Multi Jet Fusion
SLS
Selective Laser Sintering
DMLS / SLM
Direct Metal Laser Sintering
Selective Laser Melting
EBM
Electron Beam Melting
eos
SINTERIT
Sintratec
SLM
RENISHAW
CONCEPTLASER
arcam
Direct energy deposition
LENS
Laser Engineering Net Shape
EBAM
Electron Beam Additive Manufacturing
OPTOMEC
SCIAKY INC
Sheet lamination
LOM
Laminated Object Manufacturing
Paper
Mcor
IMPOSSIBLE OBJECTS
HUBS

Figure 4. AM technologies categories, commercial name of the technologies and related vendors [71].

2.1.2 Workflow

Regardless the AM technology used for manufacturing a part, some steps are recurrent in the production process. Gibson et al. [2] subdivided the AM process into eight steps: CAD, STL conversion, file transfer to machine and STL manipulation, machine setup, part build, part removal, post-processing, and application. First, the part is geometrically modeled in a computer aided design (CAD) environment. Then, the model is converted in a suitable file format for the AM machine; usually, the STL format is used since it has become the de-facto industry standard: all the software can export such a format and all the machines can deal with it. After the conversion, the STL file is imported into the AM machine and some adjustments like size and orientation are performed. Then, the machine and process parameters are set to obtain a successful build; in this phase, the parameters depend on the AM technology chosen to produce the part. The build is then started and once it ends, the part is removed from the machine. The next phase deals with all the post-process operations that, again, depends on the adopted technology; for instance, MEX and VP parts may require support removal, whereas metal PBF parts usually undergo sandblasting, thermal cycles, or hot isostatic pressing. The last phase, "Application", considers the utilization of the final part.

Loh et al. [27] proposed a similar workflow, concentrating on the possibility of producing functionally graded additive manufacturing (FGAM) parts, defined as parts in which the material organization gradually varies to achieve an intended function; the flow is divided into five steps: design and modeling, part description, which in turn is divided in material description, product description, and manufacturing description, additive manufacturing, post-processing, and final product. In step 2, they stressed the importance of describing the triptych material-product-manufacturing for obtaining the desired functionality. Loh's workflow also highlights that the "STL conversion" and "File transfer to machine and STL manipulation" phases of Gibson's workflow may be belittling since STL format only carries discretized boundary information that could be insufficient to describe all the characteristics of an object that fully exploits AM capabilities, such as multi-material.

As reported in Figure 5, a more generic and correct terminology could be "Data exchange", where no file formats are mentioned but the essence of the phase is maintained. Furthermore, the "Qualification" phase has been added, due to the need of assessing the quality of the part concerning structural integrity, surface texture, tolerances, etc…

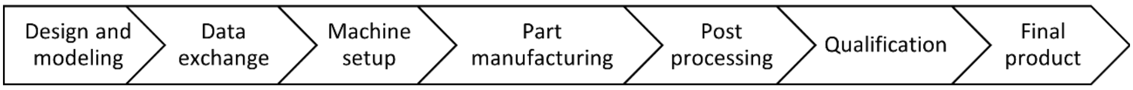

Figure 5. AM workflow, adapted from the ones proposed by Gibson et al. [2] and Loh et al. [27].

2.1.3 AM related international standards

AM is a relatively new technology, therefore international standards regulating the most critical phases of the workflow are still under development or completely missing. This lack has been highlighted in the literature too. In a 2014 article [22], Bourell et al. analyzed the steps done in the AM field since the publication of the 2009 Roadmap for Additive Manufacturing research agenda [72]; the need for recognized standards for product, process, and material certification was raised in the agenda and they noted that both the American Society for Testing and Materials (ASTM) and the International Organization for Standardization (ISO) started publishing AM related standards. Seifi et al. [73] concentrated on the standardization in the AM for metals and presented a clear image of the standardization activities and the collaborations between the organizations in charge of developing the standards; they finally recommended to keep on developing AM standards as an enabler for effective qualification and certification processes and they also recommended to publish some industry best practice documents.

For what concerns the international organizations, both ASTM and ISO have technical committees working on AM-related standards. ASTM Committee F42 on AM technologies was established in 2009 and has 8 technical subcommittees [74]. ISO Technical Committee 261 was established in 2011 [75] and soon after its creation, in September 2011, ISO and ASTM signed a cooperative agreement to adopt and jointly develop international standards on the AM subject. In their "Joint Plan for Additive Manufacturing Standards Development" [76] a hierarchy of AM standards based on three levels was proposed (Figure 6):

1. General standards: standards that specify general concepts, common requirements, or are generally applicable to most types of AM materials, processes, and applications.

2. Category standards: standards that specify requirements that are specific to a material category or process category.
3. Specialized standards: standards that specify requirements that are specific to a material, process, or application.

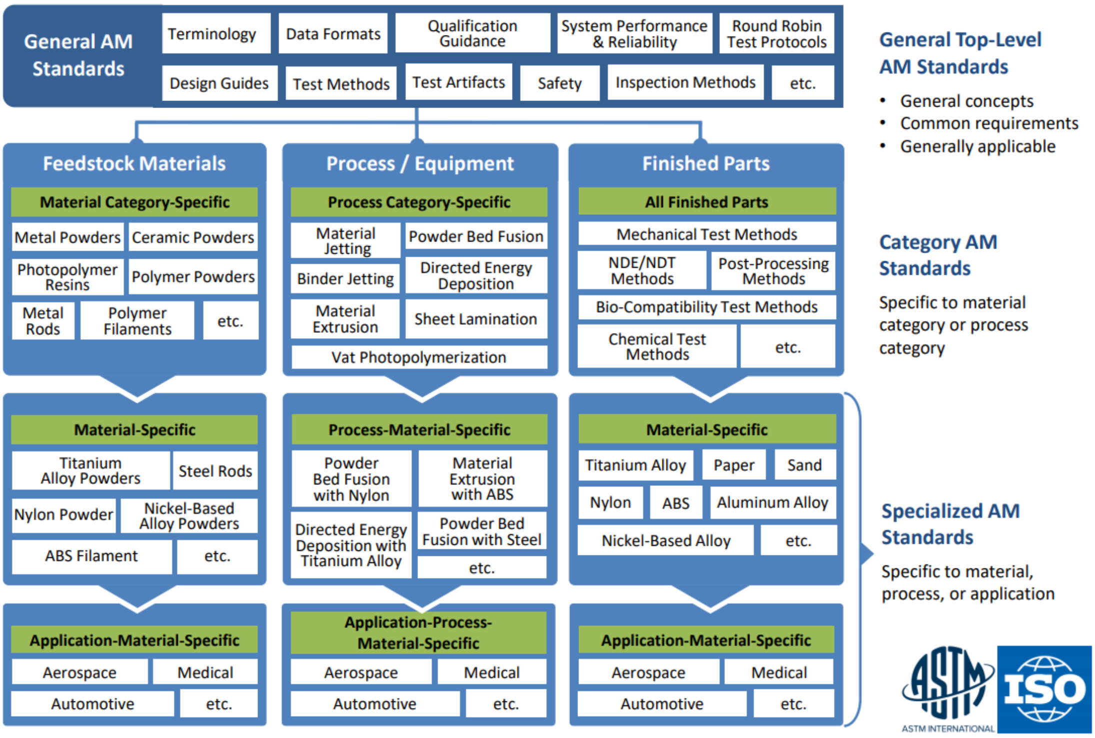
General AM Standards
Terminology
Data Formats
Qualification Guidance
System Performance & Reliability
Round Robin Test Protocols
Design Guides
Test Methods
Test Artifacts
Safety
Inspection Methods
etc.
General Top-Level AM Standards
• General concepts
• Common requirements
• Generally applicable
Feedstock Materials
Material Category-Specific
Metal Powders
Ceramic Powders
Photopolymer Resins
Polymer Powders
Metal Rods
Polymer Filaments
etc.
Process / Equipment
Process Category-Specific
Material Jetting
Powder Bed Fusion
Binder Jetting
Directed Energy Deposition
Material Extrusion
Sheet Lamination
Vat Photopolymerization
Finished Parts
All Finished Parts
Mechanical Test Methods
NDE/NDT Methods
Post-Processing Methods
Bio-Compatibility Test Methods
Chemical Test Methods
etc.
Category AM Standards
Specific to material category or process category
Material-Specific
Titanium Alloy Powders
Steel Rods
Nylon Powder
Nickel-Based Alloy Powders
ABS Filament
etc.
Process-Material-Specific
Powder Bed Fusion with Nylon
Material Extrusion with ABS
Directed Energy Deposition with Titanium Alloy
Powder Bed Fusion with Steel
etc.
Material-Specific
Titanium Alloy
Paper
Sand
Nylon
ABS
Aluminum Alloy
Nickel-Based Alloy
etc.
Specialized AM Standards
Specific to material, process, or application
Application-Material-Specific
Aerospace
Medical
Automotive
etc.
Application-Process-Material-Specific
Aerospace
Medical
Automotive
etc.
Application-Material-Specific
Aerospace
Medical
Automotive
etc.
ASTM INTERNATIONAL
ISO

Figure 6. Three-levels hierarchy AM standard structure proposed by ISO and ASTM organizations [77].

At the time of writing, ISO declares that, including the updates, 19 standards have been published under the direct responsibility of ISO/TC 261, whereas 37 standards are under development. Among them, some of the most significant published ones are:

- ISO/ASTM 52900:2015 - Additive manufacturing — General principles — Terminology, where all the definitions of AM-related terms are given.
- ISO/ASTM 52902:2019 - Additive manufacturing — Test artifacts — Geometric capability assessment of additive manufacturing systems, where benchmarking test piece geometries are described and directions are given to perform quantitative and qualitative measurements. The results can be used to evaluate the capability and/or to calibrate the AM systems.
- ISO/ASTM 52911-1:2019 - Additive manufacturing — Design — Part 1: Laser-based powder bed fusion of metals, where design recommendations are given to

avoid poor quality features or failure of the build when metal PBF technologies are used.

- ISO/ASTM 52911-2:2019 - Additive manufacturing — Design — Part 2: Laser-based powder bed fusion of polymers, where design recommendations are given to avoid poor quality features or failure of the build when polymers PBF technologies are used.
- ISO/ASTM TR 52912:2020 - Additive manufacturing — Design — Functionally graded additive manufacturing, which is more a technical report and presents a state of the art of functionally graded AM, dealing with the current manufacturing approaches, potentialities, and limitations.
- ISO/ASTM 52915:2020 - Specification for additive manufacturing file format (AMF) Version 1.2, where the requirements for the preparation, display, and transmission for the AMF are given.
- ISO/ASTM 52921:2013 - Standard terminology for additive manufacturing — Coordinate systems and test methodologies, where directions are given to define a coordinate system for the AM machines that is also used to identify the test specimen orientation.
- ISO 17296-3:2014 - Additive manufacturing — General principles — Part 3: Main characteristics and corresponding test methods, that will be replaced by ISO/ASTM 52927, where the principal requirements applied for testing parts manufactured by additive manufacturing processes are covered. The main quality characteristics of parts, the appropriate test procedures, and the scope and content of test and supply agreements are specified.

2.2 Design and modeling for AM

The layer-by-layer approach used by the AM technologies opens unprecedented design possibilities allowing for freedom in complexity that, most of the time, is impossible to reach with the traditional manufacturing technologies. Four types of complexity can be exploited: shape complexity, hierarchical complexity, material complexity, and functional complexity [2]. Shape complexity allows producing parts with complex geometries, such as lattice structures or internal cooling ducts, thanks to the fact that no machining tools are used; more, the ease in manufacturing different shapes enables the production of customized components, for example in the biomedical field [78], and the production of structurally optimized parts [79]. Hierarchical complexity exploits the AM possibility of controlling the structure of a part at different scales; the nano- and micro-structure of a metal component can be controlled by the processing parameters both in PBF [80] and DED [81] technologies; the meso-structure of a part is modified by introducing cellular structures or solid and voids patterns in certain areas of the part. Material complexity resides in the possibility of producing parts with different materials, or mixtures of them, in different regions, leading to different local properties [27]. Functional complexity comes from the possibility of producing fully functional assemblies and mechanisms, and reducing the number of parts in a component, since part consolidation allows reducing the number of separate parts. These four types of complexity can be employed simultaneously to fully exploit the AM capabilities. Of course, the design phase of a part becomes fundamental and adequate tools are needed to describe information in a suitable way to further produce the component. Furthermore, the designer needs to be aware of the AM capabilities – and limitations – to design innovative and manufacturable objects.

2.2.1 Design for Additive Manufacturing

In Chapter 19 of the "Additive Manufacturing Technologies" book [2], Rosen defined the Design for Additive Manufacturing (DfAM) concept as the set of all the considerations to make to "maximize product performance through the synthesis of shapes, sizes, hierarchical structures, and material compositions, subject to the capabilities of AM technologies". The DfAM is inspired by the design for manufacture and assembly (DFMA) [82], a methodology that focuses on reducing time-to-market and total production costs concentrating on the ease of the manufacture of the parts of the product and the simplified assembly of the parts into the final product. DfAM can be subdivided in restrictive and opportunistic DfAM. Restrictive DfAM only concentrates on the restrictions of the AM technologies and is basically used as a list of guidelines to design manufacturable parts taking into consideration the limits of the selected AM technique, i.e., the minimum features size, the need of support structures, the need of resin evacuation or de-powdering holes, etc. as shown if Figure 7.

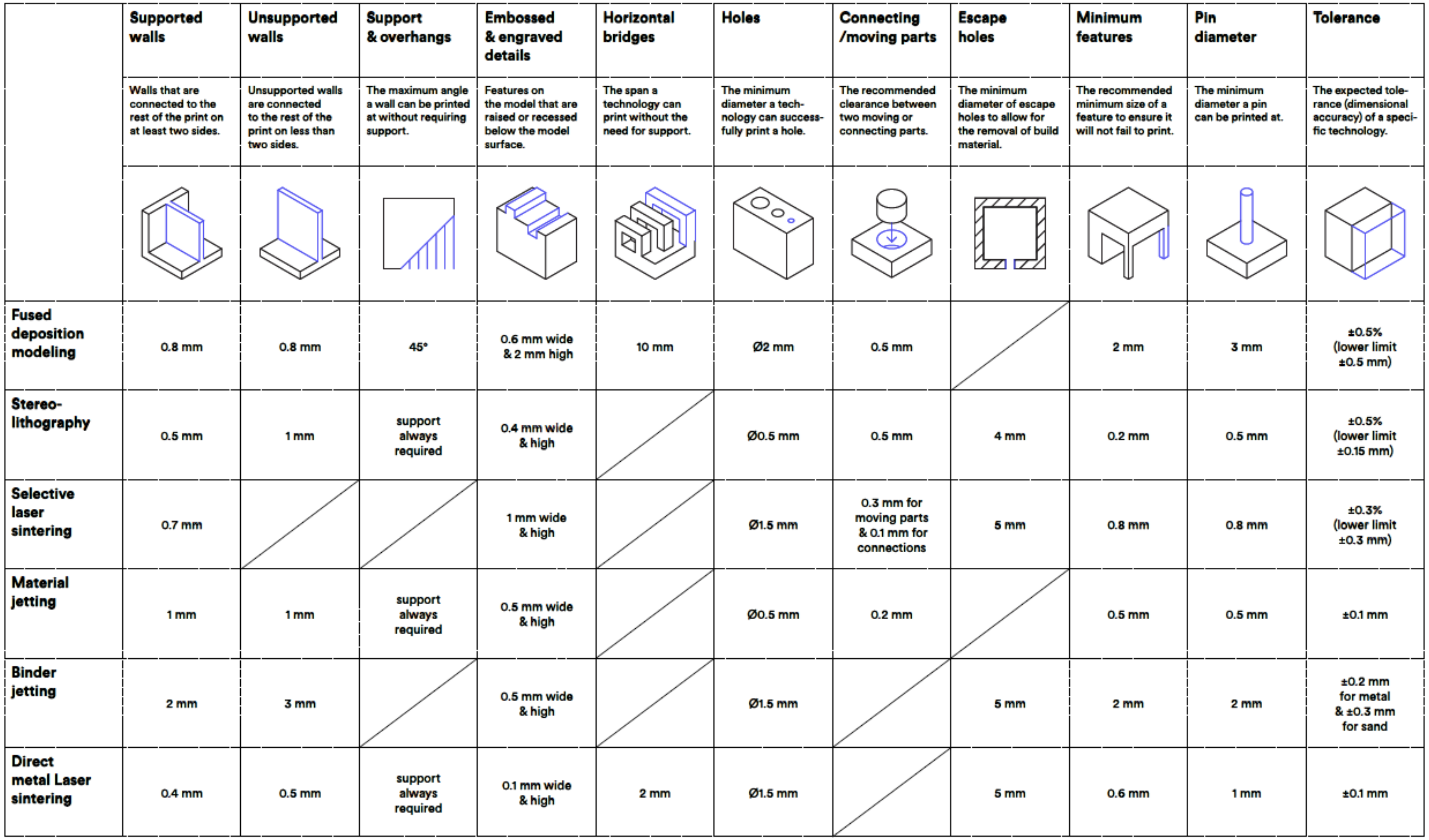

	Supported walls	Unsupported walls	Support & overhangs	Embossed & engraved details	Horizontal bridges	Holes	Connecting /moving parts	Escape holes	Minimum features	Pin diameter	Tolerance
	Walls that are connected to the rest of the print on at least two sides.	Unsupported walls are connected to the rest of the print on less than two sides.	The maximum angle a wall can be printed at without requiring support.	Features on the model that are raised or recessed below the model surface.	The span a technology can print without the need for support.	The minimum diameter a technology can successfully print a hole.	The recommended clearance between two moving or connecting parts.	The minimum diameter of escape holes to allow for the removal of build material.	The recommended minimum size of a feature to ensure it will not fail to print.	The minimum diameter a pin can be printed at.	The expected tolerance (dimensional accuracy) of a specific technology.
Fused deposition modeling	0.8 mm	0.8 mm	45°	0.6 mm wide & 2 mm high	10 mm	Ø2 mm	0.5 mm		2 mm	3 mm	±0.5% (lower limit ±0.5 mm)
Stereo-lithography	0.5 mm	1 mm	support always required	0.4 mm wide & high		Ø0.5 mm	0.5 mm	4 mm	0.2 mm	0.5 mm	±0.5% (lower limit ±0.15 mm)
Selective laser sintering	0.7 mm			1 mm wide & high		Ø1.5 mm	0.3 mm for moving parts & 0.1 mm for connections	5 mm	0.8 mm	0.8 mm	±0.3% (lower limit ±0.3 mm)
Material jetting	1 mm	1 mm	support always required	0.5 mm wide & high		Ø0.5 mm	0.2 mm		0.5 mm	0.5 mm	±0.1 mm
Binder jetting	2 mm	3 mm		0.5 mm wide & high		Ø1.5 mm		5 mm	2 mm	2 mm	±0.2 mm for metal & ±0.3 mm for sand
Direct metal Laser sintering	0.4 mm	0.5 mm	support always required	0.1 mm wide & high	2 mm	Ø1.5 mm		5 mm	0.6 mm	1 mm	±0.1 mm

Figure 7. Restrictive DfAM, design rules for different AM technologies [71]

Opportunistic DfAM, instead, focuses on the unique AM capabilities and aims at introducing in the component all the aforementioned complexities to obtain a better and innovative product. In the literature, researchers followed different approaches to reach this goal. Rosen [83] used a Process – Structure – Property – Behavior framework to describe and model a design; he further divided the Process, Structure, and Property models into geometric and material models. Moving from Geometry to Material and from Property to Process the relevant size scale decreases. More, following the traversal from Behavior to Process the design approach can be seen, where the requirements given by the Behavior are mapped to the properties and the geometry/structure, and finally the manufacturing process is defined; going from the Process to the Behavior the designed part is analyzed, and one can verify if the original requirements are satisfied. He then proposed a DfAM system organized in several modules dealing with the modeling, manufacturing simulation, and design behavior analysis phases, as reported in Figure 8.

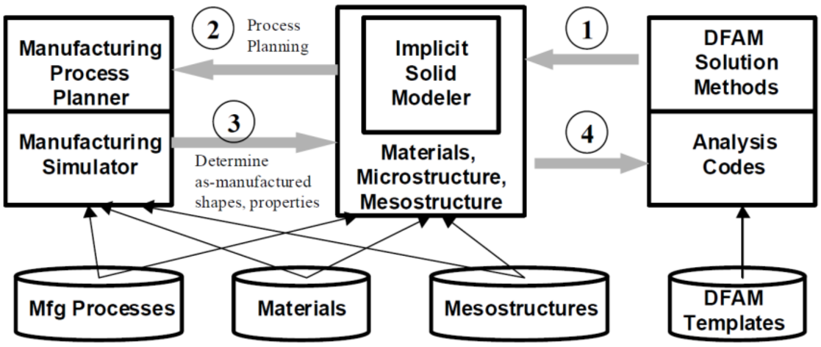
Manufacturing Process Planner
Manufacturing Simulator
② Process Planning
③ Determine as-manufactured shapes, properties
Implicit Solid Modeler
Materials, Microstructure, Mesostructure
①
④
DFAM Solution Methods
Analysis Codes
Mfg Processes
Materials
Mesostructures
DFAM Templates

Figure 8. DfAM system proposed by Rosen [83].

Ponche et al. [84] presented a DfAM methodology specifically for Additive Laser Manufacturing products that takes into account the design requirements coming from functional specifications and the manufacturing specificities depending on the selected AM process. First, the part is oriented inside the build chamber according to the global process characteristics and the required design constraints; then, it is functionally optimized through a topology optimization (TO) algorithm; finally, the manufacturing paths are defined to locally optimize the component. Vayre et al. [85] applied a four-step designing methodology. First, they identified a set of functional surfaces and the “clearing volume”, i.e., the design volume, where the material can be placed. Then, a single or multiple initial shapes are generated exploiting the expertise of the designers, or, preferably, structural optimization strategies such as the TO. Once the rough shapes have been obtained, a set of parameters that describe the part are defined and are used as optimization drivers to obtain the optimized part, according to the desired goals. Finally, the manufacturability of the optimized shape is validated. Vayre and coworkers tested this design approach on a metallic component produced by DED and EBM technologies. Briard et al. [86] presented a methodology to maximize the potential of generative design coupled with DfAM, divided into four steps: translation, initialization, AM guidelines integration, and refinement. In the translation phase, the problem is "translated" to provide suitable inputs for generative design tools; the initialization phase is an unconstrained optimization phase where possible optimized shapes are obtained; then, the AM constraints are integrated into the optimization to take into consideration the manufacturing process limitations, such as the need of supports or the minimum features size. Finally, in the refinement phase the design is pushed to its limit exploiting all the AM capabilities, for example by integrating cellular structures. Duro-Royo et al. [20] presented a computational workflow for the design and the fabrication of multi-material and multi-scale structured objects via a pneumatic extruder mounted on a 6-axes robotic arm; they focused on water-based heterogeneous materials based on polysaccharide hydrogels in 1% to 12% concentrations in w/v of 1% acetic acid aqueous solutions and these gels were also mixed with cellulose microfiber to obtain volumetric composites. They created a seamless file-to-fabrication model that starts from the design of the model and the tool paths in a CAD/CAM environment; the information is transmitted to a central interface through fabrication XML instructions and a communication applet processes input and output data generated in the design platform to and from the mechanical parts. The model considers several data coming from all the components of the chain; some of them are the parameters of the material, such as viscosity and shear rate, the combinations of base materials, the degree of concentration of material in the solvent, the type of nozzles mounted on the extruders, and the response times of the hardware. Boddeti et al. [87] presented a digital design and manufacturing workflow able to design both the macroscopic topology and the microstructure of an object; the workflow is divided into three steps: a "design automation" process that uses the mathematical homogenization approach of a two-phase microstructure and the TO for obtaining the best material distribution and its microstructure in 3D; the "material compilation" process translates the mathematical results obtained in the previous phase in a manufacturable 3D material layout and generates the code for fabrication; finally, the "digital fabrication" step involves the manufacturing of the product by a multi-material photopolymer material jetting technology. Zhang et al. [88] proposed an evaluation framework to assess the design from a process planning for AM perspective based on two sets of indicators. The first-level indicators are the "Adaptation Indicator" and the "Discrimination Indicator", where the former indicates whether the part is suitable to be produced by AM manufacturing, whereas the latter suggests the easiness of identifying the optimal AM manufacturing scenarios from a set of alternatives for a given design. The second-level indicators are the "Orientation Indicator" and the "Geometry indicator"; the former is a general indicator that analyzes the effect of the design on the orientation tasks during the process planning, and takes into consideration the amount of support structures, print time, etc. The latter is used to verify the utilization of the selected design of the advantages given by AM, such as TO or cellular structures. Similarly, Lettori et al. [89] proposed an approach to assess the compatibility and suitability of a product for the AM production through a set of fifteen reference questions and a compliance index that considers the values given as answers and the weight of the questions; the questions range from information about the mass reduction to the level of customization, from the need of multi-material areas to the batch size. They then validated the method with case studies found in the literature.

2.2.2 Geometric modeling and representation schemes

Since AM allows to produce complex parts also enabling multi-material solutions, it is fundamental to properly describe and represent the objects from a digital point of view. When dealing with geometric modeling approaches, three main classes of representation schemes can be identified, as presented in Figure 9: boundary representation (B-Rep), volume representation (V-Rep), and constructive solid geometry (CSG) [90].

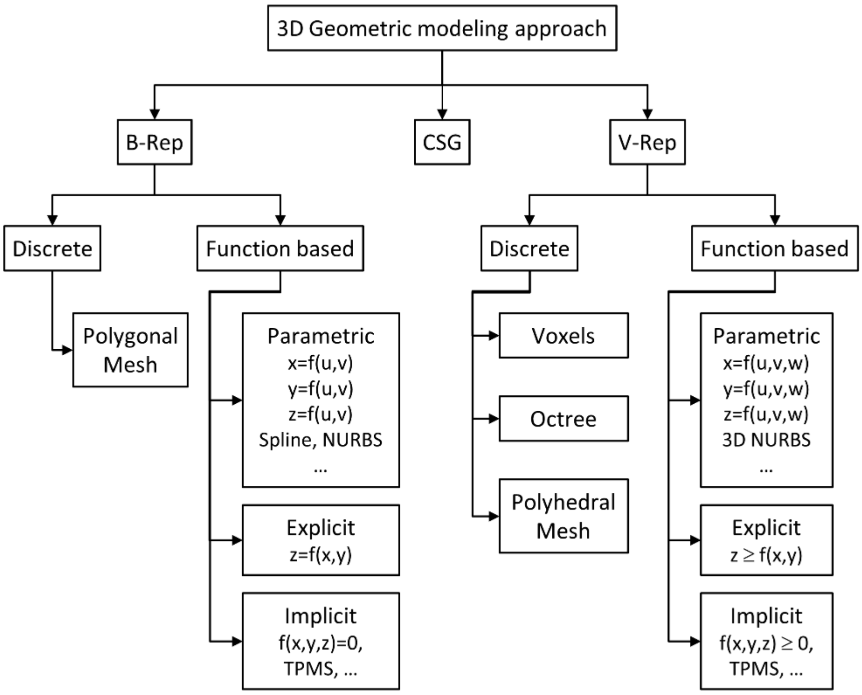
3D Geometric modeling approach
B-Rep
CSG
V-Rep
Discrete
Function based
Discrete
Function based
Polygonal Mesh
Parametric x=f(u,v) y=f(u,v) z=f(u,v) Spline, NURBS …
Explicit z=f(x,y)
Implicit f(x,y,z)=0, TPMS, …
Voxels
Octree
Polyhedral Mesh
Parametric x=f(u,v,w) y=f(u,v,w) z=f(u,v,w) 3D NURBS …
Explicit z ≥ f(x,y)
Implicit f(x,y,z) ≥ 0, TPMS, …

Figure 9. Representation schemes approaches.

B-Rep describes the shape of a part by its surface, i.e., the boundary that divides the object from the surrounding environment; this approach is adopted when the component is made by a homogeneous material, so internal information is superfluous, and the information only resides in the skin. Adopting boundary representations, a 3D surface can be described by a discrete polygonal mesh, potentially exploiting recursive subdivision algorithms [91,92], or in a continuous way by function-based approaches. In turn, these function-based methods are divided into parametric, explicit, and implicit. Implicit methods, also known as function representations (F-Rep) [26], describe the surface adopting an equation of form $f(x,y,z)=0$; in the AM field, implicit methods are suitable when describing triply periodic minimal surfaces (TPMS, they will be debated in the following sections) but are unable to represent and easily transform bounded surfaces. Parametric approaches are based on surface equation form as $S(u,v)=\big(x(u,v),y(u,v),z(u,v)\big)$ where u,v are independent parameters [93]. Several formulations have been proposed, such as Bézier surfaces [94], Bernstein polynomials [95], and Non-Uniform Rational Basis Splines (NURBS) [93]. Parametric methods allow a more natural design and representation of shapes inside a CAD environment and, more importantly, they can be expressed in the form of vectors and matrices so that complex analytical geometry problems are solved with simple methods.

The CSG approach defines a solid as a set of consecutive Boolean operations, i.e., union, intersection, and difference, applied to primitive solid objects like blocks, spheres, torus, cone, and cylinder. The Boolean operations are intended as “regularized operation”: lower-dimensional components than 3D resulting from the regularized operations are not taken into consideration. For instance, only solid (3D) parts will result from regularized operations, whereas surfaces, edges, and points are discarded [90]. A limitation of the CSG method is that CSG models need to be converted to B-Reps for visualization, data exchange, and manufacturing. Almost all the geometric kernels of the CAD 3D software are based on the CSG approach for describing and storing the modeling operations, and then they use B-Rep approaches for the visualization of the model. Usually, the primitives are homogeneous objects, but if they are heterogeneous, Fang and Srinivasan [96] presented a Volumetric-CSG (VCSG) method for the modeling and representation of volumetric objects with heterogeneous properties based on the original CSG approach.

V-Reps are needed when a part presents heterogeneous internal properties and different information are found in different point inside the volume. Dealing with discrete V-Rep, voxels (volumetric pixels) can be used to discretize the volume of a part and the resolution can be set equal to the native resolution of the AM process [97,98]; in the voxel-based methods, all the elements have the same size and are organized inside a 3D matrix or vector. The octree is an evolution of the voxel approach, based on the recursive subdivision of a cubic element into eight smaller cubes [25]; these new cubes can be inside, outside, or in the boundary of the object; the cubes at the boundary are further subdivided until the desired resolution is reached; moreover, voxels with the same properties can be joined to improve the efficiency of the data structure. Polyhedral mesh approaches are the most common in the finite element (FE) methods, they are characterized by a list of vertex coordinates, a list of polyhedra, a list of faces, a list of edges, and their reciprocal connections; again, it is possible to adopt larger elements where the variation in shape or characteristics is low and vice versa. Moving on the function-based branch of the V-Reps, implicit and explicit formulations can be adopted, but it results difficult to set different levels of inequalities or to set the desired behavior at each k value of the generic function $f(x, y, z) = k$ and make it correspond to the material and properties distribution of the real part. Parametric functions with a generic form as $V(u,v,w) = \big(x(u,v,w),\ y(u,v,w),\ z(u,v,w)\big)$ are more suitable due to the possibility of using the control points. Furthermore, the successful application of the parametric V-Rep approach in the iso-geometric analysis was demonstrated [99]; this technique allows performing FE analyses directly on the CAD model avoiding the conversion in a polyhedral mesh.

The geometric modeling of parts produced by AM technologies can be difficult if adopting the available geometric kernels. For instance, only few software are able to handle volumetric information [100], and when modeling cellular structures characterized by a high number of repetition of elements, Boolean operations are needed for joining the elements in one structure; these operations require high computational resources and often fail since the software is not able to compute the intersections between the objects; then filleting operations should be performed for eliminating sharp edges, and they need to be executed manually. If all the operations are successful, the final part becomes difficult to visualize due to the high number of surfaces to visualize. These issues are shared by all the complex geometries that exploit AM capabilities.

2.2.3 Cellular solids

Among the complex structures that can be produced by AM technologies, cellular solids gained a lot of interest in the field. According to Gibson and Ashby, cellular solids are defined as materials "made up of an interconnected network of solid struts or plates which form the edges and faces of cells" [101]. Cellular solids are often referred to also as cellular structures, lattice structures, or lattices. Placing the material only in desired zones of the part or orienting the struts according to a predefined pattern makes it possible for cellular solids to present interesting properties: they have high specific stiffness and strength since they are lightweight; they are good heat exchangers due to the large surface area with respect to the occupied volume; they can absorb and dissipate energy if the structure is designed to undergo large deformations; the large number of internal pores guarantee acoustic insulation too [101,102]. An important parameter used to describe a lattice structure is the relative density, ρ, defined as:

$$\rho = \frac{V}{V_0}$$

where V is the actual volume of the lattice, and V_0 is the volume of the region occupied by the cell. The relative density gives an idea of how much mass reduction is obtained when filling a bulk volume with the lattice.

Thanks to their characteristics, cellular structures have been widely adopted by nature as a result of millions of years of evolution; for example, the inner lattice structure of the toucan beak acts as a vascular thermal radiator and as a lightweight part [103], the skeletal microstructure of the sea urchin resembles the Schwartz P-Surface TPMS structure [104], and the internal structure of the human bones is a cellular structure randomly organized.

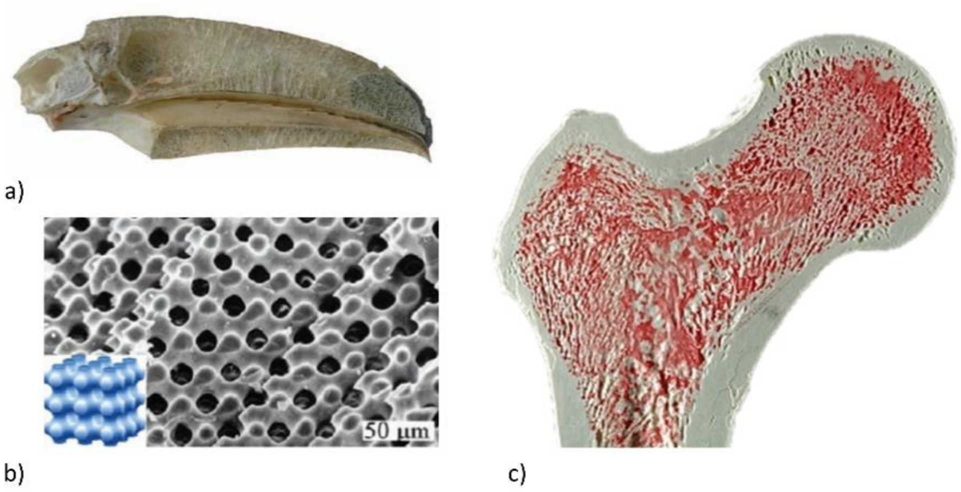

Figure 10. Examples of cellular solids found in nature: a) inner structure of the toucan beak [103], b) skeletal microstructure of the sea urchin [104], and c) internal structure of the human bone.

Before the diffusion of the AM technologies, lattice structures were produced with traditional manufacturing techniques, such as gas foaming, particulate leaching, fiber bonding, and solvent casting. As observed by Leong et al. [105] these manufacturing approaches present limitations: they require manual intervention and the final result is strongly affected by the operator expertise, they are time-consuming since post-processing is needed, toxic organic solvents are used during the production phases so this can be dangerous if the product is intended to be used for biomedical purposes and also time-consuming due to the time required for solvent evaporation, that varies from days to weeks [106]. The most critical issue is the difficulty, if not the impossibility, in controlling the final geometry of the product; the parameters can be tuned and optimize to get closer to the desired result but limits still remain. With AM technology, instead, better control on the shape of the part is obtained and it is possible to produce cellular solids with almost any desired structure.

2.2.3.1 Lattice structures classification

Lattice structures can be classified according to different properties and characteristics, and several classification schemes have been proposed in the literature. Tang et al. [107] classified the lattice structures according to the degree of order of the unit cell, considering lattices at a meso-scale, i.e., where the feature size ranges from 0.1 mm to 10 mm. They identified three groups: disordered, pseudo-periodic, and periodic lattice structures. Disordered lattices are characterized by features of different sizes and shapes and are randomly distributed, pseudo-periodic ones can have the shape of the unit cell changed in different areas of the part according to specific design purposes, and periodic ones are a simple repetition in space of the unit cell. In a following work [108], the classification method was enhanced by proposing three different classification methods. The first one was similar to the one exposed in [107]; the second one is about the geometric configuration of the unit cell and considers foam structures, divided in turn into open-cell and closed-cell foam, 2D lattice structures (honeycomb), and 3D lattice structures. The third one takes into consideration the lattice deformation criteria and is inspired by the distinction between bending-dominated and stretching-dominated structures [109]. The bending-dominated structures are characterized by low stiffness and the walls tend to bend if loaded, whereas the stretching-dominated structures have a higher elastic modulus and yield strength than the bending-dominated ones. Due to these properties, bending-dominated structures are more suitable for energy absorption application, whereas stretching-dominated structures are employed in lightweight structure design. The expected compressive behavior of these two types of lattices is presented in Figure 11 [110], where the compressive stress – strain curves are plotted.

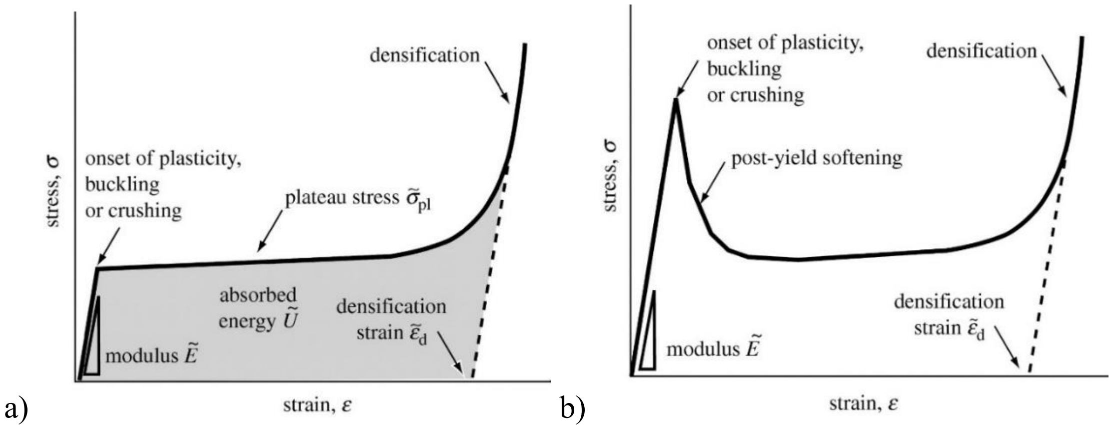

Figure 11. Compressive Stress – Strain curves of a) bending-dominated and b) stretching-dominated lattice structures [110].

These two different behaviors are described by the Maxwell stability criterion for 3D unit cells [111], further generalized by Calladine [112,113] with the equation $M = b - 3j + 6 = s - m$, where b is the number of struts, j is the number of locked joints, s is the number of states of self-stress, and m is the number of mechanisms. If $M < 12$ the cell mechanism is defined as bending-dominated, whereas if $M \geq 12$ the cell mechanism is defined as stretching-dominated. It also must be highlighted that it is not straightforward to identify the deformation mechanism of a lattice structure directly from the Maxwell criterion because the behavior depends on the unit cell topology, orientation, periodicity, and the load direction too [114]. In Chapter 11.6 of the book "Materials Selections in Mechanical Design", Ashby described the behavior of the bending- and stretching-dominated lattice structures relating the mechanical properties to the relative density, ρ [115].

Savio et al. [102] proposed a lattice structure classification based on the distribution of the cells in the whole structure, the topology of the cell, the shape of the cell, and the element dimensions of the cell, as illustrated in Figure 12.

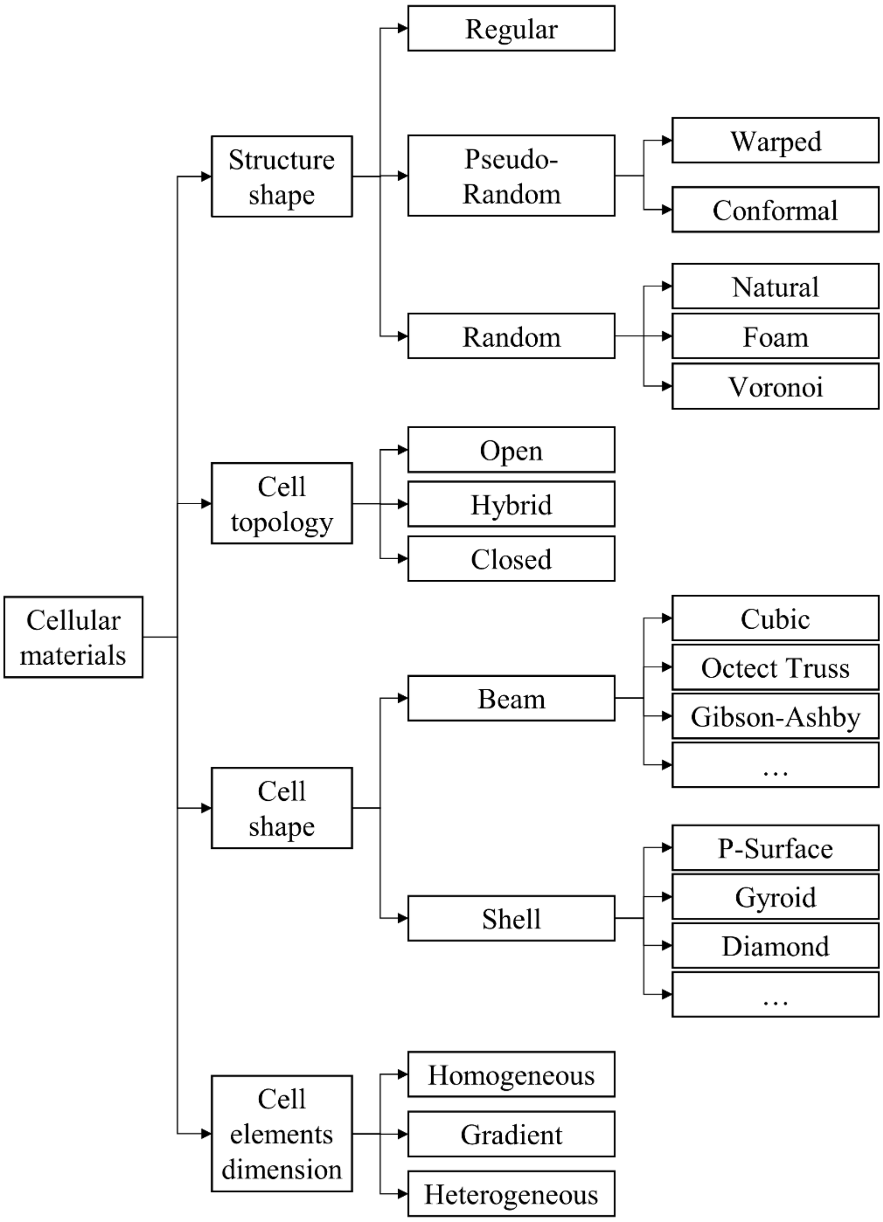
Cellular materials
Structure shape
Regular
Pseudo-Random
Warped
Conformal
Random
Natural
Foam
Voronoi
Cell topology
Open
Hybrid
Closed
Cell shape
Beam
Cubic
Octect Truss
Gibson-Ashby
…
Shell
P-Surface
Gyroid
Diamond
…
Cell elements dimension
Homogeneous
Gradient
Heterogeneous

Figure 12. Lattice structures classification. Adapted from Savio et al. [102].

Starting from the shape of the structure of the unit cell, cellular material can be divided into regular, pseudo-random, and random. Regular lattices (Figure 13a) are made by regularly repeating the unit cell along the x-, y-, and z-axis. In the pseudo-random structures, the geometry and the size of the cell are modified, but the topology is maintained. These structures can be divided, in turn, into warped and conformal. Warped cellular solids are obtained by deforming the unit cell in different zones of the volume according to the application; for instance, the size of the cells can be driven by the results of FE analyses, where high stresses could require smaller cells, or by the position of the cell with respect to a point, i.e., the closer, the smaller or vice-versa. Conformal cellular solids present unit cells with different size and geometry to adapt and conform to the external boundary of the model; conformal structures better adapt to freeform shapes since they follow the borders and the cells never interrupt, providing a better stiffness and resistance to the entire model [15]. Figure 13b shows an example of a simple cubic lattice conforming to two surfaces. Random structures present a random organization of the cells, and the size and geometry of each cell vary at the same time. As previously said, random lattice structures are frequently found in nature, for example in the cork (the material) or the cancellous bone of human beings, and in the structures produced with traditional manufacturing technologies where it is almost impossible to control the shape of the final part. Random structures are obtained also by adopting the Voronoi diagram, as shown in Figure 13c; a set of points, the seeds, are randomly positioned in the design volume and the space is partitioned in Voronoi cells, where each cell consists of all the points of the plane closer to a seed than to any other [116].

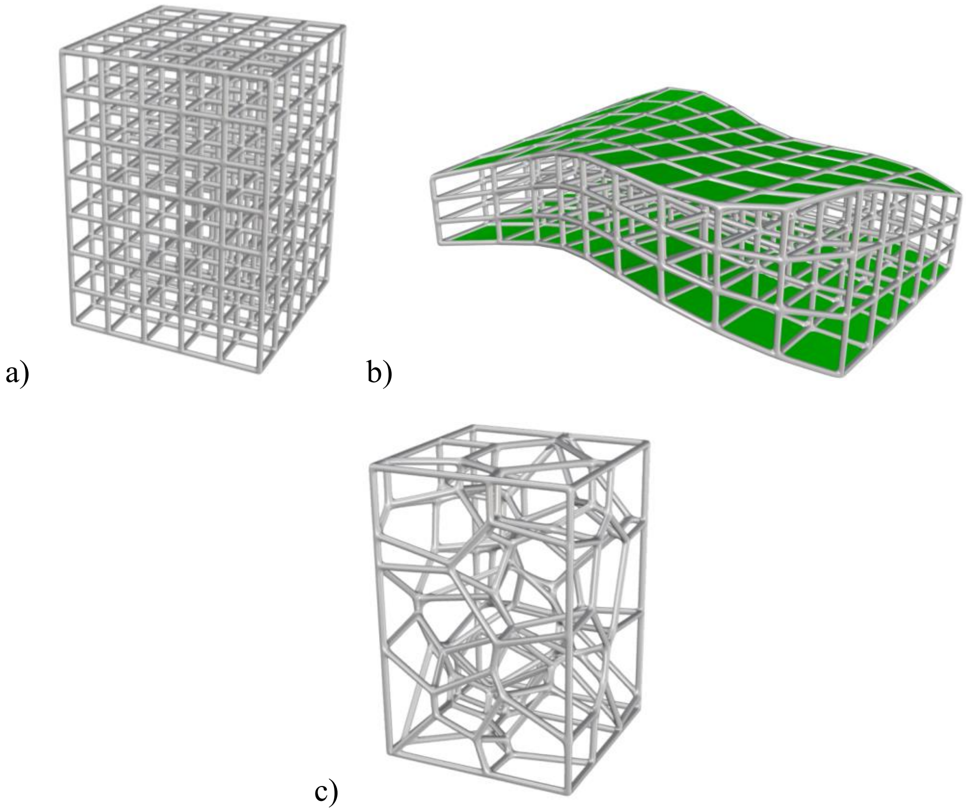

Figure 13. Cellular materials with different structure shapes: a) regular lattices obtained by repeating a simple cubic unit cell along the x-, y-, and z-direction; b) Voronoi lattice structure that fills the same box geometry as in a); c) conformal lattice structure in which the cells adapt to the shape of two surfaces.

Another classification of the cellular structures can be done depending on the topology of the cell. The lattice can present an open-cell or a closed-cell organization. In an open-cell structure, the pores and the single cells can "communicate" between each other, whereas in a closed-cell structure, the pores result inaccessible. An open-cell lattice can be preferable for biomedical applications where fluids exchange and tissue regrowth are allowed; closed-cells are better suited in mechanical applications where stiff components are required. In hybrid configurations both open and closed cells can be obtained as well. It has to be considered that closed cells cannot be produced with all the AM technologies, for example, in the PBF or VP technologies open cells are needed for evacuating the powder and the resin, respectively.

Furthermore, different cellular materials are obtained by adopting different shapes of the unit cell. A wide class of strut-based unit cells derives from the cubic cell: simple cubic (Figure 14a), body-centered cubic (Figure 14b), reinforced body-centered cubic, and face-centered cubic (Figure 14c) are characterized by an increasing number of beams [117]. The octet-truss cell (Figure 14d) derives from the face-centered cubic one and was proven to have higher stiffness and strength if compared to a randomly organized foam [118]. The modified Wallach-Gibson [111] and the modified Gibson-Ashby [119] cells are other two frequently used strut-based cells. Moving on the shell-based unit cells, the triply periodic minimal surfaces (TPMS) are some of the most adopted cells. Minimal surfaces are defined as surfaces with zero mean curvature or surfaces that minimize the surface area for given boundary conditions [120]; if minimal surfaces are repeated and duplicated along the three dimensions, they present a cubic symmetry and are called TPMS. More, TPMSs divide the space into two sub-spaces that never meet. These surfaces are defined by implicit equations; for example, the gyroid (Figure 14e) is described by $sin(x) \cdot cos(y) + sin(y) \cdot cos(z) + sin(z) \cdot cos(x) = 0$, and the Schwarz P surface (Figure 14f) is described by $cos(x) + cos(y) + cos(z) = 0$. Thanks to their curvature continuity and mechanical properties, TPMS received a lot of interest in the AM community and have been widely adopted, especially in the biomedical field and heat exchangers application, in which fluid dynamics plays a key role [121,122].

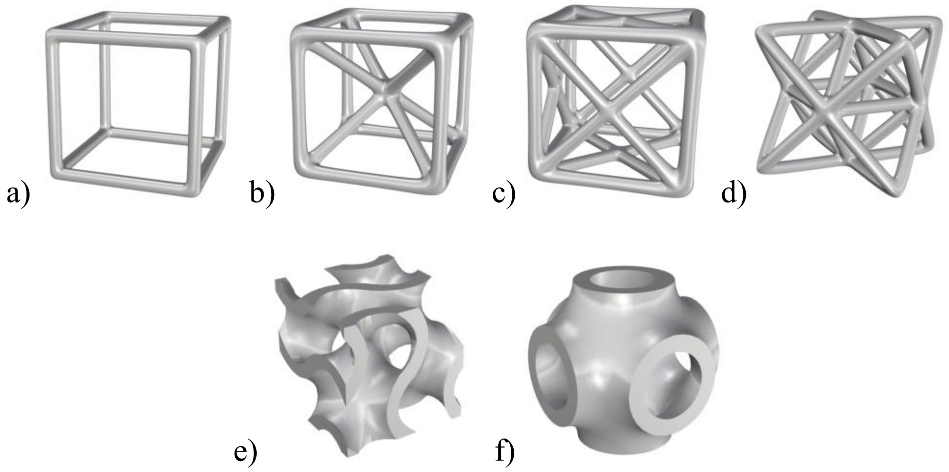

Figure 14. Different types of cell geometry: a) simple cubic, b) body centered cubic, c) face centered cubic, d) octet-truss, e) gyroid, and f) Schwarz P surface.

One last classification criterion is based on the dimension of the elements of the cell, i.e., the diameter of the beams or the thickness of the shells. If the elements of the cells of the entire lattice have the same dimension, the structure is homogeneous; if the elements of the cells have different dimensions without following an “organized” pattern, the structure is heterogeneous; if the size of the elements varies according to a defined pattern, the cellular material can be referred to as gradient elements lattice structure; as an example, in Figure 15 the diameter of the beams of the regular lattice structures linearly decreases with respect to the distance of the beams to the point at the top-right of the structure: the closer to the point, the bigger the beam dimension.

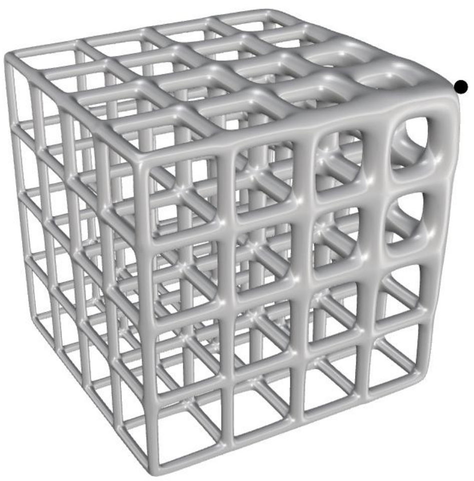

Figure 15. Lattice structure with graded elements size. The closer to the top-right point, the thicker the beam diameter.

2.2.3.2 Geometric modeling of lattice structures

Even though AM is rapidly increasing its user base and more and more products are produced with this technology, the geometric modeling tools offered for the modeling of complex structures such as the cellular solids still present limitations and issues [3]. Commercially, several CAD software offer dedicated packages for lattice modeling. ANSYS SpaceClaim [123] allows filling solid volumes with different types of regular and conformal beam-like and TPMSs lattice structures; it is possible to define the filling percentage and the size of the cell and the elements. The add-on module "Lattice Structure Design" in Siemens NX [124] enables the users to design components with lattice structures characterized by beams and shells controlling the dimension of the structure. Similar operations can be performed with other software such as the 3DEXPERIENCE Part Design App by Dassault Systèmes [125], Altair Inspire [126], the Lattice module inside Materialise 3-matic [127], the Structures module inside Materialise Magics [128], and PTC Creo [129]. The users of Rhinoceros CAD software [130] and Grasshopper plugin [131] exploited the customization freedom and developed plug-ins and add-ons for the design and modeling of lattice structures. Among them, GL Software by General Lattice [132] directly works inside Rhinoceros offering a graphical user interface enabling modeling lattices based on NURBS models; Intralattice plugin [133], developed by the Additive Design & Manufacturing Laboratory (ADML) at the McGill University, and Crystallon plugin [134], developed by Aaron Porterfield, work inside Grasshopper and allow generating lattice structures taking advantage of the parametrization and the other tools available inside Grasshopper; for instance, topology and size optimization results can be used for sizing the elements of the structures. Both Intralattice and Crystallon do not implement their modeling methods for the final lattice solid model, so it is required to use other plugins such as Dendro [135] and Cocoon [136], that create mesh models based on the marching cubes algorithm [137]. All the aforementioned tools are based on B-Rep parametric functions, NURBS, and meshes and often, when the number of elements increases, they become unstable, difficult to handle, and require a lot of computational time and resources. The nTopology software [138], instead, is based on V-Rep implicit functions, allowing to model structures with a high number of elements without failing; the implicit modeling approach handles better operations such as blending, filleting, offsetting, and Boolean operations. Moreover, the model sizes are always smaller than the same structure modeled with a B-Rep procedure, especially when dealing with TPMSs where the model size is the same regardless the number of the cells, because the software only stores the TPMSs equations. Finally, the visualization of the model is not based on B-Reps but on the sphere tracing technique [139], a variant of the ray tracing technique; these algorithms require high computational resources but, at the same time, they are highly parallel and can take advantage of the new advancements in CPUs and GPUs parallel processing capabilities that were not available in the past. As a limitation, the implicit models obtained in nTopology are often difficult to export for reusing them for further analyses in CAE software.

The scientific community proposed different approaches and solutions aimed at overcoming these limitations. Wang et al. [15] proposed a hybrid approach for geometric modeling conformal lattices. The method first models every single structure as a solid model using the ACIS geometric modeling kernel [140], directly converts the single structure to an STL model, and then stacks all the STL elements together to obtain the whole lattice; finally, it adds a sphere to each node to avoid nonmanifold geometries. The method differs from a more traditional approach because usually the entire part is first modeled as a solid and the STL conversion is performed as the last step. The authors were able to reduce the computational time. An improvement of this method was proposed by Chen [141], who developed a universal structure generating system. An XML file is used to store the information about the nodes and the struts of the cellular solid; a structure generating system is then able to create a mesh model of the part using as input the XML file previously created, like the previous approach presented by Wang et al. [15], the system firstly models the single nodes as an STL file and then joins all the nodes to obtain the complete STL mesh model. More, a filleting operation is performed by exploiting the combination of two offsetting operations, based on the Minkowski sum and difference [142]. Furthermore, Chen [143] expanded the method implementing a space warp deformation operation, able to result in smaller and thicker cells in predefined areas of the structures; again, the lattice is described by the XML file and then the space is warped by minimizing an energy function. Medeiros e Sà et al. [144] proposed a mesh modeling method able to obtain a lattice based on the dual of the structure; more precisely, given the wireframe of the starting lattice structure, called primal cell complex, the dual cell complex is obtained by connecting the central point of two adjacent cells. The new wireframe resulting from the dual operation is then used as a starting point for the creation of a solid model built thickening the beams with a mesh-faces approach. Kou and Tan [145] proposed a method to model cellular solids that present unit cells with a graded size using the Voronoi diagram; first, the seeds are generated according to a probability density function, then the vertexes of the Voronoi cells are used as control points of closed B-splines curves; finally, the curves are scaled with respect of their centroid using different scale factors depending on the position of the curve inside the part and according to the desired size of the cellular solid. Chow et al. [146] proposed a method to model 3D porous structures starting from 2D Voronoi diagrams. The Voronoi seeds are organized in concentric rings and each seed brings solid or void information that is transmitted to the relative Voronoi region; then some of the seeds receive a displacement pattern with a motion law, whereas others remain static. The structure is built along the three-dimensional direction by expanding the time dimension of the dynamic pattern. The Voronoi diagram was used also by Fantini et al. [147] that proposed a modeling workflow inside Grasshopper and Rhinoceros software to design porous structures for producing biomedical scaffolds; they also correlated the input parameters such as the number of Voronoi seeds with the target porosity and the pores size of the final model. In a further work [148], they validated the design process by fabricating a sample in Ti6Al4V material and by performing analyses with the scanning electron microscopy and the micro computed tomography technologies.

Other works in the literature explored the possibility of modeling cellular solids using the CSG approach. Zeinalabedini et al. [149] modeled a foam-like structure by subtracting randomly organized spheres that overlap each other from the design space; by controlling several parameters such as the range of the size of the spheres and the amount of overlapping between them, they were able to control the relative density of the structures. Similarly, Gagliardi et al. [150] performed the Boolean subtraction between a bulk volume and random spheres to model and simulate foams produced by traditional manufacturing technologies. Ceruti et al. [151] developed a modeling environment inside an open-source CAD software capable of performing Boolean operations to model lightweight sandwich structures and to fill lattice structures inside solid parts.

Lattice structures can be modeled adopting V-Rep approaches as well. Pasko et al. [26] modeled regular and irregular microstructures using function-based modeling via implicit surfaces described by trivariate scalar fields and continuous real functions, calling this approach “Function Representation” (FRep); in particular, they applied the set-theoretic R-functions operations [152] (union, intersection, and subtraction) on the elementary initial objects to build up more complex parts. According to the authors, the proposed FRep approach provides a more robust and dynamic control if compared to the B-Rep methods; more, it is easier to modify the topology of the object due to the FRep parametrization. Aremu et al. [153] addressed the modeling of conformal lattice structures using voxels as discrete V-Rep approach. They started from creating a voxel representation of both the starting object to fill with the lattice and the lattice structure itself; adopting the same voxel resolution size, a trimmed lattice structure is obtained by performing a Boolean intersection between the two sets of voxels; this operation is fast because the intersection deals with 0 (no voxel, void) or 1 (voxel, solid) data. Furthermore, to avoid the presence of incomplete lattice elements at the boundaries, a lattice skin, called “net-skin”, is created and connected to the internal structure as an alternative to solid skin. Finally, the option of modeling structures with a graded size of the element is implemented. Holdstein et al. [154] proposed a method based on voxels for modeling micro-implants for bones; starting from the computed tomography model of the damaged bone, the algorithm detects the defected region, creates a mask gathering adjacent voxels, searches for a similar pattern in healthy zones of the bones, and finally performs the infilling of the bone in the defected area. Brackett et al. [155] adopted a dithering method based on error diffusion to generate lattice structures with different cells dimensions; the workflow is organized as follows: a grey-scale map is obtained as a result of FE analyses or TO of the original part; then the error diffusion dithering method is applied to convert the continuous tone image into a binary black-and-white representation and variably spaced node points are generated; finally, the points are used as seeds for applying the Voronoi diagram.

2.2.3.3 Lattice structure optimization

As previously reported, the elements of the lattice, i.e., beams or shells, can have different sizes. The size can be the same for all the elements inside the structure, the elements can present random dimensions, they can follow a gradient, or the dimension can be driven by external data. The possibility of tailoring the dimension of every single element of the lattice structure is highly beneficial if considering application where structural efficiency is required, but at the same time, lightweight structures are preferred. In these situations, structural optimization suits the needs. Structural optimization aims to organize the material inside a structure in the best way, taking into consideration the loads, the material, and the constraints applied on the part. Typical optimization objectives are the mass reduction, the stiffness maximization, and the tuning of the resonant frequencies. According to Bendsøe [156], structural optimization can be divided into three classes:

1. Size optimization, in which the dimension of the elements of the structure is optimized; for instance, size optimization can involve the cross-sections of the beams or the thickness of the skins inside a lattice structure (Figure 16a).
2. Shape optimization, in which the shape of the boundary of the structure is optimized; all the boundaries are considered, both external and internal, i.e., the shape of internal holes or voids (Figure 16b).
3. Topology optimization (TO), in which the material is arranged inside a design space to find the best distribution under a set of boundary conditions and respecting the structural and dimensional performance requirements (Figure 16c).

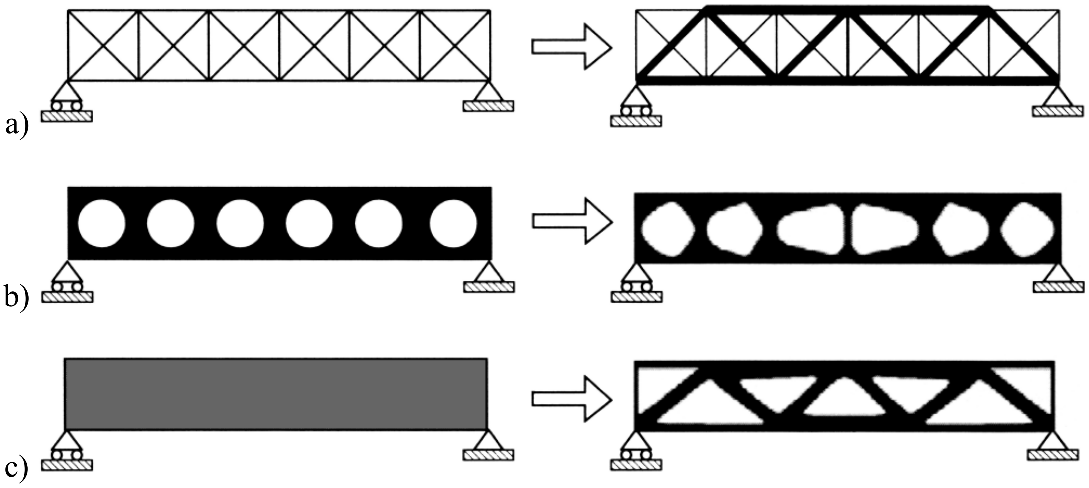

Figure 16. Structural optimization approaches: a) size optimization, b) shape optimization, c) topology optimization [156].

Size and topology optimization are the most diffused, with the latter being the most popular since it is used not only with lattice structures but with new and redesigned parts that are going to be produced with AM technologies. TO has been implemented using different algorithms [157]. Homogenization methods exploit the mathematical theory of homogenization [158] in which parts with complex geometries and microstructures are studied as a continuum domain made up of a virtual material called effective material. Density methods subdivide the model into finite elements and consider the density of each element as the only design variable, which can assume a value between 0 and 1. Usually the optimal solution is characterized by elements with intermediate density value and the solution is far from a solid (1) – void (0) situation. The Solid Isotropic Microstructure with Penalization (SIMP) method [159] is the most used method to suppress intermediate densities and exploit a power law. The so called "hard-kill" methods are another group of TO methods, aimed at avoiding the intermediate densities in the final solution. The Evolutionary Structural Optimization (ESO) method [160] calculates a criterion parameter for each element and at each iteration the elements with the lowest criterion parameter value are eliminated. As an extension of the ESO method, in the Bi-directional Evolutionary Structural Optimization (BESO) method [161], at each iteration, in addition to the removed elements, new ones can be added next to those elements with a high criterion parameter. Finally, Level-Set Methods (LSMs) consider the iso-contours of a level-set function that implicitly define the interface between the material phases and a sharp division between the solid and void zones is obtained [162]. Among the available methods, the SIMP is the most diffused, thanks to the relatively low number of iterations required, its suitability in dealing with a wide range of design constraints and large 3D models [157], and the possibility of implementing the method in a few-lines code [163,164].

Considering the optimization of lattice structures, in size optimization approaches, the size of each element is iteratively varied until the convergence is reached and the structure satisfies the starting requirements. Savio et al. [165], proposed a size optimization method for lattice structures based on the utilization of each beam defined as the ratio between the load acting on the beam and the yield stress of the material of the part; according to the boundary conditions, a FE model is set up and the diameter of the beams is modified at each iteration in order to reach the utilization target. More, technological constraints are considered and a minimum and a maximum allowed radius are defined depending on the AM technology used for the production and on the size of the unit cell. Nessi and Stankovic [166] used the Superformula [167], an extension of the Superellipse, to model an optimized domain inside a design volume; the domain is then discretized adopting a tetrahedral meshing technique and the edges of the mesh are used as the wireframe of the lattice structure; the structure is further optimized by performing a size optimization of the diameter of the beams using a FE analysis.

Moving on the implementations of TO for lattice structures, Ning and Pellegrino [168] proposed a method based on the implicit representation of the structural topology to overcome the issues of both the continuum and discrete TO approaches that when applied to lattices often result in impractical structures with floating components. In their work, the microstructure is defined by a continuous variable, i.e., the size distribution field, and the topology and the size of the structure are optimized by a genetic algorithm. Han and Lu [169] proposed a “nonuniform lattice structure design method” able to design lattice structures with unit cells of different dimensions in different areas of the design volume; this is obtained by performing a SIMP-based TO and defining a series of unit cells with the same topology, but with different cell size. The unit cells are mechanically characterized and then, depending on the TO results, are positioned in the zones of the design volume that present similar Young’s modulus. Wang et al. [170] proposed a similar method, correlating the TO results with unit cells with a constant cell size but with a variable beams size. Wu et al. [171] too proposed a TO approach for the design of hierarchical structures and developed a method called Approximation of Reduced Substructure with Penalization (ARSP); they were able to model graded cellular structures controlling the size of the elements with a parameter that, in turn, is linked to the results of the TO. Alzahrani et al. [18] proposed the Relative Density Mapping (RDM) method, that relates the size of each beam of the lattice structure depending on the relative density resulting from the TO of the elements surrounding the beam.

In some cases, the optimization of lattice structures requires improving two or more characteristics that conflict with each other. As a simple example, when reducing the mass of a structure, usually the stiffness decreases, and consequently at equal loading conditions the displacement of the structure increases; so, reducing at the same time the mass and the displacement of a lattice is not trivial. In this scenario, multi-objective optimization is widely used to solve conflicting optimization problems. Noilublao and Bureerat [172] used three multi-objective evolutionary algorithms, namely the strength Pareto evolutionary algorithm (SPEA2), the population-based incremental learning (PBIL), and the archived multi-objective simulated annealing (AMOSA), to perform the size, shape, and topology optimization of a lattice structure; they used the mass, the compliance, the natural frequencies, the frequency response function, and force transmissibility as design objectives and compared the three algorithms to determine which one is more suitable testing them on four different optimization problems of the same structure. Kaveh and Mahdavi [173] proposed the multi-objective colliding bodies optimization (MOCBO) algorithm and tested it on two case studies based on lattice structure, a 120-bar truss dome and a more complicated 582-bar truss tower, considering two conflicting objective functions containing the structural weight and nodal displacement. Angelo et al. [174] proposed two multi-objective ant colony optimization algorithms and used them to solve structural optimization problems on five structures with an increasing number of bars, with the objective of minimizing the weight of the structure and its maximum nodal displacement. They also applied the multicriteria tournament method (MTD) to select the solution from the Pareto giving different weights, i.e., importance, to the different objectives. Lemonge et al. [175] used the third evolution step of generalized differential evolution (GDE3) genetic algorithm for structurally optimizing trusses in which, other than using the "traditional" objective functions identified by the weight and nodal displacement minimization, two new types of problem were studied, the first dealing with the weight minimization and the maximization of the first natural frequency of vibration, whereas the second deals with the weight minimization and the maximization of the load factor that impacts the maximization of the elastic critical buckling load.

2.2.3.4 Numerical analysis and mechanical testing of lattice structures

The numerical analysis and mechanical testing of a newly designed part are fundamental when it comes to characterize the structural properties. Studying the behavior of cellular solids is even more important because this category of components is relatively new and is produced with recent manufacturing technology, so previous data and information are missing and need to be collected to understand how lattices behave.

Performing numerical analyses, in particular FE ones, on lattice structure is not trivial especially when dealing with parts characterized by a high number of elements and unit cells; the discretization of the whole structure by adopting a suitable resolution to study every single element of the lattice would result in a heavy model and, consequently, in high computational costs and time [149]. To overcome this issue, different simulation approaches have been proposed in the literature.

The homogenization method studies the lattice structures as a fully dense material where the mechanical properties of the lattice material, i.e., the stiffness matrix, are obtained from the unit cell [176]. The complexity of the model is reduced but, as a drawback, it is not possible to analyze anisotropic structures, so random structures or structures with elements with graded dimensions cannot be studied with the homogenization method. Vigliotti and Pasini [177] presented a matrix-based multiscale procedure for the analysis of bidimensional components filled with triangular, hexagonal, and Kagome cells; they determined the analytical expressions for the macroscopic in-plane stiffness constants and for the internal forces in the lattice edges. Arabnejad and Pasini [178] used the asymptotic homogenization theory to six different lattices, either stretching or bending dominated, for determining the effective elastic modulus and yield strength for the whole range of relative density; then, the obtained results were compared to the ones found in the literature that used other homogenization methods. Freund et al. [179] proposed and applied a computational homogenization approach on planar areas filled by eight different unit cells investigating the effective elastic parameters; they demonstrated that if the mathematical problem is well formulated, the selection of the representative volume does not influence the homogenization results. In a wider study, Ptochos and Labeas [180,181] used the homogenization method for predicting the behavior of a structure made by a thousand regular body centered cuboid unit cells and verified the numerical results by performing experimental tests, indicating good accuracy.

Moving a step further, lattice structure analysis can be performed by adopting a mono-dimensional FE approach based on the beam theory. This approach exploits the lines that compose the geometrical wireframe of the lattice, saving computational time and power introducing an error in the results [182]. Two different beam theories can be adopted: Euler-Bernoulli and Timoshenko. The Euler-Bernoulli approach neglects the shear deformation, so the cross-section of the beam remains perpendicular to its neutral axis. A relevant theory parameter is the slenderness ratio, defined as the ratio between the length and the cross-section of the beam, that affects the flexural rigidity matrix; indeed, if the ratio is low and the beam is loaded with bending forces, the flexural rigidity increases and tends to diverge, causing the underestimation of the deflection. Since the lattice structures present small-length beams, the slenderness ratio needs to be considered [16]. The Timoshenko theory, instead, includes the deformation from the shear stress and considers the rotation between the cross-section and the neutral axis of the bending curve, resulting in more accuracy. Also, this theory presents a limitation, the shear locking phenomenon, that lies in a bad schematic of the shear part of the elastic energy [183]. Bacciaglia et al. [182] compared the results obtained by analyzing a lattice structure with the Euler-Bernoulli, the homogenization, and the 3D mesh FE analysis methods; the analysis based on the beam theory was the fastest but produced a displacement estimation uncertainty of 15%. Ravari et al. [184] performed numerical analyses using the Timoshenko and the solid FE theories for studying the effects of the variation of the beam diameter on the mechanical proprieties of a lattice structure produced by MEX technology and compared the numerical data with experimental results; both the numerical methods provided similar results to the experimental ones concerning the stress distribution and Young's modulus; the Timoshenko theory better predicted the elongation of the beams and, as expected, was faster than the solid FE analysis. Campoli et al. [185] and Genovese et al. [186] found out that when simulating lattice structures produced by SLM, the results coming from the beam theory are more accurate than the ones from the solid FE analysis; Genovese et al. hypothesized that the reason could be the additional contribution of the stiffness provided by the joints of the struts. Also Dong et al. [187] focused on the nodal points of the lattices; they modified the Timoshenko beam element because the concentration of material in the nodal zones leads to different stiffness properties with respect to the central zone of the beam. They validated the hypothesis by performing experimental tests and numerical analyses, showing a better agreement than the traditional beam elements.

As it was said at the beginning of this section, mechanical testing of lattice structures is essential. More generally, mechanical tests are needed when dealing with parts produced by AM technologies because both the AM processes and the materials resulting from the processes need to be characterized [12,13,188,189]. Concentrating on cellular solids, several works investigate their mechanical properties. Smith et al. [190] studied the mechanical properties through quasi-static compression tests of lattices made up by the body-centered cubic cell and the body-centered cubic cell reinforced with vertical pillars produced in 316 L stainless steel by SLM technology. A similar approach was followed by Tsopanos et al. [191] who tested SLMed stainless steel body-centered cubic lattices finding a relation between the process parameters and the mechanical properties. Ahmadi et al. [192] tested Ti6Al4V cellular structures made by SLM technology, with different relative densities, and six different unit cell configurations, i.e., cubic, diamond, truncated cube, truncated cuboctahedron, rhombic dodecahedron, and rhombicuboctahedron; the mechanical properties were related to the relative density through a power law. Cerardi et al. [193] tensile tested and mechanically characterized lattice structures presenting three different designs of unit cell, derived from the cube and the prism edges, that, in turn, were characterized by three different porosities; the parts were produced in polyamide 12 by SLS. Similar tests were conducted also on TPMS. Al-Ketan et al. [194] performed compressive tests on both skeletal- and sheet-based TPMS such as the gyroid, the diamond, and the primitive P-surface, produced by SLM in maraging steel; they highlighted that the sheet-based structures exhibited a near stretching-dominated deformation behavior whereas the skeletal-based ones showed a bending-dominated behavior. Yu et al. [195] studied the mechanical properties and the energy absorption capabilities of gyroid and P surface lattice structures produced by stereolithography technology; they modeled and tested structures with both uniform and graded shell thickness. Furthermore, the fatigue behavior of lattice structures has been studied. Amin Yavari et al. [196] fatigue tested structures based on the cube, diamond, and truncated cuboctahedron unit cells printed at different levels of porosity in Ti6Al4V by SLM; they then normalized the fatigue curves with respect to the yield stresses, finding good agreement between structures with the same type of unit cell and were able to compare the behavior of the different unit cells. Hrabe et al. [197] fatigue tested Ti6Al4V lattice structures produced by the EBM technology; the unit cell was a diamond cell and structures with different pore sizes and beam diameters were printed by modifying the scale of the original model and changing the process parameter; the results showed that the AM produced cellular structures present a lower fatigue life compared to bulk material.

2.2.4 Functionally graded AM (FGAM) parts

In AM, complexity is also achieved through material composition. AM technologies enable the possibility to realize components with a composition that spatially varies across the volume, resulting in changes in material properties according to the functional requirements. These types of objects are called functionally graded materials (FGM). FGM are a class of advanced materials introduced in the 1980s in Japan [198]. Born for the aerospace industry and meant to be fabricated with the standard manufacturing processes, for example with bulk or surface treatments, FGM can now take advantage of the AM technologies. For this reason, the fabrication of FGM with AM leads to the term functionally graded additive manufacturing (FGAM) [27]. This brings a significant shift from contour, i.e., B-Rep, modeling to performance or volumetric modeling since it changes the traditional shape-centric fabrication towards a material-centric fabrication.

The potential gradient composition achievable can be organized in three categories: variable densification within a homogeneous composition, used by Leonardi et al. [199] to obtain heterogeneous lattice structures characterized by a variable geometry, heterogeneous composition through the simultaneous combination of two or more materials, as proposed by Huang et al. [200] that proposed a mask-image-projection based Stereolithography (MIP-SL) method for fabricating bars with heterogeneous material distribution, and variable densification within a heterogeneous composition, as presented in Figure 17.

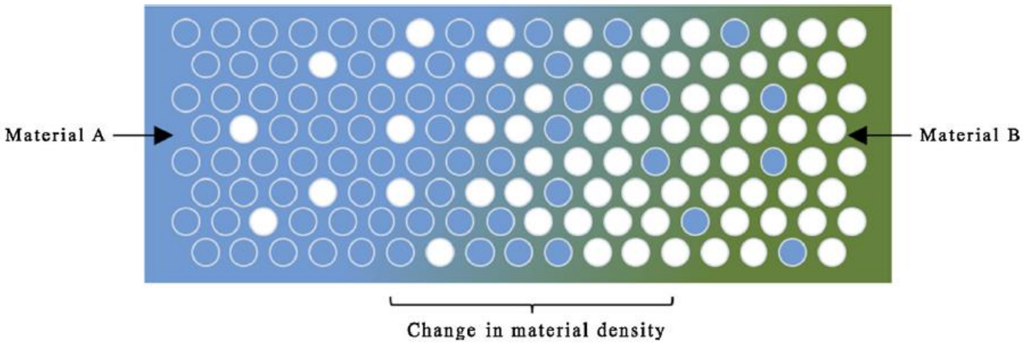

Figure 17. FGM obtained by variable densification within a heterogeneous composition [27].

Anisotropic properties can be obtained by introducing material heterogeneities into the design domain. By doing so, the different properties and advantages of multiple materials can be fully exploited, and traditional limitations due to material incompatibilities can be lessened with gradual material variations.

Not all the 7 AM technologies categories allow realizing multi-material components. The most suitable are the DED, the PBF, the MEX, and the MJ. In the laser metal deposition (LMD), a DED sub-category, the laser beam can melt previously mixed metal powders to obtain graded composition [201]. Wire arc additive manufacturing (WAAM) can use multiple metal wires where the feeding speed is controlled to obtain graded composition [202]. So, with DED it is possible to obtain both confined spaces and gradients with different compositions. Moving to PBF, the design of new selective powder dispensing methods and devices introduced the possibility to produce true gradients and confined multifunctional areas. Zhang et al. [203] combined the delivery of point-by-point selective powder with powder bed fusion for multiple material SLM. MEX technologies can be upgraded to multi-material 3D printing by adding several materials flows to the same machine [204]. This is achieved by adding nozzles or by adding extruders that converge in a single nozzle or orifice [205,206], as presented in Figure 18. Another option to achieve multi-material in a MEX system is represented by the multi-material units, from Prusa3d [207] and Mosaic [208]. More, Oxman et al. [209] proposed a method based on direct ink writing (DIW) where the printing platform can mix and extrude two materials, that are liquid at room temperature, and solidify after mixing and deposition.

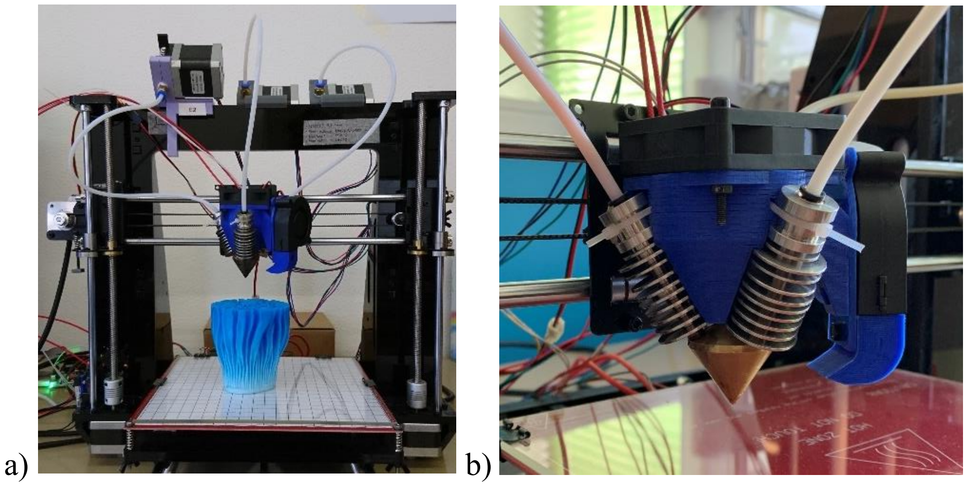

Figure 18. Commercial MEX 3D printer equipped with the 3-in-1 diamond hotend at the LIN Lab, Università degli Studi di Padova: a) entire system, b) diamond hotend close-up.

MJ, in particular the PolyJet technology by Stratasys [210], is considered the state of the art for producing multi-material objects. Various compositions can be obtained by mixing different percentages of resins before the curing step.

2.2.5 File formats for AM

During the development of a part produced by AM technologies, several stages are encountered and, often, several software are used to perform operations such as the part modeling and structural simulation, or the manufacturing process optimization. In this scenario, the product information has to be exchanged between the software, and a number of file formats for data exchange are available, each one of them with its pros and cons.

The STL file format is the de-facto industry standard for transferring the geometry of the part but is the most limited. It only includes geometrical information about the surface of the component, so it is not possible to carry information about internal characteristics, boundary colors, or any other product and manufacturing information (PMI). When exporting using the STL format, the part is approximated by planar triangles, resulting in the loss of geometrical accuracy [211]. The data structure of the STL format is made up of the triangular faces list, each one with the components of the face normal and the list of the three points at the vertexes of the triangular facet.

The PLY format is similar to the STL one because it approximates the surface geometry with discrete elements, but it can transport the colors of the textures too. The organization of the data structure slightly differs from the STL structure; indeed, each node is listed at the beginning of the file together with its coordinates and then the elements are defined calling the corresponding index of the vertexes; this allows obtaining export files with smaller dimensions.

ISO organization developed the STEP AP 242 format under the ISO 10303-242 standard [212]. The second version of the format, released in 2020, introduced several features to cover the whole product development phases as shown in Figure 19, and is now able to deal with AM-related characteristics. For instance, build information of AM parts can be specified, such as a direction vector associated with the part and the build plate size and volume, 3D scan data from reverse engineering application are supported, parts can be exported adopting 2D and 3D tessellation, and curved triangles, i.e., mesh with normal at vertices, are handled. Furthermore, according to the STEP AP 242 project webpage [213], the third edition of the standard will take into consideration some other AM capabilities as the heterogeneous materials, the representation of lattice structures, and semantic representation of the PMI for AM.

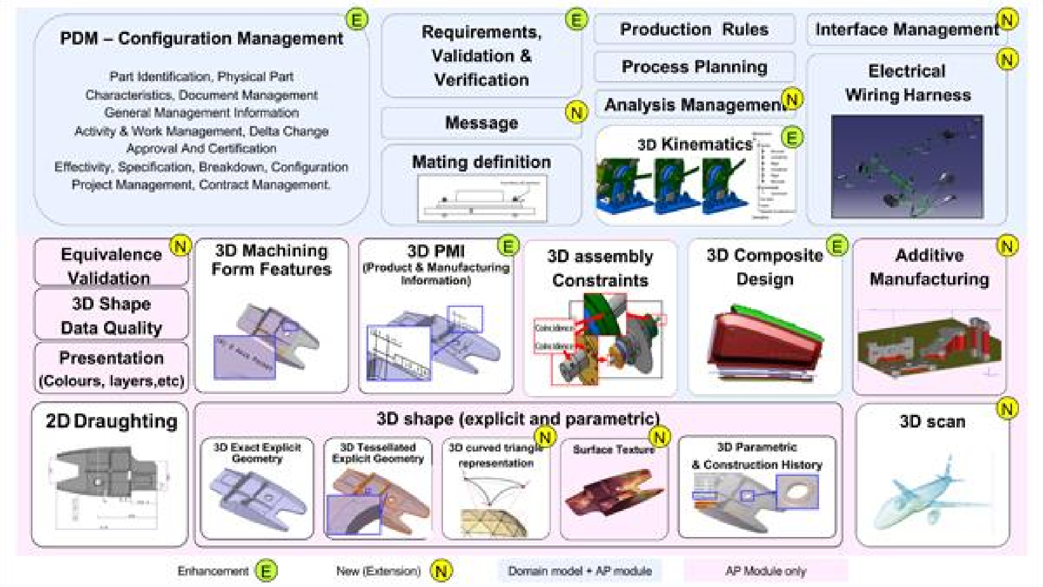
PDM – Configuration Management
Part Identification, Physical Part Characteristics, Document Management General Management Information Activity & Work Management, Delta Change Approval And Certification Effectivity, Specification, Breakdown, Configuration Project Management, Contract Management.
Requirements, Validation & Verification
Message
Mating definition
Production Rules
Process Planning
Analysis Management
3D Kinematics
Interface Management
Electrical Wiring Harness
Equivalence Validation
3D Shape Data Quality
Presentation (Colours, layers,etc)
3D Machining Form Features
3D PMI (Product & Manufacturing Information)
3D assembly Constraints
3D Composite Design
Additive Manufacturing
2D Draughting
3D shape (explicit and parametric)
3D Exact Explicit Geometry
3D Tessellated Explicit Geometry
3D curved triangle representation
Surface Texture
3D Parametric & Construction History
3D scan
E
N
Enhancement
New (Extension)
Domain model + AP module
AP Module only

Figure 19. Overview of the ISO 10303 STEP AP 242 format features [214].

ISO and ASTM organization worked together for developing a standard format called the Additive Manufacturing Format (AMF) under the standard ISO/ASTM 52915 [215]. The AMF is an XML-based format that describes parts by triangles and can store information about lattice structures, material specifications with mixed and graded materials, and new materials can be defined as compositions of other materials. The AMF file also includes provisional support for voxel-based representation. Due to these characteristics, the AMF is well suited for supporting the design and production of FGAM parts.

Another XML-based format is the 3MF, an open format free of royalties, patents, and licensing, developed by the 3MF consortium [216]. The consortium gathers a group of big players of the AM industry (3D Systems, Autodesk, EOS, General Electric, etc.) whose aim is to represent the physical object in a mark-up format with richer external and internal information supporting several code extensions considering materials and properties, production, and lattices data. They also aim to offer a cross-compatible format for multiple AM systems. A limitation of the 3MF format is that it does not support B-Rep, NURBS, and STEP modeling.

Other file formats have been proposed to support the modeling and production of parts that exploit AM features. In a work focused on FGAM, Loh et al. [27] identified also the FAV and the SVX file formats. The FAV (Fabricatable Voxel) format was developed by Fuji Xerox and Keio University, is based on voxels, and can store information about colors, materials, and connection strength through voxels; it can perform the design, analysis, and inspection of models in an integrated manner without the need of converting the data [217]. The SVX (Simple Voxels) format was proposed by Shapeways [218], is voxel-based, and is a ZIP file composed of a series of image slices and a manifest.xml file. They aim at converting the voxels in STL files, and, at the same time, keeping the information about the material, color, density, and custom data of each voxel.

2.3 Limitations and issues

Additive manufacturing has proven to be a promising technology enabling the production of components with unprecedented complexity. Nevertheless, AM is not mature yet. Periodically, experts and associations meet to discuss the progress made in the field and to draw AM roadmaps to drive and organize future developments [21,219,220]. The research community too highlights that improvements must be made in different sub-fields, as summarized in Figure 20.

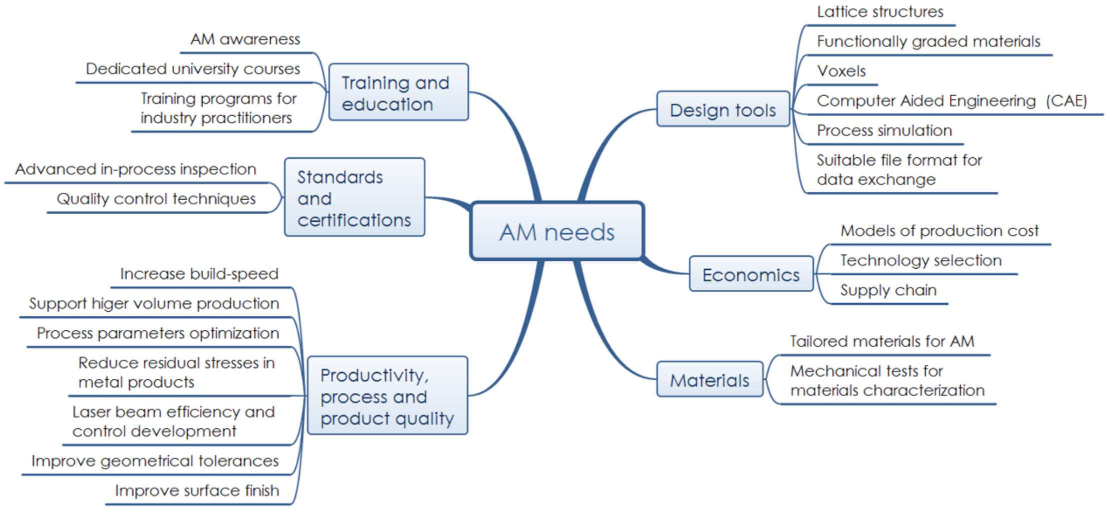
AM needs
Training and education
AM awareness
Dedicated university courses
Training programs for industry practitioners
Standards and certifications
Advanced in-process inspection
Quality control techniques
Productivity, process and product quality
Increase build-speed
Support higer volume production
Process parameters optimization
Reduce residual stresses in metal products
Laser beam efficiency and control development
Improve geometrical tolerances
Improve surface finish
Design tools
Lattice structures
Functionally graded materials
Voxels
Computer Aided Engineering (CAE)
Process simulation
Suitable file format for data exchange
Economics
Models of production cost
Technology selection
Supply chain
Materials
Tailored materials for AM
Mechanical tests for materials characterization

Figure 20. Additive manufacturing needs [221].

Some of the open issues underlined in Figure 20 have been exposed in the previous sections of the chapter, contextually to the recent advancements on that particular topic. So, the purpose of this section is to provide a recap of the current issues in AM.

Starting from the design tools for AM, the available commercial software is not suitable for designing complex parts [3]. The literature highlights the need for more robust and reliable approaches for geometric modeling cellular solids [26,222] and functionally graded objects [27]. Moreover, an exhaustive workflow that covers all the design process steps is still missing, since, according to Kumke et al. [223] the current ones focus on the utilization of a single AM potential, and they are often too specific for a single case study. Seepersad [28] stated that CAD software and CAE tools should be coupled to incorporate the DfAM knowledge into the design process. Finally, exchanging data between different software is still an issue due to the lack of a suitable and recognized standard format able to support all the features that could be adopted in a part produced by AM technologies [98].

Moving on the materials for AM production, mechanical characterization through experimental tests is fundamental to understand and predict how the parts produced by AM technologies behave with respect to the ones produced by traditional techniques [224,225]. On top of that, new materials are used to produce new shapes and features, so the static and dynamic mechanical characterization of these components is crucial [24,226]. Depending on the AM technology used, the tuning of the process parameters plays a key role in improving the mechanical properties, surface finish, and geometrical tolerances [84,227].

More, even though ISO and ASTM organizations started collaborating to jointly develop international standards, according to Bourell et al. [22] and Seifi et al. [73] efforts are still necessary to guarantee an adequate quality of the printed parts. Bacciaglia et al. [228] also highlighted the difficulty in generating 2D drawings of lattice structures, that would be useful for geometric dimensioning and tolerancing (GD&T) data or maintenance manuals.

As declared in the introduction (Chapter 1), this research project aims to overcome some of these limitations. In particular, the topics associated with the design methods and tools for the geometric modeling of complex parts have been addressed. Modeling and optimization approaches have been proposed for lattice structures characterized by conformal unit cells and with the presence of both beams and skins. The methods have been validated both numerically and experimentally by test campaigns performed on specimens of different shapes and materials. Figure 21 relates the limitations underlined to the research topic that will be exposed in the next sections, in an effort to propose solutions able to exploit AM capabilities and exceed the actual issues.

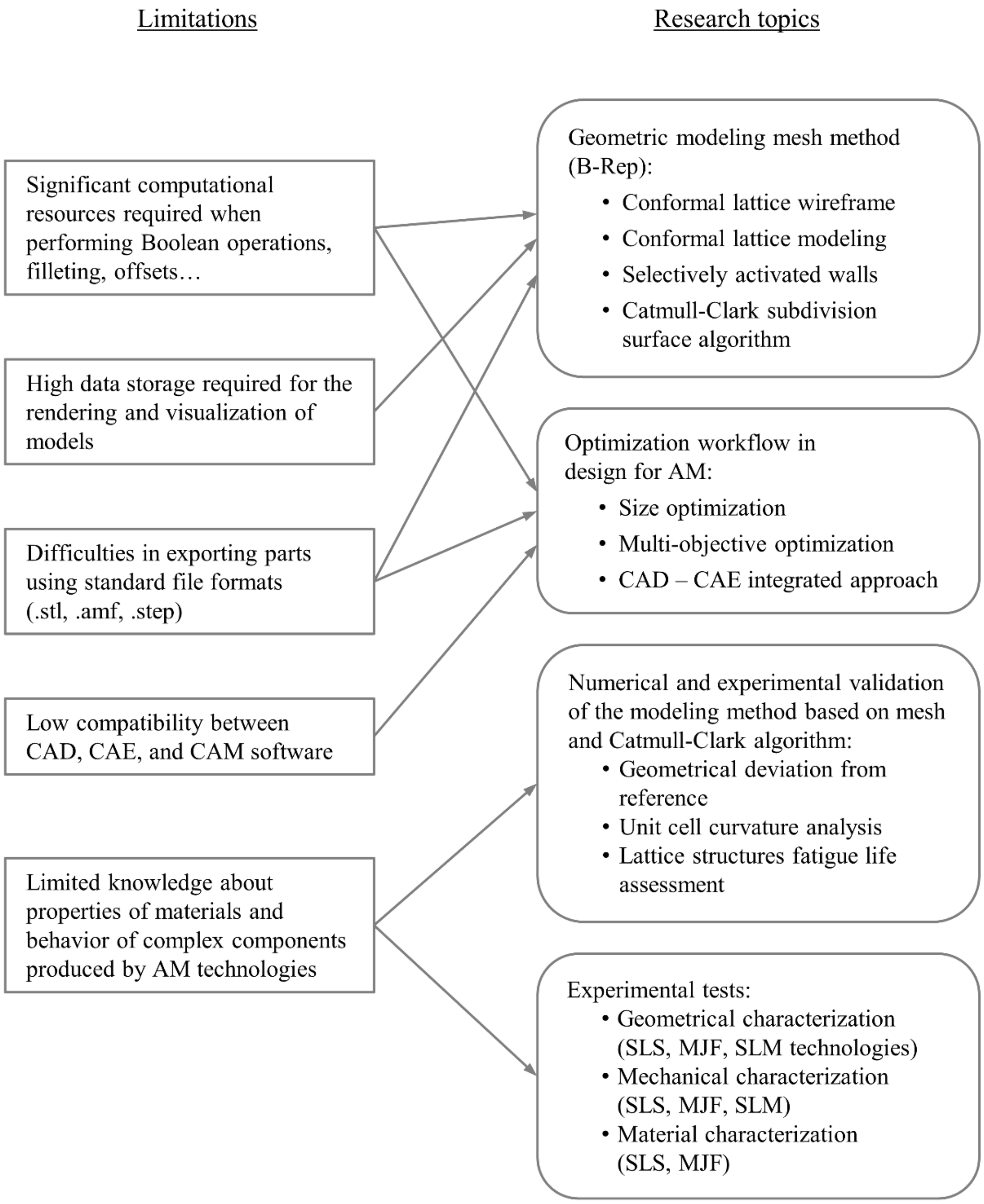
Limitations
Research topics
Significant computational resources required when performing Boolean operations, filleting, offsets…
High data storage required for the rendering and visualization of models
Difficulties in exporting parts using standard file formats (.stl, .amf, .step)
Low compatibility between CAD, CAE, and CAM software
Limited knowledge about properties of materials and behavior of complex components produced by AM technologies
Geometric modeling mesh method (B-Rep):
• Conformal lattice wireframe
• Conformal lattice modeling
• Selectively activated walls
• Catmull-Clark subdivision surface algorithm
Optimization workflow in design for AM:
• Size optimization
• Multi-objective optimization
• CAD – CAE integrated approach
Numerical and experimental validation of the modeling method based on mesh and Catmull-Clark algorithm:
• Geometrical deviation from reference
• Unit cell curvature analysis
• Lattice structures fatigue life assessment
Experimental tests:
• Geometrical characterization (SLS, MJF, SLM technologies)
• Mechanical characterization (SLS, MJF, SLM)
• Material characterization (SLS, MJF)

Figure 21. Limitations highlighted in the literature and research topics addressed in this work to overcome them.

3 Design and optimization of lattice structures

In this chapter, the approaches developed for geometric modeling lattice structures are going to be presented. First, the methods used for generating a conformal lattice wireframe are explained, then the size optimization algorithm used for defining the dimensions of the cross-section of the beams is described, finally, the mesh-based modeling method used for generating the solid model of the lattice structure is presented.

3.1 Conformal wireframe generation

When designing and modeling a lattice structure based on beam-like elements, usually, the starting step consists of the organization of the wireframe inside a design volume. The wireframe is defined as the set of all the segments describing the axes of the beams and, when first defined, does not bring information about the diameters of the struts. Being the wireframe conformal, the unit cells deform to adapt to the boundaries, are never interrupted, and maintain their original topology, as shown in the example in Figure 22.

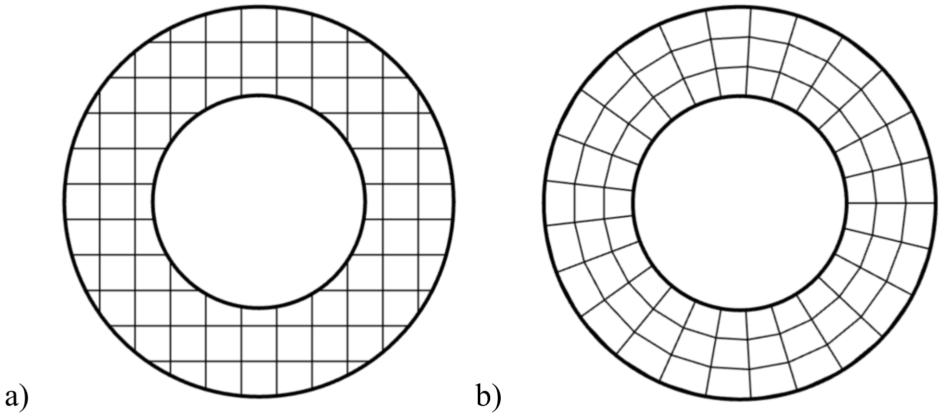

Figure 22. 2D lattice wireframe: a) regular wireframe, b) conformal wireframe. In the conformal wireframe, the topology of the unit cells is maintained at the boundary.

Different approaches for generating 3D conformal wireframes have been studied and are going to be presented below. They are based on operations on curves using commands available in traditional CAD software, on code written ad-hoc, and on the morphing of a regular wireframe to a conformal one through the Free-Form Deformation (FFD) method [229]. For the sake of clarity, the methods will be explained in two dimensions, even if they are developed for 3D applications. More, a simple cubic cell, that in 2D appears as a square, is used, but more complex cells can be implemented as well.

3.1.1 Tween curves division method

The tween curves division (TCD) method works when the bidimensional boundary of the design space can be simplified and described by four edges, namely left, right, top, and bottom curves. The method is implemented by using commands available in commercial CAD software. The steps are as follows:

1. A set of intermediate curves are obtained interpolating the two opposite edges of the design domain, i.e., from the left to the right (Figure 23a) and from the top to the bottom (Figure 23b); these intermediate curves assume a shape influenced depending to the distance to the nearest primitive. The number of curves depends on the number of unit cells desired along a direction.
2. The new curves are trimmed down to the boundaries (Figure 23c).
3. The curves are subdivided by each other.
4. Segments are drawn by connecting the starting and ending points of each curve obtained by the subdivision, and the wireframe model is constructed.

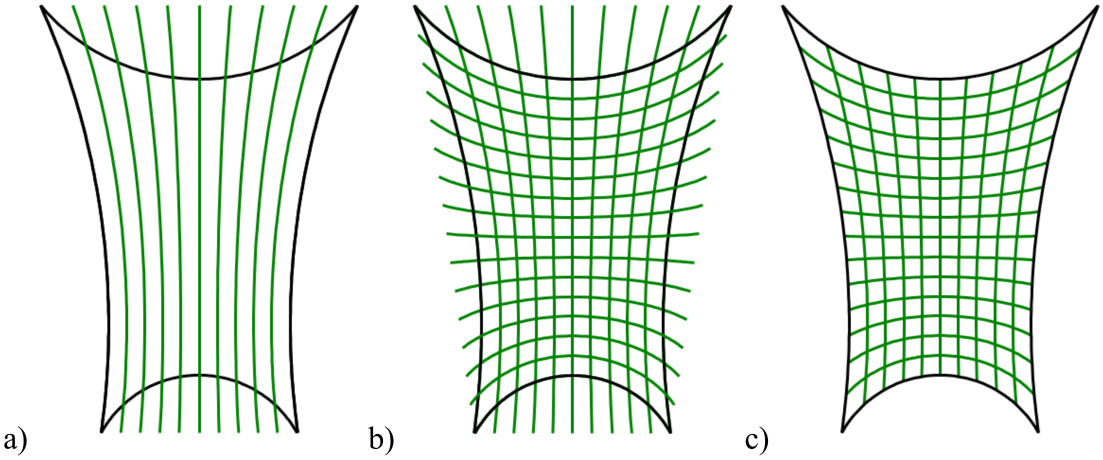

Figure 23. Tween curves division method: a) intermediate curves from left to right, b) intermediate curves from top to bottom, c) wireframe generation after trimming and intersection operations.

3.1.2 Arc division method

The arc division (AD) method uses arcs to obtain the wireframe. As the TCD, the AD method works when the bidimensional boundary of the design space can be described by four edges, and the top and the bottom ones are arcs. The method is implemented by writing an ad-hoc script. The steps are:

1. Based on the left and right curves, the vertical centerline is drawn starting from the midpoint of the upper arc to the midpoint of the lower arc.
2. The left, right, and center curves are subdivided as many times as the number of instances in the y-direction, obtaining a set of points (Figure 24a).
3. Arcs are drawn connecting the three points at each subdivision level (Figure 24b).
4. The obtained arcs are subdivided as many times as the number of the unit cells in the x-direction (Figure 24c).
5. Segments are drawn by connecting the starting and ending points of each curve obtained by the subdivision, and the wireframe model is constructed.

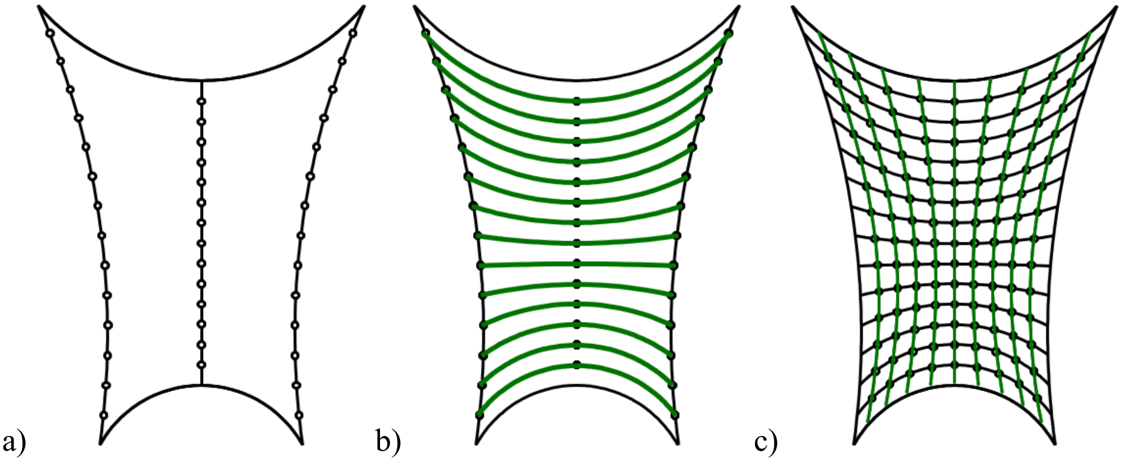

Figure 24. Arc division method: a) left, center, and right lines subdivision according to the number of instances in the y-direction, b) arcs drawing through the three points at each subdivision level, c) arcs subdivision according to the number of instances in the x-direction and final wireframe.

3.1.3 Curvature division method

The curvature division (CD) method exploits the curvature of the boundary of the design domain, and it only works if the four edges can be described as arc curves. The method is implemented by writing an ad-hoc script.

1. The curvatures k_1 and k_n of the upper and lower arc are calculated.
2. a list of *n* curvatures, k_i, $(i = 1..n)$, where n is the number of instances along the y-direction, is created by linearly interpolating the curvature of the upper and lower arc.
3. The vertical centerline is drawn connecting the midpoint of the upper and lower arcs and is divided by *n* points (Figure 25a).

4. An arc is drawn through each one of these n points: the center of the arc lays on the centerline and the radius is computed as the reciprocal of the corresponding curvature, $r_i = {}^{1}/_{k_i}$ (Figure 25b).
5. The same procedure is repeated using the left and right arcs, and the number of instances desired along the x-direction.
6. The arcs are split by each other, and the wireframe is obtained by connecting the starting and ending points of each split curve (Figure 25c).

An improvement of the method could be to connect the centers of the arcs instead of the midpoints of the arcs (at the bulleted point 3). Doing this, the symmetry of the structure is not needed, increasing the applicability of the method.

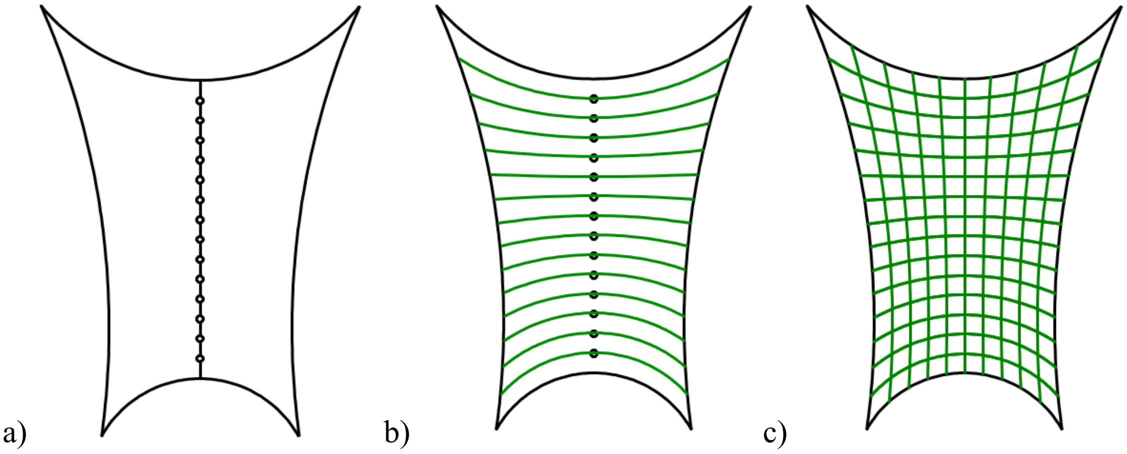

Figure 25. Curvature division method: a) centerline subdivision according to the number of instances in the y-direction, b) arcs through the center-points, with the radius value calculated as the reciprocal of the curvature, c) final wireframe.

3.1.4 NURBS free-form deformation method

The NURBS free-form deformation (NFFD) method uses the FFD approach implemented inside commercial CAD software and, unlike the previous methods, does not require the boundaries to have a specific shape and adapts to more generic design spaces. When using the FFD method [229], the object is surrounded by a trivariate tensor volume that is deformed by moving its nodes and, therefore, the captive object deforms accordingly; this basic idea has been then improved for example combining several tricubic Bezier volumes [230], or enhancing the control of the deformations through control points weighting, via NURBS-based approach [231]. The NFFD method can be performed manually by available commands, or it can be automated by defining a specific transformation of the cage. Furthermore, local warping of the wireframe can be performed by increasing the number of control points and controlling the ones in the region of interest. The steps are as follows:

1. A regular wireframe with the desired number of unit cells along the x- and y-directions is modeled.
2. A 3D NURBS cage is built around the wireframe, defining the number of control points of the cage (Figure 26a, in which the control points are 5 along the x-direction and 3 along the y-direction).
3. The control points at the far ends of the cage are moved towards the vertexes of the design space (Figure 26b).
4. The cage is better adapted to the design space by moving the internal control points (Figure 26c).

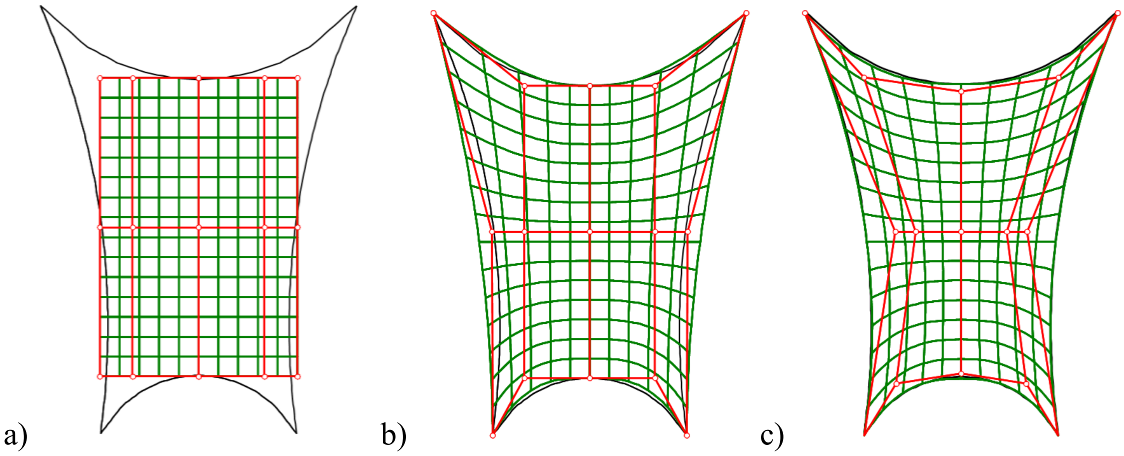

Figure 26. NURBS free-form deformation method: a) regular wireframe, cage around it, and target design space, b) far ends control points of the cage moved through the vertexes of the design space, c) cage adaptation and final wireframe.

3.2 Optimization of lattice structures

Once the conformal wireframe has been modeled, the dimensions of the diameters of the structure need to be assigned. This can be done by adopting different optimization approaches and algorithms. In the following sections, two approaches are presented. The first deals with the size optimization of the diameter of the lattice structure, whereas the second implements a multi-objective optimization based on a genetic algorithm.

3.2.1 Size optimization of lattice structures

The proposed size optimization approach aims to optimize the dimensions of the diameters of the structure, which results in a lightweight model able, at the same time, to withstand the acting loads. The algorithm is developed as described by the workflow in Figure 27 and it allows obtaining heterogeneous lattice structures characterized by beams with different sizes, depending on the position inside the lattice and on the boundary conditions, leading to better performance if compared to homogeneous structures, as stressed by the literature [232,233]. Moreover, it is directly implemented in the CAD software and performs an analysis based on beam elements, resulting in fast results that can be used in the further modeling of the structure in a straightforward way.

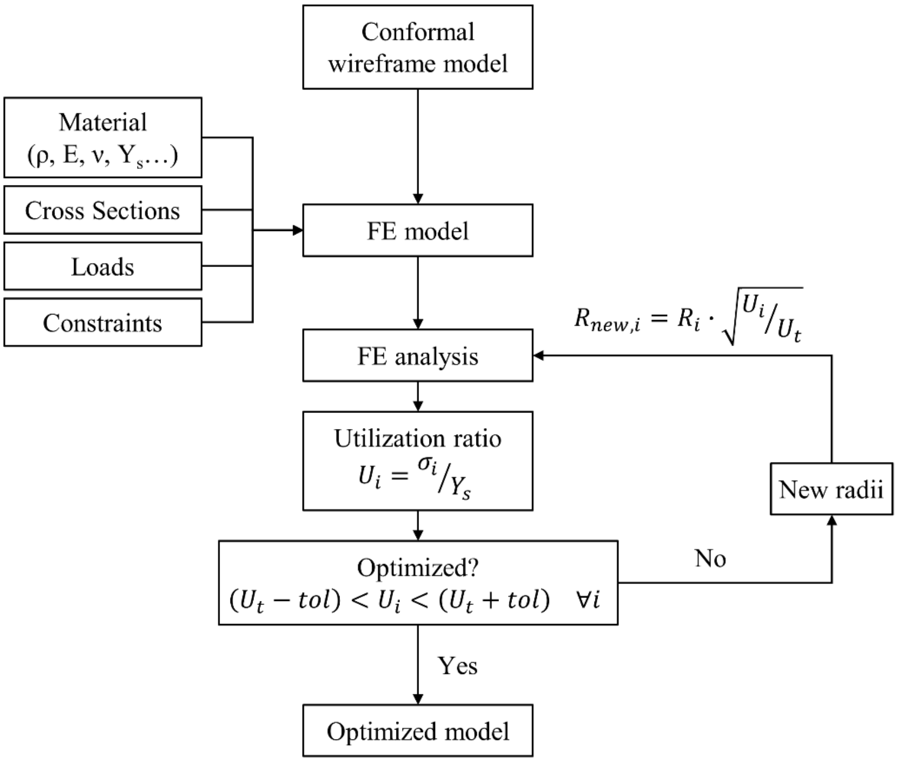
Conformal wireframe model
Material (ρ, E, ν, Y_s…)
Cross Sections
Loads
Constraints
FE model
FE analysis
$R_{new,i} = R_i \cdot \sqrt{U_i/U_t}$
Utilization ratio $U_i = \sigma_i / Y_s$
New radii
No
Optimized? $(U_t - tol) < U_i < (U_t + tol) \quad \forall i$
Yes
Optimized model

Figure 27. Size optimization workflow.

A FE model is set up gathering the required information: loads applied to the original part, constrained nodes, material data (density, ρ, Young's modulus, E, Poisson ratio, ν, Yield stress, Y_s, …), and starting cross-sections. Each segment of the wireframe is treated as a beam element and, as a simplification, the cross-sections are circular. A FE analysis is then performed and among the results, the utilization ratio U is considered. The utilization ratio U quantitively defines the level of usage of the element and is calculated approximating the procedure described in Eurocode 3 [234]. In traction it ranges between 0 when the load on the element is null, and 1, when the Von Mises stress on the element equals the yield stress. In compression the buckling effect is considered too.

The size optimization aims to obtain a structure in which the elements are loaded in the "best possible way" to provide a lightweight part that can bear the external loads at the same time. The objective of this optimization is to guarantee that all the beam elements present the same target utilization ratio U_t, net of a tolerance tol; this is achieved by modifying the radius of the beams not observing the inequality:

$$(U_t - tol) < U_i < (U_t + tol) \qquad \forall\, i$$

If the utilization is higher than required, the beam is thickened, if the utilization is lower than required, the beam is thinned following the radius update rule, and taking into consideration upper and lower bounds for the value of the radius that can depend on the minimum manufacturable feature of the AM technology and the maximum beam size according to the size of the cell:

$$R_{new,i} = R_i \cdot \sqrt{\frac{U_i}{U_t}}$$

$$if\ R_{new,i} < R_{min} \quad then \quad R_{new,i} = R_{min}$$

$$if\ R_{new,i} > R_{max} \quad then \quad R_{new,i} = R_{max}$$

The equation for the update of the radius is obtained considering a cylindrical beam under tensile load, in which the stress σ and the utilization U are defined as:

$$\sigma = \frac{F}{\pi R^2}$$

$$U = \frac{\sigma}{Y_s} = \frac{F}{\pi R^2 Y_s}$$

where Y_s is the yield stress of the material, R is the radius of the beam and F is the axial load. To obtain a utilization U in a beam, the required radius is:

$$R = \sqrt{\frac{F}{\pi U Y_s}}$$

So the radius R_n needed to reach the target utilization U_t is:

$$R_n = \sqrt{\frac{F}{\pi U_t Y_s}}$$

The ratio between R_n and R is:

$$\frac{R_n}{R} = \frac{\sqrt{\frac{F}{\pi U Y_s}}}{\sqrt{\frac{F}{\pi U_t Y_s}}} = \sqrt{\frac{U}{U_t}}$$

So the radius of the next iteration R_n for obtaining the target Utilization U_t is defined as:

$$R_n = R \cdot \sqrt{\frac{U}{U_t}}$$

The FE analyses are iteratively performed until the convergence is reached and the model is optimized, with beams presenting the desired utilization ratio.

The size optimization workflow is implemented in Rhinoceros 7 (Robert McNeel & Associates) CAD software, inside the Grasshopper environment, using Karamba3D plugin [234] blocks and libraries for the FE analyses. Code instructions are written in IronPython programming language to manage the iterative process of size optimization. Figure 28 shows some of the Grasshopper blocks describing the workflow into the canvas; on the left, the four methods for generating the wireframe described in Section 3.1 are connected (one at a time) to the blocks in the central part of the figure. Here, the boundary conditions are set indicating the loads, the constrained nodes, the cross-section shapes, and the material properties (on the top right). On the right can be found the optimization algorithms implemented in IronPython, together with the input parameters such as the minimum and maximum diameters and the Utilization ratio. On the far right, Karamba3D blocks can be used for the visualization of the results directly in the Rhinoceros viewport. Figure 29 shows a section of the code dealing with the size optimization of the beams.

It must be mentioned that the results of the simulations and optimization are preliminary; at the same time, they remain useful in the first design phases, where approximate and quick results are tolerable.

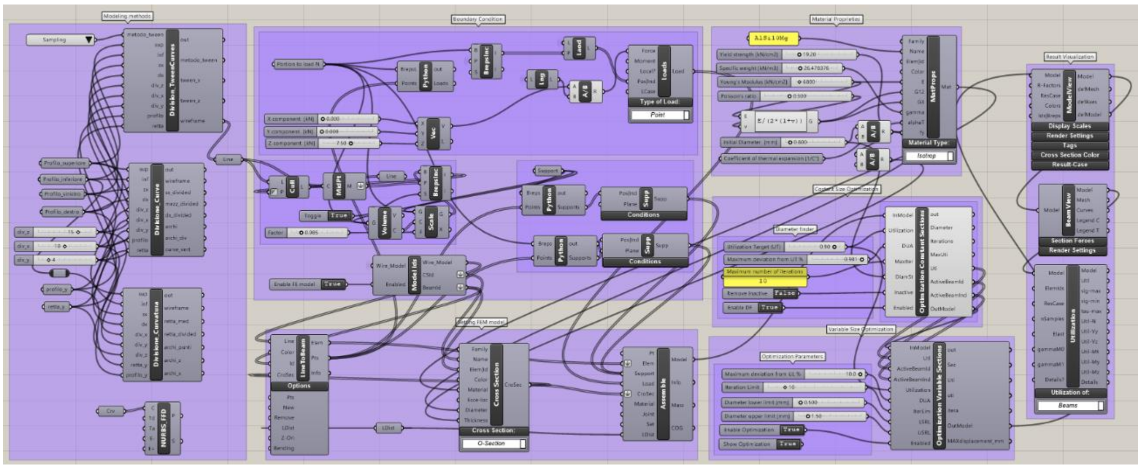

Figure 28. Grasshopper canvas with some of the blocks describing the size optimization workflow. Wireframe generation on the left, FE model setup on the center, size optimization algorithm on the right, visualization tools on the far right.

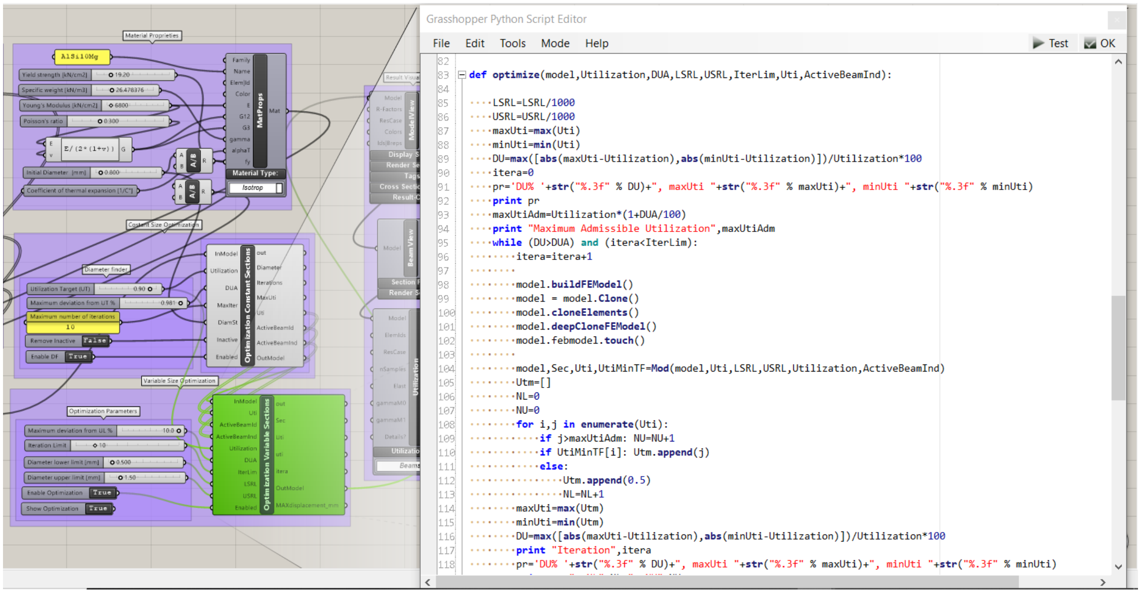

```
def optimize(model,Utilization,DUA,LSRL,USRL,IterLim,Uti,ActiveBeamInd):

    LSRL=LSRL/1000
    USRL=USRL/1000
    maxUti=max(Uti)
    minUti=min(Uti)
    DU=max([abs(maxUti-Utilization),abs(minUti-Utilization)])/Utilization*100
    itera=0
    pr='DU% '+str("%.3f" % DU)+", maxUti "+str("%.3f" % maxUti)+", minUti "+str("%.3f" % minUti)
    print pr
    maxUtiAdm=Utilization*(1+DUA/100)
    print "Maximum Admissible Utilization",maxUtiAdm
    while (DU>DUA) and (itera<IterLim):
        itera=itera+1
        
        model.buildFEModel()
        model = model.Clone()
        model.cloneElements()
        model.deepCloneFEModel()
        model.febmodel.touch()
        
        model,Sec,Uti,UtiMinTF=Mod(model,Uti,LSRL,USRL,Utilization,ActiveBeamInd)
        Utm=[]
        NL=0
        NU=0
        for i,j in enumerate(Uti):
            if j>maxUtiAdm: NU=NU+1
            if UtiMinTF[i]: Utm.append(j)
            else:
                Utm.append(0.5)
                NL=NL+1
        maxUti=max(Utm)
        minUti=min(Utm)
        DU=max([abs(maxUti-Utilization),abs(minUti-Utilization)])/Utilization*100
        print "Iteration",itera
        pr='DU% '+str("%.3f" % DU)+", maxUti "+str("%.3f" % maxUti)+", minUti "+str("%.3f" % minUti)
```

Figure 29. Detail on the implemented code of the size optimization algorithm inside the GhPython block.

3.2.2 Multi-objective optimization of lattice structures

The proposed multi-objective optimization method allows obtaining compromise solutions when dealing with two or more conflicting objectives. The workflow is presented in Figure 30.

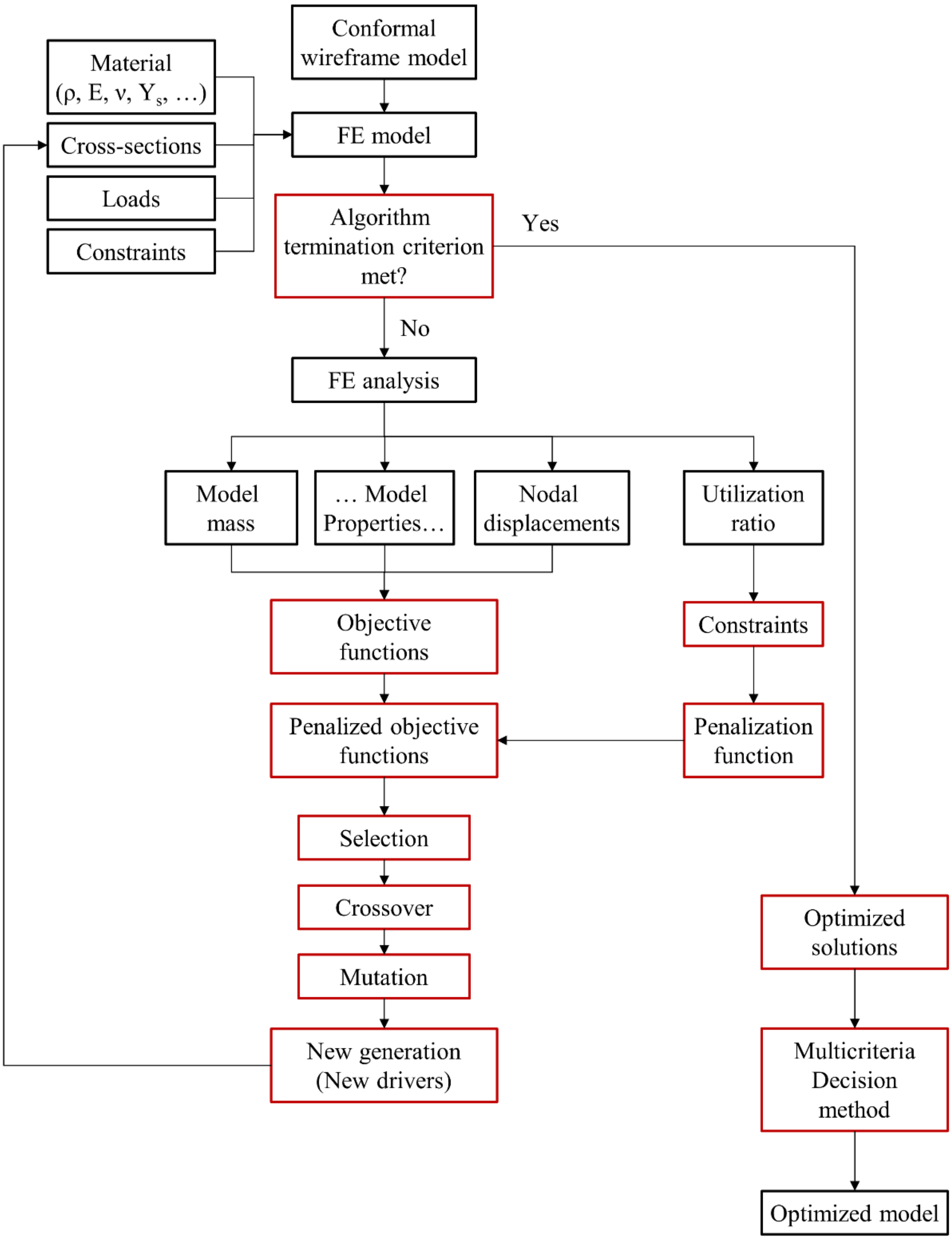
Material
(ρ, E, ν, Y_s, …)
Conformal wireframe model
Cross-sections
FE model
Loads
Constraints
Algorithm termination criterion met?
Yes
No
FE analysis
Model mass
… Model Properties…
Nodal displacements
Utilization ratio
Objective functions
Constraints
Penalized objective functions
Penalization function
Selection
Crossover
Mutation
New generation (New drivers)
Optimized solutions
Multicriteria Decision method
Optimized model

Figure 30. Multi-objective optimization workflow. Blocks in red deal with the multi-optimization phases.

As for the size optimization, the conformal wireframe is used as an input for the creation of the FE model, together with the boundary conditions such as the material, the cross-section types and initial diameters of the beams, the loads, and the constraints; among them, the size of the diameters of the beams act as optimization driver and is iteratively varied by the algorithm. The FE analysis is then performed and the following information is extracted:

- The objective properties that are being optimized. They can be the mass of the model, the nodal displacements, the natural frequencies, …
- The utilization ratio U.

The utilization ratio acts as a constraint in the optimization algorithm because it cannot exceed a predefined value U_{lim}. A penalization function is introduced to penalize the solution if U_{lim} is exceeded. The variable $g(x)$ is defined as:

$$g(x) = U_{max,sol} - U_{lim}$$

$$\left(if\ U_{max,sol} > U_{lim} \quad then \ \ g(x) > 0\right)$$

Where $U_{max,sol}$ is the maximum utilization of the beams of the model of the currently evaluated solution. Then, the violation variable v is defined as:

$$v(x) = max\{0, -g(x)\}$$

The penalization function $P(x)$ is obtained as:

$$P(x) = k \cdot \big(v(x)\big)^2$$

Where k is a penalty parameter tuned depending on the specific situation. Finally, the penalized objective function $F(x)$ is calculated as:

$$F(x) = f(x) + P(x)$$

Where $f(x)$ is the un-penalized objective function evaluated on the objective properties of the solution.

After that, the typical operations of genetic algorithms are performed [235]. After choosing the number of individuals of the population, i.e., the number of FE models to compare between each other, and the number of generations, i.e., the number of times new groups of individuals are created, the selection, crossover, and mutation phases are executed. In the selection phase (Figure 31a), the natural selection of the fittest individual in nature is simulated; the FE models presenting the optimization drivers that minimize or maximize the objective properties will have a higher chance to survive and “reproduce”. The crossover (or recombination) phase (Figure 31b) deals with the creation of the new generation; two of the individuals selected in the previous phase, the parents, will produce two new solutions, the children, by the combination of their “chromosomes”, i.e., the information about the optimization drivers. The mutation (Figure 31c) is the last operator, in which some of the chromosomes of the children’s solutions are randomly modified; the mutation phase is important because it avoids to stuck in local solutions.

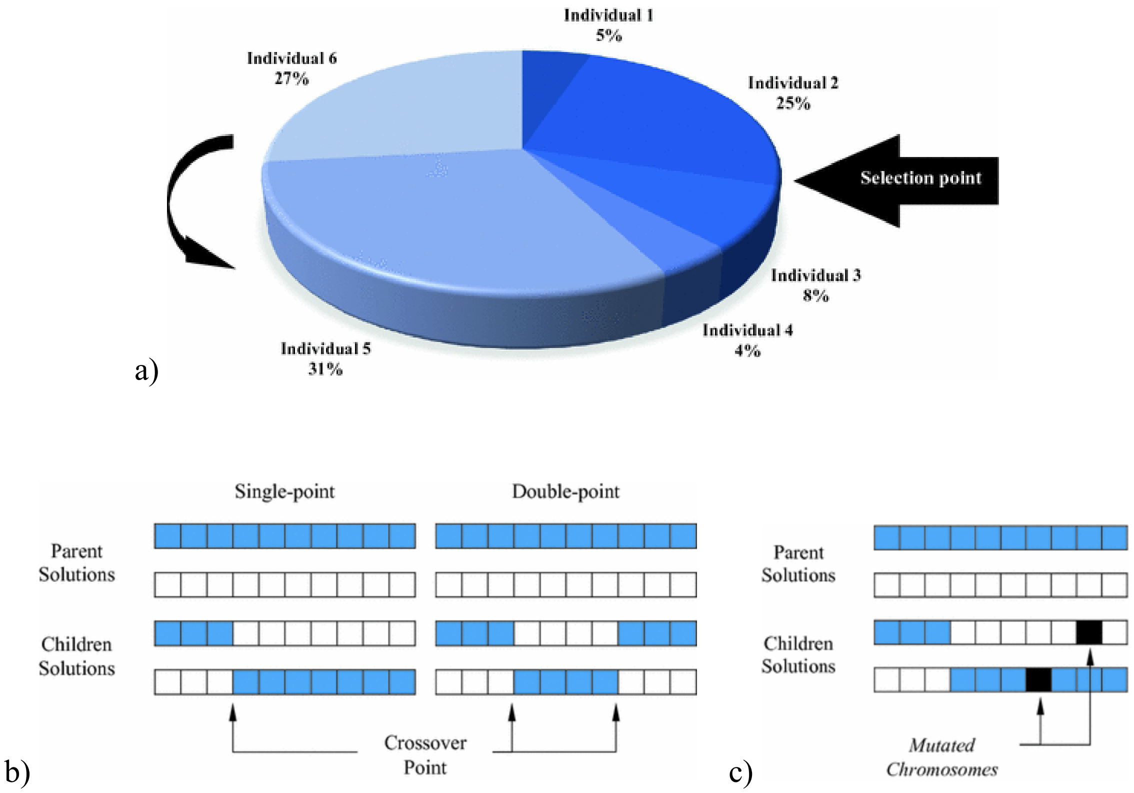
Individual 1
5%
Individual 6
27%
Individual 2
25%
Selection point
Individual 3
8%
Individual 4
4%
Individual 5
31%
a)
Single-point
Double-point
Parent
Solutions
Children
Solutions
Crossover
Point
b)
Parent
Solutions
Children
Solutions
Mutated
Chromosomes
c)

Figure 31.Genetic algorithm phases [235]: a) selection phase, b) crossover phase, and c) mutation phase.

Once the mutation has been performed, a new generation of individuals with new drivers is available for repeating the workflow. The procedure is iteratively repeated until the number of generations reaches the set value. As a result, the last generation of individuals includes the most promising solutions for the multi-objective optimization problem. Since there is not the best solution among the others, an algorithm exists to establish which solution to select. One of the methods could be the multicriteria decision method (MCDM) using a multicriteria tournament decision (MTD), where a tournament-based method ranks the solutions in the Pareto frontier according to the objectives of the problem and the preferences of the user adopting weights [175,236].

The multi-optimization workflow is implemented in Rhinoceros 7 (Robert McNeel & Associates) CAD software, inside the Grasshopper environment and using Karamba3D plugin [234] as FE solver and Octopus plugin [237] as multi-objective evolutionary optimization. Figure 32 shows the Grasshopper canvas with the implemented workflow. From the left, the blocks used for modeling the external shell and the internal lattice structures are highlighted, then the FE model is set up and analyzed using the blocks from the Karamba 3D plugin; the mass and the first natural frequency are obtained from the FE analysis and are used for the calculation of the penalty functions. Finally, the penalized objective functions are used as inputs for the genetic algorithm solver, Octopus. The solver is connected to the first block on the left to control the optimization drivers.

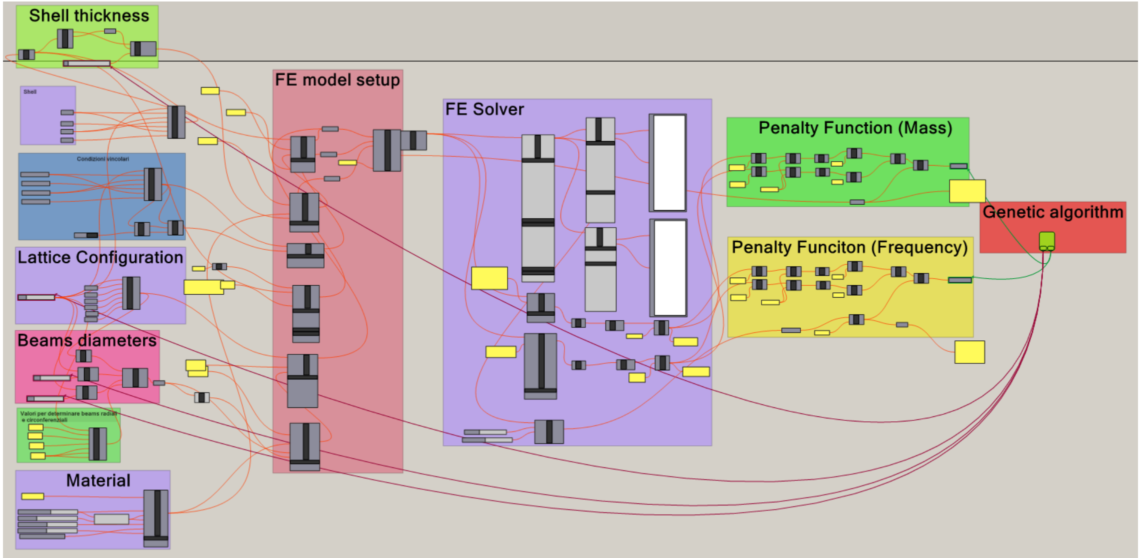
Shell thickness
Shell
Condizioni vincolari
Lattice Configuration
Beams diameters
Valori per determinare beams radiali e circonferenziali
Material
FE model setup
FE Solver
Penalty Function (Mass)
Penalty Funciton (Frequency)
Genetic algorithm

Figure 32. Multi-objective optimization workflow implemented in Grasshopper (Rhinoceros 7). (Connecting lines are red because the solver was locked)

Figure 33 shows the graphic user interface of the Octopus plugin. The central zone is occupied by the Pareto chart, showing the solutions of the current and previous generations. On the left side, the display settings for the Pareto chart and the statistics of the optimization process can be found. On the right side, the parameters related to the genetic algorithm can be set. In the lower part of the interface, on the left, the genetic distance graph is plotted and gives an overview of the convergence of the search (the denser, the better). In the middle, the list of the optimization objectives is shown and the corresponding axes of the Pareto chart can be decided; on the bottom right, the convergence graphs for each objective parameter are plotted.

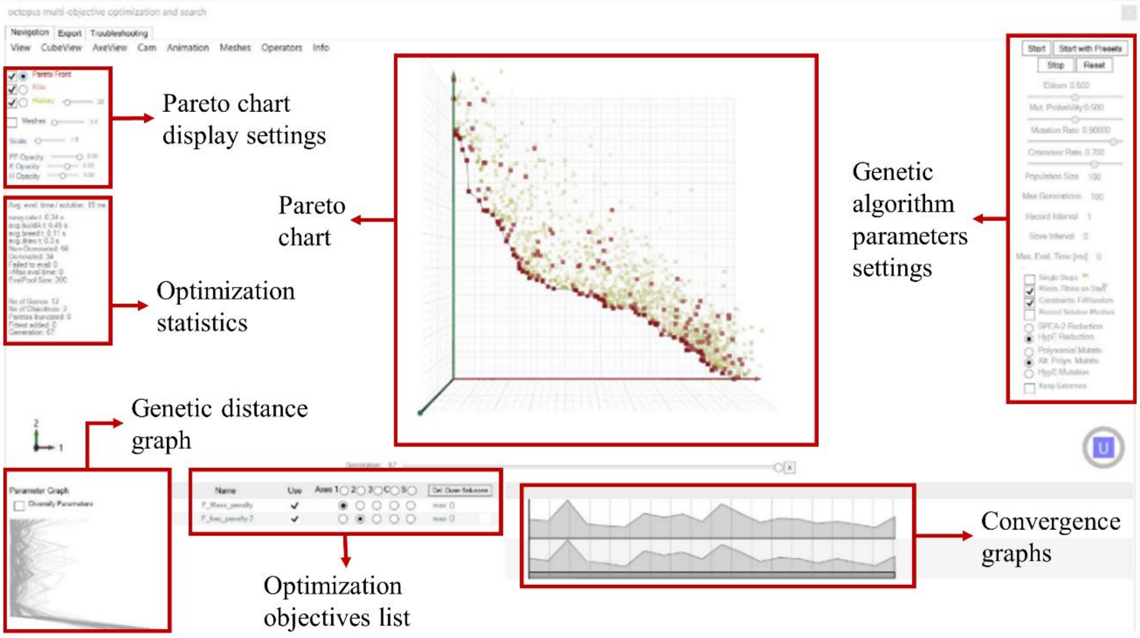
Pareto chart display settings
Pareto chart
Optimization statistics
Genetic algorithm parameters settings
Genetic distance graph
Optimization objectives list
Convergence graphs

Figure 33. Graphical user interface of Octopus plugin.

3.3 Geometric modeling of conformal lattice structures

When the wireframe has been generated and the size optimization has been performed, the geometric modeling of the solid model of the lattice structure is carried out. An approach based on the B-Rep mesh modeling method is adopted. Two methods are presented in the following sections. The first allows the geometric modeling of conformal lattice structures computing the nodal vertexes of the mesh by the intersection of cylinders; the second selectively introduces internal walls in desired zones of the lattice by closing the faces of the cells of the lattice.

3.3.1 Geometric modeling of lattice structures with beam elements

In order to model lattice structures characterized by beam elements, a suitable data structure was developed (Figure 34). The nodes are stored in an indexed position and contain information about the coordinates to identify their spatial position, the list of the indexes of the beams that arrive at the node, and the maximum diameter of the ones of the beams arriving at the node. The beams too are stored in an indexed position and as information, they bring the index of the node at the starting point, the index of the node of the ending point, and the value of the diameter resulting from the size optimization.

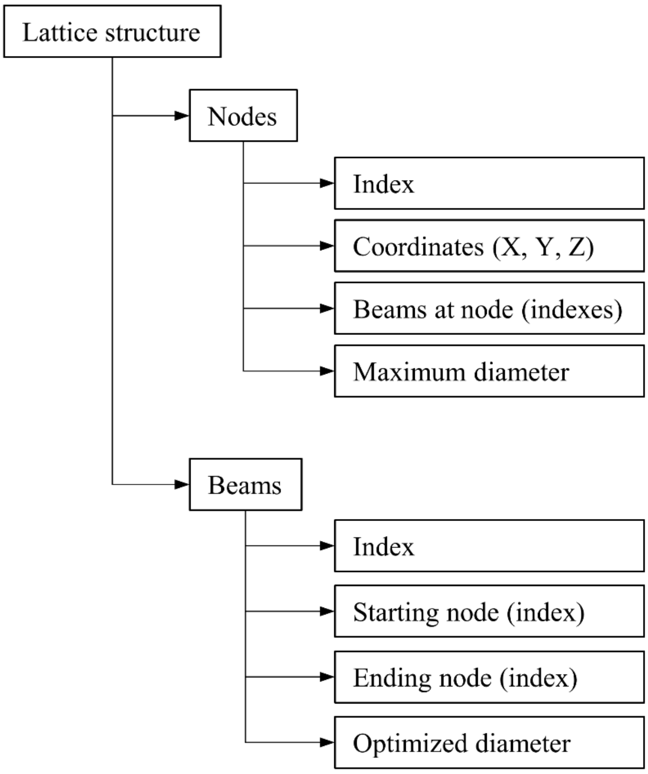
Lattice structure
Nodes
Index
Coordinates (X, Y, Z)
Beams at node (indexes)
Maximum diameter
Beams
Index
Starting node (index)
Ending node (index)
Optimized diameter

Figure 34. Data structure for the modeling method of conformal lattice structures with beams elements.

The meshed lattice structure is then modeled performing the following operations:

1. In the proximity of each nodal point, cylinders are modeled around the segments of the wireframes; the diameter of the cylinders equals the maximum diameter of the optimized ones of the beams arriving at that node (Figure 35b).
2. The intersections between the cylinders are performed and the resulting points will be the vertexes of the mesh (Figure 35b, points in blue).
3. For each beam, four lines linking the eight vertexes (four at the starting node, and four at the ending node) are drawn (Figure 35c, lines in green).
4. The midpoints of the four lines are extracted, obtaining four new vertexes of the mesh model. These vertexes are repositioned according to the optimized value of the radius of the beam (Figure 35c).
5. Each beam is modeled with an eight-faces mesh, resulting from the connection of the twelve vertexes, and assuming a double truncated pyramidal shape (Figure 35d).

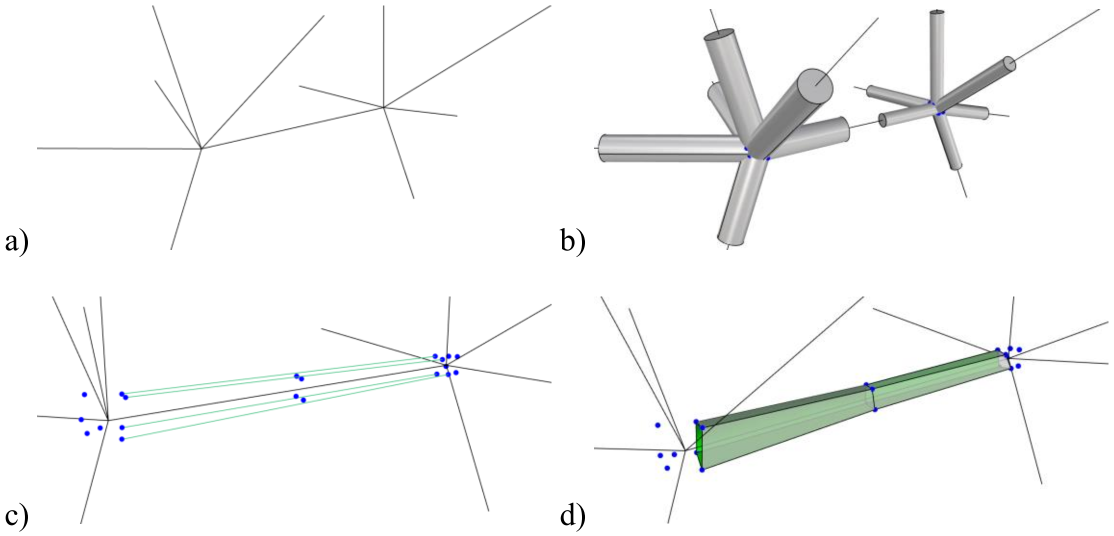

Figure 35. Geometric modeling of conformal lattice structures with beam elements: a) starting conformal wireframe, b) cylinders at the nodal points with their mutual intersections (points in blue), c) lines connecting the eight corresponding vertexes and rescaled midpoints, and d) eight-face mesh modeling a beam.

3.3.1.1 Subdivision surface schemes

The resulting lattice structure appears as a coarse mesh, with sharp edges. To smooth the model, subdivision surface schemes can be applied. The subdivision surface modeling dates back in the late 1970s, with the publication of the works of Catmull and Clark [92] and Doo and Sabin [91], and have gained popularity both in the computer graphics and in engineering applications [238,239]. A subdivision scheme enables to define a smooth surface as the limit of a sequence of successive refinements of a starting coarser mesh. Usually, these schemes act on regular meshes, i.e., meshes with identical faces, that can be squares, equilateral triangles, and regular hexagons. Since the meshes based on hexagons are not common, two types of regular subdivision schemes are found: those defined for quadrilateral meshes and those defined for triangular ones. A variety of subdivision schemes exists, and they can be classified according to several criteria: the type of refinement rule, whether the scheme is approximating or interpolating, and the degree of achievable smoothness (C1, C2, etc…). The refinement rule used by the subdivision schemes can be face-split, also called primal schemes, or vertex-split, also called dual schemes. In the face-split methods, each face of the starting mesh is divided into four faces by inserting new vertices on the edges. In the vertex-split methods, instead, for each old vertex new vertexes are generated in the faces adjacent to the vertex; depending on the starting mesh, the vertex split approaches can result in meshes containing hexagonal faces. Table 1 organizes the most diffused subdivision schemes according to this classification.

Table 1. Subdivision schemes classification.

	Face-split		Vertex-split
	Triangular meshes	Quadrangular meshes	Doo-Sabin [91] (C1), Mid-Edge [240] (C1), Biquartic [241] (C2)
Approximating	Loop [242] (C2)	Catmull-Clark [92] (C2)	
Interpolating	Mod. Butterfly [243] (C1)	Kobbelt [244] (C1)	

At each iteration of the subdivision algorithm, new vertexes are computed averaging the old vertexes coordinates and considering the weights attributed to the old vertexes. Different subdivision approaches present different weights at the vertexes, as shown in Figure 36 [222].

Among the methods, the Catmull-Clark subdivision surface algorithm [92] is applied. At every iteration, the Catmull-Clark algorithm splits each quad face of the mesh into four smaller quad faces. As a feature, this algorithm always results in meshes characterized by quad faces, independent of the starting mesh that could present arbitrary polygonal faces;

indeed, they can be reduced to a quadrilateral mesh prior to the execution of the subdivision algorithm.

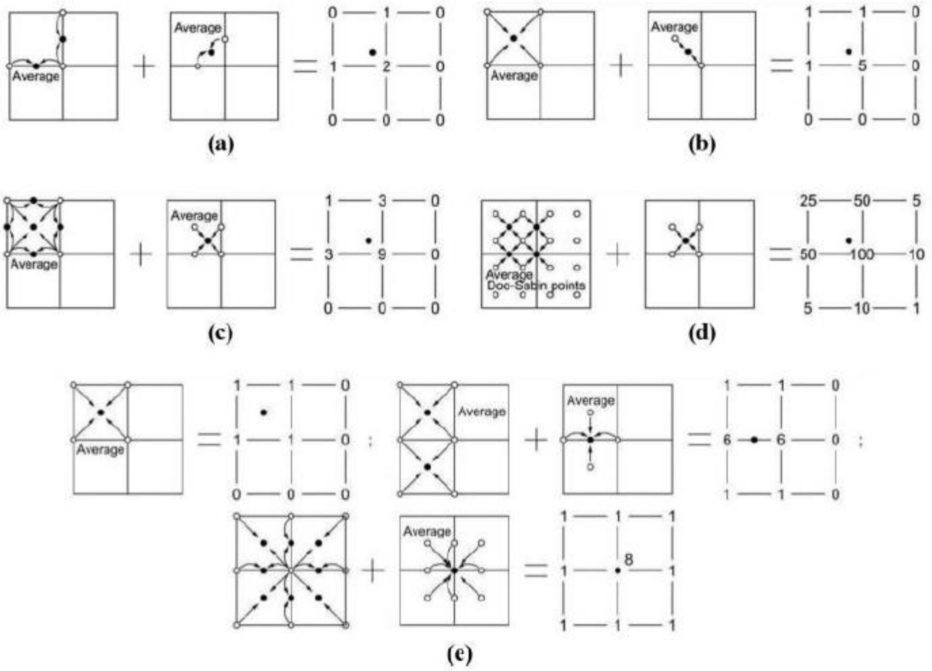

Figure 36. Vertexes generation in different subdivision surface algorithms: a) Mid-Edge, b) Proposed by Savio et al. [222], c) Doo-Sabin, d) Bi-Quartic, e) Catmull-Clark. [222]

The subdivided mesh presents a C2 (curvature) continuity everywhere, except at the extraordinary vertexes, that are vertexes with valence higher than four, i.e., vertexes that are shared by more than four edges, where the continuity is C1 (tangency) [245]. Figure 37 shows an example of refinement based on a lattice structure with the gyroid TPMS unit cell after 4 iterations of the Catmull-Clark algorithm.

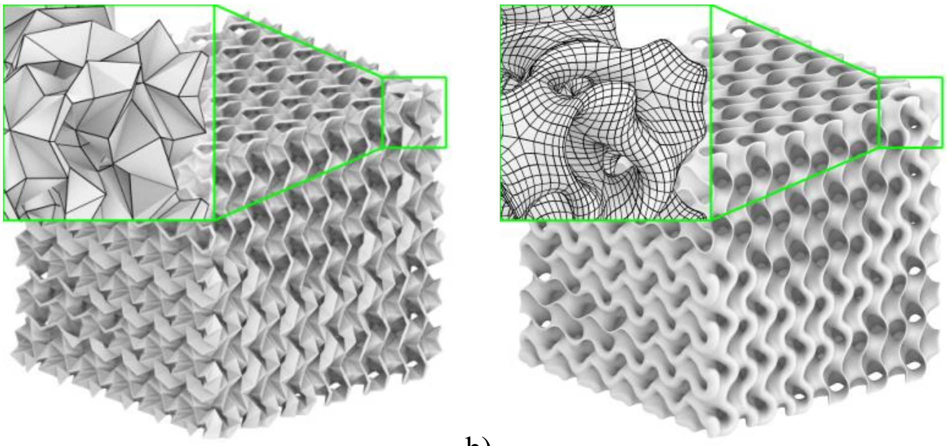

a) b)

Figure 37. Refinement of a gyroid lattice structure: a) starting mesh, b) refined mesh after 4 iterations of the Catmull-Clark algorithm [246].

3.3.2 Internal walls and external skin integration

An important attribute for cellular structures is the possibility of introducing surfaces acting as walls and skins. Figure 38 shows two simple lattice structures; they both present external skins on the top, bottom, and sides, defined as surfaces that connect the beams at the extremities of the structure. More, the lattice at the right presents an internal wall, defined as a surface between two internal adjacent cells that hinders the communication between these cells. Adding an external skin increases the stiffness of the part, isolates the parts from the outside preventing the entrance of undesired material and/or the leakage of internal liquids. Internal walls can locally play the same role as the external skin; for instance, the stiffness properties can be changed along the component adding or deleting walls; furthermore, the presence of internal walls can be designed to create internal ducts in which one or more fluids can flow acting as heat exchangers or materials transporters.

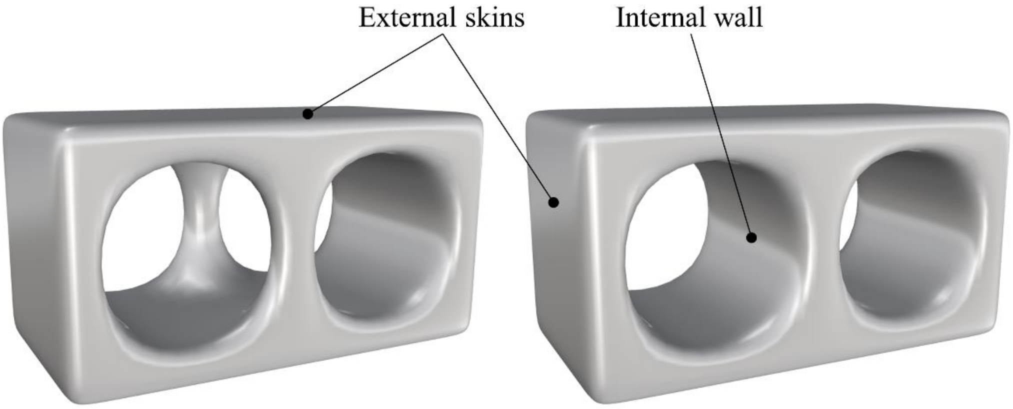

Figure 38. Definition of external skins and internal walls.

A geometric modeling method was developed to design lattice structures with selectively activated internal walls and external skin. First, the data structure was organized as shown in Figure 39. The lattice structure is considered as a 3D matrix containing the unit cells, ordered according to the number of repetitions along the x-, y-, and z-direction, n_x, n_y and n_z (Figure 40a). Each cell can be retrieved by its index number, $Cell_{index}$, or by the relative position inside the lattice; these two values are related by the equation:

$$Cell_{index} = k \cdot n_x \cdot n_y + j \cdot n_x + i$$

where n_x, n_y are the number of instances along the x- and y-direction, and i, j, k are the relative positions inside the lattice, along the x-, y-, and z-direction, respectively. The

i, j, k indexes are also used to test if a cell is internal or at the boundary and are defined as:

$$0 \leq i < n_x, \qquad if\ \big((i = 0)\ or\ (\ i =\ n_x - 1)\big)\ \rightarrow then\ boundary$$

$$0 \leq j < n_y, \qquad if\ \big((j = 0)\ or\ (\ j =\ n_y - 1)\big)\ \rightarrow then\ boundary$$

$$0 \leq k < n_z, \qquad if\ \big((k = 0)\ or\ (\ k =\ n_z - 1)\big)\ \rightarrow then\ boundary$$

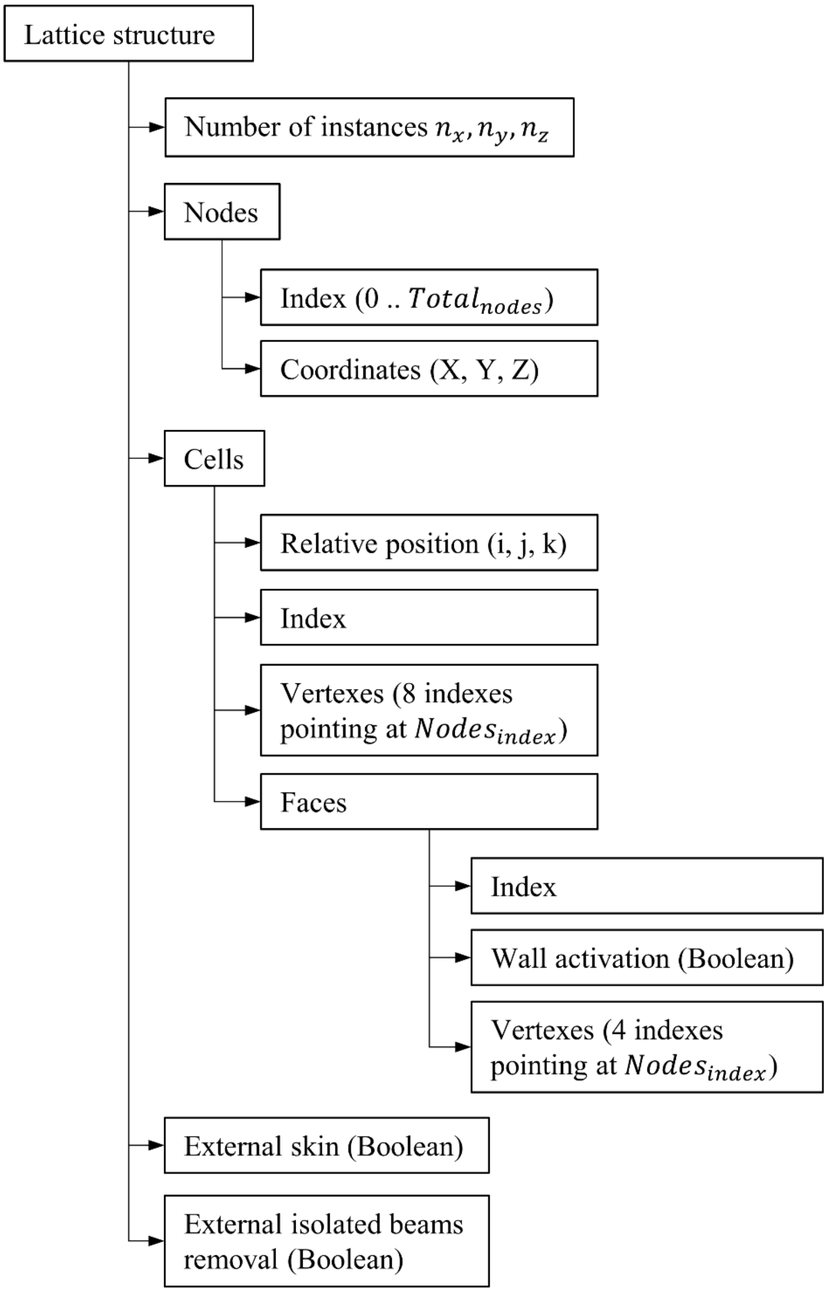
Lattice structure
Number of instances n_x, n_y, n_z
Nodes
Index (0 .. $Total_{nodes}$)
Coordinates (X, Y, Z)
Cells
Relative position (i, j, k)
Index
Vertexes (8 indexes pointing at $Nodes_{index}$)
Faces
Index
Wall activation (Boolean)
Vertexes (4 indexes pointing at $Nodes_{index}$)
External skin (Boolean)
External isolated beams removal (Boolean)

Figure 39. Data structure for the modeling method of lattice structures with internal walls and external skin.

More, the ordered list of the nodes of the cellular structure is stored to quickly obtain point information through the indexes of the node. This list contains all the nodes of the structure.

Each cell contains data about the eight vertexes. They are ordered in a list, so the position in the list, from 0 to 7, identifies the vertex position in the considered cell, as in Figure 40b, and the values stored inside the list identify the indexes of the nodes to retrieve the spatial position. Furthermore, the faces information is stored. The six faces of the cell gather a Boolean variable indicating whether the wall on that face will be activated or not. Finally, the four indexes of the vertexes of each one of the six faces are available. As for the vertexes, the faces of a cell are identified by six indexes, from 0 to 5, as shown in Figure 40c.

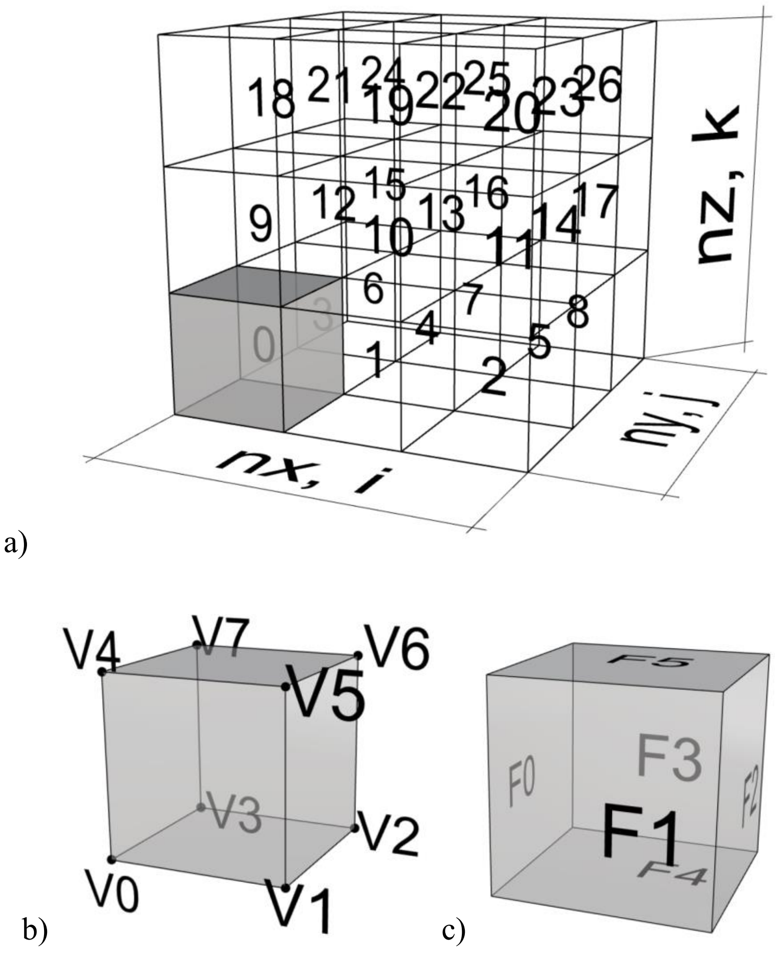

Figure 40. Data structure visualization for the modeling of lattice structures with skins and walls integration: a) organization of the cells with the cell_{index} displayed, b) cell vertexes with internal index, i.e., the position in the vertexes list in the cell structure, and c) cell faces with internal index, i.e., the position in the faces list in the cell structure.

The creation of the lattice structure is operated starting from the first unit cell and then moving on the next cells by iterating on the x-, y-, and z-direction using a “look forward, look sideward, and look upward” approach. For clarity’s sake, the modeling of the beams and the modeling of the skins will be first described separately.

When modeling the beams, the starting cells of the structure in Figure 40 are first scaled with respect to the centroid by a factor that allows obtaining the desired beam dimensions; the organization of the data structure, i.e., the indexes of the elements is maintained, and the new vertexes coordinates are updated. The result is shown in Figure 41.

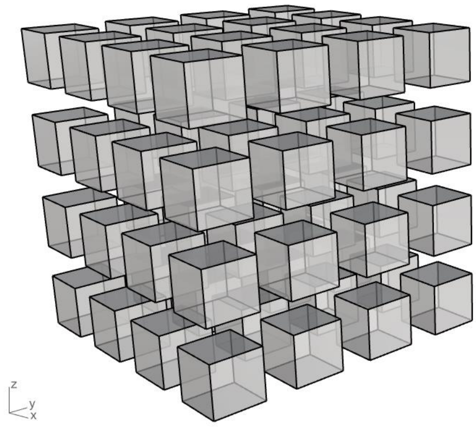

Figure 41. Scaled cells used for the modeling of the lattice structure.

Then, each cell is cycled to model the beams of the structure. Using the “look forward, look sideward, and look upward” approach, three beams for each internal cell are modeled: one aligned to the x-axis, one aligned to the y-axis, and one aligned to the z-axis. Figure 42 considers the current cell (red), identified by the indexes i, j, k and the surrounding ones (cyan) for the beam creation.

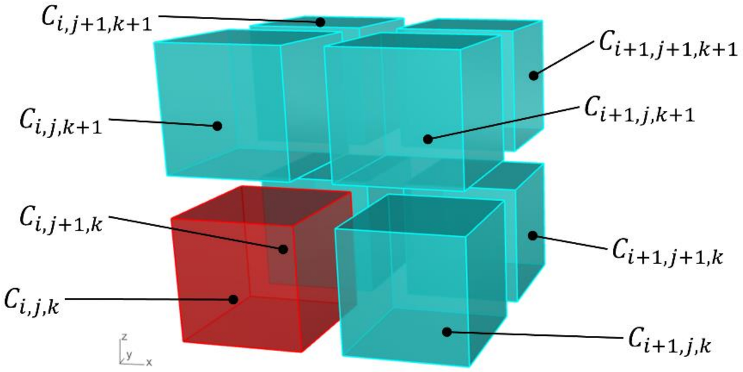
$C_{i,j+1,k+1}$
$C_{i+1,j+1,k+1}$
$C_{i,j,k+1}$
$C_{i+1,j,k+1}$
$C_{i,j+1,k}$
$C_{i+1,j+1,k}$
$C_{i,j,k}$
$C_{i+1,j,k}$
z
y
x

Figure 42. Cells considered for the modeling of the beams. The red cell is the one that is currently considered, the cyan cells are the adjacent ones used for creating the faces of the beams.

For the creation of the beam aligned to the x-axis, the following adjacent cells and the relative vertexes are considered (the index of the vertex refers to Figure 40b):

- Cell position: $i, j + 1, k$; vertex indexes: 4, 5.
- Cell position: $i, j, k + 1$, vertex indexes: 2, 3.
- Cell position: $i, j + 1, k + 1$, vertex indexes: 0, 1.

Four quad mesh faces are then created to obtain the beam by using the vertexes of the considered cell and of the adjacent ones:

- Face 1 vertexes: 6 (i, j, k), 7 (i, j, k), 4 $(i, j + 1, k)$, 5 $(i, j + 1, k)$.
- Face 2 vertexes: 5 $(i, j + 1, k)$, 4 $(i, j + 1, k)$, 0 $(i, j + 1, k + 1)$, 1 $(i, j + 1, k + 1)$.
- Face 3 vertexes: 1 $(i, j + 1, k + 1)$, 0 $(i, j + 1, k + 1)$, 3 $(i, j, k + 1)$, 2 $(i, j, k + 1)$.
- Face 4 vertexes: 2 $(i, j, k + 1)$, 3 $(i, j, k + 1)$, 7 (i, j, k), 6 (i, j, k).

The beam along the x-direction is shown in Figure 43.

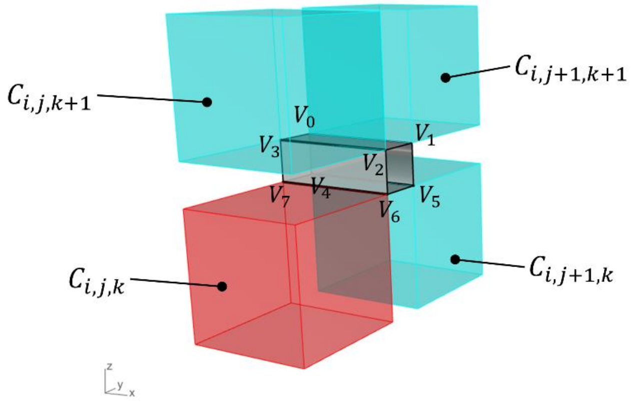
$C_{i,j,k+1}$
$C_{i,j+1,k+1}$
V_0
V_1
V_3
V_2
V_7
V_4
V_5
V_6
$C_{i,j,k}$
$C_{i,j+1,k}$
z
y
x

Figure 43. Modeling of the beam aligned to the x-axis. Current cell in red, adjacent cells in cyan.

The same procedure is followed for the modeling of the beams aligned to the y- and z-axis.

For the creation of the beam aligned to the y-axis, the following adjacent cells and the relative vertexes are considered:

- Cell position: $i + 1, j, k$; vertex indexes: 4, 7.
- Cell position: $i, j, k + 1$, vertex indexes: 1, 2.
- Cell position: $i + 1, j, k + 1$, vertex indexes: 0, 3.

Four quad mesh faces are then created to obtain the beam by using the vertexes of the considered cell and of the adjacent ones:

- Face 1 vertexes: 6 (i, j, k), 5 (i, j, k), 1 $(i, j, k + 1)$, 2 $(i, j, k + 1)$.
- Face 2 vertexes: 2 $(i, j, k + 1)$, 1 $(i, j, k + 1)$, 0 $(i + 1, j, k + 1)$, 3 $(i + 1, j, k + 1)$.
- Face 3 vertexes: 3 $(i + 1, j, k + 1)$, 0 $(i + 1, j, k + 1)$, 4 $(i + 1, j, k)$, 7 $(i + 1, j, k)$.
- Face 4 vertexes: 7 $(i + 1, j, k)$, 4 $(i + 1, j, k)$, 5 (i, j, k), 6 (i, j, k).

The beam along the y-direction is shown in Figure 44.

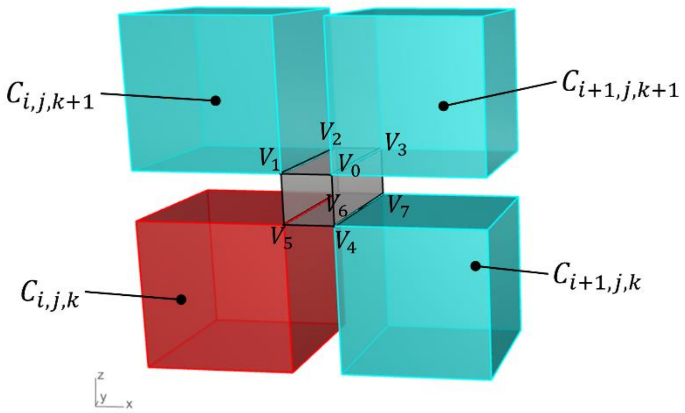

Figure 44. Modeling of the beam aligned to the y-axis. Current cell in red, adjacent cells in cyan.

Finally, for the creation of the beam aligned to the z-axis, the following adjacent cells and the relative vertexes are considered:

- Cell position: $i + 1, j, k$; vertex indexes: 3, 7.
- Cell position: $i, j + 1, k$, vertex indexes: 1, 5.
- Cell position: $i + 1, j + 1, k$, vertex indexes: 0, 4.

Four quad mesh faces are then created to obtain the beam by using the vertexes of the considered cell and of the adjacent ones:

- Face 1 vertexes: 6 (i, j, k), 2 (i, j, k), 3 $(i + 1, j, k)$, 7 $(i + 1, j, k)$.
- Face 2 vertexes: 7 $(i + 1, j, k)$, 3 $(i + 1, j, k)$, 0 $(i + 1, j + 1, k)$, 4 $(i + 1, j + 1, k)$.
- Face 3 vertexes: 4 $(i + 1, j + 1, k)$, 0 $(i + 1, j + 1, k)$, 1 $(i, j + 1, k)$, 5 $(i, j + 1, k)$.
- Face 4 vertexes: 5 $(i, j + 1, k)$, 1 $(i, j + 1, k)$, 2 (i, j, k), 6 (i, j, k).

The beam along the z-direction is shown in Figure 45.

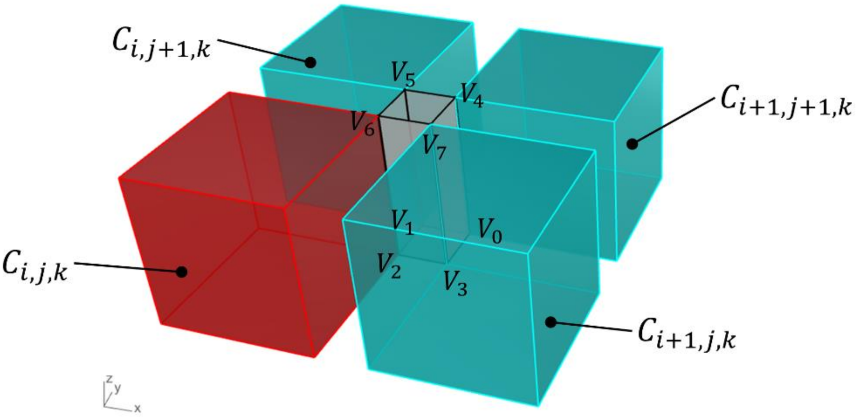

Figure 45. Modeling of the beam aligned to the z-axis. Current cell in red, adjacent cells in cyan

For the cells at the boundaries, only one beam is modeled depending on which axis limit is reached. For the boundary beams, the caps are added as quad faces.

$$if\ i = n_x - 1\ (x_{axis}\ limit), then\ model\ x_{beam}$$

$$if\ j = n_y - 1\ (y_{axis}\ limit), then\ model\ y_{beam}$$

$$if\ k = n_z - 1\ (z_{axis}\ limit), then\ model\ z_{beam}$$

Once all the beams have been modeled, a simple regular lattice structure is obtained as in Figure 46.

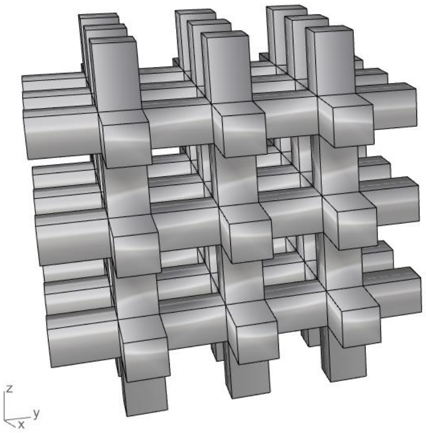

Figure 46. Regular lattice structure resulting from the beam modeling.

After the modeling of the beams, the modeling of the faces of the internal skins is addressed. Again, each cell is cycled and the Boolean value indicating whether a face needs a skin or not is checked. For each cell, using the "look forward, look sideward, and look upward" approach, three faces are checked, whose indexes are 2, 3, and 5 (referring to Figure 40c). Figure 47 shows the current cell (red) and the adjacent cells (blue) that are linked when dealing with the skin creation:

- Face 2 is linked to face 0 of the $i+1, j, k$ cell.
- Face 3 is linked to face 1 of the $i, j+1, k$ cell.
- Face 5 is linked to face 4 of the $i, j, k+1$ cell.

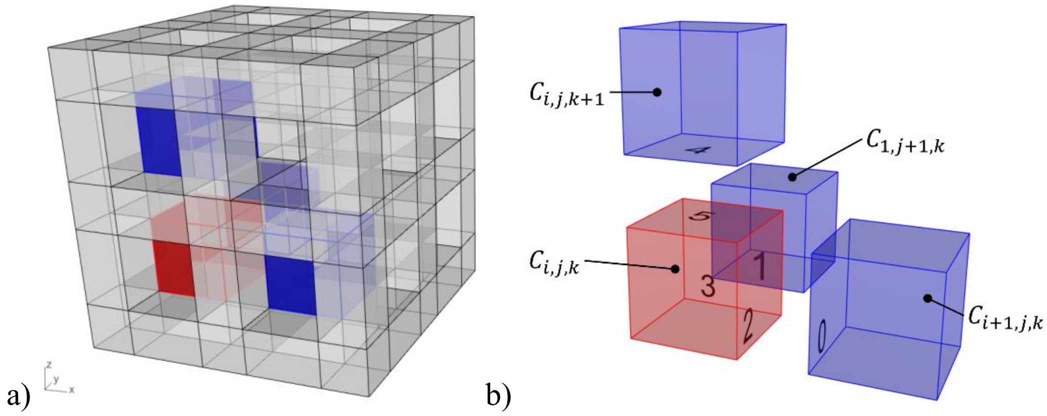

Figure 47. Cell considered for the modeling of the internal skins. The red cell is the one that is currently considered, the blue cells are the adjacent ones used for creating the faces of the beams: a) cells inside the lattice, b) cells and faces indexes.

When the Boolean value of the face 2 of the i, j, k cell is True, indicating that the face will present a skin, two quad faces are modeled, closing exactly the two involved faces:

- Vertex indexes 1, 2, 6, 5 (face 2) of the i, j, k cell.
- Vertex indexes 3, 0, 4, 7 (face 0) of the $i + 1, j, k$ cell.

Similarly, the same procedure is performed for the other two considered faces.

If the Boolean value of the face 3 of the i, j, k cell is True, the following mesh faces are created:

- Vertex indexes 3, 2, 6, 7 (face 3) of the i, j, k cell.
- Vertex indexes 1, 0, 4, 5 (face 1) of the $i, j + 1, k$ cell.

If the Boolean value of the face 5 of the i, j, k cell is True, the following mesh faces are created:

- Vertex indexes 5, 4, 7, 6 (face 5) of the i, j, k cell.
- Vertex indexes 0, 1, 2, 3 (face 4) of the $i, j + 1, k$ cell.

The creation of these faces is not enough for obtaining the internal walls: the mesh would contain non-manifold edges. Non-manifold edges are edges belonging to three or more faces; when this happens, it is not possible to determine the inside and the outside of the mesh. Figure 48a shows the creation of the skin for the face 2 of the current cell (in red) and the face 0 of the next cell (in cyan) along the x-direction; the situation is extremely simplified and only the interested beams are represented. Figure 48b shows the created faces describing the wall in transparency, and the manifold edges can be noted. The faces of the beams that are enclosed between the two faces are removed in Figure 48c and the final mesh is no more non-manifold.

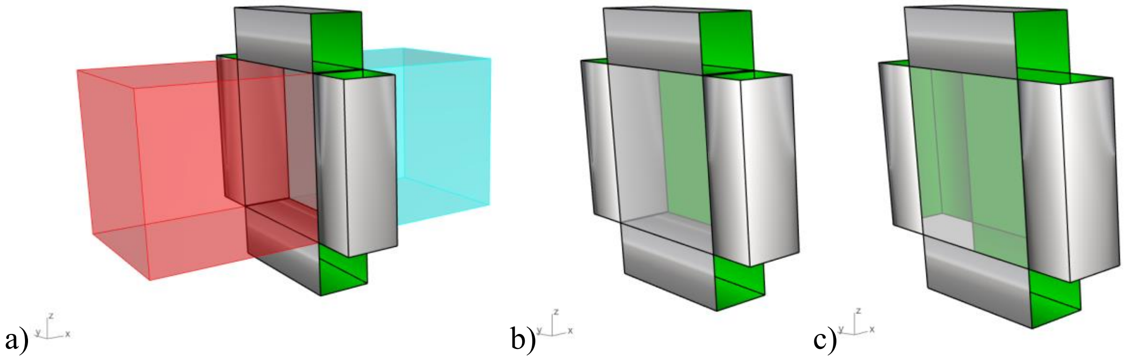

Figure 48. Modeling of the internal wall in a simplified environment: a) current cell (red) and next cell (cyan), b) wall faces modeling and non-manifold edges, c) removal of the beams faces for solving the non-manifold issue.

In the proposed method, the two phases of beams modeling and internal skins modeling are performed simultaneously. The Boolean value for the activation of the skins is read before modeling the beams, avoiding modeling the faces that then would be deleted, saving computational time and physical memory.

The method then allows modeling an external skin around the lattice. This is done by identifying the unit cells at the boundary comparing the i, j, k indexes with the n_x, n_y, n_z number of instances. Similarly, as the creation of the faces of the internal walls, mesh faces are modeled to connect the external beams (Figure 49a). Then the beams at the boundaries with valence equal to one and not connected to the external skin can be optionally removed (Figure 49b). Finally, the coarse mesh is refined by applying the Catmull-Clark subdivision surface algorithm (Figure 49c).

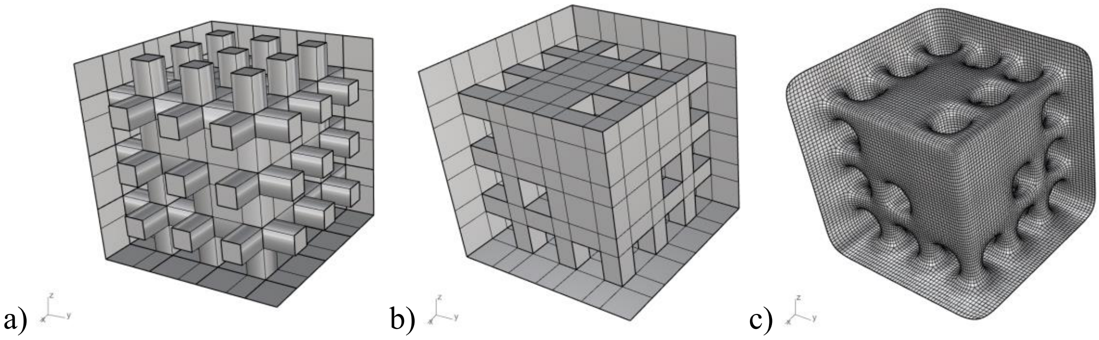

Figure 49. Last steps of the modeling of the lattice with internal walls: a) modeling of the external skin, b) removal of the beams with valence equal to 1, c) application of the Catmull-Clark subdivision surface algorithm.

The method is implemented in Rhinoceros 7 (Robert McNeel & Associates) CAD software, inside the Grasshopper environment, and using IronPython as programming language for writing the modeling code. Figure 50 shows the used environment: Rhinoceros viewport, Grasshopper canvas with blocks used as inputs for the code, and the GhPython block for writing the procedure. A part of the code that implements the operations is reported in Appendix A.

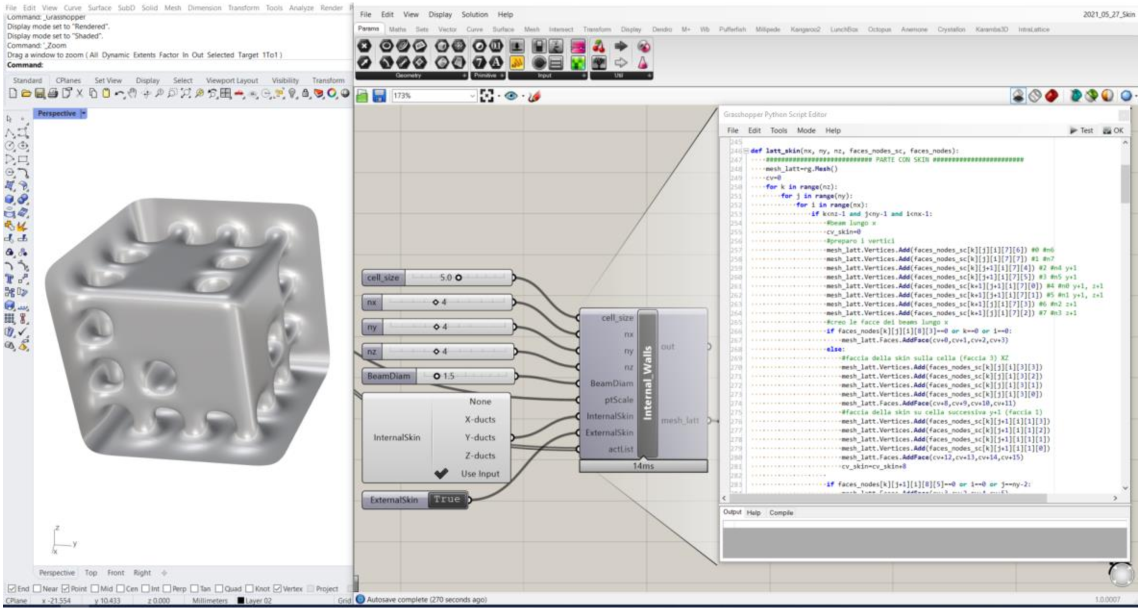

```
Command: _Grasshopper
Display mode set to "Rendered".
Display mode set to "Shaded".
Command: '_Zoom
Drag a window to zoom ( All Dynamic Extents Factor In Out Selected Target 1To1 )
Command:
```

```
def latt_skin(nx, ny, nz, faces_nodes_sc, faces_nodes):
    ############################ PARTE CON SKIN ########################
    mesh_latt=rg.Mesh()
    cv=0
    for k in range(nz):
        for j in range(ny):
            for i in range(nx):
                if k<nz-1 and j<ny-1 and i<nx-1:
                    #beam lungo x
                    cv_skin=0
                    #preparo i vertici
                    mesh_latt.Vertices.Add(faces_nodes_sc[k][j][i][7][6]) #0 #n6
                    mesh_latt.Vertices.Add(faces_nodes_sc[k][j][i][7][7]) #1 #n7
                    mesh_latt.Vertices.Add(faces_nodes_sc[k][j+1][i][7][4]) #2 #n4 y+1
                    mesh_latt.Vertices.Add(faces_nodes_sc[k][j+1][i][7][5]) #3 #n5 y+1
                    mesh_latt.Vertices.Add(faces_nodes_sc[k+1][j+1][i][7][0]) #4 #n0 y+1, z+1
                    mesh_latt.Vertices.Add(faces_nodes_sc[k+1][j+1][i][7][1]) #5 #n1 y+1, z+1
                    mesh_latt.Vertices.Add(faces_nodes_sc[k+1][j][i][7][3]) #6 #n2 z+1
                    mesh_latt.Vertices.Add(faces_nodes_sc[k+1][j][i][7][2]) #7 #n3 z+1
                    #creo le facce dei beams lungo x
                    if faces_nodes[k][j][i][8][3]==0 or k==0 or i==0:
                        mesh_latt.Faces.AddFace(cv+0,cv+1,cv+2,cv+3)
                    else:
                        #faccia della skin sulla cella (faccia 3) XZ
                        mesh_latt.Vertices.Add(faces_nodes_sc[k][j][i][3][3])
                        mesh_latt.Vertices.Add(faces_nodes_sc[k][j][i][3][2])
                        mesh_latt.Vertices.Add(faces_nodes_sc[k][j][i][3][1])
                        mesh_latt.Vertices.Add(faces_nodes_sc[k][j][i][3][0])
                        mesh_latt.Faces.AddFace(cv+8,cv+9,cv+10,cv+11)
                        #faccia della skin su cella successiva y+1 (faccia 1)
                        mesh_latt.Vertices.Add(faces_nodes_sc[k][j+1][i][1][3])
                        mesh_latt.Vertices.Add(faces_nodes_sc[k][j+1][i][1][2])
                        mesh_latt.Vertices.Add(faces_nodes_sc[k][j+1][i][1][1])
                        mesh_latt.Vertices.Add(faces_nodes_sc[k][j+1][i][1][0])
                        mesh_latt.Faces.AddFace(cv+12,cv+13,cv+14,cv+15)
                        cv_skin=cv_skin+8

                    if faces_nodes[k][j+1][i][8][5]==0 or i==0 or j==ny-2:
```

Perspective
cell_size
5.0
nx
4
ny
4
nz
4
BeamDiam
1.5
InternalSkin
None
X-ducts
Y-ducts
Z-ducts
Use Input
ExternalSkin
True
cell_size
nx
ny
nz
BeamDiam
ptScale
InternalSkin
ExternalSkin
actList
Internal_Walls
out
mesh_latt
14ms
Grasshopper Python Script Editor
File
Edit
Tools
Mode
Help
Test
OK
Output
Help
Compile
Autosave complete (270 seconds ago)

Figure 50. Environment used for the implementation of the methods for modeling internal walls and external skins: Rhinoceros viewport, Grasshopper canvas with input blocks, and GhPython block for writing the procedure.

Concentrating on the Boolean values indicating the activation of the internal skins, at the moment they can be specified following different criteria. Simple straight ducts parallel to one of the X-, Y-, and Z-axis can be created; depending on the selected direction, the Boolean values are as in Table 2. Figure 51 shows a lattice structure with straight ducts, beams with valence equal to 1 not removed, and external skin not activated, before (Figure 51a) and after (Figure 51b) the application of the subdivision surface algorithm.

Table 2. Boolean values of faces 2, 3, and 5 for modeling straight ducts parallel to one of the X-, Y-, and Z-axis.

	Face 2 Boolean	Face 3 Boolean	Face 5 Boolean
Ducts along X-direction	False	True	True
Ducts along Y-direction	True	False	True
Ducts along Z-direction	True	True	False

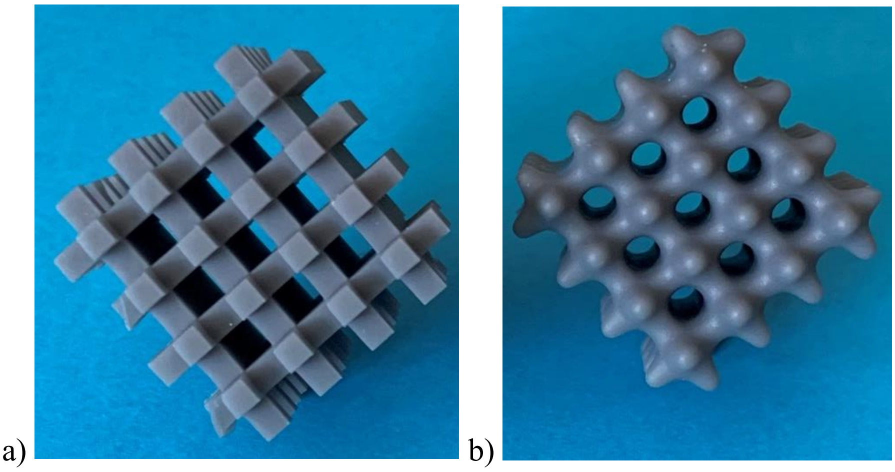

Figure 51. Lattice structure with straight ducts, beams with valence equal to 1 not removed, and external skin not activated: a) before and b) after the application of the subdivision surface algorithm. Parts produced by the Formlabs Form 3 machine (SLA technology), using the Formlabs Grey V4 resin.

The activation of the internal skins can then be controlled to obtain custom paths. This is achieved by drawing the lines that describe the desired duct; these lines are taken as an input by the implemented method, the intersections between the lines and the cells of the structure are computed to obtain the faces crossed by the lines, and the “True” Boolean value is associated if an intersection happens. Figure 52 shows a fully enclosed lattice structure with a custom internal duct and beams with valence equal to 1 removed; the inner spheres represent void areas inside the part, so this particular example can be produced by AM technologies that do not require material evacuation; for instance, FFF technologies could be suitable for the manufacturing. Otherwise, resin and powders could be left inside for damping purposes.

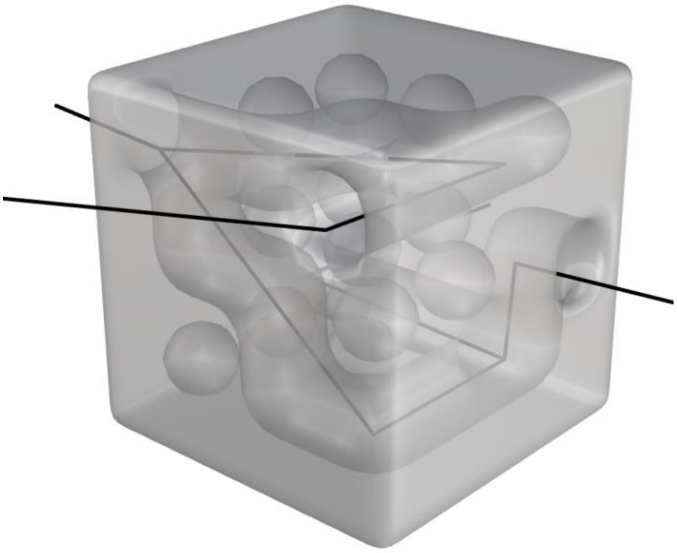

Figure 52. Lattice structure presenting an internal duct that follows a path driven by lines given as an input by the designer. The inner spheres represent void areas inside the part.

The sample in Figure 53 was printed using a transparent material and this allows to see the ducts generated by selectively activating some of the internal walls.

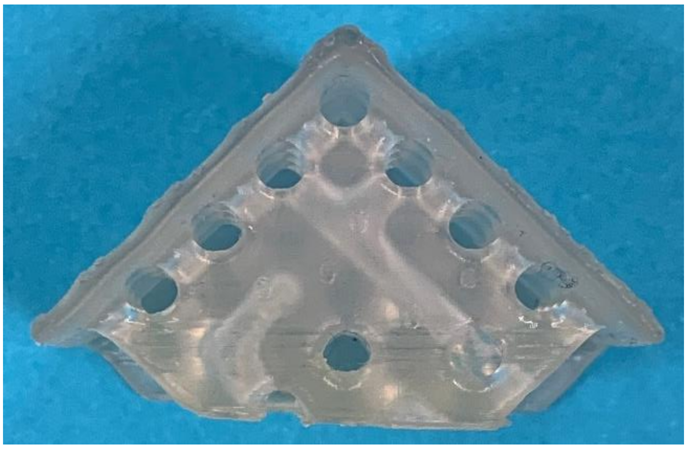

Figure 53. Sample presenting internal ducts obtained by adopting the proposed geometric modeling method. Parts produced by the Formlabs Form 3 machine (SLA technology), using the Formlabs Elastic resin.

As underlined at the beginning of the session, the presented modeling method gives the possibility of tailoring the stiffness in different areas of the model and allows to connect some areas of the part, isolating them from other zones creating internal ducts in which one or more fluids can flow acting as heat exchangers or transporters, such as in the hydraulic manifold blocks.

3.4 Optimization workflow in design for AM

As it was previously discussed in section 2.2.1, when modeling new components or when re-designing parts that are going to be produced with AM technologies, considerations dealing with the DfAM need to be made. An optimization workflow to be used in the DfAM has been proposed trying to fill up the lacks highlighted in the literature where it is stated that DfAM workflows do not completely cover the entire design process [223] or do not integrate CAD and CAE software [28]. The workflow focuses on the product design phase, also known as the embodiment design phase [247,248], where the design is developed up to the production. It exploits CAD and CAE software and tools for modeling the part and optimizing and validating the model, respectively. The available methods, both proposed in this research and commercially accessible, have been integrated in a workflow. By following this workflow, the designers are guided during the decisions that lead to the introduction of peculiar AM features in a new component.

Figure 54 shows the proposed optimization workflow that is initiated by identifying the design space, defined as the volume where the optimization and modeling approaches are allowed to operate and distribute the material. The workflow then forks into two possible paths: one dealing with the TO, the other dealing with the size optimization. Both the optimization approaches require a FE analysis to be performed, so a FE model is set up. As boundary conditions, information about the material, the load, and the constraints are provided. More, it is possible to supply additional information related to the objectives of the optimization process, such as the targeted mass or the desired stiffness, and technological constraints related to the AM manufacturing technology, like the limit for the overhanging angle or the minimum size of the features. If the TO is performed, a polyhedral mesh of the design space is used as the model of the FE analysis; depending on the optimization algorithm used (see Section 2.2.3.3) the material is iteratively distributed, eliminated, and/or re-added inside the design volume until the convergence of the method and the objectives are reached. The result of the most diffused method for TO, the SIMP method, is a grey-scale density map that is further contoured to the desired level of density, the threshold, and a mesh surface is obtained. This mesh is coarse due to the discretization operated during the FE analyses, often present disconnected areas, and cannot be produced as is. So, remodeling is required; even though in the literature methods to automatically remodel the mesh have been proposed [17,249] and some software tool for automatic remodeling is available, usually the part is remodeled manually inside a CAD environment and using the mesh as a guideline. If instead of the TO, the size optimization is performed, a wireframe model conformal to the design space and characterized by a cell type with a pre-selected size is created; then, the segments of the wireframe are considered as beam elements and are iteratively optimized; finally, the optimized lattice structure is modeled. For modeling the wireframe, optimizing the beams, and modeling the structure, the methods proposed in Sections 3.1, 3.2, and 3.3 can be adopted, respectively. Furthermore, size and topology optimizations can be bridged by assigning the diameters of the beams mapping the densities values of the TO [18,171].

When the modeling is completed, the final part needs to undergo a FE analysis for structural validation. This step is absolutely needed for the TO path because the manual remodeling could introduce weak zones and critical spots, whereas it could be neglected for the lattice modeling since the results are expected to be similar to the FE analyses based on beam elements performed during the optimization phase; indeed, the mesh modeling approach even adds more material at nodal points than what is considered in the beam model.

After the final FE validation, the process planning is faced. The AM technology and machine used for the production guide this phase because, depending on them, the part orientation, the supports, and the print path strategy are generated. The literature shows that accurately planning the process decreases the production time and the energy and material consumption [250], and is beneficial for the mechanical properties and the surface finish [84].

Finally, the last step deals with the process simulation that aims at predicting geometric distortion and residual stress of the printed parts, collision between the parts and the manufacturing machine components, and possible delamination effects during the printing process. From this information, it is possible to correct the CAD model to compensate for the expected distortion. This final step is important when manufacturing metal parts due to the formation of defects that lead to crack initiation and propagation, and consequent failure of the part [251]. Although the process simulation is mainly conducted for AM metals processes [252–254], material extrusion [255] and powder bed fusion [256] of polymers have been studied too.

As indicated by the arrows in the workflow of Figure 54, at every phase concerned with simulations the model validation could fail, requiring the remodeling of the part, a new optimization, or, even worse, the modification of the initial boundary conditions.

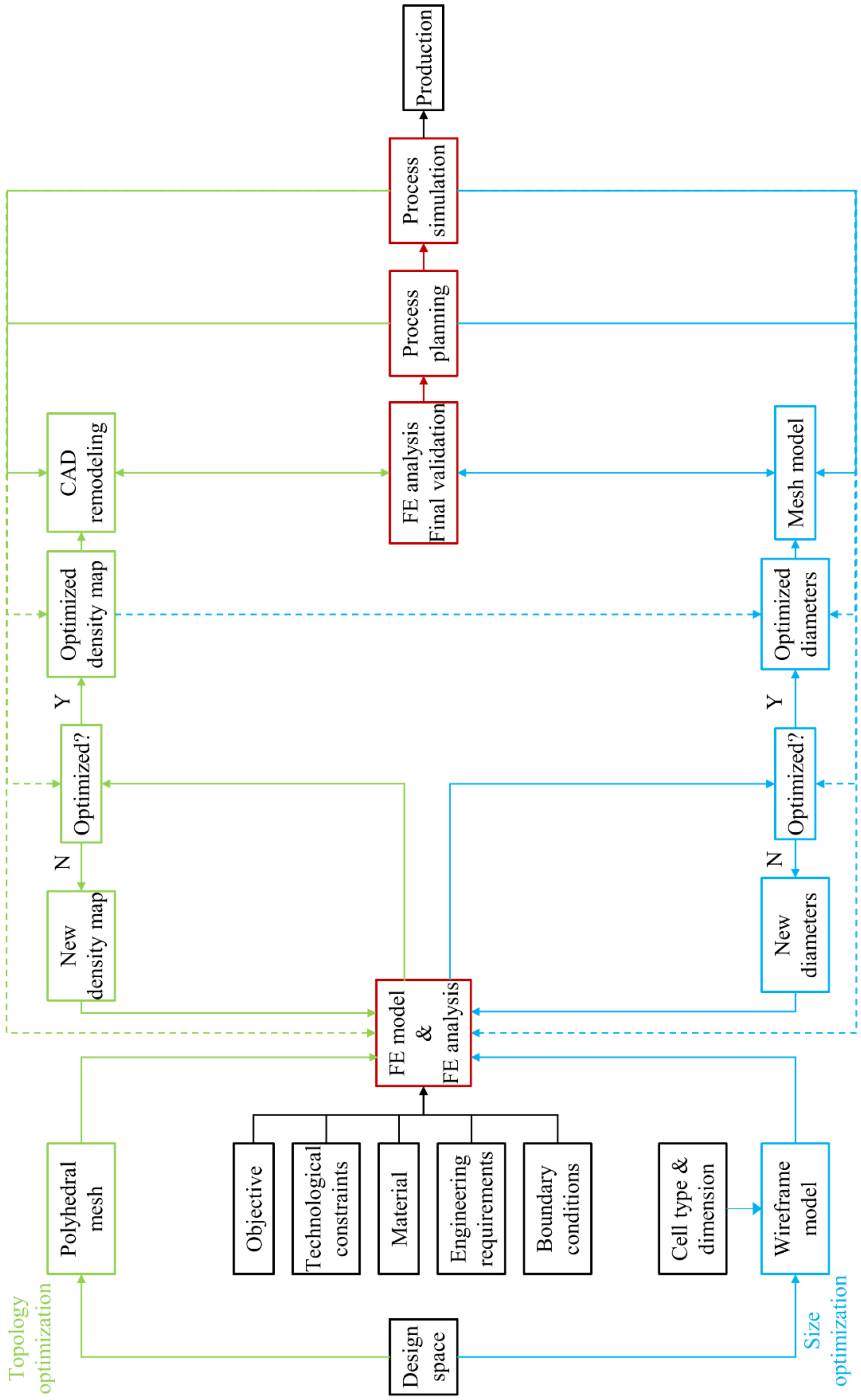
Topology optimization
Size optimization
Design space
Polyhedral mesh
Objective
Technological constraints
Material
Engineering requirements
Boundary conditions
Cell type & dimension
Wireframe model
FE model & FE analysis
New density map
N
Optimized?
Y
Optimized density map
CAD remodeling
New diameters
N
Optimized?
Y
Optimized diameters
Mesh model
FE analysis Final validation
Process planning
Process simulation
Production

Figure 54. Proposed optimization workflow in DfAM. Black blocks: boundary conditions; green blocks: topology optimization; blue blocks: size optimization; red blocks: computer-aided engineering (CAE) simulation.

4 Test cases

In this section, two test cases dealing with the design, optimization, and modeling of lattice structures are presented. The first one presents the re-modeling of a piston rod, executed by following all the steps of the optimization workflow introduced in Section 3.4. Piston rods are extensively used in the automotive and industrial fields. The structural optimization of a piston rod, with a consequent reduction of the mass, is beneficial in the automotive competitions where the performance is pushed to the limit, and in more "conservative" fields, where light-weighting allows for the reduction of inertia and energy consumption. The second test case proposes the multi-objective optimization of a liquid propellant tank for small satellites; the optimization aims to reduce the mass and increase the first natural frequency at the same time; lower mass means lower launch cost, whereas a high first natural frequency is sought to avoid the resonance phenomenon to happen during the first moment of the launch. These two objectives clash with each other, so a compromise is needed.

4.1 Piston rod

The piston rod used for this test case is currently produced with a pressure die-casting manufacturing process and the re-design aims to obtain a component suitable to be produced by the AM SLM technology, using the aluminum AlSi10Mg. The properties of the material are:

- Density: 2700 kg/m^3
- Young modulus: 68 GPa
- Yield strength 190 MPa
- Ultimate tensile strength 335 MPa
- Poisson ratio 0.30

The overall dimensions of the piston rod are presented in Figure 55.

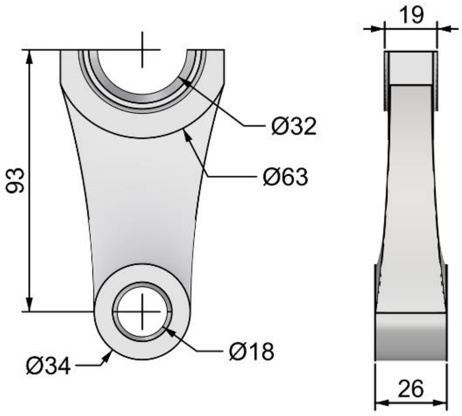

Figure 55. Overall dimensions of the piston rod.

According to the optimization workflow, the design space is defined as the central part of the piston rod, whose geometry has been simplified as in Figure 56. More, the boundary conditions are set. Two load cases are considered:

- A 7.5 kN axial traction load, applied to the upper face of the big rod's end along the z-axis.
- A 10 kN axial compression load, applied to the upper face of the big rod's end along the z-axis.

The applied constraints are:

- The 6 degrees of freedom of the elements of the small rod's end are locked, i.e., no rotations nor translations are allowed.
- Translations along the x- and y-direction of the elements of the big rod's end are locked.

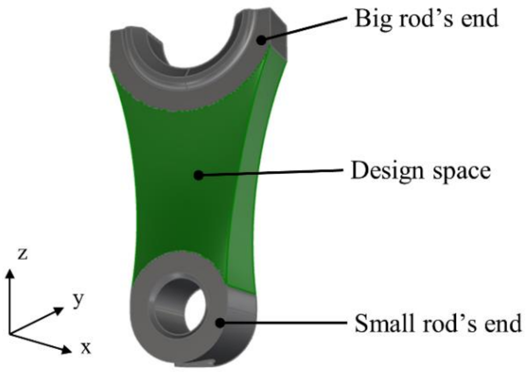

Figure 56. Zones of the piston rod.

Dealing with the size optimization path of the workflow, the design space was filled with a conformal wireframe. The simple cubic cell was used as unit cell and the number of repetitions of the cell along the x-, y-, and z-direction is 10, 4, and 14 respectively. As presented in Section 3.1, the four methods were applied to generate the wireframe, namely TCD, AD, CD, and NFFD methods, and the resulting 3D wireframes are presented in Figure 57, together with the frontal and side views.

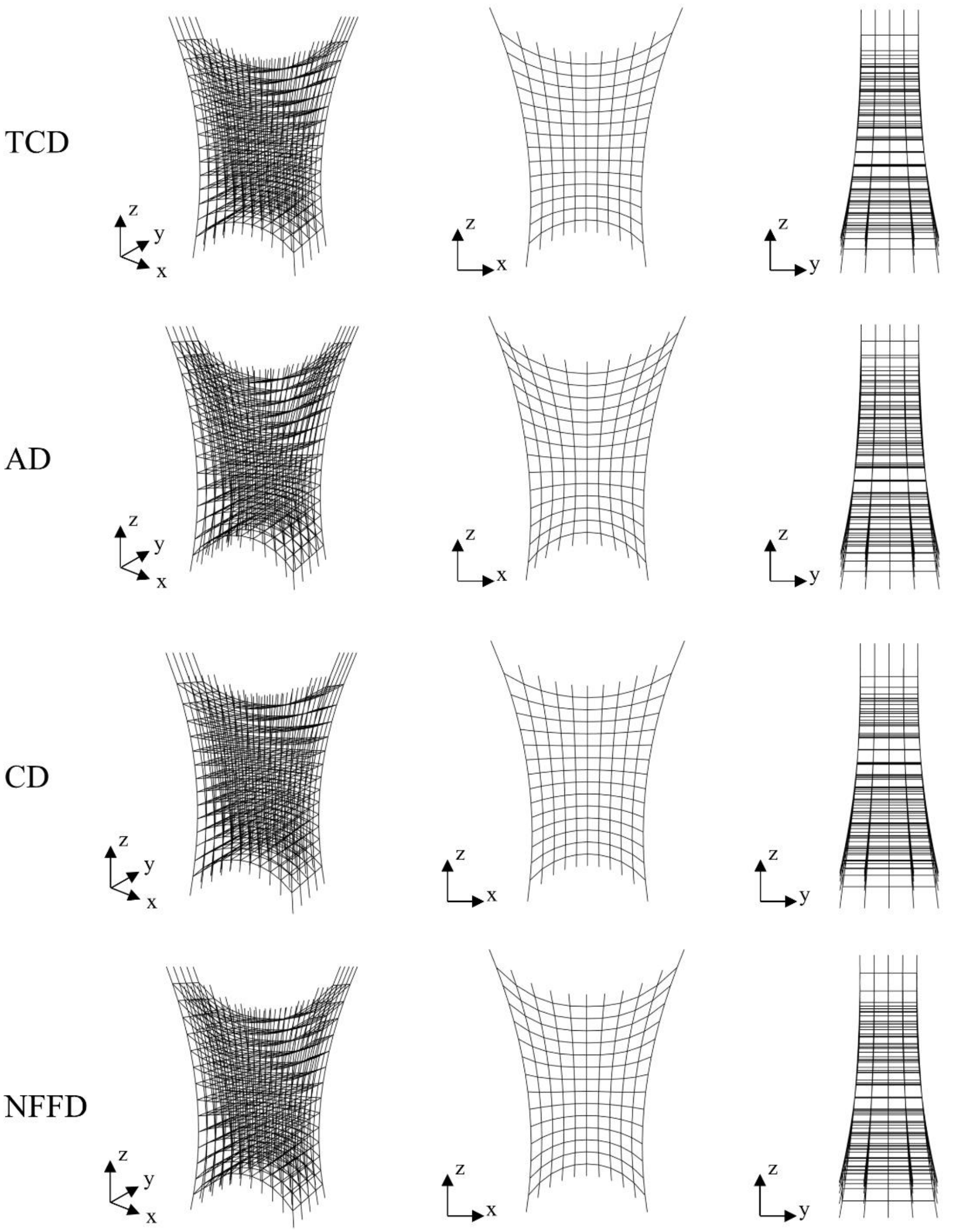

Figure 57. Wireframes of the piston rod obtained by different methods. From left to right: perspective, front, and side view.

If looking at the frontal view, the cells tend to maintain a squared shape in the central zone, whereas they deform at the boundaries. The bar plot in Figure 58 shows a comparison between the average, minimum, and maximum lengths of the beams of the four wireframes. The minimal length is similar. The maximum length curves, instead, presents higher differences mainly due to the lines at the boundary of the design space, close to the big rod end; the CD method has the longest beam dimension whereas, the AD method presents the lowest beam due to the regular division of the design space edges.

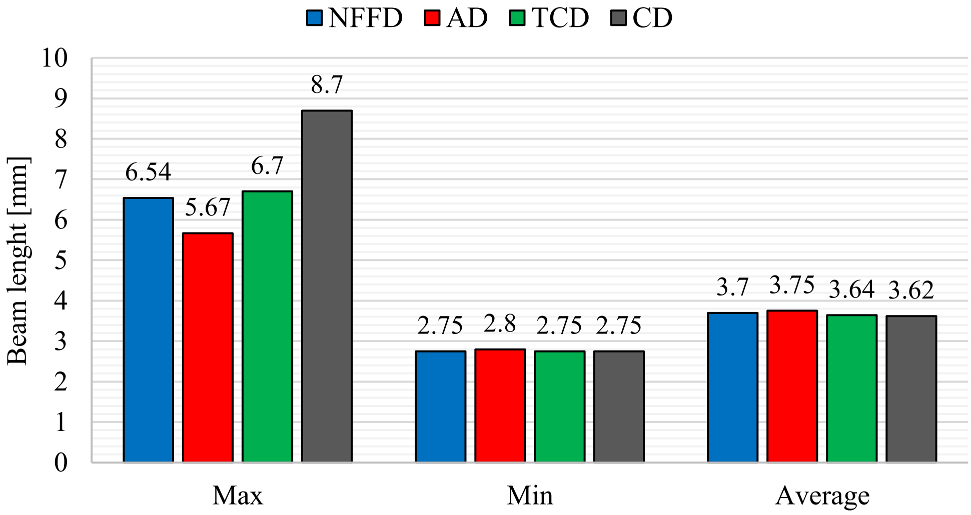

Figure 58. Comparison between the average, minimum, and maximum length of the beams of the four types of wireframes.

The wireframe was then used as the input for the FE beams model and the size optimization was performed as described in Section 3.2.1. The optimization algorithm was implemented in Rhinoceros 7 (Robert McNeel & Associates) CAD software, inside the Grasshopper environment and using Karamba3D plugin [234] as FE solver; Karamba3D uses the Timoshenko beam theory. The target utilization ratio was set to 90% with a ±1% tolerance. The upper bound for the diameter of the beams was defined as 1.5 mm taking into consideration the size of the cells, whereas the lower bound was defined as 0.5 mm according to the manufacturing capabilities of the SLM technology [257].

Figure 59a and Figure 59b show the results of the size optimization for the four methods. All the configurations present a similar average diameter (Figure 59b), about 0.70 mm for the traction and 0.76 mm for the compression load case, due to the similar beam distribution in the central area of the wireframe. The TCD lattice structure has the highest diameter in both traction, 1.15 mm, and compression, 1.44 mm, load cases. NFFD and CD methods have the lowest maximum diameter in traction, 1.05 mm. The minimum beam diameter is not plotted because it equals the lower limit imposed by the technological constraint, i.e., 0.5 mm; since the loads are aligned to the z-direction, the beams following the x- and y-direction are less loaded and would require an optimized diameter lower than the 0.5 mm limit; for this reason, some of the beams of the structure are over-dimensioned. Figure 59c and Figure 59d reports the results of the structural analysis of the optimized model. The AD configuration presents the highest relative density in both the load cases and the lattice structure is less compliant. Finally, the CD configuration has the best compromise between relative density and structure stiffness.

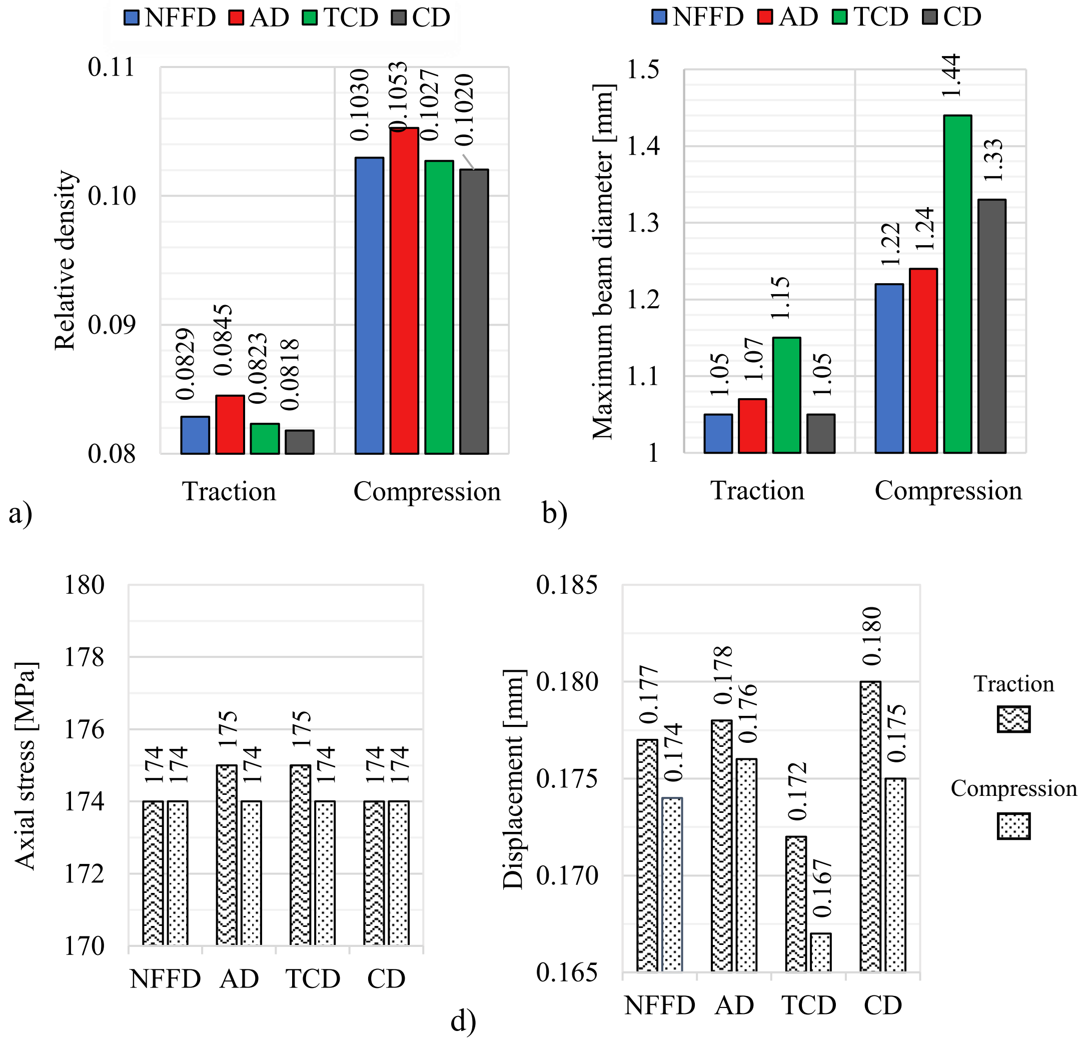

Figure 59. Results of the size optimization for the four methods: a) relative density, b) maximum beam diameter, c) maximum axial stress, and d) maximum displacement of the structures.

Given the results, the further steps of the workflow are executed on the wireframe obtained with the CD method and optimized for the 7.5 kN traction load. The CD method was selected among the others since it offers a good compromise; indeed, it has the lowest relative density presenting the lowest value of the maximum beam diameter but can withstand the applied load having just slightly higher compliance. More in general, without focusing on the piston rod case, the selection of the best wireframe creation method depends on the specific test case; this is due to the different design spaces that lead to different organization of the lattice cells inside the volume, boundary conditions, and design requirements. For instance, a high stiffness (and low maximum displacement) of the structure could be required disregarding the relative density and leading to a consequent higher mass of the part. As a further implementation, a decision driven by weighting the output parameters of the modeling method (the lengths of the beams) and of the size optimization (the relative density, the maximum beam diameter, the maximum axial stress, and the maximum displacement) according to the needs of the application could be introduced to automate the selection of the most suitable wireframe modeling method.

Focusing back on the piston rod, the optimized values of the diameters are used to model the lattice structure applying the geometric modeling method based on coarse quad mesh faces and the subsequent application of the Catmull-Clark subdivision surface algorithm, as described in Section 3.3.1. Figure 60a shows the resulting model, with a close-up of the smooth surfaces obtained at the nodal points of the structure (Figure 60b).

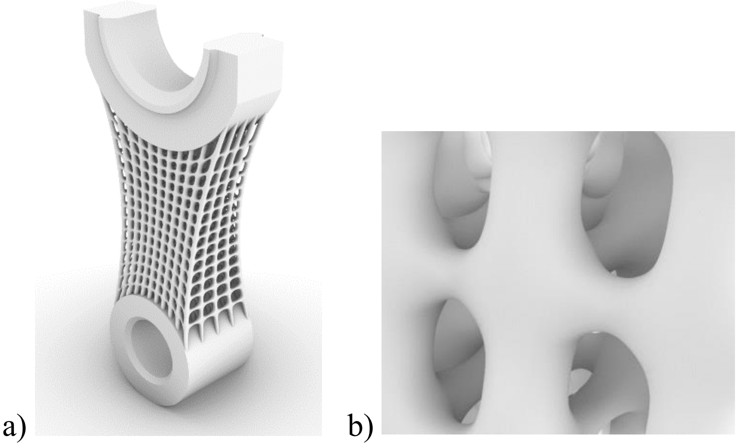

Figure 60. Modeling of the optimized CD lattice structure in the traction load case adopting the mesh modeling method and the Catmull-Clark subdivision surface algorithm: a) entire piston rod, b) close-up at the nodal points of the lattice.

Moving on the topology optimization path, the traction load case was studied. SolidWorks 2019 (Dassault Systèmes) software with the SolidWorks Simulation module that implements the TO SIMP method was used for performing the simulation. The goal was set to the best stiffness-to-weight ratio and a constraint on the final mass was imposed to be 25% of the initial one; more, the symmetry with respect to the YZ and ZX planes is requested. The mesh in Figure 61a is the result of the TO setting a threshold level of 0.3; even though it does not present disjointed areas, it is too coarse and thin to be manufactured as is. So, the manual NURBS remodeling was performed in Inspire Studio CAD 3D (Altair) software and is presented in Figure 61b.

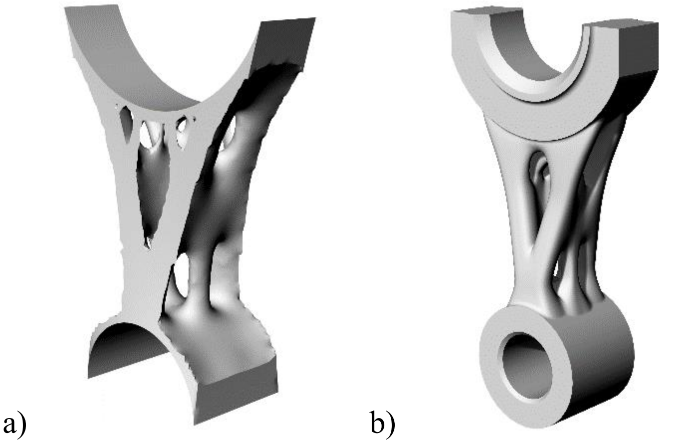

Figure 61. Topology optimization performed on the design space of the piston rod: a) coarse mesh resulting from the topology optimizer (SolidWorks Simulation), b) manual remodeling of the design space (Inspire Studio CAD 3D).

The two final models resulting from the size and topology optimizations are then mechanically validated in Ansys Mechanical 2019 R1 software. 3D tetrahedron elements ranging from 0.1 mm to 1 mm are used to discretize the models adopting a patch-independent method with automatic refinement in curvature and proximity. Since the CAD remodeling of the TO model maintained the symmetries with respect to the YZ and ZX planes, only a quarter of the model is simulated. The Von Mises stress distributions are shown in Figure 62. Being the yield stress of the aluminum AlSi10Mg material 190 MPa, the models are validated.

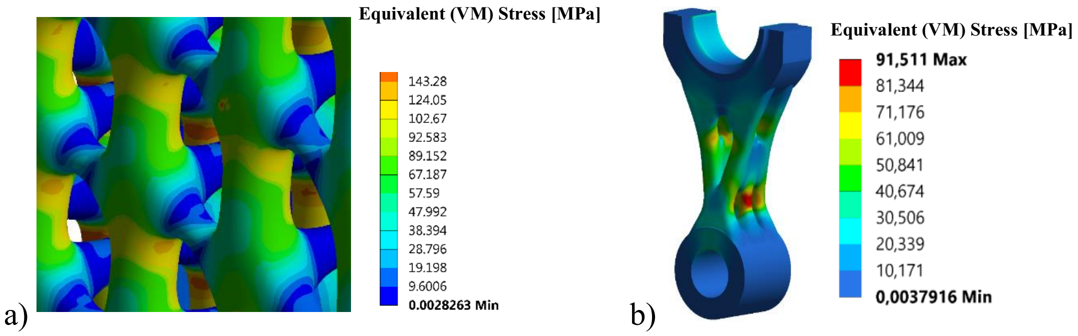
a)
Equivalent (VM) Stress [MPa]
143.28
124.05
102.67
92.583
89.152
67.187
57.59
47.992
38.394
28.796
19.198
9.6006
0.0028263 Min
b)
Equivalent (VM) Stress [MPa]
91,511 Max
81,344
71,176
61,009
50,841
40,674
30,506
20,339
10,171
0,0037916 Min

Figure 62. Mechanical validation of the final models, equivalent Von Mises stress: a) size optimization, b) topology optimization.

After the mechanical validation of the models, the process planning was performed in Netfabb Premium 2020.3 (Autodesk) software considering the part orientation and supports creation. The Renishaw AM 400 SLM machine is selected, combined with the Aluminum AlSi10Mg-0403 printed at 25 µm, as suggested by the manufacturer [258]. The configurations proposed in Figure 63 show some of the possible solutions. The bar plots in Figure 64 report information about the configurations. Configurations from Figure 63a to Figure 63c concern the TO model; there is not a “best solution”, and the decision is made depending on several considerations. The lowest height in Figure 63a guarantees a low printing time and the circular features are expected to be manufactured with a high dimensional and geometrical accuracy because they lay on the plate; at the same time, the highest supported area leads to long post-processing time for support removal and operations such as sandblasting for surface finishing. The orientation in Figure 63b has the highest height, the longest build time, and the highest volume of supports, i.e., the highest waste of material, but the lowest supported area allows for the best surface finish if no post-process operations are performed and requires less time for supports removal. Figure 63c is a compromise, allowing for a contained build time and supported area; more, the volume of the support material is the lowest. Finally, Figure 63d shows the orientation proposed for the piston rod remodeled with a lattice structure. Only one configuration is proposed because the absence of supports in the lattice zone is mandatory, due to the difficulty of their removal.

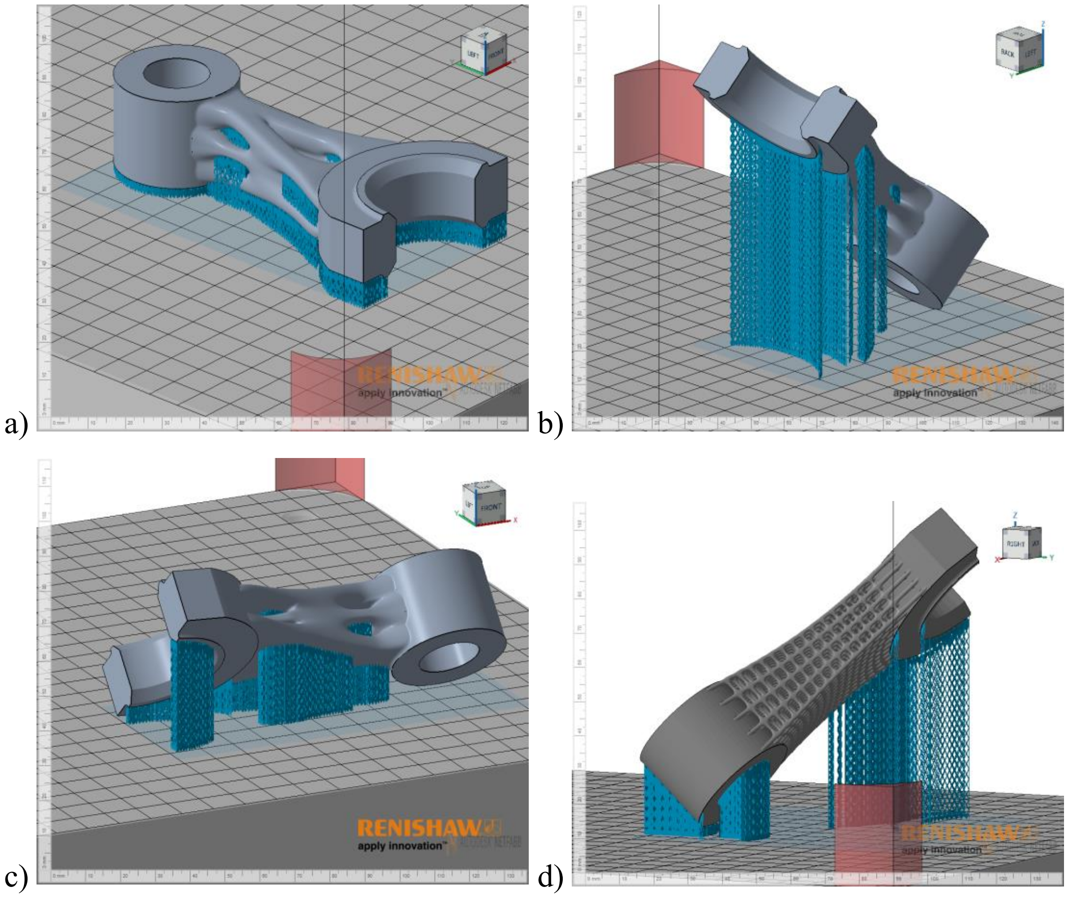
a) b) c) d)

RENISHAW
apply innovation™
RENISHAW
apply innovation™
RENISHAW
apply innovation™
RENISHAW
apply innovation™

Figure 63. Configurations proposed in the process planning phase: a) to c) topology optimization model, d) size optimization model.

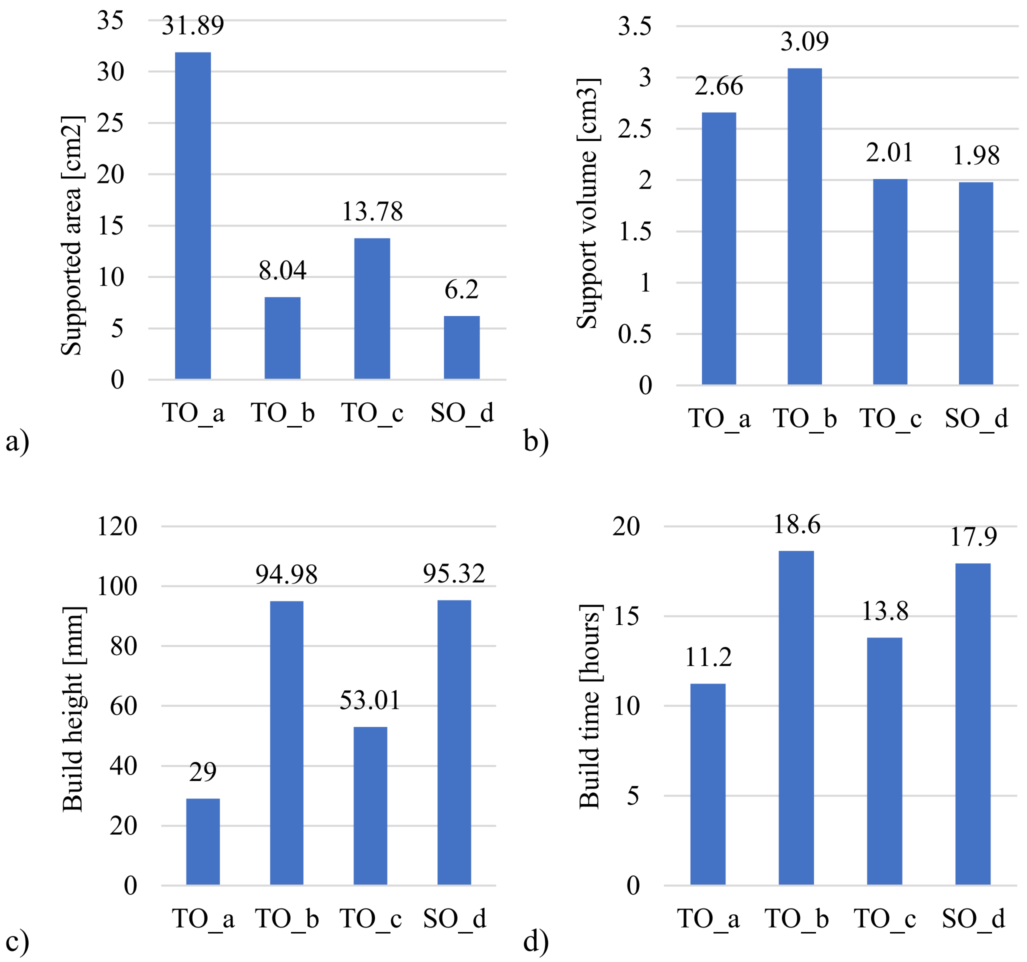

Figure 64. Information about the configuration of the process planning: a) supported area, b) support volume, c) build height, and d) build time. The labels of the horizontal axis stand for topology optimization (TO) and size optimization (SO), whereas the a, b, c, and d letters refer to the configurations in Figure 63.

The last step of the optimization workflow is the process simulation. This phase was not performed and is listed as future work. Simulating the manufacturing process is a fundamental stage to avoid failure during the production of the parts. Furthermore, the information of residual stress and geometrical warping give directions on how to compensate for the geometrical model.

Supposing the validation of the model also by the process simulation phase, the re-modeling of the piston rod allows obtaining an optimized component with a reduction of mass of the 71% and 80% depending on whether the topology optimization or the size optimization is adopted, respectively. Table 3 reports the data regarding the mass reduction.

Table 3. Mass comparison of the initial model and the optimized ones. The rod's ends are not considered in the mass computation since they were not part of the optimization.

Re-design method	Mass [g]	Mass reduction [%]
Initial design space	104.7	
Topology optimization	29.99	-71%
Size optimization	20.98	-80%

Other than the mass reduction, some considerations can be done when comparing the two proposed approaches. The lattice structure is automatically generated starting from the wireframe generation to the geometric modeling of the mesh part; if the NFFD method is used, the intervention of the operator is required but is only limited to the translation of the control points of the cage. In the TO approach, instead, the model needs to be remodeled by a qualified CAD user, requiring more time and increasing the risk of failure during the final FE analysis verification, due to possible human errors in the remodeling phase. Even though a FE validation analysis is always suggested, numerical simulations on lattice models are computationally demanding but could be omitted since the wireframe is previously optimized and the proposed geometric modeling method does not reduce the diameters of the beams and, actually, increases the mass at the nodal points where the beams meet. A limitation found in the size optimization approach is the difficulty in managing the connection between the lattice structure and the surrounding objects since, at the moment, Boolean operations are needed.

4.2 Aerospace propellant tank

The aerospace sector is one of the fields that can fully exploit the AM capabilities; for instance, some of the advantages of using AM technologies for producing aerospace components are the reduced lead time and associated cost, and the relative ease at obtaining complex geometries that leads to improved performance and lightweight parts [259]. Among the components, propellant tanks too have been produced by AM [260,261].

In this context, the design of an aerospace propellant tank for small satellites is used as a test case. In particular, an internal conformal lattice structure was introduced in the model and a multi-objective optimization was performed. The aims of the optimization are the minimization of the mass and the maximization of the first natural frequency of the tank. As stated by Jones [262] and presented in Figure 65, if excluding the affordable launchers lately produced by SpaceX, launching one kilogram into space is still expensive.

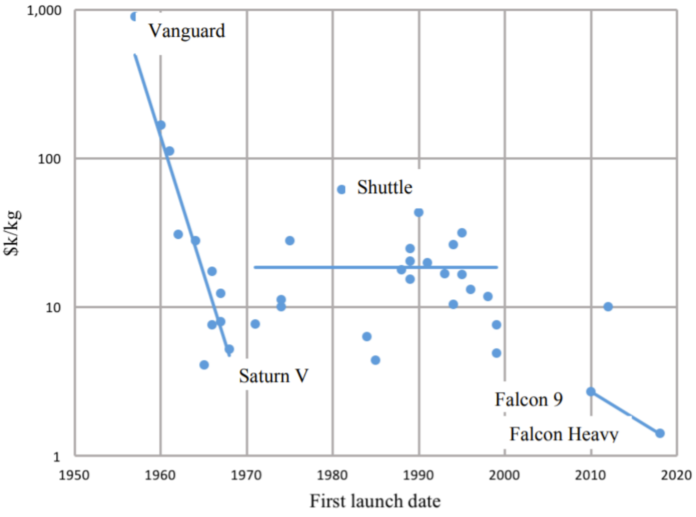

Figure 65. Costs necessary for launching one kilogram into space [262]

Moreover, in the first phases of the launch, excitation occurs in the low spectrum of frequencies and it is highly recommended to design the aerospace components to guarantee that the first natural frequency is high enough to avoid the excitation frequencies; if not, the resonance phenomenon could arise, damaging the parts. As an example, Figure 66 reports the sine-equivalent vibrations of the Vega launcher by Arianespace [263].

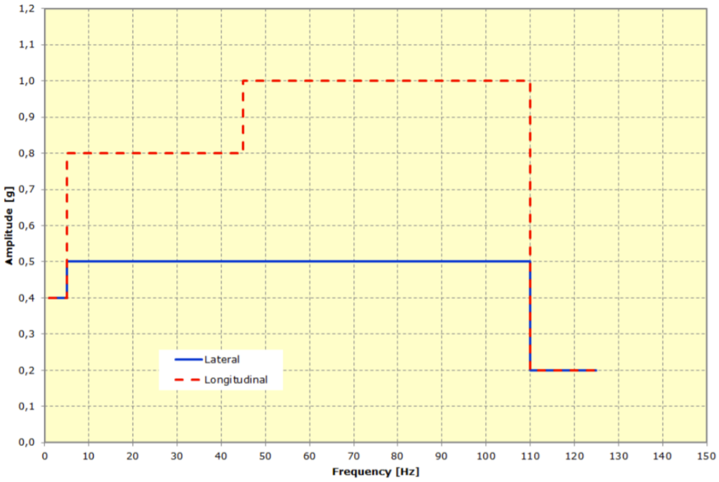

Figure 66. Sine-equivalent vibrations at spacecraft-to-adapter interface of the Vega launcher, Arianespace [263].

Thus, the mass minimization and the first frequency maximization are properties that have to be taken into consideration when designing a propellant tank. But since they are conflicting objectives, multi-objective optimization is required.

The characteristics and the boundary conditions of the tank used in this case study are inspired by the literature:

- Tank diameter: 130 mm.
- Holes diameter: 5 mm.
- Constraints: four points along the equator constrained blocking all the degrees of freedom except the radial translations.
- Load: 60 MPa of internal pressure acting radially towards the outside. The pressure was obtained by imposing a Maximum Expected Operative Pressure (MEOP) of 30 MPa and defining the burst pressure, i.e., the pressure the tank must resist during qualification tests, as the double of the MEOP, as suggested by the military standard MIL-STD 1522A [264].

Moreover, the tank is intended to be produced by SLM technology using the Titanium Ti-6Al-4V material, which has the following properties:

- Density: 4340 kg/m^3.
- Young modulus: 113.8 GPa.
- Poisson ratio: 0.342.

- Yield strength: 880 MPa.

The external shell of the tank with the overall dimensions is presented in Figure 67a, whereas in Figure 67b the constraints are shown.

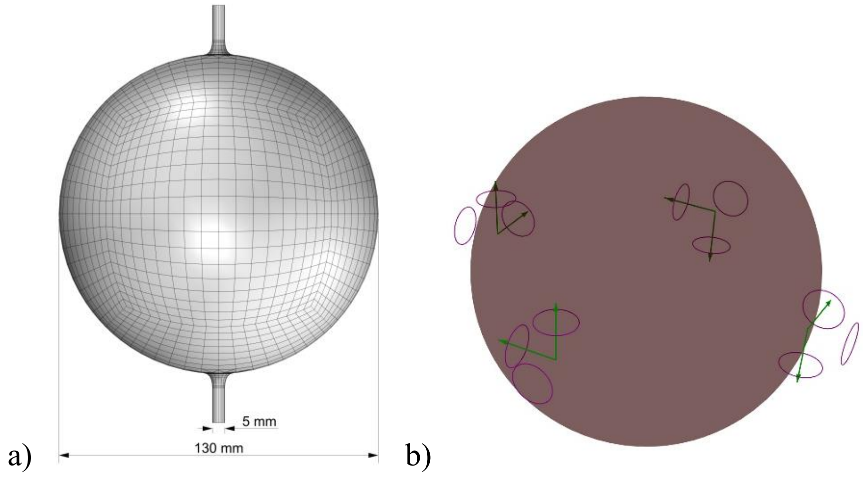

Figure 67. Propellant tank: a) overall dimensions, b) constraints of the model.

First, the internal conformal lattice structure, based on the simple cubic cell, is modeled. Given the spherical shape of the tank, it results more advantageous to adopt an ad-hoc modeling strategy taking advantage of the radial and circumferential directions instead of using the wireframe creation methods described in Section 3.1. Starting from an external mesh that discretizes a sphere with quad-faces mesh elements (Figure 68a), an internal concentrical sphere is obtained that adopts the same topology of the external one (Figure 68b) and with a radius R_{int} given by:

$$R_{int} = R_{ext} - average\left(length_{external\ mesh\ edges}\right)$$

Where R_{ext} is the radius of the external sphere, i.e., 65 mm in this case study. The beams of the internal sphere are referred to as circumferential beams. The same topology of the external and internal mesh allows connecting the corresponding nodes, creating the radial beams of the internal lattice (Figure 68c). Figure 68d shows the final internal conformal lattice, including both the circumferential and the radial beams.

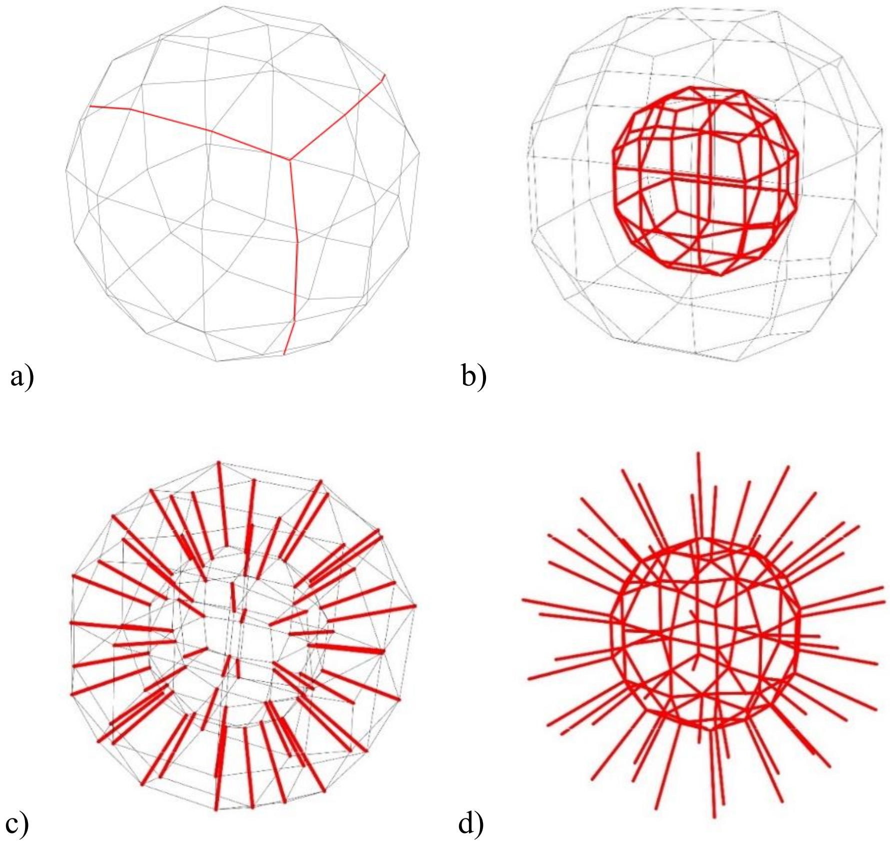

Figure 68. Internal conformal lattice structure modeling: a) sphere discretized by a quad-faces mesh, b) circumferential beams, c) radial beams, d) complete internal lattice structure.

Depending on the discretization level of the external mesh, different configurations can be obtained for the internal lattice. Figure 69 shows configurations with a fewer number of cells with bigger beams length and, vice versa, a higher number of cells with smaller beams length.

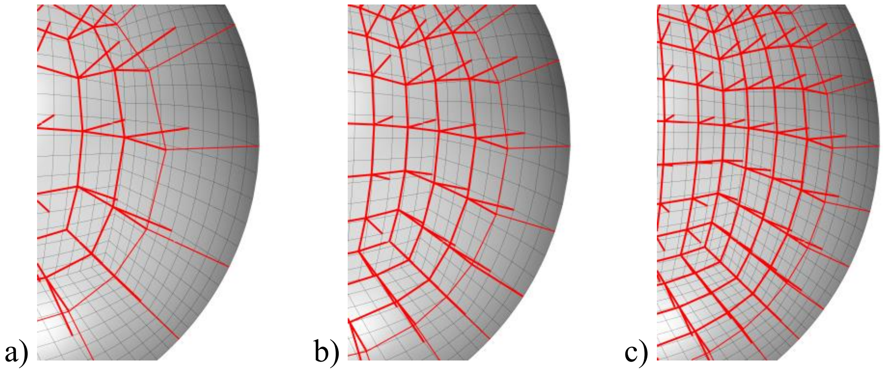

Figure 69. Different configurations of lattice structures, depending on the number and dimension of the unit cell: a) C4 configuration, b) C6 configuration, c) C8 configuration

Table 4 reports the mean dimension of the beams for each configuration. Being the structure a conformal one, given a configuration, the length of the beams is not constant.

Table 4. Mean beams dimensions for each lattice structure configuration.

Configuration	C3	C4	C5	C6	C7	C8
Mean beams dimension [mm]	30.6	23.1	18.6	15.6	13.2	11.7

To better describe the spherical shape of the tank, the external mesh is discretized with a higher number of quad faces. An important precaution is that the number of final subdivisions of the external shell is multiple of the number of the subdivision used for the creation of the internal lattice. This allows the radial beams to connect exactly at the nodes of the shell mesh, as shown in Figure 70.

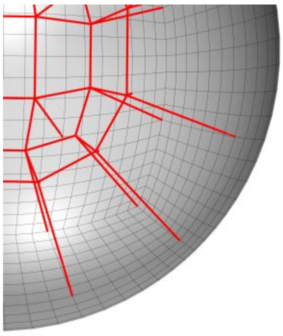

Figure 70. Connection between the beams and the shell: the node of the beam must coincide with the node of the quad face of the shell.

Once the tank with the internal structure has been modeled, the workflow for the multi-objective optimization presented in Section 3.2.2 can be initialized. As previously said, the optimization objectives are the mass minimization and the first natural frequency maximization. The drivers of the optimization are the lattice configuration, the diameters of the lattice beams and the thickness of the shell. Dealing with the diameters, the circumferential and the radial ones have been separately optimized as two different drivers. Taking into consideration the geometry and manufacturing constraints, admissible ranges for the drivers were imposed. The shell thickness ranges between 0.5 mm and 6.5 mm; the maximum value, 6.5 mm, was calculated as the limit for a structure to be considered a “thin wall” is that the thickness does not exceed 1/20 of the diameter. Both the circumferential and the radial beams diameter ranges between 0.5 mm and 1/3 of the cell size, depending on the configuration; the maximum beam diameter according to the configuration is reported in Table 5.

Table 5. Maximum beams diameter admissible for each lattice structure configuration.

Configuration	C3	C4	C5	C6	C7	C8
Maximum acceptable beam diameter [mm]	10.2	7.7	6.2	5.2	4.4	3.9

A fundamental constraint adopted by the proposed optimization algorithm is the utilization ratio of the structure; it is required for all the elements of the model, both beams and shells, to not exceed 95% of utilization. If a solution presents a utilization ratio higher than 95%, it is going to be penalized adopting the penalization function $P(x) = k \cdot \left(v(x)\right)^2$(see Section 3.2.2), with the k coefficient set to 5. The design phases and the workflow of Figure 30 have been implemented in Rhinoceros 7 (Robert McNeel & Associates) CAD software, inside the Grasshopper environment and using Karamba3D plugin [234] as FE solver and Octopus plugin [237] as multi-objective evolutionary optimization. Octopus plugin implements the HypeE algorithm [265]. The parameters used by the genetic algorithm and the setup of the multi-objective optimization are summarized in Table 6.

Table 6. Multi-objective optimization and genetic algorithm parameters.

Optimization objectives	
Mass	Minimize
First natural frequency	Maximize
Optimization drivers	
Lattice configuration	C3 to C8
Shell thickness	0.5 mm to 6.5 mm
Radial beams diameter	0.5 mm to 1/3 of cell dimension (see Table 5)
Circumferential beams diameter	0.5 mm to 1/3 of cell dimension (see Table 5)
Optimization constraints	
Utilization ratio	< 95%
Penalization coefficient	5

HypE algorithm parameters	
Elitism	0.5
Mutation probability	0.2
Mutation rate	0.9
Crossover rate	0.8
Population size	50
Max generations	50

Once the genetic algorithm has analyzed the last generation of individuals, the population can be represented by a Pareto chart, as in Figure 71, where the two axes present the two objectives of the optimization. As expected, the higher the mass, the higher the first frequency. As highlighted by the four zones, some configuration is more suitable than others depending on the area of the Pareto chart. The solutions characterized by the higher mass (Zone 1) are represented by the C3 configuration, with a shell thickness closer to the upper limit, 6.5 mm, and the diameter of the beams that ranges between 4.2 mm and 10.2 mm exploiting all the upper range of the allowable diameters for the C3 configuration. The Zone 2 is characterized by C7 configuration structures with a shell thickness closer to the 6.5 mm limit whereas the diameter of the beams ranges between 1.4 mm and 4.4 mm. The Zone 3 presents both C3 and C7 configurations; the shell thickness starts decreasing, presenting solution with a thickness down to 5.2 mm, and the beams too are thinner with diameters ranging from 0.5 mm to 0.8 mm. Finally, in the Zone 4 C7 and C8 configurations can be found with shell thicknesses always lower than 2.5 mm whereas the diameter of the beam covers the full admittable range going from 0.5 mm to 4.4 mm (C7 maximum diameter).

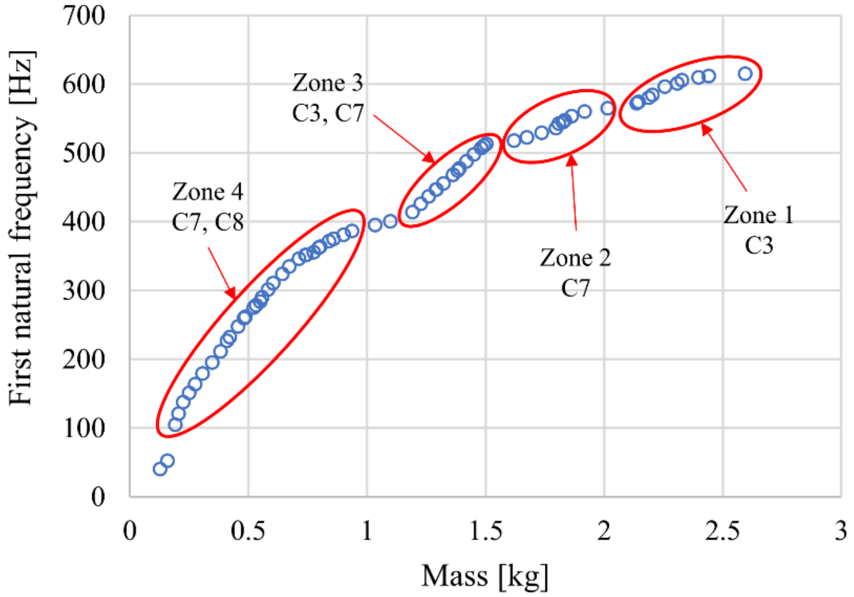

Figure 71. Multi-objective optimization results after 50 generations.

As previously said, when a multi-objective optimization is performed, the algorithms propose a set of compromise solutions and there is not a solution better than the others. The final choice is under the responsibility of the decision-maker. In the present case study, two approaches have been followed for selecting the final configuration. The first method simply selects the lighter solution that presents a first natural frequency higher than 100 Hz; the solution is presented in Figure 72 and its characteristics are reported in Table 7. It is worth mentioning that to obtain the same first frequency (103.5 Hz) with a tank without the internal lattice structure, the mass would be 0.299 kg, about 50 % more than the optimized one.

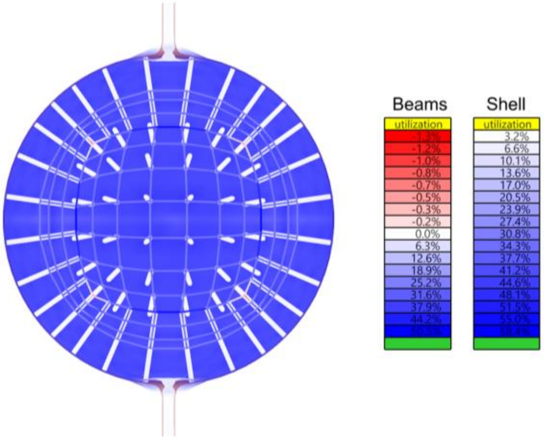
Beams
utilization
-1.3%
-1.2%
-1.0%
-0.8%
-0.7%
-0.5%
-0.3%
-0.2%
0.0%
6.3%
12.6%
18.9%
25.2%
31.6%
37.9%
44.2%
50.5%
Shell
utilization
3.2%
6.6%
10.1%
13.6%
17.0%
20.5%
23.9%
27.4%
30.8%
34.3%
37.7%
41.2%
44.6%
48.1%
51.5%
55.0%
58.4%

Figure 72. Section view of the multi-objective optimization solution presenting the lighter configuration and a first frequency higher than 100 Hz. The color map represents the utilization ratio.

Table 7. Characteristics of the solution presenting the lighter configuration and a first frequency higher than 100 Hz.

Configuration	Shell thickness [mm]	Radial beams diameter [mm]	Circumferential beams diameter [mm]	Mass [kg]	Frequency [Hz]
C7	0.5	1.98	0.76	0.192	103.5

This first method leads to a risky decision because even though almost all the launchers excite the payloads at frequencies lower than 100 Hz, the preliminary model that is being studied does not take into consideration the influence of the propellant inside the tank on the natural frequencies of the model. The second method is based on a multicriteria tournament decision (MTD) and allows to select the most suitable solution according to the weights given to the objectives, $W_{frequency}$ and W_{mass}. Three cases were simulated, with three different weights distributions. The first seeks a lightweight solution and the weights are distributed as $W_{frequency} = 0.3$ and $W_{mass} = 0.7$; the results are presented in Figure 73 and Table 8.

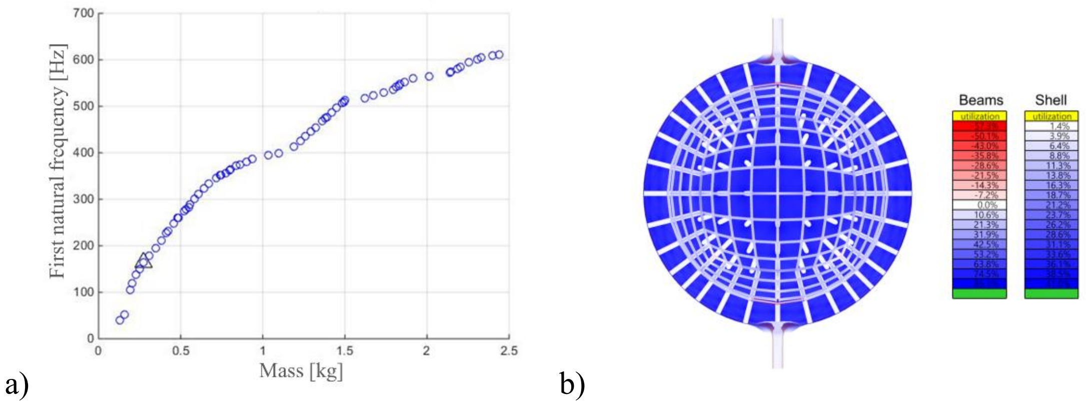

Figure 73. MTD solution obtained adopting the weights $W_{frequency} = 0.3$ and $W_{mass} = 0.7$: a) position in the Pareto chart, b) section view of the configuration. The color map represents the utilization ratio.

Table 8. Characteristics of the MTD solution obtained adopting the weights $W_{frequency} = 0.3$ and $W_{mass} = 0.7$.

Configuration	Shell thickness [mm]	Radial beams diameter [mm]	Circumferential beams diameter [mm]	Mass [kg]	Frequency [Hz]
C8	0.58	2.40	1.31	0.276	163.4

The second case proposes a balanced solution using $W_{frequency} = 0.5$ and $W_{mass} = 0.5$; the results are presented in Figure 74 and Table 9.

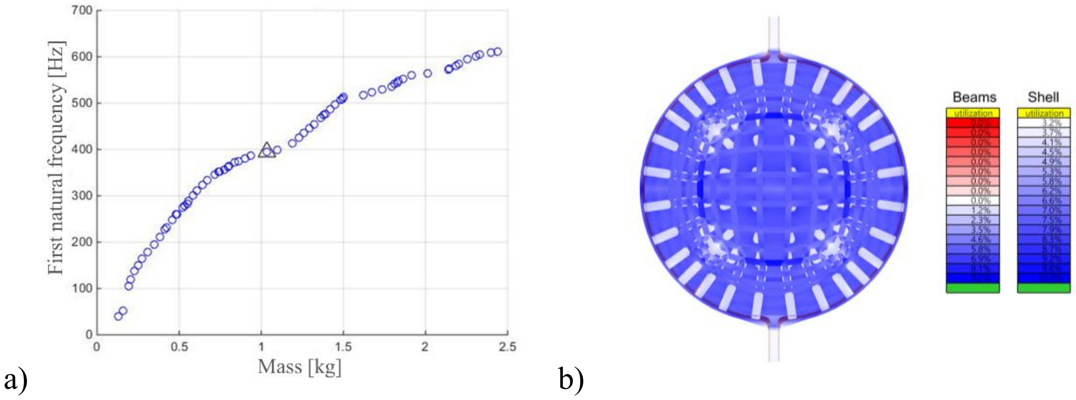

Figure 74. MTD solution obtained adopting the weights $W_{frequency} = 0.5$ and $W_{mass} = 0.5$: a) position in the Pareto chart, b) section view of the configuration. The color map represents the utilization ratio.

Table 9. Characteristics of the MTD solution obtained adopting the weights $W_{frequency} = 0.5$ and $W_{mass} = 0.5$.

Configuration	Shell thickness [mm]	Radial beams diameter [mm]	Circumferential beams diameter [mm]	Mass [kg]	Frequency [Hz]
C7	2.44	4.40	3.11	1.034	394.5

Finally, the third case gives more importance to a high first frequency adopting $W_{frequency} = 0.7$ and $W_{mass} = 0.3$; the results are presented in Figure 75 and Table 10. Note that the red color nearby the shell represents the mesh describing the shell elements and does not refer to the results of the structural analysis.

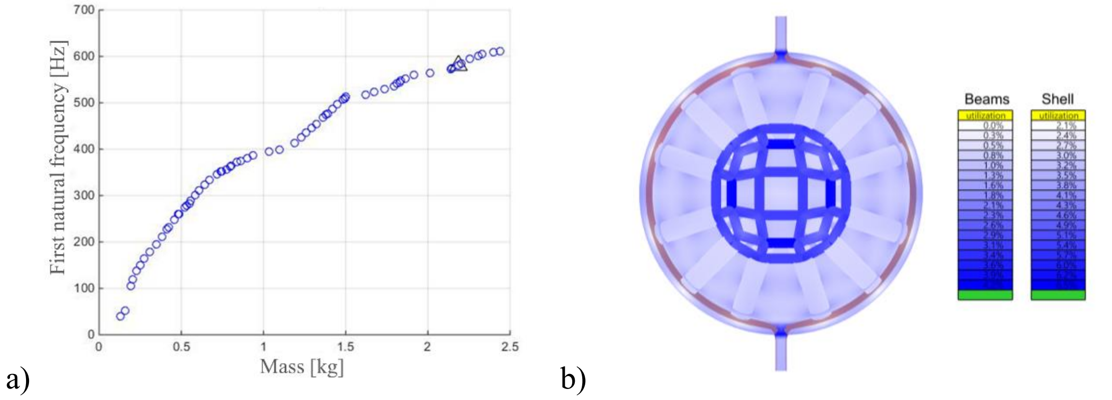

Figure 75. MTD solution obtained adopting the weights $W_{frequency} = 0.7$ *and* $W_{mass} = 0.3$*: a) position in the Pareto chart, b) section view of the configuration. The color map represents the utilization ratio. The red color nearby the shell represents the mesh describing the shell elements and does not refer to the results of the structural analysis.*

Table 10. Characteristics of the MTD solution obtained adopting the weights $W_{frequency} = 0.7$ *and* $W_{mass} = 0.3$*.*

Configuration	Shell thickness [mm]	Radial beams diameter [mm]	Circumferential beams diameter [mm]	Mass [kg]	Frequency [Hz]
C3	6.29	10.16	4.86	2.188	580.0

The introduction of an internal conformal lattice structure inside the propellant tank, allows, at equal first natural frequencies of the structures, for a mass reduction of about the 33% with respect to the structure without the structure. Moreover, an internal lattice structure could be beneficial to prevent the sloshing phenomenon, defined as the movement of a liquid, i.e., the propellant, inside another object, i.e., the tank, which is in turn undergoing motion [266]. Furthermore, the cellular structures, with their achievable porosity, could be exploited for propellant management devices helping to guide the propellant towards the outlet valve of the tank in low-gravity environments [267].

5 Numerical and experimental tests

This chapter presents the numerical and experimental tests performed for validating the mesh modeling method based on the subdivision surface. The geometrical accuracy of the model is verified by analyzing the Schwartz P-Surface and the gyroid TPMS unit cells; then a curvature analysis is performed on a unitary nodal point of a truss-like simple cubic unit cell. Furthermore, experimental tests are performed on lattice structures based on the regular repetition of the simple cubic unit cell manufactured by powder bed fusion (PBF) technologies, both of metallic and polymer materials. Contextually, a comparison between the selective laser sintering (SLS) and the multi-jet fusion (MJF) PBF technologies is proposed when producing polyamide 12 (PA12) parts.

5.1 Numerical validations of the subdivision surface modeling method

5.1.1 Geometrical deviation

As described in Section 2.2.3.1, the TPMS are frequently adopted as unit cells when modeling lattice structures due to their interesting properties, such as the smooth surfaces deriving from the zero mean curvature at each point of the surface. TPMS are defined by implicit functions and when they are modeled by adopting modeling methods based on different approaches, approximations are unavoidably done. These approximations can be compensated but high computational resources and time are required; due to computational efficiency, the geometry is often left as is and the geometrical deviation is evaluated. Approximations especially happen when discretizing the model using mesh-based approaches. A solution proposed by commercial software is the possibility of selecting the accuracy of the mesh, deciding the maximum deviation from the implicit function. The TPMS can be modeled by adopting the subdivision surface algorithm too [268]. Figure 76 shows the mesh modeling of the Schwartz P-surface, whose implicit equation is $cos(x) + cos(y) + cos(z) = 0$, and the gyroid, whose implicit equation is $sin(x) \cdot cos(y) + sin(y) \cdot cos(z) + sin(z) \cdot cos(x) = 0$. Starting from an elementary portion of the unit cell (Figure 76a and Figure 76d), the unit cell is obtained by roto-translation of the elementary portion (Figure 76b and Figure 76e), and the Catmull-Clark subdivision surface is applied (Figure 76c and Figure 76f).

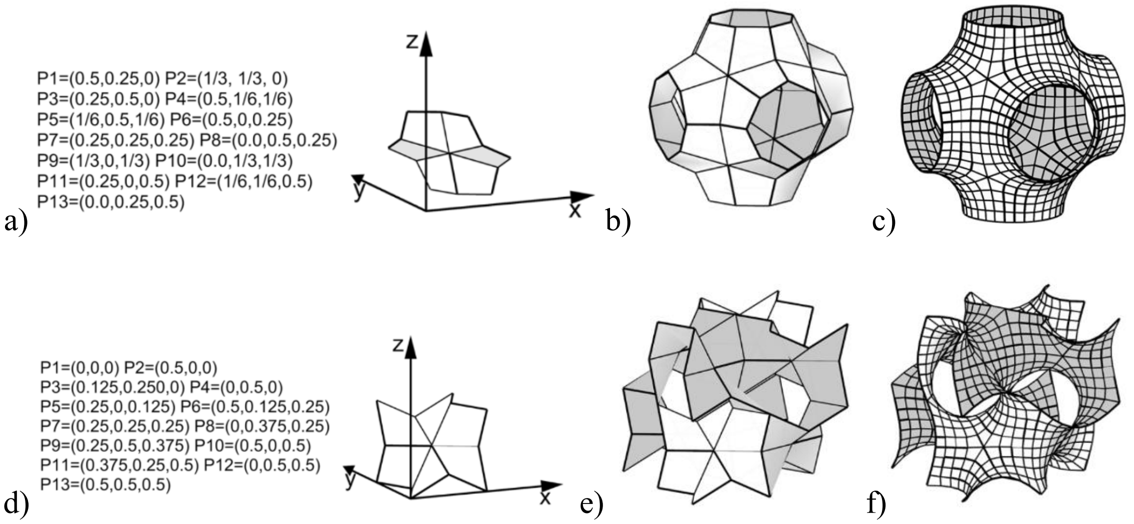
P1=(0.5,0.25,0) P2=(1/3, 1/3, 0)
P3=(0.25,0.5,0) P4=(0.5,1/6,1/6)
P5=(1/6,0.5,1/6) P6=(0.5,0,0.25)
P7=(0.25,0.25,0.25) P8=(0.0,0.5,0.25)
P9=(1/3,0,1/3) P10=(0.0,1/3,1/3)
P11=(0.25,0,0.5) P12=(1/6,1/6,0.5)
P13=(0.0,0.25,0.5)
z
y
x
a)
b)
c)
P1=(0,0,0) P2=(0.5,0,0)
P3=(0.125,0.250,0) P4=(0,0.5,0)
P5=(0.25,0,0.125) P6=(0.5,0.125,0.25)
P7=(0.25,0.25,0.25) P8=(0,0.375,0.25)
P9=(0.25,0.5,0.375) P10=(0.5,0,0.5)
P11=(0.375,0.25,0.5) P12=(0,0.5,0.5)
P13=(0.5,0.5,0.5)
z
y
x
d)
e)
f)

Figure 76. Mesh modeling of TPMS: a) to c) Schwartz P-Surface, d) to f) gyroid. a) and d): elementary portion, b) and e): coarse unit cell, c) and f) subdivided unit cell (after two iterations of the Catmull-Clark algorithm) [268].

By adopting this method, the selection of the accuracy is not available. So it is important to verify the geometrical deviation of the TPMS cells from a reference mesh available in commercial software obtained by implicit equations. To do so, the geometrical deviation of the subdivided P-Surface and the Gyroid unit cells from a reference mesh has been investigated. This research topic is an extension and continuation of the work by Savio et al. [268] who proposed a modeling method for obtaining TPMSs exploiting a mesh approach and the Catmull-Clark subdivision surface algorithm. The information achieved by these analyses is also beneficial for the methods presented in Chapter 3 since they share the modeling approach.

The size of the studied cell is 1 mm. The subdivided unit cells are modeled in Rhinoceros 7 (Robert McNeel & Associates) software, whereas the reference mesh is obtained from Netfabb 2020.3 (Autodesk) software by imposing a 0.008 mm accuracy. Figure 77 shows the comparison between the subdivided meshes and the reference ones after three iterations of the Catmull-Clark algorithm. As can be seen by the data reported in Table 11, the reference meshes have a higher number of vertexes and faces, resulting in a model difficult to handle, especially if the cell is repeated and thickened to obtain a lattice structure.

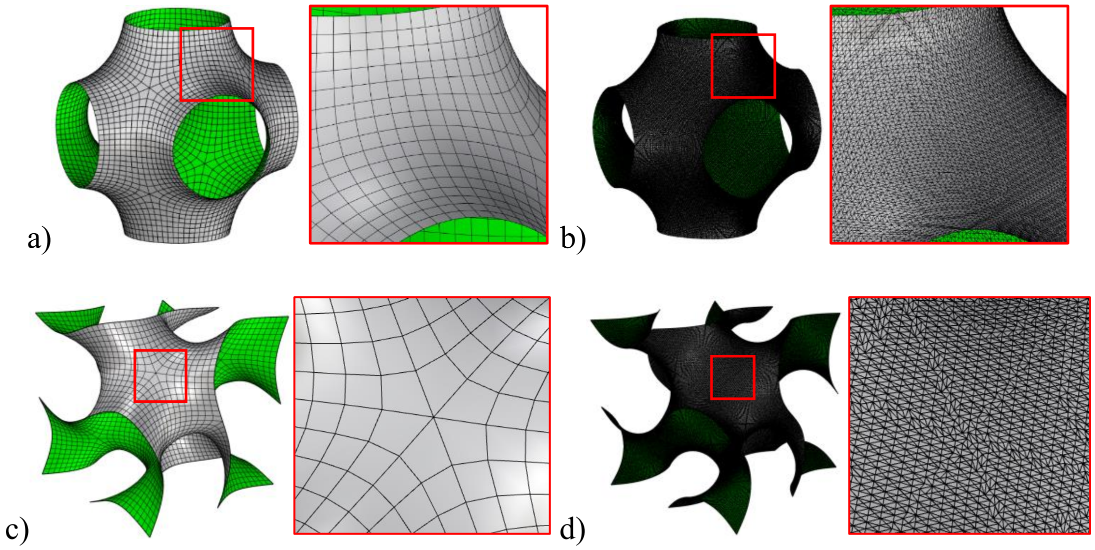

Figure 77. Comparison between the subdivided meshes and the reference ones: a) subdivided P-Surface, b) reference P-Surface, c) subdivided gyroid, d) reference gyroid. Three Catmull-Clark iterations were performed on the subdivided meshes.

Table 11. Comparison between the number of vertexes and faces of the subdivided meshes and the reference ones.

		Subdivided (3 iterations)	Reference
P-Surface	Vertexes	3260	62844
	Faces	3072	124160
Gyroid	Vertexes	3261	80589
	Faces	3072	158853

The geometrical deviation of the subdivided unit cells after up to three iterations of the Catmull-Clark algorithm was evaluated by using the Mesh-Mesh Deviation tool of the Rhino Open Projects [269] in Rhinoceros 7. The results are presented in Table 12. Figure 78 graphically shows the deviation at the third iteration of the Catmull-Clark algorithm. It is observed that the deviation of the subdivided cell never exceeds 1.3 % and 1.1 % in the P-Surface and the Gyroid cell, respectively. The deviation committed by using the subdivided TPMS cell is neglectable if considering the error introduced by the manufacturing machines [270]; more, if compared to the reference meshes, the subdivided ones have a number of vertexes an order of magnitude lower, and a number of faces two orders of magnitude lower. As previously said, this is computationally beneficial when dealing with lattice structures with a high number of cells.

Table 12. Geometrical deviation results.

Subdivision level	Maximum deviation [mm]	
	P-Surface	Gyroid
1	± 0.0127	± 0.0105
2	± 0.0126	± 0.0104
3	± 0.0129	±0.0111

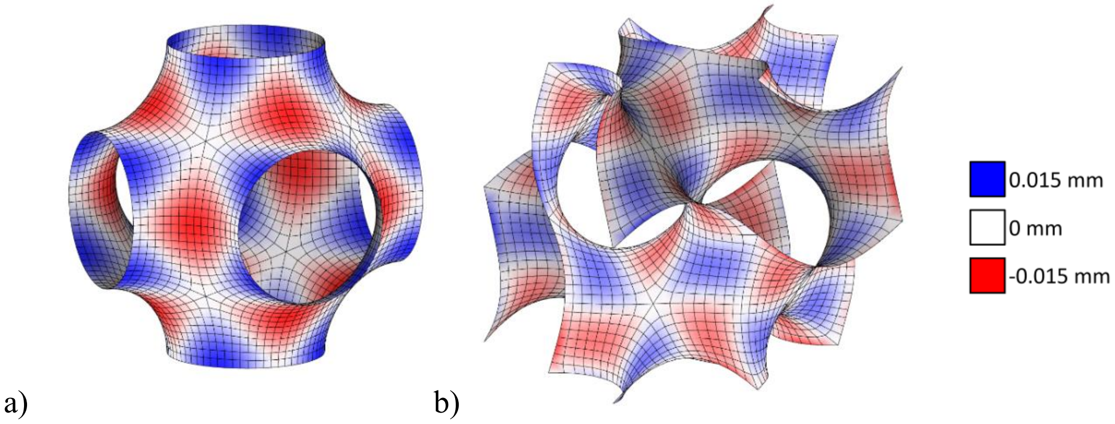

Figure 78. Geometrical deviation results after three Catmull-Clark algorithm iterations.

5.1.2 Curvature analysis

Another investigated property of the proposed modeling method is the continuity level of the surfaces that are obtained. A high level of continuity is preferable because it allows for less stress concentration in structural applications, fewer pressure drops in fluids transportations, and results in more aesthetical and smooth surfaces. Usually, the sharp edges that arise during the geometric modeling of components are removed by performing filleting operations. A situation of interest in the AM context is the modeling of truss-like lattice structures, where a common approach in standard CAD environments is to obtain the lattice element that will be repeated by intersecting cylinders meeting at the nodal point (Figure 79a) and further eliminating the sharp edges by filleting (Figure 79b).

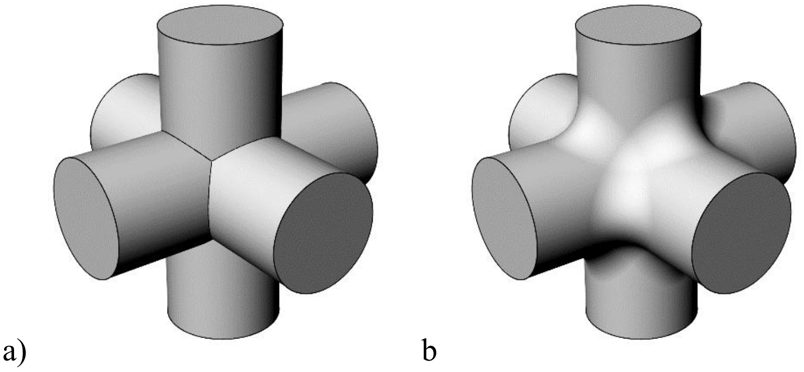

Figure 79. Truss-like unit cell modeled in a conventional CAD environment: a) trusses intersecting at nodal points, b) filleting operations for eliminating sharp edges.

The Catmull-Clark subdivision surface algorithm, instead, does not require further filleting operations since the mesh is iteratively smoothed by the algorithm itself. This can be seen in Figure 80, in which a starting single cubic mesh cell characterized by quad faces that generate sharp edges when meeting each other undergoes one, two, and three iterations of the Catmull-Clark algorithm.

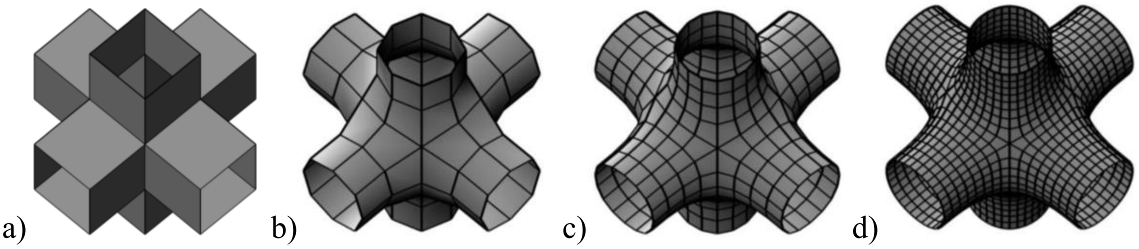

Figure 80. Single cubic cell subdivided with the Catmull-Clark algorithm: a) starting mesh, b) mesh after one iteration, c) mesh after two iterations, d) mesh after three iterations [222].

For defining the curvature of a surface, lets first recall the Frenet-Serret formula for planar curves, as the one in Figure 81:

$$\frac{d\boldsymbol{T}}{ds} = k\,\boldsymbol{N}$$

Where $\boldsymbol{T}$ is the tangent unit vector, and $\boldsymbol{N}$ is the normal unit vector. They are respectively defined as:

$$T = \frac{d\boldsymbol{r}}{ds}$$

$$\boldsymbol{N} = \frac{\frac{d\boldsymbol{T}}{ds}}{\left\|\frac{d\boldsymbol{T}}{ds}\right\|}$$

Where $\boldsymbol{r}(t)$ is a curve in the space representing the position of a point (particle) as a function of the time, and $s(t)$ is the arc length which the point has moved along the curve in the time t. By calling the curvature k as

$$k = \left\|\frac{d\boldsymbol{T}}{ds}\right\|$$

The Frenet-Serret formula is automatically obtained. So curvature describes the speed of rotation of the frame composed by $\boldsymbol{T}$ and $\boldsymbol{N}$.

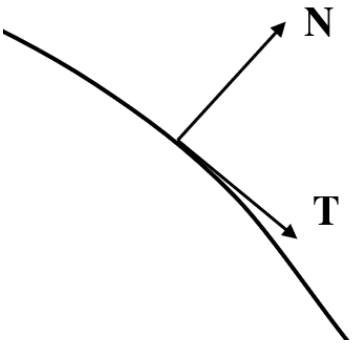

*Figure 81. **T** and **N** unit vectors in a planar curve*

When considering a surface and a point on it, it is possible to identify the unit tangent vector $\boldsymbol{T}$ and the corresponding normal unit vector N; if then the surface is intersected by the plane containing both the unit tangent and the normal, a planar curve is obtained and the curvature can be defined as described. At any given point, the two directions that identify the minimum and maximum curvatures are called principal directions, and the relative curvature are called principal curvatures.

In the present research, curvature analyses were conducted to compare the proposed mesh modeling method to filleted unit cells obtained by performing a filleting command in commercial CAD software. In particular, the cell obtained by applying the modeling approach and the Catmull-Clark algorithm (CC cell, Figure 82a) was compared to a cell obtained by intersecting beams with a squared cross-section (SF cell, Figure 82b) and with a circular cross-section (CYF cell, Figure 82c) that were filleted at the beams sharp intersections. The unit cells are designed to have the same cross-sectional area, i.e., 6.25 mm^2 and the side of the square, the diameter of the circumference, and the linear dimension of the CC cell are obtained accordingly. The dimension of the cell is 7.50 mm.

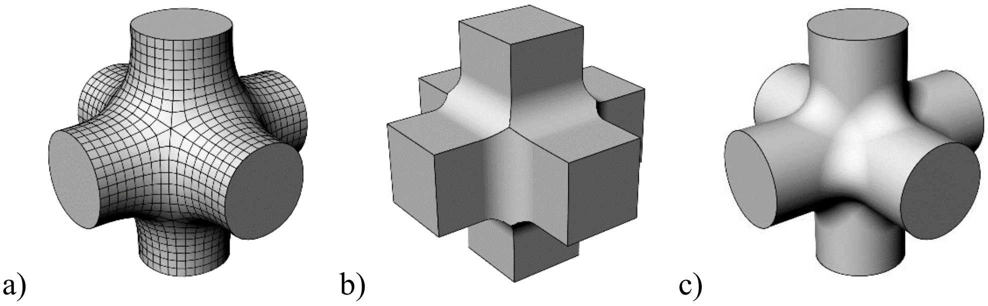

Figure 82. Simple cubic unit cells obtained by different modeling approaches: a) CC cell, b) SF cell, c) CYF cell.

The results of the curvature analysis are shown in Figure 83 where the principal curvatures are presented. The CC unit cell presents a C2 (curvature) continuity except at the extraordinary vertexes, i.e., vertexes with valence higher than 4, where continuity is C1. The SF and CYF unit cells, instead, present a C1 (tangency) continuity.

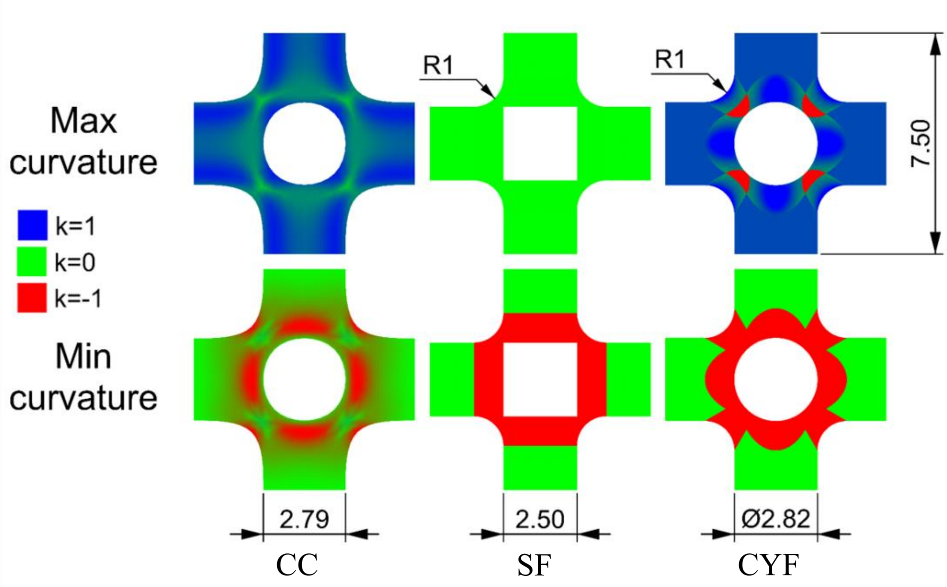

Figure 83. Curvature analysis results.

The effects of the different continuity are investigated by computing the stress concentration factor K_t, defined as:

$$K_t = \frac{\sigma_{peak}}{\sigma_{nom}}$$

Where σ_{nom} is the applied force divided by the strut section area and σ_{peak} is the maximum Von Mises stress on the cell. Linear elastic FE analyses were performed on the CC, CYF, and SF single cells, imposing boundary conditions to simulate the presence of the surrounding cells of a lattice structure and imposing a displacement to introduce a mean stress in the beam equal to 10 MPa. The analyses were performed in ANSYS Release 16 software using ″8nodes Solid185″ 3-D brick elements. According to Amado-Becker et al. [271] the material (Polyamide 12 , PA2200 by EOS [272]) was assumed to be isotropic and a Young's modulus equal to 1870 MPa and a Poisson ratio equal to 0.35 were used[273]. The trend of the K_t was studied by varying the filleting radius of the cells. The distribution of the Von Mises stress for the CC, CYF, and SF cells is presented in Figure 84.

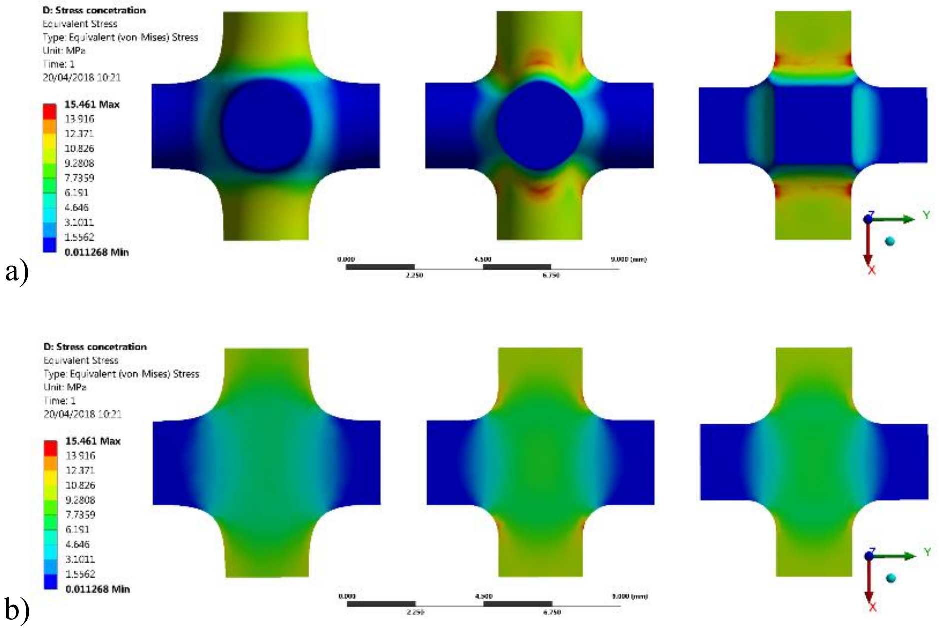
D: Stress concetration
Equivalent Stress
Type: Equivalent (von Mises) Stress
Unit: MPa
Time: 1
20/04/2018 10:21
15.461 Max
13.916
12.371
10.826
9.2808
7.7359
6.191
4.646
3.1011
1.5562
0.011268 Min
a)
0.000
4.500
9.000 (mm)
2.250
6.750
Y
Z
X
D: Stress concetration
Equivalent Stress
Type: Equivalent (von Mises) Stress
Unit: MPa
Time: 1
20/04/2018 10:21
15.461 Max
13.916
12.371
10.826
9.2808
7.7359
6.191
4.646
3.1011
1.5562
0.011268 Min
b)
0.000
4.500
9.000 (mm)
2.250
6.750
Y
Z
X

Figure 84. Distribution of the Von Mises stress for CC, CYF and SF cells: a) on the surface, b) in the median section.

The plot in Figure 85 shows the trend of the K_t as the fillet radius of the CYF and SF cells changes. The value of K_t is constant for the CC cell since it does not present fillets, whereas the value decreases as the filleting radius of the CYF and SF cells increases. Nevertheless, the K_t of the cells obtained by commercial CAD software is not going to decrease enough to reach the CC value, 1.1. So, the proposed mesh modeling method for lattice structures offers a better stress distribution along the cells if compared to more traditional approaches.

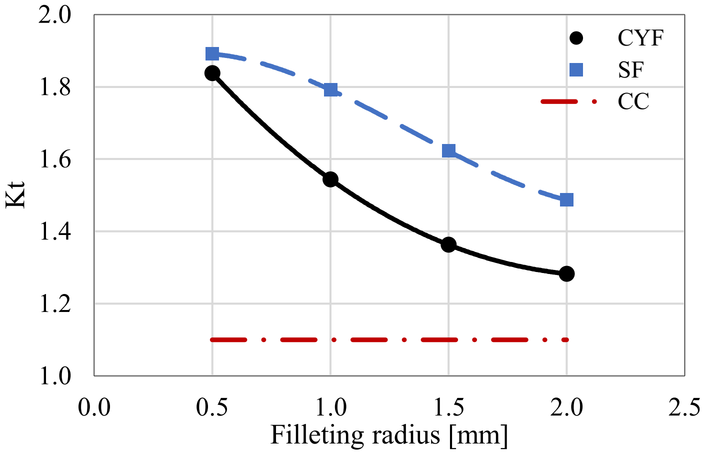

Figure 85. Stress concentration factor K_t at different values of the filleting radius.

5.2 Material and mechanical characterization of AM parts

Experimental campaigns are executed to test specimens manufactured by different AM technologies, concentrating on the PBF of both metals and polymers. The experimental tests aim to characterize the material and, above all, to validate the proposed modeling methods. Standardized specimens and lattice structure samples have been produced in stainless steel 316L material by the SLM technology and in polyamide 12 material by the SLS and the MJF technologies.

5.2.1 Test campaign on stainless steel 316L samples manufactured by SLM

In this test campaign, three types of specimens were produced in stainless steel 316L (SS316L) material by SLM PBF technology; one type according to international standards, and two types characterized by the presence of a lattice structure. The first type of sample, referred to as bulk cylindrical (BC), was adapted from the ASTM E606/606M standard [274] and the dimensions are shown in Figure 86. The diameter of the cross-section of the central part of the specimens was designed to be 2.8 mm to obtain a cross-sectional area of 6.16 mm^2 close to 6 mm^2, that is the value of the cross-sectional area of the lattice structure specimens.

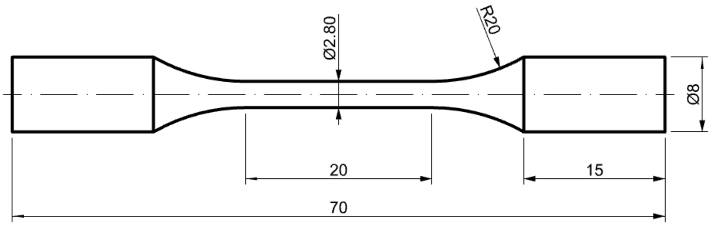

Figure 86. Dimensions of the BC specimen type, adapted from ASTM E606/606M standard.

The remaining two types of specimens present a regular lattice structure made up by the repetition of the simple cubic unit cell. The number of instances along the x-, y-, and z-axis are 3, 2, and 7, respectively and the cell size is 3 mm (Figure 87a). The cylindrical beams of the lattice have been modeling adopting two different modeling methods. The fist simply intersects cylinders at the nodal points of the lattice and results in sharp edges at the intersections and the samples are referred to as CY (Figure 87b); the second method adopts the mesh modeling approach previously described in Section 3.3.1, uses the Catmull-Clark algorithm (3 iterations), and the resulting specimens are referred to as CC (Figure 87c). The diameter of the CY sample beams measures 1.128 mm, whereas the CC has a beam dimension ranging between 1.116 mm and 1.150 mm (the section of a CC beam is not a circle). The cross-sectional area of each beam of both the CY and CC is 1 mm^2, for a total cross-sectional area of 6 mm^2.

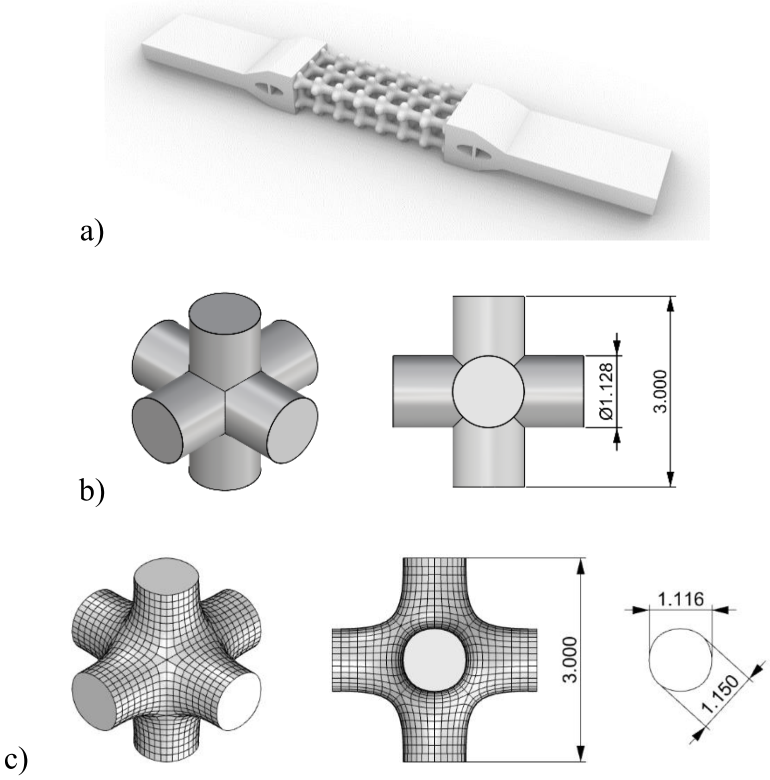

Figure 87. Lattice structure specimens type: a) specimen design, b) dimensions of the CY sample, c) dimensions of the CC samples.

Twelve specimens for each type of sample were produced in SS316L material by the SLM process adopting a Renishaw AM400 machine and using the Renishaw SS316L-0409 powder. The properties of the powder were transmitted by the producer and are presented in Table 13, whereas the process parameters of the manufacturing machine are reported in Table 14. Different process parameters were used at the borders for the BC samples; the CY and CC ones were manufactured only adopting the standard interior parameters to avoid skin related effects.

Table 13. Properties of the Renishaw SS316L-0409 powder.

Powder composition

Element	Mass (%)
Iron	Balance
Chromium	17.6
Nickel	12.7
Molybdenum	2.32
Manganese	1.31

Particle size*

Percentile	Diameter [μm]
$d_{10\%}$	18.8
$d_{50\%}$	29.4
$d_{90\%}$	45.5

*Laser diffraction analysis

Table 14. Process parameters used in the Renishaw AM400 machine.

	Interior	Borders
Laser power [W]	200	110
Exposure time [μs]	80	100
Point distance [μm]	60	20
Layer thickness [μm]	50	50
Layer rotation angle [°]	67	67
Scan pattern	Stripe	Contour

All the samples were built “standing” on the build plate, with the longitudinal axis aligned to the z-axis of the machine. No post-processing operations were performed on the manufactured parts, except for the powder evacuation and the support removal. One sample for each type of design is presented in Figure 88.

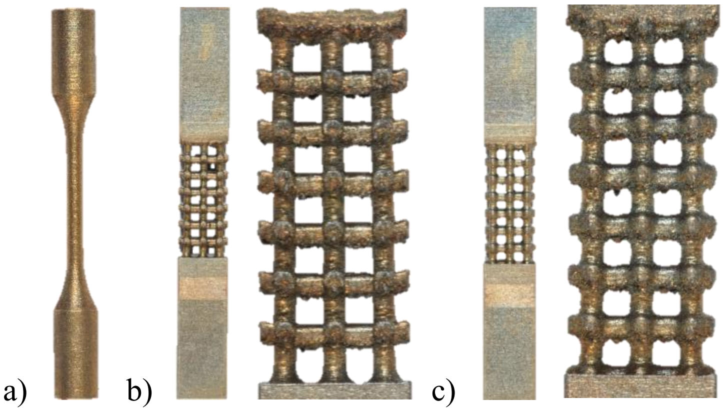

Figure 88. Printed samples: a) BC, b) CY, c) CC.

The geometries of the samples were then measured by a coordinate measuring machine (CMM) OGP SmartScope Flash 200. In particular, the diameters of the central zone of the BC samples and the diameters of the beams composing the lattices of the CY and CC samples were measured. In the CY and CC samples the beams were measured both in the front, i.e., the 3x7 cells face, and side, i.e., the 2x7 cells face, view of the lattice. Table 15 reports the mean value and the nominal dimension of the beams for the three types of samples; the diameters of the CY and CC cells only refer to the beams aligned to building direction. The low standard deviation highlights the precision and repeatability of the manufacturing method. The dimension of the BC samples is close to the nominal values. This does not happen to the CY and CC samples, probably due to the higher complexity of the specimens; more, since no post-processing such as sandblasting was performed, partially melted powders that remained attached to the part could have deceived the optical measurements of the CMM.

Table 15. CMM measured diameters: diameter of the central zone for the BC samples, diameters of the lattice beams aligned to building direction for the CY and CC samples.

	Mean [mm]	Nominal [mm]
BC	2.829 ± 0.012	2.800
CY	1.259 ± 0.006	1.128
CC	1.265 ± 0.007	1.116

The surface roughness along the building direction was also investigated. A Talysurf i-Series instrument was used to measure the roughness of the central section of the BC samples (Figure 89), whereas for the CY and CC types, the measurements were performed in the gripping zones at the extremity of the samples due to the impossibility of measuring the beams of the lattices. The measurements and analyses of the roughness were conducted using an evaluation length of 12.5 mm and a 2.5 mm sampling length, according to ISO 4287 [275] and ISO 4288 [276] standards. The results are shown in Table 16, where the R_a, R_z, and R_t parameters are reported. The roughness values of the CC and CY specimens are higher than the BC ones. This could be explained by the dedicated boundary scanning strategy adopted for manufacturing the BC parts, leading to a better surface texture.

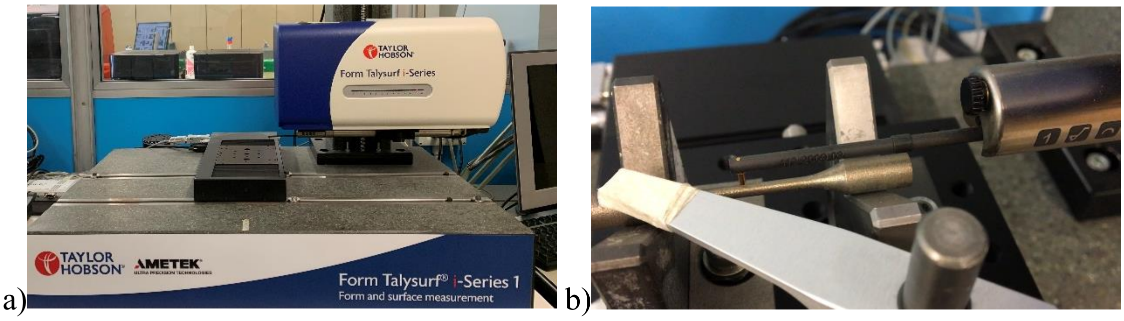

Figure 89. Roughness measurements on BC SS316L samples: a) Talysurf i-Series instrument, b) measurement of the roughness of the central section.

Table 16. Roughness parameters for SS316L samples produced by SLM technology..

	R_a [μm]	R_z [μm]	R_t [μm]
BC	5.5 ± 0.5	30.8 ± 2.7	49.2 ± 6.9
CY	7.7 ± 0.8	49.6 ± 6.2	60.0 ± 8.0
CC	8.4 ± 1.0	55.0 ± 6.7	69.2 ± 11.8

The specimens were then dynamically tensile tested on an MTS Acumen 3 Electrodynamic Test System equipped with a 3 kN load cell. The tests were performed with a stress ratio $R = 0$ to avoid buckling phenomenon; the stress ratio R is defined as:

$$R = \frac{\sigma_{min}}{\sigma_{max}}$$

Where σ_{min} and σ_{max} are the minimum and maximum excitation calculated on the cross-sectional area of the tested specimens. The test frequency was 10 Hz. For each type of specimen, groups of three samples were tested at four different stress levels, i.e., 473.2 MPa, 405.6 MPa, 338 MPa, and 270.4 MPa, that are the 70%, 60%, 50%, and 40% of the ultimate tensile strength (UTS) of the SS316L material, 676 MPa, according to the manufacturer datasheet [277]. Data was acquired with a 64 Hz timed trigger to store entire cycles signals and with a peak-and-valley trigger to store minimum and maximum signals at every cycle. No artificial cooling was applied. The number of cycles to failure was noted and further used to estimate the Stress – Number of cycles curves (S – N curves), also known as Wöhler curves, that were statistically computed according to ISO 12017 standard [278] using the method of linear least squares [279].

The used model equation is:

$$\log_{10} N = b_0 + b_1 \cdot \log_{10} S$$

Where N is the number of cycles, S is the stress, and b_0 and b_1 are curve parameters.

Table 17 reports the results of the fatigue tests, with the applied stress and the number of cycles to failure.

Table 17. Fatigue tests results for the SLM SS316L specimens.

Sample	Stress [MPa]	Number of cycles to failure		
		BC	CY	CC
1	473.2	112964	21402	43308
2	473.2	131073	24137	38776
3	473.2	110796	26737	39409
4	405.6	160491	65934	78566
5	405.6	221711	52926	83248
6	405.6	174883	56684	79870
7	338.0	439419	95161	170322
8	338.0	390904	103190	154972
9	338.0	296922	108765	167428
10	270.4	994627	213761	333488
11	270.4	1305787	224659	419924
12	270.4	905279	211225	388223

Table 18 presents the b_0 and b_1 parameters, the standard deviation SD, and the correlation coefficient R^2 of the interpolated S – N curves. Figure 90, Figure 91, and Figure 92 show the S – N curves of the three types of samples, together with the 10% and 90% limit curves at a 90% probability level. In Figure 93 and Figure 94 the 50 % and 90 % curves respectively are plotted together for comparison. According to ISO 12107 [278] and ISO 3534-1 [280] international standards, the limits curves indicate the confidence, that reflects the proportion of cases that the confidence interval would contain the true parameter value in a long series of repeated random samples under identical conditions; the probability, instead, corresponds to the reliability of the prediction.

Table 18. b_0 and b_1 parameters, SD, and R^2 of the interpolated S – N curves.

Specimen type	b_0	b_1	SD	R^2
BC	15.58	-3.94	0.076	0.96
CY	14.63	-3.81	0.064	0.97
CC	15.26	-3.98	0.032	0.99

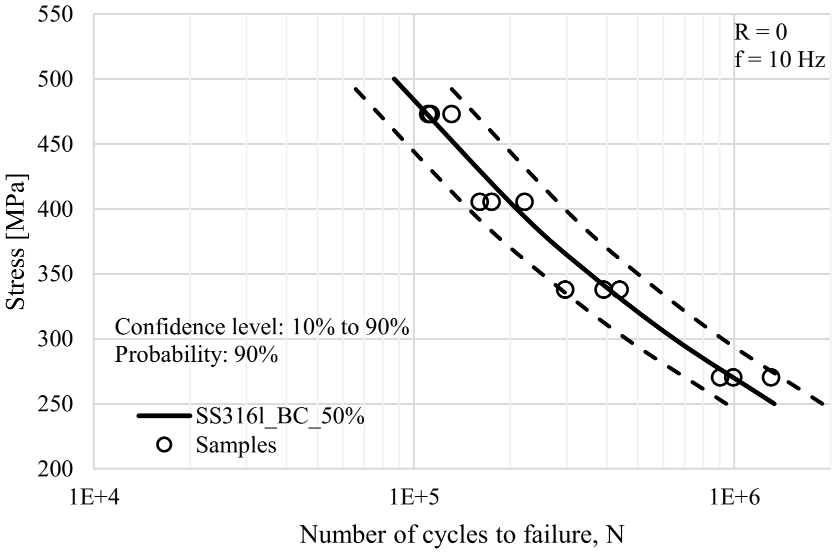

Figure 90. S – N curve of the BC samples.

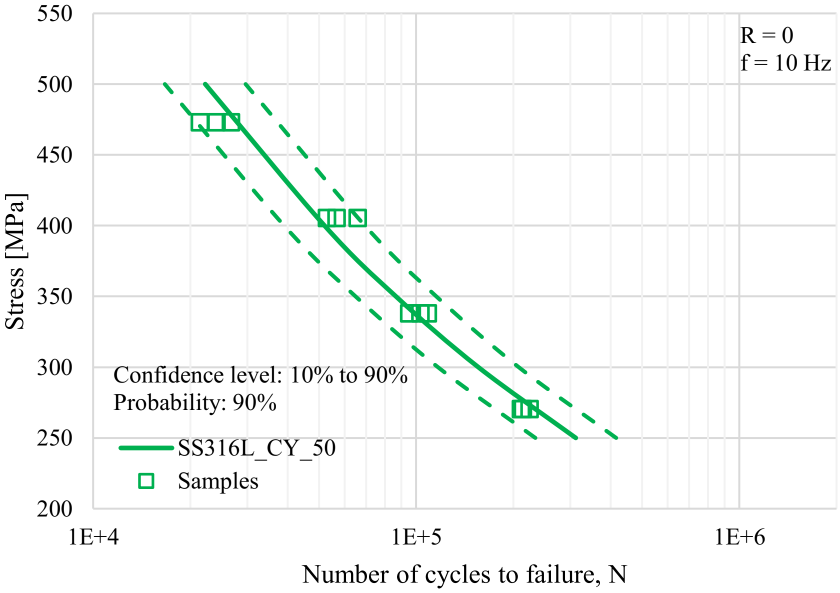

Figure 91. S – N curve of the CY samples.

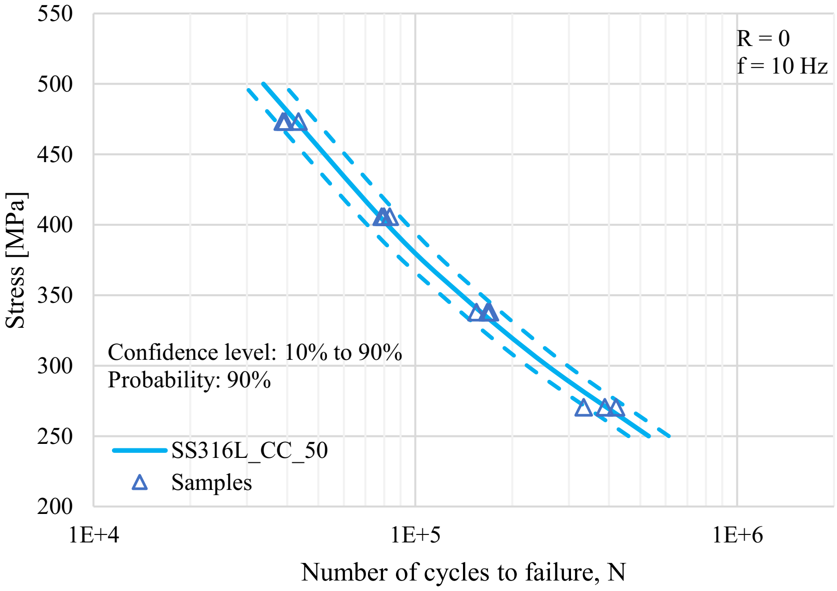

Figure 92. S – N curve of the CC samples.

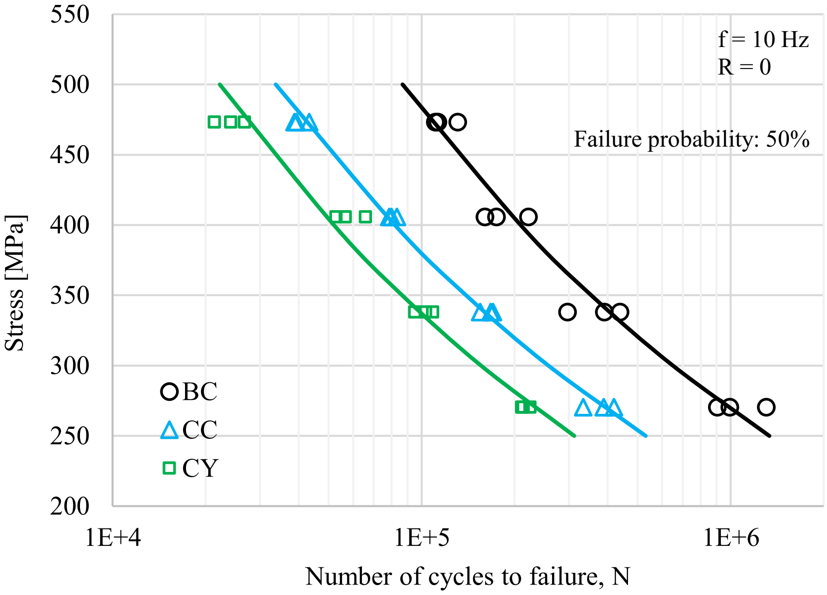

Figure 93. Comparison of the CY, CC, and BC S – N curves describing 50 % of probability of failure.

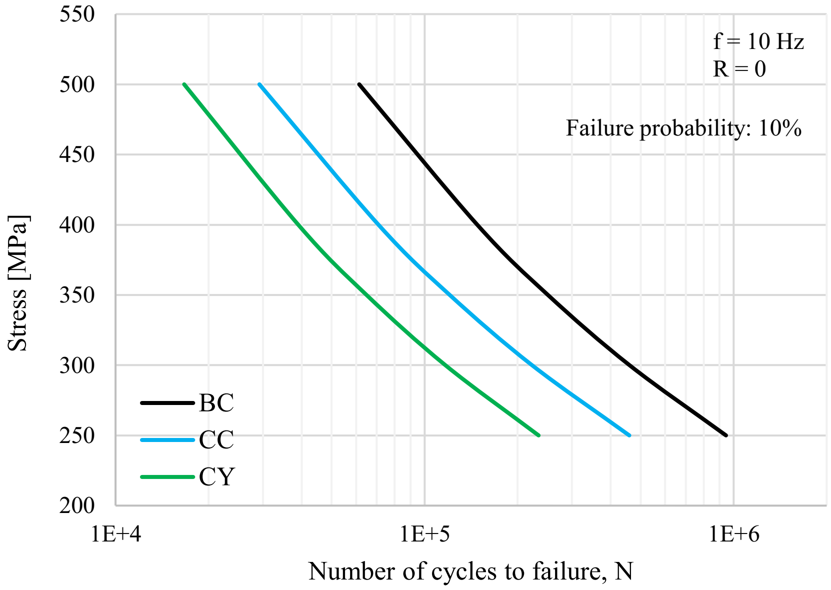

Figure 94. Comparison of the CY, CC, and BC S – N curves describing 10 % of probability of failure.

The results show that the number of cycles to failure of the CC samples is about one and a half times the number of cycles to failure of the CY ones. This is reasonable because the modeling method adopted for obtaining the lattice structure in the CC models allows for the elimination of the sharp edges and, therefore, a lower concentration of the stress at the nodal points. If comparing the fatigue life of the lattice structures with the results of the BC samples, the bulk material performs better. This behavior could be explained by various aspects. In the BC samples, there is no concentration of the stress at nodal points; the cross-sectional profile of the CY and CC lattices is greater than the BC design, increasing the possibility of crack initiation; more, since the cross-sectional area of a single lattice beam is smaller than the one of the cylindrical samples, at equal dimensions of internal defects, being the manufacturing technology the same, the lattices will be more prone to failure. In any case, these are only hypotheses and need to be verified with further studies, for example concentrating on the crack initiation and propagation phenomena with dedicated experimental tests.

5.2.2 Comparison between polyamide 12 parts manufactured by SLS and MJF

Another experimental campaign was conducted concentrating on polyamide 12 (PA12) polymer material produced by PBF technologies. In particular, a comparative study was realized between selective laser sintering and multi-jet fusion technologies. As mentioned in Section 2.1.1, the SLS and MJF technologies are both categorized as PBF techniques and can both produce PA12 parts. SLS and MJF differ by the way the thermal energy is provided and the way the sintering of the surrounding powders is prevented. In the SLS, the powder is sintered by a spot laser that scans the section of the component and heats only the areas defined by the 3D model. In the MJF, an array of inkjet print heads releases two types of printing ink: a so-called “fusing agent” inside the model boundaries, and a “detailing agent” edges of the model to inhibit the sintering of powders not wetted by the fusing agent; then, the layer is exposed to infrared (IR) heating lights to build the part. The MJF technology works line-by-line, thus is faster than the SLS. Having said that, a series of different types of specimens were produced both by the SLS and the MJF technologies and were compared. Among them, bulk and lattice structure specimens were fatigue tested covering a lack in the literature because, at the date of the tests, no Wöhler curves describing the behavior of the MJF parts were available. Moreover, the effect of different modeling methods for lattice structures on the fatigue life of the samples was investigated. For the sake of completeness, other aspects were explored, such as material microstructure, porosity and density of the printed parts, roughness of the samples, etc…

As the SLS machine and powders, an EOS FORMIGA P110 machine and the EOS PA2200-Performance [272] PA12 powder were used. For the MJF, the HP Jet Fusion 4200 machine and the HP 3D high-reusability PA12 powder [281] were used. The SLS process parameters are listed in Table 19, whereas the balanced print mode preset was used in the HP machine because it is not allowed to manually set and modify the parameters. Virgin and reused powders were mixed, using a refresh ratio (virgin: reused) of 1:1 for SLS and 1:4 for MJF.

Table 19. Process parameters and preset mode respectively used for SLS and MJF processes.

SLS		MJF	
Laser beam power	20 W	Preset mode	Balanced mode: one rolling step, two injection passes 10.5 s per layer
Laser scan speed	3000 mm/s		
Layer thickness	100 µm		
Laser spot size	~0.4 mm		
Building platform temperature	160 °C		
Virgin: reused powder ratio	1:1	Virgin: reused powder ratio	1:4

Seven different types of specimens were manufactured to undergo different characterization tests:

- The plates in Figure 95a were used for X-Ray Diffractometry (XRD) and SEM analyses.
- The cylinders in Figure 95b were used for He-pycnometry and Thermogravimetric Analysis and Differential Scanning Calorimetry (TGA-DSC).
- The ISO 527 type 1A specimens in Figure 95c had the geometries and the surface roughness measured, they were static tensile tested, and the fracture surfaces were analyzed by SEM.
- The ASTM E606 specimens in Figure 95d were fatigue tested and analyzed by SEM.
- Three types of lattice structures specimens in Figure 95e, Figure 95f, and Figure 95g were fatigue tested and analyzed by SEM.

(The powders used for the build were used too for X-Ray Diffractometry, TGA-DSC, and SEM analyses).

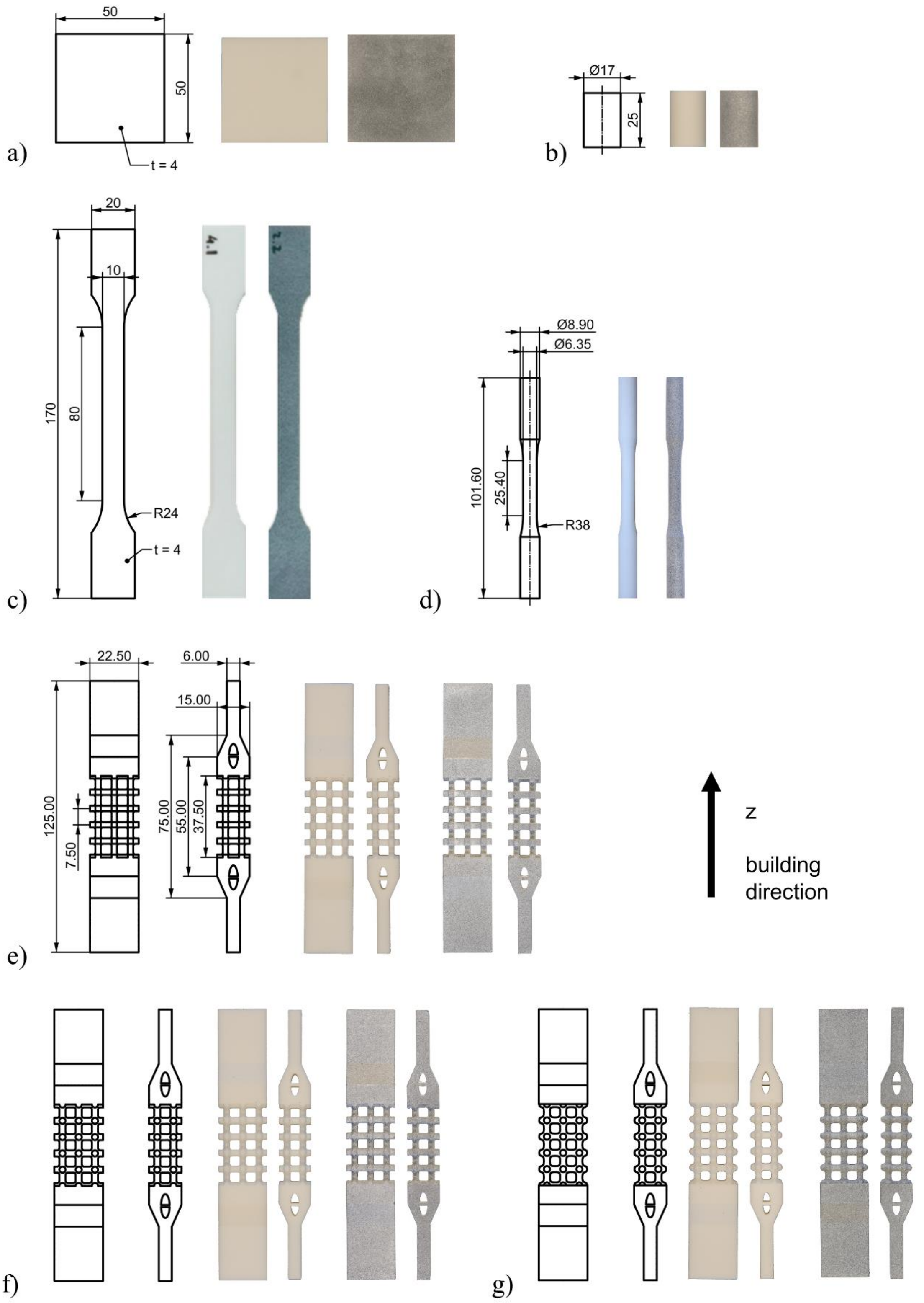
a)
50
50
t = 4
b)
Ø17
25
c)
20
10
170
80
R24
t = 4
4.1
2.1
d)
Ø8.90
Ø6.35
101.60
25.40
R38
e)
22.50
6.00
15.00
125.00
7.50
75.00
55.00
37.50
z
building
direction
f)
g)

Figure 95. Types of manufactured samples for characterizations: a) plates for XRD and SEM, b) cylinders for He-pycnometry and TGA-DSC, c) ISO 527-1A for static tensile tests, roughness, and SEM, d) ASTM E606/E606M for dynamic tensile tests and SEM, e) SF lattice structures for dynamic tensile tests and SEM, f) CYF lattice structures for dynamic tensile tests and SEM, g) CC lattice structures for dynamic tensile tests and SEM. Left: nominal dimensions, center: SLS part, right: MJF part.

The design of the lattice structures specimens is inspired by the one used during the SS316L campaign (Section 5.2.1). A simple cubic unit cell was regularly repeated along the x-, y- and z-direction 3, 2, and 5 times respectively. The unit cells are obtained by three different modeling methods. The so-called SF cell is obtained by intersecting 6 beams with squared cross-sections at the nodal points of the lattice and performing a filleting operation at the sharp edges generated at the intersections (Figure 96a). The so-called CYF cell is obtained by intersecting 6 beams with circular cross-sections at the nodal points of the lattice and performing a filleting operation at the sharp edges generated at the intersections (Figure 96b). The last cell, the CC cell (Figure 96c), is obtained by applying the Catmull-Clark subdivision surface algorithm. The curvature analysis of these three types of unit cells was previously studied as discussed in Section 5.1.2. The size of the cell is 7.5 mm. The dimensions of the cross-section of the three types of cells are set to obtain a 6.25 mm^2 cross-sectional area. So, the SF cell has a 2.50 mm strut size, the CYF cell has a 2.821 mm strut diameter, and the CC cell has a strut section that ranges between 2.79 mm and 2.88 mm.

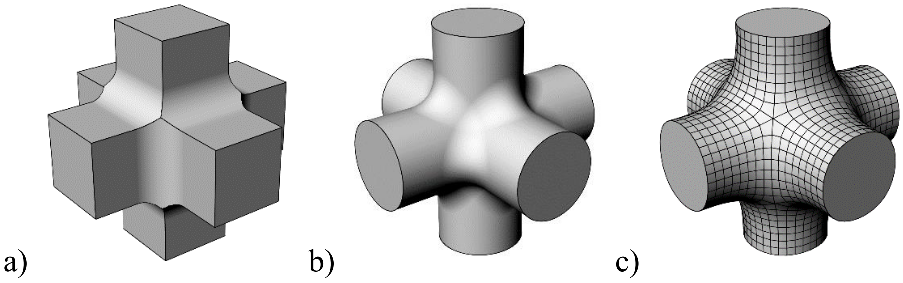

Figure 96. Simple cubic unit cells used in the lattice structure samples types: a) SF, b) CYF, c) CC.

First, the morphology of the powders and the printed parts was characterized by a Field Emission Gun electron microscope (FEI Quanta 200) in low vacuum mode. As can be seen in Figure 97a some of the SLS powders show cracks; the presence of these cracks is not yet fully understood but it has been supposed to be related to the synthesis process, where powders are obtained by dissolution in ethanol at high pressure and temperature, followed by slow crystallization [53,282]; the evaporation of the remaining ethanol could be the cause of the cracks. Even though MJF powders are in contact with the solvents of the fusing and detailing agents, cracks in Figure 97b are not as evident as in the SLS; this could be due to elements of the agents because they contain 2-pyrrolidone and triethylene glycol, that have boiling points of 251°C and 288°C respectively [283], higher than ethanol (78°C), and the temperature during the printing process does not exceed 185 °C [8].

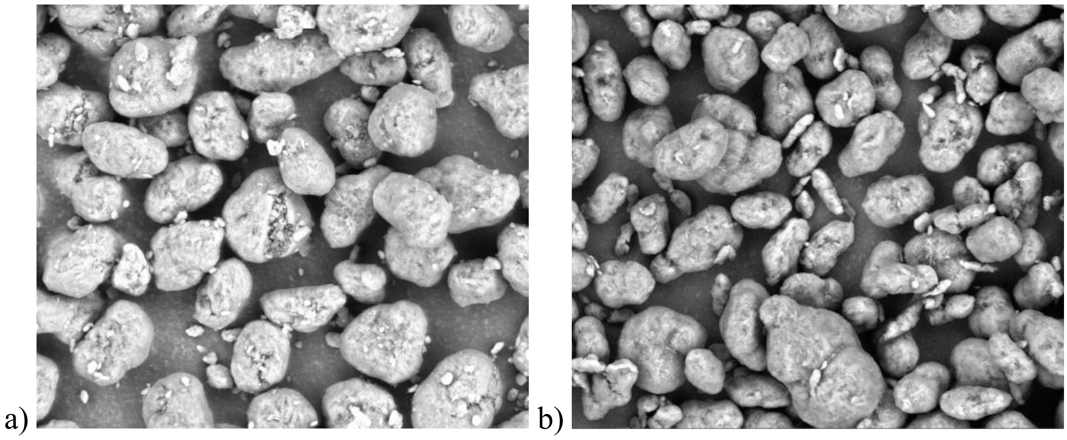

Figure 97. SEM analyses of the starting powders used for the manufacturing process: a) SLS, b) MJF.

XRD analyses were performed with a Bruker D8 Advance platform on both the starting powders and the rectangular plates (Figure 95a) using a Cu-Ka radiation with a scan speed of 5°/sec and a scan step of 0.01 in the range $2\theta = 10° - 40°$. The results in Figure 98 highlight the presence of both α-phase and γ-phase in the starting powders, whereas the printed parts mainly present γ-phase and a small shoulder of α-phase. The two technologies do not present significant differences, in accordance with other studies in the literature [53,54,284].

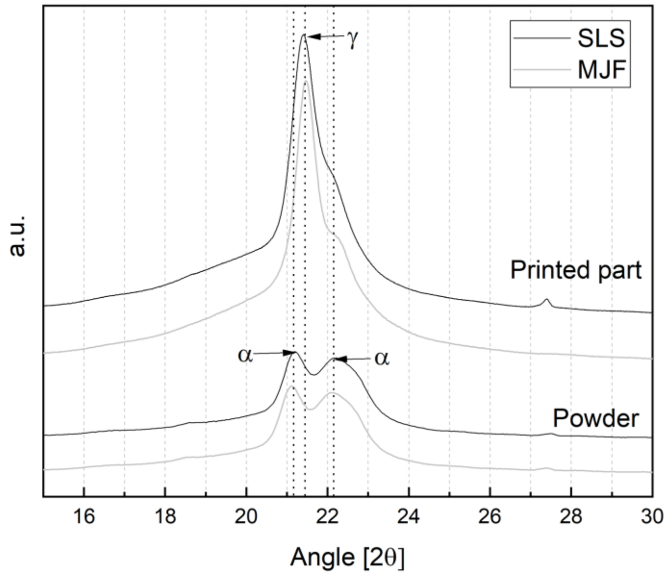

Figure 98. XRD results for powders and printed parts of SLS and MJF technologies.

Then TGA-DSC analyses were performed on the powders and the core parts of the cylindrical samples in Figure 95b using a Mettler-Toledo TGA/DSC 3+ instrument on 5 ± 0.5 mg samples in the range 25 °C – 300 °C, at a heating rate of 10 °C/min under nitrogen flow. The crystallinity percentage (C%) was calculated as the ratio between the specific heat of fusion of the sample and the specific heat of fusion of 100% crystalline PA12, equal to 209.3 J/g [285]. The heat of fusion was calculated as the integral of the peak. The curves in Figure 99 show a single peak corresponding to the melting temperature of 188.6 ± 0.1 °C for SLS and 187.7 ± 0.2 °C for MJF. Similar results were obtained by Cai et al. [52] that measured 188.9 °C for the SLS EOS PA2200 and 188.4 °C for the HP PA12 3D High Reusability. In the printed samples, the peak decreases to 183.1 ± 0.5 °C and 182.7 ± 0.4 °C for SLS and MJF, in accordance with the study of Chen et al. [286]. Finally, the percentage of crystallinity drops when moving from the powders to the printed parts; in the SLS the crystallinity decreases from 49.1 ± 0.5 % to 24.5 ± 0.1, and in the MJF it decreases from 48.3 ± 0.4 % to 31.5 ± 0.2 %. The measured melting temperature, enthalpy of fusion, and crystallinity are also reported in Table 20.

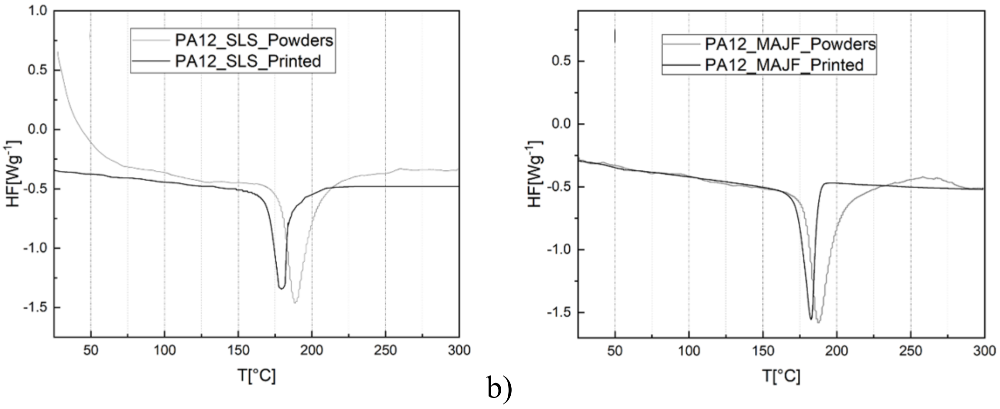

a) b)

Figure 99. TGA-DSC analyses on powders and printed parts: a) SLS, b) MJF.

Table 20. TGA-DSC results for the powders and printed parts manufactured by SLS and MJF: melting temperature, enthalpy of fusion, and crystallinity.

	T_m [°C]	H_m [J/g]	Crystallinity [%]
SLS Powder	188.6 ± 0.1	102.9 ± 1.1	49.1 ± 0.5
SLS Part	183.1 ± 0.5	52.3 ± 0.4	24.5 ± 0.1
MJF Powder	187.7 ± 0.2	101.2 ± 0.9	48.3 ± 0.4
MJF Part	182.7 ± 0.4	65.9 ± 0.3	31.5 ± 0.2

Density measurements were performed by He-pycnometry analyses using an Accupyc 1340 instrument; the density of the starting powders, ρ_{th}, and the apparent density, ρ_{app}, of three cylindrical samples (Figure 95b) for each technology were obtained. The bulk density of the cylinders, ρ_{bulk}, was calculated as:

$$\rho_{bulk} = \frac{mass_{cylinder}}{volume_{cylinder}}$$

Then, the total porosity, P_{tot}, of the printed parts was calculated as [287]:

$$P_{tot} = 1 - \frac{\rho_{bulk}}{\rho_{th}}$$

The open porosity, P_{open}, as:

$$P_{open} = 1 - \frac{\rho_{app}}{\rho_{th}}$$

Finally, the closed porosity, P_{close}, was calculated as:

$$P_{close} = P_{tot} - P_{open}$$

The results of the measurements are reported in Table 21.

Table 21. Densities and porosities of the SLS and MJF powders and parts.

	SLS	MJF
ρ_{th} [g/cm^3]	1.058 ± 0.001	1.056 ± 0.001
ρ_{bulk} [g/cm^3]	0.974 ± 0.011	0.985 ± 0.025
ρ_{app} [g/cm^3]	0.991 ± 0.002	0.997 ± 0.011
$\rho_{datasheet}$ [g/cm^3]	0.93	1.01
P_{tot} [%]	7.95 ± 0.09	6.75 ± 0.18
P_{open} [%]	6.35 ± 0.01	5.62 ± 0.06
P_{close} [%]	1.61 ± 0.10	1.13 ± 0.24

The total porosity of SLS printed parts (7.95 %) is higher than MJF ones (6.75 %), and this is also reflected in the percentage of closed porosity, 1.61 % for SLS printed parts and 1.13 % for MJF printed parts. The porosity inside PA12 manufactured by AM technologies is a known phenomenon; the results of this campaign for the SLS parts, if compared to other studies such as the one by Van Hooreweder and Kruth [288] and O'Connor et. al [289], show a higher level of total porosity.

Measurements were done by the OGP SmartScope Flash 200 CMM. The width and thickness of the central part of the ISO 527 type 1A specimens (Figure 95c), the diameters of the central part of the specimens adapted from ASTM E606/E606M standard (Figure 95d), and the size of the beams of the three types of lattice structures (Figure 95e, Figure 95f, Figure 95g) along the z-direction both in the front and side view were measured. Figure 100 shows the setup during the measurements of the thickness of a ISO 527 type 1A specimen.

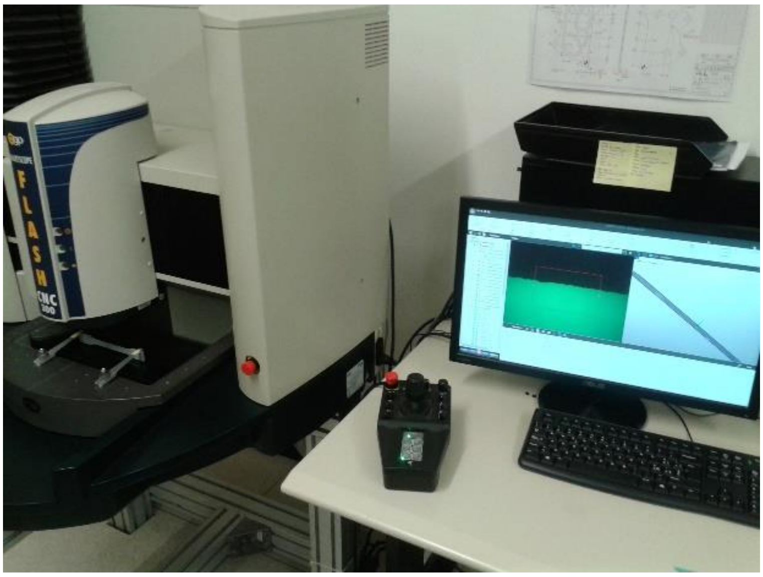

Figure 100. OGP SmartScope Flash 200 CMM setup during the measurement of the thickness of a ISO 527 type 1A specimen produced by MJF, on the testbed on the left. On the right, the software shows the optically acquired profile and the nominal CAD file.

The difference between the measured and the nominal dimensions was calculated, and the size error was obtained and is reported in Table 22. The size error can be both positive or negative, depending on whether the measured feature is bigger or smaller than the nominal. Analyzing the results for the SLS parts, the lattice samples have a dimensional error higher than the standardized samples; this could be due to the more complex geometry of the lattice structures. This trend is not found in the MJF manufactured parts, where the ISO 527 specimens have the biggest dimensional error. These linear measurements do not take into consideration the shape errors that introduce errors when acquiring linear dimensions with optical instrumentation.

Table 22. Size error in [mm] of the different specimen types.

	SLS	MJF
ISO 527	0.034 ± 0.035	0.319 ± 0.079
ASTM E606	0.052 ± 0.030	-0.053 ± 0.069
SF	0.099 ± 0.031	0.053 ± 0.061
CYF	0.095 ± 0.030	-0.091 ± 0.050
CC	0.089 ± 0.043	-0.084 ± 0.080

The surface roughness R_a parameter was measured along the growing direction, on the top surface, and on the bottom surface of the ISO 527-1A specimens (Figure 95c) with the Talysurf i-Series instrument. An evaluation length of 12.5 mm and a sampling length of 2.5 mm were adopted. Results are reported in Table 23. The bottom face presents the highest roughness in both SLS and MJF specimens. This could be explained by the absence of post-processing on the manufactured samples causing partially un-melted powders to remain stuck on the parts, especially on the bottom surface, as can be seen in the SEM images in Figure 101.

Table 23. Surface roughness R_a parameter in [μm] measured on the ISO 527-1A specimens manufactured by SLS and MJF technologies.

	SLS	MJF
Top face	10.4 ± 1.6	8.7 ± 0.9
Bottom face	15.0 ± 2.3	13.3 ± 1.0
Building direction	10.8 ± 0.8	11.2 ± 1.2

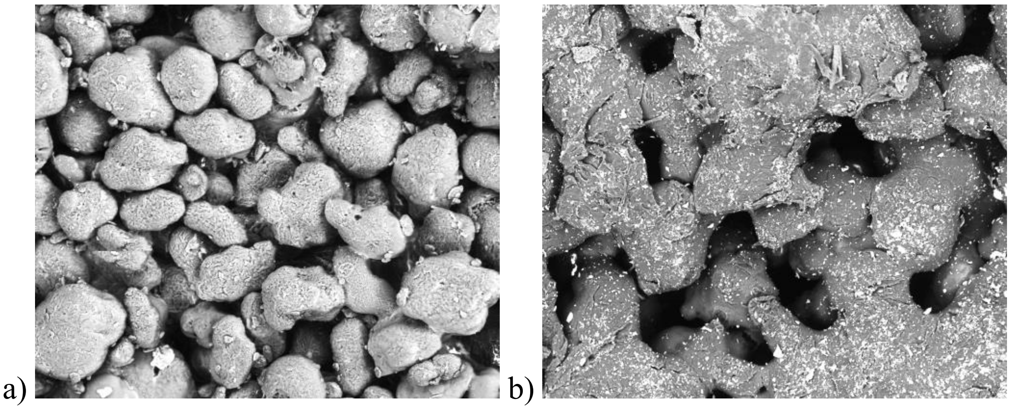

Figure 101. SEM analyses on the surfaces of the printed parts: a) SLS, b) MJF.

Tensile tests were performed on five ISO 527 type 1A specimens (Figure 95c) on the MTS Acumen 3 Electrodynamic Test System equipped with a 3kN load cell and an MTS 634.31 F extensometer. The setup is shown in Figure 102. The test speed rate was 2 mm/min and the gauge length was 10 mm.

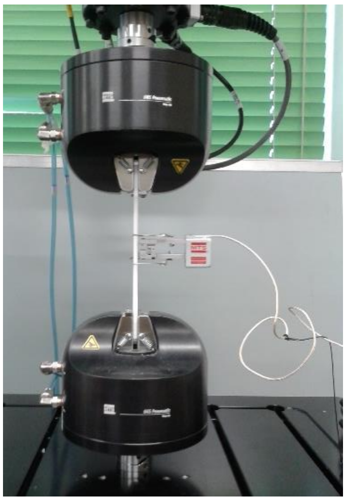

Figure 102. Tensile test setup. ISO 527 type 1A sample produced by SLS technology gripped by the MTS Acumen 3 Electrodynamic Test System and with the extensometer connected.

The Stress – Strain curves and True stress – True strain curves were plotted, and the Young's modulus, the ultimate tensile strength (UTS), the strain at break (ε_{max}), and toughness were calculated. The true strain, ϵ, and the true stress, σ', are calculated as [290]:

$$\epsilon = \ln\left(\frac{l}{l_0}\right)$$

$$\sigma' = \sigma\,(1 + \epsilon)$$

where l is the elongation, l_0 is the gauge length, and σ is the engineering stress. The material toughness, defined as the area under the true curve until fracture [291], is obtained by:

$$Toughness = \int_0^{\epsilon_f} \sigma' d\epsilon$$

The curves of the tensile tests are presented in Figure 103 and the mechanical properties are reported in Table 24.

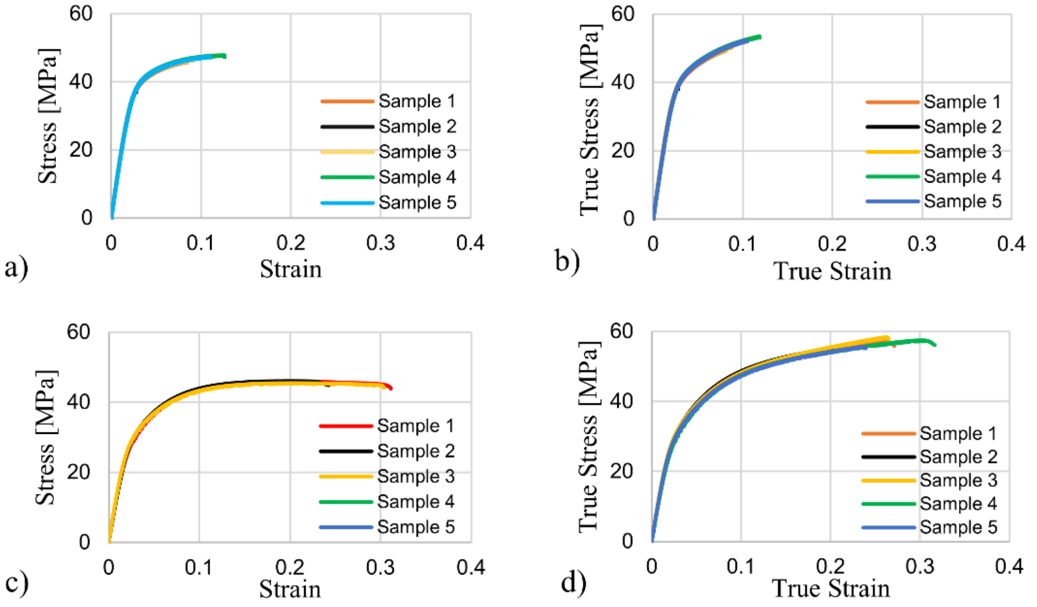

Figure 103. Static tensile test results: a) SLS Stress - Strain, b) SLS True Stress - True Strain, c) MJF Stress - Strain, d) MJF True Stress - True Strain.

Table 24.Mechanical properties of the PA12 polymer manufactured by SLS and MJF technologies.

	SLS	MJF
E [GPa]	1.87 ± 0.04	1.53 ± 0.06
UTS [MPa]	46.93 ± 0.86	45.59 ± 0.38
ε_{max} [%]	10.3 ± 1.9	30.0 ± 4.9
Toughness [J/m^3]	3.8 ± 0.9	11.7 ± 2.1

The SLS samples are stiffer with a slightly higher Young's modulus than MJF and a lower deformation at break, 10 %, against the 30 % of the MJF ones. Thanks to the higher deformation reached by the MJF specimens, they also result tougher than the SLS parts. This higher toughness is confirmed by the analyses of the fracture surfaces of the MJF samples (Figure 104c and Figure 104d), where the upper part shows a ductile fracture surface with signs of plastic deformation and meets with a smoother lower part where the failure occurs, in accordance with O'Connor et al. [289]. The fracture surfaces of the SLS in Figure 104a, instead, show a brittle behavior, with brittle fracture paths and no signs of deformation, in accordance with the findings of Van Hooreweder et al. [55].

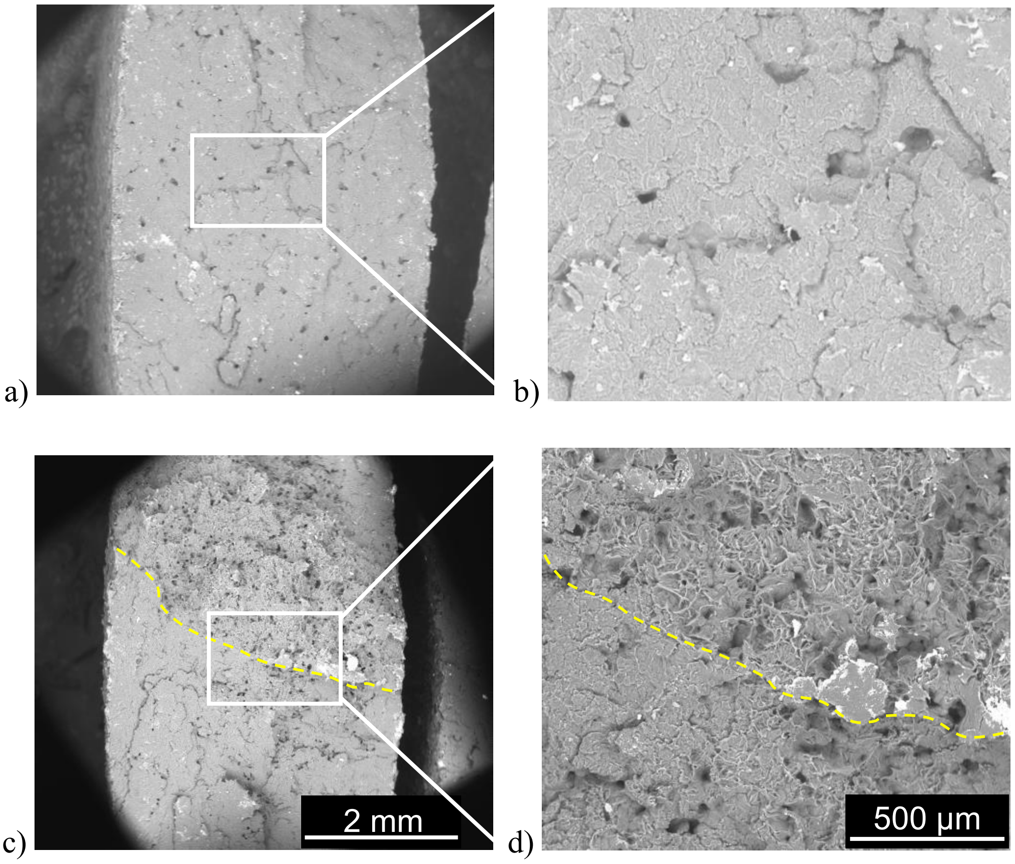

Figure 104. SEM analyses on the fracture surfaces of the tensile tested specimens: a), b) SLS, c), d) MJF.

The obtained mechanical properties have been compared with other studies available in the literature (Table 25). The properties of the SLS manufactured specimens correspond except for few occasions. Cai et al. [52] and Xu et al. [292] found higher elongations at break the tested specimens were produced with different orientations in the build plate, i.e., laying in the XY plane instead of along the z-axis; Van Hooreweder and Kruth [288] found a higher modulus and a lower elongation at break, but they stated that the process parameters were optimized to increase the stiffness of the parts. Moving to MJF technology, Morales-Planas et al. [293] found a Young's modulus higher than all the other studies in the literature testing the specimens in a similar way if compared to the others. Furthermore, the results obtained by the experimental campaign show a slightly higher Young's modulus than the others and an elongation at break comparable to the one of the samples printed along the y-axis (YZ plane) by O'Connor [289] and the ones printed along the x-axis (XY plane) by Cai et al. [52]. Considering other studies that compared the two PBF technologies, Sillani et al. [294] similarly obtained MJF parts tougher than the SLS ones, but they used the SLS process parameters optimized for the best surface finish and not for the best mechanical properties. Xu et al. [292], instead, found a contrasting behavior with SLS samples showing a higher Young's modulus, UTS, and elongation than MJF, but the study reported that the parts were manufactured laying on the build plate, i.e., on the XY plane and not along the z-direction, and it was proven that the properties of parts manufactured by the MJF techniques differ depending on the building direction [289,293]; more, the experimental conditions of the studies could have been different influencing the results.

Table 25. Comparison of the obtained mechanical characteristics with other studies in the literature.

Technology	E [GPa]	UTS [MPa]	ε_{max} %	Printing direction	Machine	Powder	Ref.
SLS	1.76 ± 0.02	43.6 ± 0.5	31.6 ± 2.9	XY plane	EOS FORMIGA P 110	Not specified	[292]
	1.68 ± 0.04	47.6 ± 1.4	6.6 ± 0.5	X axis	DTM 2500plus	3D Systems Duraform PA12	[294]
	1.61 ± 0.06	40.6 ± 3.2	3.7 ± 0.5	Z axis			
	1.72 ± 0.01	45.1 ± 0.5	10.0 ± 0.1	XY plane	Not specified	3D Systems Duraform PA12	[295]
	1.64 ± 0.01	46.4 ± 0.1	16.9 ± 0.1	X axis	EOS FORMIGA P 100	EOS PA 2200	[296]
	2.16 ± 0.05	49.0 ± 1.7	4.0 ± 0.3	Z axis	EOS P 730	EOS PA2200	[288]
	1.39 ± 0.03	44.0 ± 0.1	27.6 ± 2.6	X axis	EOS P 396	EOS PA2200	[52]
	1.61 ± 0.10	43.9 ± 0.7	26.6 ± 2.9	Y axis			
	1.22 ± 0.03	39.6 ± 0.2	14.7 ± 1.1	Z axis			
	1.87 ± 0.04	46.9 ± 0.9	10.3 ± 1.9	Z axis	EOS FORMIGA P 110	EOS PA2200-Perf.	(Current)
MJF	1.42 ± 0.04	40.1 ± 1.5	17.5 ± 3.9	XY plane	HP Jet Fusion 3D 4200	HP 3D High Reusability PA12	[292]
	1.13 ± 0.07	45.8 ±3.5	11.2 ±1.8	X axis	HP Jet Fusion 3D 4200	HP 3D High Reusability PA12	[294]
	1.20 ± 0.08	47.9 ± 0.9	13.2 ± 1.5	Y axis			
	1.34 ± 0.10	53.7 ± 1.1	11.4 ± 1.3	Z axis			

MJF (cont.)	1.24 ± 0.03	47.0 ± 0.9	19.0 ± 2.8	X axis	HP Jet Fusion 3D 4200	HP 3D High Reusability PA12	[289]
	1.15 ± 0.04	48.0 ± 0.8	27.0 ± 1.2	Y axis			
	1.25 ± 0.04	49.0 ± 0.6	16.0 ± 1.9	Z axis			
	3.94 ± 0.36	49.9 ± 1.9	3.3 ± 0.8	X axis	HP Jet Fusion 3D 4200	HP 3D High Reusability PA12	[293]
	3.97 ± 0.31	49.3 ± 3.4	2.2 ± 0.3	Z axis			
	1.37 ± 0.03	48.7 ± 0.8	27.4 ± 2.2	X axis	HP Jet Fusion 3D 4200	HP 3D High Reusability PA12	[52]
	1.37 ± 0.07	44.5 ± 0.7	15.9 ± 1.1	Y axis			
	1.67 ± 0.07	49.6 ± 1.2	14.8 ± 0.3	Z axis			
	1.53 ± 0.06	45.6 ± 0.4	30.0 ± 4.9	Z axis	HP Jet Fusion 3D 4200	HP 3D High Reusability PA12	(Current)

Then, the fatigue tests on the specimens adapted from the ASTM E606/E606M standard (Figure 95d) and the SF (Figure 95e), CYF (Figure 95f), and CC (Figure 95g) lattice structure specimens were performed. The test procedure was similar to the one used for the fatigue tests of the SS316L samples and the setup used for testing the lattice structure is shown in Figure 105. All the MJF samples (ASTM, SF, CYF, and CC) and the SLS ASTM samples were tested at the 38 MPa, 36 MPa, 34 MPa, and 32 MPa stress levels (three specimens per level), whereas the SLS lattice structures were tested at the 37.5 MPa, 35 MPa, and 32.5 MPa stress levels (three specimens per level). The test frequency was 3 Hz, to avoid the heating of the polymeric material.

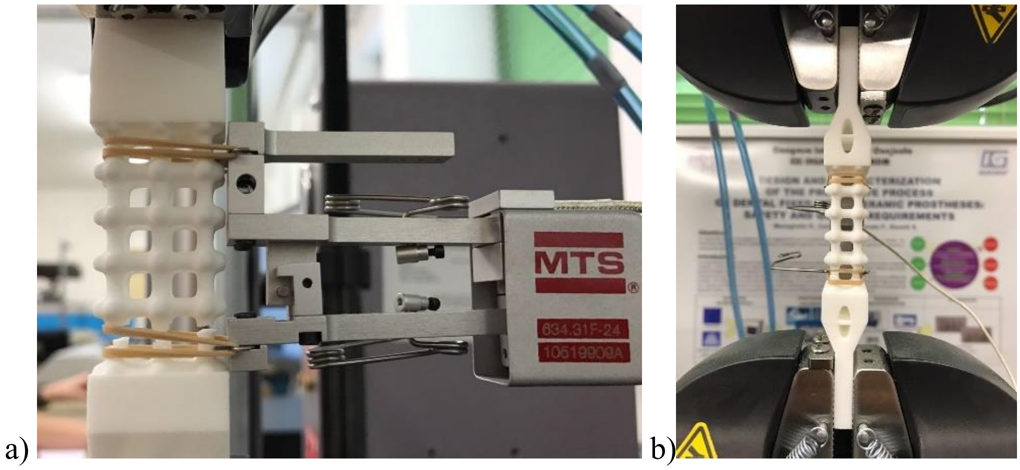

Figure 105. Fatigue test setup for a CC sample produced by SLS technology: a) front view of the specimen, b) side view of the specimen.

As for the stainless steel tests, the number of cycles to failure was used to estimate the Stress – Number of cycles curves (S – N curves) using the equation:

$$\log_{10} N = b_0 + b_1 \cdot \log_{10} S$$

Table 26 and Table 27 shows the results of the fatigue tests, with the number of cycles to failure of the tested samples, of the MJF and SLS technology, respectively.

Table 26. Fatigue tests results for the SLS ASTM E606 specimens and for the MJF ASTM E606, SF, CYF, and CC specimens.

Sample	Stress [MPa]	Number of cycles to failure				
		ASTM E606 (SLS)	ASTM E606 (MJF)	SF	CYF	CC
1	38	1639	542	1828	1128	70403
2	38	1349	763	1383	1506	856
3	38	1416	875	1298	626	45051
4	36	2826	1250	4986	1971	255880
5	36	2244	699	9108	1626	4128
6	36	2262	929	53613	659	4257
7	34	3153	1839	67100	23014	181464
8	34	4543	979	28560	615	225711
9	34	2700	1425	217205	4619	99261
10	32	8472	11119	4478	59603	450051
11	32	4513	74579	87857	865	42275
12	32	5691	88171	68741	146229	270746

Table 27. Fatigue tests results for the SLS SF, CYF, and CC specimens.

Sample	Stress [MPa]	Number of cycles to failure		SF	
		CYF	CC	Stress [MPa]	Number of cycles to failure
1	37.5	1666	36258	36.0	918
2	37.5	911	69688	35.3	646
3	37.5	5438	2836	33.6	8177
4	35	45002	224915	33.6	23699
5	35	1969	65878	33.5	2024
6	35	2094	160308	31.5	49701
7	32.5	156089	459355	31.3	61506
8	32.5	177740	436536	31.2	83917
9	32.5	150360	533086	28.8	404622

Table 28 presents the b_0 and b_1 parameters, the standard deviation SD, and the correlation coefficient R^2 of the interpolated S – N curves.

Table 28. Fitting parameters for the S – N curves of the specimens produced by SLS and MJF

Technology	Specimen type	b_0	b_1	SD	R^2
SLS	ASTM E606	15.79	-7.99	0.09	0.88
	SF	49.59	-30.00	0.35	0.89
	CYF	51.58	-30.77	0.53	0.74
	CC	39.48	-22.32	0.43	0.69
MJF	ASTM E606	12.13	-5.88	0.12	0.57
	(ASTM E606 knee)	85.49	-53.73	0.34	0.85
	SF	32.57	-18.41	0.60	0.47
	CYF	30.67	-17.60	0.67	0.39
	CC	31.11	-17.12	0.74	0.33

From Figure 106 to Figure 113 the interpolated S – N curves of the sample tested, together with the 10% and 90% limit curves at a 90% confidence level, are presented.

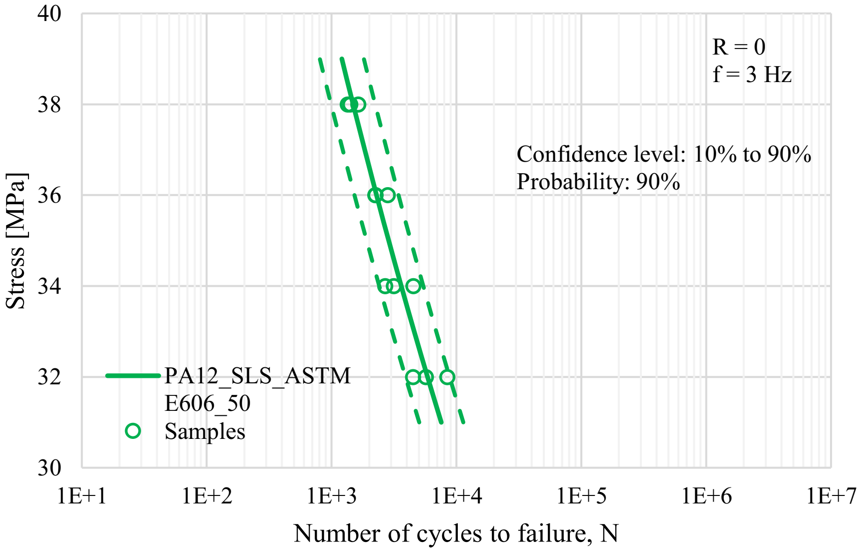

Figure 106. S – N curve of the ASTM E606 samples manufactured by SLS.

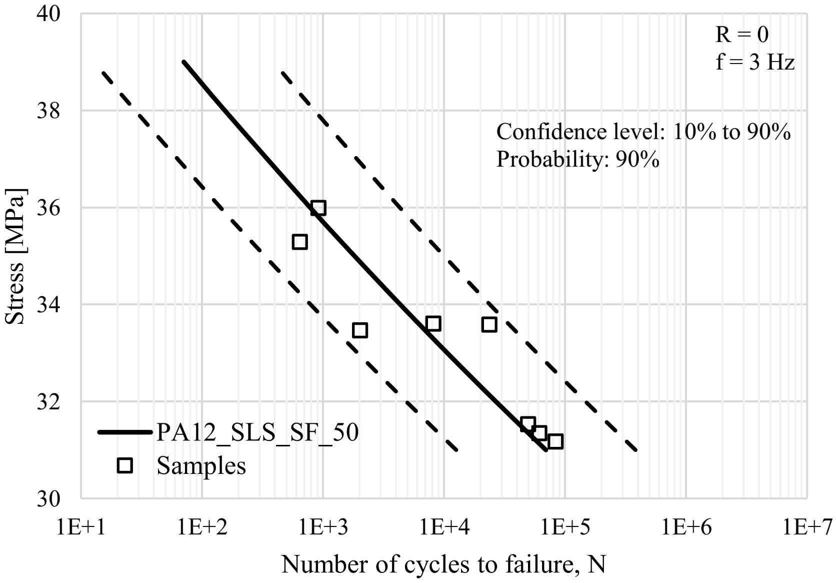

Figure 107. S – N curve of the SF lattice samples manufactured by SLS.

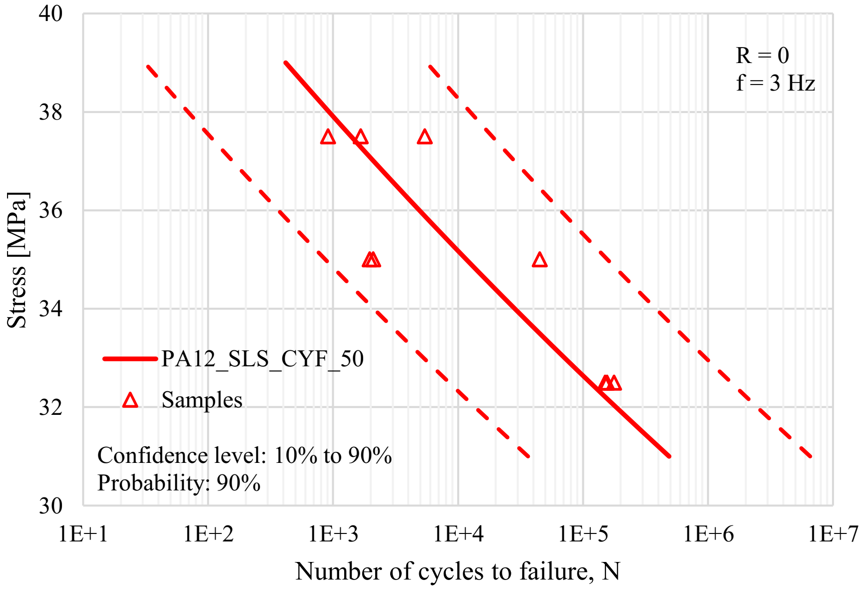

Figure 108. S – N curve of the CYF lattice samples manufactured by SLS.

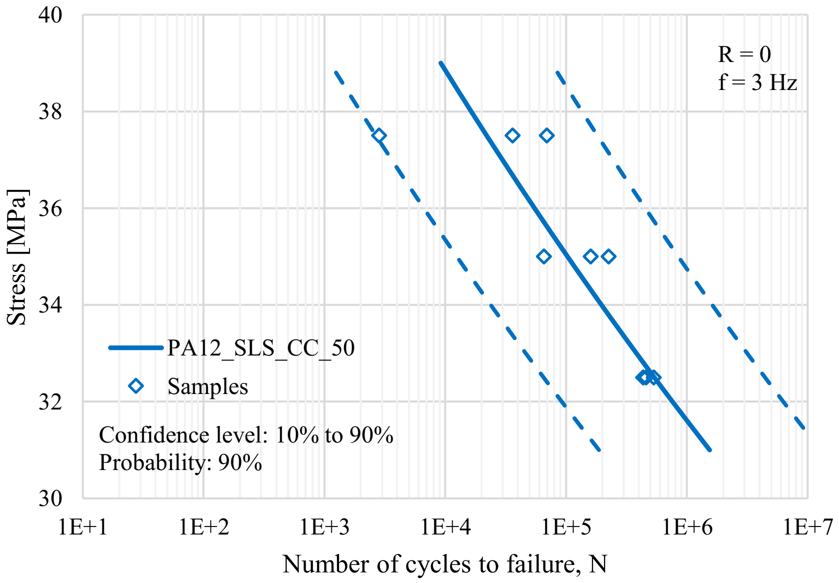

Figure 109. S – N curve of the CC lattice samples manufactured by SLS.

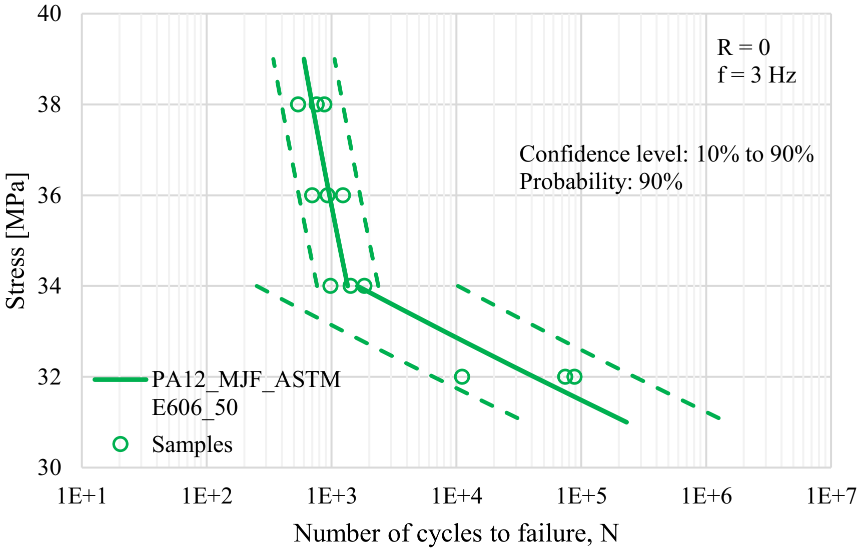

Figure 110. S – N curve of the ASTM E606 samples manufactured by MJF. The confidence level lines are different in the two segments because the standard deviations and the statistical coefficient are different (two different sets of data were used for the statistical analysis).

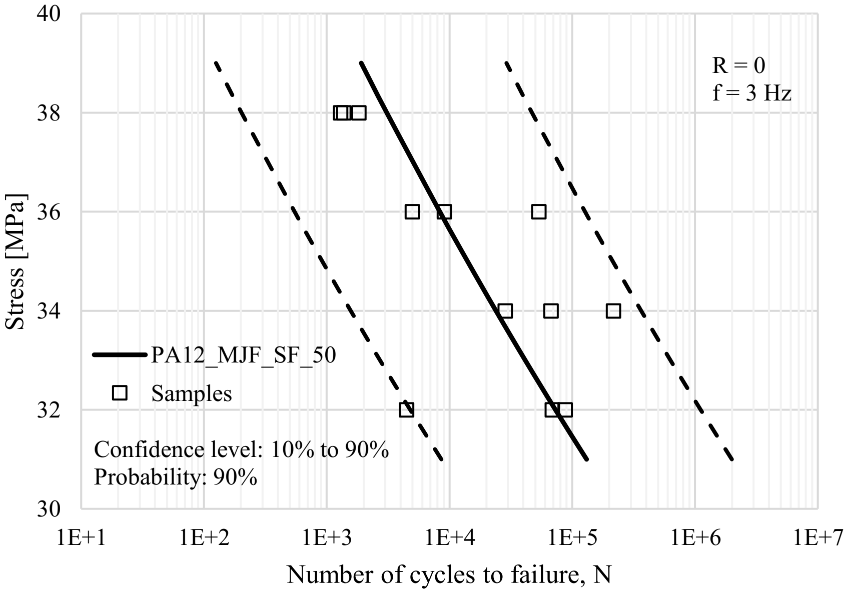

Figure 111. S – N curve of the SF lattice samples manufactured by MJF.

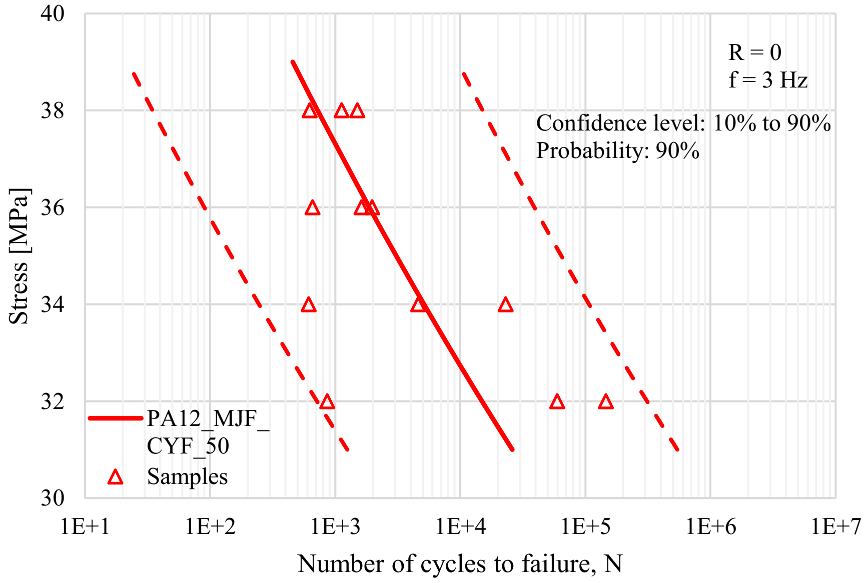

Figure 112. S – N curve of the CYF lattice samples manufactured by MJF.

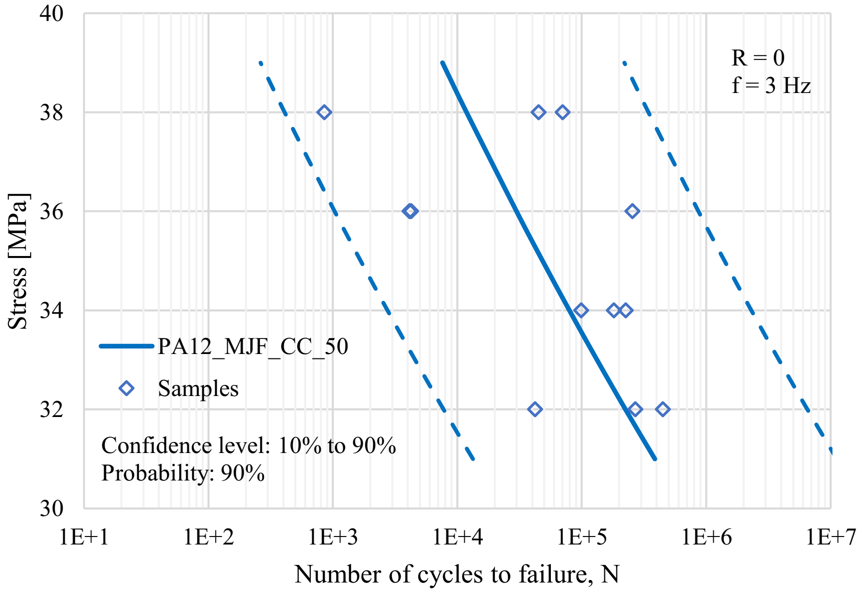

Figure 113. S – N curve of the CC lattice samples manufactured by MJF.

Figure 114 and Figure 115 show the comparison between the mean S – N lines, i.e., with 50 % of probability of failure, of the different types of fatigue tested samples for SLS and MJF, respectively.

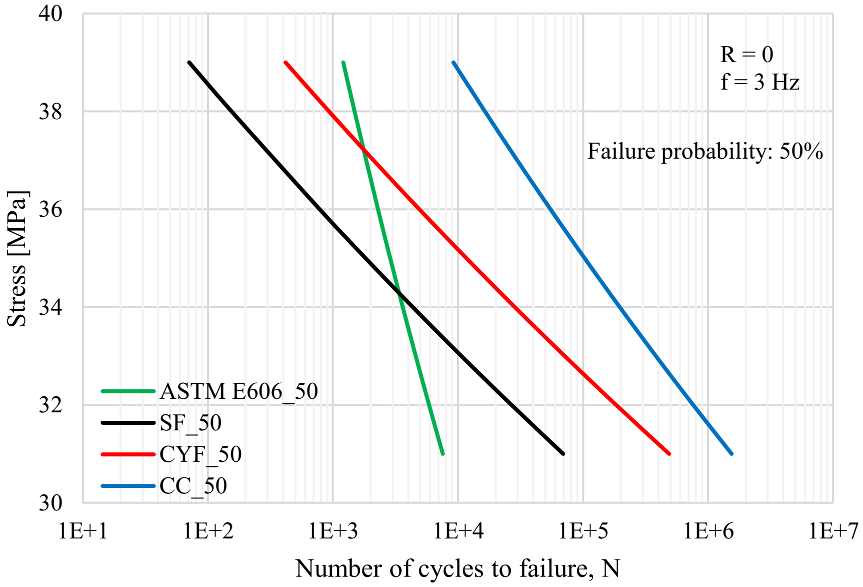

Figure 114. Comparison between the fatigue tested sample types manufactured by SLS. The curves represent 50 % of probability of failure.

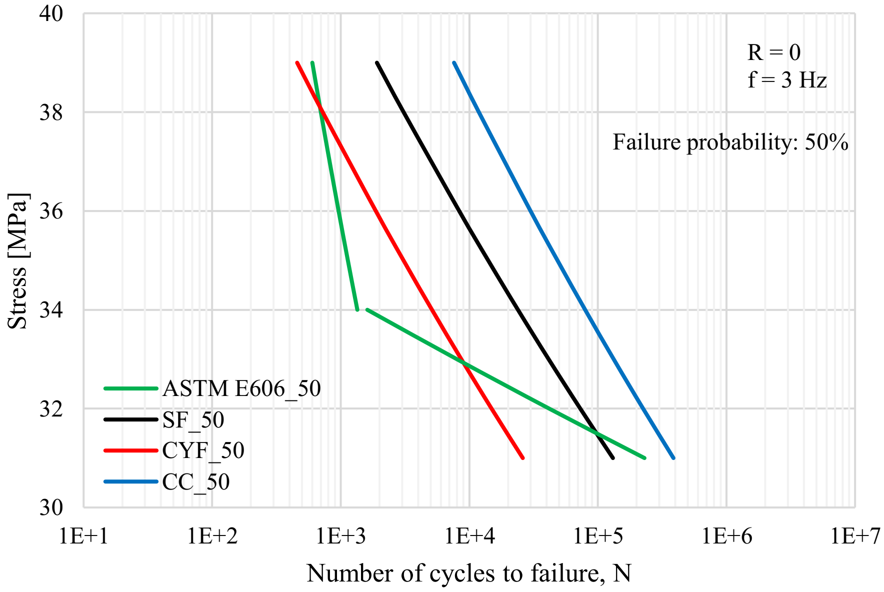

Figure 115. Comparison between the fatigue tested sample types manufactured by MJF. The curves represent 50 % of probability of failure.

Similarly, Figure 116 and Figure 117 show the comparison between the S – N lines with 10 % of probability of failure, of the different types of fatigue tested samples for SLS and MJF, respectively

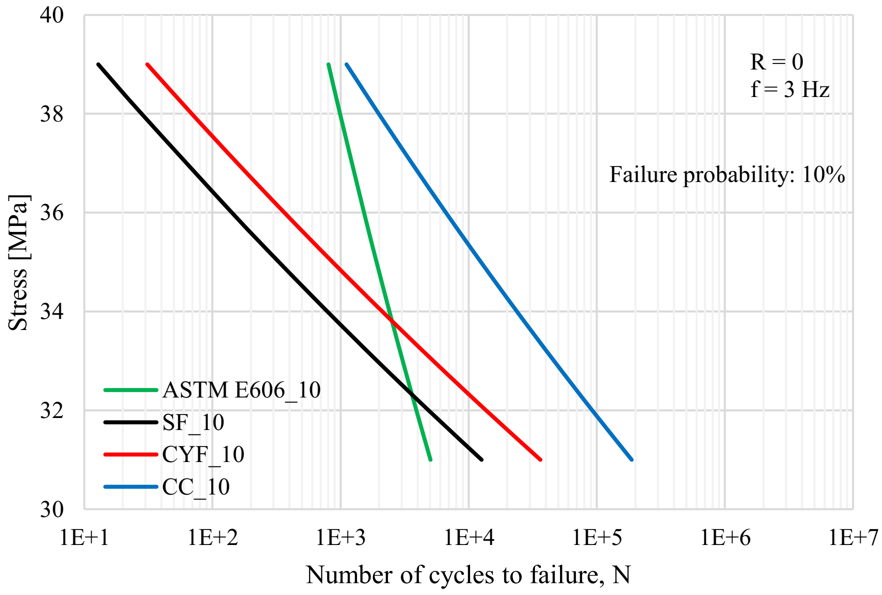

Figure 116. Comparison between the fatigue tested sample types manufactured by SLS. The curves represent 10 % of probability of failure.

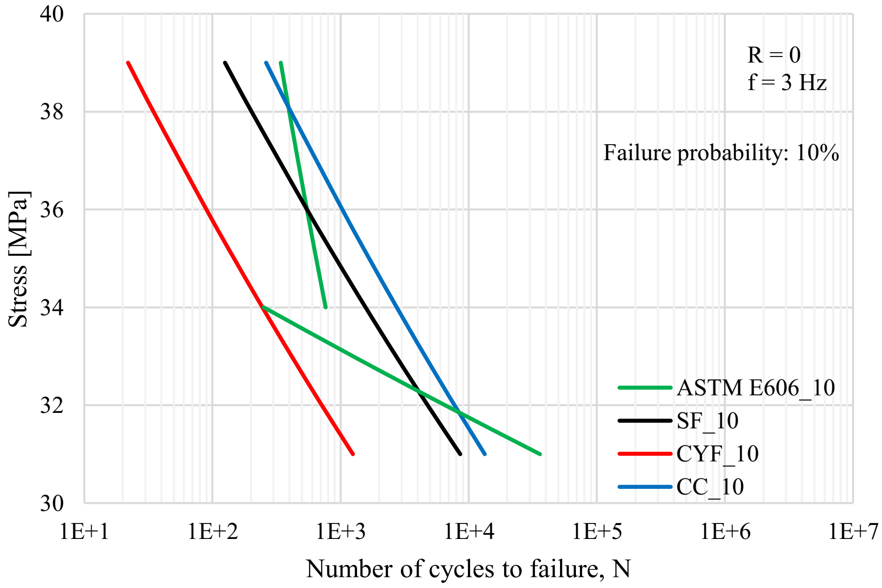

Figure 117. Comparison between the fatigue tested sample types manufactured by MJF. The curves represent 10 % of probability of failure. The confidence level lines are different in the two segments of the ASTM E606 samples because the standard deviations and the statistical coefficient are different (two different sets of data were used for the statistical analysis).

Observing the resulting curves, the MJF bulk samples, i.e., the MJF ASTM E606 types, are the only ones that present the knee of the Wöhler curve, approaching the fatigue limit at 32 MPa. Comparing the SLS and MJF ASTM E606 samples, the SLS ones perform slightly better than the MJF at high stress until 34 MPa, where the MJF curve presents the knee and allows for better fatigue behavior at lower stress. More, the correlation coefficient R^2 of the SLS bulk specimens, 0.88, is higher than the one of the MJF bulk specimens, 0.57 (for the section between 38 MPa and 34 MPa), showing a less dispersion of the tested samples. More in general, all the interpolated curves of the parts manufactured by SLS present a higher R^2 than the ones manufactured by MJF. The fracture surfaces of the tested samples were analyzed by the SEM and in Figure 118 some of the images taken to the SLS and MJF ASTM E606 samples are reported. The fracture of the SLS parts (Figure 118a and Figure 118b) presents a brittle crazing mechanism with large dimple areas, in accordance with the findings of Salazar et al. [295,297]. The fracture mechanism of the MJF parts (Figure 118c and Figure 118d) shows the initiation of the fracture at the contour of the sample, the crack propagation on the smooth region of the surface, and the final fracture happens on the rough central part of the surface, as described also by Sauer and Richardson [298]. Pores are noted in both the technologies, but to a higher extent in the SLS part.

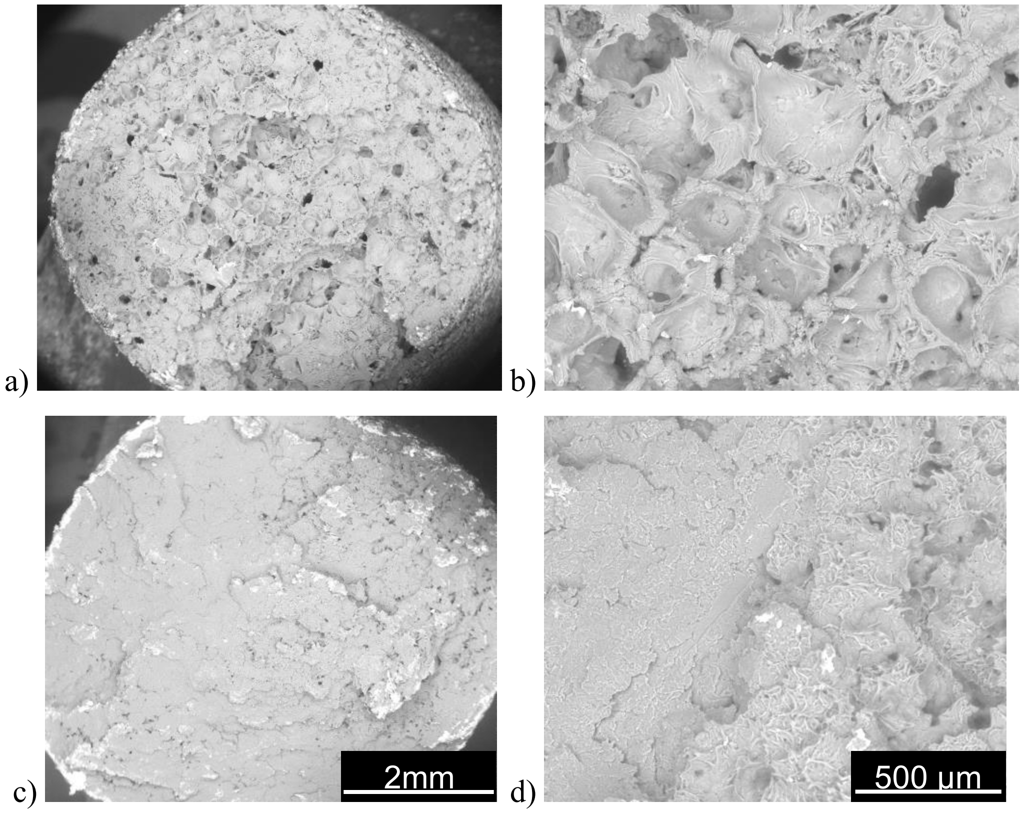

Figure 118. SEM analyses on the fracture surfaces of the fatigue tested ASTM E606 samples: a), b): SLS, c), d) MJF.

Moving on the fatigue curves of the lattice structures, some considerations stand out. At equal manufacturing technology, the slopes of the three lattices are similar but differ from the slope of the bulk material curve, which is higher in modulus; for the SLS parts, this implies a better behavior of the bulk material with respect to the SF and CYF lattices at higher stress, and a worse behavior at lower stress; the MJF SF and CYF lattices behave respectively similarly and better than the bulk parts at high stresses and worst at low stresses, due to the knee of the ASTM E606 curve. Both in the SLS and MJF technologies, the CC lattice performs better than all the other types of tested specimens. Another point to note is that the behavior of the SF and CYF lattices is inverted in the two technologies, with the CYF behaving better than SF in SLS, and, vice versa, the SF behaving better than CYF in MJF. SEM analyzed fracture surfaces of the lattices are presented in Figure 119. The failure mechanisms reflect the ones found in the bulk specimens, with the brittle crazing mechanism in the SLS SF (Figure 119a) and CC lattices (Figure 119e), and the crack propagation before the failure for the MJF samples.

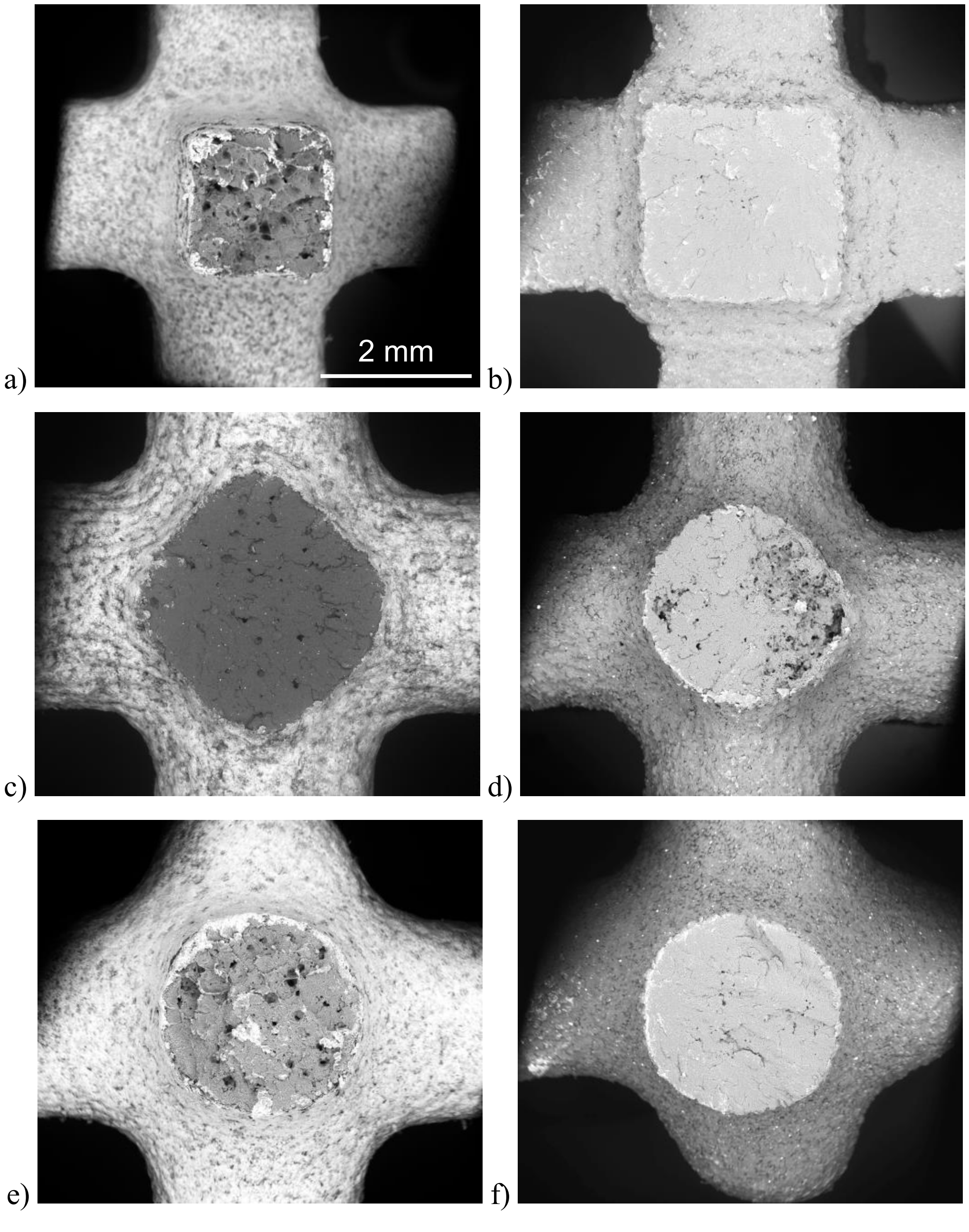

Figure 119. SEM analyses on the fracture surfaces of the fatigue tested lattice types: a) SF SLS, b) SF MJF, c) CYF SLS, d) CYF MJF, e) CC SLS, f) CC MJF.

Furthermore, a comparison can be made between the fatigue results of this campaign and the results obtained from fatigue testing the samples produced by SLM in SS316L material (Section 5.2.1). First, it is observed that the results of the SS316L tests are less dispersed. Then, as a common result, among the lattices, the structures obtained adopting the proposed mesh modeling method with the application of the Catmull-Clark algorithm present the best fatigue life behavior, failing on average at a higher number of cycles than the others. As previously said, this is due to the higher continuity of the surfaces and the lower concentration of stress at the nodal points. The bulk cylindrical samples behave differently: in the SS316L tests performed better than all the other types of samples, whereas in the PA12 tests they did not stand out. One reason for the observed behavior could be the different sizes of the tested samples; the cross-sectional area of each beam of the PA12 lattice samples measure 6.25 mm^2, whereas for the SS316L samples the cross-sectional area measures 1 mm^2. The bigger dimensions of the PA12 samples could avoid premature failures due to internal porosities and defects. Nevertheless, this is just a conjecture and further dedicated tests need to be performed to detect the causes of the observed behavior.

As a conclusion for this section, a summary of the information acquired from the comparison of the SLS and MJF technologies is presented:

- The SEM analyses on the powders showed that the MJF powders are smoother than the SLS ones. The SLS powders also presented some cracks, a phenomenon that could be related to the solution–precipitation process in ethanol used during the production of the powders, or it can be caused by the evaporation during the printing process of the remaining ethanol of the production phases.
- The XRD analyses highlighted that the microstructure of both the powders and the printed parts of the two technologies are similar. The starting powders present both α-phase and γ-phase, whereas the printed samples show mainly γ-phase and a small shoulder of α-phase.
- The TGA-DSC analyses on the powders and the printed samples showed a translation of the peak to lower temperatures together with the broadening of the peak itself. The crystallinity of the powders, 49.1 ± 0.5% for SLS and 48.3 ± 0.4% for MJF, decreased during the printing process to 24.5 ± 0.1% for SLS and 31.5 ± 0.2% for MJF.
- The He-pycnometry measurements showed a higher total porosity in the SLS samples (7.95 ± 0.09%) with respect to the MJF ones (6.75 ± 0.18%).
- The roughness measurements (R_a parameter) resulted in similar values for the two technologies. More, both the SLS and MJF presented a rougher surface at the bottom face (15.0 ± 2.3 μm for SLS and 13.3 ± 1.0 μm for MJF) than the side face (10.8 ± 0.8 μm for SLS and 11.2 ± 1.2 μm for MJF) and the top face

(10.4 ± 1.6 μm for SLS and 8.7 ± 0.9 μm for MJF). This could be related to the fact that no post-processing was performed and some partially un-melted powders remained stuck on the parts.

- The main differences highlighted by the static tensile tests were the slightly higher Young's modulus of the SLS samples (1.87 ± 0.04 GPa) than the MJF ones (1.53 ± 0.06 GPa) and the higher deformation at break of the MJF parts (30.0 ± 4.9%) than the SLS ones (10.3 ± 1.9%), three times on average. This, together with a similar UTS, led to a higher toughness of the parts produced by the MJF technology.
- The SEM analyses on the fracture surface of the ISO 527 specimens revealed a brittle fracture mechanism for the SLS specimens, whereas a ductile fracture for the MJF ones. SEM analyses on fatigue-tested cylindrical specimens highlighted a brittle crazing mechanism for the SLS samples, whereas in the MJF parts the crack initiated on the contour and slowly grew until the failure. The analyses on the fatigue-tested lattice structures confirmed the mechanism observed on the bulk specimens.
- Focusing on the geometric modeling methods, the CC structures showed the best behavior among the lattice samples due to the Catmull–Clark subdivision surface algorithm, which results in smoother surfaces with respect to standard filleting operations in the CAD software and leads to a lower stress concentration and better fatigue life.

Reasoning about which one of the two technologies could be the most suitable when deciding the manufacturing technology to adopt, some considerations need to be made. The mechanical characterization showed that the parts produced by the SLS technology are stiffer than the ones produced by the MJF technology; The MJF parts, instead, are tougher and allow for a higher deformation before failure. Depending on the specific application, the SLS technology could be preferred for components with structural purposes, whereas MJF could be exploited in situations in which a high energy absorption is required before the failure of the structure. Furthermore, HP declares that the MJF technology is up to ten times faster if compared to similar technologies such as the SLS technique [299], enabling higher production volumes. Finally, the cost of an MJF machine is located in the hundreds of thousands of dollars range, whereas it is possible to find SLS systems starting from an order of magnitude lower, i.e., tens of thousands of dollars [6]; cheaper SLS systems will have smaller build volumes, requiring a compromise between costs and production volumes.

6 Conclusions

AM brought a revolution with its new approach of producing objects in a layer-by-layer fashion, adding material instead of removing it. The freedom of manufacturing complex parts with shapes, functions, and combinations of materials that were impossible to create with the standard technologies requires suitable design and modeling tools able to handle these new paradigms allowing to exploit the new manufacturing possibilities. However, the literature highlighted that the most diffused CAD software are inappropriate to the purpose because they were developed and meant to describe components manufactured with traditional technologies. More in general, the lack of tools for modeling AM-oriented objects was noted.

So, the present research project aimed to overcome these limitations and develop new geometric modeling methods suitable for designing parts that fully exploit the possibilities offered by AM.

For reaching the research aim, different topics were addressed; the main focus of the work was the development of modeling and optimization approaches for lattice structures. Starting from the creation of the lattice wireframe, four methods based on commands available in commercial software, ad-hoc written code procedures, and a freeform deformation method based on trivariate NURBS were proposed to obtain wireframes that conform to the boundary of the design volume. The results show that the developed methods outperform the results obtainable from the commercial software, allowing for a more regular shape of the single cells inside the lattice and higher ease in conforming to the design volume. Then, two optimization workflows were implemented. The first deals with the size optimization of the beams of the lattice structure, and iteratively cycles until the size of each beam of the structure is optimized, i.e., the utilization of the beams reaches a target value; manufacturing constraints are introduced to avoid elements that are too small and impossible to produce or elements that are too big with respect to the size of the cell. The second workflow performs a multi-objective optimization on lattice structures allowing to obtain compromise solutions when trying to optimize conflicting objectives; the optimization phase adopts a genetic algorithm based on the selection, crossover, and mutation operations. The utilization of the beams acts as an optimization constraint and the upper and lower size limits of the beams are introduced in the control of the optimization drivers. Adopting these optimization approaches allows obtaining lightweight structures that, at the same time, can bear the acting loads and boundary conditions safely, presenting optimized properties.

After that, two methods for the geometric modeling of lattice structures were proposed. Both the methods are based on a B-Rep mesh approach and, at first, they produce a coarse mesh composed of quadrangular faces and characterized by sharp edges; then, the Catmull-Clark subdivision surface algorithm is applied and a refined mesh is obtained without the need for further manual filleting operations. In particular, the first approach is meant to model conformal lattice structures given the conformal wireframe and the information about the optimized diameter of the beams; it creates the vertexes of the mesh by intersecting cylinders modeled around the nodal points and then connecting the corresponding vertexes. The second method allows introducing shell elements in the lattice structures by selectively closing faces around the beams or creating an external skin isolating the lattice from the outside; the opening or closing of every single face is independent from the other and can be controlled separately. The implemented methods can produce mesh models of complex lattice structures in a reliable way and bring several advantages. Conformal lattices avoid the truncation of the cells at the boundaries thus increasing the stiffness of the part; internal walls can create optimized ducts and paths for fluids circulation and heat exchanging and can locally modify the stiffness of the component; external skins can isolate the lattice structure from the "external word" avoiding the wear of the lattice or the leakage of fluids. More, the adoption of the Catmull-Clark algorithm enables dealing with coarse meshes, avoiding the need for high computational resources, that become then smooth without the need for further operations.

The presented methods were then included in a wider optimization workflow for AM (Figure 54), conceived for describing the steps related to the embodiment design phase of a component produced by AM technologies. The optimization workflow has a design volume as a starting point and includes two main paths, one dealing with the design and modeling of size-optimized conformal lattice structures that fill the volume, and one dealing with the topology optimization of the design volume, with the consecutive manual remodeling of the topology optimized shape. Then, the workflow includes the final mechanical validation through FE analyses, the process planning, and the process simulation through CAE software. The proposed workflow addressed the needs highlighted in the literature that noted the lack of workflows for the DfAM incorporating CAD software and CAE tools and comprehensive methods exploiting multiple AM advantages.

Two test cases were used for evaluating the proposed methods. The remodeling of a piston rod was performed by applying the entire optimization workflow; the topology optimization path was followed by using commercial CAD and CAE software, whereas in the size-optimization path the previously described methods for the design, optimization, and modeling of conformal lattice structures were adopted; the topology- and size-optimized solutions were then mechanically validated and the process planning was performed, highlighting the benefits and limitations of choosing one solution with respect to the other; both the solutions presented a significant mass reduction with respect to the starting design volume. Then, an aerospace propellant tank for small satellites redesigned with the introduction of an internal conformal lattice structure was optimized following the proposed multi-objective optimization workflow. The optimization objectives were the minimization of the mass and the maximization of the first natural frequency; the optimization drivers were the thickness of the shell of the tank, the diameters of the beams of the lattice, and the configuration of the lattice itself, since it was possible to model structures with a high number of small cells or, vice versa, a low number of big cells. As a constraint, the solutions that exceeded the maximum allowed utilization of the beams and the shells were penalized. The results contained a set of optimal solutions, and it was shown that at equal first natural frequencies, the optimized configuration with the internal lattice structure allowed for about 30 % of mass reduction if compared to the optimized solution without the lattice structure.

The mesh modeling method based on the Catmull-Clark algorithm was numerically validated. The geometrical deviation of the Schwartz P-Surface and the gyroid TPMSs modeled with the subdivision method from a reference mesh directly obtained from the implicit equations that describe the two TPMSs was evaluated. The results showed that adopting the subdivided meshes leads to a geometrical deviation from the reference meshes of a maximum of 1.3 %, which is acceptable if considering that the proposed modeling approach results in meshes with an extremely lower number of vertexes and faces, allowing for faster computations when working with lattice structure with a high number of unit cells. An elementary portion of the simple cubic unit cell obtained by the mesh subdivision method underwent a curvature analysis, and it was compared to the curvature of the cells obtained in commercial CAD software where fileting operations are manually performed at the sharp edges using the available command. The results of the analysis showed that the subdivided cell has a surface with a C2 level continuity (curvature continuity) whereas the cells obtained by the CAD modeling have a surface with a C1 level continuity (tangency continuity). The higher continuity of the subdivided mesh also reflects on the stress distribution at the nodal point of the lattice structures; indeed, the subdivided mesh presented a lower stress concentration factor than the other analyzed cells, where the factor depends on the filleting radius and remains higher regardless the filleting radius value.

Finally, experimental campaigns were executed to validate the mesh modeling method and assess the fatigue life behavior of lattice structures adopting the subdivided unit cell. The lattices with the subdivided cell were compared to lattices obtained by modeling the unit cells with commercial CAD software and with bulk specimens. The samples were produced in SS316L material by SLM technology and in PA12 material by SLS and MJF technologies. The results of the experimental tests showed that at equal material, the lattice structures modeled with the proposed method have a better fatigue behavior than the others, failing at a higher number of cycles. More, the PA12 lattices manufactured by both the SLS and MJF technology behave better than cylindrical bulk specimens, whereas the SS316L lattices performed worse than the cylindrical samples; this could be explained by the smaller size of the metallic samples, closer to the manufacturing limits, and probably more prone to failure due to internal defects. The experimental campaign performed on the SLS and MJF technologies, allowed for an in-depth comparison of the two technologies, both belonging to the powder bed fusion category of the AM processes, but with a different way of sintering the parts.

Summing up, the research project allowed for the implementation of methods for the modeling and optimization of lattice structures, leading to an advancement in the AM field, and overcoming some of the limitations that emerged from the literature. Thanks to the broad versatility of AM, the outcomes of the research can be adopted in different fields. Lattice structures can be used in the automotive field both for lightweight applications and for energy absorption, reducing fuel consumption and increasing the performance and the safety of the vehicles; in the aerospace field too, lightweight components are required; also, applications can be found in compliant structures, sports apparel, i.e., shoe soles, and equipment, i.e., bike saddles. More, lattices with optimized internal ducts can be employed for high-performance heat exchangers, microfluidic applications, and biomedical scaffolds.

Improvements to the works are still needed. As future works, the enhancement of the proposed methods and further validations are planned. Even though the implementation of different unit cells during the generation of the conformal wireframe and the size optimization is straightforward, issues are still present when moving on the geometric modeling of the final mesh, especially at nodal points where a different number of beams can meet and different interfaces are needed. Similarly, the implementation of the internal wall at the moment works with faces enclosed by four beams and further adaptations to different wall shapes are planned. Another issue that will be addressed is the difficulty in simulating lattice structures due to the high number of elements needed to discretize the geometry; dedicated homogenization or volumetric approaches will be considered as possible solutions.

References

[1] ISO/ASTM, ISO/ASTM 52900:2015 (ASTM F2792) - Additive manufacturing -- General principles -- Terminology, (2015).

[2] I. Gibson, D. Rosen, B. Stucker, M. Khorasani, Additive Manufacturing Technologies, Springer International Publishing, Cham, 2021. https://doi.org/10.1007/978-3-030-56127-7.

[3] M.K. Thompson, G. Moroni, T. Vaneker, G. Fadel, R.I. Campbell, I. Gibson, A. Bernard, J. Schulz, P. Graf, B. Ahuja, F. Martina, Design for Additive Manufacturing: Trends, opportunities, considerations, and constraints, CIRP Ann. 65 (2016) 737–760. https://doi.org/10.1016/j.cirp.2016.05.004.

[4] J. Holmström, J. Partanen, J. Tuomi, M. Walter, Rapid manufacturing in the spare parts supply chain, J. Manuf. Technol. Manag. 21 (2010) 687–697. https://doi.org/10.1108/17410381011063996.

[5] N.M. Terry Wohlers, Robert Ian Campbell, Olaf Diegel, Joseph Kowen, Ray Huff, Wohlers Report 2021, Wohlers Associates, 2021. https://wohlersassociates.com/2021report.htm (accessed September 23, 2021).

[6] T. Wohlers, I. Campbell, O. Diegel, J. Kowen, T. Caffrey, Wohlers Report 2019, 2019.

[7] Scopus - Document search, (n.d.). https://www.scopus.com/search/form.uri#basic (accessed September 28, 2021).

[8] N. Hopkinson, P. Erasenthiran, High speed sintering—early research into a new rapid manufacturing process, in: Solid Free. Fabr. Symp., 2004: pp. 312–320.

[9] B.E. Kelly, I. Bhattacharya, H. Heidari, M. Shusteff, C.M. Spadaccini, H.K. Taylor, Volumetric additive manufacturing via tomographic reconstruction, Science (80-.). 363 (2019) 1075–1079. https://doi.org/10.1126/science.aau7114.

[10] H. Chen, Y.F. Zhao, Process parameters optimization for improving surface quality and manufacturing accuracy of binder jetting additive manufacturing process, Rapid Prototyp. J. 22 (2016) 527–538. https://doi.org/10.1108/RPJ-11-2014-0149.

[11] J.M. Chacón, M.A. Caminero, E. García-Plaza, P.J. Núñez, Additive manufacturing of PLA structures using fused deposition modelling: Effect of process parameters on mechanical properties and their optimal selection, Mater. Des. 124 (2017) 143–157. https://doi.org/10.1016/j.matdes.2017.03.065.

[12] W.E. Frazier, Metal additive manufacturing: A review, J. Mater. Eng. Perform. 23 (2014) 1917–1928. https://doi.org/10.1007/s11665-014-0958-z.

[13] S.C. Ligon, R. Liska, J. Stampfl, M. Gurr, R. Mülhaupt, Polymers for 3D Printing and Customized Additive Manufacturing, Chem. Rev. 117 (2017) 10212–10290. https://doi.org/10.1021/acs.chemrev.7b00074.

[14] A. Zocca, P. Colombo, C.M. Gomes, J. Günster, Additive Manufacturing of Ceramics: Issues, Potentialities, and Opportunities, J. Am. Ceram. Soc. 98 (2015) 1983–2001. https://doi.org/10.1111/jace.13700.

[15] H. Wang, Y. Chen, D.W. Rosen, A Hybrid Geometric Modeling Method for Large Scale Conformal Cellular Structures, in: Vol. 3 25th Comput. Inf. Eng. Conf. Parts A B, ASMEDC, Long Beach, CA, 2005: pp. 421–427. https://doi.org/10.1115/DETC2005-

85366.

[16] F. Tamburrino, S. Graziosi, M. Bordegoni, The Design Process of Additively Manufactured Mesoscale Lattice Structures: A Review, J. Comput. Inf. Sci. Eng. 18 (2018) 1–16. https://doi.org/10.1115/1.4040131.

[17] T. Zegard, G.H. Paulino, Bridging topology optimization and additive manufacturing, Struct. Multidiscip. Optim. 53 (2016) 175–192. https://doi.org/10.1007/s00158-015-1274-4.

[18] M. Alzahrani, S.K. Choi, D.W. Rosen, Design of truss-like cellular structures using relative density mapping method, Mater. Des. 85 (2015) 349–360. https://doi.org/10.1016/j.matdes.2015.06.180.

[19] A. Garland, G. Fadel, Design and Manufacturing Functionally Gradient Material Objects with an off the Shelf Three-Dimensional Printer: Challenges and Solutions, J. Mech. Des. Trans. ASME. 137 (2015). https://doi.org/10.1115/1.4031097.

[20] J. Duro-Royo, L. Mogas-Soldevila, N. Oxman, Flow-based fabrication: An integrated computational workflow for design and digital additive manufacturing of multifunctional heterogeneously structured objects, Comput. Des. 69 (2015) 143–154. https://doi.org/10.1016/j.cad.2015.05.005.

[21] America Makes, ANSI, Standardization Roadmap for Additive Manufacturing - Version 2.0, 2018.

[22] D.L. Bourell, D.W. Rosen, M.C. Leu, The roadmap for additive manufacturing and its impact, 3D Print. Addit. Manuf. 1 (2014) 6–9. https://doi.org/10.1089/3dp.2013.0002.

[23] G. Avventuroso, M. Silvestri, E.M. Frazzon, Additive Manufacturing Plant for Large Scale Production of Medical Devices: A Simulation Study, in: IFAC-PapersOnLine, Elsevier, 2018: pp. 1442–1447. https://doi.org/10.1016/j.ifacol.2018.08.312.

[24] M. Benedetti, A. du Plessis, R.O. Ritchie, M. Dallago, S.M.J. Razavi, F. Berto, Architected cellular materials: A review on their mechanical properties towards fatigue-tolerant design and fabrication, Mater. Sci. Eng. R Reports. 144 (2021) 100606. https://doi.org/10.1016/j.mser.2021.100606.

[25] M.E. Mortenson, Geometric modeling, (1997).

[26] A. Pasko, O. Fryazinov, T. Vilbrandt, P. Fayolle, V. Adzhiev, Procedural function-based modelling of volumetric microstructures, Graph. Models. 73 (2011) 165–181. https://doi.org/10.1016/j.gmod.2011.03.001.

[27] G.H. Loh, E. Pei, D. Harrison, M.D. Monzón, An overview of functionally graded additive manufacturing, Addit. Manuf. 23 (2018) 34–44. https://doi.org/10.1016/j.addma.2018.06.023.

[28] C.C. Seepersad, Challenges and Opportunities in Design for Additive Manufacturing, 3D Print. Addit. Manuf. 1 (2014) 10–13. https://doi.org/10.1089/3dp.2013.0006.

[29] ASTM F2792-09, Standard Terminology for Additive Manufacturing Technologies, ASTM Int. (2009) 1–3. https://doi.org/10.1520/F2792-09.

[30] J.J. Beaman, D.L. Bourell, C.C. Seepersad, D. Kovar, Additive Manufacturing Review: Early Past to Current Practice, J. Manuf. Sci. Eng. 142 (2020). https://doi.org/10.1115/1.4048193.

[31] F. Willeme, Photo-sculpture, U.S. Patent 43,822, 1864.

[32] J.E. Blanther, Manufacture of Contour Relief Maps, U.S. Patent 473,901, 1892.

[33] W.K. Swainson, Method, medium and apparatus for producing three-dimensional figure product, U.S. Patent 4,041,476, 1971.

[34] L. Ciraud, Method and Device for Producing Any Objects From Any Meltable Material, EUR Patent DE 22 63 777 A1, 1971.

[35] C.W. Hull, Apparatus for production of three-dimensional objects by stereolithography, U.S. Patent 4,575,330, 1986.

[36] S. Crump, Apparatus and method for creating three-dimensional objects, U.S. Patent 5,121,329, 1992.

[37] M. Feygin, Apparatus and method for forming an integral object from laminations, U.S. Patent 4,752,352, 1988.

[38] C.R. Deckard, Method and apparatus for producing parts by selective sintering, U.S. Patent 4,863,538, 1989.

[39] T.S. Srivatsan, Materials Processing Handbook , Joanna R. Groza, James F. Shackelford, Enrique J. Lavernia, and Michael T. Powers, Editors, Mater. Manuf. Process. 27 (2012) 1146–1147. https://doi.org/10.1080/10426914.2012.689459.

[40] P.K. Gokuldoss, S. Kolla, J. Eckert, Additive manufacturing processes: Selective laser melting, electron beam melting and binder jetting-selection guidelines, Materials (Basel). 10 (2017) 672. https://doi.org/10.3390/ma10060672.

[41] M. Ziaee, N.B. Crane, Binder jetting: A review of process, materials, and methods, Addit. Manuf. 28 (2019) 781–801. https://doi.org/10.1016/j.addma.2019.05.031.

[42] A. Dass, A. Moridi, State of the art in directed energy deposition: From additive manufacturing to materials design, Coatings. 9 (2019) 418. https://doi.org/10.3390/COATINGS9070418.

[43] T.J. Gordelier, P.R. Thies, L. Turner, L. Johanning, Optimising the FDM additive manufacturing process to achieve maximum tensile strength: a state-of-the-art review, Rapid Prototyp. J. 25 (2019) 953–971. https://doi.org/10.1108/RPJ-07-2018-0183.

[44] R.J. Zaldivar, T.D. Mclouth, G.L. Ferrelli, D.N. Patel, A.R. Hopkins, D. Witkin, Effect of initial filament moisture content on the microstructure and mechanical performance of ULTEM ® 9085 3D printed parts, Addit. Manuf. 24 (2018) 457–466. https://doi.org/10.1016/j.addma.2018.10.022.

[45] T. Hofstätter, D.B. Pedersen, G. Tosello, H.N. Hansen, State-of-the-art of fiber-reinforced polymers in additive manufacturing technologies:, Http://Dx.Doi.Org/10.1177/0731684417695648. 36 (2017) 1061–1073. https://doi.org/10.1177/0731684417695648.

[46] D. Chimene, R. Kaunas, A.K. Gaharwar, Hydrogel Bioink Reinforcement for Additive Manufacturing: A Focused Review of Emerging Strategies, Adv. Mater. 32 (2020) 1902026. https://doi.org/10.1002/ADMA.201902026.

[47] L.J. Tan, W. Zhu, K. Zhou, Recent Progress on Polymer Materials for Additive Manufacturing, Adv. Funct. Mater. (2020) 2003062. https://doi.org/10.1002/adfm.202003062.

[48] H. Fayazfar, F. Liravi, U. Ali, E. Toyserkani, Additive manufacturing of high loading concentration zirconia using high-speed drop-on-demand material jetting, Int. J. Adv. Manuf. Technol. 2020 1099. 109 (2020) 2733–2746. https://doi.org/10.1007/S00170-020-05829-2.

[49] W.E. King, A.T. Anderson, R.M. Ferencz, N.E. Hodge, C. Kamath, S.A. Khairallah, A.M. Rubenchik, Laser powder bed fusion additive manufacturing of metals; physics, computational, and materials challenges, Appl. Phys. Rev. 2 (2015) 041304. https://doi.org/10.1063/1.4937809.

[50] C.A. Chatham, T.E. Long, C.B. Williams, A review of the process physics and material screening methods for polymer powder bed fusion additive manufacturing, Prog. Polym. Sci. 93 (2019) 68–95. https://doi.org/10.1016/j.progpolymsci.2019.03.003.

[51] B. Khoshnevis, B. Asiabanpour, M. Mojdeh, K. Palmer, SIS - A new SFF method based on powder sintering, Rapid Prototyp. J. 9 (2003) 30–36. https://doi.org/10.1108/13552540310455638.

[52] C. Cai, W.S. Tey, J. Chen, W. Zhu, X. Liu, T. Liu, L. Zhao, K. Zhou, Comparative study on 3D printing of polyamide 12 by selective laser sintering and multi jet fusion, J. Mater. Process. Technol. 288 (2021) 116882. https://doi.org/10.1016/j.jmatprotec.2020.116882.

[53] S. Dadbakhsh, L. Verbelen, O. Verkinderen, D. Strobbe, P. Van Puyvelde, J.-P. Kruth, Effect of PA12 powder reuse on coalescence behaviour and microstructure of SLS parts, Eur. Polym. J. 92 (2017) 250–262. https://doi.org/https://doi.org/10.1016/j.eurpolymj.2017.05.014.

[54] G. V. Salmoria, J.L. Leite, R.A. Paggi, The microstructural characterization of PA6/PA12 blend specimens fabricated by selective laser sintering, Polym. Test. 28 (2009) 746–751. https://doi.org/10.1016/j.polymertesting.2009.06.010.

[55] B. Van Hooreweder, F. De Coninck, D. Moens, R. Boonen, P. Sas, Microstructural characterization of SLS-PA12 specimens under dynamic tension/compression excitation, Polym. Test. 29 (2010) 319–326. https://doi.org/10.1016/j.polymertesting.2009.12.006.

[56] S. Yuan, F. Shen, J. Bai, C.K. Chua, J. Wei, K. Zhou, 3D soft auxetic lattice structures fabricated by selective laser sintering: TPU powder evaluation and process optimization, Mater. Des. 120 (2017) 317–327. https://doi.org/10.1016/J.MATDES.2017.01.098.

[57] L.J. Tan, W. Zhu, K. Sagar, K. Zhou, Comparative study on the selective laser sintering of polypropylene homopolymer and copolymer: processability, crystallization kinetics, crystal phases and mechanical properties, Addit. Manuf. 37 (2021) 101610. https://doi.org/10.1016/J.ADDMA.2020.101610.

[58] M. Schmidt, D. Pohle, T. Rechtenwald, Selective laser sintering of PEEK, CIRP Ann. - Manuf. Technol. 56 (2007) 205–208. https://doi.org/10.1016/j.cirp.2007.05.097.

[59] C.Y. Yap, C.K. Chua, Z.L. Dong, Z.H. Liu, D.Q. Zhang, L.E. Loh, S.L. Sing, Review of selective laser melting: Materials and applications, Appl. Phys. Rev. 2 (2015) 041101. https://doi.org/10.1063/1.4935926.

[60] L.E. Murr, S.M. Gaytan, D.A. Ramirez, E. Martinez, J. Hernandez, K.N. Amato, P.W. Shindo, F.R. Medina, R.B. Wicker, Metal Fabrication by Additive Manufacturing Using Laser and Electron Beam Melting Technologies, J. Mater. Sci. Technol. 28 (2012) 1–14. https://doi.org/10.1016/S1005-0302(12)60016-4.

[61] J. Romano, L. Ladani, J. Razmi, M. Sadowski, Temperature distribution and melt

geometry in laser and electron-beam melting processes – A comparison among common materials, Addit. Manuf. 8 (2015) 1–11. https://doi.org/10.1016/J.ADDMA.2015.07.003.

[62] M. Rombouts, J.P. Kruth, L. Froyen, P. Mercelis, Fundamentals of Selective Laser Melting of alloyed steel powders, CIRP Ann. 55 (2006) 187–192. https://doi.org/10.1016/S0007-8506(07)60395-3.

[63] J. Zhang, B. Song, Q. Wei, D. Bourell, Y. Shi, A review of selective laser melting of aluminum alloys: Processing, microstructure, property and developing trends, J. Mater. Sci. Technol. 35 (2019) 270–284. https://doi.org/10.1016/J.JMST.2018.09.004.

[64] S. Leuders, M. Thöne, A. Riemer, T. Niendorf, T. Tröster, H.A. Richard, H.J. Maier, On the mechanical behaviour of titanium alloy TiAl6V4 manufactured by selective laser melting: Fatigue resistance and crack growth performance, Int. J. Fatigue. 48 (2013) 300–307. https://doi.org/10.1016/j.ijfatigue.2012.11.011.

[65] B. Vandenbroucke, J.P. Kruth, Selective laser melting of biocompatible metals for rapid manufacturing of medical parts, Rapid Prototyp. J. 13 (2007) 196–203. https://doi.org/10.1108/13552540710776142.

[66] D. Ahn, J.H. Kweon, J. Choi, S. Lee, Quantification of surface roughness of parts processed by laminated object manufacturing, J. Mater. Process. Technol. 212 (2012) 339–346. https://doi.org/10.1016/J.JMATPROTEC.2011.08.013.

[67] T. Himmer, T. Nakagawa, M. Anzai, Lamination of metal sheets, Comput. Ind. 39 (1999) 27–33. https://doi.org/10.1016/S0166-3615(98)00122-5.

[68] R.J. Friel, R.A. Harris, Ultrasonic Additive Manufacturing – A Hybrid Production Process for Novel Functional Products, Procedia CIRP. 6 (2013) 35–40. https://doi.org/10.1016/J.PROCIR.2013.03.004.

[69] S. Maruo, O. Nakamura, S. Kawata, Three-dimensional microfabrication with two-photon-absorbed photopolymerization, Opt. Lett. 22 (1997) 132. https://doi.org/10.1364/OL.22.000132.

[70] J. Crivello, Photoinitiators for free radical cationic and anionic photopolymerization, Surf. Coatings Technol. 168 (1998). https://ci.nii.ac.jp/naid/10024038243 (accessed August 6, 2021).

[71] Hubs, Additive manufacturing technologies: An overview | Hubs, (2021). https://www.hubs.com/knowledge-base/additive-manufacturing-technologies-overview/ (accessed August 16, 2021).

[72] D.L. Bourell, M.C. Leu, D.W. Rosen, Roadmap for Additive Manufacturing: Identifying the Future of Freeform Processing, 2009. https://wohlersassociates.com/roadmap2009A.pdf.

[73] M. Seifi, M. Gorelik, J. Waller, N. Hrabe, N. Shamsaei, S. Daniewicz, J.J. Lewandowski, Progress Towards Metal Additive Manufacturing Standardization to Support Qualification and Certification, JOM. 69 (2017) 439–455. https://doi.org/10.1007/s11837-017-2265-2.

[74] ASTM, Committee F42 on Additive Manufacturing Technologies, (2021). https://www.astm.org/COMMITTEE/F42.htm (accessed August 10, 2021).

[75] ISO, ISO/TC 261 on Additive Manufacturing, (2021). https://committee.iso.org/home/tc261 (accessed August 10, 2021).

[76] ISO/TC 261, ASTM-F24, Joint Plan for Additive Manufacturing Standards Development,

(2013). https://www.astm.org/COMMIT/AM_Standards_Development_Plan_v2.docx.

[77] ASTM, F42 AM Standards Structure And Primer, (n.d.). https://www.astm.org/COMMIT/F42_AMStandardsStructureAndPrimer.pdf (accessed August 10, 2021).

[78] A.D. Lantada, P.L. Morgado, Rapid Prototyping for Biomedical Engineering: Current Capabilities and Challenges, Annu. Rev. Biomed. Eng. 14 (2012) 73–96. https://doi.org/10.1146/annurev-bioeng-071811-150112.

[79] D. Brackett, I. Ashcroft, R. Hague, Topology optimization for additive manufacturing, in: Proc. Solid Free. Fabr. Symp. Austin, TX, S, 2011: pp. 348–362.

[80] A. Kudzal, B. McWilliams, C. Hofmeister, F. Kellogg, J. Yu, J. Taggart-Scarff, J. Liang, Effect of scan pattern on the microstructure and mechanical properties of Powder Bed Fusion additive manufactured 17-4 stainless steel, Mater. Des. 133 (2017) 205–215. https://doi.org/10.1016/J.MATDES.2017.07.047.

[81] Z. Wang, T.A. Palmer, A.M. Beese, Effect of processing parameters on microstructure and tensile properties of austenitic stainless steel 304L made by directed energy deposition additive manufacturing, Acta Mater. 110 (2016) 226–235. https://doi.org/10.1016/J.ACTAMAT.2016.03.019.

[82] G. Boothroyd, P. Dewhurst, W.A. Knight, Product Design for Manufacture and Assembly, Third Edition (Manufacturing Engineering and Ma..., (2010).

[83] D.W. Rosen, Computer-Aided Design for Additive Manufacturing of Cellular Structures, Comput. Aided. Des. Appl. 4 (2007) 585–594. https://doi.org/10.1080/16864360.2007.10738493.

[84] R. Ponche, O. Kerbrat, P. Mognol, J.Y. Hascoet, A novel methodology of design for Additive Manufacturing applied to Additive Laser Manufacturing process, Robot. Comput. Integr. Manuf. 30 (2014) 389–398. https://doi.org/10.1016/j.rcim.2013.12.001.

[85] B. Vayre, F. Vignat, F. Villeneuve, Designing for additive manufacturing, in: Procedia CIRP, Elsevier B.V., 2012: pp. 632–637. https://doi.org/10.1016/j.procir.2012.07.108.

[86] T. Briard, F. Segonds, N. Zamariola, G-DfAM: a methodological proposal of generative design for additive manufacturing in the automotive industry, Int. J. Interact. Des. Manuf. 14 (2020) 875–886. https://doi.org/10.1007/s12008-020-00669-6.

[87] N. Boddeti, Z. Ding, S. Kaijima, K. Maute, M.L. Dunn, Simultaneous Digital Design and Additive Manufacture of Structures and Materials, Sci. Rep. 8 (2018) 15560. https://doi.org/10.1038/s41598-018-33454-3.

[88] Y. Zhang, A. Bernard, R.K. Gupta, R. Harik, Evaluating the design for additive manufacturing: A process planning perspective, in: Procedia CIRP, Elsevier B.V., 2014: pp. 144–150. https://doi.org/10.1016/j.procir.2014.03.179.

[89] J. Lettori, R. Raffaeli, M. Peruzzini, J. Schmidt, M. Pellicciari, Additive manufacturing adoption in product design: an overview from literature and industry, Procedia Manuf. 51 (2020) 655–662. https://doi.org/10.1016/j.promfg.2020.10.092.

[90] C.M. Hoffmann, J.R. Rossignac, A Road Map to Solid Modeling, IEEE Trans. Vis. Comput. Graph. 2 (1996) 3–10. https://doi.org/10.1109/2945.489381.

[91] D. Doo, M. Sabin, Behaviour of recursive division surfaces near extraordinary points, Comput. Des. 10 (1978) 356–360. https://doi.org/10.1016/0010-4485(78)90111-2.

[92] E. Catmull, J. Clark, Recursively generated B-spline surfaces on arbitrary topological meshes, Comput. Des. 10 (1978) 350–355. https://doi.org/10.1016/0010-4485(78)90110-0.

[93] L. Piegl, W. Tiller, The NURBS book, Springer Science & Business Media, 2012.

[94] P. Bézier, Numerical control: Mathematics and applications, John Wiley & Sons, Ltd, London, UK, 1972. https://doi.org/10.1002/nme.1620060322.

[95] S. Bernšteın, Démonstration du théoreme de Weierstrass fondée sur le calcul des probabilities, Comm. Soc. Math. Kharkov. 13 (1912) 1–2.

[96] S. Fang, R. Srinivasan, Volumetric-CSG -- a model-based volume visualization approach, in: Proc. Sixth Int. Conf. Cent. Eur. Comput. Graph. Vis., Václav Skala-UNION Agency, 1998.

[97] E.L. Doubrovski, E.Y. Tsai, D. Dikovsky, J.M.P. Geraedts, H. Herr, N. Oxman, Voxel-based fabrication through material property mapping: A design method for bitmap printing, CAD Comput. Aided Des. 60 (2015) 3–13. https://doi.org/10.1016/j.cad.2014.05.010.

[98] A. Bacciaglia, A. Ceruti, A. Liverani, A systematic review of voxelization method in additive manufacturing, Mech. Ind. 20 (2019) 630. https://doi.org/10.1051/meca/2019058.

[99] J.A. Cottrell, T.J.R. Hughes, Y. Bazilevs, Isogeometric analysis: toward integration of CAD and FEA, John Wiley & Sons, Hoboken, New Jersey, US, 2009.

[100] Luca Grigolato, Stefano Rosso, Roberto Meneghello, Gianmaria Concheri, Gianpaolo Savio, Heterogeneous objects representation for Additive Manufacturing: a review, Instant J. Mech. Eng. (2019) 14–23. https://doi.org/10.36811/ijme.2019.110002.

[101] L.J. Gibson, M.F. Ashby, Cellular Solids, Cambridge University Press, Cambridge, 1997. https://doi.org/10.1017/CBO9781139878326.

[102] G. Savio, S. Rosso, R. Meneghello, G. Concheri, Geometric Modeling of Cellular Materials for Additive Manufacturing in Biomedical Field: A Review, Appl. Bionics Biomech. 2018 (2018) 1–14. https://doi.org/10.1155/2018/1654782.

[103] G.J. Tattersall, D. V. Andrade, A.S. Abe, Heat exchange from the toucan bill reveals a controllable vascular thermal radiator, Science (80-.). 325 (2009) 468–470. https://doi.org/10.1126/science.1175553.

[104] M. Lai, A.N. Kulak, D. Law, Z. Zhang, F.C. Meldrum, D.J. Riley, Profiting from nature: Macroporous copper with superior mechanical properties, Chem. Commun. (2007) 3547–3549. https://doi.org/10.1039/b707469g.

[105] K.F. Leong, C.M. Cheah, C.K. Chua, Solid freeform fabrication of three-dimensional scaffolds for engineering replacement tissues and organs, Biomaterials. 24 (2003) 2363–2378. https://doi.org/10.1016/S0142-9612(03)00030-9.

[106] A. Kantaros, N. Chatzidai, D. Karalekas, 3D printing-assisted design of scaffold structures, Int. J. Adv. Manuf. Technol. 82 (2016) 559–571. https://doi.org/10.1007/s00170-015-7386-6.

[107] Y. Tang, A. Kurtz, Y.F. Zhao, Bidirectional Evolutionary Structural Optimization (BESO) based design method for lattice structure to be fabricated by additive manufacturing, CAD Comput. Aided Des. 69 (2015) 91–101. https://doi.org/10.1016/j.cad.2015.06.001.

[108] Y. Tang, Y.F. Zhao, A survey of the design methods for additive manufacturing to improve functional performance, Rapid Prototyp. J. 22 (2016) 569–590. https://doi.org/10.1108/RPJ-01-2015-0011.

[109] V.S. Deshpande, M.F. Ashby, N.A. Fleck, Foam topology: bending versus stretching dominated architectures, Acta Mater. 49 (2001) 1035–1040. https://doi.org/10.1016/S1359-6454(00)00379-7.

[110] M.F. Ashby, The properties of foams and lattices, Philos. Trans. R. Soc. A Math. Phys. Eng. Sci. 364 (2006) 15–30. https://doi.org/10.1098/rsta.2005.1678.

[111] J.C. Wallach, L.J. Gibson, Mechanical behavior of a three-dimensional truss material, Int. J. Solids Struct. 38 (2001) 7181–7196. https://doi.org/10.1016/S0020-7683(00)00400-5.

[112] C.R. Calladine, Buckminster Fuller's "Tensegrity" structures and Clerk Maxwell's rules for the construction of stiff frames, Int. J. Solids Struct. 14 (1978) 161–172. https://doi.org/10.1016/0020-7683(78)90052-5.

[113] N.A. Fleck, V.S. Deshpande, M.F. Ashby, Micro-architectured materials: Past, present and future, in: Proc. R. Soc. A Math. Phys. Eng. Sci., Royal Society, 2010: pp. 2495–2516. https://doi.org/10.1098/rspa.2010.0215.

[114] T. Maconachie, M. Leary, B. Lozanovski, X. Zhang, M. Qian, O. Faruque, M. Brandt, SLM lattice structures: Properties, performance, applications and challenges, Mater. Des. 183 (2019) 108137. https://doi.org/10.1016/j.matdes.2019.108137.

[115] M.F. Ashby, Materials selection in Mechanical Design, 4th ed., Elsevier Ltd, 2011.

[116] A.P. Roberts, E.J. Garboczi, Elastic moduli of model random three-dimensional closed-cell cellular solids, Acta Mater. 49 (2001) 189–197. https://doi.org/10.1016/S1359-6454(00)00314-1.

[117] M.H. Luxner, J. Stampfl, H.E. Pettermann, Finite element modeling concepts and linear analyses of 3D regular open cell structures, in: J. Mater. Sci., 2005: pp. 5859–5866. https://doi.org/10.1007/s10853-005-5020-y.

[118] V.S. Deshpande, N.A. Fleck, M.F. Ashby, Effective properties of the octet-truss lattice material, J. Mech. Phys. Solids. 49 (2001) 1747–1769. https://doi.org/10.1016/S0022-5096(01)00010-2.

[119] A.P. Roberts, E.J. Garboczi, Elastic properties of model random three-dimensional open-cell solids, J. Mech. Phys. Solids. 50 (2002) 33–55. https://doi.org/10.1016/S0022-5096(01)00056-4.

[120] E.A. Lord, A.L. Mackay, Periodic minimal surfaces of cubic symmetry, Curr. Sci. 85 (2003) 346–362. http://www.jstor.org/stable/24108665.

[121] F.S.L. Bobbert, K. Lietaert, A.A. Eftekhari, B. Pouran, S.M. Ahmadi, H. Weinans, A.A. Zadpoor, Additively manufactured metallic porous biomaterials based on minimal surfaces: A unique combination of topological, mechanical, and mass transport properties, Acta Biomater. 53 (2017) 572–584. https://doi.org/10.1016/j.actbio.2017.02.024.

[122] W. Li, G. Yu, Z. Yu, Bioinspired heat exchangers based on triply periodic minimal surfaces for supercritical CO2 cycles, Appl. Therm. Eng. 179 (2020) 115686. https://doi.org/10.1016/J.APPLTHERMALENG.2020.115686.

[123] Ansys, Ansys SpaceClaim, (2021). https://www.ansys.com/products/3d-design/ansys-spaceclaim (accessed February 20, 2021).

[124] Siemens, Design for Additive Manufacture, (2021). https://www.plm.automation.siemens.com/global/en/products/mechanical-design/design-for-additive-manufacture.html (accessed June 16, 2021).

[125] Dassault Systèmes, The 3DEXPERIENCE platform, a Game Changer for Business and Innovation, (2021). https://www.3ds.com/3dexperience (accessed November 18, 2021).

[126] Altair, Accelerate Simulation-driven Design | Altair Inspire, (2021). https://www.altair.com/inspire/ (accessed November 18, 2021).

[127] Materialise, 3-matic Lattice Structures Module, (2021). https://www.materialise.com/en/software/3-matic/modules/lattice-module (accessed November 18, 2021).

[128] Materialise, Structures Module | Materialise Magics | 3D Printing Software, (2021). https://www.materialise.com/en/software/magics/structures-module (accessed November 18, 2021).

[129] PTC, Creo CAD Software: Enable the Latest in Design, (n.d.). https://www.ptc.com/en/products/creo (accessed November 18, 2021).

[130] Robert McNeel & Associates, Rhino - Rhinoceros 3D, (2021). https://www.rhino3d.com/en/ (accessed November 22, 2021).

[131] S. Davidson, Grasshopper - algorithmic modeling for Rhino, (2021). https://www.grasshopper3d.com/ (accessed February 20, 2021).

[132] General Lattice, GL Software, (n.d.). https://www.generallattice.com/software (accessed November 22, 2021).

[133] ADML Lab - McGill Univeristy, INTRA|LATTICE, (n.d.). http://www.intralattice.com/ (accessed November 22, 2021).

[134] A. Porterfield, Crystallon, (2019). https://www.food4rhino.com/en/app/crystallon (accessed November 22, 2021).

[135] Ecrlabs, Dendro, (n.d.). https://www.ecrlabs.com/dendro/ (accessed November 22, 2021).

[136] Bespoke geometry, Cocoon, (2015). http://www.bespokegeometry.com/2015/07/22/cocoon/ (accessed November 22, 2021).

[137] W.E. Lorensen, H.E. Cline, MARCHING CUBES: A HIGH RESOLUTION 3D SURFACE CONSTRUCTION ALGORITHM., Comput. Graph. 21 (1987) 163–169. https://doi.org/10.1145/37402.37422.

[138] nTopology, Next-Generation Design & Engineering Software | nTopology, (2021). https://ntopology.com/ (accessed June 16, 2021).

[139] J.C. Hart, Sphere tracing: A geometric method for the antialiased ray tracing of implicit surfaces, Vis. Comput. 12 (1996) 527–545. https://doi.org/10.1007/s003710050084.

[140] J. Corney, 3d Modeling Using the Acis Kernel and Toolkit, 1st ed., John Wiley &amp; Sons, Inc., USA, 1997.

[141] Y. Chen, A mesh-based geometric modeling method for general structures, in: Proc. ASME Des. Eng. Tech. Conf., American Society of Mechanical Engineers Digital Collection, 2006: pp. 269–281. https://doi.org/10.1115/detc2006-99513.

[142] J.R. Rossignac, A.A.G. Requicha, Offsetting operations in solid modelling, Comput.

Aided Geom. Des. 3 (1986) 129–148. https://doi.org/10.1016/0167-8396(86)90017-8.

[143] Y. Chen, 3D Texture Mapping for Rapid Manufacturing, Comput. Des. Appl. 4 (2007) 761–771. www.ptc.com (accessed August 25, 2021).

[144] A. Medeiros e Sá, K. Rodriguez Echavarria, D. Arnold, Dual joints for 3D-structures: Producing skins for skeletons by exploring duality, Vis. Comput. 30 (2014) 1321–1331. https://doi.org/10.1007/s00371-013-0883-4.

[145] X.Y. Kou, S.T. Tan, Microstructural modelling of functionally graded materials using stochastic Voronoi diagram and B-Spline representations, Https://Doi.Org/10.1080/0951192X.2011.627948. 25 (2012) 177–188. https://doi.org/10.1080/0951192X.2011.627948.

[146] H.N. Chow, S.T. Tan, W.S. Sze, Layered Modeling of Porous Structures with Voronoi Diagrams, Comput. Aided. Des. Appl. 4 (2007) 321–330. https://doi.org/10.1080/16864360.2007.10738552.

[147] M. Fantini, M. Curto, F. De Crescenzio, A method to design biomimetic scaffolds for bone tissue engineering based on Voronoi lattices, Virtual Phys. Prototyp. 11 (2016) 77–90. https://doi.org/10.1080/17452759.2016.1172301.

[148] M. Fantini, M. Curto, Interactive design and manufacturing of a Voronoi-based biomimetic bone scaffold for morphological characterization, Int. J. Interact. Des. Manuf. 12 (2018) 585–596. https://doi.org/10.1007/s12008-017-0416-x.

[149] H. Zeinalabedini, Y.O. Yildiz, P. Zhang, K. Laux, M. Kirca, A.C. To, Homogenization of additive manufactured polymeric foams with spherical cells, Addit. Manuf. 12 (2016) 274–281. https://doi.org/10.1016/j.addma.2016.04.008.

[150] F. Gagliardi, L. De Napoli, L. Filice, D. Umbrello, A comparison among FE models to simulate metallic foams forming – An experimental validation, Mater. Des. 30 (2009) 1282–1287. https://doi.org/10.1016/J.MATDES.2008.06.051.

[151] A. Ceruti, R. Ferrari, A. Liverani, Design for additive manufacturing using LSWM: A CAD tool for the modelling of lightweight and lattice structures, in: Smart Innov. Syst. Technol., 2017: pp. 756–765. https://doi.org/10.1007/978-3-319-57078-5_71.

[152] V. Shapiro, Theory of R-functions and Applications: A Primer, (1991). https://ecommons.cornell.edu/handle/1813/7059 (accessed August 27, 2021).

[153] A.O. Aremu, J.P.J. Brennan-Craddock, A. Panesar, I.A. Ashcroft, R.J.M. Hague, R.D. Wildman, C. Tuck, A voxel-based method of constructing and skinning conformal and functionally graded lattice structures suitable for additive manufacturing, Addit. Manuf. 13 (2017) 1–13. https://doi.org/10.1016/j.addma.2016.10.006.

[154] Y. Holdstein, A. Fischer, L. Podshivalov, P.Z. Bar-Yoseph, Volumetric texture synthesis of bone micro-structure as a base for scaffold design, in: 2009 IEEE Int. Conf. Shape Model. Appl. SMI 2009, 2009: pp. 81–88. https://doi.org/10.1109/SMI.2009.5170167.

[155] D.J. Brackett, I.A. Ashcroft, R.D. Wildman, R.J.M. Hague, An error diffusion based method to generate functionally graded cellular structures, Comput. Struct. 138 (2014) 102–111. https://doi.org/10.1016/j.compstruc.2014.03.004.

[156] M.P. Bendsøe, Optimization of Structural Topology, Shape, and Material, Springer Berlin Heidelberg, Berlin, Heidelberg, 1995. https://doi.org/10.1007/978-3-662-03115-5.

[157] G.I.N. Rozvany, A critical review of established methods of structural topology

optimization, Struct. Multidiscip. Optim. 37 (2009) 217–237. https://doi.org/10.1007/s00158-007-0217-0.

[158] M.P. Bendsøe, N. Kikuchi, Generating optimal topologies in structural design using a homogenization method, Comput. Methods Appl. Mech. Eng. 71 (1988) 197–224. https://doi.org/10.1016/0045-7825(88)90086-2.

[159] M.P. Bendsøe, Optimal shape design as a material distribution problem, Struct. Optim. 1 (1989) 193–202.

[160] Y.M. Xie, G.P. Steven, A simple evolutionary procedure for structural optimization, Comput. Struct. 49 (1993) 885–896. https://doi.org/10.1016/0045-7949(93)90035-C.

[161] O.M. Querin, G.P. Steven, Y.M. Xie, Evolutionary structural optimisation (ESO) using a bidirectional algorithm, Eng. Comput. (Swansea, Wales). 15 (1998) 1031–1048. https://doi.org/10.1108/02644409810244129.

[162] N.P. Van Dijk, K. Maute, M. Langelaar, F. Van Keulen, Level-set methods for structural topology optimization: A review, Struct. Multidiscip. Optim. 48 (2013) 437–472. https://doi.org/10.1007/s00158-013-0912-y.

[163] O. Sigmund, A 99 line topology optimization code written in matlab, Struct. Multidiscip. Optim. 21 (2001) 120–127. https://doi.org/10.1007/s001580050176.

[164] E. Andreassen, A. Clausen, M. Schevenels, B.S. Lazarov, O. Sigmund, Efficient topology optimization in MATLAB using 88 lines of code, Struct. Multidiscip. Optim. 43 (2011) 1–16. https://doi.org/10.1007/s00158-010-0594-7.

[165] G. Savio, F. Gaggi, R. Meneghello, G. Concheri, Design method and taxonomy of optimized regular cellular structures for additive manufacturing technologies, Proc. Int. Conf. Eng. Des. ICED. 4 (2015) 235–244. https://www.designsociety.org/publication/37788/design_method_and_taxonomy_of_optimized_regular_cellular_structures_for_additive_manufacturing_technologies.

[166] A. Nessi, T. Stanković, Topology, Shape, and Size Optimization of Additively Manufactured Lattice Structures Based on the Superformula, in: Int. Des. Eng. Tech. Conf. Comput. Inf. Eng. Conf. Vol. 2A 44th Des. Autom. Conf., ASME, 2018: p. V02AT03A042. https://doi.org/10.1115/detc2018-86191.

[167] J. Gielis, Inventing the Circle - The geometry of Nature, Geniaal bvba, 2003. http://scholar.google.com/scholar?hl=en&btnG=Search&q=intitle:No+Title#0%0Ahttps://www.evernote.com/shard/s89/sh/cb8da877-1405-4f53-9094-67b249ca7bce/3f875e367c3c73ce88335885bf2a3404.

[168] X. Ning, S. Pellegrino, Design of Lightweight Structural Components for Direct Digital Manufacturing, in: 53rd AIAA/ASME/ASCE/AHS/ASC Struct. Struct. Dyn. Mater. Conf., American Institute of Aeronautics and Astronautics, 2012: pp. 1–21. https://doi.org/10.2514/6.2012-1807.

[169] Y. Han, W.F. Lu, A Novel Design Method for Nonuniform Lattice Structures Based on Topology Optimization, J. Mech. Des. 140 (2018) 91403–91410. http://dx.doi.org/10.1115/1.4040546.

[170] C. Wang, J.H. Zhu, W.H. Zhang, S.Y. Li, J. Kong, Concurrent topology optimization design of structures and non-uniform parameterized lattice microstructures, Struct. Multidiscip. Optim. 58 (2018) 35–50. https://doi.org/10.1007/s00158-018-2009-0.

[171] Z. Wu, L. Xia, S. Wang, T. Shi, Topology optimization of hierarchical lattice structures

with substructuring, Comput. Methods Appl. Mech. Eng. 345 (2019) 602–617. https://doi.org/10.1016/j.cma.2018.11.003.

[172] N. Noilublao, S. Bureerat, Simultaneous topology, shape and sizing optimisation of a three-dimensional slender truss tower using multiobjective evolutionary algorithms, Comput. Struct. 89 (2011) 2531–2538. https://doi.org/10.1016/j.compstruc.2011.08.010.

[173] A. Kaveh, V.R. Mahdavi, Multi-objective colliding bodies optimization algorithm for design of trusses, J. Comput. Des. Eng. 6 (2019) 49–59. https://doi.org/10.1016/j.jcde.2018.04.001.

[174] J.S. Angelo, H.S. Bernardino, H.J.C. Barbosa, Ant colony approaches for multiobjective structural optimization problems with a cardinality constraint, Adv. Eng. Softw. 80 (2015) 101–115. https://doi.org/10.1016/j.advengsoft.2014.09.015.

[175] A.C.C. Lemonge, J.P.G. Carvalho, P.H. Hallak, D.E.C. Vargas, Multi-objective truss structural optimization considering natural frequencies of vibration and global stability, Expert Syst. Appl. 165 (2021) 113777. https://doi.org/10.1016/j.eswa.2020.113777.

[176] A.L. Kalamkarov, I. V. Andrianov, V. V. Danishevs'kyy, Asymptotic homogenization of composite materials and structures, Appl. Mech. Rev. 62 (2009) 1–20. https://doi.org/10.1115/1.3090830.

[177] A. Vigliotti, D. Pasini, Linear multiscale analysis and finite element validation of stretching and bending dominated lattice materials, Mech. Mater. 46 (2012) 57–68. https://doi.org/10.1016/J.MECHMAT.2011.11.009.

[178] S. Arabnejad, D. Pasini, Mechanical properties of lattice materials via asymptotic homogenization and comparison with alternative homogenization methods, Int. J. Mech. Sci. 77 (2013) 249–262. https://doi.org/10.1016/j.ijmecsci.2013.10.003.

[179] J. Freund, A. Karakoç, J. Sjölund, Computational homogenization of regular cellular material according to classical elasticity, Mech. Mater. 78 (2014) 56–65. https://doi.org/10.1016/J.MECHMAT.2014.07.018.

[180] E. Ptochos, G. Labeas, Elastic modulus and Poisson's ratio determination of micro-lattice cellular structures by analytical, numerical and homogenisation methods, J. Sandw. Struct. Mater. 14 (2012) 597–626. https://doi.org/10.1177/1099636212444285.

[181] E. Ptochos, G. Labeas, Shear modulus determination of cuboid metallic open-lattice cellular structures by analytical, numerical and homogenisation methods, Strain. 48 (2012) 415–429. https://doi.org/10.1111/j.1475-1305.2012.00837.x.

[182] A. Bacciaglia, A. Ceruti, A. Liverani, Structural Analysis of Voxel-Based Lattices Using 1D Approach, 3D Print. Addit. Manuf. (2021). https://doi.org/10.1089/3dp.2020.0178.

[183] J. Rakowski, The interpretation of the shear locking in beam elements, Comput. Struct. 37 (1990) 769–776. https://doi.org/10.1016/0045-7949(90)90106-C.

[184] M.R. Karamooz Ravari, M. Kadkhodaei, M. Badrossamay, R. Rezaei, Numerical investigation on mechanical properties of cellular lattice structures fabricated by fused deposition modeling, Int. J. Mech. Sci. 88 (2014) 154–161. https://doi.org/10.1016/j.ijmecsci.2014.08.009.

[185] G. Campoli, M.S. Borleffs, S. Amin Yavari, R. Wauthle, H. Weinans, A.A. Zadpoor, Mechanical properties of open-cell metallic biomaterials manufactured using additive manufacturing, Mater. Des. 49 (2013) 957–965. https://doi.org/10.1016/j.matdes.2013.01.071.

[186] K. Genovese, S. Leeflang, A.A. Zadpoor, Microscopic full-field three-dimensional strain measurement during the mechanical testing of additively manufactured porous biomaterials, J. Mech. Behav. Biomed. Mater. 69 (2017) 327–341. https://doi.org/10.1016/j.jmbbm.2017.01.010.

[187] G. Dong, Y.F. Zhao, Numerical and experimental investigation of the joint stiffness in lattice structures fabricated by additive manufacturing, Int. J. Mech. Sci. 148 (2018) 475–485. https://doi.org/10.1016/J.IJMECSCI.2018.09.014.

[188] J.J. Lewandowski, M. Seifi, Metal Additive Manufacturing: A Review of Mechanical Properties, Annu. Rev. Mater. Res. 46 (2016) 151–186. https://doi.org/10.1146/annurev-matsci-070115-032024.

[189] J.R.C. Dizon, A.H. Espera, Q. Chen, R.C. Advincula, Mechanical characterization of 3D-printed polymers, Addit. Manuf. 20 (2018) 44–67. https://doi.org/10.1016/j.addma.2017.12.002.

[190] M. Smith, Z. Guan, W.J. Cantwell, Finite element modelling of the compressive response of lattice structures manufactured using the selective laser melting technique, Int. J. Mech. Sci. 67 (2013) 28–41. https://doi.org/10.1016/j.ijmecsci.2012.12.004.

[191] S. Tsopanos, R. a. W. Mines, S. McKown, Y. Shen, W.J. Cantwell, W. Brooks, C.J. Sutcliffe, The Influence of Processing Parameters on the Mechanical Properties of Selectively Laser Melted Stainless Steel Microlattice Structures, J. Manuf. Sci. Eng. 132 (2010) 041011. https://doi.org/10.1115/1.4001743.

[192] S.M. Ahmadi, S.A. Yavari, R. Wauthle, B. Pouran, J. Schrooten, H. Weinans, A.A. Zadpoor, Additively manufactured open-cell porous biomaterials made from six different space-filling unit cells: The mechanical and morphological properties, Materials (Basel). 8 (2015) 1871–1896. https://doi.org/10.3390/ma8041871.

[193] A. Cerardi, M. Caneri, R. Meneghello, G. Concheri, M. Ricotta, Mechanical characterization of polyamide cellular structures fabricated using selective laser sintering technologies, Mater. Des. 46 (2013) 910–915. https://doi.org/10.1016/j.matdes.2012.11.042.

[194] O. Al-Ketan, R. Rowshan, R.K. Abu Al-Rub, Topology-mechanical property relationship of 3D printed strut, skeletal, and sheet based periodic metallic cellular materials, Addit. Manuf. 19 (2018) 167–183. https://doi.org/10.1016/j.addma.2017.12.006.

[195] S. Yu, J. Sun, J. Bai, Investigation of functionally graded TPMS structures fabricated by additive manufacturing, Mater. Des. 182 (2019) 108021. https://doi.org/10.1016/j.matdes.2019.108021.

[196] S. Amin Yavari, S.M. Ahmadi, R. Wauthle, B. Pouran, J. Schrooten, H. Weinans, A.A. Zadpoor, Relationship between unit cell type and porosity and the fatigue behavior of selective laser melted meta-biomaterials, J. Mech. Behav. Biomed. Mater. 43 (2015) 91–100. https://doi.org/10.1016/j.jmbbm.2014.12.015.

[197] N.W. Hrabe, P. Heinl, B. Flinn, C. Körner, R.K. Bordia, Compression-compression fatigue of selective electron beam melted cellular titanium (Ti-6Al-4V), J. Biomed. Mater. Res. - Part B Appl. Biomater. 99 B (2011) 313–320. https://doi.org/10.1002/jbm.b.31901.

[198] R.G. Miyamoto, Y., Kaysser, W.A., Rabin, B.H., Kawasaki, A., Ford, Functionally Graded Materials: Design, Processing and Applications (Materials Technology Series), Springer Science & Business Media, 1999.

[199] F. Leonardi, S. Graziosi, R. Casati, F. Tamburrino, M. Bordegoni, Additive manufacturing of heterogeneous lattice structures: An experimental exploration, in: Proc. Int. Conf. Eng. Des. ICED, Cambridge University Press, 2019: pp. 669–678. https://doi.org/10.1017/dsi.2019.71.

[200] P. Huang, D. Deng, Y. Chen, Modeling and fabrication of heterogeneous three-dimensional objects based on additive manufacturing, in: ASME Int. Mech. Eng. Congr. Expo. Proc., American Society of Mechanical Engineers Digital Collection, 2013. https://doi.org/10.1115/IMECE2013-65724.

[201] N. Shamsaei, A. Yadollahi, L. Bian, S.M. Thompson, An overview of Direct Laser Deposition for additive manufacturing; Part II: Mechanical behavior, process parameter optimization and control, Addit. Manuf. 8 (2015) 12–35. https://doi.org/10.1016/j.addma.2015.07.002.

[202] J. Wang, Z. Pan, Y. Ma, Y. Lu, C. Shen, D. Cuiuri, H. Li, Characterization of wire arc additively manufactured titanium aluminide functionally graded material: Microstructure, mechanical properties and oxidation behaviour, Mater. Sci. Eng. A. 734 (2018) 110–119. https://doi.org/10.1016/j.msea.2018.07.097.

[203] X. Zhang, C. Wei, Y.H. Chueh, L. Li, An integrated dual ultrasonic selective powder dispensing platform for three-dimensional printing of multiple material metal/glass objects in selective laser melting, J. Manuf. Sci. Eng. Trans. ASME. 141 (2019). https://doi.org/10.1115/1.4041427.

[204] M. Rafiee, R.D. Farahani, D. Therriault, Multi-Material 3D and 4D Printing: A Survey, Adv. Sci. 7 (2020) 1902307. https://doi.org/10.1002/advs.201902307.

[205] S.E. Bakarich, R. Gorkin, R. Gately, S. Naficy, M. in het Panhuis, G.M. Spinks, 3D printing of tough hydrogel composites with spatially varying materials properties, Addit. Manuf. 14 (2017) 24–30. https://doi.org/10.1016/j.addma.2016.12.003.

[206] RepRap, Diamond Hotend, (2018). https://reprap.org/wiki/Diamond_Hotend (accessed September 16, 2021).

[207] Prusa Research, Original Prusa i3 Multi Material 2.0 - Prusa3D - 3D Printers from Josef Průša, (2021). https://www.prusa3d.com/original-prusa-i3-multi-material-2-0/ (accessed September 16, 2021).

[208] Mosaic Manufacturing, Palette 2S, (n.d.). https://www.mosaicmfg.com/products/palette-2s (accessed September 16, 2021).

[209] N. Oxman, E. Tsai, M. Firstenberg, Digital Anisotropy, J. Virtual Phys. Prototyp. 4 (2011) 261–274.

[210] Stratasys, PolyJet Technology for 3D Printing, (2021). https://www.stratasys.com/polyjet-technology (accessed September 16, 2021).

[211] S. Hällgren, L. Pejryd, J. Ekengren, 3D Data Export for Additive Manufacturing-Improving Geometric Accuracy, in: Procedia CIRP, Elsevier, 2016: pp. 518–523. https://doi.org/10.1016/j.procir.2016.05.046.

[212] ISO International Organization for Standardization, ISO 10303-242:2020 - Industrial automation systems and integration — Product data representation and exchange — Part 242: Application protocol: Managed model-based 3D engineering, (2020) 11. https://www.iso.org/standard/66654.html (accessed September 6, 2021).

[213] AP 242 Edition 2 capabilities for Additive Manufacturing interoperability, (2020).

http://www.ap242.org/additive-manufacturing (accessed September 6, 2021).

[214] AP242 Ed2 - Introduction, (2020). http://www.ap242.org/edition-2 (accessed September 6, 2021).

[215] ISO International Organization for Standardization ASTM American Society for Testing and Materials, ISO/ASTM 52915:2020 - Specification for additive manufacturing file format (AMF) Version 1.2, (2020). https://www.iso.org/standard/74640.html (accessed September 6, 2021).

[216] Enabling the full potential of 3D printing - 3MF Consortium, (2020). https://3mf.io/ (accessed September 6, 2021).

[217] Y. Yokoyama, N. Hiji, T. Takahashi, Application of Attribute Information of Voxel-Based 3D Data Format FAV for Metamaterials Structure Design, NIP Digit. Fabr. Conf. 2019 (2019) 109–114. https://doi.org/10.2352/ISSN.2169-4451.2019.35.109.

[218] Shapeways, Shapeways Launches SVX, a Voxel Based File Format for 3D Printing - Shapeways Blog, (2014). https://www.shapeways.com/blog/archives/17972-shapeways-launches-svx-voxel-file-format-for-3d-printing.html (accessed September 6, 2021).

[219] SASAM, Additive Manufacturing: SASAM Standardisation Roadmap, 2015.

[220] FoFAM, Additive Manufacturing roadmap: gaps and actions on market driven value chains, 2016.

[221] S. Rosso, F. Uriati, L. Grigolato, R. Meneghello, G. Concheri, G. Savio, An Optimization Workflow in Design for Additive Manufacturing, Appl. Sci. 11 (2021) 2572. https://doi.org/10.3390/app11062572.

[222] G. Savio, R. Meneghello, G. Concheri, Geometric modeling of lattice structures for additive manufacturing, Rapid Prototyp. J. 24 (2018) 351–360. https://doi.org/10.1108/RPJ-07-2016-0122.

[223] M. Kumke, H. Watschke, T. Vietor, A new methodological framework for design for additive manufacturing, Virtual Phys. Prototyp. 11 (2016) 3–19. https://doi.org/10.1080/17452759.2016.1139377.

[224] F. Calignano, M. Lorusso, I. Roppolo, P. Minetola, Investigation of the mechanical properties of a carbon fibre-reinforced nylon filament for 3d printing, Machines. 8 (2020) 1–13. https://doi.org/10.3390/machines8030052.

[225] G. Allevi, L. Capponi, P. Castellini, P. Chiariotti, F. Docchio, F. Freni, R. Marsili, M. Martarelli, R. Montanini, S. Pasinetti, A. Quattrocchi, R. Rossetti, G. Rossi, G. Sansoni, E.P. Tomasini, Investigating Additive Manufactured Lattice Structures: A Multi-Instrument Approach, IEEE Trans. Instrum. Meas. 69 (2020) 2459–2467. https://doi.org/10.1109/TIM.2019.2959293.

[226] S. Raghavendra, A. Molinari, M. Dallago, G. Zappini, F. Zanini, S. Carmignato, M. Benedetti, Uniaxial static mechanical properties of regular, irregular and random additively manufactured cellular materials: Nominal vs. real geometry, Forces Mech. 2 (2021) 100007. https://doi.org/10.1016/j.finmec.2020.100007.

[227] P. Cicconi, M. Mandolini, C. Favi, F. Campi, M. Germani, Metal Additive Manufacturing for the Rapid Prototyping of Shaped Parts: A Case Study, Comput. Aided. Des. Appl. 18 (2021) 1061–1079. https://doi.org/10.14733/cadaps.2021.1061-1079.

[228] A. Bacciaglia, A. Ceruti, A. Liverani, Proposal of a standard for 2D representation of bio-

inspired lightweight lattice structures in drawings, Proc. Inst. Mech. Eng. Part C J. Mech. Eng. Sci. (2020) 095440622095159. https://doi.org/10.1177/0954406220951595.

[229] T.W. Sederberg, S.R. Parry, Free-form deformation of solid geometric models, Proc. 13th Annu. Conf. Comput. Graph. Interact. Tech. SIGGRAPH 1986. 20 (1986) 151–160. https://doi.org/10.1145/15922.15903.

[230] S. Coquillart, Extended Free-Form Deformation : A Sculpturing Tool for 3D Geometric Modeling, Comput. Graph. (ACM). 24 (1990) 187–196.

[231] H.J.L. and W.N. Waggenspack, NURBS-Based Free-Form Deformations, IEEE Comput. Graph. Appl. (1994) 59–65.

[232] Y. Tang, G. Dong, Q. Zhou, Y.F. Zhao, Lattice Structure Design and Optimization with Additive Manufacturing Constraints, IEEE Trans. Autom. Sci. Eng. 15 (2018) 1546–1562. https://doi.org/10.1109/TASE.2017.2685643.

[233] W. Chen, X. Zheng, S. Liu, Finite-element-mesh based method for modeling and optimization of lattice structures for additive manufacturing, Materials (Basel). 11 (2018) 2073. https://doi.org/10.3390/ma11112073.

[234] C. Preisinger, Linking structure and parametric geometry, Archit. Des. 83 (2013) 110–113. https://doi.org/10.1002/ad.1564.

[235] S. Mirjalili, Genetic algorithm, in: Stud. Comput. Intell., Springer, Cham, 2019: pp. 43–55. https://doi.org/10.1007/978-3-319-93025-1_4.

[236] R.O. Parreiras, J.A. Vasconcelos, Decision making in multiobjective optimization aided by the multicriteria tournament decision method, Nonlinear Anal. Theory, Methods Appl. 71 (2009) e191–e198. https://doi.org/10.1016/j.na.2008.10.060.

[237] S. Künzli, S. Bleuler, L. Thiele, E. Zitzler, Application of Multi-Objective Evolutionary Algorithms, in: C.C. Coello, G.B. Lamont (Eds.), World Scientific, 2004: pp. 269–294.

[238] J. Peters, U. Reif, Subdivision Surfaces, Springer Berlin Heidelberg, Berlin, Heidelberg, 2008. https://doi.org/10.1007/978-3-540-76406-9.

[239] P. Schröder, D. Zorin, T. DeRose, D.R. Forsey, L. Kobbelt, M. Lounsbery, J. Peters, Subdivision for modeling and animation, ACM SIGGRAPH Course Notes. 12 (1998) 43.

[240] D. Zorin, Subdivision zoo, Subdiv. Model. Animat. (2000) 65–104.

[241] R. Qu, Recursive subdivision algorithms for curve and surface design, (1990). http://bura.brunel.ac.uk/handle/2438/5447 (accessed November 29, 2021).

[242] C. Loop, Smooth Subdivision Surfaces Based on Triangles, Master's Thesis, Univ. Utah, Dep. Math. (1987). https://ci.nii.ac.jp/naid/10000144165 (accessed November 29, 2021).

[243] N. Dyn, D. Levin, J.A. Gregory, A butterfly subdivision scheme for surface interpolation with tension control, ACM Trans. Graph. 9 (1990) 160–169. https://doi.org/10.1145/78956.78958.

[244] L. Kobbelt, Interpolatory Subdivision on Open Quadrilateral Nets with Arbitrary Topology, Comput. Graph. Forum. 15 (1996) 409–420. https://doi.org/10.1111/1467-8659.1530409.

[245] A.A. Ball, D.J.T. Storry, Conditions for Tangent Plane Continuity over Recursively Generated B-Spline Surfaces, ACM Trans. Graph. 7 (1988) 83–102. https://doi.org/10.1145/42458.42459.

[246] G. Savio, R. Meneghello, S. Rosso, G. Concheri, 3D model representation and data exchange for additive manufacturing, in: Lect. Notes Mech. Eng., Springer International Publishing, 2019: pp. 412–421. https://doi.org/10.1007/978-3-030-12346-8_40.

[247] D.G. Ullman, The Mechanical Design Process, 4th ed., McGraw-Hill, 2010. https://doi.org/10.1201/b18147.

[248] G. Pahl, W. Beitz, J. Feldhusen, K.H. Grote, Engineering design: A systematic approach, Springer London, 2007. https://doi.org/10.1007/978-1-84628-319-2.

[249] L. Jiu, W. Zhang, L. Meng, Y. Zhou, L. Chen, A CAD-oriented structural topology optimization method, Comput. Struct. 239 (2020) 106324. https://doi.org/10.1016/j.compstruc.2020.106324.

[250] J. Jiang, X. Xu, J. Stringer, Optimization of process planning for reducing material waste in extrusion based additive manufacturing, Robot. Comput. Integr. Manuf. 59 (2019) 317–325. https://doi.org/10.1016/j.rcim.2019.05.007.

[251] X. Song, S. Feih, W. Zhai, C.N. Sun, F. Li, R. Maiti, J. Wei, Y. Yang, V. Oancea, L. Romano Brandt, A.M. Korsunsky, Advances in additive manufacturing process simulation: Residual stresses and distortion predictions in complex metallic components, Mater. Des. 193 (2020) 108779. https://doi.org/10.1016/j.matdes.2020.108779.

[252] S. Jayanath, A. Achuthan, A computationally efficient hybrid model for simulating the additive manufacturing process of metals, Int. J. Mech. Sci. 160 (2019) 255–269. https://doi.org/10.1016/j.ijmecsci.2019.06.007.

[253] R. Martukanitz, P. Michaleris, T. Palmer, T. DebRoy, Z.K. Liu, R. Otis, T.W. Heo, L.Q. Chen, Toward an integrated computational system for describing the additive manufacturing process for metallic materials, Addit. Manuf. 1 (2014) 52–63. https://doi.org/10.1016/j.addma.2014.09.002.

[254] B. Schoinochoritis, D. Chantzis, K. Salonitis, Simulation of metallic powder bed additive manufacturing processes with the finite element method: A critical review, Proc. Inst. Mech. Eng. Part B J. Eng. Manuf. 231 (2017) 96–117. https://doi.org/10.1177/0954405414567522.

[255] B. Brenken, E. Barocio, A. Favaloro, V. Kunc, R.B. Pipes, Development and validation of extrusion deposition additive manufacturing process simulations, Addit. Manuf. 25 (2019) 218–226. https://doi.org/10.1016/j.addma.2018.10.041.

[256] S. Kolossov, E. Boillat, R. Glardon, P. Fischer, M. Locher, 3D FE simulation for temperature evolution in the selective laser sintering process, Int. J. Mach. Tools Manuf. 44 (2004) 117–123. https://doi.org/10.1016/j.ijmachtools.2003.10.019.

[257] J.M. Weaver, T.J. Barton, J. Linn, D. Jenkins, M.P. Miles, R. Smith, Quantifying accuracy of a concept laser metal additive machine through the NIST test artifact, Rapid Prototyp. J. 25 (2019) 221–231. https://doi.org/10.1108/RPJ-01-2018-0029.

[258] Renishaw, Data sheets - Additive manufacturing - AlSi10Mg-0403 (400 W), (2021). https://www.renishaw.com/en/data-sheets-additive-manufacturing--17862 (accessed February 19, 2021).

[259] B. Blakey-Milner, P. Gradl, G. Snedden, M. Brooks, J. Pitot, E. Lopez, M. Leary, F. Berto, A. du Plessis, Metal additive manufacturing in aerospace: A review, Mater. Des. 209 (2021) 110008. https://doi.org/10.1016/j.matdes.2021.110008.

[260] A.M. Haque, A. Bell, C.T. Morgan, M. Crossley, K. Swar, L. Shadbolt, D. Staab, A.

Garbayo, Development of an Additive Manufactured Mass , Volume and Cost Optimised Ti-6AL-4V Fuel Tank for Microsatellite Propulsion Systems MiniTANK, in: 36th Int. Electr. Propuls. Conf., 2019: pp. 1–20.

[261] W. Tam, K. Wlodarczyk, J. Hudak, Additive manufactured pressure vessel development: An update, in: Am. Soc. Mech. Eng. Press. Vessel. Pip. Div. PVP, American Society of Mechanical Engineers Digital Collection, 2019. https://doi.org/10.1115/PVP2019-94033.

[262] H.W. Jones, The Recent Large Reduction in Space Launch Cost, 48th Int. Conf. Environ. Syst. (2018) 81. https://ttu-ir.tdl.org/handle/2346/74082 (accessed September 18, 2021).

[263] Arianespace, Vega User's Manual, (2014). https://www.arianespace.com/wp-content/uploads/2018/05/Vega-Users-Manual_Issue-04_April-2014.pdf (accessed September 18, 2021).

[264] USA Department of Air Force, MIL-STD 1522A - Standard general requirements for safe design and operation of pressurized missile and space systems, (1984).

[265] J. Bader, E. Zitzler, HypE: An algorithm for fast hypervolume-based many-objective optimization, Evol. Comput. 19 (2011) 45–76. https://doi.org/10.1162/EVCO_a_00009.

[266] Raouf A. Ibrahim, Liquid Sloshing Dynamics: Theory and Applications, 2005. https://books.google.com/books?id=ctvhvH74ZzEC.

[267] O. Mireles, C. Gomez, W. Tilson, T. Belcher, B. Abranovic, M. Chaidez, J. Lopez, C. Romanowski, L. Wesche, Thermal, Fluid, Mechanical, and Microstructural Property Characterization of Additively Manufactured Lattice Structures - NASA Technical Reports Server (NTRS), (2018). https://ntrs.nasa.gov/citations/20180006367 (accessed November 26, 2021).

[268] G. Savio, R. Meneghello, G. Concheri, Design of variable thickness triply periodic surfaces for additive manufacturing, Prog. Addit. Manuf. 4 (2019) 281–290. https://doi.org/10.1007/s40964-019-00073-x.

[269] G. Savio, Rhino Open Projects, (n.d.). https://www.food4rhino.com/app/rhino-open-projects (accessed February 6, 2020).

[270] T.L. Leirmo, O. Semeniuta, Investigating the Dimensional and Geometric Accuracy of Laser-Based Powder Bed Fusion of PA2200 (PA12): Experiment Design and Execution, Appl. Sci. 11 (2021) 2031. https://doi.org/10.3390/app11052031.

[271] A. Amado-Becker, J. Ramos-Grez, M.J. Yañez, Y. Vargas, L. Gaete, Elastic tensor stiffness coefficients for SLS Nylon 12 under different degrees of densification as measured by ultrasonic technique, Rapid Prototyp. J. 14 (2008) 260–270. https://doi.org/10.1108/13552540810907929.

[272] PA 2200 Performance 1.0, EOS GmbH - Electro Opt. Syst., (2018). https://eos.materialdatacenter.com/eo/ (accessed November 18, 2019).

[273] G. Savio, S. Rosso, A. Curtarello, R. Meneghello, G. Concheri, Implications of modeling approaches on the fatigue behavior of cellular solids, Addit. Manuf. 25 (2019) 50–58. https://doi.org/10.1016/j.addma.2018.10.047.

[274] ASTM, ASTM E606/E606M - 2012 -- Standard Test Method for Strain-Controlled Fatigue Testing, (2012).

[275] ISO International Organization for Standardization, ISO 4287:1997 - Geometrical Product Specifications (GPS) -- Surface texture: Profile method -- Terms, definitions and surface

texture parameters, (1997).

[276] ISO International Organization for Standardization, ISO 4288:1996 - Geometrical Product Specifications (GPS) -- Surface texture: Profile method -- Rules and procedures for the assessment of surface texture, (1996).

[277] Renishaw, Data sheets - Additive manufacturing - SS 316L-0407, (2018). https://www.renishaw.com/en/data-sheets-additive-manufacturing--17862 (accessed June 4, 2019).

[278] ISO International Organization for Standardization, ISO 12107:2012 -- Metallic materials -- Fatigue testing -- Statistical planning and analysis of data, (2012).

[279] N.R. Draper, H. Smith, Applied regression analysis, John Wiley & Sons, 1998.

[280] ISO International Organization for Standardization, ISO 3534-1:2006 - Statistics — Vocabulary and symbols — Part 1: General statistical terms and terms used in probability, (2006). https://www.iso.org/standard/40145.html (accessed September 30, 2021).

[281] HP 3D High Reusability PA 12 - Datasheet, (2017). https://cimquest-inc.com/resource-center/HP/Materials/HP-PA12-Datasheet.pdf (accessed February 3, 2020).

[282] L. Verbelen, S. Dadbakhsh, M. Van Den Eynde, J.P. Kruth, B. Goderis, P. Van Puyvelde, Characterization of polyamide powders for determination of laser sintering processability, Eur. Polym. J. 75 (2016) 163–174. https://doi.org/10.1016/j.eurpolymj.2015.12.014.

[283] B. Scherer, I.L. Kottenstedde, F.M. Matysik, Material characterization of polyamide 12 and related agents used in the multi-jet fusion process: complementary application of high-resolution mass spectrometry and other advanced instrumental techniques, Monatshefte Fur Chemie. 151 (2020) 1203–1215. https://doi.org/10.1007/s00706-020-02646-x.

[284] B. Van Hooreweder, D. Moens, R. Boonen, J.P. Kruth, P. Sas, On the difference in material structure and fatigue properties of nylon specimens produced by injection molding and selective laser sintering, Polym. Test. 32 (2013) 972–981. https://doi.org/10.1016/j.polymertesting.2013.04.014.

[285] S. Gogolewski, K. Czerntawska, M. Gastorek, Effect of annealing on thermal properties and crystalline structure of polyamides. Nylon 12 (polylaurolactam), Colloid Polym. Sci. Kolloid Zeitschrift Zeitschrift Für Polym. 258 (1980) 1130–1136. https://doi.org/10.1007/BF01382456.

[286] P. Chen, H. Wu, W. Zhu, L. Yang, Z. Li, C. Yan, S. Wen, Y. Shi, Investigation into the processability, recyclability and crystalline structure of selective laser sintered Polyamide 6 in comparison with Polyamide 12, Polym. Test. 69 (2018) 366–374. https://doi.org/10.1016/j.polymertesting.2018.05.045.

[287] L. Biasetto, P. Zanonato, S. Carturan, P. Di Bernardo, P. Colombo, A. Andrighetto, G. Prete, Lanthanum carbide-based porous materials from carburization of lanthanum oxide and lanthanum oxalate mixtures, J. Nucl. Mater. 378 (2008) 180–187. https://doi.org/10.1016/j.jnucmat.2008.06.016.

[288] B. Van Hooreweder, J.P. Kruth, High cycle fatigue properties of selective laser sintered parts in polyamide 12, CIRP Ann. - Manuf. Technol. 63 (2014) 241–244. https://doi.org/10.1016/j.cirp.2014.03.060.

[289] H.J. O’Connor, A.N. Dickson, D.P. Dowling, Evaluation of the mechanical performance of polymer parts fabricated using a production scale multi jet fusion printing process, Addit. Manuf. 22 (2018) 381–387. https://doi.org/10.1016/j.addma.2018.05.035.

[290] R.G. Budynas, Shigley's Mechanical Engineering Design ,10th edition, Tenth edit, McGraw-Hill Education, New York NY, 2015.

[291] S. Kalpakjian, S. Schmid, Manufacturing Engineering and Technology, 7th ed., Pearson, 2013.

[292] Z. Xu, Y. Wang, D. Wu, K.P. Ananth, J. Bai, The process and performance comparison of polyamide 12 manufactured by multi jet fusion and selective laser sintering, J. Manuf. Process. 47 (2019) 419–426. https://doi.org/10.1016/j.jmapro.2019.07.014.

[293] S. Morales-Planas, J. Minguella-Canela, J. Lluma-Fuentes, J.A. Travieso-Rodriguez, A.A. García-Granada, Multi Jet Fusion PA12 manufacturing parameters for watertightness, strength and tolerances, Materials (Basel). 11 (2018) 1472. https://doi.org/10.3390/ma11081472.

[294] F. Sillani, R.G. Kleijnen, M. Vetterli, M. Schmid, K. Wegener, Selective laser sintering and multi jet fusion: Process-induced modification of the raw materials and analyses of parts performance, Addit. Manuf. 27 (2019) 32–41. https://doi.org/10.1016/j.addma.2019.02.004.

[295] A. Salazar, A. Rico, J. Rodríguez, J. Segurado Escudero, R. Seltzer, F. Martin De La Escalera Cutillas, Fatigue crack growth of SLS polyamide 12: Effect of reinforcement and temperature, Compos. Part B Eng. 59 (2014) 285–292. https://doi.org/10.1016/j.compositesb.2013.12.017.

[296] A. Pilipović, T. Brajlih, I. Drstvenšek, Influence of Processing Parameters on Tensile Properties of SLS Polymer Product, Polymers (Basel). 10 (2018) 1208. https://doi.org/10.3390/polym10111208.

[297] A. Salazar, A. Rico, J. Rodríguez, J. Segurado Escudero, R. Seltzer, F. Martin De La Escalera Cutillas, Monotonic loading and fatigue response of a bio-based polyamide PA11 and a petrol-based polyamide PA12 manufactured by selective laser sintering, Eur. Polym. J. 59 (2014) 36–45. https://doi.org/10.1016/j.eurpolymj.2014.07.016.

[298] J.A. Sauer, G.C. Richardson, Fatigue of polymers, Int. J. Fract. 16 (1980) 499–532. https://doi.org/10.1007/BF02265215.

[299] HP, HP Multi Jet Fusion technology - Technical white paper, (2018). https://h20195.www2.hp.com/v2/GetDocument.aspx?docname=4AA5-5472ENW (accessed November 28, 2021).

Appendix A – Internal walls implementation code

In this appendix, a part of the code that implements the modeling of the internal walls inside a lattice structure is presented. As highlighted in Section 3.3.2, for clarity's sake, the modeling phases of the beams and the walls were described separately, but the code performs them simultaneously, reducing the computational time and the physical memory required to store the information about the mesh model.

The code is written in IronPython, an implementation of the Python programming language, inside the Grasshopper environment for Rhinoceros 7 CAD 3D software (Robert McNeel & Associates). The RhinoCommon API libraries were used to directly control the geometries from the code.

```
import rhinoscriptsyntax as rs
import Rhino as rc
import Rhino.Geometry as rg

…

def latt_skin(nx, ny, nz, faces_nodes_sc, faces_nodes):
    ############################ PARTE CON SKIN ########################
    mesh_latt=rg.Mesh()
    cv=0
    for k in range(nz):
        for j in range(ny):
            for i in range(nx):
                if k<nz-1 and j<ny-1 and i<nx-1:
                    #beam lungo x
                    cv_skin=0
                    #preparo i vertici
                    mesh_latt.Vertices.Add(faces_nodes_sc[k][j][i][7][6]) #0 #n6
                    mesh_latt.Vertices.Add(faces_nodes_sc[k][j][i][7][7]) #1 #n7
                    mesh_latt.Vertices.Add(faces_nodes_sc[k][j+1][i][7][4]) #2 #n4 y+1
                    mesh_latt.Vertices.Add(faces_nodes_sc[k][j+1][i][7][5]) #3 #n5 y+1
                    mesh_latt.Vertices.Add(faces_nodes_sc[k+1][j+1][i][7][0])  #4  #n0
y+1, z+1
                    mesh_latt.Vertices.Add(faces_nodes_sc[k+1][j+1][i][7][1])  #5  #n1
y+1, z+1
                    mesh_latt.Vertices.Add(faces_nodes_sc[k+1][j][i][7][3]) #6 #n2 z+1
                    mesh_latt.Vertices.Add(faces_nodes_sc[k+1][j][i][7][2]) #7 #n3 z+1
                    #creo le facce dei beams lungo x
                    if faces_nodes[k][j][i][8][3]==0 or k==0 or i==0:
                        mesh_latt.Faces.AddFace(cv+0,cv+1,cv+2,cv+3)
                    else:
                        #faccia della skin sulla cella (faccia 3) XZ
                        mesh_latt.Vertices.Add(faces_nodes_sc[k][j][i][3][3])
                        mesh_latt.Vertices.Add(faces_nodes_sc[k][j][i][3][2])
                        mesh_latt.Vertices.Add(faces_nodes_sc[k][j][i][3][1])
                        mesh_latt.Vertices.Add(faces_nodes_sc[k][j][i][3][0])
                        mesh_latt.Faces.AddFace(cv+8,cv+9,cv+10,cv+11)
                        #faccia della skin su cella successiva y+1 (faccia 1)
                        mesh_latt.Vertices.Add(faces_nodes_sc[k][j+1][i][1][3])
    mesh_latt.Vertices.Add(faces_nodes_sc[k][j+1][i][1][2])
    mesh_latt.Vertices.Add(faces_nodes_sc[k][j+1][i][1][1])
    mesh_latt.Vertices.Add(faces_nodes_sc[k][j+1][i][1][0])
    mesh_latt.Faces.AddFace(cv+12,cv+13,cv+14,cv+15)
    cv_skin=cv_skin+8

if faces_nodes[k][j+1][i][8][5]==0 or i==0 or j==ny-2:
    mesh_latt.Faces.AddFace(cv+3,cv+2,cv+4,cv+5)

if faces_nodes[k+1][j][i][8][3]==0 or i==0 or k==nz-2:
    mesh_latt.Faces.AddFace(cv+5,cv+4,cv+6,cv+7)

if faces_nodes[k][j][i][8][5]==0 or j==0 or i==0:
    mesh_latt.Faces.AddFace(cv+7,cv+6,cv+1,cv+0)

cv=cv+8+cv_skin

#beam lungo y
cv_skin=0
#preparo i vertici
mesh_latt.Vertices.Add(faces_nodes_sc[k][j][i][7][6]) #0 #n6
mesh_latt.Vertices.Add(faces_nodes_sc[k][j][i][7][5]) #1 #n5
mesh_latt.Vertices.Add(faces_nodes_sc[k+1][j][i][7][1]) #2 #n1 z+1
mesh_latt.Vertices.Add(faces_nodes_sc[k+1][j][i][7][2]) #3 #n2 z+1
mesh_latt.Vertices.Add(faces_nodes_sc[k+1][j][i+1][7][0])  #4  #n0 x+1, z+1
mesh_latt.Vertices.Add(faces_nodes_sc[k+1][j][i+1][7][3])  #5  #n3 x+1, z+1
mesh_latt.Vertices.Add(faces_nodes_sc[k][j][i+1][7][4]) #6 #n4 x+1
mesh_latt.Vertices.Add(faces_nodes_sc[k][j][i+1][7][7]) #7 #n7 x+1

#creo le facce dei beams lungo y o delle pelli della faccia piano XY
if faces_nodes[k][j][i][8][5]==0 or j==0 or i==0:
    mesh_latt.Faces.AddFace(cv+0,cv+1,cv+2,cv+3)
else:
    #faccia della skin sulla cella (faccia 5) XY
    mesh_latt.Vertices.Add(faces_nodes_sc[k][j][i][5][3])
    mesh_latt.Vertices.Add(faces_nodes_sc[k][j][i][5][2])
    mesh_latt.Vertices.Add(faces_nodes_sc[k][j][i][5][1])
    mesh_latt.Vertices.Add(faces_nodes_sc[k][j][i][5][0])
    mesh_latt.Faces.AddFace(cv+8,cv+9,cv+10,cv+11)
    #faccia della skin su cella successiva z+1 (faccia 4)
    mesh_latt.Vertices.Add(faces_nodes_sc[k+1][j][i][4][3])
    mesh_latt.Vertices.Add(faces_nodes_sc[k+1][j][i][4][2])
    mesh_latt.Vertices.Add(faces_nodes_sc[k+1][j][i][4][1])
    mesh_latt.Vertices.Add(faces_nodes_sc[k+1][j][i][4][0])
    mesh_latt.Faces.AddFace(cv+12,cv+13,cv+14,cv+15)
    cv_skin=cv_skin+8


if faces_nodes[k][j][i+1][8][5]==0 or j==0 or i==nx-2:
    mesh_latt.Faces.AddFace(cv+5,cv+4,cv+6,cv+7)

if faces_nodes[k+1][j][i][8][2]==0 or j==0 or k==nz-2:
    mesh_latt.Faces.AddFace(cv+3,cv+2,cv+4,cv+5)

if faces_nodes[k][j][i][8][2]==0 or j==0 or k==0:
    #faccia del beam
    mesh_latt.Faces.AddFace(cv+7,cv+6,cv+1,cv+0)
```

```
                    cv=cv+8+cv_skin

                    #beam lungo z
                    cv_skin=0
                    #preparo i vertici
                    mesh_latt.Vertices.Add(faces_nodes_sc[k][j][i][7][6]) #0 #n6
                    mesh_latt.Vertices.Add(faces_nodes_sc[k][j][i][7][2]) #1 #n2
                    mesh_latt.Vertices.Add(faces_nodes_sc[k][j][i+1][7][3]) #2 #n3 x+1
                    mesh_latt.Vertices.Add(faces_nodes_sc[k][j][i+1][7][7]) #3 #n7 x+1
                    mesh_latt.Vertices.Add(faces_nodes_sc[k][j+1][i+1][7][0])  #4  #n0
x+1, y+1

                    mesh_latt.Vertices.Add(faces_nodes_sc[k][j+1][i+1][7][4])  #5  #n4
x+1, y+1

                    mesh_latt.Vertices.Add(faces_nodes_sc[k][j+1][i][7][1]) #6 #n1 y+1
                    mesh_latt.Vertices.Add(faces_nodes_sc[k][j+1][i][7][5]) #7 #n5 y+1

                    #creo le facce dei beams lungo z
                    if faces_nodes[k][j][i][8][2]==0 or k==0 or j==0:
                        mesh_latt.Faces.AddFace(cv+0,cv+1,cv+2,cv+3)
                    else:
                        #faccia della skin sulla cella (faccia 2) ZY
                        mesh_latt.Vertices.Add(faces_nodes_sc[k][j][i][2][3])
                        mesh_latt.Vertices.Add(faces_nodes_sc[k][j][i][2][2])
                        mesh_latt.Vertices.Add(faces_nodes_sc[k][j][i][2][1])
                        mesh_latt.Vertices.Add(faces_nodes_sc[k][j][i][2][0])
                        mesh_latt.Faces.AddFace(cv+8,cv+9,cv+10,cv+11)
                        #faccia della skin su cella successiva x+1 (faccia 0)
                        mesh_latt.Vertices.Add(faces_nodes_sc[k][j][i+1][0][3])
                        mesh_latt.Vertices.Add(faces_nodes_sc[k][j][i+1][0][2])
                        mesh_latt.Vertices.Add(faces_nodes_sc[k][j][i+1][0][1])
                        mesh_latt.Vertices.Add(faces_nodes_sc[k][j][i+1][0][0])
                        mesh_latt.Faces.AddFace(cv+12,cv+13,cv+14,cv+15)
                        cv_skin=cv_skin+8

                    if faces_nodes[k][j][i+1][8][3]==0 or k==0 or i==nx-2:
                        mesh_latt.Faces.AddFace(cv+3,cv+2,cv+4,cv+5)

                    if faces_nodes[k][j+1][i][8][2]==0 or k==0 or j==ny-2:
                        mesh_latt.Faces.AddFace(cv+5,cv+4,cv+6,cv+7)

                    if faces_nodes[k][j][i][8][3]==0 or i==0 or k==0:
                        mesh_latt.Faces.AddFace(cv+7,cv+6,cv+1,cv+0)

                    cv=cv+8+cv_skin

                elif k<nz-1 and j<ny-1 and i==nx-1:
                    #beam lungo x
                    #preparo i vertici
                    mesh_latt.Vertices.Add(faces_nodes_sc[k][j][i][7][6]) #0 #n6
                    mesh_latt.Vertices.Add(faces_nodes_sc[k][j][i][7][7]) #1 #n7
                    mesh_latt.Vertices.Add(faces_nodes_sc[k][j+1][i][7][4]) #2 #n4 y+1
                    mesh_latt.Vertices.Add(faces_nodes_sc[k][j+1][i][7][5]) #3 #n5 y+1
                    mesh_latt.Vertices.Add(faces_nodes_sc[k+1][j+1][i][7][0])  #4  #n0
y+1, z+1

                    mesh_latt.Vertices.Add(faces_nodes_sc[k+1][j+1][i][7][1])  #5  #n1
y+1, z+1

                    mesh_latt.Vertices.Add(faces_nodes_sc[k+1][j][i][7][3]) #6 #n3 z+1
                    mesh_latt.Vertices.Add(faces_nodes_sc[k+1][j][i][7][2]) #7 #n2 z+1
                    #creo le facce dei beams lungo x
                    mesh_latt.Faces.AddFace(cv+0,cv+1,cv+2,cv+3)
                    mesh_latt.Faces.AddFace(cv+3,cv+2,cv+4,cv+5)
                    mesh_latt.Faces.AddFace(cv+5,cv+4,cv+6,cv+7)
                    mesh_latt.Faces.AddFace(cv+7,cv+6,cv+1,cv+0)
                    cv=cv+8

                elif k<nz-1 and j==ny-1 and i<nx-1:
                    #beam lungo y
                    #preparo i vertici
                    mesh_latt.Vertices.Add(faces_nodes_sc[k][j][i][7][6]) #0 #n6
                    mesh_latt.Vertices.Add(faces_nodes_sc[k][j][i][7][5]) #1 #n5
                    mesh_latt.Vertices.Add(faces_nodes_sc[k+1][j][i][7][1]) #2 #n1 z+1
                    mesh_latt.Vertices.Add(faces_nodes_sc[k+1][j][i][7][2]) #3 #n2 z+1
                    mesh_latt.Vertices.Add(faces_nodes_sc[k+1][j][i+1][7][0])  #4  #n0
x+1, z+1

                    mesh_latt.Vertices.Add(faces_nodes_sc[k+1][j][i+1][7][3])  #5  #n3
x+1, z+1

                    mesh_latt.Vertices.Add(faces_nodes_sc[k][j][i+1][7][4]) #6 #n4 x+1
                    mesh_latt.Vertices.Add(faces_nodes_sc[k][j][i+1][7][7]) #7 #n7 x+1
                    #creo le facce dei beams lungo y
                    mesh_latt.Faces.AddFace(cv+0,cv+1,cv+2,cv+3)
                    mesh_latt.Faces.AddFace(cv+3,cv+2,cv+4,cv+5)
                    mesh_latt.Faces.AddFace(cv+5,cv+4,cv+6,cv+7)
                    mesh_latt.Faces.AddFace(cv+7,cv+6,cv+1,cv+0)
                    cv=cv+8

                elif k==nz-1 and j<ny-1 and i<nx-1:
                    #beam lungo z
                    #preparo i vertici
                    mesh_latt.Vertices.Add(faces_nodes_sc[k][j][i][7][6]) #0 #n6
                    mesh_latt.Vertices.Add(faces_nodes_sc[k][j][i][7][2]) #1 #n2
                    mesh_latt.Vertices.Add(faces_nodes_sc[k][j][i+1][7][3]) #2 #n3 x+1
                    mesh_latt.Vertices.Add(faces_nodes_sc[k][j][i+1][7][7]) #3 #n7 x+1
                    mesh_latt.Vertices.Add(faces_nodes_sc[k][j+1][i+1][7][0])  #4  #n0
x+1, y+1

                    mesh_latt.Vertices.Add(faces_nodes_sc[k][j+1][i+1][7][4])  #5  #n4
x+1, y+1

                    mesh_latt.Vertices.Add(faces_nodes_sc[k][j+1][i][7][1]) #6 #n1 y+1
                    mesh_latt.Vertices.Add(faces_nodes_sc[k][j+1][i][7][5]) #7 #n5 y+1
                    #creo le facce dei beams lungo z
                    mesh_latt.Faces.AddFace(cv+0,cv+1,cv+2,cv+3)
                    mesh_latt.Faces.AddFace(cv+3,cv+2,cv+4,cv+5)
                    mesh_latt.Faces.AddFace(cv+5,cv+4,cv+6,cv+7)
                    mesh_latt.Faces.AddFace(cv+7,cv+6,cv+1,cv+0)
                    cv=cv+8


    mesh_latt.Normals.ComputeNormals()

    mesh_latt.Compact()

    return mesh_latt
```

Appendix B – Materials data sheets

In the following pages, the datasheets of the powders used for manufacturing the tested samples are reported. In particular, the materials are:

- Stainless Steel 316L “SS 316L-0407” produced by Renishaw plc.
- Polyamide 12 “PA2200 Performance 1.0” produced by EOS GmBH.
- Polyamide 12 “HP 3D High Reusability PA 12” produced by HP Inc.

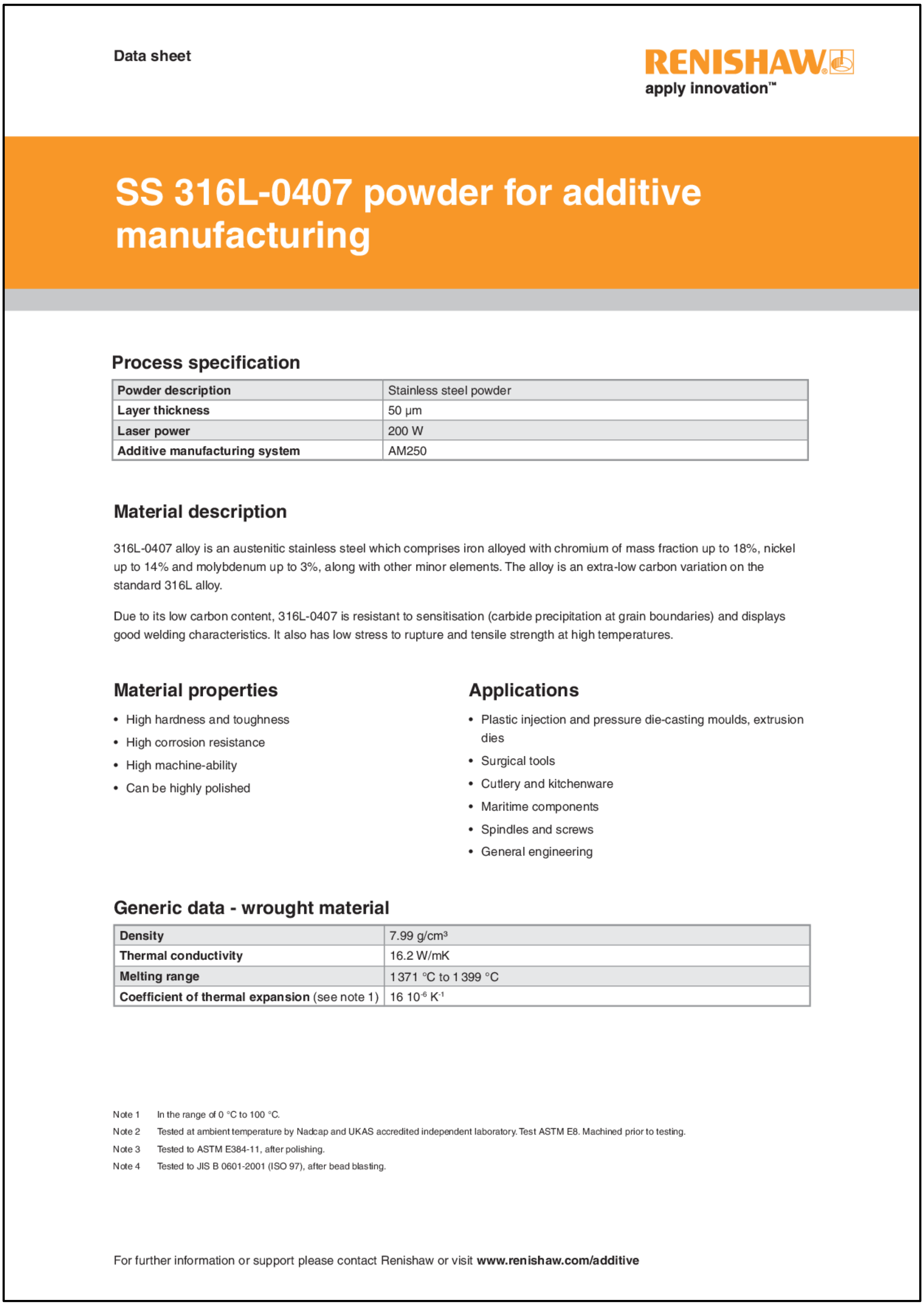

Data sheet

RENISHAW
apply innovation™

SS 316L-0407 powder for additive manufacturing

Process specification

Powder description	Stainless steel powder
Layer thickness	50 µm
Laser power	200 W
Additive manufacturing system	AM250

Material description

316L-0407 alloy is an austenitic stainless steel which comprises iron alloyed with chromium of mass fraction up to 18%, nickel up to 14% and molybdenum up to 3%, along with other minor elements. The alloy is an extra-low carbon variation on the standard 316L alloy.

Due to its low carbon content, 316L-0407 is resistant to sensitisation (carbide precipitation at grain boundaries) and displays good welding characteristics. It also has low stress to rupture and tensile strength at high temperatures.

Material properties

- High hardness and toughness
- High corrosion resistance
- High machine-ability
- Can be highly polished

Applications

- Plastic injection and pressure die-casting moulds, extrusion dies
- Surgical tools
- Cutlery and kitchenware
- Maritime components
- Spindles and screws
- General engineering

Generic data - wrought material

Density	7.99 g/cm³
Thermal conductivity	16.2 W/mK
Melting range	1 371 °C to 1 399 °C
Coefficient of thermal expansion (see note 1)	16 10^{-6} K^{-1}

Note 1 In the range of 0 °C to 100 °C.

Note 2 Tested at ambient temperature by Nadcap and UKAS accredited independent laboratory. Test ASTM E8. Machined prior to testing.

Note 3 Tested to ASTM E384-11, after polishing.

Note 4 Tested to JIS B 0601-2001 (ISO 97), after bead blasting.

For further information or support please contact Renishaw or visit **www.renishaw.com/additive**

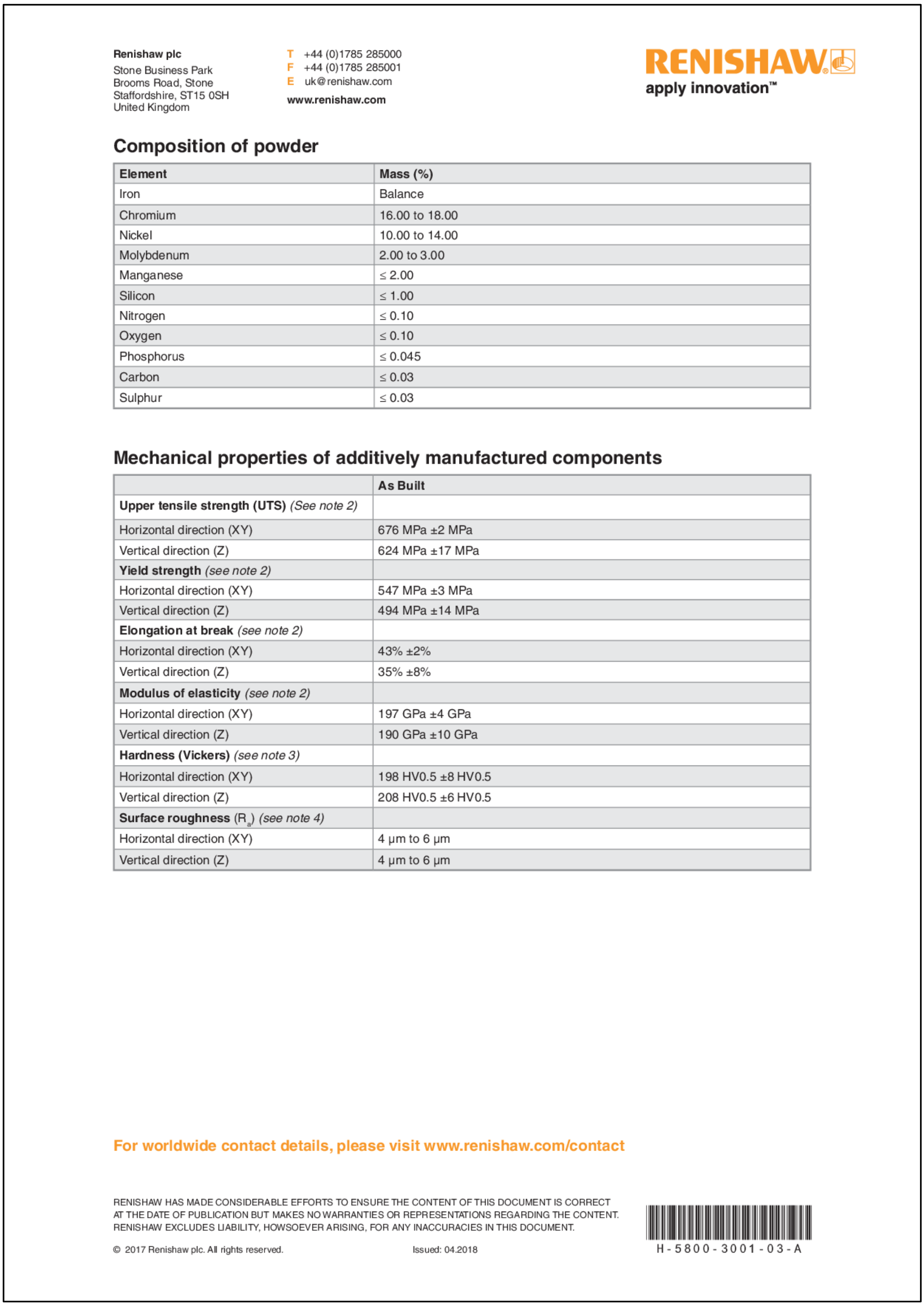

Renishaw plc
Stone Business Park
Brooms Road, Stone
Staffordshire, ST15 0SH
United Kingdom

T +44 (0)1785 285000
F +44 (0)1785 285001
E uk@renishaw.com
www.renishaw.com

RENISHAW
apply innovation™

Composition of powder

Element	Mass (%)
Iron	Balance
Chromium	16.00 to 18.00
Nickel	10.00 to 14.00
Molybdenum	2.00 to 3.00
Manganese	≤ 2.00
Silicon	≤ 1.00
Nitrogen	≤ 0.10
Oxygen	≤ 0.10
Phosphorus	≤ 0.045
Carbon	≤ 0.03
Sulphur	≤ 0.03

Mechanical properties of additively manufactured components

	As Built
Upper tensile strength (UTS) *(See note 2)*	
Horizontal direction (XY)	676 MPa ±2 MPa
Vertical direction (Z)	624 MPa ±17 MPa
Yield strength *(see note 2)*	
Horizontal direction (XY)	547 MPa ±3 MPa
Vertical direction (Z)	494 MPa ±14 MPa
Elongation at break *(see note 2)*	
Horizontal direction (XY)	43% ±2%
Vertical direction (Z)	35% ±8%
Modulus of elasticity *(see note 2)*	
Horizontal direction (XY)	197 GPa ±4 GPa
Vertical direction (Z)	190 GPa ±10 GPa
Hardness (Vickers) *(see note 3)*	
Horizontal direction (XY)	198 HV0.5 ±8 HV0.5
Vertical direction (Z)	208 HV0.5 ±6 HV0.5
Surface roughness (R_a) *(see note 4)*	
Horizontal direction (XY)	4 µm to 6 µm
Vertical direction (Z)	4 µm to 6 µm

For worldwide contact details, please visit www.renishaw.com/contact

RENISHAW HAS MADE CONSIDERABLE EFFORTS TO ENSURE THE CONTENT OF THIS DOCUMENT IS CORRECT AT THE DATE OF PUBLICATION BUT MAKES NO WARRANTIES OR REPRESENTATIONS REGARDING THE CONTENT. RENISHAW EXCLUDES LIABILITY, HOWSOEVER ARISING, FOR ANY INACCURACIES IN THIS DOCUMENT.

© 2017 Renishaw plc. All rights reserved.

Issued: 04.2018

H-5800-3001-03-A

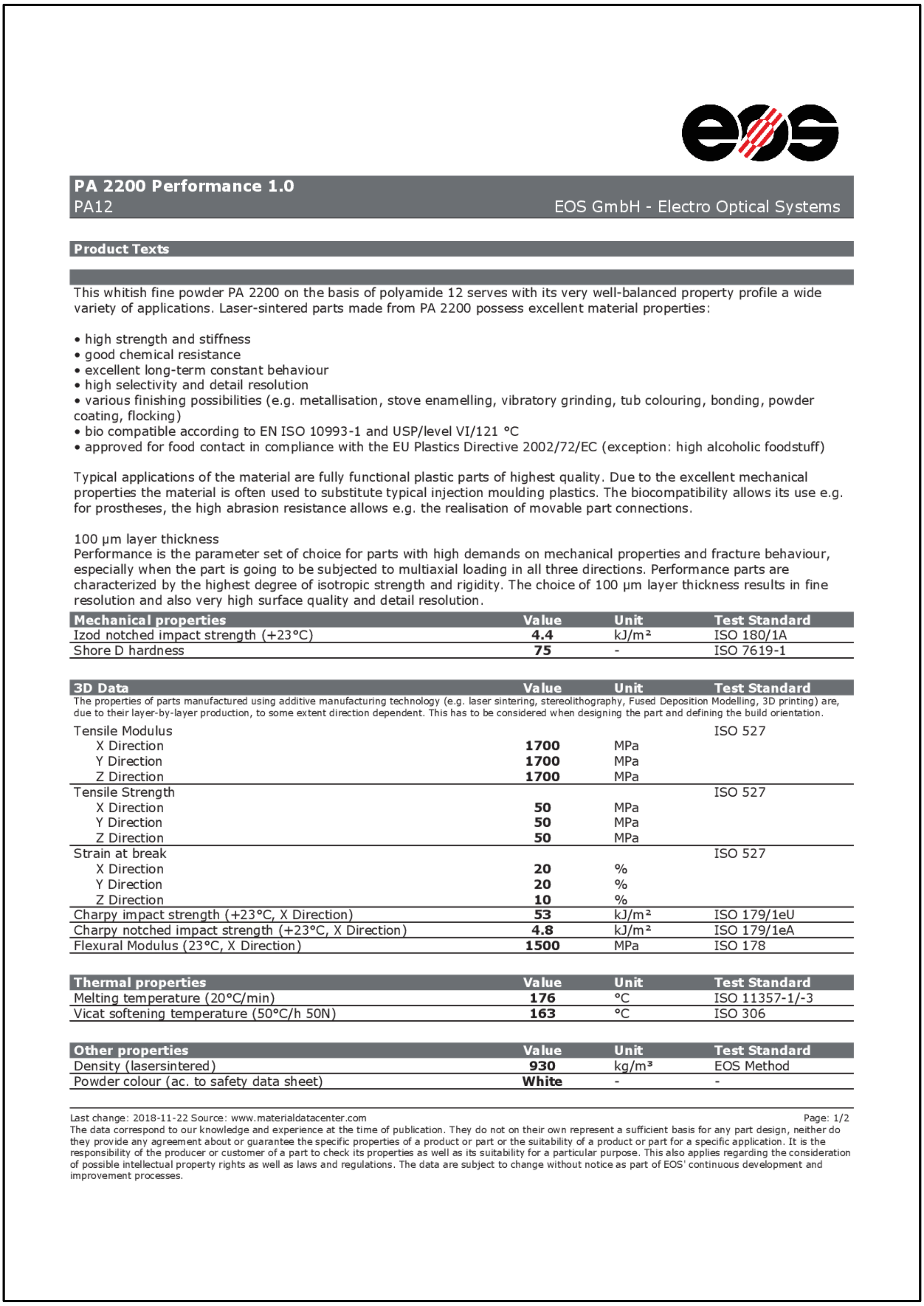

PA 2200 Performance 1.0

PA12 EOS GmbH - Electro Optical Systems

Product Texts

This whitish fine powder PA 2200 on the basis of polyamide 12 serves with its very well-balanced property profile a wide variety of applications. Laser-sintered parts made from PA 2200 possess excellent material properties:

- high strength and stiffness
- good chemical resistance
- excellent long-term constant behaviour
- high selectivity and detail resolution
- various finishing possibilities (e.g. metallisation, stove enamelling, vibratory grinding, tub colouring, bonding, powder coating, flocking)
- bio compatible according to EN ISO 10993-1 and USP/level VI/121 °C
- approved for food contact in compliance with the EU Plastics Directive 2002/72/EC (exception: high alcoholic foodstuff)

Typical applications of the material are fully functional plastic parts of highest quality. Due to the excellent mechanical properties the material is often used to substitute typical injection moulding plastics. The biocompatibility allows its use e.g. for prostheses, the high abrasion resistance allows e.g. the realisation of movable part connections.

100 µm layer thickness
Performance is the parameter set of choice for parts with high demands on mechanical properties and fracture behaviour, especially when the part is going to be subjected to multiaxial loading in all three directions. Performance parts are characterized by the highest degree of isotropic strength and rigidity. The choice of 100 µm layer thickness results in fine resolution and also very high surface quality and detail resolution.

Mechanical properties	Value	Unit	Test Standard
Izod notched impact strength (+23°C)	**4.4**	kJ/m²	ISO 180/1A
Shore D hardness	**75**	-	ISO 7619-1

3D Data	Value	Unit	Test Standard

The properties of parts manufactured using additive manufacturing technology (e.g. laser sintering, stereolithography, Fused Deposition Modelling, 3D printing) are, due to their layer-by-layer production, to some extent direction dependent. This has to be considered when designing the part and defining the build orientation.

Tensile Modulus			ISO 527
X Direction	**1700**	MPa	
Y Direction	**1700**	MPa	
Z Direction	**1700**	MPa	
Tensile Strength			ISO 527
X Direction	**50**	MPa	
Y Direction	**50**	MPa	
Z Direction	**50**	MPa	
Strain at break			ISO 527
X Direction	**20**	%	
Y Direction	**20**	%	
Z Direction	**10**	%	
Charpy impact strength (+23°C, X Direction)	**53**	kJ/m²	ISO 179/1eU
Charpy notched impact strength (+23°C, X Direction)	**4.8**	kJ/m²	ISO 179/1eA
Flexural Modulus (23°C, X Direction)	**1500**	MPa	ISO 178

Thermal properties	Value	Unit	Test Standard
Melting temperature (20°C/min)	**176**	°C	ISO 11357-1/-3
Vicat softening temperature (50°C/h 50N)	**163**	°C	ISO 306

Other properties	Value	Unit	Test Standard
Density (lasersintered)	**930**	kg/m³	EOS Method
Powder colour (ac. to safety data sheet)	**White**	-	-

Last change: 2018-11-22 Source: www.materialdatacenter.com Page: 1/2

The data correspond to our knowledge and experience at the time of publication. They do not on their own represent a sufficient basis for any part design, neither do they provide any agreement about or guarantee the specific properties of a product or part or the suitability of a product or part for a specific application. It is the responsibility of the producer or customer of a part to check its properties as well as its suitability for a particular purpose. This also applies regarding the consideration of possible intellectual property rights as well as laws and regulations. The data are subject to change without notice as part of EOS' continuous development and improvement processes.

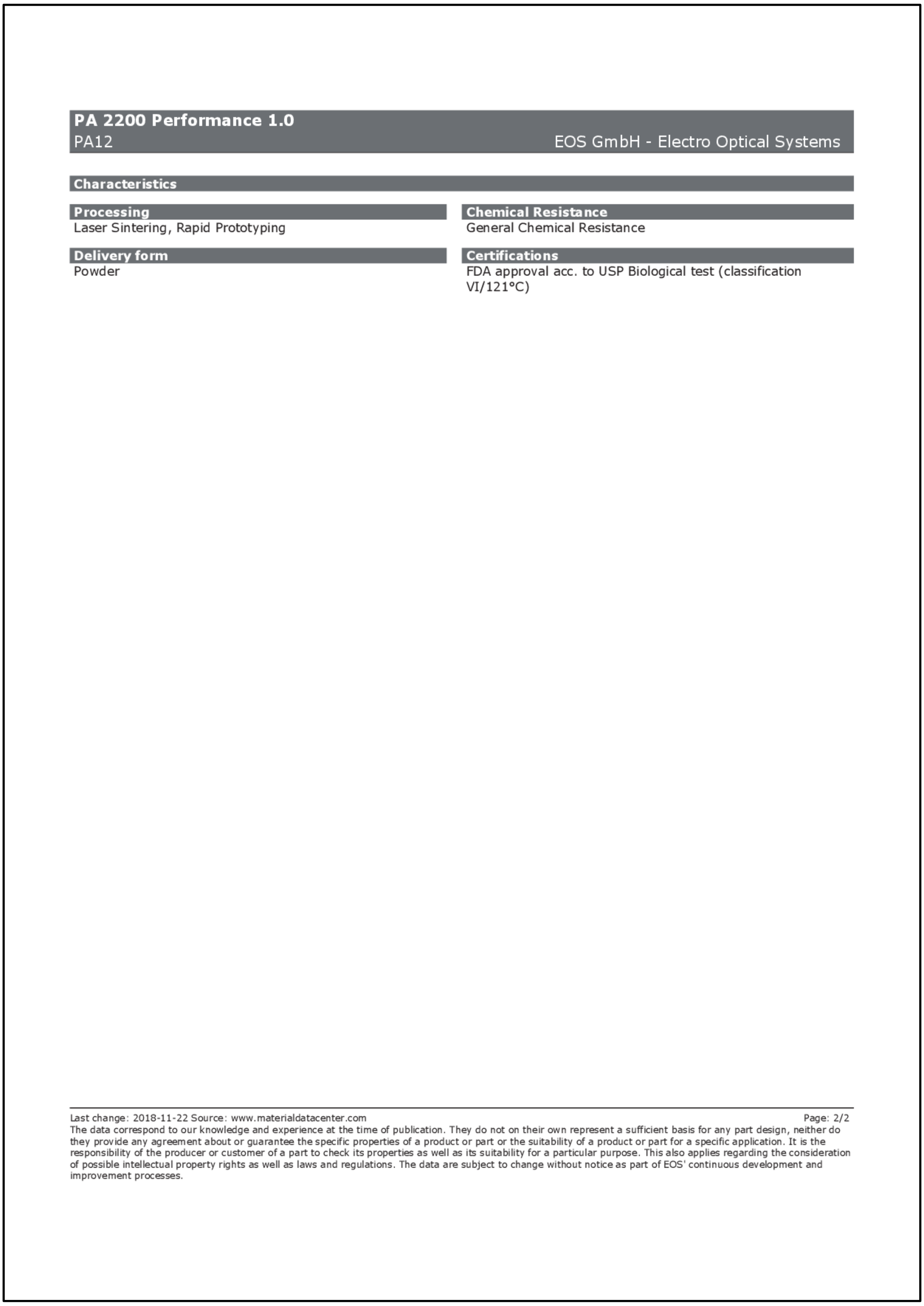

PA 2200 Performance 1.0
PA12
EOS GmbH - Electro Optical Systems

Characteristics

Processing
Laser Sintering, Rapid Prototyping

Chemical Resistance
General Chemical Resistance

Delivery form
Powder

Certifications
FDA approval acc. to USP Biological test (classification VI/121°C)

Last change: 2018-11-22 Source: www.materialdatacenter.com
Page: 2/2

The data correspond to our knowledge and experience at the time of publication. They do not on their own represent a sufficient basis for any part design, neither do they provide any agreement about or guarantee the specific properties of a product or part or the suitability of a product or part for a specific application. It is the responsibility of the producer or customer of a part to check its properties as well as its suitability for a particular purpose. This also applies regarding the consideration of possible intellectual property rights as well as laws and regulations. The data are subject to change without notice as part of EOS' continuous development and improvement processes.

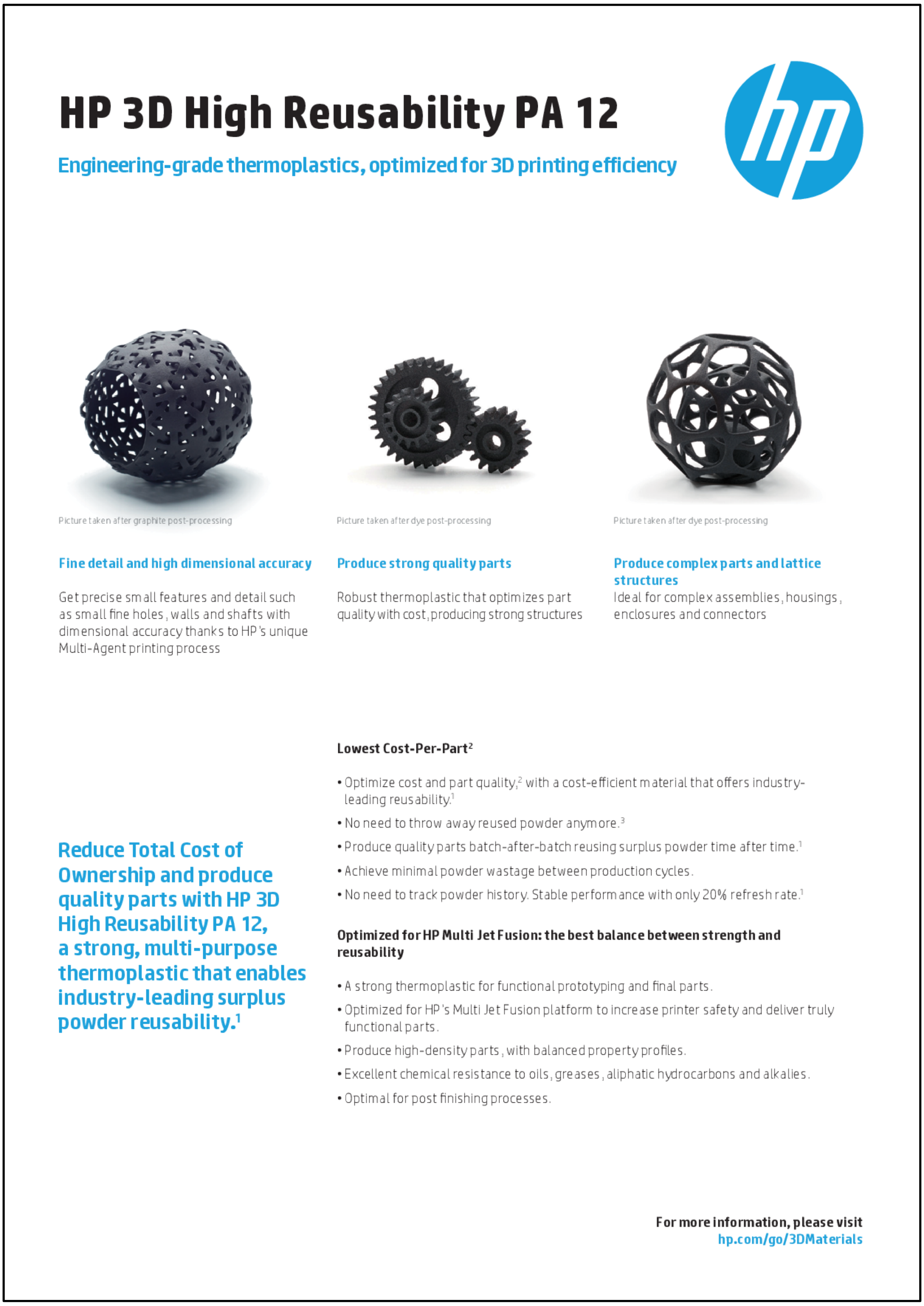

HP 3D High Reusability PA 12

Engineering-grade thermoplastics, optimized for 3D printing efficiency

Picture taken after graphite post-processing

Picture taken after dye post-processing

Picture taken after dye post-processing

Fine detail and high dimensional accuracy

Get precise small features and detail such as small fine holes, walls and shafts with dimensional accuracy thanks to HP's unique Multi-Agent printing process

Produce strong quality parts

Robust thermoplastic that optimizes part quality with cost, producing strong structures

Produce complex parts and lattice structures

Ideal for complex assemblies, housings, enclosures and connectors

Reduce Total Cost of Ownership and produce quality parts with HP 3D High Reusability PA 12, a strong, multi-purpose thermoplastic that enables industry-leading surplus powder reusability.[1]

Lowest Cost-Per-Part[2]

- Optimize cost and part quality,[2] with a cost-efficient material that offers industry-leading reusability.[1]
- No need to throw away reused powder anymore.[3]
- Produce quality parts batch-after-batch reusing surplus powder time after time.[1]
- Achieve minimal powder wastage between production cycles.
- No need to track powder history. Stable performance with only 20% refresh rate.[1]

Optimized for HP Multi Jet Fusion: the best balance between strength and reusability

- A strong thermoplastic for functional prototyping and final parts.
- Optimized for HP's Multi Jet Fusion platform to increase printer safety and deliver truly functional parts.
- Produce high-density parts, with balanced property profiles.
- Excellent chemical resistance to oils, greases, aliphatic hydrocarbons and alkalies.
- Optimal for post finishing processes.

For more information, please visit
hp.com/go/3DMaterials

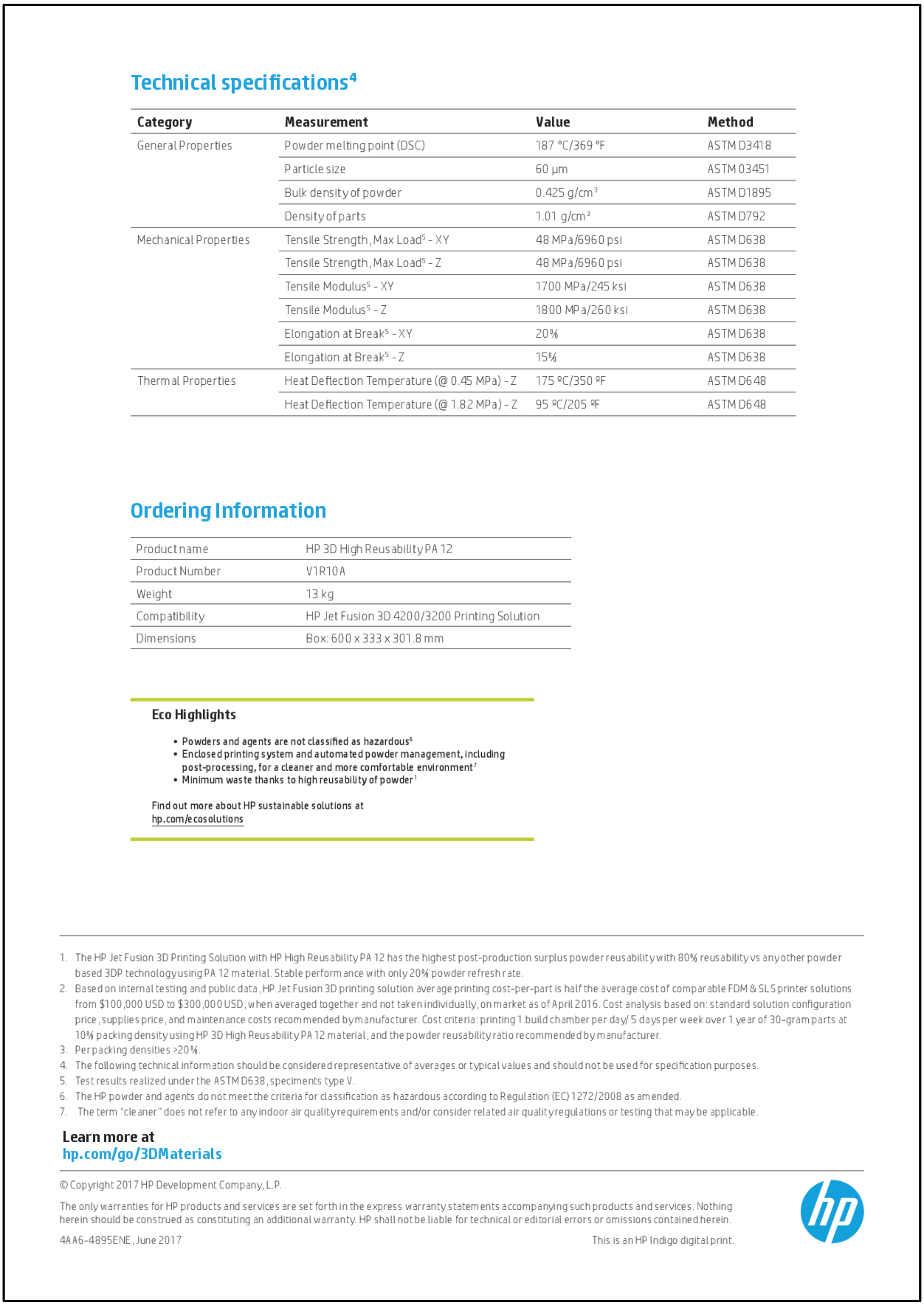

Technical specifications[4]

Category	Measurement	Value	Method
General Properties	Powder melting point (DSC)	187 °C/369 °F	ASTM D3418
	Particle size	60 µm	ASTM 03451
	Bulk density of powder	0.425 g/cm^3	ASTM D1895
	Density of parts	1.01 g/cm^3	ASTM D792
Mechanical Properties	Tensile Strength, Max Load[5] - XY	48 MPa/6960 psi	ASTM D638
	Tensile Strength, Max Load[5] - Z	48 MPa/6960 psi	ASTM D638
	Tensile Modulus[5] - XY	1700 MPa/245 ksi	ASTM D638
	Tensile Modulus[5] - Z	1800 MPa/260 ksi	ASTM D638
	Elongation at Break[5] - XY	20%	ASTM D638
	Elongation at Break[5] - Z	15%	ASTM D638
Thermal Properties	Heat Deflection Temperature (@ 0.45 MPa) - Z	175 °C/350 °F	ASTM D648
	Heat Deflection Temperature (@ 1.82 MPa) - Z	95 °C/205 °F	ASTM D648

Ordering Information

Product name	HP 3D High Reusability PA 12
Product Number	V1R10A
Weight	13 kg
Compatibility	HP Jet Fusion 3D 4200/3200 Printing Solution
Dimensions	Box: 600 x 333 x 301.8 mm

Eco Highlights

- Powders and agents are not classified as hazardous[6]
- Enclosed printing system and automated powder management, including post-processing, for a cleaner and more comfortable environment[7]
- Minimum waste thanks to high reusability of powder[1]

Find out more about HP sustainable solutions at
hp.com/ecosolutions

---

1. The HP Jet Fusion 3D Printing Solution with HP High Reusability PA 12 has the highest post-production surplus powder reusability with 80% reusability vs any other powder based 3DP technology using PA 12 material. Stable performance with only 20% powder refresh rate.
2. Based on internal testing and public data, HP Jet Fusion 3D printing solution average printing cost-per-part is half the average cost of comparable FDM & SLS printer solutions from $100,000 USD to $300,000 USD, when averaged together and not taken individually, on market as of April 2016. Cost analysis based on: standard solution configuration price, supplies price, and maintenance costs recommended by manufacturer. Cost criteria: printing 1 build chamber per day/ 5 days per week over 1 year of 30-gram parts at 10% packing density using HP 3D High Reusability PA 12 material, and the powder reusability ratio recommended by manufacturer.
3. Per packing densities >20%.
4. The following technical information should be considered representative of averages or typical values and should not be used for specification purposes.
5. Test results realized under the ASTM D638, speciments type V.
6. The HP powder and agents do not meet the criteria for classification as hazardous according to Regulation (EC) 1272/2008 as amended.
7. The term "cleaner" does not refer to any indoor air quality requirements and/or consider related air quality regulations or testing that may be applicable.

Learn more at
hp.com/go/3DMaterials

© Copyright 2017 HP Development Company, L.P.

The only warranties for HP products and services are set forth in the express warranty statements accompanying such products and services. Nothing herein should be construed as constituting an additional warranty. HP shall not be liable for technical or editorial errors or omissions contained herein.

4AA6-4895ENE, June 2017

This is an HP Indigo digital print.

Appendix C – Related publications

In this appendix, the published articles related to the topics of this research project are reported.

In particular, the following works are attached:

- S. Rosso, A. Curtarello, F. Basana, L. Grigolato, R. Meneghello, G. Concheri, G. Savio, Modeling Symmetric Minimal Surfaces by Mesh Subdivision, in: Roucoules L., Paredes M., Eynard B., Morer Camo P., Rizzi C. (eds) Advances on Mechanics, Design Engineering and Manufacturing III. JCM 2020. Lecture Notes in Mechanical Engineering. Springer, Cham:, 2021: pp. 249–254. https://doi.org/10.1007/978-3-030-70566-4_40.
- S. Rosso, F. Uriati, L. Grigolato, R. Meneghello, G. Concheri, G. Savio, An Optimization Workflow in Design for Additive Manufacturing, Appl. Sci. 11 (2021) 2572. https://doi.org/10.3390/app11062572.
- S. Rosso, R. Meneghello, L. Biasetto, L. Grigolato, G. Concheri, G. Savio, In-depth comparison of polyamide 12 parts manufactured by Multi Jet Fusion and Selective Laser Sintering, Addit. Manuf. 36 (2020) 101713. https://doi.org/10.1016/j.addma.2020.101713.
- S. Rosso, R. Meneghello, G. Concheri, G. Savio, Scale and Shape Effects on the Fatigue Behaviour of Additively Manufactured SS316L Structures: A Preliminary Study, in: Lect. Notes Mech. Eng., Springer, 2020: pp. 879–890. https://doi.org/10.1007/978-3-030-31154-4_75.
- Luca Grigolato, Stefano Rosso, Roberto Meneghello, Gianmaria Concheri, Gianpaolo Savio, Heterogeneous objects representation for Additive Manufacturing: a review, Instant J. Mech. Eng. (2019) 14–23. https://doi.org/10.36811/ijme.2019.110002.
- S. Rosso, G. Savio, F. Uriati, R. Meneghello, G. Concheri, Optimization approaches in design for additive manufacturing, in: Proc. Int. Conf. Eng. Des. ICED, Cambridge University Press, 2019: pp. 809–818. https://doi.org/10.1017/dsi.2019.85.

- G. Savio, R. Meneghello, S. Rosso, G. Concheri, 3D model representation and data exchange for additive manufacturing, in: Lect. Notes Mech. Eng., Springer International Publishing, 2019: pp. 412–421. https://doi.org/10.1007/978-3-030-12346-8_40.
- G. Savio, S. Rosso, A. Curtarello, R. Meneghello, G. Concheri, Implications of modeling approaches on the fatigue behavior of cellular solids, Addit. Manuf. 25 (2019) 50–58. https://doi.org/10.1016/j.addma.2018.10.047.
- G. Savio, A. Curtarello, S. Rosso, R. Meneghello, G. Concheri, Homogenization driven design of lightweight structures for additive manufacturing, Int. J. Interact. Des. Manuf. (2019). https://doi.org/10.1007/s12008-019-00543-0.

Modeling Symmetric Minimal Surfaces by Mesh Subdivision

Stefano Rosso[1](✉), Andrea Curtarello[2], Federico Basana[2], Luca Grigolato[2], Roberto Meneghello[1], Gianmaria Concheri[2], and Gianpaolo Savio[2]

[1] Department of Management and Engineering, University of Padova, Padua, Italy
stefano.rosso.3@phd.unipd.it
[2] Department of Civil, Environmental and Architectural Engineering, University of Padova, Padua, Italy

Abstract. Thanks to the great diffusion of additive manufacturing technologies, the interest in lattice structures is growing. Among them, minimal surfaces are characterized by zero mean curvature, allowing enhanced properties such as mechanical response and fluidynamic behavior. Recent works showed a method for geometric modeling triply periodic minimal surfaces (TPMS) based on subdivision surface. In this paper, the deviation between the subdivided TPMS and the implicit defined ones is investigated together with mechanical properties computed by numerical methods. As a result, a model of mechanical properties as a function of the TPMS thickness and relative density is proposed.

Keywords: Lattice structures · Additive manufacturing · Triply periodic minimal surfaces · Design for additive manufacturing

1 Introduction

The spreading of additive manufacturing (AM) technologies makes it possible to produce parts with unprecedented complexity, such as biomimicry products, organic shapes and lightweight components. Nevertheless, anisotropic materials, surface finish, costs and security are just some of the open issues [1]. Among the lightweight structures, cellular solids or lattice structures are characterized by superior properties: they have high specific stiffness and strength, and they are good heat exchangers, energy absorbers and acoustic insulators [2, 3, 4]. Lattice structures, indeed, can find application from microscale to macroscale, from tissue engineering [5], to construction [6]. Minimal surfaces are a kind of lattice structures defined as surfaces with zero mean curvature or surfaces that minimize the surface area for given boundary conditions [7]. Minimal surfaces repeating themselves in three dimensions are called triply periodic minimal surfaces (TPMS) [8]. These surfaces have received huge attention in the research community due to their intrinsic properties [9], especially in the biomedical field, where it is mandatory to use porous scaffolds designed to allow fluid exchange and tissue regrowth [10, 11]. Furthermore, due to their curvature continuity, the stress concentration at nodal points is eliminated and fatigue life is improved compared to beam-like lattice structures [12].

© The Author(s) 2021
L. Roucoules et al. (Eds.): JCM 2020, LNME, pp. 249–254, 2021.
https://doi.org/10.1007/978-3-030-70566-4_40

TPMS can be modeled adopting different methods: boundary representation (BRep), volume representation (VRep) and constructive solid geometry (CSG) [2, 13]. As emerged in recent studies, current mesh or parametric models are not ideal for modeling lattice structures, due to the significant computational resources required, processing times, robustness, rendering and visualization issues [14, 15]. To overcome these limitations, a novel method for geometric modeling variable thickness triply periodic surfaces based on a subdivision surface algorithm has been recently proposed [13]. Nevertheless, the geometrical accuracy of the modeling method and the mechanical characterization of the thickened structure still need to be investigated.

As an extension of the aforementioned work, in this study, the geometrical deviation of the subdivided TPMS P-Surface from the implicit defined one is investigated, then the mechanical properties of the unit cell are computed by finite element analyses. As a result, a model of mechanical properties as a function of the cell relative density is proposed and compared to the ones available in literature. The findings show the accuracy of the proposed modeling method; more, the numerical model allows to relate the thickness of the part to the mechanical properties by simulating a single cell inside the lattice structure, saving computational time, and giving directions for tailored applications with lattices that present variable properties in the design volume. Furthermore, knowing the properties of a single cell is a key feature when integrating topology optimization in the design workflow and also for applying the homogenization method [16] during the mechanical characterization of lattice structures.

2 Methods

A 1 mm unit cell of P-Surface type was modeled as described in [13]. A coarse mesh was used to model the unit cell of a P-surface; the Catmull-Clark subdivision surface algorithm was then adopted to achieve a smooth geometric model; finally, a thickness is assigned adopting a differential offset algorithm.

The deviation of the subdivided mesh at the third iteration of the Catmull-Clark subdivision scheme from the reference minimal surface was then computed in Rhinoceros 6 by “Mesh-Mesh Deviation” tool from “Rhino Open Projects” [17, 18]. The reference minimal surface was built in Netfabb introducing the minimal surface implicit equation in the mathematical part library (accuracy at 0.05 mm).

The finite element analysis software ANSYS R18.1 was then used to obtain the mechanical properties of the TPMS cells: Young’s modulus (E), Poisson’s ratio (ν), and Shear modulus (G). The used material was a titanium alloy, Ti6Al4V ELI (Grade 23), with the following bulk properties: $E_0 = 113800$ MPa, $\nu_0 = 0.342$, $G_0 = 42400$ MPa [19]. The stl file of the cell after three iterations of the subdivision algorithm was imported in the software and a second order tetrahedral elements mesh was used. Then, a set of constraints was imposed to the single cell. Even if a single cell is studied, the boundary conditions have been imposed in order to simulate an entire lattice structure, so the cell must deform accordingly. As Fig. 1 shows, for E and ν determination, a 0.05 mm displacement along Y axis is imposed to the upper face, while X and Z directions are free; the bottom face is fixed along Y axis (i.e., a 0 mm displacement is imposed), and X and Z direction displacements are free. Remote points are used to control the degrees of freedom of the cell faces; this technique allows to relate a point (the remote point) to a node, a face, or to the entire body, and to control the behavior of the connected part by directly imposing loads and/or constraints to the remote point. A remote point with a deformable behavior, i.e. the geometry is free to deform, is assigned to the bottom face; remote points are also connected to the lateral faces of the unit cell, along the normal direction of each face, with a coupled behavior. To take into account the presence of the adjacent cells, coupling equations are assigned to the nodes of opposite faces [16], so each node of a face moves with the same displacement of the opposite node. To obtain E and ν, the reaction force of the bottom face and the contraction of lateral faces are evaluated. Similarly, another set is imposed to the P-Surface cell to determine G. A displacement along the X direction is imposed to the upper face, and reaction force of the bottom face are used to calculate G; the remote displacement and coupling equations of opposite faces are also assigned to ensure a displacement compatible with adjacent cells. The simulations were run four times, targeting four different thickness of the P-Surface cell, 0.1 mm, 0.2 mm, 0.3 mm and 0.4 mm, corresponding to a relative density of 0.23, 0.45, 0.64, 0.80, respectively.

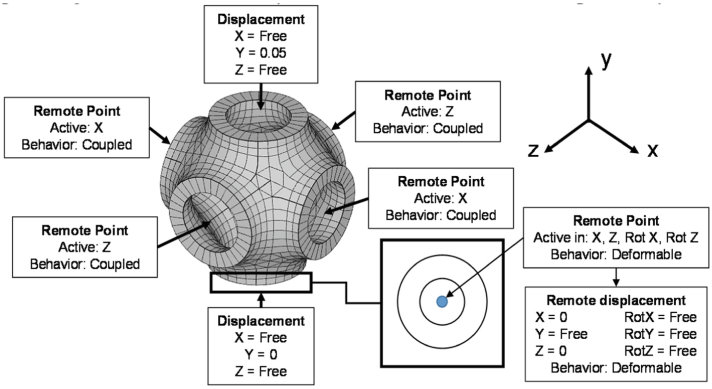
Displacement
X = Free
Y = 0.05
Z = Free
Remote Point
Active: X
Behavior: Coupled
Remote Point
Active: Z
Behavior: Coupled
y
z
x
Remote Point
Active: X
Behavior: Coupled
Remote Point
Active: Z
Behavior: Coupled
Remote Point
Active in: X, Z, Rot X, Rot Z
Behavior: Deformable
Remote displacement
X = 0
RotX = Free
Y = Free
RotY = Free
Z = 0
RotZ = Free
Behavior: Deformable
Displacement
X = Free
Y = 0
Z = Free

Fig. 1. Set of constraints for E and ν determination.

3 Results

Figure 2 shows the deviation map between the subdivided and the implicit minimal surface on a 1 mm unit cell. Subdivided minimal surfaces slightly differ from the ones defined by implicit equations, less than 1.3% of the cell dimension.

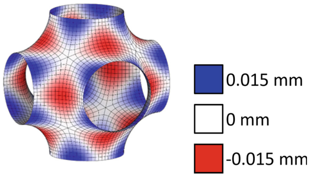

Fig. 2. Deviation map between subdivided and implicit minimal surfaces on a 1 mm P-surface unit cella. Max range: ±0.0127 mm.

Figure 3 shows the results for the elastic modulus E. The ratio between the obtained modulus E and the modulus of the bulk material E_0 is plotted against relative density (ρ). A power law well fits the results (Standard Deviation = 0.0146). The experimental data are also described by a quadratic equation so, as a first approximation, the model can be simplified (Standard Deviation = 0.0301).

In the same graph, a comparison with the results by Bobbert et al. [9] and Lee et al. [20] is presented. Lee's results are close to the ones obtained in this study; the trend found by Bobbert et al., instead, slightly differs but their results were experimentally obtained from compression tests, while the ones of the present study refer to numerical analyses of tensile tests. The proposed numerical model also extends in a wider relative density range, 0.2–0.8, if compared to Bobbert's, 0.3–0.5, and Lee's, 0.02–0.3. Graphs in Fig. 4 show the results for the determination of ν and G.

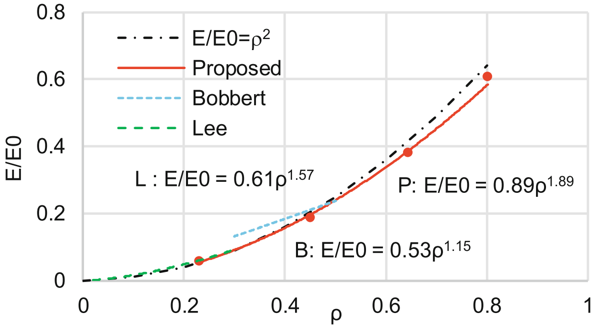

Fig. 3. Elastic modulus simulation results for P-Surface cell, and comparison with the literature.

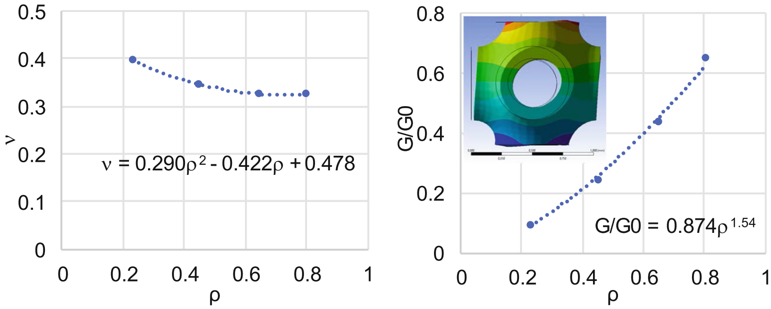

Fig. 4. Poisson's ratio (left) and shear modulus (right) simulation results for P-Surface cell. The figure in the shear plot highlights the effects of the deformable and coupled conditions.

4 Conclusions

In this work, a TPMS P-Surface modeled with a subdivision surface method was geometrically and mechanically characterized, and a model of the mechanical properties as a function of the relative density was obtained. The numerical method that was used only requires a single unit cell resulting in accurate solutions, and reducing computational time, since computational time and cost increase cubically as the number of cells increases.

The results show that Young's and shear modulus increase with relative density. The results for Young's modulus, if compared with data available in the literature, present a good agreement and extend for a wider relative density range.

Mechanical characterization of subdivided TPMS opens new possibilities for the implementation of the topology optimization in the modeling workflow of lattices with variable properties and allows to simulate this type of structures using the homogenization method, reducing time and computational costs.

Acknowledgments. This work was partially funded by Fondazione Cassa Di Risparmio di Padova e Rovigo (CARIPARO) and grant "BIRD 190850" by Department of Civil, Environmental and Architectural Engineering, University of Padova.

References

1. Bacciaglia, A., Ceruti, A., Liverani, A.: Additive manufacturing challenges and future developments in the next ten years, pp. 891–902 (2020). https://doi.org/10.1007/978-3-030-31154-4_76
2. Savio, G., Rosso, S., Meneghello, R., Concheri, G.: Geometric modeling of cellular materials for additive manufacturing in biomedical field: a review. Appl. Bionics Biomech., 1–14 (2018). https://doi.org/10.1155/2018/1654782
3. Tamburrino, F., Graziosi, S., Bordegoni, M.: The design process of additively manufactured mesoscale lattice structures: a review. J. Comput. Inf. Sci. Eng. **18**(4), 1–6 (2018). https://doi.org/10.1115/1.4040131
4. Plocher, J., Panesar, A.: Review on design and structural optimisation in additive manufacturing: towards next-generation lightweight structures. Mater. Des. **183** (2019). https://doi.org/10.1016/j.matdes.2019.108164
5. Lanzotti, A., Martorelli, M., Russo, T., Gloria, A.: Design of additively manufactured lattice structures for tissue regeneration. Mater. Sci. Forum MSF **941**, 2154–2159 (2018). https://doi.org/10.4028/www.scientific.net/MSF.941.2154
6. Paolini, A., Kollmannsberger, S., Rank, E.: Additive manufacturing in construction: a review on processes, applications, and digital planning methods. Addit. Manuf. **30**(July), 100894 (2019). https://doi.org/10.1016/j.addma.2019.100894
7. Lord, E.A., Mackay, A.L.: Periodic minimal surfaces of cubic symmetry. Curr. Sci. **85**(3), 346–362 (2003)
8. Schoen, A.H.: Infinite periodic minimal surfaces without self-intersections (1970)
9. Bobbert, F.S.L., et al.: Additively manufactured metallic porous biomaterials based on minimal surfaces: a unique combination of topological, mechanical, and mass transport properties. Acta Biomater. **53**, 572–584 (2017). https://doi.org/10.1016/j.actbio.2017.02.024

10. Kapfer, S.C., Hyde, S.T., Mecke, K., Arns, C.H., Schröder-Turk, G.E.: Minimal surface scaffold designs for tissue engineering. Biomaterials **32**(29), 6875–6882 (2011). https://doi.org/10.1016/J.BIOMATERIALS.2011.06.012
11. Ambu, R., Morabito, A.E.: Modeling, assessment, and design of porous cells based on schwartz primitive surface for bone scaffolds. Sci. World J. **2019** (2019). https://doi.org/10.1155/2019/7060847
12. Speirs, M., Van Hooreweder, B., Van Humbeeck, J., Kruth, J.-P.: Fatigue behaviour of NiTi shape memory alloy scaffolds produced by SLM, a unit cell design comparison. J. Mech. Behav. Biomed. Mater. **70**, 53–59 (2017). https://doi.org/10.1016/j.jmbbm.2017.01.016
13. Savio, G., Meneghello, R., Concheri, G.: Design of variable thickness triply periodic surfaces for additive manufacturing. Prog. Addit. Manuf. **4**(3), 281–290 (2019). https://doi.org/10.1007/s40964-019-00073-x
14. Feng, J., Fu, J., Lin, Z., Shang, C., Li, B.: A review of the design methods of complex topology structures for 3D printing. Vis. Comput. Ind. Biomed. Art **1**(1), 5 (2018). https://doi.org/10.1186/s42492-018-0004-3
15. Pasko, A., Fryazinov, O., Vilbrandt, T., Fayolle, P., Adzhiev, V.: Procedural function-based modelling of volumetric microstructures. Graph. Models **73**(5), 165–181 (2011). https://doi.org/10.1016/j.gmod.2011.03.001
16. Savio, G., Curtarello, A., Rosso, S., Meneghello, R., Concheri, G.: Homogenization driven design of lightweight structures for additive manufacturing. Int. J. Interact. Des. Manuf. (2019). https://doi.org/10.1007/s12008-019-00543-0
17. Savio, G.: Rhino Open Projects. https://www.food4rhino.com/app/rhino-open-projects. Accessed 06 Feb 2020
18. Savio, G., Meneghello, R., Concheri, G.: Optical properties of spectacle lenses computed by surfaces differential quantities. Adv. Sci. Lett. **19**(2), 595–600 (2013). https://doi.org/10.1166/asl.2013.4724
19. AZoM, Grade 23 Ti 6Al 4V ELI Alloy (UNS R56401). AZO Materials (2013). https://www.azom.com/article.aspx?ArticleID=9365. Accessed 07 Feb 2020
20. Lee, D.-W., Khan, K.A., Abu Al-Rub, R.K.: Stiffness and yield strength of architectured foams based on the Schwarz Primitive triply periodic minimal surface. Int. J. Plast. **95**, 1–20 (2017). https://doi.org/10.1016/J.IJPLAS.2017.03.005

Open Access This chapter is licensed under the terms of the Creative Commons Attribution 4.0 International License (http://creativecommons.org/licenses/by/4.0/), which permits use, sharing, adaptation, distribution and reproduction in any medium or format, as long as you give appropriate credit to the original author(s) and the source, provide a link to the Creative Commons license and indicate if changes were made.

The images or other third party material in this chapter are included in the chapter's Creative Commons license, unless indicated otherwise in a credit line to the material. If material is not included in the chapter's Creative Commons license and your intended use is not permitted by statutory regulation or exceeds the permitted use, you will need to obtain permission directly from the copyright holder.

applied sciences

Article

An Optimization Workflow in Design for Additive Manufacturing

Stefano Rosso [1,*], Federico Uriati [2], Luca Grigolato [3,4], Roberto Meneghello [1], Gianmaria Concheri [4] and Gianpaolo Savio [4]

[1] Department of Management and Engineering, University of Padova, Stradella S. Nicola, 3, 36100 Vicenza, Italy; roberto.meneghello@unipd.it
[2] Department of Engineering and Architecture, University of Parma, Parco Area delle Scienza, 181/A, 43124 Parma, Italy; federico.uriati@unipr.it
[3] Department of Industrial Engineering, University of Padova, Via Gradenigo, 6/a, 35131 Padova, Italy; luca.grigolato@phd.unipd.it
[4] Department of Civil, Environmental, and Architectural Engineering, University of Padova, Via Venezia, 1, 35131 Padova, Italy; gianmaria.concheri@unipd.it (G.C.); gianpaolo.savio@unipd.it (G.S.)
* Correspondence: stefano.rosso.3@phd.unipd.it

Abstract: Additive Manufacturing (AM) brought a revolution in parts design and production. It enables the possibility to obtain objects with complex geometries and to exploit structural optimization algorithms. Nevertheless, AM is far from being a mature technology and advances are still needed from different perspectives. Among these, the literature highlights the need of improving the frameworks that describe the design process and taking full advantage of the possibilities offered by AM. This work aims to propose a workflow for AM guiding the designer during the embodiment design phase, from the engineering requirements to the production of the final part. The main aspects are the optimization of the dimensions and the topology of the parts, to take into consideration functional and manufacturing requirements, and to validate the geometric model by computer-aided engineering software. Moreover, a case study dealing with the redesign of a piston rod is presented, in which the proposed workflow is adopted. Results show the effectiveness of the workflow when applied to cases in which structural optimization could bring an advantage in the design of a part and the pros and cons of the choices made during the design phases were highlighted.

Keywords: DfAM; design for additive manufacturing; size optimization; topology optimization; design workflow; computational geometry; geometric modeling

check for updates

Citation: Rosso, S.; Uriati, F.; Grigolato, L.; Meneghello, R.; Concheri, G.; Savio, G. An Optimization Workflow in Design for Additive Manufacturing. *Appl. Sci.* **2021**, *11*, 2572. https://doi.org/10.3390/app11062572

Academic Editor: Marco Mandolini

Received: 22 February 2021
Accepted: 11 March 2021
Published: 13 March 2021

Publisher's Note: MDPI stays neutral with regard to jurisdictional claims in published maps and institutional affiliations.

Copyright: © 2021 by the authors. Licensee MDPI, Basel, Switzerland. This article is an open access article distributed under the terms and conditions of the Creative Commons Attribution (CC BY) license (https://creativecommons.org/licenses/by/4.0/).

1. Introduction

From the works of the early pioneers, additive manufacturing (AM) technologies were characterized by great growth in the last 35 years [1]. According to ISO/ASTM standards "AM is the general term for those technologies that, based on a geometrical representation, create physical objects by successive addition of material" [2]. Depending on the method of layer manufacturing, it is possible to organize the AM technologies in the following categories: vat photopolymerization, material jetting, binder jetting, powder bed fusion, material extrusion, directed energy deposition, and sheet lamination [2].

This technology brings new opportunities especially in design freedom, allowing very complex shapes, integrating cinematics and multi-material parts, reducing the number of components through part consolidation, and increasing mass customization. On the other hand, to fully exploit the AM technologies' potential, many needs in different sub-fields were highlighted [1,3–8], as summarized in Figure 1. For example, a highly skilled workforce is required, file formats for exchanging the data related to the AM workflow need enhancements [8,9], and design methods and tools for complex structures, multi-material parts, and functionally graded materials need to be improved [10,11]. The concerns over the structural integrity of these complex parts require static and dynamic mechanical characterization [12,13]; also, experimental tests help to mechanically characterize the materials, and the obtained information is used in numerical simulations to predict the different mechanical behavior between the products obtained through additive manufacturing and the ones obtained by traditional techniques of material subtraction [14,15]. More, dedicated qualification standards for AM are needed to guarantee an adequate quality of the printed parts [16,17] and their representation in 2D drawings [18].

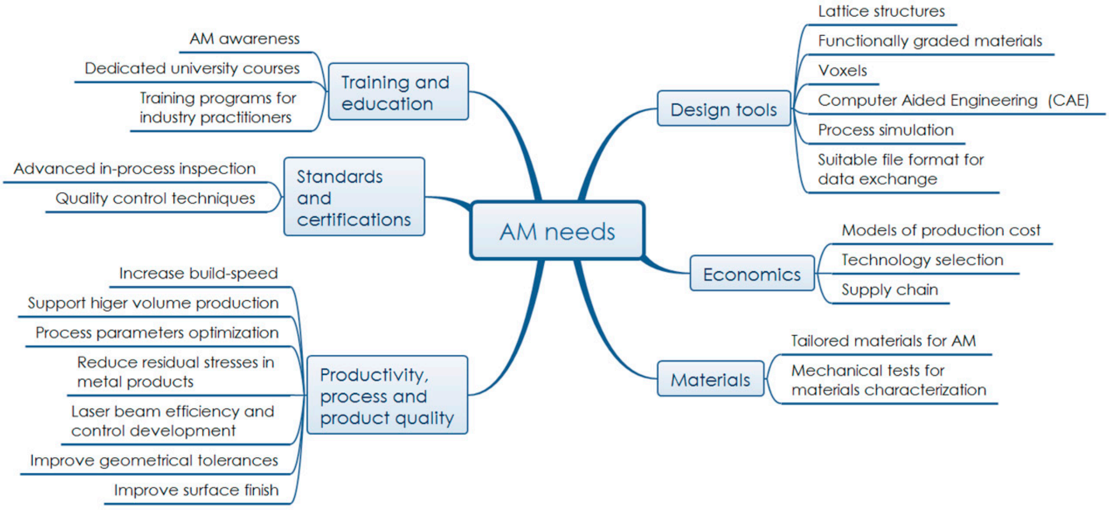
AM needs
Training and education
AM awareness
Dedicated university courses
Training programs for industry practitioners
Standards and certifications
Advanced in-process inspection
Quality control techniques
Productivity, process and product quality
Increase build-speed
Support higer volume production
Process parameters optimization
Reduce residual stresses in metal products
Laser beam efficiency and control development
Improve geometrical tolerances
Improve surface finish
Design tools
Lattice structures
Functionally graded materials
Voxels
Computer Aided Engineering (CAE)
Process simulation
Suitable file format for data exchange
Economics
Models of production cost
Technology selection
Supply chain
Materials
Tailored materials for AM
Mechanical tests for materials characterization

Figure 1. Additive Manufacturing needs.

In a recent work, *The Economist* claims that the value of AM products will no longer be in the physical item, but in its design [19]. These reflections lead to a reconsideration of the design approaches for AM. According to Ullman [20], the design process can be divided into six major phases: product discovery, project planning, product definition, conceptual design, product development, and product support. During the conceptual design phase, several concepts are generated and evaluated; however, the knowledge of the concepts is limited and the goal in this phase is to select the best alternatives with the least expenditure of time and other resources. In the product development phase, instead, once the product is generated, it is fundamental to compare its performance to the engineering specifications. This is done both with virtual simulations and physical prototypes, often resulting in a time-consuming iterative process due to part modifications and redesigns. A different approach that exploits the higher computational capabilities available nowadays is the computational design synthesis [21], where the tasks needed to obtain a solution are divided into four main steps: "representation" deals with the creation of a mental model of the object, "generation" deals with the object creation, "evaluation" verifies if the constraints and design goals are met, and "guidance" gives a feedback for the design improvements [22]. The last three phases are iteratively repeated until a final design is obtained. In design synthesis, optimization is performed in the representation and generation phases, where the design has not a specific topology yet. Usually, stochastic methods are applied to obtain different designs that satisfy the requirements [23].

Furthermore, when designing parts that are going to be produced by AM technologies, several thoughts must be considered to "maximize product performance through the synthesis of shapes, sizes, hierarchical structures, and material compositions, subject to the capabilities of AM technologies" [24]. All these considerations can be grouped within the Design for Additive Manufacturing (DfAM) concept. Gibson et al. [24] distinguished between opportunistic and restrictive DfAM; the former allows to take advantages of the unique capabilities of AM, such as cellular solids, part consolidation, and multi-material, whereas the latter focuses on the restrictions and limitations of the AM technologies, such as the minimum feature size and the need of support structures. Rosen [25] used a Process–Structure–Property–Behavior framework to describe and model a design and proposed a DfAM system organized in several modules dealing with the modeling, manufacturing simulation, and design behavior analysis phases. Ponche et al. [26] presented a DfAM methodology that takes into account the design requirements and the manufacturing specificities, adopting a redesign strategy based on the functional surface approach; they concentrated on metallic components produced by Additive Laser Manufacturing. Vayre et al. [27] applied a four-step designing methodology consisting of initial shape generation, set of geometrical parameter definition, shape optimization through the tuning of the parameters, and final validation of a metallic part produced by direct metal deposition and electron beam melting AM technologies. Briard et al. [28] presented a four-step methodology to maximize the potential of generative design coupled with DfAM; the first phase deals with the translation of the problem to a suitable input for generative design, whereas the following three phases deal with an unconstrained iterative optimization, an iterative optimization driven by the AM guidelines, and a final iterative optimization refining the part including AM-enabled structures, such as lattices. Duro-Royo et al. [29] presented a computational workflow for the design and the fabrication of multi-material and multi-scale structured objects; they focused on water-based heterogeneous materials based on polysaccharide hydrogels in 1% to 12% concentrations in *w/v* of 1% acetic acid aqueous solutions and these gels were also mixed with cellulose microfiber to obtain volumetric composites. They created a model that considers the input data, like materials and geometry, and calculates all the instructions for the object fabrication via a pneumatic extruder mounted on a six-axes robotic arm. Boddeti et al. [30] presented a digital design and manufacturing workflow able to design both the macroscopic topology and the microstructure of an object; the workflow is divided into three steps: a design automation process that optimizes the material distribution and its microstructure, a material compilation process that creates a material layout and generates the code for fabrication, and a digital fabrication step with multi-material photopolymer material jetting technology. Zhang et al. [31] proposed an evaluation framework to assess the design from the perspective of process planning for AM; two sets of indicators were used to check whether the part is suitable to be produced by AM manufacturing and to verify the design's utilization of the characteristics of an AM process. Similarly, Lettori et al. [32] proposed an approach to assess the compatibility and suitability of a product for the AM production through a set of reference questions and a compliance index; then, they validated the method with case studies found in the literature. Motyl and Filippi [33] reviewed the scientific literature to explore the relationship between AM processes and product design, concentrating on the conceptual design phase and the theory of inventive problem solving (TRIZ) [34]; some of the analyzed works use the TRIZ for the definition of the DfAM guidelines.

Nonetheless, the literature highlights the lack of exhaustive frameworks that describe the design process and take full advantage of the possibilities offered by AM. Seepersad [35] stated that advances are still needed to couple computer-aided design (CAD) software and computer-aided engineering (CAE) tools to incorporate the DfAM knowledge into the design process. Kumke et al. [36] highlighted some limitations on the existing DfAM frameworks too: they do not cover the entire design process steps, they focus on the utilization of a single AM potential, and they are often too specific for a single case study.

In this contribution, a heuristic design workflow for AM is proposed aimed at exploiting the new possibilities offered by AM technologies and the high computational resources available nowadays. The workflow focuses on the product design phase, also referred to as embodiment design [20,37], where the design is developed up to the production. It specifically concentrates on cases in which mechanical performances are required, together with a reduction of the weight of the parts. Different geometric modeling opportunities and structural optimization techniques are presented: commercial software is used to perform the topology optimization and the redesign of the optimized results. As an alternative, a method developed by the research group designs conformal lattice structures with size optimization performed on the beams and allows to automatically obtain a smooth mesh model. The proposed workflow is then validated on a test case, adopting different design methods based on lattice structures, PolyNurbs, and parametric CAD to reach innovative solutions.

2. Design Workflow

The proposed workflow helps the designer during the product development process of AM components, guiding him throughout decisions that allow to fully exploit AM potential. AM-related engineering requirements and technological constraints are considered in the first phases of the workflow and simulation tools are used to optimize and validate the geometric model. In particular, the workflow can be adopted during the embodiment design phase of parts in which the mechanical performance needs to be maximized and the weight needs to be as low as possible. Structural optimization approaches such as size and topology optimization perfectly suit this scenario.

Figure 2 shows the proposed design workflow for AM. First, the design space is identified. The design space is a volume where the material distribution is going to be optimized; it can be obtained from an existing model or it can be specifically designed considering the maximum allowable size of the component. Then, two paths can be followed: the first one performs a topology optimization on the entire design space, whereas the second one performs a size optimization on a lattice structure. Regardless of the selected approach, a finite element (FE) model is created taking into consideration not only the "usual" boundary conditions such as the material, the loads, and the constraints but also the constraints and conditions strictly related to the design for AM. For instance, the technological constraints could include a limit for the inclination of the structure to avoid overhang angles (if required by the manufacturing technology) and the upper and lower limits for the most critical features, i.e., hole size, strut dimension, wall thickness, etc. Furthermore, since AM allows the production of complex geometrical shapes, it is easier to create parts resulting from multi-objective optimization; the optimization goals like targeted mass and natural frequencies, or desired heat exchanging properties can be considered as engineering requirements. Including this information in the first part of the workflow enables to obtain a design with the desired functionalities that is likely to be produced without the need of stepping back to the product development phase.

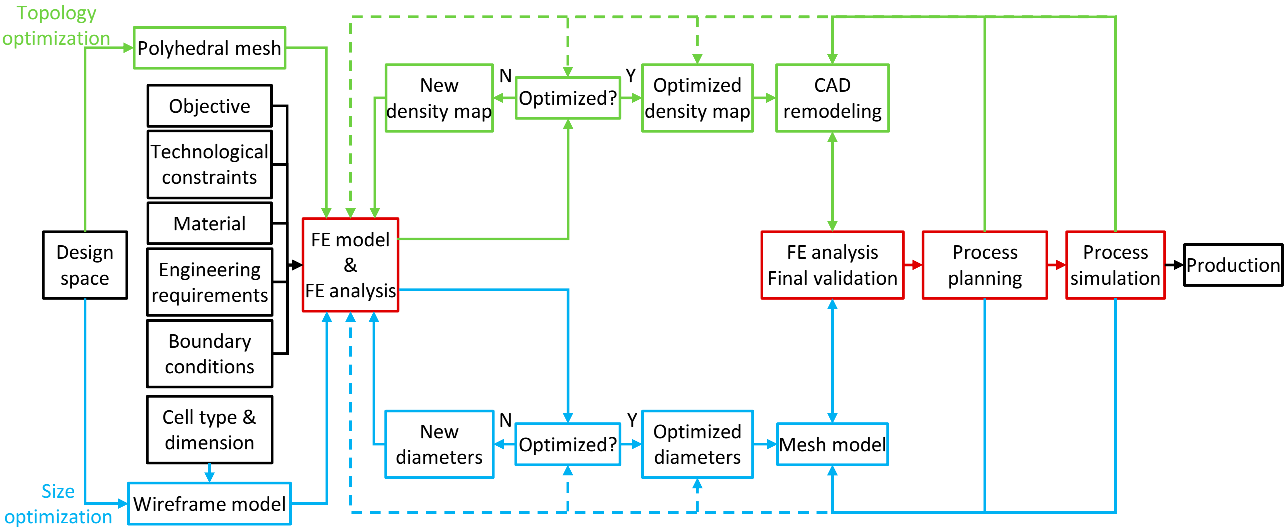
Topology optimization
Polyhedral mesh
Objective
Technological constraints
Material
Engineering requirements
Boundary conditions
Cell type & dimension
Design space
Size optimization
Wireframe model
FE model & FE analysis
New density map
N
Optimized?
Y
Optimized density map
CAD remodeling
FE analysis Final validation
Process planning
Process simulation
Production
New diameters
N
Optimized?
Y
Optimized diameters
Mesh model

Figure 2. The proposed design workflow for additive manufacturing. Black blocks: steps related to the boundary conditions; green blocks: steps related to the topology optimization; blue blocks: steps related to the size optimization; red blocks: steps related to computer-aided engineering (CAE) simulation software.

If the topology optimization approach is chosen, the design space is discretized and a polyhedral mesh is obtained; then, the topology optimization is performed. During this process, the material is arranged inside the design space to find the best distribution of material under a set of boundary conditions and respecting the structural and dimensional performance requirements. According to the literature, several topology optimization algorithms can be used [38]. Homogenization methods use the mathematical theory of homogenization [39,40] to study a complex domain previously divided into microstructures, i.e., the finite elements, as a continuum domain made up of a virtual material called effective material [41]. Density methods consider the density as the only design variable for each finite element, and the variable can assume a value between 0 and 1; since the optimal solutions would consist of elements with values mostly between 0 and 1, the results would be far from a solid (1)–void (0) situation. The most popular numerical method for suppressing intermediate densities is the Solid Isotropic Microstructure with Penalization (SIMP) method, proposed by Bendsoe [42], which penalizes elements with intermediate densities exploiting a power law. To avoid intermediate densities in the optimized solution, discrete methods, also called “hard-kill” methods, can be used; in the Evolutionary Structural Optimization (ESO) method proposed by Xie and Steven [43], a criterion parameter is calculated for each element and at each iteration the elements with the lowest criterion parameter value are eliminated. Furthermore, Bi-directional Evolutionary Structural Optimization (BESO) method [44] is an extension of ESO, in which new elements can be added next to those elements with a high criterion parameter at each iteration. Level-set Methods (LSMs) are another category of topology optimization methods where the iso-contours of a level-set function implicitly define the interface between the material phases [45,46]; this approach allows to obtain a sharp transition between void and solid regions. In the proposed workflow, a SIMP density method is adopted because this method requires relatively few iterations, is suitable for a combination of a wide range of design constraints, multiple load conditions, multi-physics problems, and extremely large (often 3D) systems, is extensively used in industrial software [38], and can be easily implemented with a simple code [47,48]. As a result of the SIMP method, a density map is obtained, which is contoured to a specific level of density (threshold), obtaining a mesh surface. Often, the resulting mesh cannot be directly used for the production phase due to the lack of connection zones or the presence of coarse regions due to the process discretization. The remodeling of the topology optimization mesh is a research topic of interest, indeed. Zegard and Paulino [49] presented a tool that generates suitable outputs for AM by using filters and the continuation approach on the penalization parameter; Jiu et al. [50] proposed a CAD-oriented topology optimization method able to perform the optimization directly on the CAD model instead of on the mesh. Most of the time the procedure is operated manually, and the part is modeled in a CAD environment using the mesh as guideline during the modeling. Alternatively, software tools for automatic remodeling are available; these mainly adopt quad-remesh and subdivision surface approaches.

If the size optimization approach is followed, given a cell type and the unit cell dimension, a wireframe model is obtained filling the design space with a conformal lattice structure. In a conformal structure, the unit cell can deform to adapt to the boundary of the part or the lines of the stress field; this feature eliminates weakness at boundaries and provides stiffness and resistance to the entire model [51]. The size optimization is then performed on the wireframe [52,53]. The diameter of the beams iteratively varies until all the beams reach the target utilization, defined as the ratio between the maximum Von Mises stress measured on the beam and the admissible stress; as previously highlighted, the size of the beam is controlled to ensure that the beam diameter is thick enough to be manufactured and that it does not exceed the upper bound to avoid interferences with the surrounding beams. The optimized wireframe is then modeled with a boundary representation mesh-based approach as proposed by Savio et al. [54]. The obtained coarse mesh is then smoothed adopting the Catmull–Clark subdivision surface algorithm [55]: each quad face is subdivided into four smaller quad faces at every iteration. The algorithm produces a surface with continuity in curvature (C2 surface), except at extraordinary vertices where they are C1. This allows to reduce stress concentration, especially at nodal points, enhancing the mechanical properties and the fatigue life of the lattice [56–58].

Alternatively, it is possible to combine topology and size optimization. The literature shows how the density map of the topology optimization can be used to assign an optimized dimension to the diameter of a beam-like lattice structure [59,60] and to the thickness of a shell-like lattice structure [61].

Once the optimized part is modeled, it is necessary to perform an additional FE analysis to mechanically validate the final model. This step is mandatory in topology optimization because during the modeling phase weak zones could arise, especially if manual remodeling is adopted. After that, process-related considerations are done. Process planning deals with all the necessary operations needed once the AM production technology and machine have been selected. The orientation of the part inside the manufacturing machine, the generation of the supports (if needed), and the generation of the print path strategy affect the quality of the printed part, i.e., the surface texture and the mechanical properties [26], the material and energy consumption, and the production time [62–64]. Then, process simulation helps to predict residual stress and geometric distortion of the printed parts, avoiding time-consuming and expensive experimental campaigns based on trial and error. The evaluation of residual stresses and thermal distortions allows compensating the geometrical CAD model obtaining parts with the desired dimensional specifications and mechanical properties, reducing the probability of defects that lead to crack initiation, propagation, and failure both during the printing and the utilization of the product, especially when dealing with metallic components [65]. Process simulation methods that concentrate not only on metals AM techniques [66–69] but also on material extrusion [70,71] and powder bed fusion [72,73] of polymers can be found. If the FE analysis fails to validate the component or if the manufacturing process simulation highlights dimensional deformation and residual stresses higher than requirements, it is necessary to remodel the part or to step back to the optimization phase, changing the boundary conditions of the model.

When all these steps are successfully completed, the part is ready to be produced. The component is optimized for the intended use and it is likely to not encounter manufacturing issues during the printing phase. An important consideration is whether to use the topology optimization or the size optimization approach. One option could be to apply both and compare the solutions, choosing the one that best suits the application, but it is computationally demanding. Some a priori thoughts can help to decide as well. If the part is metallic, the struts of the lattice could act as internal supports, heat dissipators, and prevent thermal warping. Furthermore, being less bulky, the lattice structure could present lower residual stress. The mechanical validation of a lattice structure requires high computational resources and it is time consuming due to the high number of 3D elements needed to mesh the structure; at the same time, while the FE validation analysis is mandatory for the topology optimized part because the manual remodeling phase can introduce weak areas, it is less necessary for the lattice structure model because the diameters of the beams were previously optimized through a FE analysis and in the presented mesh modeling approach the optimized value is adopted at the middle of the beam, whereas the diameter tends to increase towards the nodal points.

3. Case Study

The proposed workflow was applied to the remodeling of a piston rod. Reducing the weight of a piston rod while maintaining the mechanical performance is an important goal, especially in competitions in the automotive fields, but also in the industry where weight reduction leads to less inertia and to a reduction of energy consumption.

The part is currently produced with a pressure die-casting process and is intended to be produced with the Selective Laser Melting (SLM) powder bed fusion AM technology. The material is an aluminum AlSi10Mg with properties as in Table 1.

Table 1. Aluminum AlSi10Mg properties.

Density	2700 kg/m^3
Young modulus	68 GPa
Yield strength	190 MPa
Ultimate tensile strength	335 MPa
Poisson Ratio	0.30

Overall dimensions, loads, and constraints applied to the piston rod are shown in Figure 3a,b, respectively. The loads and constraints are summarized in Table 2.

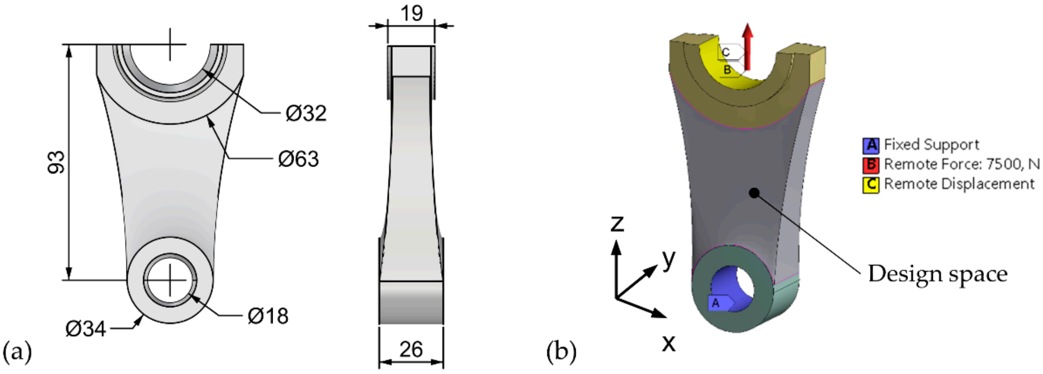

Figure 3. Piston rod: (**a**) overall dimension, (**b**) boundary conditions and design space.

Table 2. Load and constraints applied to the piston rod.

Load	7.5 kN axial traction along z-axis. Applies to big rod's end face.
Constraints	All the displacements and rotations locked. Applies to inner face of the small rod's end. Displacements along x- and y-directions locked. Applies to big rod's end face.

The topology optimization of the design space was performed in SolidWorks 2019 (Dassault Systèmes) using the SolidWorks Simulation module; the software adopts the SIMP method for solving the optimization problem. The "best stiffness to weight ratio" goals was set, using the constraint of a final mass equal to 25% of the original part. The symmetry of the final part with respect to the YZ and ZX plane was imposed. Figure 4a shows the mesh resulting from the topology optimization. This mesh was then used as a starting point for the manual remodeling phase, performed in Inspire Studio CAD 3D software (Altair), as in Figure 4b.

The size optimization section of the workflow was performed in Rhinoceros 6 (Robert McNeel & Associates) inside Grasshopper environment. The design space was filled with a conformal wireframe based on the simple cubic unit cell; the number of instances is 10, 4, and 15 along the x-, y-, and z-axis, respectively, and the minimum element size equals 3 mm. The FE beams model was set-up using Karamba3D plugin [74]. The loads and the constraints were directly applied at the nodes of the beams placed at the interface between the design space and the big and small rod's ends; the 7.5 kN load was equally distributed on each node of the upper part of the wireframe, so as the rotation and translation constraints on each node of the lower and upper part of the wireframe. The target utilization ratio was set to (90 ± 1)% with respect to the yield strength. The upper and lower bound for the diameter of the beams were defined as 1.5 mm and 0.5 mm, respectively. Figure 5 shows the conformal wireframe and the utilization ratio of the optimized structure. Some beams do not reach the required utilization ratio; indeed, they present a utilization ratio lower than the target because the optimized diameter was smaller than the minimum allowable size (i.e., 0.5 mm), so, being assigned the 0.5 mm diameter, they are under-utilized.

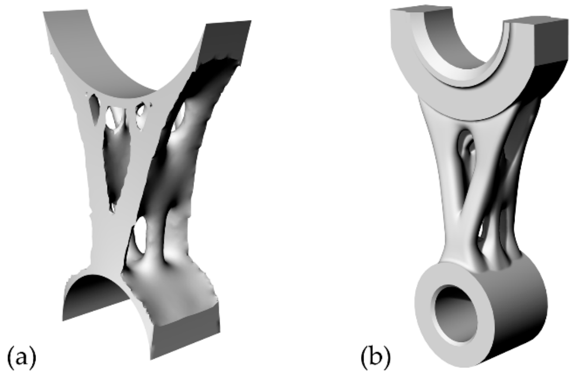

Figure 4. Topology optimization: (**a**) SolidWorks Simulation result (mesh), (**b**) Inspire Studio manual remodeling result (NURBS).

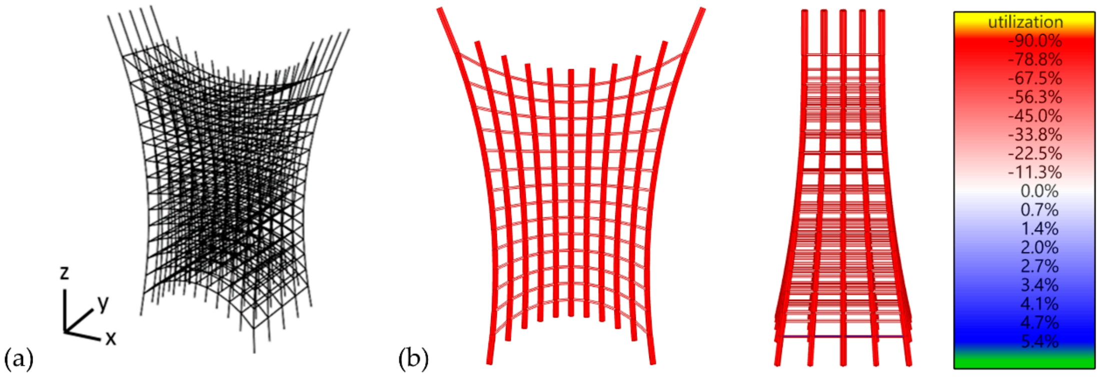

Figure 5. Size optimization: (**a**) wireframe model, (**b**) utilization ratio of the optimized structure (compression is positive).

The lattice structure was then modeled adopting the mesh approach and the Catmull–Clark subdivision surface algorithm. As can be seen in Figure 6, smooth surfaces are obtained, especially at nodal points.

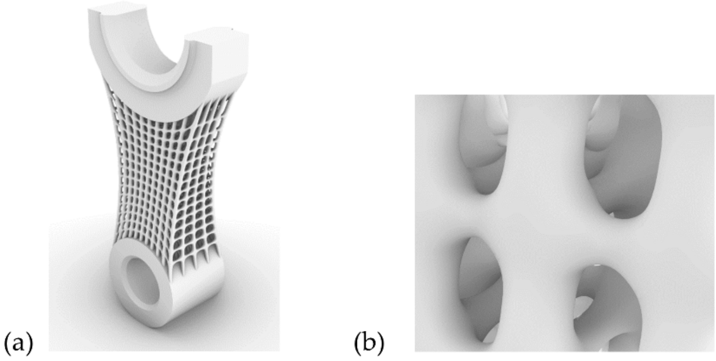

Figure 6. Modeled lattice structure: (**a**) lattice connected to the piston rod's ends, (**b**) detail on the smooth surfaces at nodal points.

Then, the two models obtained from the topology and the size optimization were validated through FE analyses in Ansys Mechanical 2019 R1. The parts were meshed with tetrahedron elements using an element minimum size of 0.1 mm and an element maximum size of 1 mm. The meshing method is patch-independent and includes automatic refinement in curvature and proximity. The symmetry of the topology optimized part with respect to the ZX and YZ plane was exploited to simulate only one quarter of the model. The results are represented in Figure 7. In the size optimized model (Figure 7b), the higher value of stress observed on the legend is related to the absence of fillet between the lattice structure and the body and does not depend on the modeling method of the lattice.

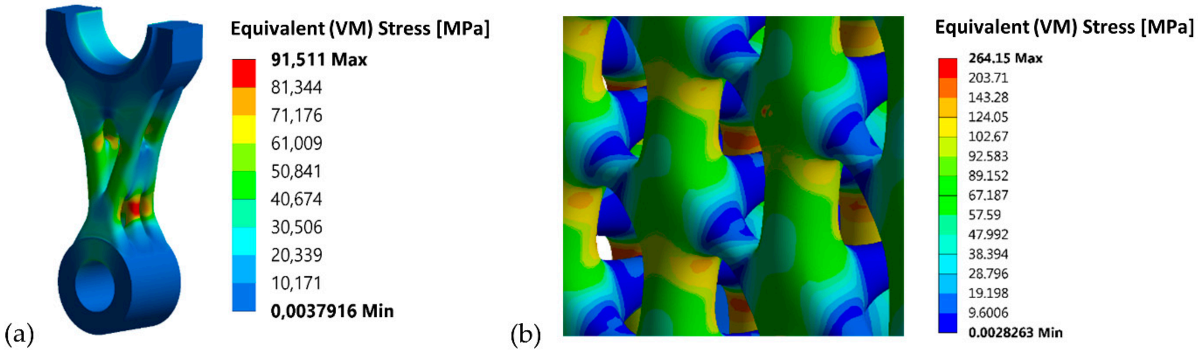
(a)
Equivalent (VM) Stress [MPa]
91,511 Max
81,344
71,176
61,009
50,841
40,674
30,506
20,339
10,171
0,0037916 Min
(b)
Equivalent (VM) Stress [MPa]
264.15 Max
203.71
143.28
124.05
102.67
92.583
89.152
67.187
57.59
47.992
38.394
28.796
19.198
9.6006
0.0028263 Min

Figure 7. FE analyses validation, equivalent Von Mises stress: (**a**) topology optimization, (**b**) size optimization.

Netfabb Premium 2020.3 (Autodesk) was used for preliminary process planning, choosing for the best part orientation. Supports too were created inside the software. The Renishaw AM 400 SLM machine was selected, together with the default material configuration for Aluminum AlSi10Mg-0403 printed with a 25 µm layer thickness, as suggested by the powders manufacturer [75]. First, the topology optimized model was oriented. Among the proposed orientations, three are reported in Figure 8. The final decision is driven by several considerations. The orientation in Figure 8a has the lowest height, resulting in faster printing time, but presents the highest supported area, requiring more time for supports removal and post-process such as sandblasting to avoid the lower quality of the surface finish in the supported areas; the configuration in Figure 8b has the less supported area, but has the highest support volume and height, resulting in a long build time and high material waste; the configuration in Figure 8c has the lower support volume and a relatively low supported area and build time. Moreover, since the configuration in Figure 8a lays on the platform, the circular functional surfaces on the rod's ends will have the best dimensional and geometrical accuracy. Further milling operations could be needed to comply with the requested tolerances.

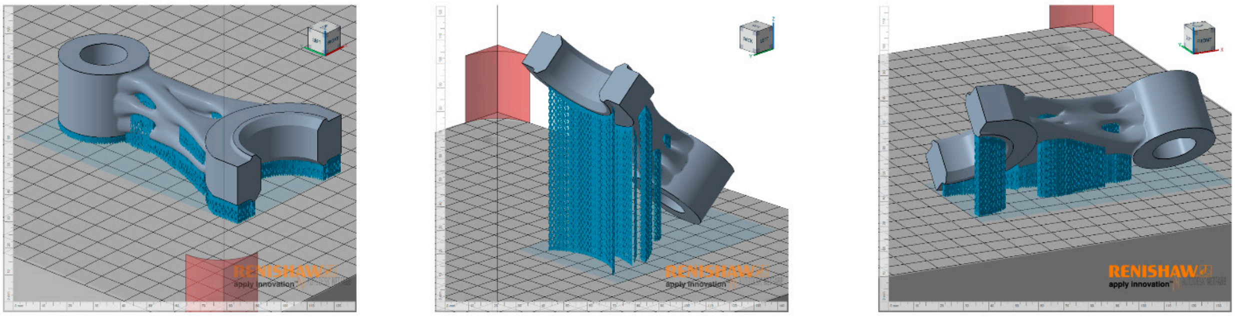
RENISHAW
apply innovation
RENISHAW
apply innovation
RENISHAW
apply innovation

(a)

Supported area	31.89 cm^2
Support Volume	2.66 cm^3
Height	29.00 mm
Build time	11h 14m

(b)

Supported area	8.04 cm^2
Support Volume	3.09 cm^3
Height	94.98 mm
Build time	18h 38m

(c)

Supported area	13.78 cm^2
Support Volume	2.01 cm^3
Height	53.01 mm
Build time	13h 48m

Figure 8. Part orientation and support generation for the topologically optimized piston rod. (**a**–**c**) show three possible orientations.

The same procedure was followed for the orientation of the piston rod with the lattice structure. This time, due to the extreme difficulty of removing the supports between the beams of the lattice, the only orientation that did not present supports in the central part of the model was chosen, as shown in Figure 9.

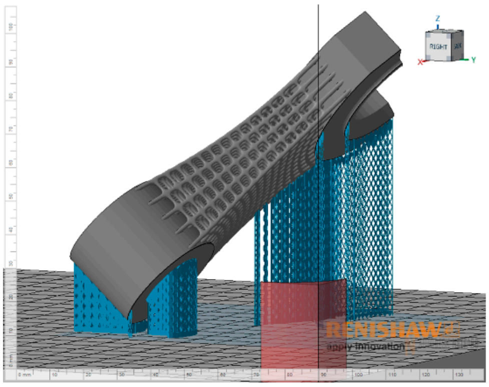

Supported area	6.20 cm^2
Support Volume	1.98 cm^3
Height	95.32 mm
Build time	17h 56m

Figure 9. Part orientation and support generation for the size optimized piston rod.

Finally, the next step would be to perform the process simulation of the oriented part to assess the printability of the models, the geometrical distortions, and the residual stresses. According to the results, the designer can consider geometrically compensating the part, changing the part orientation, or going back to the modeling phase and remodel the part.

The application of the workflow for redesigning the piston rod enabled to obtain two optimized parts and a considerable reduction of the mass, as shown in Table 3. The two methods present some drawbacks too. The topology optimized model requires manual remodeling, and it is more prone to failure during the final FE analysis verification, due to human errors during the remodeling phase. The proposed method for the size optimization is in its prototypal stage and it still has a limited choice of unit cells and does not correctly manage the connection between the lattice structure and the adjacent objects. Numerical analyses on the lattice model are computationally demanding but less necessary since the wireframe was previously optimized and the mesh modeling method does not alter the diameter of the beams.

Table 3. Mass reduction of the optimized models. The mass only considers the design space volume and not the rod's ends, which were not optimized.

Model/Approach	Mass [g]	% of Mass Reduction
Starting design space	104.7	
Topology optimization	29.99	−71%
Size optimization	20.98	−80%

4. Conclusions

In this work, a design workflow for Additive Manufacturing was proposed, trying to overcome the limits highlighted in the literature, where it is stated that the available frameworks do not exploit all the advantages offered by AM and do not cover the entire design process. The presented workflow considers the embodiment design phase, from the definition of a design volume to the production of the part, integrating both CAD tools for the geometric modeling of the part and CAE tools for the optimization and simulation phases; more, it considers the possibility to use the size optimization to obtain lattice structures with optimized beams, and the topology optimization to obtain more organic shapes. The workflow was then applied to the remodeling and optimization of a piston rod in which both commercial and custom tools were adopted, showing its ease and universality of implementation.

As future works, the process simulation will be performed on the oriented parts. Then, a hybrid method that combines size and topology optimization is going to be developed to further expand the workflow possibilities; the 0–1 density parameter will drive the dimension of the beams, shell, or solid elements. The connection between the lattice structures and the adjacent objects will be addressed to obtain smoother links and enhance the mechanical properties of the parts. Moreover, aspects related to hybrid manufacturing technologies will be addressed.

Author Contributions: Conceptualization, S.R., F.U., L.G., G.S., R.M., and G.C.; Formal analysis, S.R., F.U., and L.G.; Funding acquisition, G.S., R.M., and G.C.; Investigation, S.R.; Methodology, S.R., and G.S.; Supervision, G.S., R.M., and G.C.; Writing—original draft, S.R.; Writing—review and editing, S.R., F.U., L.G., G.S., R.M., and G.C. All authors have read and agreed to the published version of the manuscript.

Funding: This research was funded by a Ph.D. grant of Fondazione Cassa di Risparmio di Padova e Rovigo (CARIPARO), by the grant "FSE 2105-37-11-2018: Hybrid manufacturing strategies through selective laser sintering for the customization of series components" by Regione Veneto, and by the grant "BIRD 190850—Design, geometric modeling and analysis of components with functionally graded variation for additive manufacturing technologies" by the Department of Civil, Environmental, and Architectural Engineering, University of Padova, Italy.

Institutional Review Board Statement: Not applicable.

Informed Consent Statement: Not applicable.

Data Availability Statement: The raw/processed data required to reproduce these findings can be partially shared upon request.

Conflicts of Interest: The authors declare no conflict of interest.

References

1. Pei, E. Editorial PIAM October 2019. *Prog. Addit. Manuf.* **2019**, *4*, 355–356. [CrossRef]
2. *ISO/ASTM, ISO/ASTM 52900:2015 (ASTM F2792)—Additive Manufacturing–General Principles—Terminology*; ISO International Organization for Standardization, ASTM American Society for Testing and Materials: Geneva, Switzerland; West Conshohocken, PA, USA, 2015.
3. AM Platform, Additive Manufacturing Strategic Research Agenda. 2014. Available online: https://www.rm-platform.com/linkdoc/AM%20SRA%20-%20February%202014.pdf (accessed on 12 March 2021).
4. SASAM. Additive Manufacturing: SASAM Standardisation Roadmap. 2015. Available online: https://www.rm-platform.com/downloads2/summary/50-strategic-research-agenda/608-sasam-standardisation-roadmap-open-june-2015 (accessed on 12 March 2021).
5. FoFAM. Additive Manufacturing Roadmap: Gaps and Actions on Market Driven Value Chains. 2016. Available online: https://portal.effra.eu/result/show/1080 (accessed on 12 March 2021).
6. America Makes, ANSI, Standardization Roadmap for Additive Manufacturing—Version 1.0. 2017. Available online: https://share.ansi.org/Shared%20Documents/Standards%20Activities/AMSC/AMSC_Roadmap_February_2017.pdf (accessed on 12 March 2021).
7. America Makes, ANSI, Standardization Roadmap for Additive Manufacturing—Version 2.0. 2018. Available online: https://www.americamakes.us/america-makes-ansi-standardization-roadmap-additive-manufacturing-presented-formnext-conference/ (accessed on 12 March 2021).
8. Savio, G.; Meneghello, R.; Rosso, S.; Concheri, G. 3D model representation and data exchange for additive manufacturing. In *Lecture Notes in Mechanical Engineering*; Springer: Cham, Switzerland, 2019; pp. 412–421. [CrossRef]
9. Bacciaglia, A.; Ceruti, A.; Liverani, A. A systematic review of voxelization method in additive manufacturing. *Mech. Ind.* **2019**, *20*, 630. [CrossRef]
10. Grigolato, L.; Rosso, S.; Meneghello, R.; Concheri, G.; Savio, G. Heterogeneous objects representation for Additive Manufacturing: A review. *Instant J. Mech. Eng.* **2019**, 14–23. [CrossRef]
11. Thompson, M.K.; Moroni, G.; Vaneker, T.; Fadel, G.; Campbell, R.I.; Gibson, I.; Bernard, A.; Schulz, J.; Graf, P.; Ahuja, B.; et al. Design for Additive Manufacturing: Trends, opportunities, considerations, and constraints. *CIRP Ann.-Manuf. Technol.* **2016**, *65*, 737–760. [CrossRef]
12. Benedetti, M.; du Plessis, A.; Ritchie, R.; Dallago, M.; Razavi, S.; Berto, F. Architected cellular materials: A review on their mechanical properties towards fatigue-tolerant design and fabrication. *Mater. Sci. Eng. R Rep.* **2021**, *144*, 100606. [CrossRef]

13. Raghavendra, S.; Molinari, A.; Dallago, M.; Zappini, G.; Zanini, F.; Carmignato, S.; Benedetti, M. Uniaxial static mechanical properties of regular, irregular and random additively manufactured cellular materials: Nominal vs. real geometry. *Forces Mech.* **2021**, *2*, 100007. [CrossRef]
14. Calignano, F.; Lorusso, M.; Roppolo, I.; Minetola, P. Investigation of the Mechanical Properties of a Carbon Fibre-Reinforced Nylon Filament for 3D Printing. *Machines* **2020**, *8*, 52. [CrossRef]
15. Allevi, G.; Capponi, L.; Castellini, P.; Chiariotti, P.; Docchio, F.; Freni, F.; Marsili, R.; Martarelli, M.; Montanini, R.; Pasinetti, S.; et al. Investigating Additive Manufactured Lattice Structures: A Multi-Instrument Approach. *IEEE Trans. Instrum. Meas.* **2020**, *69*, 2459–2467. [CrossRef]
16. Bourell, D.L.; Rosen, D.W.; Leu, M.C. The roadmap for additive manufacturing and its impact. *3D Print. Addit. Manuf.* **2014**, *1*, 6–9. [CrossRef]
17. Seifi, M.; Gorelik, M.; Waller, J.; Hrabe, N.; Shamsaei, N.; Daniewicz, S.; Lewandowski, J.J. Progress Towards Metal Additive Manufacturing Standardization to Support Qualification and Certification. *JOM* **2017**, *69*, 439–455. [CrossRef]
18. Bacciaglia, A.; Ceruti, A.; Liverani, A. Proposal of a standard for 2D representation of bio-inspired lightweight lattice structures in drawings. *Proc. Inst. Mech. Eng. Part C J. Mech. Eng. Sci.* **2020**, 095440622095159. [CrossRef]
19. The Economist Intelligence Unit. *Adding It Up: The Economic Impact of Additive Manufacturing*; Agency for Science, Technology and Research (A* STAR): Singapore, 2018; 24p.
20. Ullman, D.G. *The Mechanical Design Process*, 4th ed.; McGraw-Hill: New York, NY, USA, 2010. [CrossRef]
21. Chakrabarti, A. *Engineering Design Synthesis: Understanding, Approaches, and Tools*; Springer: London, UK, 2002.
22. Cagan, J.; Campbell, M.I.; Finger, S.; Tomiyama, T. A Framework for Computational Design Synthesis: Model and Applications. *J. Comput. Inf. Sci. Eng.* **2005**, *5*, 171. [CrossRef]
23. Shea, K.; Cagan, J. Innovative dome design: Applying geodesic patterns with shape annealing. *Artif. Intell. Eng. Des. Anal. Manuf.* **1997**, *11*, 379. [CrossRef]
24. Gibson, I.; Rosen, D.; Stucker, B.; Khorasani, M. *Additive Manufacturing Technologies*; Springer International Publishing: Cham, Switzerland, 2021. [CrossRef]
25. Rosen, D.W. Computer-Aided Design for Additive Manufacturing of Cellular Structures. *Comput. Aided Des. Appl.* **2007**, *4*, 585–594. [CrossRef]
26. Ponche, R.; Kerbrat, O.; Mognol, P.; Hascoet, J.Y. A novel methodology of design for Additive Manufacturing applied to Additive Laser Manufacturing process. *Robot. Comput. Integr. Manuf.* **2014**, *30*, 389–398. [CrossRef]
27. Vayre, B.; Vignat, F.; Villeneuve, F. Designing for Additive Manufacturing. *Procedia CIRP* **2012**, 632–637. [CrossRef]
28. Briard, T.; Segonds, F.; Zamariola, N. G-DfAM: A methodological proposal of generative design for additive manufacturing in the automotive industry. *Int. J. Interact. Des. Manuf.* **2020**, *14*, 875–886. [CrossRef]
29. Duro-Royo, J.; Mogas-Soldevila, L.; Oxman, N. Flow-based fabrication: An integrated computational workflow for design and digital additive manufacturing of multifunctional heterogeneously structured objects. *Comput. Des.* **2015**, *69*, 143–154. [CrossRef]
30. Boddeti, N.; Ding, Z.; Kaijima, S.; Maute, K.; Dunn, M.L. Simultaneous Digital Design and Additive Manufacture of Structures and Materials. *Sci. Rep.* **2018**, *8*, 15560. [CrossRef]
31. Zhang, Y.; Bernard, A.; Gupta, R.K.; Harik, R. Evaluating the design for additive manufacturing: A process planning perspective. *Procedia CIRP* **2014**, *21*, 144–150. [CrossRef]
32. Lettori, J.; Raffaeli, R.; Peruzzini, M.; Schmidt, J.; Pellicciari, M. Additive manufacturing adoption in product design: An overview from literature and industry. *Procedia Manuf.* **2020**, *51*, 655–662. [CrossRef]
33. Motyl, B.; Filippi, S. Investigating the Relationships between Additive Manufacturing and TRIZ: Trends and Perspectives. In *Lecture Notes in Mechanical Engineering*; Springer: Cham, Switzerland, 2019; pp. 903–911. [CrossRef]
34. Altshuller, G. And Suddenly the Inventor Appeared: TRIZ, the Theory of Inventive Problem Solving, Worcester. 1996. Available online: http://books.google.com/books?hl=en&lr=&id=s7Qk_6WELWUC&oi=fnd&pg=PA1&dq=And+Suddenly+the+Inventor+Appeared&ots=2Fc3TJGicr&sig=b5C0LEyulNyiMQVfz-cOx0FPdrU (accessed on 19 November 2020).
35. Seepersad, C.C. Challenges and Opportunities in Design for Additive Manufacturing. *3D Print. Addit. Manuf.* **2014**, *1*, 10–13. [CrossRef]
36. Kumke, M.; Watschke, H.; Vietor, T. A new methodological framework for design for additive manufacturing. *Virtual Phys. Prototyp.* **2016**, *11*, 3–19. [CrossRef]
37. Pahl, G.; Beitz, W.; Feldhusen, J.; Grote, K.-H. *Engineering Design: A Systematic Approach*; Springer: London, UK, 2007. [CrossRef]
38. Rozvany, G.I.N. A critical review of established methods of structural topology optimization. *Struct. Multidiscip. Optim.* **2009**, *37*, 217–237. [CrossRef]
39. Bendsøe, M.P.; Kikuchi, N. Generating optimal topologies in structural design using a homogenization method. *Comput. Methods Appl. Mech. Eng.* **1988**, *71*, 197–224. [CrossRef]
40. Hassani, B.; Hinton, E. *Homogenization and Structural Topology Optimization*; Springer: London, UK, 1999. [CrossRef]
41. Savio, G.; Curtarello, A.; Rosso, S.; Meneghello, R.; Concheri, G. Homogenization driven design of lightweight structures for additive manufacturing. *Int. J. Interact. Des. Manuf.* **2019**. [CrossRef]
42. Bendsøe, M.P. Optimal shape design as a material distribution problem. *Struct. Optim.* **1989**, *1*, 193–202. [CrossRef]
43. Xie, Y.; Steven, G. A simple evolutionary procedure for structural optimization. *Comput. Struct.* **1993**, *49*, 885–896. [CrossRef]

44. Querin, O.; Steven, G.; Xie, Y. Evolutionary structural optimisation (ESO) using a bidirectional algorithm. *Eng. Comput.* **1998**, *15*, 1031–1048. [CrossRef]
45. Haber, R.; Bendsøe, M. Problem formulation, solution procedures and geometric modeling: Key issues in variable-topology optimization. In *Proceedings of the 7th AIAA/USAF/NASA/ISSMO Symposium on Multidisciplinary Analysis and Optimization, St. Louis, MO, USA, 2–4 September 1998*; American Institute of Aeronautics and Astronautics Inc., AIAA: Reston, VA, USA; pp. 1864–1873. [CrossRef]
46. van Dijk, N.P.; Maute, K.; Langelaar, M.; van Keulen, F. Level-set methods for structural topology optimization: A review. *Struct. Multidiscip. Optim.* **2013**, *48*, 437–472. [CrossRef]
47. Sigmund, O. A 99 line topology optimization code written in matlab. *Struct. Multidiscip. Optim.* **2001**, *21*, 120–127. [CrossRef]
48. Andreassen, E.; Clausen, A.; Schevenels, M.; Lazarov, B.S.; Sigmund, O. Efficient topology optimization in MATLAB using 88 lines of code. *Struct. Multidiscip. Optim.* **2011**, *43*, 1–16. [CrossRef]
49. Zegard, T.; Paulino, G.H. Bridging topology optimization and additive manufacturing. *Struct. Multidiscip. Optim.* **2016**, *53*, 175–192. [CrossRef]
50. Jiu, L.; Zhang, W.; Meng, L.; Zhou, Y.; Chen, L. A CAD-oriented structural topology optimization method. *Comput. Struct.* **2020**, *239*, 106324. [CrossRef]
51. Wang, H.V. A Unit Cell Approach for Lightweight Structure and Compliant Mechanism. Ph.D. Dissertation, Georgia Institute of Technology, Atlanta, GA, USA, 2005.
52. Savio, G.; Gaggi, F.; Meneghello, R.; Concheri, G. Design method and taxonomy of optimized regular cellular structures for additive manufacturing technologies. *Proc. Int. Conf. Eng. Des. ICED* **2015**, *4*, 235–244. Available online: https://www.designsociety.org/publication/37788/design_method_and_taxonomy_of_optimized_regular_cellular_structures_for_additive_manufacturing_technologies (accessed on 12 March 2021).
53. Savio, G.; Meneghello, R.; Concheri, G. Optimization of lattice structures for additive manufacturing technologies. In *Advances on Mechanics, Design Engineering and Manufacturing. Lecture Notes in Mechanical Engineering*; Springer: Cham, Switzerland, 2016; pp. 213–222. [CrossRef]
54. Savio, G.; Meneghello, R.; Concheri, G. Geometric modeling of lattice structures for additive manufacturing. *Rapid Prototyp. J.* **2018**, *24*, 351–360. [CrossRef]
55. Catmull, E.; Clark, J. Recursively generated B-spline surfaces on arbitrary topological meshes. *Comput. Des.* **1978**, *10*, 350–355. [CrossRef]
56. Rosso, S.; Meneghello, R.; Biasetto, L.; Grigolato, L.; Concheri, G.; Savio, G. In-depth comparison of polyamide 12 parts manufactured by Multi Jet Fusion and Selective Laser Sintering. *Addit. Manuf.* **2020**, *36*, 101713. [CrossRef]
57. Rosso, S.; Meneghello, R.; Concheri, G.; Savio, G. Scale and Shape Effects on the Fatigue Behaviour of Additively Manufactured SS316L Structures: A Preliminary Study. In *Lecture Notes in Mechanical Engineering*; Springer: Cham, Switzerland, 2019; pp. 879–890. [CrossRef]
58. Savio, G.; Rosso, S.; Curtarello, A.; Meneghello, R.; Concheri, G. Implications of modeling approaches on the fatigue behavior of cellular solids. *Addit. Manuf.* **2019**, *25*, 50–58. [CrossRef]
59. Wu, Z.; Xia, L.; Wang, S.; Shi, T. Topology optimization of hierarchical lattice structures with substructuring. *Comput. Methods Appl. Mech. Eng.* **2019**, *345*, 602–617. [CrossRef]
60. Alzahrani, M.; Choi, S.K.; Rosen, D.W. Design of truss-like cellular structures using relative density mapping method. *Mater. Des.* **2015**, *85*, 349–360. [CrossRef]
61. Savio, G.; Meneghello, R.; Concheri, G. Design of variable thickness triply periodic surfaces for additive manufacturing. *Prog. Addit. Manuf.* **2019**, *4*, 281–290. [CrossRef]
62. Jiang, J.; Xu, X.; Stringer, J. Optimization of process planning for reducing material waste in extrusion based additive manufacturing. *Robot. Comput. Manuf.* **2019**, *59*, 317–325. [CrossRef]
63. Ahsan, A.N.; Habib, A.; Khoda, B. Resource based process planning for additive manufacturing. *CAD Comput. Aided Des.* **2015**, *69*, 112–125. [CrossRef]
64. Cicconi, P.; Mandorli, M.; Favi, C.; Campi, F.; Germani, M. Metal Additive Manufacturing for the Rapid Prototyping of Shaped Parts: A Case Study. *Comput. Des. Appl.* **2021**, *18*, 1061–1079. [CrossRef]
65. Song, X.; Feih, S.; Zhai, W.; Sun, C.-N.; Li, F.; Maiti, R.; Wei, J.; Yang, Y.; Oancea, V.; Brandt, L.; et al. Advances in additive manufacturing process simulation: Residual stresses and distortion predictions in complex metallic components. *Mater. Des.* **2020**, *193*, 108779. [CrossRef]
66. Schoinochoritis, B.; Chantzis, D.; Salonitis, K. Simulation of metallic powder bed additive manufacturing processes with the finite element method: A critical review. *Proc. Inst. Mech. Eng. Part B J. Eng. Manuf.* **2016**, *231*, 96–117. [CrossRef]
67. Gong, X.; Cheng, B.; Price, S.; Chou, K. Powder-bed electron-beam-melting additive manufacturing: Powder characterization, process simulation and metrology. In Proceedings of the 2013 ASME Early Career Technical Conference (ECTC), Birmingham, AL, USA, 2–3 November 2013; pp. 55–66. Available online: https://www.researchgate.net/publication/275960612 (accessed on 23 December 2020).
68. Martukanitz, R.; Michaleris, P.; Palmer, T.; DebRoy, T.; Liu, Z.-K.; Otis, R.; Heo, T.W.; Chen, L.-Q. Toward an integrated computational system for describing the additive manufacturing process for metallic materials. *Addit. Manuf.* **2014**, *1*, 52–63. [CrossRef]

69. Jayanath, S.; Achuthan, A. A computationally efficient hybrid model for simulating the additive manufacturing process of metals. *Int. J. Mech. Sci.* **2019**, *160*, 255–269. [CrossRef]
70. Watanabe, N.; Shofner, M.L.; Treat, N.; Rosen, D.W. A model for residual stress and part warpage prediction in material extrusion with application to polypropylene. In *Solid Freeform Fabrication 2016, Proceedings of the 27th Annual International Solid Freeform Fabrication Symposium—An Additive Manufacturing Conference, Austin, TX, USA, 8–10 August 2016*; TMS: Pittsburgh, PA, USA, 2016; pp. 2437–2455.
71. Brenken, B.; Barocio, E.; Favaloro, A.; Kunc, V.; Pipes, R.B. Development and validation of extrusion deposition additive manufacturing process simulations. *Addit. Manuf.* **2019**, *25*, 218–226. [CrossRef]
72. Fradl, D.; Panditaratne, J.; Bi, J.; Fu, R.; Oancea, V. Finite Element Simulation of the Multi Jet Fusion (MJFTM) Process using Abaqus. In Proceedings of the SIMULIA Science in the Age of Experience, Chicago, IL, USA, 15–18 May 2017; pp. 440–469. Available online: https://pdfs.semanticscholar.org/fb66/17aab5ff74f47709ebfecb694d32f23ceff2.pdf (accessed on 23 January 2020).
73. Kolossov, S.; Boillat, E.; Glardon, R.; Fischer, P.; Locher, M. 3D FE simulation for temperature evolution in the selective laser sintering process. *Int. J. Mach. Tools Manuf.* **2004**, *44*, 117–123. [CrossRef]
74. Preisinger, C. Linking Structure and Parametric Geometry. *Arch. Des.* **2013**, *83*, 110–113. [CrossRef]
75. Renishaw, Data Sheets—Additive Manufacturing—AlSi10Mg-0403 (400 W). 2021. Available online: https://www.renishaw.com/en/data-sheets-additive-manufacturing--17862 (accessed on 19 February 2021).

Additive Manufacturing 36 (2020) 101713

Contents lists available at ScienceDirect

Additive Manufacturing

journal homepage: www.elsevier.com/locate/addma

Research Paper

In-depth comparison of polyamide 12 parts manufactured by Multi Jet Fusion and Selective Laser Sintering

Stefano Rosso [a,b,*], Roberto Meneghello [a,b], Lisa Biasetto [a], Luca Grigolato [b,c], Gianmaria Concheri [b,c], Gianpaolo Savio [b,c]

[a] University of Padova, Department of Management and Engineering, Stradella S. Nicola, 3, 36100 Vicenza, Italy
[b] University of Padova, Laboratory of Design Tools and Methods in Industrial Engineering, Viale G. Colombo, 5, 35131 Padova, Italy
[c] University of Padova, Department of Civil, Environmental, and Architectural Engineering, Via Venezia, 1, 35131 Padova, Italy

ARTICLE INFO

Keywords:
Polyamide 12
Selective Laser Sintering
Multi Jet Fusion
Lattice structure
Fatigue

ABSTRACT

Recently, the possibility of producing medium-to-large batches has increased the interest in polymer powder bed fusion technologies such as selective laser sintering (SLS) and multi jet fusion (MJF). Only scant data about the characterization of parts produced by MJF can be found in the literature, and fatigue behavior studies are absent. This study analyzes the material properties of Polyamide 12 (PA12) powders and printed specimens using both SLS and MJF technologies. The morphology, crystalline phases, density, porosity, dimensional accuracy, and roughness are measured and compared; tensile and fatigue tests are performed to assess the effect of the technologies on the mechanical behavior of the produced structures. In addition, lattice structure specimens obtained by different geometric modeling approaches are tested to understand the influence of modeling methods on the fatigue life. The PA12 powders printed by both SLS and MJF mainly show by X-Ray Diffraction γ-phase and a small shoulder of α-phase. The crystallinity decreases after printing the powders both in SLS and MJF technology. The printed parts fabricated using the two technologies present a total porosity of 7.95% for SLS and 6.75% for MJF. The roughness values are similar, $Ra \approx 11$ μm along the building direction. During tensile tests, SLS samples appear to be stiffer, with a lower plastic deformation than MJF samples, that are tougher than SLS ones. Fatigue tests demonstrate higher dispersion for MJF specimens and an enhancement of fatigue life for both SLS and MJF printed lattice structures modeled with a novel geometric modeling approach that allows the creation of smoother surfaces at nodal points. Scanning electron microscopy on fracture surfaces shows a brittle failure for the SLS tensile specimens, a more ductile failure for the MJF tensile specimens, a crazing failure mechanism for the SLS fatigue tested samples, and a crack initiation and slow growth and propagation for the MJF fatigue tested samples.

1. Introduction

The additive or layer-by-layer production of components, in contrast to subtractive manufacturing methodologies, allows for freedom in shape and complexity, reduction of waste, product optimization, production of small batches, and shorter lead times [1,2]. Owing to these recognized capabilities, in 2018, the worldwide additive manufacturing (AM) industry grew 33.5% to $9.795 billion at a rate higher than that in 2017 (21.0%) [3]. Among the materials that can be used with AM techniques, polymers are widely used due to the optimal properties and vast potential of their printed parts, and the advances made in polymer material development are significant [4]. In addition, an analysis of the worldwide material sales data indicates that consumption of polymers for powder bed fusion (PBF) systems represents 26.9% of the total, with a growth from $291 million to $402.1 million in 2018 [3]. This increased interest in the polymer PBF is also driven by the rather new technology called multi jet fusion (MJF). According to international standards [5], SLS and MJF are both PBF technologies. The PBF

Abbreviations: AM, Additive Manufacturing; PA12, Polyamide 12; PBF, Powder Bed Fusion; SLS, Selective Laser Sintering; MJF, Multi Jet Fusion; HSS, High Speed Sintering; SIS, Selective Inhibition Sintering; XRD, X-Ray Diffraction; SEM, Scanning Electron Microscopy; TGA-DSC, Thermogravimetric Analysis and Differential Scanning Calorimetry.

[*] Corresponding author at: University of Padova, Department of Management and Engineering, Stradella S. Nicola, 3, 36100 Vicenza, Italy.
E-mail address: stefano.rosso.3@phd.unipd.it (S. Rosso).

https://doi.org/10.1016/j.addma.2020.101713
Received 26 June 2020; Received in revised form 9 November 2020; Accepted 11 November 2020
Available online 14 November 2020
2214-8604/© 2020 The Authors. Published by Elsevier B.V. This is an open access article under the CC BY-NC-ND license (http://creativecommons.org/licenses/by-nc-nd/4.0/).

manufacturing method can be summarized as follows:

1. a CAD model is sectioned (sliced) at different heights to create layers that contain object sections;
2. the AM machine is initialized by preheating the building platform (mandatory for PBF of polymers, not necessary for PBF of metals);
3. the first layer of powders is evenly distributed on the base plate using a coating mechanism;
4. the 2D slice of the part geometry is fused by selectively sintering the powders that lay on the plate;
5. the base plate is lowered to a height equal to the layer thickness;
6. points from 3 to 5 are repeated until the entire part is built.

The main difference between SLS and MJF lies in the manner how powders are bonded in order to create the solid part; in the SLS process, a laser selectively sinters the powder only in the space defined by a 3D model; in the MJF technology, an array of inkjet print heads releases two types of printing ink: a so-called "fusing agent" is applied inside the model boundaries, while a "detailing agent" is applied at the edges of the model to inhibit the sintering of powders not wetted by the fusing agent and create fine details and smooth surfaces; the layer is then exposed to infrared (IR) heating lights to build the part. The higher speed of MJF technology than SLS is because in SLS the laser sinters the powders point by point, while in MJF the layer is processed line by line, in accordance with the arrangement of the print heads and the infrared lamps. SLS was developed by Carl R. Deckard at the University of Texas [6,7]. MJF can be considered a hybrid between Neil Hopkinson's high-speed sintering (HSS) [8,9] and Behrokh Khoshnevis' selective inhibition sintering (SIS) [10,11]. The former is a technique developed by Loughborough University that aims at sintering 2D profiles of powder layers by adding carbon black that absorbs infrared radiations and increases the rate of sintering, and using an infrared lamp to sinter without the need for a laser. The latter was developed by the University of Southern California and is characterized by the deposition of a sintering-inhibitor liquid along the layer profiles/boundaries to prevent the sintering of selected areas; the uninhibited powder is then sintered by a heated nichrome filament, without the need for a laser. Similarly to the HSS, in MJF the "fusing agent" contains carbon black (5.2%) to absorb infrared radiations, suspended in a solution of water (65%), 2-pyrrolidone (18.7%), and triethylene glycol (8.4%); the "detailing agent", instead, mostly contains water (83%), 2-pyrrolidone (3.7%), and triethylene glycol (11.1%) [12].

SLS process is a mature and widely used material forming technology, thanks to several advantages over other polymer additive techniques [13]. This technology does not require support structures for overhangs and thin walls because the part is supported by the surrounding unfused powders; binders are not required, post-processing steps may be avoided, and there is not a risk of toxicity in biomedical applications [14]; moreover, a variety of materials can be processed using this technique [15,16], from polyamides [17,18] to polyetheretherketone (PEEK) [19]. The SLS processing of polyamide 12 (PA12) has been widely studied. Virgin and reused PA12 powders have been characterized to understand the influence on the microstructure and mechanical properties of printed parts [20,21]; the process parameters have been investigated and optimized to obtain the best mechanical properties and surface finish [22–24]; a 3D failure criterion for SLS PA12 parts undergoing tension, compression, and shear loads as single or combined loads was implemented and verified [25]. Fatigue behavior of SLS PA12 printed parts has been studied under dynamic tension/tension excitation [26], tension/compression excitation [18], four-point rotating bending [27], and load increase method [28], and compared to the PA12 parts obtained with more traditional manufacturing techniques, such as injection molding [29,30]. On the contrary, MJF technology is new in the AM scenario, and few scientific works are available in the literature [31–40]. During the development of the High-Speed Sintering process, Majewski et al. [41] studied the effects of the IR lamp power on the degree of sintering and achievable depth of sintering, eventually concluding that there is a maximum obtainable layer thickness (~200 μm), and that a greater degree of sintering occurs at the higher power levels of IR lamps. Later on, Ellis et al. [42] assessed the influence of print density that corresponds to the amount of "Radiation Absorbing Material" (i.e. carbon black) deposited on the surface, on the crystallinity and mechanical properties of PA12; they found out that when the print density increases, the percentage of crystallinity decreases, while the degree of particle melting increases linearly; moreover, when the print density increases, the stiffness and tensile strength increase, while ductility decreases. For the SIS process, Khoshnevis et al. [11] proposed four theories depending on the inhibitor used: a) macroscopic mechanical inhibition, where droplets of the inhibitor penetrate the powder layer in an impact event, distancing them and avoiding adhesion during the sintering phase; b) microscopic mechanical inhibition, where the inhibitor penetrates the powder layer and obstructs adhesion; c) thermal inhibition, where the inhibitor penetrates the powder layer, cools the polymer particles during the heating step of the process via evaporation and prevents sintering; d) chemical inhibition, where the inhibitor penetrates the powder layer and reacts with the powder particles at their surface, thereby producing a chemical species that is resistant to sintering. Asiabanpour et al. [43] optimized the surface quality and dimensional accuracy of SIS printed parts, setting up a Design of Experiment and using the response surface methodology, studying the effects of several process parameters such as layer thickness, inhibitor liquid pressure and feed rate, heater temperature, and obtaining a mathematical model so as a set of optimized process parameters. They also discussed the inhibitor liquid choice [44] and discarded water, isopropyl alcohol, and other liquids because no inhibition phenomena other than impact cutting and cooling were found, while dichlorobenzene and butylbenzene were not considered due to their toxicity and tendency to damage the printer head system; they found a solution of soluble salt, water, and small amount of alcohol to be the best inhibitor liquid.

O'Connor et al. [31] thoroughly investigated the morphology, chemistry, and mechanical performance of parts produced with MJF technology. The specimens were printed in three build orientations and results showed isotropic behavior in terms of tensile strength with a moderately ductile failure mode. The mechanical properties stayed in the range specified by other works dealing with PA 12 parts. Another study [32] concentrated on the properties of MJF PA12 glass-bead filled parts, showing an increase in the surface roughness and tensile modulus as well as a decrease in the maximum tensile strength and elongation compared to MJF PA12-only specimens; these results were influenced by the poor glass sphere-polymer matrix adhesion. Studies on the water tightness of samples produced with MJF were conducted by Morales-Planas et al. [33], who demonstrated that this technology can be used to produce fluid-handling parts due to the lack of open porosity in their structure, in compliance with ISO standards. Mele et al. [34] investigated the capillarity effect in the MJF process, that comes from the interaction between the detailing and fusing agents, and leads to a non-planar surface, especially when close to the border edges; they first performed experimental measurements on benchmark geometries, and then used the collected data to propose a numerical model.

Habib et al. [35] performed nonlinear finite element analyses to study the compressive response and energy-absorbing characteristics of different lattice structures in both bending-dominated and stretching-dominated cases [45]; they used PA12 samples produced using an MJF machine to conduct the analyses and verify the mathematical model; a comparison between lattices produced with MJF and fused deposition modeling technologies was also done, showing that MJF provides better quality parts in a fraction of the time. Fradl et al. [36] simulated the MJF process with the commercial finite element software Abaqus. They created a modeling framework to predict the thermal behavior, part distortions, and residual stresses at the end of the print by coupling the thermal and mechanical problems. The model was validated using a medical device as a case study. Kim et al. [46] proposed an approach for the process-level simulation of the MJF technology; they used a cyber-physical system where the cyber part pertains to the printer with the printing controller and process modules, and the physical part is the model of multiple layers of build material; the results of the simulations show a reduction of several orders of magnitude in the computational time when compared with an FEM analysis, while having reasonable accuracy.

Focusing on the comparison between SLS and MJF technologies, only a few studies can be found in the literature. Xu et al. [38] investigated the powders and the performance of PA12 parts fabricated with these two technologies. They found out that the MJF powders have a higher crystallinity and wider sintering window compared to SLS powders; on the other hand, SLS parts have a higher degree of crystallinity, in accordance with the instant heating capability of the laser source; also, SLS parts have better mechanical performance. A similar study was conducted by Sillani et al. [39], in which they compared virgin, reused, and artificially aged powders; they highlighted that MJF powder is end-capped, allowing for higher recyclability of the raw material. Mechanical properties of the printed parts differ slightly from [38]; indeed, in [39], MJF parts have higher elongation at break and higher tensile strength (when printed along z direction), but it is recognized that different process parameters and level of reuse of the powders highly affect the properties of the final parts [20–22,31,47]. Cai et al. [40] proposed a comparison of both the powders and the parts obtained by SLS and MJF technologies. The thermal features, phase constitutions, functional groups, and chemical states of both powders are nearly identical; the printed parts have similar porosity but different pore morphology and volume distributions. A clear anisotropy is detected when changing the printing direction from the XY plane to the Z axis, especially on the UTS, that decreases for the SLS parts and increases for the MJF ones; this different behavior was supposed by the authors to be due to the different sintering approach of the two technologies, with MJF resulting in a better sinter quality between the layers.

It also must be noted that no studies about the fatigue behavior of parts printed with HP MJF have been published yet.

In this work, a comparison between SLS and MJF technologies is presented through the analysis of PA12 powders and printed specimens. Material characterization of powder and samples are obtained by scanning electron microscope, x-ray diffraction, thermogravimetric analysis and differential scanning calorimetry, He-pycnometry, dimensional and roughness measurements, and tensile and fatigue tests, which is the main innovative contribution of this study, especially with regards to MJF technology. Lattice structure specimens obtained by different geometric modeling approaches are also tested to understand the influence of both technologies and modeling methods on the fatigue life; the results obtained from the comparison of the modeling methods depend neither on the material of the part nor on the manufacturing technology, so they can be used as general guidelines when designing parts that require an optimal fatigue behavior. Moreover, the results of the comparison between the two technologies can help both researchers and industry users choose between them, depending on the application and the required mechanical properties.

2. Materials and methods

2.1. Sample preparation

Samples were produced with both SLS and MJF technology. An SLS EOS FORMIGA P110 machine and EOS PA2200-performance [48] PA12 powder were used to produce SLS samples; the powder and process parameters are reported in Table 1; the set of process parameters is a standard set for biomedical applications and was used in a previous work [26]; a similar set of parameters used on the same machine and powders was proved to be one of the best for optimal tensile properties [49]. The HP Jet Fusion 4200 machine and HP3D high-reusability PA12 powder [50] were used to produce MJF samples; the HP machine does not allow parameter modification, and so, the balanced print mode preset was used, consisting of one rolling step and two injection passes spending 10.5 s per layer, as reported in Table 1 [31,33]. For each technology, the powders suggested by the machine vendor (Table 2) were used to achieve the best results. The parts were produced by mixing virgin and reused powders in a refresh ratio (virgin: reused) of 1:1 for SLS, reflecting a standard operating procedure adopted by the lab, and 1:4 for MJF according to the manufacturer's datasheet [50].

Table 1
Process parameters for SLS and MJF process.

	SLS	MJF
Laser beam power	20 W	Balanced mode: one rolling step, two injection passes 10.5 s per layer
Laser scan speed	3000 mm/s	
Layer thickness	100 μm	
Laser spot size	~0.4 mm	
Building platform temperature	160 °C	
Virgin: reused powder ratio	1:1	1:4

For each printing technology, specimens with seven different geometries were manufactured depending on the characterization tests, with shape and dimensions as in Fig. 1. All the specimens belong to the same batch, i.e. the same print job. Three types of lattice structure specimens were designed using different unit cells: cells with a squared section and fillet radius (SF, Fig. 1e), cells with a circular section and fillet radius (CYF, Fig. 1f), and a unit cell obtained by the Catmull–Clark surface subdivision algorithm (CC, Fig. 1g) [26,52]. Adopting the Catmull–Clark subdivision [53], it is possible to obtain a smooth mesh from an initial coarse mesh by recursively applying the algorithm; in CC specimens, three iterations of the algorithm were applied. Lattice structures were obtained by repeating the unit cell along the x, y, and z-axes, three, two, and five times, respectively. The cell dimension is 7.5 mm and the fillet radius is 1 mm for the SF and CYF cells; each cell has a resistant area of 6.25 mm^2, corresponding to a 2.50 mm strut size for the SF cell, and 2.821 mm strut diameter for the CYF cell. The CC cell has a continuous shape variation and the size of the minimum strut section ranges between 2.79 mm and 2.88 mm.

2.2. Powders and sample characterization

A Field Emission Gun electron microscope (FEI Quanta 200 Eindhoven, The Netherlands) in low vacuum mode was used to characterize the powders morphology and the samples after static (Fig. 1c) and dynamic (Fig. 1d–g) mechanical testing. X-Ray diffraction analyses (XRD, Bruker D8 Advance, Mannheim, Germany) were performed on both the starting powders and the rectangular plates (Fig. 1a) using Cu-Kα radiation (scan speed 5°/sec, scan step 0.01) in the range $2\theta = 10^{\circ} – 40^{\circ}$. The powders used during SLS and MJF processes and the core parts of printed cylindrical samples (Fig. 1b) were analyzed by Thermogravimetric Analysis and Differential Scanning Calorimetry (TGA-DSC) using a Mettler-Toledo TGA/DSC 3 + on 5 ± 0.5 mg samples in the range 25–300 °C, at a heating rate of 10 °C/min under nitrogen flow. The crystallinity percentage (C%) was calculated as the ratio between the specific heat of fusion of the sample (J/g) and the specific heat of fusion

Table 2
Properties of used PA12 powders.

	PA2200 Performance (SLS)	PA12 3D High Reusability (MJF)
Density [g/cm^3]	0.440 [38]	0.425 [50]
Powder average size [μm]	56 [51]	60 [50]
Melting point [°C]	176 [48]	187 [50]

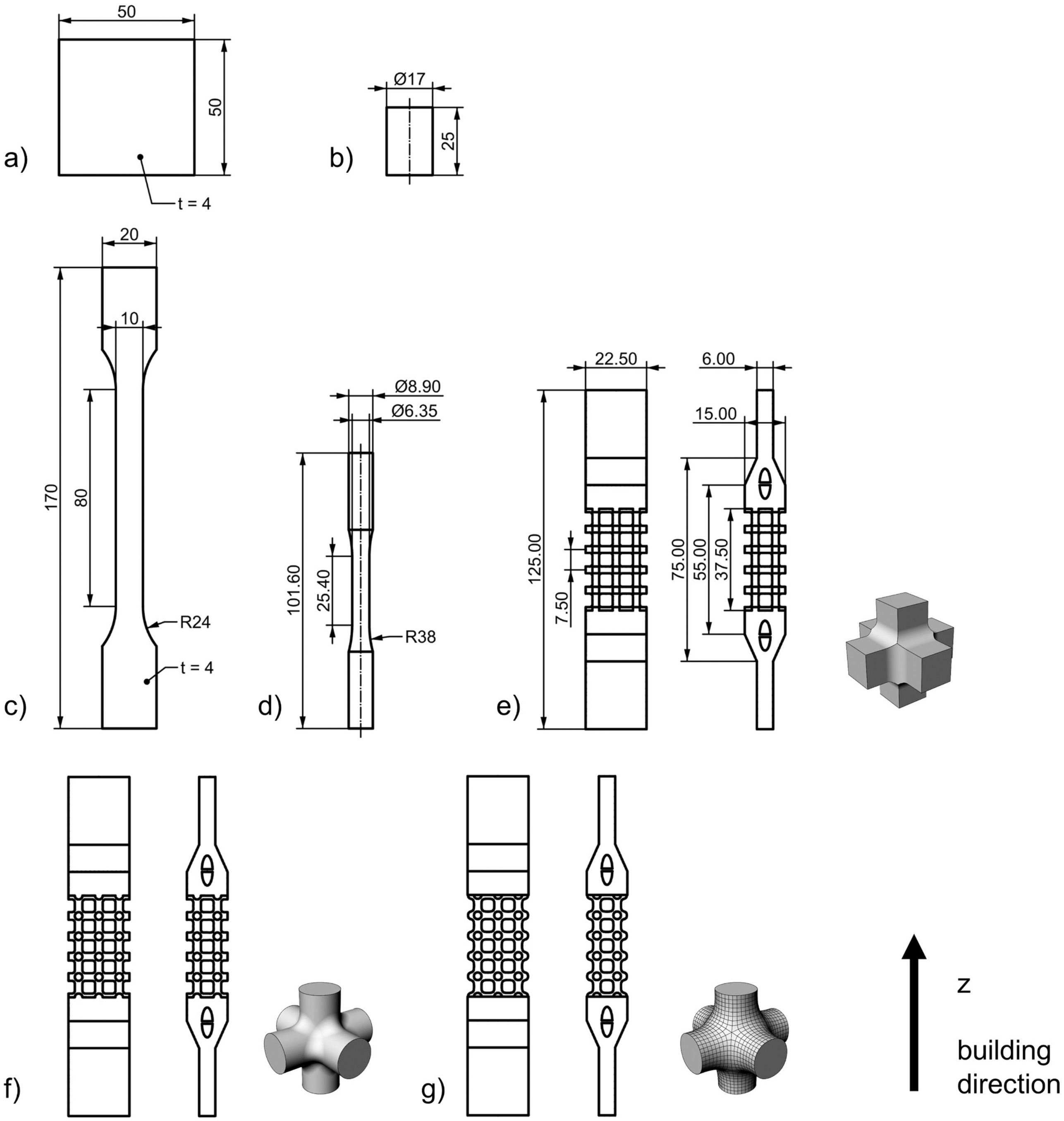

Fig. 1. Specimen dimensions: a) plates for XRD, b) cylinders for He-pycnometry, c) ISO 527 type 1A specimens for static tensile tests, d) ASTM E606 specimens for fatigue tests, e) SF lattice structure for fatigue tests, f) CYF lattice structure for fatigue tests, g) CC lattice structure for fatigue tests. Specimens are in scale.

of 100% crystalline PA12, equal to 209.3 J/g as reported in [54]. The heat of fusion was calculated by the DSC software as integral of the peak. He-pycnometry (Accupyc 1340, Micromeritics) was performed to measure the density of the starting powders (ρ_{th}) and the apparent density (ρ_{app}) of the three cylindrical samples produced by SLS and MJF (Fig. 1b). The bulk density (ρ_{bulk}) of the cylinders was measured as mass over volume ratio, where the mass was measured by a digital balance and the volume by a digital caliper.

The total porosity P_{tot} of the printed parts was calculated as [55]:

$$P_{tot} = 1 - \frac{\rho_{bulk}}{\rho_{th}} \tag{1}$$

The open porosity P_{open} as:

$$P_{open} = 1 - \frac{\rho_{app}}{\rho_{th}} \tag{2}$$

Being the total porosity P_{tot} equal to the sum of open and closed porosity, the closed porosity P_{close} was calculated as:

$$P_{close} = P_{tot} - P_{open} \tag{3}$$

Specimens type 1A that follow the ISO 527 standard [56] (Fig. 1c), specimens adapted from ASTM E606/E606M standard [57] (Fig. 1d), and lattice structures (Fig. 1e–g) were measured with a coordinate measuring machine (OGP SmartScope Flash 200): width and thickness of the ISO 527 specimens central part and diameters of the central part of the ASTM E606 specimens were measured, whereas for the lattice structures, the size of the struts along the z direction was measured both in the front and in the side view. The error in size was then calculated by the difference between the measured dimensions and the nominal ones. Surface roughness was measured using a Talysurf i-Series on ISO 527 specimens, reporting the Ra parameter (arithmetic mean deviation of the assessed profile) along the growing direction, on the top surface, and on the bottom surface, according to ISO 4287 [58] and ISO 4288 [59] standards (evaluation length = 12.5 mm, sampling length = 2.5 mm).

Mechanical tests were executed on an MTS Acumen 3 Electrodynamic Test System equipped with a 3 kN load cell and an MTS 634.31 F extensometer. Tensile tests were performed according to the ISO 527 standard on five specimens as in Fig. 1c, measuring the mechanical properties of the bulk material at a speed rate of 2 mm/min and with a gauge length of 10 mm. Stress-strain curves and True stress – True strain curves were plotted and Young's modulus, ultimate tensile strength (UTS), strain at break (ε_{max}), and toughness were calculated. The True stress – True strain curves are obtained according to the following equation for the true strain, ϵ, and the true stress σ' [60]:

$$\epsilon = \ln\left(\frac{l}{l_0}\right) \tag{4}$$

$$\sigma' = \sigma(1+\epsilon) \tag{5}$$

where l is the elongation, l_0 is the gauge length, and σ is the engineering

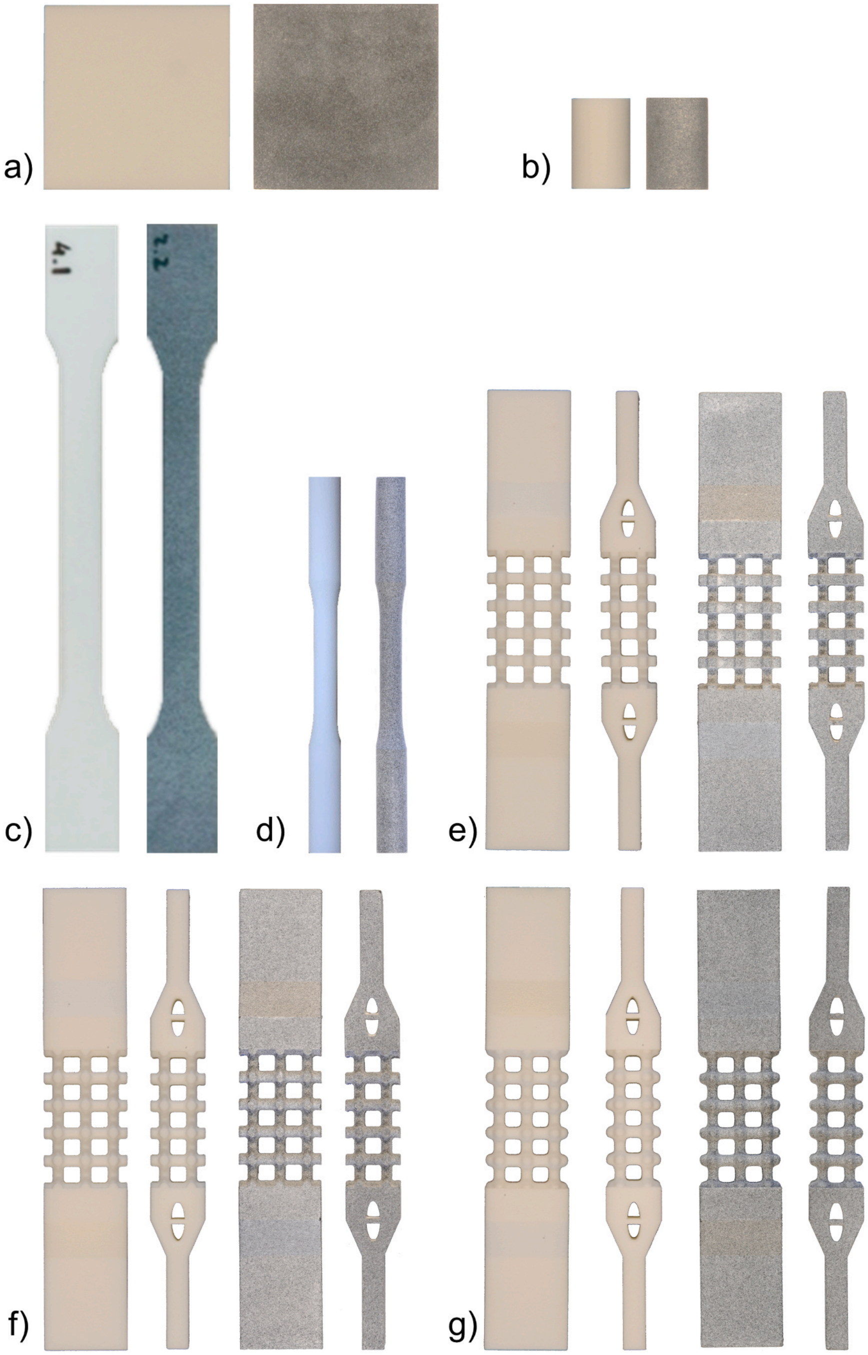

Fig. 2. Printed specimens: a) plates for XRD, b) cylinders for He-pycnometry, c) ISO 527 type 1A specimens for static tensile tests, d) ASTM E606 specimens for fatigue tests, e) SF lattice structure for fatigue tests, f) CYF lattice structure for fatigue tests, g) CC lattice structure for fatigue tests. For each sample, left: SLS, right: MJF. Specimens are in scale.

stress. The material toughness, defined as the area under the true curve until fracture [61], was obtained by:

$$Toughness = \int_0^{\epsilon_f} \sigma' d\epsilon \tag{6}$$

Fatigue tests on SLS and MJF specimens adapted from the ASTM E606/E606M standard (Fig. 1d) and on MJF lattice specimens (Fig. 1e–g) were performed for four load steps (32 MPa, 34 MPa, 36 MPa, 38 MPa) at 3 Hz frequency with zero stress ratio (R = 0, i.e. $R = \sigma_{min}/\sigma_{max}$, where σ is the stress) to avoid buckling phenomena. Data were acquired with a timed trigger at 64 Hz to store signals for the entire cycle and with a peak-and-valley trigger to store the minimum and maximum signals at every cycle. No artificial cooling was applied. Guidelines from the ISO 12107 standard [62] were followed to statistically estimate the stress–number of cycles (S–N) curves, also known as the Wöhler curves. Fatigue tests on SLS SF, CYF, and CC lattice specimens were performed in a previous study [26]. Finally, fracture surfaces of the static tensile tested and fatigue tested cylindrical bulk specimens and lattice structures were analyzed using SEM.

3. Results and discussion

Fig. 2 shows a printed specimen for each type of printing technology (SLS samples on the left, MJF samples on the right) and shape.

3.1. Powders properties and process effect

The SLS and MJF powders used in this study were a mixture of virgin and recycled powders, as recommended by the printers' producers. The reason why producers recommend the use of a mixture of powders lays behind the presence of a mixture of crystalline structures and the consequent positive effect on the mechanical properties of the printed parts [20]. Powders used for SLS can be synthesized in different ways as reported in [20]. SLS polyamide 12 can be obtained by dissolution in ethanol at high pressure and temperature, followed by slow crystallization; alternatively, PA12 powders or granules are heated in steam for a long time (up to 100 h). The main scope of these treatments is to increase the melting temperature of the powders and to improve whiteness and flowability. As an effect, some of the SLS powders show cracks (Fig. 3a). The presence of these cracks is not yet fully understood but it has been supposed to be related to the synthesis process as reported in [21,63]; the evaporation of the remaining ethanol could be a clue. Less is known from the literature on MJF powders, being this an emerging technology. However, the presence of both a melting and a detailing agent on the powder bed is a fundamental prerequisite for the MJF technology. MJF powders regularly come in contact with the solvents of the fusing and detailing agents, but this cracking effect is not as evident as for SLS; this could be explained by the fact that the agents contain 2-pyrrolidone and triethylene glycol, that have boiling points of 251 °C and 288 °C respectively [12], higher than ethanol (78 °C), and the temperature during the printing process does not exceed 185 °C [8,36].

The starting powders and a part of the cylindrical samples were analyzed by TGA-DSC in order to define the melting point and the crystallinity degree. In Fig. 4 both SLS and MJF powders show a single peak corresponding to the melting temperature of 188.6 ± 0.1 °C and 187.7 ± 0.2 °C respectively, as reported in Table 3. These results are in accordance with Cai et. al [40], that used the same PA12 powders, i.e. EOS PA2200 (188.9 °C) and HP PA12 3D High Reusability (188.4 °C), and Schmid et al. [64], that tested 3D-Systems Duraform PA12 powders for SLS machines (186.1 °C), that come from the same PA12 supplier as EOS PA2200, Evonik [65]. In [64] the higher melting temperature of PA12 powders for SLS compared to standard PA12 powders (178 °C) was observed and attributed to the presence of crystalline phases with larger unit cells. Powders for additive manufacturing are subjected to a very special thermal treatment history to enlarge the processability window. The exact thermal cycle of powders is confidential and not revealed by the producers.

The printed samples show a translation of the peak to lower temperature, 183.1 ± 0.5 °C for SLS parts and 182.7 ± 0.4 °C for MJF parts. It is well known from the literature that PA12 may exhibit two crystalline forms. The monoclinic or triclinic α-phase and the pseudohexagonal γ-phase [17]. As reported in [66] films of PA12 showed α-phase with a

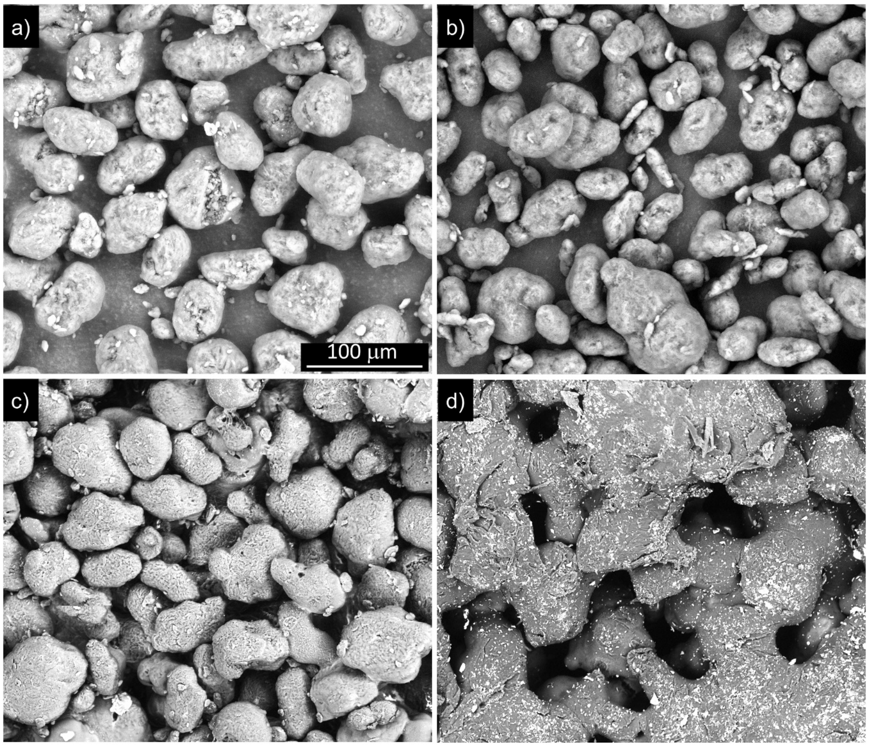

Fig. 3. SEM analyses of the morphology of the powders: a) SLS, b) MJF. Surface morphology of printed parts, c) SLS and d) MJF.

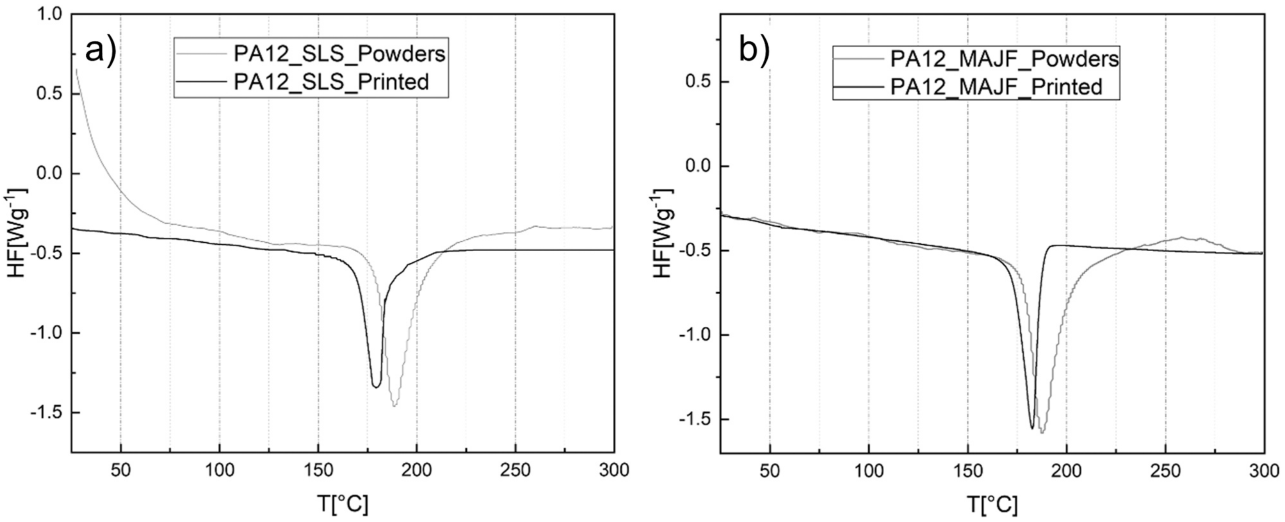

Fig. 4. DSC curves of starting SLS and MJF powders and printed parts: a) SLS, b) MJF.

Table 3
Melting temperature, enthalpy of fusion, and crystallinity of the two sets of samples.

Sample	T_m [°C]	H_m [J/g]	Crystallinity [%]
SLS Powder	188.6 ± 0.1	102.9 ± 1.1	49.1 ± 0.5
SLS Part	183.1 ± 0.5	52.3 ± 0.4	24.5 ± 0.1
MJF Powder	187.7 ± 0.2	101.2 ± 0.9	48.3 ± 0.4
MJF Part	182.7 ± 0.4	65.9 ± 0.3	31.5 ± 0.2

melting temperature of 175 °C, whereas the γ-phase of 182 °C. In this work we used a mixture of starting powders that, as shown later by XRD, are characterized by a mixture of these two phases and values are in accordance with [67].

The calculated crystallinity percentage is reported in Table 3. It can be observed an important decrease of crystallinity both on SLS and MJF printed parts, in accordance with several studies in the literature [21,38,40].

Fig. 5 shows XRD analyses of both starting powders and printed parts. In the starting powders both α-phase and γ-phase are present, whereas after printing mainly γ-phase and a small shoulder of α-phase can be detected. No significant differences emerge between the two technologies in terms of microstructure. This behavior is in accordance with [17,21,29].

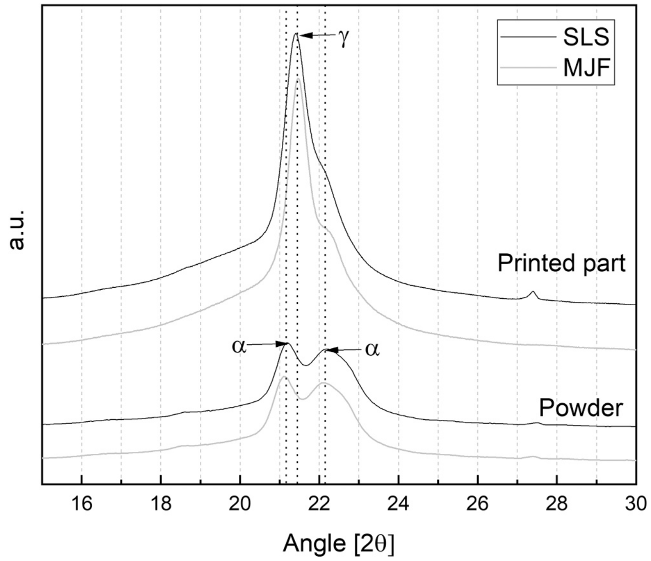

Fig. 5. XRD microstructural characterization of both powders and printed parts (rectangular parallelepiped, as shown in Fig. 1a).

In Table 4, the density of the starting powders (ρ_{th}), the bulk density (ρ_{bulk}), the apparent density (ρ_{app}), the density of the printed parts from the datasheets ($\rho_{datasheet}$), so as the values of the total porosity (P_{tot}), the open porosity (P_{open}), and the closed porosity (P_{close}), calculated by Eqs. (1–3) are reported. The total porosity of SLS printed parts is higher than MJF ones, and this is also reflected in the percentage of closed porosity, 1.61% for SLS printed parts and 1.13% for MJF printed parts. The presence of porosity on PA12 printed parts is well known from the literature, in this study we measured a total porosity higher than average values reported in the literature for SLS and MJF PA12 printed parts [30,31]. A more detailed study on morphological characteristics of porosity is planned in order to assess the pore size distribution, morphology, and their effect on the mechanical performance of the printed parts.

Table 5 shows the mean size error for each type of static and fatigue specimen and technology, obtained by the difference between the measured dimension and the nominal one, as described in Section 2.2. The size error can be positive or negative, depending on the measured size of the sample with respect to the nominal dimension. Lattices produced with SLS present a dimensional error close to 0.1 mm; this does not happen for MJF lattices, where dimensional errors appear to be more dispersed. ISO 527 specimens produced with MJF have the biggest dimensional error, that is, almost one order of magnitude higher than SLS ISO 527 samples. Furthermore, standard deviations are smaller for SLS technology. It has to be highlighted that the samples are embossed and bended [34,38] and these geometrical shape errors induce errors while performing linear measurements. An X-ray computed tomography would allow acquiring the actual printed geometry, and more accurate geometrical information would be available.

Table 4
Density and porosity for SLS and MJF samples.

Property	SLS	MJF
ρ_{th} [g/cm^3]	1.058 ± 0.001	1.056 ± 0.001
ρ_{bulk} [g/cm^3]	0.974 ± 0.011	0.985 ± 0.025
ρ_{apparent} [g/cm^3]	0.991 ± 0.002	0.997 ± 0.011
$\rho_{\text{datasheet}}$ [g/cm^3]	0.93	1.01
P_{tot} [%]	7.95 ± 0.09	6.75 ± 0.18
P_{open} [%]	6.35 ± 0.01	5.62 ± 0.06
P_{close} [%]	1.61 ± 0.10	1.13 ± 0.24

Table 5
Size error of samples used for mechanical tests.

	SLS	MJF
	Size error [mm]	Size error [mm]
ISO 527	0.034 ± 0.035	0.319 ± 0.079
ASTM E606	0.052 ± 0.030	-0.053 ± 0.069
SF	0.099 ± 0.031	0.053 ± 0.061
CYF	0.095 ± 0.030	-0.091 ± 0.050
CC	0.089 ± 0.043	-0.084 ± 0.080

Table 6 shows the measured roughness profile (Ra) on the top face, bottom face, and building direction of the ISO 527 specimens, for both technologies. As previously observed for SLS [26], MJF specimens present a rougher surface on the bottom face compared to the building direction. Usually, surface roughness in the building direction is higher than at the top surface [30], but it has been shown that the results are highly dependent on the process parameters, filter wavelength, and measurement techniques [27]. In [31], specimens produced by MJF technology presented greater roughness on the top surface Ra = 10.29 μm) than the bottom surface Ra = 2.54 μm); however, they were glass-bead blasted prior to the experiment. In the present study, the specimens were not post-processed, and partially un-melted powder could stick to the part and modify the surface texture, especially on the bottom face.

Fig. 6 shows the results of the tensile tests on ISO 527 specimens, generating both the engineering (Fig. 6a and d) and true (Fig. 6b and e) stress–strain curves. The tensile behavior of the tested samples is reported in the tables is Fig. 6c and f: the Young's modulus is similar for the two sets of samples, with SLS showing stiffer behavior. MJF samples, on the other hand, show a more ductile behavior that is expressed by a deformation at break of 30% versus the 10% of samples printed by SLS. The UTSs of the two technologies overlap. The MJF samples show a higher toughness.

The results of the tensile tests are supported by the SEM analyses performed on the fracture surface of the ISO 527 specimens (Fig. 7). The SLS specimen, in Fig. 7a and b, shows a brittle fracture surface, brittle fracture paths can be recognized, and hardly any signs of deformation can be distinguished; a similar failure mechanism for SLS parts was noted by Van Hooreweder et al. [18]. The upper part of the fracture surface of the MJF specimen (Fig. 7c and d) shows a ductile fracture surface with signs of plastic deformation, as noted by O'Connor et al. [31], and meets with a smoother lower part where the failure occurs. The ductile fracture of the MJF sample allows for a higher energy absorption before the failure, leading to a higher toughness of the parts, as confirmed by the tables in Fig. 6. Spherical voids are present without distinct PA12 particles in both technologies.

A comparison between the obtained mechanical properties and data available in the literature can be found in Table 7. SLS results are in accordance with other studies, except for the high elongation at break found by Xu et al. [38] and Cai et al. [40] but in both cases the specimens were printed with different orientations (on the XY plane) with respect to the current work (along Z axis), and the results obtained by Van Hooreweder and Kruth [30] where a higher Young's modulus and a lower elongation at break could be explained by the optimization of parameters to increase the stiffness of the printed parts. Among the available data for MJF, the highest stiffness was obtained by Morales-Planas et al. [33]; even though their specimens were tested according to the ASTM D638–14 standard instead of ISO 527, the specimen dimensions, section area, and test procedures are similar. The results of the current study for MJF printed parts present a slightly higher Young's modulus than that obtained in previous studies, and an elongation at break similar to the elongation of the samples printed along the Y axis (YZ plane) obtained by O'Connor et al. [31], and the ones printed along X axis (XY plane) by Cai et al. [40]. Considering studies that compare SLS and MJF technology, MJF samples tougher than SLS ones were also found in Sillani et al. [39], but the set of parameters for SLS was optimized for the best surface finish and not for the maximum mechanical properties. Also the MJF specimens printed along the Z axis (the same as in the current study) by Cai et al. [40] presented a higher UTS and Young's modulus than SLS specimens. Xu et al. [38] obtained a behavior that is in contrast: SLS parts have higher Young's modulus, UTS, and elongation than MJF. This behavior could be due to the different orientation of the printed samples, namely, flat in Xu's research and along the building direction in the present one; indeed, the mechanical properties of MJF printed parts were found to differ depending on the building direction [31,33]. Furthermore, the differences between the results mentioned in the literature are because of the possible differences in the experimental conditions, such as temperature and humidity, level of powder reuse, different set of process parameters for SLS machines, and different firmware that could change the preset configuration for MJF machines.

Table 6
Ra roughness parameter measured on ISO 527 specimens.

	SLS	MJF
	Ra [μm]	Ra [μm]
Top face	10.4 ± 1.6	8.7 ± 0.9
Bottom face	15.0 ± 2.3	13.3 ± 1.0
Building direction	10.8 ± 0.8	11.2 ± 1.2

Fig. 8 shows the S–N curves obtained from fatigue tests. The curves are statistically estimated according to the ISO 12107 standard, for ASTM E606 samples and SF, CYF, and CC lattice specimens, fabricated with both SLS (Fig. 8a) and MJF (Fig. 8b) technologies.

In Table 8 the fitting parameters b_0 and b_1 for the fitting model equation

$$\log_{10}N = b_0 + b_1 \cdot \log_{10}S \tag{7}$$

are reported, together with the standard deviation SD and the correlation parameter R^2.

SLS bulk specimens perform better than MJF ones for stresses higher than 34 MPa. At 32 MPa, the MJF samples fail at a greater number of cycles, approaching the knee of the curve and the fatigue limit. In Fig. 9a and b, the SEM analyses on the fracture surface of the SLS cylindrical samples show a brittle crazing mechanism with large dimple areas, in accordance with Salazar et al. studies [68,69]. The SEM analyses on the MJF specimens fracture surface in Fig. 9c show a different failure mechanism, already described in the literature [70]: the fracture initiates on the contour of the sample, then the crack propagates on the smooth region of the surface, and the final fracture happens on the rough central part of the surface. Porosities are detected in both the technologies, but to a greater extent in the SLS one, in accordance with He-pycnometry measurements in Table 4. Nevertheless, the porosity of a single section does not necessarily reflect the porosity of the entire geometry, especially when considering the section where the failure occurs, where the worst scenario is expected, i.e. higher porosity and defects. Furthermore, the pores do not necessarily affect the fatigue life of thermoplastic materials negatively. When loaded, the porous material deforms and micro-void coalescence occurs; at this point, three possible mechanisms can arise [29]:

1. Local melt zone formation, that stabilizes the crack growth;
2. If the temperature stays under the glass transition temperature, relative sliding between chain molecules occurs, allowing more elasticity;
3. the increasing of the temperature leads to a change in crystalline phases from the γ-form to the α-form; this can cause the molecular chains to shift in a preferential orientation, resulting in an improved fatigue resistance.

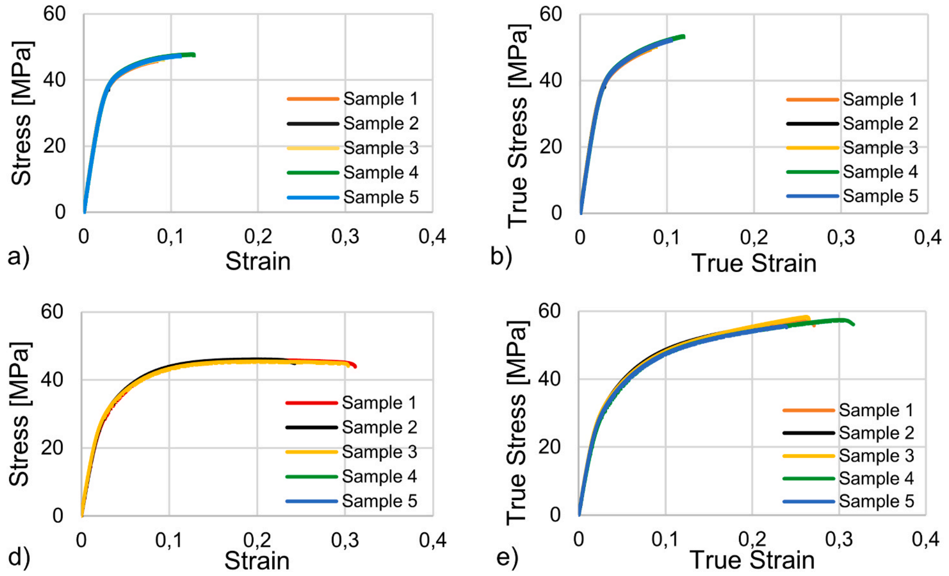

c)

SLS	
E [GPa]	1.87±0.04
UTS [MPa]	46.93±0.86
ε_{max} %	10.3±1.9
Toughness [J/m^3]	3.8±0.9

f)

MJF	
E [GPa]	1.53±0.06
UTS [MPa]	45.59±0.38
ε_{max} %	30.0±4.9
Toughness [J/m^3]	11.7±2.1

Fig. 6. Tensile test curves for ISO 527 specimens. a) SLS Stress–Strain, b) SLS True stress–True strain, c) SLS specimens mechanical properties, d) MJF Stress–Strain, e) MJF True stress–True strain, f) MJF specimens mechanical properties.

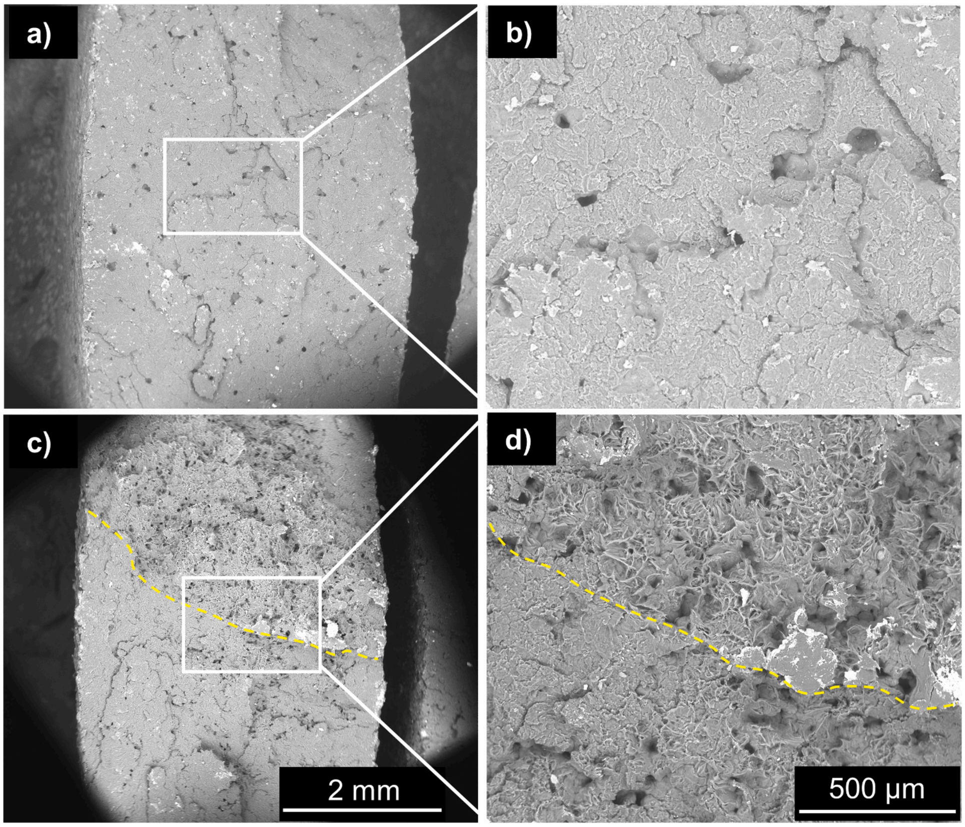

Fig. 7. SEM analyses on fracture surface from static tests on ISO 527 specimens: a) and b) SLS, c) and d) MJF.

To have a wider vision on the phenomenon, further studies are needed where the temperature of the samples in the fracture zone is monitored during the fatigue tests.

Analyzing lattice structures, at high stresses CYF and CC have a behavior similar to the two technologies, but since the slope of MJF is higher, the SLS samples have a longer life at low stresses; the same slope is found in SF samples, but the ones manufactured by MJF have a life behavior better than even CYF, as opposed to SLS where the CYF type behaves better than SF. In general, CC structures show the best behavior between the lattice samples. This is owing to the Catmull–Clark subdivision approach that results in smoother surfaces with respect to standard filleting operations inside the CAD software; as can be seen in Fig. 10, surface curvature for the CC specimens is G2 (curvature continuity), except at extraordinary vertices (i.e. vertices in a quadrilateral mesh in which the number of incident edges differs from 4 [71]), whereas the surfaces of fillets realized with software command are G1

Table 7
Comparison of the tensile properties of PA12 parts, fabricated by powder bed fusion processes.

Technology	E [GPa]	UTS [MPa]	ε_{max} %	Printing direction	Ref.
SLS	1.76 ± 0.02	43.6 ± 0.5	31.6 ± 2.9	XY plane	[38]
	1.68 ± 0.04	47.6 ± 1.4	6.6 ± 0.5	X axis	[39]
	1.61 ± 0.06	40.6 ± 3.2	3.7 ± 0.5	Z axis	
	1.72 ± 0.01	45.1 ± 0.5	10.0 ± 0.1	XY plane	[68]
	1.64 ± 0.01	46.4 ± 0.1	16.9 ± 0.1	X axis	[49]
	2.16 ± 0.05	49.0 ± 1.7	4.0 ± 0.3	Z axis	[30]
	1.39 ± 0.03	44.0 ± 0.1	27.6 ± 2.6	X axis	
	1.61 ± 0.10	43.9 ± 0.7	26.6 ± 2.9	Y axis	[40]
	1.22 ± 0.03	39.6 ± 0.2	14.7 ± 1.1	Z axis	
	1.87 ± 0.04	46.9 ± 0.9	10.3 ± 1.9	Z axis	(Current study)
MJF	1.42 ± 0.04	40.1 ± 1.5	17.5 ± 3.9	XY plane	[38]
	1.13 ± 0.07	45.8 ± 3.5	11.2 ± 1.8	X axis	[39]
	1.20 ± 0.08	47.9 ± 0.9	13.2 ± 1.5	Y axis	
	1.34 ± 0.10	53.7 ± 1.1	11.4 ± 1.3	Z axis	
	1.24 ± 0.03	47.0 ± 0.9	19.0 ± 2.8	X axis	[31]
	1.15 ± 0.04	48.0 ± 0.8	27.0 ± 1.2	Y axis	
	1.25 ± 0.04	49.0 ± 0.6	16.0 ± 1.9	Z axis	
	3.94 ± 0.36	49.9 ± 1.9	3.3 ± 0.8	X axis	[33]
	3.97 ± 0.31	49.3 ± 3.4	2.2 ± 0.3	Z axis	
	1.37 ± 0.03	48.7 ± 0.8	27.4 ± 2.2	X axis	
	1.37 ± 0.07	44.5 ± 0.7	15.9 ± 1.1	Y axis	[40]
	1.67 ± 0.07	49.6 ± 1.2	14.8 ± 0.3	Z axis	
	1.53 ± 0.06	45.6 ± 0.4	30.0 ± 4.9	Z axis	(Current study)

XY plane is used as the printing direction whether the specimens were printed flat, and no printing direction axes were specified.

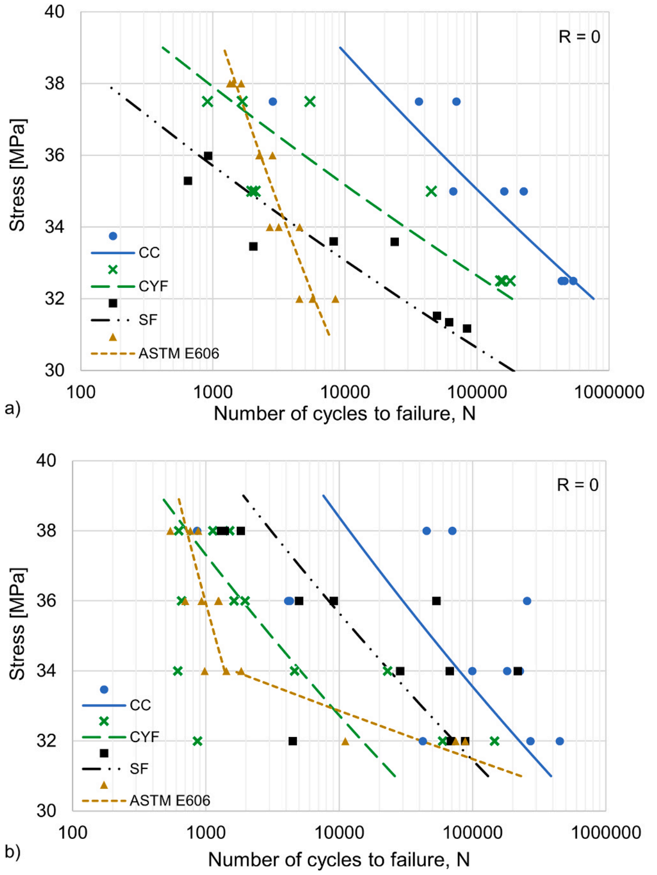

Fig. 8. Wöhler curves obtained from bulk and lattice structures samples: a) SLS, b) MJF.

Table 8
Statistical parameters for S–N curves, according to ISO 12107.

Technology	Specimen type	b_0	b_1	SD	R^2
SLS	ASTM E606	15.79	− 7.99	0.09	0.88
	SF	49.59	− 30.00	0.35	0.89
	CYF	51.58	− 30.77	0.53	0.74
	CC	39.48	− 22.32	0.43	0.69
MJF	ASTM E606	12.13	− 5.88	0.12	0.57
	(ASTM E606 knee)	85.49	− 53.73	0.34	0.85
	SF	32.57	− 18.41	0.60	0.47
	CYF	30.67	− 17.60	0.67	0.39
	CC	31.11	− 17.12	0.74	0.33

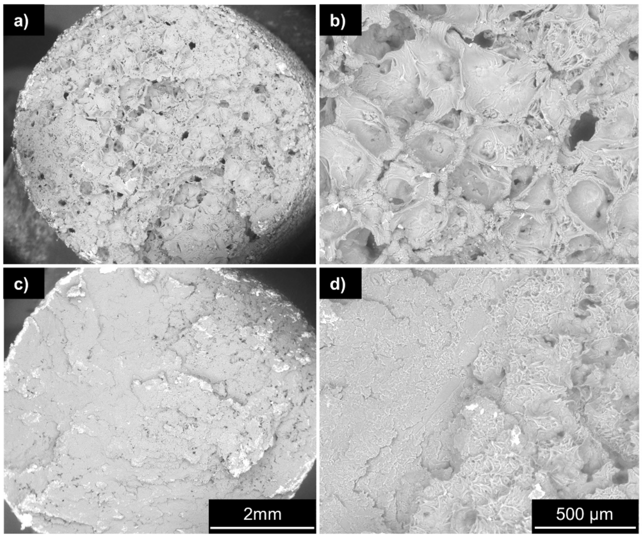

Fig. 9. SEM analyses on fracture surface from fatigue test from ASTM E606 bulk specimen: a) and b) SLS, c) and d) MJF.

(tangency continuity) [26]. This better surface curvature leads to a lower stress concentration and consequently, to a better fatigue life.

Some of the lattice specimens, especially the CC type, behave better than bulk ones, as opposed to the observations of a previous study that used selective laser-melted 316 stainless steel parts [72]. The different behavior could be explained firstly by the difference in the materials used (polymers vs metals) and secondly, by a scale effect due to the different size of the beams of the lattice structures; indeed, bigger beams as in PA12 specimens could help avoid failure driven by internal defects and porosities that reduce the effective area on a cross-section, and surface texture where roughness represents a weakness [28,73]. SEM analyses on the fracture surface of the different types of lattice structures confirm the failure mechanisms observed for the ASTM E606 specimens. The SLS lattices show the brittle crazing mechanism, especially the SF lattices (Fig. 11a) and the CC lattices (Fig. 11c), while the MJF lattices present more planar surfaces where the crack propagated before the failure of the samples. Some dimples are found in the MJF CYF specimen (Fig. 11e).

4. Conclusions

In this work, a comparison between SLS and MJF technologies used to produce PA12 components is presented. Both the powders and the printed parts underwent different experimental tests to characterize the microstructure and morphology; the printed parts also underwent dimensional and roughness measurements as well as mechanical and fatigue tests. In addition, fatigue tests on three types of lattice specimens were performed; the lattices were obtained by the regular repetition of a simple cubic unit cell, but each type of unit cell was geometrically

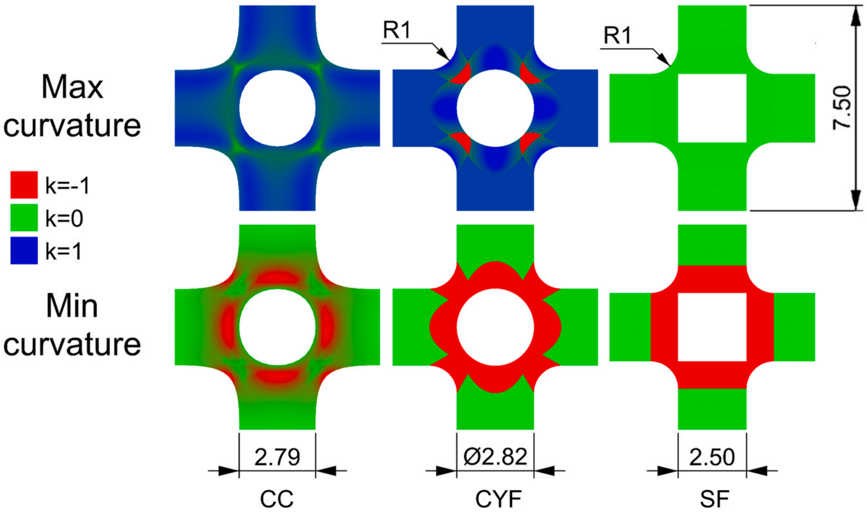

Fig. 10. Surface curvature analysis results performed on the lattice structures unit cells.

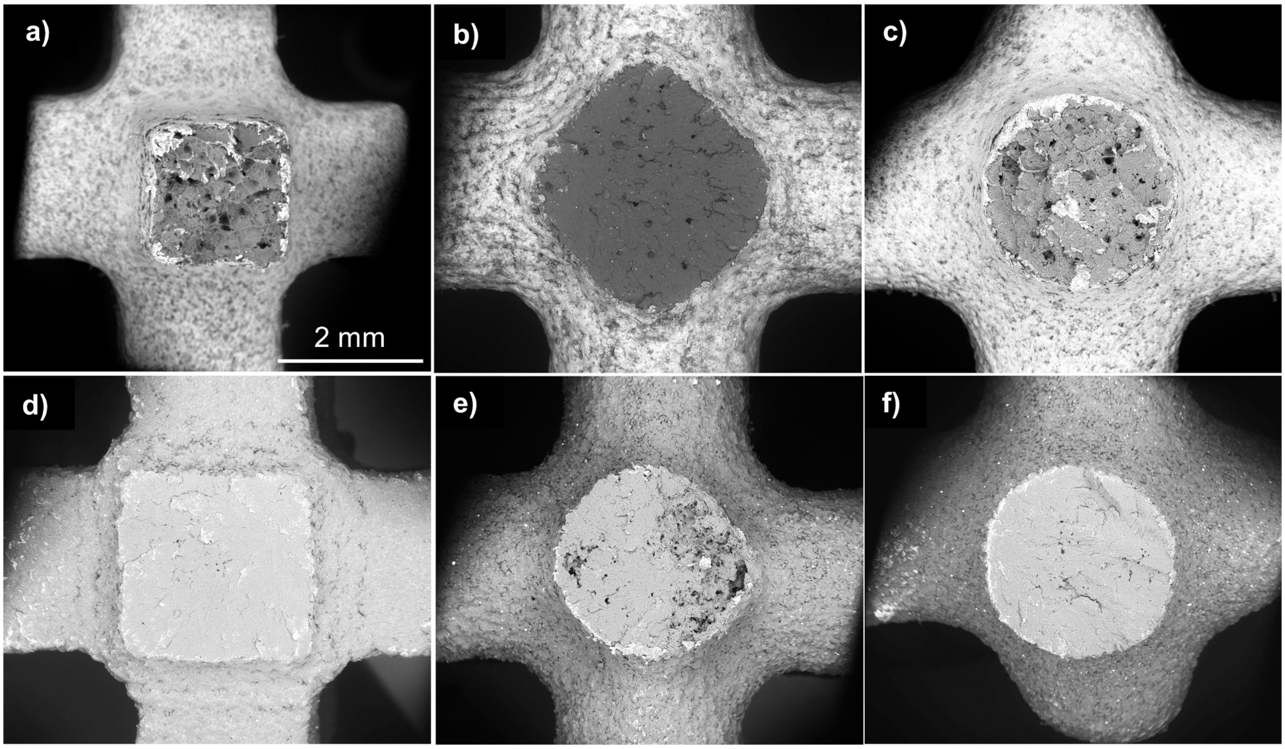

Fig. 11. SEM analyses on fracture surface of fatigue tested lattice structure specimens: a) SF SLS, b) CYF SLS, c) CC SLS, d) SF MJF, e) CYF MJF, and f) CC MJF.

modeled by adopting different approaches, resulting in three different filleting designs at nodal points; these modeling procedures do not depend on the material, and the results are applicable not only for parts with different materials, but also for parts fabricated by different processes. The obtained results can be summarized as follows:

- SEM analyses show MJF powders to be smoother than SLS ones. Some of the SLS powders are cracked, probably due to the solution – precipitation process in ethanol, at elevated temperature, used to produce the powders, or due to the evaporation of the remaining ethanol during the printing process.
- TGA-DSC analyses on SLS and MJF powders showed a single peak corresponding to the melting temperature of 188.6 ± 0.1 °C and 187.7 ± 0.2 °C, respectively. The printed samples show a translation of the peak to lower temperature, 183.1 ± 0.5 °C for SLS parts and 182.7 ± 0.4 °C for MJF parts, so as a broadening of the same peak. The crystallinity of the powders, 49.1 ± 0.5% for SLS and 48.3 ± 0.4% for MJF, decreased during the printing process to 24.5 ± 0.1% for SLS and 31.5 ± 0.3% for MJF.
- XRD on both the powders and final parts showed that in the starting powders both α-phase and γ-phase are present, whereas after printing mainly γ-phase and a small shoulder of α-phase can be detected. The microstructure of the two technologies does not show significant differences.
- He-pycnometry measurements indicated a total porosity of the final parts of 7.95 ± 0.09% for SLS and 6.75 ± 0.18% for MJF.
- Roughness measurements on the sample profile (Ra) showed similar values for the two processes, and they both resulted in a rougher

surface at the bottom face (15.0 ± 2.3 μm for SLS and 13.3 ± 1.0 μm for MJF) compared to the lateral face in the building direction (10.8 ± 0.8 μm for SLS and 11.2 ± 1.2 μm for MJF) and the top face (10.4 ± 1.6 μm for SLS and 8.7 ± 0.9 μm for MJF). This can be attributed to the presence of unmelted powders on the surface of the specimens, that did not undergo post-process operations.
- Static tensile tests showed that SLS specimens have a higher Young's modulus than MJF ones (1.87 ± 0.04 GPa for SLS and 1.53 ± 0.06 GPa for MJF), but a smaller deformation at break (0.10 ± 0.02 for SLS and 0.30 ± 0.05 MPa for MJF). The UTSs are similar (46.93 ± 0.86 MPa for SLS and 45.59 ± 0.38 MPa for MJF).
- SEM analyses on the fracture surface of ISO 527 specimens showed a brittle fracture mechanism for the SLS specimens, whereas a ductile fracture for the MJF ones. SEM analyses on fatigue tested cylindrical specimens highlighted a brittle crazing mechanism for the SLS samples, whereas in the MJF parts the crack initiated on the contour and slowly grew until the failure. The failure surfaces of the different types of lattice structures confirmed the fatigue behavior observed on the bulk specimens.
- Focusing on the geometric modeling methods, CC structures show the best behavior among the lattice samples due to the Catmull–Clark subdivision approach, which results in smoother surfaces with respect to standard filleting operations in the CAD software and leads to a lower stress concentration and better fatigue life. The Wöhler curves associated with MJF specimens present lower R^2 values than SLS. Compared to the lattice structures, bulk specimens highlighted better behavior at high stress but a worse behavior at low stress.

CRediT authorship contribution statement

Stefano Rosso: Investigation, Formal analysis, Writing - original draft, Writing - review & editing. **Roberto Meneghello:** Writing - review & editing, Supervision. **Lisa Biasetto:** Investigation, Formal analysis, Writing - review & editing. **Luca Grigolato:** Investigation, Formal analysis. **Gianmaria Concheri:** Supervision, Writing - review & editing, Funding acquisition. **Gianpaolo Savio:** Conceptualization, Project administration, Supervision, Writing - review & editing, Funding acquisition.

Declaration of Competing Interest

The authors declare that they have no known competing financial interests or personal relationships that could have appeared to influence the work reported in this paper.

Acknowledgments

This work was partially funded by Fondazione Cassa di Risparmio di Padova e Rovigo (CARIPARO), Italy, and grant 'BIRD 190850' by the Department of Civil, Environmental, and Architectural Engineering, University of Padova, Italy. The authors gratefully acknowledge generous in-kind support from 3Dfast s.r.l and 3DZ Franchising Limited Treviso for fabricating the test specimens. The authors acknowledge Anna De Marzi (University of Padova, Department of Industrial Engineering) for TGA-DSC measurements.

Data availability

The raw/processed data required to reproduce these findings can be partially shared upon request.

References

[1] J. Holmström, J. Partanen, J. Tuomi, M. Walter, Rapid manufacturing in the spare parts supply chain, J. Manuf. Technol. Manag. 21 (2010) 687–697, https://doi.org/10.1108/17410381011063996.

[2] M.K. Thompson, G. Moroni, T. Vaneker, G. Fadel, R.I. Campbell, I. Gibson, A. Bernard, J. Schulz, P. Graf, B. Ahuja, F. Martina, Design for additive manufacturing: trends, opportunities, considerations, and constraints, CIRP Ann. Manuf. Technol. 65 (2016) 737–760, https://doi.org/10.1016/j.cirp.2016.05.004.

[3] T. Wohlers, I. Campbell, O. Diegel, J. Kowen, T. Caffrey, Wohlers Report 2019, (2019).

[4] L.J. Tan, W. Zhu, K. Zhou, Recent progress on polymer materials for additive manufacturing, Adv. Funct. Mater. 30 (2020), 2003062, https://doi.org/10.1002/adfm.202003062.

[5] ISO/ASTM, ISO/ASTM 52900:2015 (ASTM F2792) - Additive manufacturing – general principles – terminology, (2015).

[6] C. Deckard, Selective Laser Sintering, University of Texas,, Austin, 1988.

[7] C. Deckard, Method and apparatus for producing parts by selective sintering, US4863538A, (1989).

[8] N. Hopkinson, P. Erasenthiran, High speed sintering—early research into a new rapid manufacturing process, in: Proceedings of the Solid Freeform Fabrication Symposium, (2004), pp. 312–320.

[9] H.R. Thomas, N. Hopkinson, P. Erasenthiran, High speed sintering—continuing research into a new rapid manufacturing process, in: Proceedings of the 17th SFF Symposium Austin, TX, (2006), pp. 682–691.

[10] B. Khoshnevis, B. Asiabanpour, M. Mojdeh, B. Koraishy, K. Palmer, Z. Deng, SIS-A New SFF Method Based on Powder Sintering, in: Proceedings of the 2002 International Solid Freeform Fabrication Symposium, (2002).

[11] B. Khoshnevis, B. Asiabanpour, M. Mojdeh, K. Palmer, SIS - a new SFF method based on powder sintering, Rapid Prototyp. J. 9 (2003) 30–36, https://doi.org/10.1108/13552540310455638.

[12] B. Scherer, I.L. Kottenstedde, F.M. Matysik, Material characterization of polyamide 12 and related agents used in the multi-jet fusion process: complementary application of high-resolution mass spectrometry and other advanced instrumental techniques, Mon. Fur Chem. 151 (2020) 1203–1215, https://doi.org/10.1007/s00706-020-02646-x.

[13] R.D. Goodridge, C.J. Tuck, R.J.M. Hague, Laser sintering of polyamides and other polymers, Prog. Mater. Sci. 57 (2012) 229–267, https://doi.org/10.1016/j.pmatsci.2011.04.001.

[14] A. Mazzoli, Selective laser sintering in biomedical engineering, Med. Biol. Eng. Comput. 51 (2013) 245–256, https://doi.org/10.1007/s11517-012-1001-x.

[15] J.P. Kruth, X. Wang, T. Laoui, L. Froyen, Lasers and materials in selective laser sintering, Assem. Autom. 23 (2003) 357–371, https://doi.org/10.1108/01445150310698652.

[16] K.H. Tan, C.K. Chua, K.F. Leong, C.M. Cheah, W.S. Gui, W.S. Tan, F.E. Wiria, Selective laser sintering of biocompatible polymers for applications in tissue engineering, Biomed. Mater. Eng. 15 (2005) 113–124.

[17] G.V. Salmoria, J.L. Leite, R.A. Paggi, The microstructural characterization of PA6/PA12 blend specimens fabricated by selective laser sintering, Polym. Test. 28 (2009) 746–751, https://doi.org/10.1016/j.polymertesting.2009.06.010.

[18] B. Van Hooreweder, F. De Coninck, D. Moens, R. Boonen, P. Sas, Microstructural characterization of SLS-PA12 specimens under dynamic tension/compression excitation, Polym. Test. 29 (2010) 319–326, https://doi.org/10.1016/j.polymertesting.2009.12.006.

[19] M. Schmidt, D. Pohle, T. Rechtenwald, Selective laser sintering of PEEK, CIRP Ann. Manuf. Technol. 56 (2007) 205–208, https://doi.org/10.1016/j.cirp.2007.05.097.

[20] H. Zarringhalam, N. Hopkinson, N.F. Kamperman, J.J. de Vlieger, Effects of processing on microstructure and properties of SLS Nylon 12, Mater. Sci. Eng. A 435–436 (2006) 172–180, https://doi.org/10.1016/j.msea.2006.07.084.

[21] S. Dadbakhsh, L. Verbelen, O. Verkinderen, D. Strobbe, P. Van Puyvelde, J.-P. Kruth, Effect of PA12 powder reuse on coalescence behaviour and microstructure of SLS parts, Eur. Polym. J. 92 (2017) 250–262, https://doi.org/10.1016/j.eurpolymj.2017.05.014.

[22] B. Caulfield, P.E. McHugh, S. Lohfeld, Dependence of mechanical properties of polyamide components on build parameters in the SLS process, J. Mater. Process. Technol. 182 (2007) 477–488, https://doi.org/10.1016/j.jmatprotec.2006.09.007.

[23] S. Singh, V.S. Sharma, A. Sachdeva, S.K. Sinha, Optimization and analysis of mechanical properties for selective laser sintered polyamide parts, Mater. Manuf. Process. 28 (2013) 163–172, https://doi.org/10.1080/10426914.2012.677901.

[24] A. Sachdeva, S. Singh, V.S. Sharma, Investigating surface roughness of parts produced by SLS process, Int. J. Adv. Manuf. Technol. 64 (2013) 1505–1516, https://doi.org/10.1007/s00170-012-4118-z.

[25] P. Obst, M. Launhardt, D. Drummer, P.V. Osswald, T.A. Osswald, Failure criterion for PA12 SLS additive manufactured parts, Addit. Manuf. 21 (2018) 619–627, https://doi.org/10.1016/j.addma.2018.04.008.

[26] G. Savio, S. Rosso, A. Curtarello, R. Meneghello, G. Concheri, Implications of modeling approaches on the fatigue behavior of cellular solids, Addit. Manuf. 25 (2019) 50–58, https://doi.org/10.1016/j.addma.2018.10.047.

[27] J. Munguia, K. Dalgarno, Fatigue behaviour of laser-sintered PA12 specimens under four-point rotating bending, Rapid Prototyp. J. 20 (2014) 291–300, https://doi.org/10.1108/RPJ-07-2012-0064.

[28] M. Blattmeier, G. Witt, J. Wortberg, J. Eggert, J. Toepker, Influence of surface characteristics on fatigue behaviour of laser sintered plastics, Rapid Prototyp. J. 18 (2012) 161–171, https://doi.org/10.1108/13552541211212140.

[29] B. Van Hooreweder, D. Moens, R. Boonen, J.P. Kruth, P. Sas, On the difference in material structure and fatigue properties of nylon specimens produced by injection molding and selective laser sintering, Polym. Test. 32 (2013) 972–981, https://doi.org/10.1016/j.polymertesting.2013.04.014.

[30] B. Van Hooreweder, J.P. Kruth, High cycle fatigue properties of selective laser sintered parts in polyamide 12, CIRP Ann. Manuf. Technol. 63 (2014) 241–244, https://doi.org/10.1016/j.cirp.2014.03.060.

[31] H.J. O'Connor, A.N. Dickson, D.P. Dowling, Evaluation of the mechanical performance of polymer parts fabricated using a production scale multi jet fusion printing process, Addit. Manuf. 22 (2018) 381–387, https://doi.org/10.1016/j.addma.2018.05.035.

[32] H.J.O.' Connor, D.P. Dowling, Comparison between the properties of polyamide 12 and glass bead filled polyamide 12 using the multi jet fusion printing process, Addit. Manuf. 31 (2019), 100961, https://doi.org/10.1016/j.addma.2019.100961.

[33] S. Morales-Planas, J. Minguella-Canela, J. Lluma-Fuentes, J.A. Travieso-Rodriguez, A.A. García-Granada, Multi Jet Fusion PA12 manufacturing parameters for watertightness, strength and tolerances, Materials 11 (2018) 1472, https://doi.org/10.3390/ma11081472.

[34] M. Mele, G. Campana, G.L. Monti, Modelling of the capillarity effect in Multi Jet Fusion technology, Addit. Manuf. 30 (2019), 100879, https://doi.org/10.1016/j.addma.2019.100879.

[35] F.N. Habib, P. Iovenitti, S.H. Masood, M. Nikzad, Fabrication of polymeric lattice structures for optimum energy absorption using Multi Jet Fusion technology, Mater. Des. 155 (2018) 86–98, https://doi.org/10.1016/j.matdes.2018.05.059.

[36] D. Fradl, J. Panditaratne, J. Bi, R. Fu, V. Oancea, Finite element simulation of the Multi Jet Fusion (MJF^{TM}) process using Abaqus, Sci. Age Exp. (2017) 440–469. ⟨https://pdfs.semanticscholar.org/fb66/17aab5ff74f47709ebfecb694d32f23ceff2.pdf⟩. accessed January 23, 2020.

[37] https://doi.org/10.1109/CPPS.2016.7483916H. Kim, Y. Zhao, L. Zhao, Process-level modeling and simulation for HP's Multi Jet Fusion 3D printing technology, in: Proceedings of the 2016 1st Int. Work. Cyber-Physical Prod. Syst. CPPS 2016, Institute of Electrical and Electronics Engineers Inc., (2016).

[38] Z. Xu, Y. Wang, D. Wu, K.P. Ananth, J. Bai, The process and performance comparison of polyamide 12 manufactured by multi jet fusion and selective laser sintering, J. Manuf. Process. 47 (2019) 419–426, https://doi.org/10.1016/j.jmapro.2019.07.014.

[39] F. Sillani, R.G. Kleijnen, M. Vetterli, M. Schmid, K. Wegener, Selective laser sintering and multi jet fusion: process-induced modification of the raw materials and analyses of parts performance, Addit. Manuf. 27 (2019) 32–41, https://doi.org/10.1016/j.addma.2019.02.004.

[40] C. Cai, W.S. Tey, J. Chen, W. Zhu, X. Liu, T. Liu, L. Zhao, K. Zhou, Comparative study on 3D printing of polyamide 12 by selective laser sintering and multi jet fusion, J. Mater. Process. Technol. 288 (2021), 116882, https://doi.org/10.1016/j.jmatprotec.2020.116882.

[41] C.E. Majewski, D. Oduye, H.R. Thomas, N. Hopkinson, Effect of infra-red power level on the sintering behaviour in the high speed sintering process, Rapid Prototyp. J. 14 (2008) 155–160, https://doi.org/10.1108/13552540810878012.

[42] A. Ellis, C.J. Noble, N. Hopkinson, High speed sintering: assessing the influence of print density on microstructure and mechanical properties of nylon parts, Addit. Manuf. 1 (2014) 48–51, https://doi.org/10.1016/j.addma.2014.07.003.

[43] B. Asiabanpour, K. Palmer, B. Khoshnevis, An experimental study of surface quality and dimensional accuracy for selective inhibition of sintering, Rapid Prototyp. J. 10 (2004) 181–192, https://doi.org/10.1108/13552540410539003.

[44] B. Asiabanpour, B. Khoshnevis, K. Palmer, Advancements in the selective inhibition sintering process development, Virtual Phys. Prototyp. 1 (2006) 43–52, https://doi.org/10.1080/17452750500289910.

[45] V.S. Deshpande, M.F. Ashby, N.A. Fleck, Foam topology: bending versus stretching dominated architectures, Acta Mater. 49 (2001) 1035–1040, https://doi.org/10.1016/S1359-6454(00)00379-7.

[46] H. Kim, Y. Zhao, L. Zhao, Process-level modeling and simulation for HP's Multi Jet Fusion 3D printing technology, in: Proceedings of the 2016 1st Int. Work. Cyber-Physical Prod. Syst. CPPS 2016, (2016), pp. 1–4. ⟨https://doi.org/10.1109/CPPS.2016.7483916⟩.

[47] M. Pavan, T. Craeghs, P. Van Puyvelde, J. Kruth, W. Dewulf, Understanding the link between process parameters, microstructure and mechanical properties of laser sintered PA12 parts through X-ray computed tomography, (2016).

[48] PA 2200 Performance 1.0, EOS GmbH - Electro Opt. Syst., (2018). ⟨https://eos.materialdatacenter.com/eo/⟩ (Accessed November 18, 2019).

[49] A. Pilipović, T. Brajlih, I. Drstvenšek, Influence of processing parameters on tensile properties of SLS Polymer product, Polymers 10 (2018) 1208, https://doi.org/10.3390/polym10111208.

[50] HP 3D High Reusability PA 12 - Datasheet, (2017). ⟨https://cimquest-inc.com/resource-center/HP/Materials/HP-PA12-Datasheet.pdf⟩ (Accessed February 3, 2020).

[51] EOS, PA 2200 Material data sheet, (2008). ⟨http://www.shapeways.com/topics/udesign/materials/white_strong_flexible/pa2200_material_data_sheet_12_08_en_.pdf⟩ (Accessed September 17, 2020).

[52] G. Savio, R. Meneghello, G. Concheri, Geometric modeling of lattice structures for additive manufacturing, Rapid Prototyp. J. 24 (2018) 351–360, https://doi.org/10.1108/RPJ-07-2016-0122.

[53] E. Catmull, J. Clark, Recursively generated B-spline surfaces on arbitrary topological meshes, Comput. Des. 10 (1978) 350–355, https://doi.org/10.1016/0010-4485(78)90110-0.

[54] S. Gogolewski, K. Czerntawska, M. Gastorek, Effect of annealing on thermal properties and crystalline structure of polyamides. Nylon 12 (polylaurolactam), Colloid Polym. Sci. Kolloid Z. Z. Für Polym. 258 (1980) 1130–1136, https://doi.org/10.1007/BF01382456.

[55] L. Biasetto, P. Zanonato, S. Carturan, P. Di Bernardo, P. Colombo, A. Andrighetto, G. Prete, Lanthanum carbide-based porous materials from carburization of lanthanum oxide and lanthanum oxalate mixtures, J. Nucl. Mater. 378 (2008) 180–187, https://doi.org/10.1016/j.jnucmat.2008.06.016.

[56] ISO International Organization for Standardization, ISO 527–1:2012 - Plastics – determination of tensile properties – Part 1: general principles, (2012).

[57] ASTM, ASTM E606/E606M - 2012 – Standard test method for strain-controlled fatigue testing, (2012).

[58] ISO International Organization for Standardization, ISO 4287:1997 - Geometrical Product Specifications (GPS) – surface texture: profile method – terms, definitions and surface texture parameters, (1997).

[59] ISO International Organization for Standardization, ISO 4288:1996 - Geometrical Product Specifications (GPS) – surface texture: profile method – rules and procedures for the assessment of surface texture, (1996).

[60] R.G. Budynas. Shigley's Mechanical Engineering Design, 10th ed.,, McGraw-Hill Education,, New York NY, 2015.

[61] S. Kalpakjian, S. Schmid. Manufacturing Engineering and Technology, 7th ed.,, Pearson,, 2013.

[62] ISO International Organization for Standardization, ISO 12107:2012 – Metallic materials – fatigue testing – statistical planning and analysis of data, (2012).

[63] L. Verbelen, S. Dadbakhsh, M. Van Den Eynde, J.P. Kruth, B. Goderis, P. Van Puyvelde, Characterization of polyamide powders for determination of laser sintering processability, Eur. Polym. J. 75 (2016) 163–174, https://doi.org/10.1016/j.eurpolymj.2015.12.014.

[64] M. Schmid, A. Amado, K. Wegener, Materials perspective of polymers for additive manufacturing with selective laser sintering, J. Mater. Res. 29 (2014) 1824–1832, https://doi.org/10.1557/jmr.2014.138.

[65] M. Schmid, R. Kleijnen, M. Vetterli, K. Wegener, Influence of the origin of polyamide 12 powder on the laser sintering process and laser sintered parts, Appl. Sci. 7 (2017) 462, https://doi.org/10.3390/app7050462.

[66] T. Ishikawa, S. Nagai, N. Kasai, Thermal behavior of α nylon-12, J. Polym. Sci. Polym. Phys. Ed. 18 (1980) 1413–1419, https://doi.org/10.1002/pol.1980.180180619.

[67] P. Chen, H. Wu, W. Zhu, L. Yang, Z. Li, C. Yan, S. Wen, Y. Shi, Investigation into the processability, recyclability and crystalline structure of selective laser sintered Polyamide 6 in comparison with Polyamide 12, Polym. Test. 69 (2018) 366–374, https://doi.org/10.1016/j.polymertesting.2018.05.045.

[68] A. Salazar, A. Rico, J. Rodríguez, J. Segurado Escudero, R. Seltzer, F. Martin De La Escalera Cutillas, Fatigue crack growth of SLS polyamide 12: effect of reinforcement and temperature, Compos. Part B Eng. 59 (2014) 285–292, https://doi.org/10.1016/j.compositesb.2013.12.017.

[69] A. Salazar, A. Rico, J. Rodríguez, J. Segurado Escudero, R. Seltzer, F. Martin De La Escalera Cutillas, Monotonic loading and fatigue response of a bio-based polyamide PA11 and a petrol-based polyamide PA12 manufactured by selective laser sintering, Eur. Polym. J. 59 (2014) 36–45, https://doi.org/10.1016/j.eurpolymj.2014.07.016.

[70] J.A. Sauer, G.C. Richardson, Fatigue of polymers, Int. J. Fract. 16 (1980) 499–532, https://doi.org/10.1007/BF02265215.

[71] D. Zorin, Subdivision zoo, Subdiv. Model. Animat. (2000) 65–104.

[72] S. Rosso, R. Meneghello, G. Concheri, G. Savio, Scale and shape effects on the fatigue behaviour of additively manufactured SS316L structures: a preliminary study, in: C. Rizzi, A.O. Andrisano, F. Leali, F. Gherardini, F. Pini, A. Vergnano (Eds.), Des. Tools Methods Ind. Eng., Springer International Publishing, Cham, 2020, pp. 879–890.

[73] L. Safai, J.S. Cuellar, G. Smit, A.A. Zadpoor, A review of the fatigue behavior of 3D printed polymers, Addit. Manuf. 28 (2019) 87–97, https://doi.org/10.1016/j.addma.2019.03.023.

Scale and Shape Effects on the Fatigue Behaviour of Additively Manufactured SS316L Structures: A Preliminary Study

Stefano Rosso[1](✉), Roberto Meneghello[1], Gianmaria Concheri[2], and Gianpaolo Savio[2]

[1] Department of Management and Engineering,
Laboratory of Design Tools and Methods in Industrial Engineering,
University of Padova, Stradella S. Nicola, 3, 36100 Vicenza, Italy
`stefano.rosso.3@phd.unipd.it`
[2] Department of Civil, Environmental and Architectural Engineering,
Laboratory of Design Tools and Methods in Industrial Engineering,
University of Padova, Via Venezia, 1, 35131 Padua, Italy

Abstract. The freedom in geometry given by additive manufacturing allows to produce cellular materials, also called lattice structures, with unit cells and mesoscale features that are impossible to obtain with traditional manufacturing techniques. The geometric modeling of lattice structures still presents issues such as robustness and automation, but, with a novel modeling approach based on subdivision surface algorithm, these troubles were limited. Furthermore, the subdivision method smooths surfaces, avoiding sharp edges at nodal points and increasing performances in fatigue properties. The aim of this work is twofold; a. The subdivision surface method is validated through fatigue tests on specimen additively manufactured by selective laser melting technology in SS316L stainless steel; dynamic tests were carried out on two types of lattice structures based on cubic cell: one obtained with a traditional modeling method, one obtained with a subdivision surface approach. b. Additional tests on bulk cylindrical samples, allowed to propose a preliminary model that describes the fatigue behaviour of additively manufactured lattices as a function of the bulk material properties, considering the shape and scale effects coming from stress concentration factor, increased area, surface roughness and porosity of the part. Results show that the subdivision surface approach improves the fatigue life of lattice structures, as expected. More, the lattices have a worse fatigue life compared to the bulk samples due to the scale and shape effects, that results in a higher sensibility to surface and internal defects related to the manufacturing process.

Keywords: Additive manufacturing · Lattice structure · Fatigue behaviour · Scale effect · Shape effect

© Springer Nature Switzerland AG 2020
C. Rizzi et al. (Eds.): ADM 2019, LNME, pp. 879–890, 2020.
https://doi.org/10.1007/978-3-030-31154-4_75

1 Introduction

Additive manufacturing (AM) and its layer-by-layer approach allow producing parts with extreme freedom in geometry. More, AM presents other benefits if compared to conventional techniques: design can be optimized for function and customized for different users, design of the final part can quickly change, small production batches become more feasible and economical, and material wasting is reduced [1]. Looking at the market, it is also possible to see an exponential rise in metal AM systems sales, supported by the significant growth of the revenues from metals for AM [2]. Furthermore, the layer-wise approach of AM technology enables the production of cellular materials [3], also called lattice structures. In addition to the fact of being lightweight, lattices present other interesting properties: they are stiff in relation to their low mass, they are good energy absorbers thanks to the possibility to undergo large deformations, good acoustic insulators thanks to the internal porosity and good heat exchangers due to their large surface area [4]. While the static behaviour of metal lattice structures produced by SLM has been extensively studied, the fatigue behaviour still needs to be analyzed deeper [5]. In this scenario, the need for characterization of materials tailored for AM has been highlighted in [6] and [7] and is an essential task that has to be addressed in order to guarantee that AM parts have the same mechanical performance of parts produced with more traditional subtractive technologies. Another important point for the characterization of additively manufactured parts is the understanding of the influence of surface texture and porosity on mechanical properties, considering also the sensitivity of these two parameters to the size and shape of the geometry [8].

Greitemeier et al. [9] studied the effect of surface roughness on fatigue life of AM Ti6Al4V samples, showing that the fatigue properties highly depend on this parameter, and formulating a model based on an equivalent initial flaw size (EIFS). Masuo et al. [10] identified the major factors that influence the fatigue strength of AM materials as microstructure, build direction [11, 12], defects (i.e. surface roughness, pores, lack of fusion, shrinkage and inclusions) and residual stress, and proposed a method for estimating the effect of defects with the $\sqrt{area}$ parameter. Wycisk et al. [13] analyzed and simulated the fatigue life and crack propagation considering AM defects, such as porosity and surface roughness.

Nevertheless, further studies that investigate the effect on fatigue behaviour of typical AM defects on parts with respect to the wrought material are needed, especially when dealing with complex geometries such as lattice structures.

The aim of this study is twofold. a. A previously presented method for modeling lattice structures based on a subdivision surface algorithm [14] was tested to verify its actual effectiveness in enhancing the fatigue life of the parts with respect to a more standard method; b. A preliminary model was proposed in order to describe the sensitivity of AM parts to typical AM defects, coming from the technology, i.e. porosity and surface roughness, and from the modeling phase, i.e. sharp edges, especially when dealing with scale and shape effects. To do so, three types of specimens were additively manufactured with selective laser melting (SLM) technology in 316L stainless steel (SS316L): bulk parts, lattice structures modeled with a traditional approach, and lattice structures modeled with the subdivision surface method.

2 Materials and Methods

2.1 Specimens

Three types of specimens were designed. Bulk cylindrical (BC) specimens were adapted from ASTM E606/606M – 12 standard [15], adopting the dimensions in Fig. 1. The diameter of the central uniform section was reduced to 2.8 mm to obtain an area close to 6 mm^2, similar to the resistant area of 6 beams with unitary area as in the lattice samples.

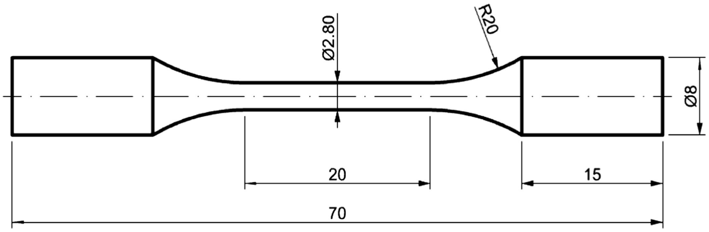

Fig. 1. Bulk cylindrical specimens dimensions.

Then, two types of lattice structures were modeled, cylindrical (CY) and Catmull-Clark (CC); both of them are made up from a regular repetition of a simple cubic cell; the number of instances is 3, 2 and 7 along x-, y-, z- axes, respectively. The cylindrical beams around the wireframe have been modeled with two different approaches; in the CY unit cell, the beams approaching nodal points are simply intersected, generating sharp edges; the CC unit cell, instead, is modelled adopting the Catmull-Clark subdivision surface algorithm [14, 16]: starting from a quadrilateral mesh, the initial vertices are iteratively averaged following the subdivision rule, splitting into four each quad face and resulting in a smooth surface, especially at nodal points, without the need for additional filleting operations. Figure 2 shows the CY and CC unit cell, and a lattice specimen. The dimension of the beams of the lattice specimens are obtained in order to ensure a cross-section area of 1 mm^2 for each beam, and cell size of 3 mm; the beams of the CY specimens have a diameter of 1.128 mm, while the CC has a beam dimension ranging between 1.116 mm and 1.150 (the section of a CC beam is not a circle). Moreover, all the specimen types have a similar cross-section area, 6.16 mm^2 for BC, 6 mm^2 for CY and CC lattices; this allows to concentrate on the mechanical fatigue behaviour of specimens originating from different modeling approaches. More, the adopted dimensions respect technological constraints, such as minimum hole size for de-powdering and minimum struts size.

A total of 36 specimens, 12 for each specimen type, were manufactured in 316L stainless steel by SLM technology, using the AM400 machine by Renishaw. Renishaw SS316L-0409 powder was used, and its main properties are reported in Table 1. The SS316L is an austenitic stainless steel and presents good weldability, machinability and high corrosion resistance; it is widely used in cyclically loaded components in a variety of engineering sectors such as automotive, construction, refinery, oil and gas, and chemical and petrochemical industries [17].

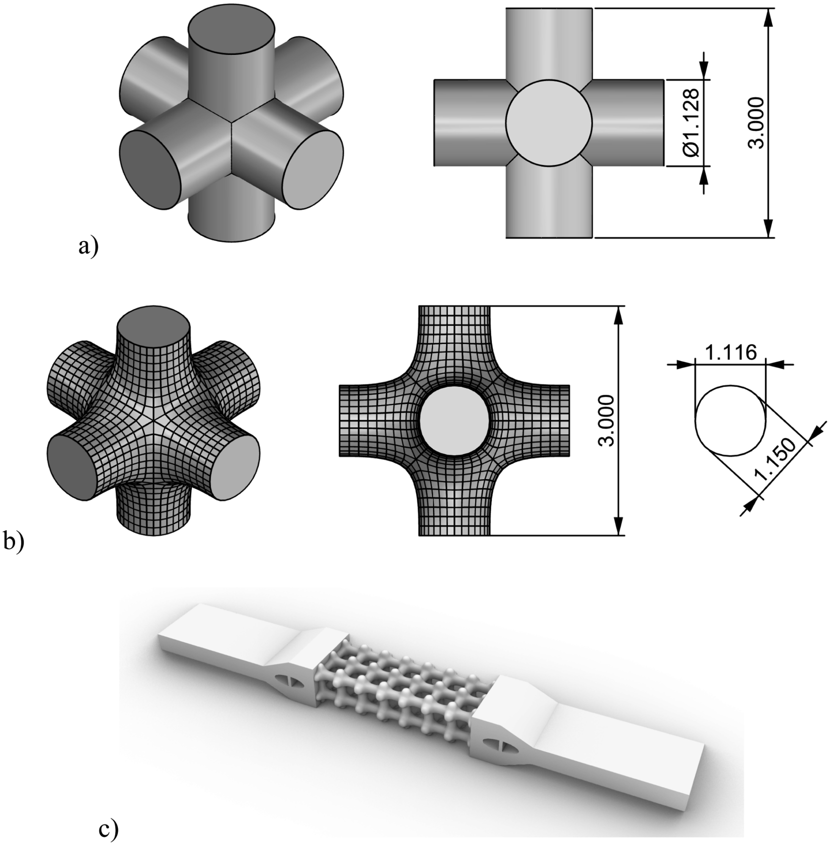

Fig. 2. (a) Cylindrical unit cell, (b) Catmull-Clark unit cell, (c) lattice specimen.

Table 1. Renishaw SS316L-0409 stainless steel powder properties.

Powder composition	
Element	Mass (%)
Iron	Balance
Chromium	17.6
Nickel	12.7
Molybdenum	2.32
Manganese	1.31

Particle size*	
Percentile	Diameter [μm]
$d_{10\%}$	18.8
$d_{50\%}$	29.4
$d_{90\%}$	45.5

*Laser diffraction analysis

All specimens were manufactured adopting the process parameters summarized in Table 2, “Interior” column; only for BC parts, different process parameters were used at the borders. The build direction was parallel to the longitudinal axis of the specimens and to the loading direction. The samples were tested as-built, i.e. no post-processing operations were performed, except for powder evacuation and supports removal.

Table 2. Process parameters.

	Interior	Borders
Laser power [W]	200	110
Exposure time [µs]	80	100
Point distance [µm]	60	20
Layer thickness [µm]	50	50
Layer rotation angle [°]	67	67
Scan pattern	Stripe	Contour

2.2 Experimental Tests

Specimens were weighed, and measured by the optical coordinate measuring machine (CMM) OGP SmartScope Flash 200: diameters of the central section were measured for BC samples and diameters of the beams were measured for CY and CC ones; a routine was created in Zone3 software, in which the beams are optically detected and measured; measurements were taken both in the front (3 × 7 cells) and side (2 × 7 cells) face of the lattice. Surface roughness along building direction was measured by a Talysurf i-Series. Measurement was taken in the central section of 2.80 mm diameter for the BC samples, while for the lattice structures specimens, due to the difficulty to measure the beams of the lattice, measurements were taken on the flat surfaces at the extremity of the samples, where they are gripped to the testing machine. The following parameters were used for roughness measurement and analysis: evaluation length = 12.5 mm, sampling length = 2.5 mm, according to ISO 4287 [18] and ISO 4288 [19] standards.

For CY and CC cells, numerical analyses were done to calculate the curvature and the stress concentration factor k_t, defined as $k_t = \sigma_{peak}/\sigma_{nom}$, where σ_{nom} is the applied force divided by the strut section area and σ_{peak} is the maximum Von Mises stress on the cell. Minimum and maximum surface curvature were analysed in Rhinoceros 6 using AdvMesh tool from Rhino Open Projects. k_t was obtained in ANSYS® Release 16 by the finite element analysis (FEA) of a simplified model allowing to study a single cell, as if it was surrounded by others [20].

Then, fatigue tests were executed on an MTS Acumen 3 Electrodynamic Test System equipped with a 3 kN load cell and an MTS 634.31 F extensometer. Tests were performed at 10 Hz frequency with 0 stress ratio (R = 0, i.e. $\sigma_{max}/\sigma_{min} = 0$, where σ is the stress). Each type of specimen was tested at 4 different stress levels, 473.2 MPa, 405.6 MPa, 338 MPa and 270.4 MPa, equal to 70%, 60%, 50% and 40% of the ultimate tensile strength (UTS), 676 MPa, according to Renishaw's SS316L datasheet [21]. Data were acquired with a timed trigger at 64 Hz to store entire cycles signals and with a peak-and-valley trigger to store minimum and maximum signals at every cycle. No artificial cooling was applied. The estimated Stress – Number of cycles (S-N) curves, also known as Wöhler curves, were statistically computed according to standard ISO/DIS 12107 [22].

3 Results and Discussions

Figure 3 shows one printed sample for each type of specimen. Due to the lack of post-processing procedures such as sandblasting or chemical etching [23], in the magnified view of the lattice structure of CY and CC specimens, it is possible to observe some partially melted powder, especially at bottom surfaces.

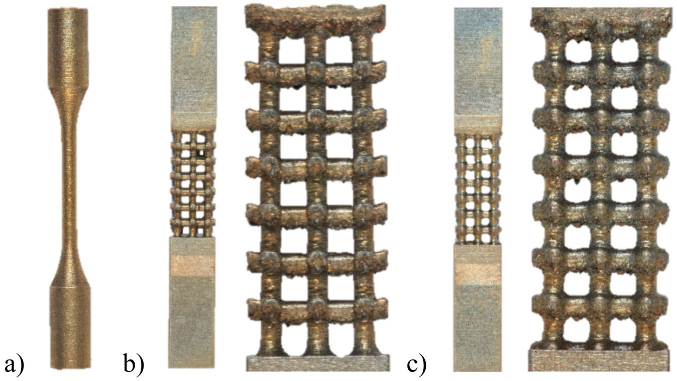

Fig. 3. SLM SS316L specimens: (a) BC sample, (b) CY sample, (c) CC sample.

Table 3 presents the average values and the standard deviations for mass and diameter dimension of the specimens, compared with nominal values. Nominal mass is obtained adopting a density of 7.99 g/cm^3, according to the datasheet, and calculating the volume of the geometric model. For CY and CC models only the diameters of the beams aligned with the building direction were reported. Table 3 also shows the roughness parameters Ra, Rz, and Rt of specimens. The mass and dimensions of the specimens are always higher than the nominal value; this is probably due to the absence of offset compensation preset in the build preparation software. The lack of a contour strategy for the lattice specimens affects the quality of their surfaces in terms of size and roughness [24]. Moreover, the more complex shape of the CY and CC samples could result in higher dimensional errors.

Table 3. Mass, diameter and roughness measurements.

	Mass [g]			Diameter [mm]			Roughness [µm]					
							Ra		Rz		Rt	
	Mean	SD	Nominal	Mean	SD	Nominal	Mean	SD	Mean	SD	Mean	SD
BC	16.09	0.15	15.93	2.829	0.012	2.800	5.5	0.5	30.8	2.7	49.2	6.9
CY	13.72	0.11	12.85	1.259	0.006	1.128	7.7	0.8	49.6	6.2	60.0	8.0
CC	14.06	0.08	13.20	1.265	0.007	1.116	8.4	1.0	55.0	6.7	69.2	11.8

Figure 4a presents the curvature analysis for CC (subdivided) and CY (circular section) specimens. CY geometry does not have fillet radius but during the manufacturing of the parts, sharp edges are slightly filleted; an approximated fillet radius of 0.1 mm was measured by the CMM. The minimum and maximum curvature analysis highlights that while the CY geometry has a C^1 surface (tangent continuous surfaces), the Catmull-Clark subdivision algorithm produces a surface with curvature continuity (C^2 surface), except at extraordinary vertices where they are C^1 [16, 25] (for a quadrilateral mesh an extraordinary vertex is a vertex in which the number of incident edges differs from 4). Thanks to its curvature continuity, CC cells surfaces are smoother than CY ones. This also reflects on the stress concentration factor k_t; in Fig. 4b, k_t is plotted as a function of the Fillet radius/Cell dimension ratio. CC cell has a constant k_t = 1.15 deriving from the subdivision algorithm, while CY cell has a decreasing behaviour as the ratio increases. This is due to the beneficial effects that large fillet radii have on the peak stresses. Nevertheless, as far as the ratio increases, k_t of CY will not reach the k_t of CC.

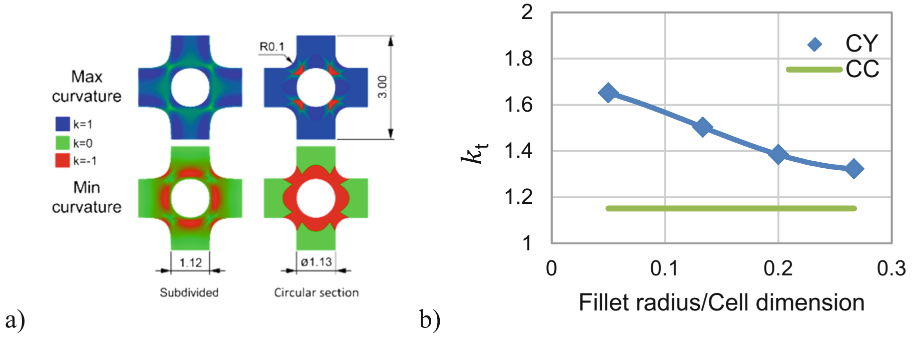

Fig. 4. (a) Curvature analysis for CC (subdivided) and CY (circular section) specimens. (b) stress concentration factor k_t as a function of fillet radius/Cell dimension ratio.

Figure 5 shows the results of fatigue tests as Stress – Number of cycles (S-N) curves (Wöhler curves) obtained according to ISO/DIS 12107 standard. The curves were obtained by the model equation:

$$\log_{10} N = b_0 + b_1 \cdot \log_{10} S \tag{1}$$

that can be rewritten as:

$$N = k \cdot S^{b_1} \tag{2}$$

where $k = 10^{b_0}$.

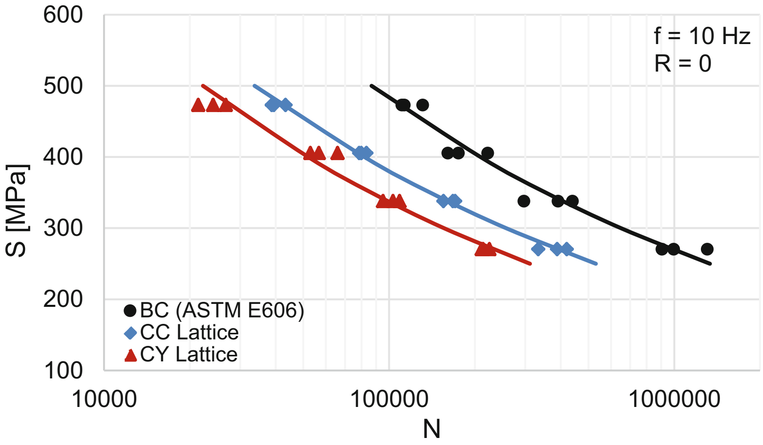

Fig. 5. S-N curves, according to ISO/DIS 12107 standard.

In Table 4 the parameters b_0 and b_1 are reported, together with the standard deviation SD and the correlation coefficient R^2, that is close to 1 for all of the specimen types, that means the model well describes the behaviour of the samples.

Table 4. Statistical parameters for S-N curve, according to ISO/DIS 12107.

Specimen type	b_0	b_1	SD	R^2
BC	15.58	−3.94	0.076	0.96
CC	15.26	−3.98	0.032	0.99
CY	14.63	−3.81	0.064	0.97

CC lattice specimens fail about one and a half times later with respect to CY ones. This is due to the different modeling approach adopted. As previously analyzed, the lattice structure modeled with the Catmull-Clark subdivision method presents smoother surfaces than the CY, especially at nodal points where the CY model has sharp edges, except for the small fillet radii resulting from the manufacturing technology; the lower stress concentration factor improves the fatigue behaviour. So the surface subdivision method results in lattices with an enhanced fatigue life, that are modeled in an efficient way, and that can be exploited in different applications and fields, for example, scaffolds in biomedical field, lightweight and energy absorber structures in the automotive industry, and bearing structures in industrial field.

The BC samples fail at a higher number of cycles if compared to lattice structures; indeed, they resist more than twice the CC lattices. This is explained at least by 3 aspects:

- the stress concentration factor, k_t, is negligible for the BC sample;
- the effective resistant area is more sensitive to the porosity in a small section;
- the cross-section profile of the sample is greater for the lattice sample and increases the opportunity of cracks initiation.

k_t, mainly related to the shape of the sample, is higher in CY lattices than in CC ones and, especially, in BC models can be neglected thanks to the axisymmetrical shape that does not present sharp edges, but filleted edges with large radii instead.

The cross-section and the porosity are related to the scale effect, that appears in this work due to the “segmentation” of one bigger element in several smaller ones. Let d be the diameter of a pore and let suppose that a pore is present in a beam, which could be the weak link in the chain of a lattice. The effective area will be:

$$A_{eff} = A_n - \frac{\pi d^2}{4} \tag{3}$$

where A_n is the nominal area. The coefficient k_A that keeps in consideration the sensitivity to the porosity depending on the number N of beams can be defined as a function of the effective areas:

$$k_A = \frac{\sigma_N}{\sigma_1} = \frac{A_{eff,1}}{A_{eff,N}} = \frac{A_n - \frac{\pi d^2}{4}}{A_n - \frac{\pi N d^2}{4}} = \frac{D^2 - d^2}{D^2 - Nd^2} \tag{4}$$

where D is the diameter of a single beam of area A_n, σ is the stress applied, and subscripts 1 and N indicate how many sections are present in the model.

The cross-section profile of the lattice structure is greater due to the absence of a contour strategy that results in a higher roughness, and to the shape of the sample: to obtain the same area with more beams, the length of the profile increases. Since the relation between area A and perimeter p of a circumference can be written as $p = 2\sqrt{A\pi}$, if the same area is divided in N equal smaller areas, the ratio between the perimeter of a single bigger beam p_1 and the perimeters of N smaller beams p_N will be:

$$\frac{p_1}{p_N} = \frac{2\sqrt{A\pi}}{2\sqrt{A\pi N}} = \frac{1}{\sqrt{N}} \tag{5}$$

The coefficient k_P that describes the scale effect of the cross-section profile will consider the ratio between the roughness parameters Rt_1/Rt_N as well, and can be described as follows:

$$k_P = f\left(\frac{1}{\sqrt{N}}, \frac{Rt_1}{Rt_N}\right) \tag{6}$$

To better understand Eq. (6), further studies are needed to confirm these hypotheses, which are not yet confirmed in the literature. Indeed, studies exist that state that larger parts experience lower fatigue limits with respect to smaller parts [26].

Combining all the coefficients, Eq. (2) can be re-written as:

$$N = k \cdot k_p \cdot (k_t \cdot k_A \cdot S)^{b_1} \tag{7}$$

Equation (7) allows to describe the fatigue behaviour of geometries in which the circular cross-section of a part has been divided in smaller cross-sections, keeping in consideration the scale and shape effects; this perfectly suits the situation where lattice structures made of struts are compared to the bulk material. The development of an accurate and effective model in fatigue life of lattice structures is fundamental in the design phase, allowing reliable simulations of the mechanical behaviour. For instance, this model can be introduced in homogenization methods, reducing the complexity in the simulation of trabecular components [27].

4 Conclusions

In this work, three types of specimen were modeled and produced by AM SLM technology in SS316L: bulk specimens (BC), regular lattice structures modeled with a traditional modeling method (CY), and regular lattice structures modeled adopting a previously proposed modeling approach based on a subdivision surface algorithm (CC). All the parts were fatigue tested to better understand the fatigue behaviour of the geometric modeling approach.

In particular, the comparison between CY and CC modeling approaches highlights that CC samples fail at a higher number of cycles, thanks to a modeling method that results in smooth surfaces, avoiding sharp edges and reducing the negative consequences of shape effects. The comparison between bulk and lattice specimens allows to understand the scale effects on porosity and surface roughness: when the diameter of a beam decreases, the percentage of area occupied by a porosity is bigger if compared to the same porosity in a beam with a bigger diameter, and this weakens the structure; moreover, when the area of a beam is subdivided into several smaller beams, the total perimeter of a cross-section increases, enhancing the probability of points for crack initiation. Thanks to these observations, confirmed by experimental tests, it was possible to propose a preliminary model that takes into consideration the scale and shape effects and describes the fatigue behaviour of AM parts characterized by the reduction of the elements dimension and by the increase of the shape complexity, allowing to predict the fatigue behaviour of lattice structures.

The proposed model is still in an early stage and further studies are needed to complete and validate it through an extensive fatigue test campaign, with samples with different shapes and element sizes. Nevertheless, it is already possible to assert that the surface subdivision modeling method allows overcoming issues in lattice structure modeling highlighted in literature, such as robustness and scalability. Finally, the development of a model in fatigue life of lattice structures is fundamental in the design phase, where can be implemented in Computer Aided Engineering software, reducing the complexity of the analyses.

Acknowledgments. This work was partially funded by Fondazione Cassa Di Risparmio di Padova e Rovigo (CARIPARO) and by Regione Friuli Venezia Giulia "FESR D23D1800-0160007" to Tesolin S.p.A.

References

1. Holmström, J., Partanen, J., Tuomi, J., Walter, M.: Rapid manufacturing in the spare parts supply chain. J. Manuf. Technol. Manag. **21**, 687–697 (2010). https://doi.org/10.1108/17410381011063996
2. Wohlers, T., Campbell, I., Diegel, O., Kowen, J., Caffrey, T.: Wohlers report 2019 (2019)
3. Gibson, L.J., Ashby, M.F.: Cellular Solids. Cambridge University Press, Cambridge (1997). https://doi.org/10.1017/CBO9781139878326
4. Savio, G., Rosso, S., Meneghello, R., Concheri, G.: Geometric modeling of cellular materials for additive manufacturing in biomedical field: a review. Appl. Bionics Biomech. **2018**, 1–14 (2018). https://doi.org/10.1155/2018/1654782
5. Van Hooreweder, B., Kruth, J.-P.: Advanced fatigue analysis of metal lattice structures produced by selective laser melting. CIRP Ann. **66**, 221–224 (2017). https://doi.org/10.1016/J.CIRP.2017.04.130
6. SASAM: Additive Manufacturing: SASAM Standardisation Roadmap (2015)
7. AMSC: Standardization Roadmap for Additive Manufacturing (version 1.0) (2017)
8. Yadollahi, A., Shamsaei, N.: Additive manufacturing of fatigue resistant materials: challenges and opportunities. Int. J. Fatigue **98**, 14–31 (2017). https://doi.org/10.1016/J.IJFATIGUE.2017.01.001
9. Greitemeier, D., Dalle Donne, C., Syassen, F., Eufinger, J., Melz, T.: Effect of surface roughness on fatigue performance of additive manufactured Ti–6Al–4V. Mater. Sci. Technol. **32**, 629–634 (2016). https://doi.org/10.1179/1743284715Y.0000000053
10. Masuo, H., Tanaka, Y., Morokoshi, S., Yagura, H., Uchida, T., Yamamoto, Y., Murakami, Y.: Influence of defects, surface roughness and HIP on the fatigue strength of Ti-6Al-4V manufactured by additive manufacturing. Int. J. Fatigue **117**, 163–179 (2018). https://doi.org/10.1016/J.IJFATIGUE.2018.07.020
11. Croccolo, D., De Agostinis, M., Fini, S., Olmi, G., Vranic, A., Ciric-Kostic, S.: Influence of the build orientation on the fatigue strength of EOS maraging steel produced by additive metal machine. Fatigue Fract. Eng. Mater. Struct. **39**, 637–647 (2016). https://doi.org/10.1111/ffe.12395
12. Bača, A., Konečná, R., Kunz, L.: Influence of build direction on the fatigue behaviour of Ti6Al4V alloy produced by direct metal laser sintering. Mater. Today Proc. **3**, 921–924 (2016). https://doi.org/10.1016/J.MATPR.2016.03.021
13. Wycisk, E., Solbach, A., Siddique, S., Herzog, D., Walther, F., Emmelmann, C.: Effects of defects in laser additive manufactured Ti-6Al-4V on fatigue properties. Phys. Procedia **56**, 371–378 (2014). https://doi.org/10.1016/J.PHPRO.2014.08.120
14. Savio, G., Meneghello, R., Concheri, G.: Geometric modeling of lattice structures for additive manufacturing. Rapid Prototyp. J. **24**, 351–360 (2018). https://doi.org/10.1108/RPJ-07-2016-0122
15. ASTM: ASTM E606/E606M - 2012 – Standard Test Method for Strain-Controlled Fatigue Testing (2012)
16. Catmull, E., Clark, J.: Recursively generated B-spline surfaces on arbitrary topological meshes. Comput. Des. **10**, 350–355 (1978). https://doi.org/10.1016/0010-4485(78)90110-0

17. Elangeswaran, C., Cutolo, A., Muralidharan, G.K., de Formanoir, C., Berto, F., Vanmeensel, K., Van Hooreweder, B.: Effect of post-treatments on the fatigue behaviour of 316L stainless steel manufactured by laser powder bed fusion. Int. J. Fatigue **123**, 31–39 (2019). https://doi.org/10.1016/J.IJFATIGUE.2019.01.013
18. ISO International Organization for Standardization: ISO 4287:1997 - Geometrical Product Specifications (GPS) – Surface texture: Profile method – Terms, definitions and surface texture parameters (1997)
19. ISO International Organization for Standardization: ISO 4288:1996 - Geometrical Product Specifications (GPS) – Surface texture: Profile method – Rules and procedures for the assessment of surface texture (1996)
20. Savio, G., Rosso, S., Curtarello, A., Meneghello, R., Concheri, G.: Implications of modeling approaches on the fatigue behavior of cellular solids. Addit. Manuf. **25**, 50–58 (2019). https://doi.org/10.1016/j.addma.2018.10.047
21. Renishaw: Data sheets - Additive manufacturing - SS 316L-0407. https://www.renishaw.com/en/data-sheets-additive-manufacturing–17862
22. ISO International Organization for Standardization: ISO/DIS 12107 – Metallic materials – Fatigue testing – Statistical planning and analysis of data (2017)
23. Van Hooreweder, B., Apers, Y., Lietaert, K., Kruth, J.P.: Improving the fatigue performance of porous metallic biomaterials produced by selective laser melting. Acta Biomater. **47**, 193–202 (2017). https://doi.org/10.1016/j.actbio.2016.10.005
24. Yadroitsev, I., Yadroitsava, I., Bertrand, P., Smurov, I.: Factor analysis of selective laser melting process parameters and geometrical characteristics of synthesized single tracks. Rapid Prototyp. J. **18**, 201–208 (2012). https://doi.org/10.1108/13552541211218117
25. Zorin, D.: Subdivision zoo. Subdiv. Model. Animat. 65–104 (2000)
26. Murakami, Y.: Metal Fatigue: Effects of Small Defects and Nonmetallic Inclusions. Elsevier, Boston (2002)
27. Savio, G., Curtarello, A., Rosso, S., Meneghello, R., Concheri, G.: Homogenization driven design of lightweight structures for additive manufacturing. Int. J. Interact. Des. Manuf. (2019). https://doi.org/10.1007/s12008-019-00543-0

Instant Journal of Mechanical Engineering
Review Article Open Access

Heterogeneous objects representation for Additive Manufacturing: a review

Luca Grigolato[1,2*], Stefano Rosso[1,3], Roberto Meneghello[1,3], Gianmaria Concheri[1,2] and Gianpaolo Savio[1,2]

[1]Laboratory of Design Tools and Methods in Industrial Engineering, University of Padova, Italy
[2]Department of Civil, Environmental and Architectural Engineering, University of Padova, Italy
[3]Department of Management and Engineering, University of Padova, Italy

***Corresponding Author:** Luca Grigolato, Laboratory of Design Tools and Methods in Industrial Engineering, University of Padova, Italy, Email: luca.grigolato@unipd.it

Received Date: *Dec 04, 2019 /* ***Accepted Date:*** *Dec 12, 2019/* ***Published Date:*** *Dec 14, 2019*

Abstract
Recent advances in additive manufacturing technologies demand for extremely customized, complex shape and multi-fold functional products. Heterogeneous objects, such as functionally graded materials, represent an attractive solution for researchers and industries in many application fields. Combining geometric modelling and material assignment in a definitive and accessible CAD tool is still a challenge. In this review the key aspects of heterogenous object representation related to additive manufacturing processes are reported. After the presentation of the various methodologies for geometric modelling found in the literature, additive manufacturing applications for heterogeneous objects are summarized.

Keywords: Geometric modeling; Computational geometry; Additive manufacturing; CAD; FGM; Heterogeneous objects

Cite this article as: Luca Grigolato, Stefano Rosso, Roberto Meneghello, et al. 2019. Heterogeneous objects representation for Additive Manufacturing: a review. I J Mech Eng. 1: 14-23.

Copyright: This is an open-access article distributed under the terms of the Creative Commons Attribution License, which permits unrestricted use, distribution, and reproduction in any medium, provided the original author and source are credited. Copyright © 2019; Luca Grigolato

Introduction

Thanks to the exploitation of design freedom guaranteed by additive manufacturing (AM) technologies, heterogenous object modelling and production is receiving a renewed interest. These lead to a paradigm shift that is taking place in industry, from a shape-centred approach to a functional requirement approach [1]. Nowadays, AM processes can create heterogeneous objects, but the lack of suitable geometric modelling and material representation techniques for this type of objects limits the ability of product development [2,3]. Current CAD tools and workflows have been designed to represent homogeneous objects suitable for traditional manufacturing technologies, modelling shapes by their boundaries without information about the material distribution inside the part.

We experienced heterogeneous objects much more than homogeneous ones. Manmade objects are usually almost constant in their internal material distribution and they can be modelled as homogeneous solids. In contrast, natural objects are rarely homogeneous, fitting together functions, shapes and materials. Nature reveals every day optimized heterogeneous objects such as animal tissues (e.g. human bones), plant structures (e.g. wood) and geological materials (e.g. soil and rocks) [2,4,5]. For this reason, also related to biomimicry design approach, the interest in heterogeneous objects has increased exponentially [6]. Heterogeneous object modelling is not a novelty in computational design, as it represented the natural evolution of homogeneous object modelling [7,8]. A heterogeneous object is referred to a solid component consisting in more than two attributes distributed discontinuously or continuously inside geometry boundaries [9,10]. If a discontinuous change in attributes distribution, i.e. material distribution, generates distinct regions separated by distinct interfaces in the solid, it is called a composite (Figure 1a) [10]. On the other hand, if the continuous variation of an attribute produces gradient in material distribution, it is often referred to as functionally graded material (FGM) [10]. In the simplest FGM, two different materials change gradually from one to the other, as schematically shown in figure 1b. In addition, distribution can be even random or irregular [4,5,11]. Sometimes, authors use FGM and multi-material terms interchangeably [12] while they use composite for the discontinuous change. The effective material properties such as Young’s modulus, Poisson’s ratio, density, thermal conductivity, and thermal expansion can be determined by several rules such as the mixture, the three-phase model by Frohlich and Sack, the self-consistent scheme, the Mori-Tanaka technique, and the mean field approach [13].

FGM are now a consolidate argument in scientific research. This is demonstrated by the growing number of publications in the literature. Indeed, according to Scopus database, the number of papers containing the keyword "functionally graded materials" increased from 153 in 2000 to 924 in 2018. For all the reasons above, a shared systematic design methodology is urgently required, specifically integrated with additive manufacturing methods and tools [1,4,12]. This means to elaborate an overall design approach, in order to consider object multi-fold functions, shape and material distribution in specific environmental and boundary conditions. As a first step in this direction, in this work firstly a taxonomy of geometric modelling approaches for heterogeneous objects is proposed, and then, the opportunities highlighted in literature for manufacturing heterogeneous objects by AM technologies are presented.

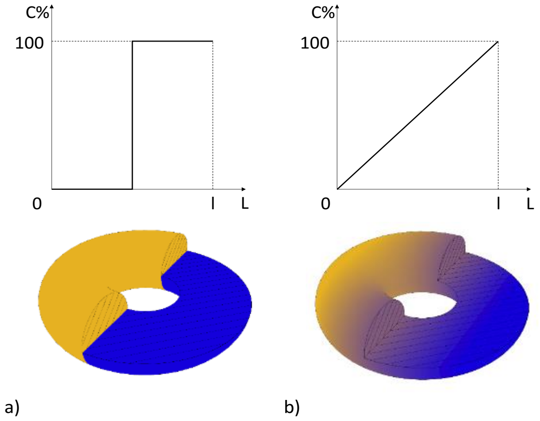

Figure 1: A heterogeneous model of a torus, (a) with discrete material distribution and (b) with graded material distribution. Yellow and blue colors represent two different materials. In the length axis (L), l represents the length of the object. C% is the percentage of blue material: when C%=0 the object is totally made of yellow material, if C%=100 the object is blue.

Heterogeneous object modelling and representation

Current CAD software are designed to operate with homogeneous solids and not with heterogeneous ones, because the modelling objective until now was to describe mainly geometrical information [14]. Many models exist for representing the outer shape of an object, but modelling the inner composition is still a challenge [1,15,16]. Since heterogeneous objects modelling is not trivial, because includes more than the shape representation, there are different approaches to model the volumetric property distribution in a solid [4,12,17], some of those take advantages from the analogies with other disciplines such as geosciences or colour representation [18].

In general, heterogeneous object geometric modelling requires the connection of properties information, such as material, to the solid model. This procedure includes two concurrent phases: shape modelling and material modelling or properties assignment [4,12,17,19,20]. Geometric modelling is concerned with both shape representations of the objects and properties assignment that is targeted at defining property distribution and composition over the geometric domain [4]. The procedures for heterogeneous object modelling can intuitively be sequential or parallel, that is whether the shape is modelled before material distribution, or the geometry and the material are defined simultaneously, respectively. As almost all the commercial CAD software packages can only create geometric models, now sequential process is the simpler strategy to model FGM object [12]. Alternatively, as Boddeti et al. [21] or Garland et al. [15] proposed, it is possible to simultaneously define topology and material distribution by an original algorithm based on topology and material gradient optimization within a single part. Zhang et al. [12] refers to boundary modelling and property assignment in terms of attributes. Indeed, shape attribute is usually already defined, while other properties or attributes that may differ from the material, can be defined as well. FGM fundamental attributes/properties are geometry and material. Other attributes/properties are for example microstructure [22-26], tolerances and operating conditions, which could also be included in a complete model description [2,8,14,27]. In order to define the better distribution of material, new design and optimization approaches are needed. For instance, Tornabene et al. [28,29] proposed a method for designing shells with graded composition between ceramic and metal along the lamina thickness, to optimize frequency and static deflection.

Geometric modelling approaches

Geometric modelling approaches for solids can be classified in 3 main classes (Figure 2): boundary representation (B-Rep), volume representation (V-Rep) and constructive solid geometry (CSG) [30,31]. In B-rep solids are described in terms of connected surfaces or faces representing the surface of an object. V-rep allows the description of both the surface and the internal portion of an object, and consequently the representation of the internal properties' distribution and not only of the boundaries. CSG is a description of a solid geometry through sequential logical operations (Boolean), starting from simple primitive geometries that could be homogeneous or heterogeneous. In the second case, Boolean operations should be redefined to manage heterogeneous primitives [30,32]. In other to visualize and manufacture the model, depending on the primitives, it is possible to shift to a B-rep or a V-rep.

Both B-rep and V-rep can be represented by discrete models or by functions. In the case of discrete V-rep, spatial decomposition can be reached by voxel, octree and polyhedral mesh. Typical discrete representation can be found in computed tomography (CT) image representation, in voxel form, or in finite element (FE) method, as polyhedral mesh. Beside discrete representation methods, bi-variate or tri-variate parametric functions are often used in CAD software for intuitively modify shape by moving control points. Usually, bi-variate parametric functions are used for surface representation, while tri-variate are implemented for morphing objects. Implicit and explicit functions can be implemented in CAD software and can be useful in the representation of particular shapes such as minimal surfaces, but do not allow an easy modification of the shape as in the case of parametric functions.

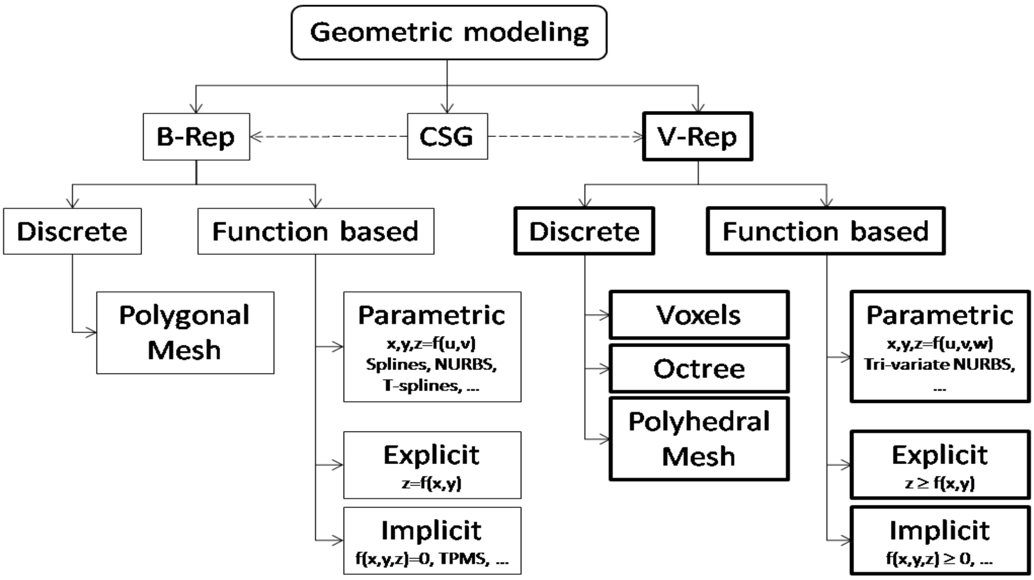
Geometric modeling
B-Rep
CSG
V-Rep
Discrete
Function based
Polygonal Mesh
Parametric
x,y,z=f(u,v)
Splines, NURBS, T-splines, ...
Explicit
z=f(x,y)
Implicit
f(x,y,z)=0, TPMS, ...
Discrete
Function based
Voxels
Octree
Polyhedral Mesh
Parametric
x,y,z=f(u,v,w)
Tri-variate NURBS, ...
Explicit
z ≥ f(x,y)
Implicit
f(x,y,z) ≥ 0, ...

Figure 2: Geometric modelling approaches.

Discrete V-rep representation

Discrete volumetric models are often classified as evaluated models or representations [4], since the volumetric information stored in the model is directly available for further application, such as numerical analysis and simulation [11]. The easiest way to discretize a volume is to subdivide it in small and equal cubes (i.e. voxel). Octrees is a partition of a three-dimensional space by recursively subdividing a cube into eight cubes; each cube can be inside, outside or in the boundary of an object; for each cube in the boundary the subdivision is repeated until the desired resolution is obtained. The space decomposition can be reached by other approaches that can better follow the external shape or the internal characteristics, using polyhedra. In this case, it is possible to adopt larger elements where the variation in shape or characteristics is low and vice versa. The discrete representation schemes are based on different data structures: for instance, voxel based methods rely on the distribution of the elements inside a tree-dimensional matrix or a vector, octree is based on a tree, while for polyhedral mesh it is necessary to define a list of vertex coordinates, a list of polyhedra, a list of faces, a list of edges and the reciprocal connections [30,33,34].

Function based V-rep representation

The most common way to define a geometry in a CAD environment is based on parametric functions. In the volumetric case, these functions map a domain of the parameter space (u,v,w) in the design space (x,y,z). Function adopted for mapping the (u,v,w) space in the (x,y,z), can be simple polynomials, but for an easier geometry management, control points were introduced together with basis function in the Bézier representation. In this formulation, moving a point, the whole geometry is modified. To overcome this limitation, B-splines and NURBS were introduced, where rational non uniform basis functions are recursively defined. Using NURBS, with a single equation, any type of geometry can be obtained. Differently, using explicit or implicit functions, each geometry is represented by a different equation, making difficult modeling complex geometries [33].

Properties assignment approaches

For heterogeneous objects, in particular for FGM, the volumetric property information consists in material data, and it can be divided in two branches: material composition and distribution [12]. Composition at each point of the volume is identified by a vector m. This represents a complication, because material information adds dimensions to the model. Distribution, that model the variation of m in the volume, can be described in various way and can be classified in three main classes [12]. The first ones is the extension of conventional geometric modelling approaches in order to consider material representation, i.e. the material description is dependent to the geometry approach used. This is called geometric model-based. The second class contains schemes wherein the material assignment is based on other geometry information, e.g. coordinate system-based. In the last class, special control feature-based schemes, also referred to as material primitives' features, are used to describe material distribution in FGM objects [11]. Other classifications are possible and not in contrast with the previous one [4]. Anyway, the material assignment needs a geometric support. Conceptually, next to a build space where the geometry is defined with any of the approaches previously described, a geometric model for material distribution is added. The basic concept of any heterogeneous modelling method is to define a function associating the material to all the points in the geometric model [20].

Geometric model-based

In geometric model-based, geometric modelling approaches are utilized as the basis for modelling the material attribute. In this case, material distribution is geometric representation dependent. In discrete V-rep, at each voxel, polyhedron or vertex within a boundary, a material composition is assigned [30]. These models permit complex FGM modelling with great accuracy that is directly related to the domain resolution, but computational and memory costs can be high [4,30]. For example, voxels approach can be improved by bringing together adjacent voxel with the same properties, making the spatial-occupancy enumeration more efficient such as in octree encoding [13]. Note that the material distribution inside a voxel is not necessarily homogeneous, for instance, Bernstein polynomials or tri-linear functions have been used to represent interpolated material distributions when the material composition is assigned to a vertex [4]. Extensions to pure voxel representation has been proposed by several authors, such as Blouin et al. [35]. A more flexible approach is based on polyhedral mesh. In polyhedral mesh, objects are described with a set of adjacent polyhedra, each represented by a list of vertices. The vertices store their geometric position as well as the material composition, and can be mathematically described as:

$$heterogeneous\ object = \{V_i\} = \{T_1, T_2, \dots T_n\}$$

$$T_k = \{G(v_{k1}, v_{k2}, \dots, v_{km}), M(v_{k1}, v_{k2}, \dots, v_{km})\},\quad 1 < k < n$$

$$v_{ki} = (x_i, y_i, z_i, m_i)$$

where T_k denotes a representative polyhedron, G and M denote the geometry and material distribution of T_k, v_{ki} is a representative vertex of T_k that stores the coordinates and punctual material information m_i and n is the number of polyhedrons that compose the whole heterogeneous object. The function M is an interpolation function used for defining the material distribution inside each polyhedron.

Contrary to space subdivisions, function-based representation utilizes exact geometric data representations, such as B-Rep and f-Rep [36], and rigorous functions (explicit, implicit, parametric) to represent the material distributions [4]. For implicit and explicit functions, it is very challenging to work on different levels of inequalities to manage the distribution of different materials. For example, with an implicit function based strategy it is possible to set a property at each k_i value (a surface) of the f(x,y,z)=k_i, but it has some drawbacks. Instead, parametric functions, such as tri-variate NURBS, show several advantages and the approach can be extended in FGM representation [30,37,38].

Coordinate system-based and control features-based

Material distribution can be defined based on geometrical features which differ from the shape of the object. For instance, the definition of properties or material can be referred to the coordinate system and independent from the boundary of an FGM. This is referred as coordinate system-based [12,17]. The distribution is defined with respect to a Cartesian, cylindrical or spherical coordinates system with linear or non-linear and discrete or continuous functions. If the material is assigned to a set of equidistant points, the supporting geometric model is equivalent to a voxel model. Doubrovski et al. [39] proposed a methodology based on voxelization modelling in which the resolution is set equal to the additive manufacturing process. Another example appears when the distribution is controlled by features such as points, curves or surfaces, referred as material features. Material composition at any point in the space model is derived from these control features and distance-based weighting functions. As stated in [4,11] this approach seems to be more intuitive from a user experience point of view. Bidarra et al. [27] defined a feature as a representation of the shape aspect of a product that is mappable to generic shape and functionally significant for the product. Also, features may be entities that are not otherwise present in the shape model. These new reference entities may be point (0-D), line/curve (1-D), or plane/surface (2-D). The material distribution function can be polynomial, exponential or harmonic functions of the distance from material reference entities [1,4,5,12]. Recently developed voxel-based modeling engine called Monolith [40] permits to handle spatial variations directly in material properties, using different approaches to assign the properties to objects such as geometric model-based, coordinate system-based and control features-based. These voxel-based representation fits perfectly within a new class of 3D printers which have multiple print heads capable of depositing different types material, such as resin, within a single build volume.

Additive Manufacturing applications

Manufacturing techniques play a critical role in achieving the designed composition and thus the demanded properties of heterogeneous object for specific applications. In particular, FGMs have found applications in various fields, such as aerospace, mechanical, electrical, thermal, optical, biomedical and geophysical [1,4,12,41]. One way to categorize these techniques is based on the type of FGM objects manufactured by them. Mahamood et al. [42] classified the FGM objects into two groups: thin and bulk FGM. Thin FGM is usually in the form of surface coatings, while manufacturing techniques for bulk FGM are powder metallurgy, centrifugal method, and AM [12]. Not all the current AM technologies, classified in ISO/ASTM 52900 [43], are now used for FGM realization. The main AM techniques reported in literature are presented in figure 3: vat photopolymerization (Stereolithography – SLA), material extrusion (Fused Deposition Modelling – FDM), powder bed fusion (Selective Laser Sintering/Melting – SLS/SLM), direct energy deposition (Laser Engineered Net Shaping – LENS) and material jetting (polyjet) [12].

SLA has attractive attributes of creating objects with a high-quality surface finish, dimensional accuracy, and a variety of material options. The material distribution is homogeneous in a layer, but changes along the build direction. It is challenging to obtain heterogeneous material compositions within intralayer. However, there is a possibility of printing functionally graded material with SLA. As shown by Huang et al. [44], a mask-image-projection-based Stereolithography is proposed to build objects with multiple materials.

FDM produces parts by extruding filaments of molten thermoplastics material through heated nozzles. After extrusion from the nozzle in a desired pattern, the material solidifies to form the object. There are large varieties of materials that can be used in FDM process. FDM devices with multiple nozzles allow the construction of heterogeneous objects with discrete material distribution. On the other hand, it is possible to put different materials in the same nozzles having the potential of manufacturing functionally graded material objects as long as the machine system allows for an arbitrary mixture of different filament materials. For example, Leu et al. [45] developed a triple extruder mechanism, which can control the filaments extrusion for desired composition gradients. In the same way Garland et al. [15] used an off the shelf FDM 3D printer to produce FGM object. The printer is equipped with a nozzle that can extrude two mixed materials at once. By controlling the rate at which the two filaments are pulled into the melt chamber, FGM objects can be printed, i.e. colours or compositions changed. Khalil et al. [46] showed the possibility of constructing heterogeneous tissue with FDM process in medical applications. Their system is based on a setup with four different nozzles.

LENS and SLS-SLM are promising technologies for fabricating FGM metal parts with excellent strength, accuracy (50-100 µm), and surface roughness (<10 µm), depending upon the machine type, materials and geometry of the products. Both LENS and SLS-SLM use powders as construction unit, but the former in blown-powder while the latter in a powder-bed technique. By controlling the composition ratio of different material powders, they have the potential of producing FGM objects. LENS is mainly used for iron-, titanium-, and nickel-based alloys. Other examples of FGM parts are functionally graded tungsten carbide and tool steel parts, alloys and ceramic parts by SLM, TiC and Ti composite by LENS, and Nykon-11 and silica nanocomposites by SLS [9,12]. Stratasys PolyJet 3D printing technology jets layers of curable liquid photopolymer onto a build tray and the gradient profile is thus continuous. One application of this technology for a graded prosthesis production is proposed in [39], where a PolyJet printer permits the elimination of slicing and path planning by bitmap images. Other researchers have demonstrated workflows for modelling and fabricating material compositions with target visual properties and desired deformation behaviour [39]. Another example is given by Connex 3 by Stratasys [47]: it offers the ability to create objects by jetting material droplets in a predefined pattern from designated microscale inkjet printing nozzles. With a three-base colour system, the material droplets have a wide colour range option from 20 palettes, each one providing several colours. The process requires a specific range of viscosity and curing temperature of the jetted liquid. This limits the type of material that can be used in this process.

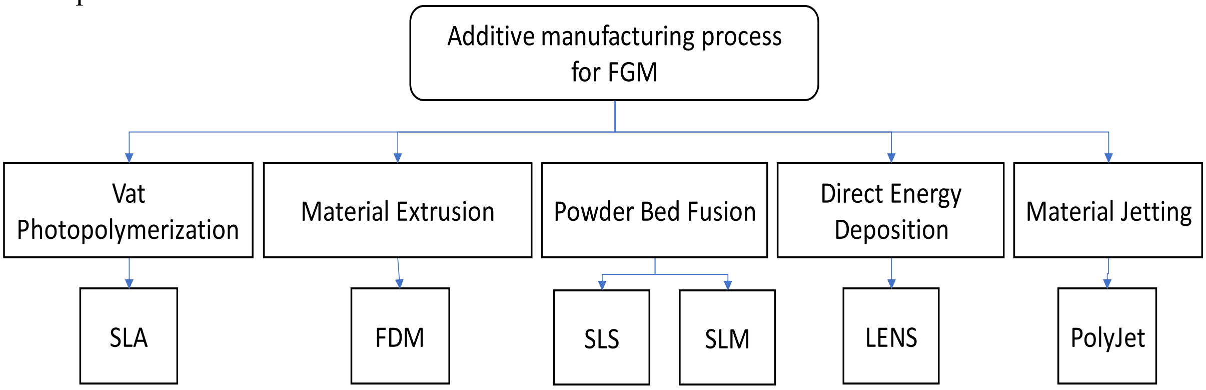

Figure 3: Additive Manufacturing processes currently used for FGM objects, classified using ISO/ASTM 52900.

Conclusions

AM can effectively build heterogeneous object, but research effort must be addressed to improve design and representation methods. In order to support these trends, this research suggested a classification of the possible approaches for volumetric modelling. Different approaches to assign properties of heterogeneous objects were described, defining a fundamental step for any design approach able to optimize the material combination and distribution on a design space. Moreover, the paper presents the major AM technologies useful for manufacturing FGMs.

Acknowledgement

This work was partially funded by grant “BIRD 190850 - Design, geometric modeling and analysis of components with functionally graded variation for additive manufacturing technologies” by Department of Civil, Environmental and Architectural Engineering, University of Padova, and Fondazione Cassa di Risparmio di Padova e Rovigo CARIPARO.

References

1. Leung YS, Kwok TH, Li X, et al. 2019. Challenges and Status on Design and Computation for Emerging Additive Manufacturing Technologies. Journal of Computing and Information Science in Engineering. Ref.: https://bit.ly/34fl6zL
2. Pasko A, Fryazinov O, Vilbrandt T, et al. 2011. Procedural function-based modelling of volumetric microstructures. Graphical Models. 73: 165-181. Ref.: https://bit.ly/2LJoUTh
3. Kou XY, Tan ST. 2005. A hierarchical representation for heterogeneous object modeling. CAD Computer Aided Design. 37: 307-319. Ref.: https://bit.ly/35bk1do
4. Kou XY, Tan ST. 2007. Heterogeneous object modeling: A review. CAD Computer Aided Design. 39:284-301. Ref.: https://bit.ly/38qEpZT
5. Miyamoto Y, Kaysser WA, Rabin BH, et al. 1999. Functionally Graded Materials. Ref.: https://bit.ly/2RBzyzj
6. Ahern J, DiCarlo A. 2016. Computationally engineered advanced manufacturing of parts. In: 2016 IEEE Aerospace Conference. 1-8. Ref.: https://bit.ly/2RMf5rk
7. Requicha AAG, Voelcker HB. 1982. Solid Modeling: A Historical Summary and Contemporary Assessment. IEEE Computer Graphics and Applications. 2: 9-24. Ref.: https://bit.ly/36pqZvG
8. Requicha AG. 1980. Representations for Rigid Solids: Theory, Methods, and Systems. ACM Computing Surveys (CSUR). 12: 437-464. https://bit.ly/2P8CHF6 b
9. Zhang C, Chen F, Huang Z, et al. 2019. Additive manufacturing of functionally graded materials: A review. Materials Science and Engineering. 764: 138209. Ref.: https://bit.ly/35bkQ5Y
10. Wu XJ, Liu WJ, Wang MY. 2007. Modeling Heterogeneous Objects in CAD. Computer-Aided Design and Applications. 4: 731-740. Ref.: https://bit.ly/2E3O8re
11. Sharma GK, Gurumoorthy B. 2019. Modelling multiply connected heterogeneous objects using mixed-dimensional material reference features. Journal of Computational Design and Engineering. 6: 337-347. Ref.: https://bit.ly/2LIjSX8
12. Zhang B, Jaiswal P, Rai R, et al. 2018. Additive Manufacturing of Functionally Graded Material Objects: A Review. Journal of Computing and Information Science in Engineering. Ref.: https://bit.ly/2PCgPkv
13. Tran LV, Ferreira AJM, Nguyen-Xuan H. 2013. Isogeometric analysis of functionally graded plates using higher-order shear deformation theory. Composites Part B: Engineering. Ref.: https://bit.ly/35aIoIb
14. Kumar V, Dutta D. 1998. An approach to modeling and representation of heterogeneous objects. Journal of Mechanical Design, Transactions of the ASME .120: 659-667. Ref.: https://bit.ly/38qPFWn
15. Garland A, Fadel G. 2015. Design and Manufacturing Functionally Gradient Material Objects with an off the Shelf Three-

Dimensional Printer: Challenges and Solutions. Journal of Mechanical Design, Transactions of the ASME. Ref.: https://bit.ly/36lBi3I
16. Garland A, Fadel G. 2016. Multi-Objective Optimal Design of Functionally Gradient Materials. Volume 2A: 42nd Design Automation Conference. Ref.: https://bit.ly/3454LgM
17. Paolini A, Kollmannsberger S, Rank E. 2019. Additive manufacturing in construction: A review on processes, applications, and digital planning methods. Additive Manufacturing. 30: 100894. Ref.: https://bit.ly/36goeg2
18. Fadel G, Morvan S. 2002. Multi-material representation and design issues. In: Gibson I (ed) Software solutions for rapid prototyping. 155-224.
19. Shin K-H, Natu H, Dutta D, et al. 2003. A method for the design and fabrication of heterogeneous objects. Materials and Design. 24: 339-353. Ref.: https://bit.ly/36mFkc1
20. Jackson TR. 2000. Analysis of functionally graded material object representation methods. Ref.: https://bit.ly/38t1dZh
21. Boddeti N, Ding Z, Kaijima S, et al. 2018. Simultaneous Digital Design and Additive Manufacture of Structures and Materials. Scientific Reports. 8: 15560. Ref.: https://go.nature.com/35czyth
22. Rosen DW, Jeong N, Wang Y. 2013. A method for reverse engineering of material microstructure for heterogeneous CAD. Computer-Aided Design. 45: 1068-1078. Ref.: https://bit.ly/2Pc6RqZ
23. Liu X, Shapiro V. 2015. Random heterogeneous materials via texture synthesis. Computational Materials Science. Ref.: https://bit.ly/2qKeGuE
24. Latief FDE, Biswal B, Fauzi U, et al. 2010. Continuum reconstruction of the pore scale microstructure for Fontainebleau sandstone. Physica A: Statistical Mechanics and its Applications. Ref.: https://bit.ly/349uYL5
25. McDowell DL, Ghosh S, Kalidindi SR. 2011. Representation and computational structure-property relations of random media. 63: 45-51. Ref.: https://b.gatech.edu/2sYEDHt
26. Bostanabad R, Bui AT, Xie W, et al. 2016. Stochastic microstructure characterization and reconstruction via supervised learning. Acta Materialia. Ref.: https://bit.ly/36mFOyR
27. Bidarra R, de Kraker KJ, Bronsvoort WF. 1998. Representation and management of feature information in a cellular model. CAD Computer Aided Design. 30: 301-313. Ref.: https://bit.ly/2qEUHxh
28. Tornabene F, Ceruti A. 2013. Mixed Static and Dynamic Optimization of Four-Parameter Functionally Graded Completely Doubly Curved and Degenerate Shells and Panels Using GDQ Method. Mathematical Problems in Engineering. 2013:1-33. Ref.: https://bit.ly/35cqZia
29. Tornabene F, Liverani A, Caligiana G. 2011. FGM and laminated doubly curved shells and panels of revolution with a free-form meridian: A 2-D GDQ solution for free vibrations. International Journal of Mechanical Sciences. 53: 460-470. Ref.: https://bit.ly/2LI0Wb6
30. Savio G, Meneghello R, Rosso S, et al. 2019. 3D Model Representation and Data Exchange for Additive Manufacturing. 412-42. Ref.: https://bit.ly/2sevk64
31. Hoffmann CM, Rossignac JR. 1996. A road map to solid modeling. IEEE Transactions on Visualization and Computer Graphics. 2: 3-10. Ref.: https://bit.ly/2ro6och
32. Shin KH, Dutta D. 2001. Constructive representation of heterogeneous objects. Journal of Computing and Information Science in Engineering. 1: 205-217. Ref.: https://bit.ly/36pk2e0
33. Mortenson ME. 1985. Geometric Modeling I. Wiley.
34. Bacciaglia A, Ceruti A, Liverani A. 2019. A systematic review of voxelization method in additive manufacturing. Mechanics & Industry. 20: 630. Ref.: https://bit.ly/36p1SsJ
35. Blouin A, Combemale B, Baudry B, et al. 2015. Kompren: modeling and generating model slicers. Software & Systems Modeling. 14: 321-337. Ref.: https://bit.ly/2E4fnSn
36. Pasko A, Adzhiev V, Schmitt B, et al. 2001. Constructive hypervolume modeling. Graphical Models .63: 413-442. Ref.: https://bit.ly/35atQsb
37. Massarwi F, Elber G. 2016. A B-spline based framework for volumetric object modeling.

CAD Computer Aided Design. 78: 36-47. Ref.: https://bit.ly/2E4fDAP

38. Martin W, Cohen E. 2001. Representation and extraction of volumetric attributes using trivariate splines. In: Proceedings of the sixth ACM symposium on Solid modeling and applications - SMA '01. 234-240. Ref.: https://bit.ly/2YzC36H
39. Doubrovski EL, Tsai EY, Dikovsky D, et al. 2015. Voxel-based fabrication through material property mapping: A design method for bitmap printing. Computer-Aided Design. 60: 3-13. Ref.: https://bit.ly/2RHBBSi
40. Panagiotis M, Payne AO. 2019. Monolith. Accessed 27. Ref.: https://bit.ly/35bWKrR
41. Wośko M, Paszkiewicz B, Piasecki T, et al. 2005. Applications of functionally graded materials in optoelectronic devices. In: Optica Applicata. 663-667. Ref.: https://bit.ly/2RIgNtY
42. Mahamood RM, Akinlabi ET, Shukla M, et al. 2012. Functionally graded material: An overview. In: Lecture Notes in Engineering and Computer Science. 1593-1597. Ref.: https://bit.ly/36kTD0T
43. ISO/ASTM (2015) ISO/ASTM 52900:2015 (ASTM F2792) - Additive manufacturing -- General principles -- Terminology.
44. Huang P, Deng D, Chen Y. 2014. Modeling and Fabrication of Heterogeneous Three-Dimensional Objects Based on Additive Manufacturing. Volume 2A: Advanced Manufacturing. Ref.: https://bit.ly/356834J
45. Liu W, Zhang YS, Heinrich MA, et al. 2017. Rapid Continuous Multimaterial Extrusion Bioprinting. Advanced Materials. 29: 1604630. Ref.: https://bit.ly/2PaZpMF
46. Khalil S, Nam J, Sun W. 2005. Multi-nozzle deposition for construction of 3D biopolymer tissue scaffolds. Rapid Prototyping Journal. 11: 9-17. Ref.: https://bit.ly/34aKqGI
47. Stratasys. 2019. Connex3 Objet500 and Objet350. https://www.stratasys.com/it/3d-printers/objet-350-500-connex3. Accessed 27 Nov 2019.

INTERNATIONAL CONFERENCE ON ENGINEERING DESIGN, ICED19
5-8 AUGUST 2019, DELFT, THE NETHERLANDS

OPTIMIZATION APPROACHES IN DESIGN FOR ADDITIVE MANUFACTURING

Rosso, Stefano; Savio, Gianpaolo; Uriati, Federico; Meneghello, Roberto; Concheri, Gianmaria

Università degli Studi di Padova, Italy

ABSTRACT

Nowadays, topology optimization and lattice structures are being re-discovered thanks to Additive Manufacturing technologies, that allow to easily produce parts with complex geometries.

The primary aim of this work is to provide an original contribution for geometric modeling of conformal lattice structures for both wireframe and mesh models, improving previously presented methods. The secondary aim is to compare the proposed approaches with commercial software solutions on a piston rod as a case study.

The central part of the rod undergoes size optimization of conformal lattice structure beams diameters using the proposed methods, and topology optimization using commercial software tool. The optimized lattice is modeled with a NURBS approach and with the novel mesh approach, while the topologically optimized part is manually remodeled to obtain a proper geometry. Results show that the lattice mesh modelling approach has the best performance, resulting in a lightweight structure with smooth surfaces and without sharp edges at nodes, enhancing mechanical properties and fatigue life.

Keywords: Additive Manufacturing, Optimisation, Case study, Lattice structures, Modeling approaches

Contact:
Rosso, Stefano
University of Padova
Department of Management and Engineering
Italy
stefano.rosso.3@phd.unipd.it

Cite this article: Rosso, S., Savio, G., Uriati, F., Meneghello, R., Concheri, G. (2019) ‘Optimization Approaches in Design for Additive Manufacturing’, in *Proceedings of the 22nd International Conference on Engineering Design (ICED19),* Delft, The Netherlands, 5-8 August 2019. DOI:10.1017/dsi.2019.85

1 INTRODUCTION

Nowadays, optimization is a fundamental phase during the development of a new product; finding the right moment when to start to optimize is essential to save time, money and obtain an innovative product. In the past decades, optimization was performed as the third phase out of four of the design process (Kirsch, 1993): after the formulation of functional requirements and the conceptual design stage, the optimization step is conducted in an iterative-intuitive way, based on trial and error. This approach tends to be time-consuming as often the first guess does not satisfy the requirements, and other solutions have to be designed and tested, in an iterative process. If, instead, computational design synthesis (Chakrabarti, 2002) is used, the tasks needed to obtain a solution can be divided in four main steps: representation, where a mental model of the object is created, generation, where the object is created, evaluation, where an analysis is performed to see how well the part meets the design goals and constraints, and guidance, in which feedback on improvements to the design for the next iteration is given (Cagan *et al.*, 2005); generation, evaluation and guidance phases are iteratively repeated until a final design is obtained. In design synthesis, optimization can occur during representation and generation phases, where the design has not yet been refined to a specific topology. Usually, stochastic methods are applied, since it is not mandatory to find exact global optima, but it is possible to explore different design that can generate suboptimal designs that satisfy the designer's needs (Shea and Cagan, 1997). Applications of stochastic methods were proposed by Shea, Aish and Gourtovaia (2005), where a generative structural design system including structural topology and shape annealing (STSA) method is combined with an associative modeling system, and by Shea and Smith (2006) where STSA is applied for improving full-scale transmission tower design. Since stochastic methods are iterative processes, they could require lot of time and computational resources, according to the number of iteration and variables of the problem. A similar approach, called Simulation-Driven Design or Optimization-Driven Design, has been adopted by both academic researchers (Sellgren, 1999; Koziel and Ogurtsov, 2014) and commercial software (Altair, 2018). Moving up and embedding the optimization in the first concept and design definition, the resulting shape will drive the following validation and production phases in a faster way, with no need for further iterations.

Among all the types of optimization, structural optimization aims to find the best way to organize material in a structure, according to loads and boundary conditions applied on the part. Objectives of the optimization can be mass reduction, stiffness maximization and resonant frequencies. Structural optimization can be mainly arranged into three classes (Bendsoe and Sigmund, 2013).

1. *Size optimization*: it deals with the optimization of the dimensions, which involve, for example, the cross sections of trusses inside a structure and/or thicknesses of plates.
2. *Shape optimization*: it deals with the optimization of the shape of boundaries of the structure; it affects not only the external boundaries but also the shape of potential internal voids.
3. *Topology optimization*, in which material is arranged in order to find the best distribution under a set of boundary conditions.

All the structures and shapes resulting from the aforementioned optimization and modeling techniques present really complicated geometries, difficult and sometimes impossible to produce with conventional manufacturing technologies. Additive Manufacturing (AM) technologies, instead, due to their layer-by-layer manufacturing approach, allow for the production of complex shapes without necessary increasing production costs and times (Holmström *et al.*, 2010). In their work, Brackett, Ashcroft and Hague (2011) presented opportunities, and practical difficulties as well, of topology optimization for AM. In (Rosen, 2016) a review of synthesis methods for AM can be found; in particular, topology optimization methods, codes, commercial software and research issues are reported. Another thorough review that summarizes the state of the art topology optimization methods and exposes current challenges and opportunities in the AM field can be found in (Liu *et al.*, 2018). Common issues and limitations are the integration of AM process constraints during topology optimization, the addressing of multi-scale modeling, multiple loading conditions and local constraints, multiple materials, robustness with respect to variations and computational efficiency of the methods. Zegard and Paulino (2016) addressed the post-processing phases needed to allow a topologically optimized part to be additively manufactured. In this scenario, lattice structures are receiving increasing attention. In addition to the fact of being lightweight, lattices present other interesting properties: they are stiff in relation to their low mass, they are good energy absorbers thanks to the possibility to undergo large deformations, good acoustic insulators thanks to the internal porosity and good heat exchangers due to their large surface area (Savio *et al.*, 2018). Moreover, structural optimization has been widely applied to lattice design. In (Ning and Pellegrino, 2012), topology optimization methods are divided in continuum methods, such as Solid isotropic material with penalization (SIMP) method (Bendsøe, 1989; Bendsøe and Sigmund, 1999) and homogenization method, and discrete methods, such as ground-structure based methods and shape-grammar methods; both of the categories present some limitations, so the authors proposed an implicit representation of the structural topology, where the microstructure is defined by a continuous variable, i.e. the size distribution field. More, an optimization loop running under a genetic algorithm is implemented to optimize the size and the topology of a lattice structure. Nessi and Stanković (2018) used the Superformula, an extension of the Superellipse, to obtain a design domain in which a tetrahedral meshing technique was applied to generate the topology of a lattice structure; the size of the struts of the lattice resulting from the edges of the tetrahedral mesh was then optimized using a finite element analysis, given a set of loads and boundary conditions. More, Stanković *et al.* (2015) developed a generalized optimality criteria method for the optimization of lattice structures, including DfAM constraints and exploiting multi material possibilities offered by these technologies; results show that multi material lattices outperform single material ones. Also, the density map resulting from topology optimization can be used to proportionally assign the dimension of the beams or the size of the cells (Han and Lu, 2018; Wang *et al.*, 2018).

The aim of this work is twofold: proposing an extension of a previous lattice structure modeling method to conformal lattices, and comparing it with other commercial approach. Different geometric modeling approaches and structural optimizations methods are presented, both developed by the group of research and available in commercial software, and applied to a piston rod. A conformal wireframe is modeled with a novel approach that uses the curvature of the profile arc curves of the central part of the rod; then, the beams of a lattice structure built around the conformal wireframe are dimensioned with a size optimization algorithm; the optimized lattice is then modeled by a Non-Uniform Rational B-Splines method (Savio, Meneghello and Concheri, 2017) and a mesh method (Savio, Meneghello and Concheri, 2018) with a new feature able to build the mesh faces around nodal points of non-regular lattices. Furthermore, the central part of the rod is topologically optimized and the geometries are remodeled and structurally analysed using commercial software. The results obtained by the three approaches (NURBS method, mesh method and topology optimization method) are finally compared. Outcomes highlight that the mesh modeling method is able to efficiently create conformal lattices with enhanced fatigue behaviour.

2 TOOLS AND METHODS

Sections 2.1 and 2.2 present an improvement of a methods previously developed by Savio, Meneghello and Concheri (2018), introducing the possibility of modeling conformal lattice structures. Section 2.3 deals with an alternative design procedure consisting in topology optimization followed by a manual remodeling and a structural analysis of the part.

The previous method has advantages, such as low computational resources requirements, it is fast and enhances the fatigue behaviour of the parts, but, at the same time, lacks in extension of the available single cells database and does not allow for the modeling of conformal lattices. In conformal structures the geometry and the size of the cells can be different inside the part in order to adapt (i.e. conform) to the external shape of the model: this feature eliminates weakness at boundaries and provides stiffness and resistance to the entire model (Wang, 2005). This new feature increases the field of application of the method, allowing to address filling situations where it is not possible to accept lattice structures with regular repetitions of uniform lattices. In Figure 1 a flow chart regarding the proposed method is presented, highlighting the main novel contribution.

The size optimization was performed in Rhinoceros 6 (Robert McNeel & Associates), using the graphical algorithm editor Grasshopper and Karamba3D as finite element (FE) solver for beams and shells, and an ad-hoc iterative process in Python programming language. The optimization follows these steps:

- A part is given as input and a lattice structure wireframe is created inside, according to the cell type and minimum dimension; the lattice structure created is a conformal one, so the geometry and the size of the cells can adapt (i.e. conform) to the external shape of the model;

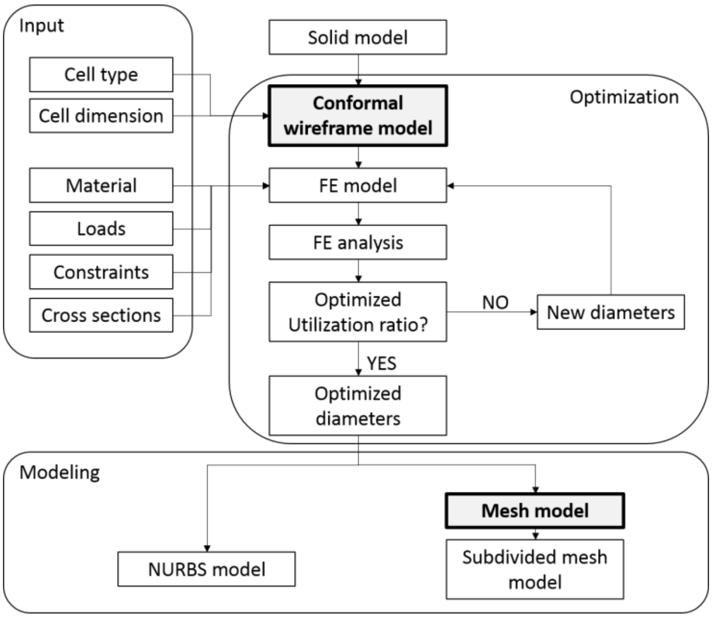

Figure 1. Flow chart of the proposed method.

- A FE beams model is obtained from the wireframe applying the boundary conditions: material, loads, constraints, initial cross-section equal for each beam.
- A FE analysis (FEA) is performed and the utilization of each beam, similar to the ratio between the maximum Von Mises stress at a beam and the admissible stress, is computed. An iterative variation of the beams diameter is carried out until the utilization ratio of each beam is inside a target range. An upper and lower bound for beam dimension are defined to allow the beam to be manufactured (i.e. the beam diameter has to be bigger than the lower bound), and to not interfere with the nearby beams (i.e. the beam diameter has to be smaller than the upper bound).

Once the FE model has been optimized, the lattice structure is modeled adopting two different boundary representation approaches: Non-Uniform Rational B-Splines (NURBS) modeling and mesh modeling.

Adopting NURBS modeling, a cylinder having the optimized diameter and spherical caps is constructed around each line of the model; Boolean union over the capped cylinders is then performed to obtain the lattice structure. The resulting model presents a lot of sharp edges that cause stress concentration at nodal points and mechanically weaken the structure.

Using mesh modeling, an 8-faces mesh is modeled around each beam, assuming a double truncated pyramidal shape. At the middle of the beam, the optimized diameter dimension is adopted, while at the ends, where the beam approaches the nodes, the diameter dimension of the biggest beam arriving at the node is used, to avoid issues in the mesh model reconstruction.

Catmull-Clark subdivision surface algorithm is finally adopted (Catmull and Clark, 1978). With Catmull-Clark subdivision, starting from a quadrilateral mesh, the initial vertices are iteratively averaged following the subdivision rule, splitting into four each quad face and resulting in a smooth surface; this algorithm produces a surface with continuity in curvature (C2 surface), except at extraordinary vertices where they are C1 (Catmull and Clark, 1978; Zorin, 2000).

2.1 Conformal wireframe model

Conformal wireframes can be obtained adopting morphing algorithms to map a regular wireframe on a specific shape, but the tested implementation provided cells with bigger surface area at vertex. Instead, exploiting curvature information guarantees a better control on the final cells.

Starting from 4 boundary profiles arcs (Figure 2a), conformal wireframe is modeled according to the following steps:

- the line connecting the mid-point of the upper and lower profiles is created and divided by the minimum cell size value, obtaining the number of arcs along this direction, *n;*
- the curvatures of the upper and lower profile arcs are extracted; these two values are linearly interpolated obtaining *n* intermediate curvature;

- the line connecting the mid-point of the upper and lower profiles is created and subdivided in *n* points (Figure 2b);
- *n* new arcs are obtained imposing the passage on the *n* subdivision points; the centres lays on an extension of the previously created line and the radius is obtained from the *n*-th interpolated curvature value (Figure 2c);
- same passages are applied to the left and right profile arcs and the complete wireframe is obtained (Figure 2d).

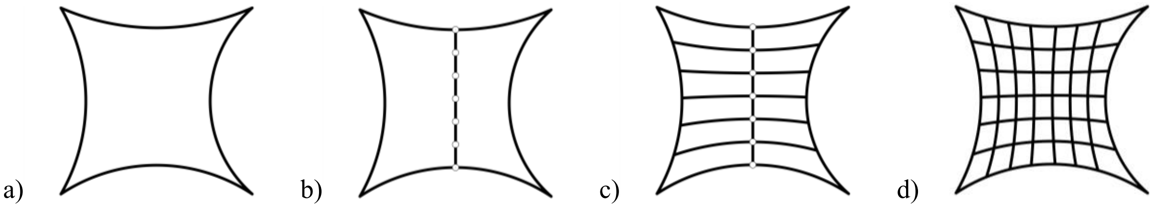

Figure 2. Conformal wireframe creation: a) starting profile arcs, b) arc mid-point line subdivision, c) one-direction wireframe, d) final wireframe.

2.2 Lattice structure mesh modeling

Since the lattice structure is conformal, it is likely to have beams at nodes that are not orthogonal with respect to each other. In order to model a mesh around the wireframe, the following operations are executed:

- cylinders are built around the wireframe model and the intersections points of cylindres approaching the same node are computed; these points will be the vertexes of the mesh; the value of the diameters of cylinders approaching the same node equal to the biggest diameter value obtained from the size optimization (Figure 3a);
- 4 lines linking two nodes are obtained connecting the previously found intersections;
- at the mid-point of each line, new vertexes are obtained and repositioned according to the values of the optimized diameters of the beams (Figure 3b);
- an 8-faces mesh is modeled around each beam, connecting the 12 vertexes, assuming a double truncated pyramidal shape (Figure 3c).

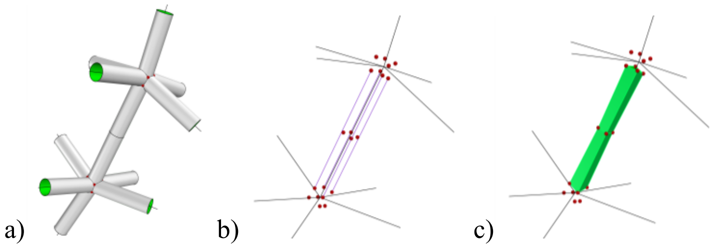

Figure 3. Mesh modeling at nodal points: a) cylinders intersections vertexes, b) mid vertexes, c) mesh beam model.

2.3 Topology optimization

Another possible structural optimization approach is given by topology optimization. With TO, a specific zone of the product, called "design space", is defined. It is recommended to simplify as much as possible the geometry, avoiding fillets, chamfers, and pocket holes, to let the optimization work better. Then, an optimization algorithm distributes the material on the design space according to loads and constraints. The goal of the optimization is usually to maximize the stiffness, imposing a desired reduction of mass, varying the density element by element, which is related to mechanical properties. As a results, a density map is obtained, which is contoured to a specific level of density (threshold), obtaining a mesh surface. The optimized mesh of the design space is taken as an "inspiration" to the further modeling of the part in a CAD tool, often operating manually. Consequently, considering the manual remodeling procedure, a FEA is needed to verify that the stress condition is respected.
Topology optimization is performed in SOLIDWORKS® 2018 Student Edition by Dassault Systemes, with the plugin SOLIDWORKS® Simulation, based on SIMP method. The optimized mesh is

remodeled in Evolve® software by Altair Engineering, Inc., and the remodeled part is then analysed in ANSYS® Workbench 2019 R1, by ANSYS, Inc.

3 RESULTS AND DISCUSSION

3.1 Case study

The case study presented in this work is a piston rod, currently produced with a pressure die-casting process in aluminum EN AC-46100 (AlSi11Cu2Fe); the properties of the material are presented in Table 1. Overall dimensions are shown in Figure 4a.

Table 1. Aluminum EN AC-46100 (AlSi11Cu2Fe) properties.

Density	Young modulus	Yield strength	Ultimate Tensile Strength	Poisson ratio
2700 kg/m3	71 GPa	140 MPa	240 MPa	0.34

The piston rod is loaded with an axial traction load of 7.5 kN along z-axis applied to the big rod's end and it is constrained by blocking all the displacements and rotations of the nodes belonging to the inner face of the small rod's end and by blocking the displacements along x and y directions of the nodes belonging to the face of the big rod's end to simulate the higher stiffness of the parts that are not optimized and maintain the original geometries. Figure 4b shows the simplified model of the rod with the design space and boundary conditions. The design space was modelled starting from the ZX plane; the arc curve at the big rod's end and the semicircle curve at the small rod's end were extracted; the profile was completed with two symmetric arcs, imposing tangency both at start and at end of the curve. On the YZ plane, two symmetrical arcs were modeled to connect the two rod's ends; tangency was imposed at the big rod's end connection and position in the small.

In order to compare different methods, the optimization and modeling approaches were applied only to the central part of the connecting rod.

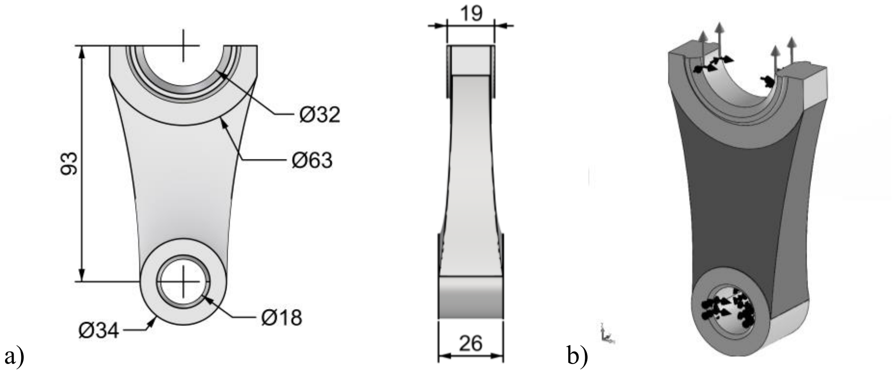

Figure 4. Piston rod: a) overall model dimensions, b) design space (dark grey), loads and constraints.

3.2 Size optimization of the lattice structure

First, the central part of the piston rod was filled with a wireframe representing a conformal lattice structure with a simple cubic unit cell of minimum length equal to 3 mm, following the procedure in Section 2.1 (Figure 5).

The FE model was set-up inside Grasshopper with Karamba3D plugin; loads and constraints previously defined were directly applied at the nodes of the beams placed at the interface between the central part and the big and small rod's ends; since the loads are applied to the nodes, the value of 7.5 kN was equally distributed in each node. The target utilization ratio was set to (90±1) % with respect to the yield strength. Upper and lower bound for beams dimeter were defined 1.5 mm and 0.5 mm, respectively. Figure 6 shows the distribution of the utilization ratio across the optimized lattice. The results coming from the size optimization, i.e. the optimized beams diameter, were used to model the lattice structure.

Figure 7a shows the piston rod with the central part filled with the optimized lattice structure modeled with NURBS surfaces. A lot of sharp edges can be found in the structure where smaller diameter beams connect at nodes with bigger ones (Figure 7b). Filleting operations would be useful to reduce stress concentration, but due to the model complexity, are quite difficult if not impossible to perform.

It is also important to remark that when dealing with complex geometries, such as organic models or lattice structures, NURBS modeling can be unsuitable due to difficulties in operating Boolean unions and due to high computational and memory resources required (Pasko *et al.*, 2011).

In order to solve the aforementioned problems, the conformal lattice structure was remodeled adopting the mesh approach presented in Section 2.2, obtaining the part shown in Figure 7c; there is no need of additional filleting operations (see Figure 7d) and it has been showed that structures modeled with a mesh surface subdivision method present better fatigue behavior (Savio *et al.*, 2019).

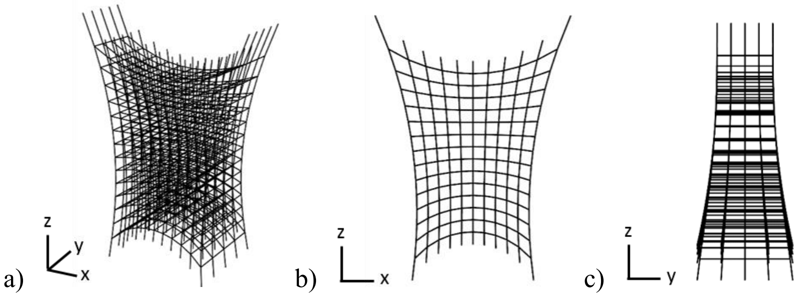

Figure 5. Lattice wireframe: a) perspective view, b) front view, c) side view.

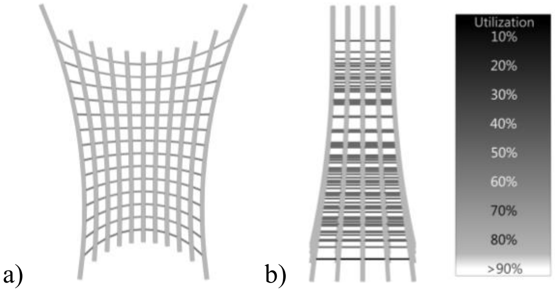

Figure 6. Utilization ratio across the optimized lattice: a) front view, b) side view.

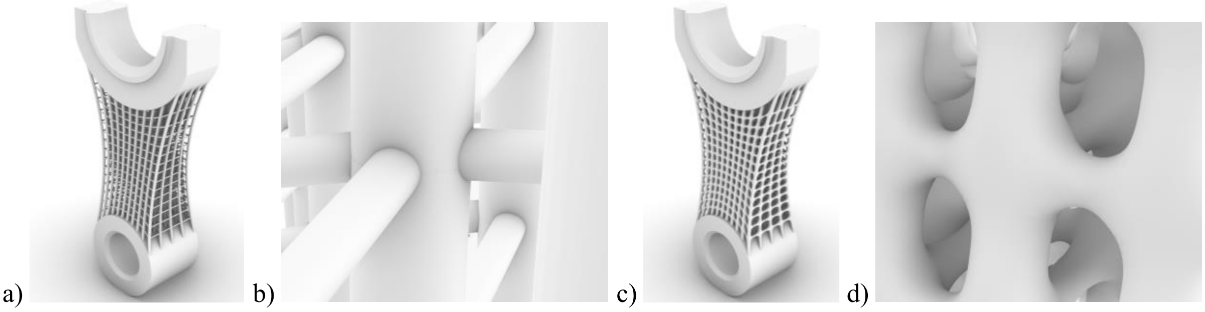

Figure 7. NURBS model: a) piston rod, b) sharp edges at nodal points. Mesh model: c) piston rod, d) smooth surfaces at nodal points due to Catmull-Clark algorithm.

3.3 Topology optimization

The piston rod was topologically optimized using SOLIDWORKS® 2018 Student Edition by Dassault Systemes, with the plugin SOLIDWORKS® Simulation.

First, the rod was remodeled, simplifying all the features. Then, the design space was selected and the loads and constraints were defined. The topology optimization was lunched with the goal of "best stiffness to weight ratio" and with the constraint of a final mass equal to 25% of the original part; the mass constraint set to 25% will control the threshold level with which the density map will be contoured. An additional symmetry constraint of the final part with respect to plane YZ and ZX was imposed. The mesh resulting from the optimization was remodeled with a NURBS approach in Altair Evolve® CAD 3D software, exploiting the PolyNURBS modeling feature and the double symmetry of the part. Figure 8 shows the result of the topology optimization (Figure 8a) and the remodeled part (Figure 8b).

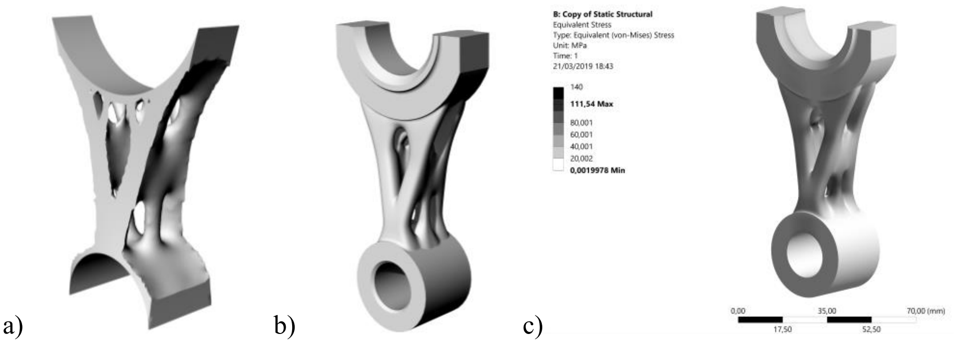

Figure 8. Topology optimization model: a) SOLIDWORKS® Simulation result, b) remodeled part in Altair Evolve, c) equivalent Von-Mises stress.

The remodeled part was then analysed with the Computer Aided Engineering (CAE) software ANSYS® 2019 R1. Boundary conditions, i.e. material, loads, constraints, was set; being the part symmetrical with respect to ZX and YZ plane, this condition was exploited to reduce the computational time. The part was meshed with tetrahedrons element imposing the element minimum size at 0.1 mm in order to obtain at least two elements on the smaller fillet that has a radius of 0.3mm; the element maximum size is 1 mm. The meshing method is patch independent and include automatic refinement in curvature and proximity. Figure 8c shows the analysis results; in particular, equivalent Von-Mises stress distribution is displayed.

3.4 Discussions

Table 2 shows a comparison between the volumes of the simplified piston rod and the ones resulting from the three different optimization and modeling approaches.

Table 2. Volumes of different piston rods.

Simplified piston rod	73613.32 mm3
Size optimization + NURBS modelling	38798.05 mm3
Size optimization + Mesh modelling	42791.94 mm3
Topology optimization + NURBS modelling	46131.88 mm3

With respect to the simplified piston rod, the size optimized NURBS model, the size optimized mesh model, and the topologically optimized model are respectively 47.29%, 41.87% and 37.33% lighter. During optimization phases, the ends of the piston rod remain untouched; so, a better comparison can be made between the central design space and the optimized geometries (Table 3).

Table 3. Volumes of different modeling approaches for central rod part (design space).

Simplified piston rod	38778.69 mm3
Size optimization + NURBS modelling	3780.30 mm3
Size optimization + Mesh modelling	7770.71 mm3
Topology optimization + NURBS modelling	11108.95 mm3

From this point of view, the size optimized NURBS model is 90.25% lighter, the size optimized mesh model is 79.96% lighter and the topologically optimized one is 71.35% lighter than the starting simplified central part of the rod.

The NURBS model is the lightest but presents sharp edges at nodal points because of the lack of fillets, that are difficult to perform due to the complexity of the structure; this affects the mechanical behavior, weakening the part. The mesh model, even if it comes from the same size optimization of the NURBS one, is heavier because Catmull-Clark subdivision surface algorithm thickens the beams with smaller diameters when approaching the nodes, resulting in more volume for the structure; but at the same time, the part presents a smooth surface with curvature continuity that guarantees better mechanical properties. Moreover, the modeling approach is automatic. The topologically optimized model is the heaviest of the three optimized models and requires manual remodeling of the mesh resulting from the optimization. However, topology optimization is useful at a conceptual design phase because allows to explore different configurations starting from boundary conditions and simple design spaces, and can be also used imposing technological constraints to produce the part with traditional techniques. Moreover, once remodeled, the topology optimized part needs to be verified again by a FE analysis, to make sure that the manual remodeling did not introduce weak points inside the part. The results of FE analysis in Figure 8c show that the maximum value for the equivalent Von-Mises stress is 111.54 MPa; since Aluminum AlSi11Cu2Fe has a yield stress of 140 MPa, the connecting rod withstand the applied load with a safety factor (SF) of 1.26, that is close to the 1.1 value used during the size optimization. While during size optimization the SF is imposed as objective of the iterative algorithm with the utilization ratio, in the topologically optimized part SF can only be verified at the end of the process with a FE analysis; also, due to manual remodeling of the part it is difficult to modify the shape in order to obtain the exact SF value.

The beam models were not analysed since it is assumed that size optimization on beam dimension gives a suitable structural verification.

4 CONCLUSIONS

In this work, an improvement of a previous modeling approach was presented, introducing the possibility of modeling conformal lattice structures thus extending the field of application of the design method. More, a piston rod was used as a case study to compare two types of structural optimization: size and topology optimization.

The topologically optimized part is the heaviest of the three models studied; the mesh resulting from TO is coarse and the geometry needs to be remodeled with a CAD software, manually by the user, and validated with FEA. The NURBS model of the lattice structure is the lightest but presents sharp edges at nodal points; this weakens the structure and filleting operations are suggested, but difficult to perform. The mesh model is heavier than the NURBS one but, at the same time, the subdivision method guarantees smooth surfaces, with no need of filleting operations, resulting in an enhanced mechanical behavior and fatigue resistance.

From these observations, the modeling method that uses mesh and subdivision surface algorithm to generate a lattice structure appears to have the best performances. Nevertheless, the method needs to be improved. Indeed, future developments will concentrate on the approaches that deal with the interface between the lattice structure and the connecting rod ends parts (or surfaces/parts to join with, in general) because, by now, the connection still generates sharp edges. More, the conformal wireframe generation method depends on the possibility of simplifying the edges of the design space with four arc curves; alternatively, morphing algorithms can be used to map a regular wireframe on a specific shape, but improvements have to be done to reach a more general method that guarantee a more uniform cell distribution. Attention will be also given to the possibility of modeling different types of single cells, enhancing the method that generates the mesh around nodal points, and also enabling the possibility to suggest the shape of the cell, according to load conditions.

ACKNOWLEDGMENTS

This work was supported by Fondazione Cassa di Risparmio di Padova e Rovigo (CARIPARO).

REFERENCES

Altair (2018), *Altair Inspire: The Future of Simulation-Driven Design*. Available at: https://solidthinking.com/product/inspire/ (Accessed: 9 November 2018).

Bendsøe, M. P. (1989), “Optimal shape design as a material distribution problem”, *Structural Optimization. Springer*, Vol 1 No. 4, pp. 193–202.

Bendsoe, M. P. and Sigmund, O. (2013), *Topology Optimization: Theory, Methods, and Applications*. Springer Science & Business Media.

Bendsøe, M. P. and Sigmund, O. (1999), “Material interpolation schemes in topology optimization”, *Archive of Applied Mechanics*, Vol. 69 No. 9, pp. 635–654. http://doi.org/10.1007/s004190050248.

Brackett, D., Ashcroft, I. and Hague, R. (2011), “Topology optimization for additive manufacturing”, in *Proceedings of the Solid Freeform Fabrication Symposium*, Austin, TX. S, pp. 348–362.

Cagan, J. et al. (2005), “A framework for computational design synthesis: model and applications”, *Journal of Computing and Information Science in Engineering*. ASME, Vol. 5 No. 3, p. 171. http://doi.org/10.1115/1.2013289.

Catmull, E. and Clark, J. (1978), “Recursively generated B-spline surfaces on arbitrary topological meshes”, *Computer-Aided Design*. Elsevier, Vol. 10 No. 6, pp. 350–355. http://doi.org/10.1016/0010-4485(78)90110-0.

Chakrabarti, A. (2002), *Engineering Design Synthesis: Understanding, Approaches, and Tools*.

Han, Y. and Lu, W. F. (2018), “A novel design method for nonuniform lattice structures based on topology optimization”, *Journal of Mechanical Design*. ASME, Vol. 140 No. 9, pp. 91403–91410. Available at: http://dx.doi.org/10.1115/1.4040546.

Holmström, J. et al. (2010), “Rapid manufacturing in the spare parts supply chain”, *Journal of Manufacturing Technology Management*. Emerald Group Publishing Limited, Vol. 21 No. 6, pp. 687–697. http://doi.org/10.1108/17410381011063996.

Kirsch, U. (1993), *Problem Statement - Structural Optimization: Fundamentals and Applications*, in Kirsch, U. (ed.). Springer Berlin Heidelberg, Berlin, Heidelberg, pp. 1–56. http://doi.org/10.1007/978-3-642-84845-2_1.

Koziel, S. and Ogurtsov, S. (2014), “*Numerically Efficient Approach to Simulation-Driven Design of Planar Microstrip Antenna Arrays by Means of Surrogate-Based Optimization - Solving Computationally Expensive Engineering Problems*”, in Koziel, S., Leifsson, L. and Yang, X.-S. (eds). Springer International Publishing, Cham, pp. 149–170.

Liu, J. et al. (2018), “Current and future trends in topology optimization for additive manufacturing”, *Structural and Multidisciplinary Optimization*, Vol. 57 No. 6, pp. 2457–2483. http://doi.org/10.1007/s00158-018-1994-3.

Nessi, A. and Stanković, T. (2018), “Topology, shape, and size optimization of additively manufactured lattice structures based on the superformula”, in *International Design Engineering Technical Conferences and Computers and Information in Engineering Conference, Volume 2A: 44th Design Automation Conference*. ASME, p. V02AT03A042. http://doi.org/10.1115/detc2018-86191.

Ning, X. and Pellegrino, S. (2012), “Design of lightweight structural components for direct digital manufacturing”, in *53rd AIAA/ASME/ASCE/AHS/ASC Structures, Structural Dynamics and Materials Conference. American Institute of Aeronautics and Astronautics (Structures, Structural Dynamics, and Materials and Co-located Conferences)*, pp. 1–21. http://doi.org/10.2514/6.2012-1807.

Pasko, A. et al. (2011), “Procedural function-based modelling of volumetric microstructures”, *Graphical Models*. Elsevier Inc., Vol. 73 No. 5, pp. 165–181. http://doi.org/10.1016/j.gmod.2011.03.001.

Rosen, D. W. (2016), “A review of synthesis methods for additive manufacturing”, *Virtual and Physical Prototyping*. Taylor & Francis, Vol. 11 No. 4, pp. 305–317. http://doi.org/10.1080/17452759.2016.1240208.

Savio, G. et al. (2018a), “Geometric modeling of cellular materials for additive manufacturing in biomedical field: A review”, *Applied Bionics and Biomechanics*, Vol. 2018, pp. 1–14. http://doi.org/10.1155/2018/1654782.

Savio, G. et al. (2019), “Implications of modeling approaches on the fatigue behavior of cellular solids”, *Additive Manufacturing*. Elsevier, Vol. 25, pp. 50–58. http://doi.org/10.1016/j.addma.2018.10.047.

Savio, G., Meneghello, R. and Concheri, G. (2017), *Optimization of lattice structures for Additive Manufacturing Technologies BT - Advances on Mechanics, Design Engineering and Manufacturing : Proceedings of the International Joint Conference on Mechanics, Design Engineering & Advanced Manufacturing (JCM)*, in Eynard, B. et al. (eds). Springer International Publishing, Cham, pp. 213–222. http://doi.org/10.1007/978-3-319-45781-9_22.

Savio, G., Meneghello, R. and Concheri, G. (2018b), “Geometric modeling of lattice structures for additive manufacturing”, *Rapid Prototyping Journal*, Vol. 24 No. 2, pp. 351–360. http://doi.org/10.1108/RPJ-07-2016-0122.

Sellgren, U. (1999), “Simulation-driven design: motives, means, and opportunities”. *KTH.*

Shea, K., Aish, R. and Gourtovaia, M. (2005), “Towards integrated performance-driven generative design tools”, *Automation in Construction*. Elsevier, Vol. 14 No. 2, pp. 253–264. http://doi.org/10.1016/J.AUTCON.2004.07.002.

Shea, K. and Cagan, J. (1997), “Innovative dome design: Applying geodesic patterns with shape annealing”, *Artificial Intelligence for Engineering, Design, Analysis and Manufacturing*. Cambridge University Press, Vol. 11 No. 05, p. 379. http://doi.org/10.1017/S0890060400003310.

Shea, K. and Smith, I. F. C. (2006), “Improving Full-Scale Transmission Tower Design through Topology and Shape Optimization”, *Journal of Structural Engineering*. American Society of Civil Engineers, Vol. 132 No. 5, pp. 781–790. http://doi.org/10.1061/(ASCE)0733-9445(2006)132:5(781).

Stanković, T. et al. (2015), “A Generalized Optimality Criteria Method for Optimization of Additively Manufactured Multimaterial Lattice Structures”, *Journal of Mechanical Design*. ASME, Vol. 137 No. 11, pp. 111405–111412. Available at: http://dx.doi.org/10.1115/1.4030995.

Wang, C. et al. (2018), “Concurrent topology optimization design of structures and non-uniform parameterized lattice microstructures”, *Structural and Multidisciplinary Optimization*, Vol. 58 No. 1, pp. 35–50. http://doi.org/10.1007/s00158-018-2009-0.

Wang, H. V. (2005), “A unit cell approach for lightweight structure and compliant mechanism”. Georgia Institute Of Technology.

Zegard, T. and Paulino, G. H. (2016), “Bridging topology optimization and additive manufacturing”, *Structural and Multidisciplinary Optimization*, Vol. 53 No. 1, pp. 175–192. http://doi.org/10.1007/s00158-015-1274-4.

Zorin, D. (2000), “Subdivision zoo”, *Subdivision for Modeling and Animation*, pp. 65–104.

3D Model Representation and Data Exchange for Additive Manufacturing

G. Savio[1,3](✉), R. Meneghello[2,3], S. Rosso[1,3], and G. Concheri[1,3]

[1] Department of Civil Environmental and Architectural Engineering,
University of Padova, Via Venezia, 1, 35131 Padova, Italy
gianpaolo.savio@unipd.it
[2] Department of Management and Engineering, University of Padova,
Stradella San Nicola 3, 36100 Vicenza, Italy
[3] Laboratory of Design Tools and Methods in Industrial Engineering,
University of Padova, Via Venezia, 1, 35131 Padova, Italy

Abstract. The unique capabilities of additive manufacturing (AM) technologies highlight limits in commercial CAD tools. In this manuscript, after a synthetic description of the main AM technologies based on international standards classification, geometric modeling methods and data exchange file formats available in the literature are presented. Twelve geometric models have been studied to evaluate the effectiveness of the file format, noting the file dimension and the time to open and close the file. As a result, a roadmap in the development of new tools for design in AM is drawn, taking into account the new possibilities offered by AM technologies.

Keywords: Design for additive manufacturing · Data exchange · Geometric modeling · Additive manufacturing

1 Introduction

Additive manufacturing (AM) technologies have unique capabilities, making possible the fabrication of (i) shape with any complexity (in the limits of the design rules, such as minimal wall thickness and escape holes), (ii) parts having desired microstructure (by controlling process parameters), mesostructure (adopting cellular solids) and macrostructure, (iii) pieces having point by point specific materials, (iv) functional mechanisms without the assembly of parts [1].

In order to fulfill these unique capabilities, dedicated design tools and methods are needed, allowing, for instance, mass customization [2], parts consolidation [3], complex free-form and organic shape modeling, voxel and 3D bitmap design [4], cellular solids and topology optimization (multiscale design) [5–9], functionally graded material design (FGM) [10], flow channels [3] and thermal optimization [11]. More broadly it is possible to "maximize product performance in terms of manufacturability, reliability, and cost, through the synthesis of shapes, sizes and material compositions, subject to the capabilities of AM technologies" (adapted from [1]) which is the objective of Design for Additive Manufacturing (DfAM). Few of the mentioned tools

© Springer Nature Switzerland AG 2019
F. Cavas-Martínez et al. (Eds.): *Advances on Mechanics, Design Engineering and Manufacturing II*, LNME, pp. 412–421, 2019.
https://doi.org/10.1007/978-3-030-12346-8_40

are available in commercial CAD software, while others are only described in research projects.

To identify the potential of AM technologies, in this paper, firstly the international standard classification of AM technologies is presented. Then, geometric modeling and analysis approaches able to exploit the AM potential are presented, especially according to the capabilities of complex shape and functionally graded materials modeling. Finally, characteristics and efficiency of file formats for data exchange are discussed, studying 12 test cases. Mesh and NURBS represent effectively and efficiently both boundary and volumetric geometric models, while the implementation tested shows the need to strengthen the data exchange file format supported by international standards.

2 AM Technologies

ISO/ASTM 52900 [12] and ISO 17296-2 [13] provide definitions, classification, and description of the main AM technologies. Seven types of additive processes are identified:

- *vat photopolymerization* in which liquid photopolymer in a vat is selectively cured by light-activated polymerization,
- *material jetting* in which droplets of build material are selectively deposited,
- *binder jetting* in which a liquid bonding agent is selectively deposited to join powder materials,
- *powder bed fusion* in which thermal energy selectively fuses regions of a powder bed,
- *material extrusion* in which material is selectively dispensed through a nozzle or orifice,
- *directed energy deposition* in which focused thermal energy is used to fuse materials by melting as they are being deposited,
- *sheet lamination* in which sheets of material are bonded to form an object.

Due to the limits of commercial CAD/CAM tools, the capabilities of AM technologies are not yet fully exploited. For instance, a number of studies show that it is possible to obtain a continuous variation in material composition, varying gradually the mechanical properties [4, 14, 15], but there are not yet adequate tools to support the relevant design process. Other examples show the ability to embed 3D colors used as a passive wear indicator or embed electronics using metal nanoparticles [16]. Moreover, recent advances in using FGM in parts and AM technologies demonstrate the need of commercial CAD systems for creating heterogeneous objects [17].

3 Geometric Modeling for AM

A number of geometric modeling approaches are available in the literature. These can be classified in 3 main groups (Fig. 1): boundary representation (BRep), volume representation (VRep) and constructive solid geometry (CSG).

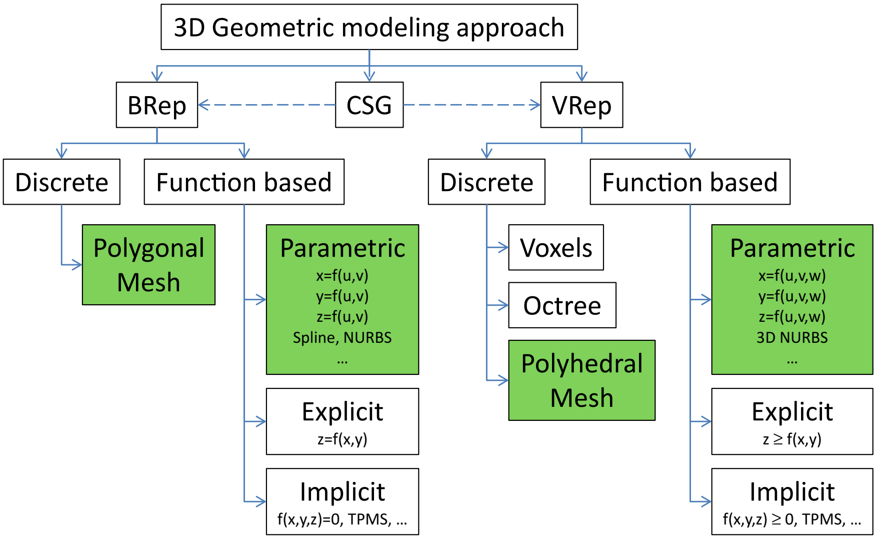
3D Geometric modeling approach
BRep
CSG
VRep
Discrete
Function based
Discrete
Function based
Polygonal Mesh
Parametric
x=f(u,v)
y=f(u,v)
z=f(u,v)
Spline, NURBS
…
Explicit
z=f(x,y)
Implicit
f(x,y,z)=0, TPMS, …
Voxels
Octree
Polyhedral Mesh
Parametric
x=f(u,v,w)
y=f(u,v,w)
z=f(u,v,w)
3D NURBS
…
Explicit
z ≥ f(x,y)
Implicit
f(x,y,z) ≥ 0, TPMS, …

Fig. 1. Geometric modeling approaches

BRep is a method for representing the shape of an object by a collection of connected surfaces describing the skin (i.e. boundary) of the solid and is the basic principle of solid modeling on which all CAD 3D geometric kernels are based since 40 years. In AM this approach is useful when the solid is made by a homogenous material and the skin is the only part that presents variable characteristics such, as colors that can be represented by a texture. A 3D surface can be represented by implicit, explicit or parametric functions, or by polygonal meshes. An equation of form $f(x, y, z) = 0$ is the implicit equation of a surface [18] also known as Function Representation (FRep), widely studied in the literature [19]. Regarding AM, FReps are able to easily design lattice structures [20]; for instance, triply periodic minimal surfaces (TPMS) are periodic implicit surfaces often used in AM for their curvature continuity. On the other hand, FReps are unable to represent and easily transform bounded surfaces. A parametric representation of a surface is given by $S(u, v) = (x(u, v), y(u, v), z(u, v))$, where u and v are independent parameters defined in an arbitrary interval usually normalized to [0, 1] [21]. The parametric surfaces, such as Bézier, Spline and Non Uniform Rational Basis-Splines (NURBS), are supported by numerically stable algorithms and allow more natural design and representation of shapes in a computer than implicit equations [21]. Parametric geometry is easy to express in the form of vector and matrices allowing to use relatively simple techniques to solve very complex analytical geometry problems, providing a common mathematical format for representing any curve and surface, drastically reducing the number and the complexity of subroutines required to solve geometric-modeling problems [22]. It is difficult, instead, to manage very complex shapes such as lattice structures by parametric functions [8]. Mesh models, which represent the surfaces by adjacent closed polygons, can improve the usability of complex shapes especially adopting subdivision surface algorithms [8]. Moreover, the geometric models adopted in AM are usually based on meshes.

When a part is made of heterogeneous materials, BReps are not enough. In this case it is necessary to describe colors or composition point by point, by means of VRep. Recently, voxel (a volumetric pixel) based modeling approach was proposed with a resolution set equal to the native resolution of the AM process [4]. This methodology can be improved by bringing together adjacent voxels with the same properties, making more efficient the spatial-occupancy enumeration (Octree encoding [18]). Alternatively, a more flexible approach based on polyhedral mesh can be adopted in the design of heterogeneous materials taking inspiration from FEA/CAE methodologies. As in the case of BReps, a VRep can be represented by implicit, explicit or parametric functions. Besides the previously mentioned troubles for implicit and explicit functions, it is very difficult to work on different level of inequalities to set the distribution of different materials: it is possible to set a material at each k value of the f (x, y, z) = k, but is quite difficult or impossible to get an adequate match between desired spatial distribution of the materials and f(x, y, z). Instead, parametric functions such as NURBS 3D, show a number of advantages especially in CAD and FEA integration (iso/geometric analysis [23–25]). This approach can be extended in FGM analysis [26]. Moreover, volumetric subdivision can be adopted in both discrete and function based approaches integrating iso-geometric analysis [27]. Additionally, this approach could be integrated into mesh modeling for cellular materials [8], allowing the design and the optimization of lattice structures.

A different approach in geometric modeling is CSG, in which a solid is represented combining a number of primitives, such as prisms and cylinders, by using Boolean operators. Usually, primitive geometries are defined as homogeneous solids and are switched to BRep for visualization, data exchange, and manufacturing. Recent studies show the feasibility of adopting heterogeneous primitives in CSG, redefining the Boolean operations concept [28]. In this case, CSG can be likened to a VRep also called VCSG.

In short, in our opinion, the geometric modeling methodologies highlighted in green in Fig. 1 are the most effective approaches for AM, allowing geometric complexity and an effective and intuitive geometric modeling approach, providing a unified mathematical basis for every shape. Moreover, mesh and NURBS have become the de facto industry standard for the acquisition, representation, design and data exchange of geometric information, supported by many standards.

4 Data Exchange File Format for AM

In AM product development, there is a number of formats for data exchange partially able to cover the different stages of the product development process such as geometric modeling, design, manufacturing, and verification [29–31].

Stl file format is the de facto industry standard for transferring geometric information, but it supports only triangles with face normal, without any other product and manufacturing information (PMI) and color information. When exporting a free-form surface in stl, the geometry is approximated with planar triangles, therefore reducing the model accuracy [32]. Many other file formats can be used in data exchange for additive manufacturing such as ply, Obj, Step, AMF, 3MF, WRLM, JT, slc, each one has its pros and cons. Unlike the other, ply format supports polygonal meshes that are not necessarily triangles.

Step AP 242 (ISO 10303-242 [33]), developed by ISO, is probably the file format that could better cover the whole product development stage, including PMI and annotations, but the implementations tested do not support triangular meshes for now, even if the next version of this standard is introducing a number of features dedicated to AM such as curved triangles (mesh with normal at vertices), building orientation, building volume, support structures. Moreover, in the 3rd edition, Step will include heterogeneous materials, representation of lattice structures and semantic representation of PMI for Additive manufacturing [34].

ISO and ASTM have developed a standard "Specification for additive manufacturing file format (AMF)". The ISO/ASTM 52915 [35] is an XML-based format describing parts by triangles. It supports color, texture mapping, few PMI (currently not tolerances), possibly lattices and FGM. Moreover, ASTM is working on a new specification for AMF supporting voxel information, CSG representations and solid texturing [36].

In 3MF consortium opinion, AMF is widely held to have gone into a standards body too early, having some features not clearly defined and other features missing [37]. AMF inspired the foundations of 3MF, that is an industry consortium working to define a 3D printing format free of royalties, patents and licensing access and implementation.

In order to evaluate the efficiency of different file formats in terms of file dimension and time to open and save a file, 12 geometric models were studied, derived adopting 0, 2 and 4 iterations of the Catmull-Clark subdivision surface algorithm [38] on 4 cases: a regular lattice [8], a random lattice [39, 40], a variable thickness triply periodic surface and an organic model (Fig. 2). Subdivision surface algorithm was used for several reasons: it allows to increase rapidly and consistently the model complexity, it is an interesting approach in designing lattice structures and organic shapes, it can be implemented in graphic card, it is widely used in visualization and rendering, and can potentially can reduce the amount of data in file exchange. Table 1 summarizes the number of vertices and faces for the test cases at different levels of subdivision: the most complex surface is the random lattice after 4 iterations of the Catmull-Clark subdivision scheme.

Table 2 shows the file dimension for each test case in MByte. The number of iterations of the subdivision increases rapidly the file dimension. Moreover in the implementation adopted (Rhinoceros 6 by Robert McNeel & Associates; native file format *.3 dm [41]), AMF uses a large amount of memory, up to 10 GByte, about 10 times the ply format and 20 times the 3MF (a compressed version of AMF consisting of a zip file exists, but requires higher computational time).

Table 3 shows time to open and save the file containing the regular lattice after 4 subdivision iterations. Stl is the fastest to save due to the few information contained, but requests more time to open because the software needs to reconstruct the data structure (stl file format describes each triangle by its vertices coordinates, duplicating the vertex shared by adjacent triangles). In the implementation adopted, 3MF shows the longest time to open and to save.

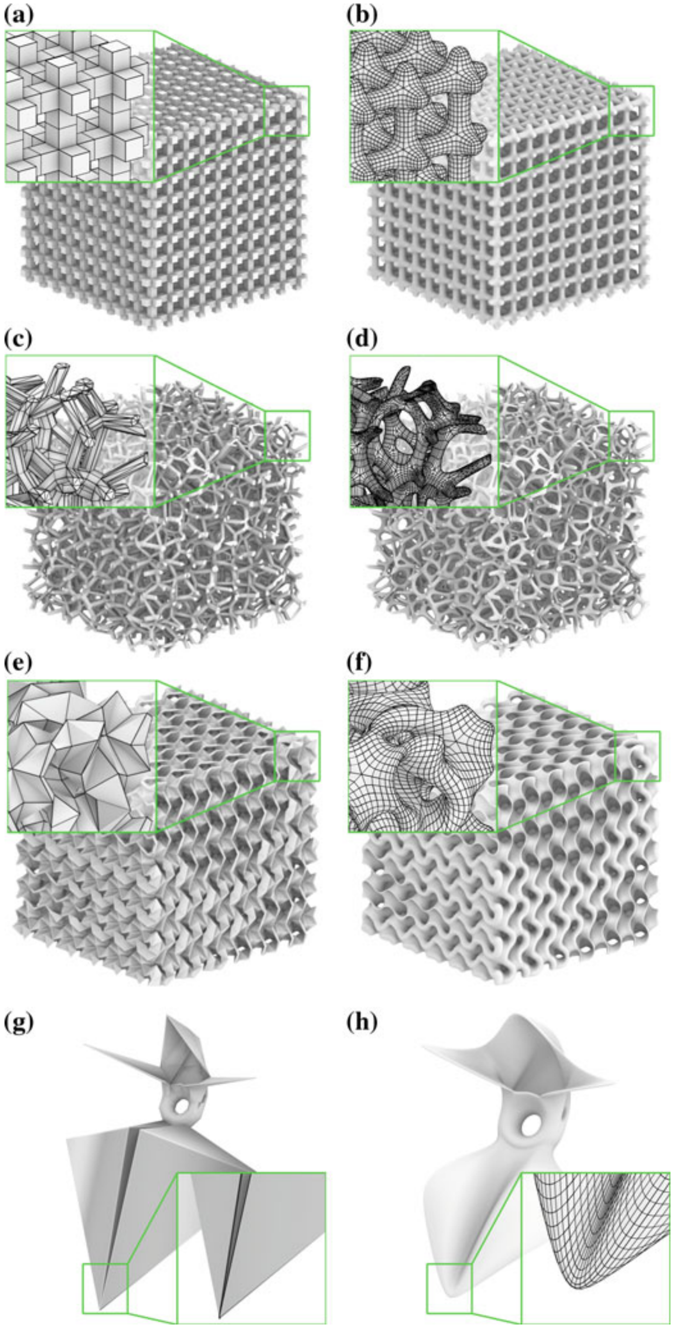

Fig. 2. Test cases adopted for the investigation of data exchange file format: initial (**a**) and subdivided mesh (**b**) of a regular lattice structures based on a cubic cell; initial (**c**) and subdivided mesh (**d**) of a random lattice; initial (**e**) and subdivided mesh (**f**) of a quasi-gyroid lattice with variable thickness; initial (**g**) and subdivided mesh (h) of an organic model

Table 1. Number of vertices and faces of the test cases at different levels of subdivision

	Vertices			Faces		
	0 iter.	2 iter.	4 iter.	0 iter.	2 iter.	4 iter.
Case 1: regular lattice	98,400	390,200	6,294,200	24,600	393,600	6,297,600
Case 2: random lattice	61,014	1,078,360	17,388,040	72,397	1,087,312	17,396,992
Case 3: gyroid lattice	22,679	356,038	5,747,398	22,464	359,424	5,750,784
Case 4: organic model	376	4294	66,174	266	4136	66,176

Table 2. File dimension in MByte of the test cases at different levels of subdivision

	Native			ply			AMF			3MF			stl		
Iter. n.	0	2	4	0	2	4	0	2	4	0	2	4	0	2	4
Case 1	0.9	9.6	177.8	3.1	21.6	387.8	9.4	215.6	3535.7	0.6	9.4	166.4	2.5	39.4	629.8
Case 2	2.0	60.1	1028.6	3.5	63.7	916.0	31.2	603.1	9836.3	1.8	33.2	511.3	6.4	108.7	1739.7
Case 3	0.7	11.1	272.4	1.2	20.7	357.7	10.7	198.6	3232.5	0.6	11.1	171.1	2.3	35.9	575.1
Case 4	0.04	0.37	4.01	0.02	0.21	3.57	0.13	2.24	36.4	0.01	0.12	1.94	0.03	0.41	6.62

Table 3. Time to open and save the file in case 1 after 4 subdivision iteration

	Time to open (s)	Time to save (s)
Native	6.8	27.9
ply	79.0	42.4
AMF	1019.1	336.9
3MF	73.0	63.2
stl	118.7	18.5

5 Conclusion

In this study, geometric modeling approaches for AM technologies were surveyed, identifying the most effective methods, considering the capabilities of AM such as shape complexity and FGM. Mesh and NURBS show the potential to handle the link between shape and function for both boundary and volumetric geometric models.

Moreover, few data exchange file formats were studied, highlighting the pros and cons of their main features. In the implementation tested, file formats supported by international standards show low efficiency. Future development of an adequate file format for data exchange should support volumetric models, complex geometry, exact geometry (tessellation is not fundamental), subdivision surfaces and hierarchical structures along the whole product development, over PMI and color information.

Acknowledgements. This work was partially supported by the University of Padova—Department of Civil, Environmental and Architectural Engineering ICEA (BIRD175287/17, 2017).

References

1. Gibson I, Rosen D, Stucker B (2015) Additive manufacturing technologies. Springer, New York, New York, NY
2. Reeves P, Tuck C, Hague R (2011) Additive manufacturing for mass customization. In: Mass customization, pp 275–289
3. Hopkinson N, Hague RJM, Dickens PM (eds) (2005) Rapid manufacturing. Wiley, Chichester
4. Doubrovski EL, Tsai EY, Dikovsky D, Geraedts JMP, Herr H, Oxman N (2015) Voxel-based fabrication through material property mapping: a design method for bitmap printing. Comput Des 60:3–13
5. Yang S, Tang Y, Zhao YF (2015) A new part consolidation method to embrace the design freedom of additive manufacturing. J Manuf Process 20:444–449
6. Tang Y, Kurtz A, Zhao YF (2015) Bidirectional evolutionary structural optimization (BESO) based design method for lattice structure to be fabricated by additive manufacturing. Comput Des 69:91–101
7. Savio G, Meneghello R, CONCHERI G (2017) Optimization of lattice structures for additive manufacturing technologies. In: Eynard B, Nigrelli V, Oliveri SM, Peris-Fajarnes G, Rizzuti S (eds) Advances on mechanics, design engineering and manufacturing. In Lecture notes in mechanical engineering. Springer, Cham, pp 213–222
8. Savio G, Meneghello R, Concheri G (2018) Geometric modeling of lattice structures for additive manufacturing. Rapid Prototyp J 24:351–360
9. Tamburrino F, Graziosi S, Bordegoni M (2018) The design process of additively manufactured mesoscale lattice structures: a review. J Comput Inf Sci Eng 18:1–16
10. Mahamood R, Akinlabi E, Shukla M, Pityana S (2012) Functionally graded materials: an overview. In: Proceedings of the world congress on engineering 2012, vol III (WCE 2012), London, UK, 4–6 July 2012. pp 1291–1299
11. Challis VJ, Roberts AP, Wilkins AH (2008) Design of three dimensional isotropic microstructures for maximized stiffness and conductivity. Int J Solids Struct 45:4130–4146
12. ASTM (2015) ISO/ASTM52900-15 Standard terminology for additive manufacturing – general principles – terminology, ASTM International, West Conshohocken, PA. https://doi.org/10.1520/ISOASTM52900-15
13. ISO 17296-2:2015 additive manufacturing—general principles—Part 2: overview of process categories and feedstock
14. Garland A, Fadel G (2015) Design and manufacturing functionally gradient material objects with an off the shelf three-dimensional printer: challenges and solutions. J Mech Des 137:111407
15. Grujicic M, Cao G, Fadel GM (2001) Effective materials properties: determination and application in mechanical design and optimization. Proc Inst Mech Eng Part L J Mater Des Appl 215:225–234
16. HP's Jet Fusion 3D Printing Technology: enabling the next industrial revolution. https://higherlogicdownload.s3.amazonaws.com/AUVSI/6322f901-72cc-424f-9550-cee46d4da1d6/UploadedImages/documents/FutureRoboticsForumPresentations/HPJetFusion3D.pdf

17. Bhashyam S, Hoon Shin K, Dutta D (2000) An integrated CAD system for design of heterogeneous objects. Rapid Prototyp J 6:119–135
18. Mortenson ME (1997) Geometric modeling. Wiley (1997)
19. Pasko A, Adzhiev V, Sourin A, Savchenko V (1995) Function representation in geometric modeling: concepts, implementation and applications. Vis Comput 11:429–446
20. Pasko A, Fryazinov O, Vilbrandt T, Fayolle P, Adzhiev V (2011) Procedural function-based modelling of volumetric microstructures. Graph Models 73:165–181
21. Piegl L, Tiller W (1997) The NURBS book. Springer, Berlin, Heidelberg
22. Mortenson ME (1985) Geometric modeling. Wiley
23. Nguyen VP, Kerfriden P, Brino M, Bordas SPA, Bonisoli E (2014) Nitsche's method for two and three dimensional NURBS patch coupling. Comput Mech 53:1163–1182
24. Cottrell JA, Hughes TJR, Bazilevs Y (2009) Isogeometric analysis: toward Integration of CAD and FEA. Wiley, Chichester
25. Tornincasa S, Bonisoli E, Kerfriden P, Brino M (2014) Investigation of crossing and veering phenomena in an isogeometric analysis framework. In: Allemang R (ed) Topics in modal analysis II, vol 8. Springer, Cham, pp 361–376
26. Tran LV, Ferreira AJM, Nguyen-Xuan H (2013) Isogeometric analysis of functionally graded plates using higher-order shear deformation theory. Compos Part B Eng 51:368–383
27. Burkhart D, Hamann B, Umlauf G (2010) Iso-geometric finite element analysis based on Catmull-Clark subdivision solids. Comput Graph Forum 29:1575–1584
28. Fang S, Srinivasan R (1998) Volumetric-CSG—a model-based volume visualization approach. In: Proceedings of sixth international conference in Central Europe on Computer Graphics and Visualization
29. Nassar AR, Reutzel EW (2013) A proposed digital thread for additive manufacturing. Solid Free Fabr 19–43
30. Xiao J, Eynard B, Anwer N, Le Duigou J, Durupt A (2016) Geometric models and standards for additive manufacturing: a preliminary survey. In: Virtual concept 2016 international workshop on major trends in product design, Bordeaux, France, 17–18 March 2016. https://hal.archives-ouvertes.fr/hal-01364825v1
31. Xiao J, Anwer N, Durupt A, Le Duigou J, Eynard B (2017) Standardisation focus on process planning and operations management for additive manufacturing. In: Eynard B, Nigrelli V, Oliveri SM, Peris-Fajarnes G, Rizzuti S (eds) Advances on mechanics, design engineering and manufacturing. In "Lecture notes in mechanical engineering." Springer, Cham, pp 223–232
32. Hällgren S, Pejryd L, Ekengren J (2016) 3D data export for additive manufacturing-improving geometric accuracy. Procedia CIRP 50:518–523
33. ISO 10303-242:2014 Industrial automation systems and integration—product data representation and exchange—Part 242: Application protocol: managed model-based 3D engineering
34. AP 242 Edition 2 capabilities for additive manufacturing interoperability. http://www.ap242.org/additive-manufacturing
35. ASTM (2016) ISO/ASTM52915-16 Standard specification for additive manufacturing file format (AMF) Version 1.2, ASTM International, West Conshohocken, PA. https://doi.org/10.1520/ISOASTM52915-16
36. ASTM WK48549 New specification for AMF support for solid modeling: voxel information, constructive solid geometry representations and solid texturing, ASTM International, West Conshohocken, PA
37. 3MF CONSORTIUM. https://3mf.io
38. Catmull E, Clark J (1978) Recursively generated B-spline surfaces on arbitrary topological meshes. Comput Des 10:350–355

39. Savio G, Rosso S, Meneghello R, Concheri G (2018) Geometric modeling of cellular materials for additive manufacturing in biomedical field: a review. Appl Bionics Biomech 2018:1–14
40. Fantini M, Curto M, De Crescenzio F (2016) A method to design biomimetic scaffolds for bone tissue engineering based on Voronoi lattices. Virtual Phys Prototyp 11:77–90
41. OpenNURBS Initiative. https://www.rhino3d.com/en/opennurbs

Additive Manufacturing 25 (2019) 50–58

Contents lists available at ScienceDirect

Additive Manufacturing

journal homepage: www.elsevier.com/locate/addma

Full length article

Implications of modeling approaches on the fatigue behavior of cellular solids

Gianpaolo Savio[a,*], Stefano Rosso[a], Andrea Curtarello[a], Roberto Meneghello[b], Gianmaria Concheri[a]

[a] University of Padova, Department of Civil, Environmental and Architectural Engineering, Laboratory of Design Tools and Methods in Industrial Engineering, Via Venezia 1, 35131, Padova, Italy
[b] University of Padova, Department of Management and Engineering, Laboratory of Design Tools and Methods in Industrial Engineering, Stradella S. Nicola, 3, 36100, Vicenza, Italy

ARTICLE INFO

Keywords:
Subdivision surface
Lattice structures
Fatigue
Selective laser sintering
Design for additive manufacturing
Geometric modeling

ABSTRACT

According to recent studies, a new paradigm in the geometric modeling of lattice structures based on subdivision surfaces for additive manufacturing overcomes the critical issues on CAD modeling highlighted in the literature, such as scalability, robustness, and automation. In this work, the mechanical behavior of the subdivided lattice structures was investigated and compared with the standard lattices. Five types of cellular structures based on cubic cell were modeled: struts based on squared or circular section, with or without fillets and cell based on the subdivision approach. Sixty-five specimens were manufactured by selective laser sintering technology in polyamide 12 and tensile and fatigue tests were performed. Furthermore, numerical analyses were carried out in order to establish the stress concentration factors.

Results show that subdivided lattice structures, at the same resistant area, improve stiffness and fatigue life and reduce stress concentration while opening new perspectives in the development of lattice structures for additive manufacturing technologies and applications.

1. Introduction

In the last decades, Additive Manufacturing (AM), defined as “a process of joining materials to make objects from 3D model data, usually layer upon layer, as opposed to subtractive manufacturing methodologies” [1], has received increasing attention from the scientific research community. The possibility of producing parts in a layer-wise fashion brings a huge freedom in shape and complexity. Among AM technologies, Selective Laser Sintering (SLS) uses a laser beam to selectively sinter thin layers of powdered materials following the cross-sectional profiles obtained from slicing a 3D modeled object. In particular, polyamide 12 (PA12) was the most widely used laser sintered polymer making up more than 95 percent of the market and 25 percent of the value of AM material sales [2]. As stated in [3], SLS polyamide can be found as finished products in the automotive, aeronautical and biomedical field, owing to its mechanical properties [4], biocompatibility [5], the ease of processability and relatively low cost compared to other available SLS materials [2]. At the same time, the lack of a deep knowledge of the long-term mechanical properties of PA12 is highlighted [6]. Trying to overcome this limit, several studies have been carried out in the last years. Blattmeier et al. [7] studied the influence of surface characteristics on fatigue behavior of laser sintered PA12. Specimens presented two different layer orientations and, for each orientation, a grinding finished surface or a non-finished surface. Munguia and Dalgrano [8] performed fatigue tests on SLS PA12 specimens under four-point rotating bar bending at 30 Hz and 50 Hz. Salmoria et al. [9] investigated the mechanical properties of PA6 and PA12 blended specimens. The 20/80 and 50/50 PA6/PA12 blends presented good fatigue strength under the test conditions. Salazar et al. [10] tested fatigue crack growth of neat PA12 and short glass fiber filled PA12-f, both at 23 °C and −50 °C. At room temperature, neat and fiber filled PA12 presented similar fatigue behavior, while at −50 °C PA12-f performed better owing to the presence of glass fibers, assuring a Young’s modulus enhancement of 144 percent. They also compared mechanical, fracture and fatigue crack propagation behavior of PA12 and PA11, a bio-based polyamide obtained from vegetable oil, instead of petroleum [11]. Moreover, Van Hooreweder et al. [12–14] presented Wohler’s curves for PA12, obtained testing notched and un-notched specimens produced with different technologies like injection molding and selective laser sintering, and with different scan direction for the

---

[*] Corresponding author.
E-mail address: gianpaolo.savio@unipd.it (G. Savio).

https://doi.org/10.1016/j.addma.2018.10.047
Received 1 August 2018; Received in revised form 5 October 2018; Accepted 31 October 2018
Available online 02 November 2018
2214-8604/ © 2018 Elsevier B.V. All rights reserved.

sintered ones.

The aforementioned freedom in shape and complexity brought by AM allows to manufacture and to fully exploit the features of cellular solids, defined as materials made up of an interconnected network of solid struts, or plates which form the edges or faces of cells [15]. Due to the appearance of the obtained material, cellular solids are usually referred to as lattice structures. The possibility of designing the unit cell to put material only where it is needed for a specific application leads to a structure with optimal properties. Geometric modeling and design of additively manufactured lattice structures were recently reviewed, proposing a classification of cellular materials from a geometric point of view and an integrated and holistic view of the design process [16,17].

A number of studies investigate the mechanical properties of lattice structures. Moongkhamklang et al. [18], Zupan et al. [19], and Coté et al. [20] studied shear and compressive behavior of two cell geometries (diamond and square) realized in titanium matrix composite by means of static tests and analytical formulations. They underlined how the buckling effects are not negligible in the failure mode. Even Deshpande et al. [21] described compressive properties of aluminum alloy octet truss cell. Smith et al. [22] investigated the mechanical performance of body-centered cubic (BCC) and body-centered cubic with vertical pillars cells (BCCZ) realized by SLM technique and compared Young’s Modulus and stress behaviors obtained through FE analysis with experimental results finding good agreement. Tsopanos et al. [23] analyzed mechanical properties of stainless steel BCC cells and found a correlation between the mechanical properties, the relative density and the SLM process parameters. Experimental and numerical analysis on metallic lattice structures were also conducted by Luxner et al. [24], Wallach et al. [25], Ptochos et al. [26], Campoli et al. [27], Dallago et al. [28] and Al-Ketan et al. [29].

Many authors investigated the mechanical properties of polymeric cellular material. Josupeit et al. [30] investigated the mechanical behavior of PA12 sandwich structures made with different cell types through four point bending tests. Sudarmadji et al. [31] studied the mechanical properties and porosity relationship of 3 different polyhedral units that can be assembled into scaffold structures made of Polycaprolactone. Cerardi et al. [32] analyzed the mechanical properties of PA12 lattice structures through both experimental and numerical analysis. Rezaei et al. [33] investigated the structural properties of polylactic acid BCCZ cell shape. Uni-axial tests on square lattice structures of different sizes made of PA12 was carried out by Lammens et al. [34]. Maskery et al. [35] studied the mechanical behavior of three types of minimal surface lattice structures made by the polymer. They concluded that the cell geometry plays a crucial role in determining the lattice deformation process and failure mode. Vasenjak et al. [36] performed uniaxial compression loading tests on PA12 regular open cell cellular structures. They pointed out that the circular cell shape provides higher structural stability and higher capability of energy absorption in comparison to the quadratic cells.

Only a few studies on fatigue behavior on porous metallic materials are available in literature [37–41]. Many researchers proposed a numerical model compared to the data from fatigue tests [42]. Hedayati et al. [43] proposed a computational approach based on the finite element method to predict the fatigue behavior of lattice structures given the type of cell, cell dimension and S-N curve of the bulk material. The obtained S-N curves well matched the experimental results conducted on Ti–6Al–4V specimens for stress levels not exceeding 60% of the yield stress of the porous material and it was found that the irregularities of the material clearly decrease the fatigue life especially for low load values. Jamshidinia et al. [44] conducted experimental and numerical fatigue analysis on dental abutment with a lattice structure made of Ti-6Al-4V; they found good agreement between tests and simulations data. Moreover, the numerical results revealed the detrimental influence of the sharp corners on the fatigue performances of the structure. Zargarian et al. [45] compared the numerical results of regular titanium lattice samples with the fatigue tests data published in the literature [39,46,47]. They showed that the fatigue curves obeyed the power law and that the coefficient of the power law depends on relative density, geometry and fatigue behavior of the bulk material while the exponent only depends on the fatigue strength of the bulk material.

Recently, a new paradigm in geometric modeling of lattice structure based on subdivision surface was proposed [48]. This approach overcomes the critical issues on CAD modeling highlighted in literature, such as scalability, robustness, and automation [49], while static and fatigue behavior and stress concentration need experimental and numerical validations, which are the aims of this work.

Subdivision surface algorithms define a smooth surface as the limit of a sequence of successive refinements of a mesh or a control polygon of a parametric surface. Since the late 1970s, when the publication of the papers by Catmull and Clark [50] and Doo and Sabin [51] marked the beginning of subdivision for surface modeling, a number of subdivision schemes have been proposed and found applications in computer graphics and computer-assisted geometric design [52–55]. Moreover, these approaches are very easy to implement and very efficient [52].

In this paper, mechanical properties, fatigue behavior and stress concentration of PA12 SLS cellular structures are analyzed. More in detail, these properties are investigated on cubic cells obtained by subdivision surface modeling approach [48] and compared to typical cells with circular and squared sections, with and without fillets. Moreover, weight and size measurements were performed.

2. Materials and methods

2.1. Subdivision surface for lattice structures

Subdivision schemes exploit recursive algorithms to smooth an initial mesh model. The Catmull–Clark subdivision surface [50] is one of the most common methods, widely used in computer graphics, for approximating points preferably lying on a quadrilateral mesh. According to the initial mesh vertices, iteratively averaging their coordinates, new vertices are computed following a subdivision rule, splitting into four each single quad [56].

The approach adopted in the design of lattice structures (Fig. 1) consists in the definition of a mesh with 8 planar faces around each cell edge, obtaining an initial mesh that is subdivided by Catmull-Clark algorithm. Applying this subdivision scheme, a smooth surface is obtained. The resulting section is slightly smaller than the initial square section and is not perfectly circular. Curvature, fillet radius, and section shape can be defined more accurately by imposing boundary conditions

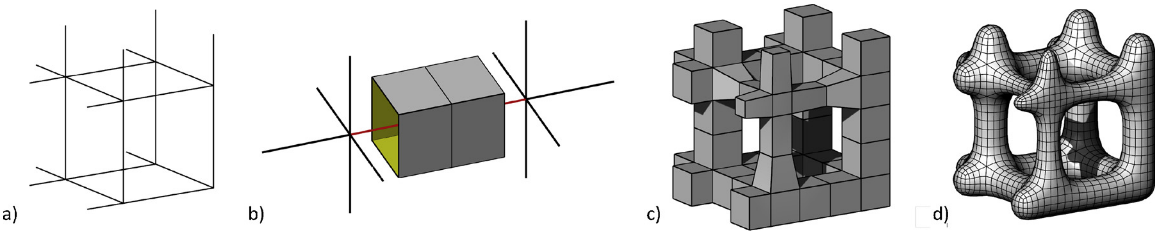

Fig. 1. Approach for modeling lattice structures: a) cell edges, b) 8-faces cell edge mesh, c) initial mesh and d) subdivided mesh [48].

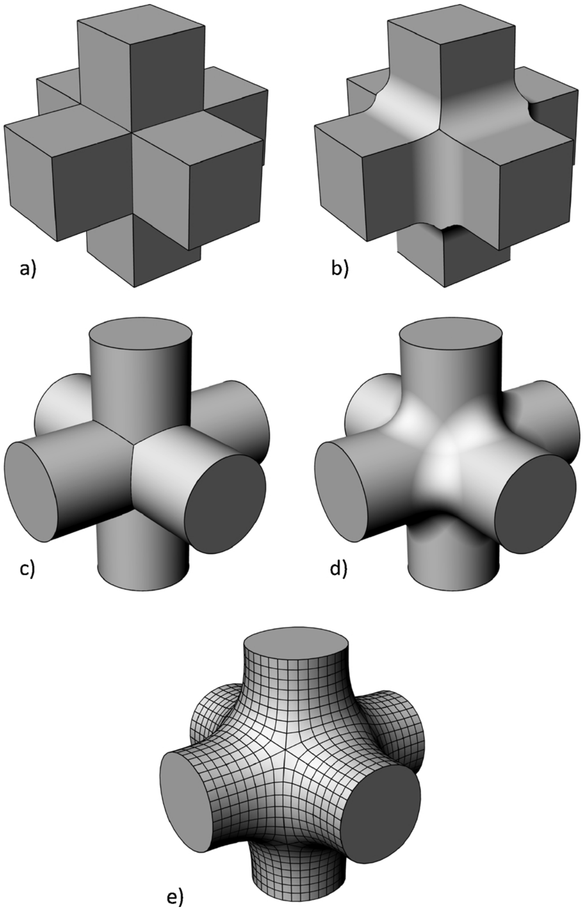

Fig. 2. Unit cells: a) S; b) SF; c) CY; d) CYF; e) CC.

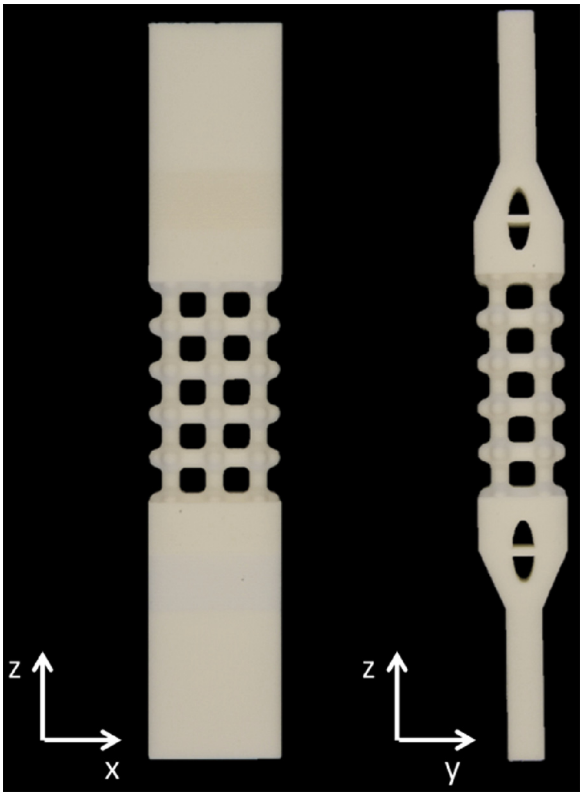

Fig. 3. Catmull-Clark specimen.

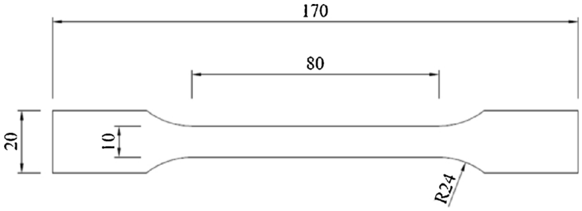

Fig. 4. Specimen type 1 A according ISO 527-2:2012 standard (thickness 4 mm).

Table 1
Powder and process parameters.

Laser beam power	20 W
Laser scan speed	3000 mm/s
Layer thickness	100 µm
Laser spot size	~ 0.4 mm
Building platform temperature	160 °C
Powder average size	60 µm
Unexposed/fresh powder	1:1

in the subdivision [57], by using an initial mesh with more polygons or by adjusting the mesh vertices coordinates. A detailed explanation of the modeling approach is available in [48].

2.2. Specimens

Five specimens were designed repeating a simple cubic cell along x, y and z-axes. Fig. 2 shows the unit cells used to design the samples: non-filleted cell with squared section (S, Fig. 2a), cell with squared section and a fillet radius (SF, Fig. 2b), non-filleted cell with circular section (CY, Fig. 2c), cell with circular section and a fillet radius (CYF, Fig. 2d) and unit cell obtained using the proposed approach after 3 iterations of the Catmull-Clark subdivision scheme (CC, Fig. 2e).

Fig. 3 shows a Catmull-Clark specimen with the reference frame, where the upper and lower holes were designed to reduce residual stress and material consumption. Each specimen had 5 unit cells along the z-axis, 3 unit cells along the x-axis and 2 unit cells along the y-axis. Taking into account the mechanical test machine and the AM process characteristics, 7.5 mm cell dimension and 1 mm fillet radius have been chosen, allowing the reduction of the ratio between dimensional and shape error, and cell size. The resistant area of each cell was equal to 6.25 mm^2, corresponding to a 2.5 mm struts size for the S and SF cells, and 2.821 mm struts diameter for the CY and CYF cells. The Catmull-Clark cell has a continuous shape variation and the size of the minimum struts section ranges between 2.79 and 2.88 mm. A constant section area allows more focused attention on the mechanical fatigue behavior of specimens originating from different modeling approaches.

A total of 65 PA12 specimens were produced by SLS EOSINT FORMIGA P110, 12 for each modeling approach and 5 additional specimens type 1 A according to ISO 527 standard [58] ("dogbone" specimen, Fig. 4). EOS "PA 2200 Performance" powder was used [59]. Build direction was parallel to specimen longitudinal axis and loading direction (z-axis). Other powder and process parameters are summarized in Table 1. All specimens were manufactured in one single batch adopting the same process parameters, and tested as build (no post processing operation was performed, excluding powder evacuation).

2.3. Experimental tests

Surface roughness of the dogbone specimens was measured by Talysurf i-Series along the growing direction, on the top surface and on the bottom surface. Specimens were weighed and measured by an optical coordinate measuring machine (OGP SmartScope Flash 200);

beams were measured both in the front and in the side views (Fig. 3) and the average value of struts' size for each sample was adopted to compute the actual area (only the struts parallel to the z-axis were considered). This area was considered in the computation of force for the fatigue tests.

Mechanical tests were executed on a MTS Acumen 3 Electrodynamic Test System equipped with a 3 kN load cell and a MTS 634.31 F extensometer, available at the Department of Neurosciences of the University of Padua. The five "dogbone" specimens were tensile tested according to ISO 527 standard [58] to measure bulk material mechanical properties at a speed rate of 2 mm/min and gauge length of 10 mm. Three samples for each cellular type were tensile tested at a speed rate of 5 mm/min and gauge length of 30 mm, in axial-displacement-controlled mode. Stress – Strain curves were plotted and Young's Modulus (E), ultimate tensile strength (UTS) or tensile strength that is referred as the maximum tensile stress, and strain at break (ε_{max}), were calculated according to standards ISO 1926 [60] and ISO 527 [58]. Fatigue tests were performed on 9 samples for each cellular type at 2 Hz frequency, with 0 stress ratio (R = 0, i.e. $\sigma_{max}/\sigma_{min} = 0$ where σ is the stress) to avoid buckling phenomena. Data were acquired with a timed trigger at 64 Hz to store entire cycles signals and with a peak-and-valley trigger to store minimum and maximum signals at every cycle. No artificial cooling was applied. The estimated Stress – Number of cycles (S-N) curves, also known as Wöhler curves, were statistically computed according to standard ISO/DIS 12107 [61].

2.4. Numerical analyses

In order to confirm the fatigue behavior, stress concentration factor (K_t) was established for the subdivided cell and for cells with circular and squared sections varying the fillet radius. K_t is defined as:

$$K_t = \sigma_{peak} / \sigma_{nom} \tag{1}$$

where σ_{nom} is the applied force divided by the strut section area and σ_{peak} is the maximum von Mises stress on the cell.

Owing to the specific boundary conditions and to the coupling equations, K_t was obtained by the finite element analysis (FEA) by a simplified model allowing to study a single cell, as if it was surrounded by others, and applying a displacement. Linear elastic analyses were performed by ANSYS® Release 16 software package using ″8nodes Solid185″ 3-D brick elements. According to the results proposed by Amado-Becker et al. [62] it can be stated that a sintered material can assume an isotropic behavior for certain values of energy density, as shown the PA 2200 Performance material datasheet [59]. Due to this assumption, the material input parameters were E (equal to 1870 MPa obtained by tensile tests) and the Poisson's ratio (ν = 0.35 found in literature [32]).

3. Results and discussion

Fig. 5 shows the manufactured specimens, one for each type of cell. Table 2 shows the arithmetical mean deviation of the roughness profile (Ra) measured on building direction, on the top surface and on the bottom surface of the dogbone specimens. Ra shows a higher value in the bottom surface. This outcome is supported by OGP images of the lattice samples (Fig. 6), where the bottom faces of the samples appear more rough. In literature prediction models and experimental results show that surface roughness on building direction is usually higher than in the top surface [8,14,63]. However, these results are closely related to the actual process parameters, especially in the top surface, to the filter wavelength and to the measurement techniques [64–66], while, a scattering of results on the top surface higher than on the growing direction is confirmed in the literature [8].

For each sample, the actual size of each strut parallel to z-axis was measured, obtaining a "mean actual size". Table 3 shows the mean size

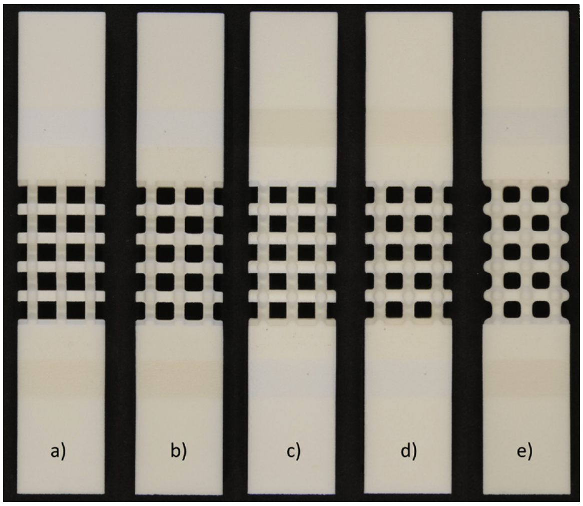

Fig. 5. Manufactured specimens one for each type of cell: a) S; b) SF; c) CY; d) CYF; e) CC.

Table 2
Surface roughness of the dogbone specimens.

	Building direction		Top Surface		Bottom surface	
	Mean	SD	Mean	SD	Mean	SD
Ra [µm]	10.8	0.8	10.4	1.6	15.0	2.3

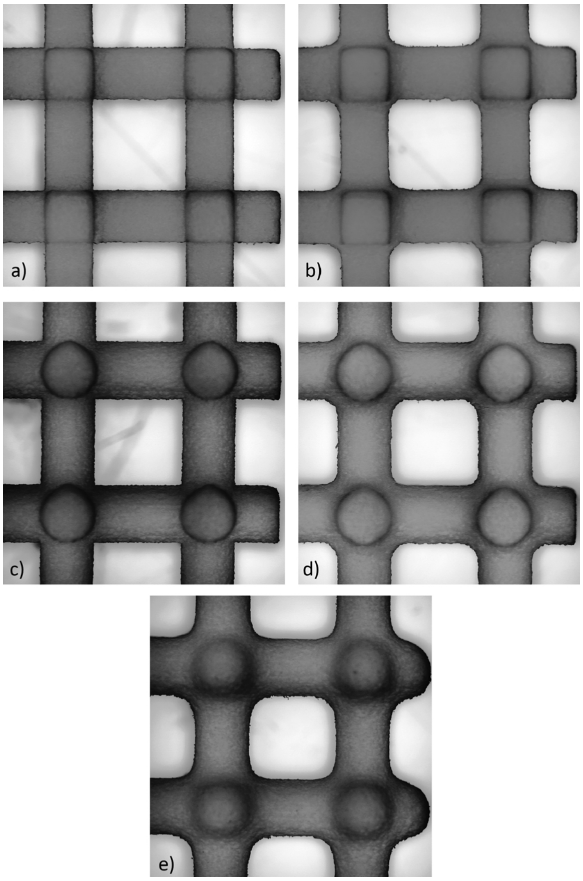

Fig. 6. OGP images of lattice samples (side 15 x 15 mm): a) S; b) SF; c) CY; d) CYF; e) CC.

Table 3
Mean dimensional error for specimen types.

	Specimen type									
	S		SF		CY		CYF		CC	
	Mean	SD	Mean	SD	Mean	SD	Mean	SD	Mean	SD
Size error [mm]	0.104	0.037	0.099	0.031	0.083	0.017	0.095	0.030	0.089	0.043

error and standard deviation (SD) of the "mean actual size" for each modeling approach. All samples sizes are greater than the nominal values (size error is always positive).

In standard finished SLS parts, after powder evacuation the surface is also cleaned by plastic bead blasting to remove any un-sintered powder sticking. For a smoother surface, parts can be polished in media tumblers or vibro machines. Unavoidably, these operations remove material, and consequently, standard SLS parts are manufactured slightly larger. Considering that no post processing operation was performed, it stands to reason that size errors are always positive. In other words, the actual size is always greater then the nominal size.

This fact reflects on mass measurements: the samples weigh more than the nominal, computed assuming a 930 kg/m^3 density [59], up to 8.0% on the average. Table 4 shows mean mass of each type of specimen compared to the nominal values.

Fig. 7 and Table 5 show the results of tensile tests of "dogbone" specimens. One of the specimens failed earlier than others, so its UTS and ε_{max} values were discarded, while E value was used to calculate the mean value. These values are in accordance with the datasheet provided by the supplier with a maximum difference on E of approximately 10% [59].

Figs. 8 and 9 show the mechanical properties of the 5 types of lattice specimens. The term "*effective*" (indicated by *) refers to mechanical properties calculated considering a bulk section of the lattice structure; in this case, the x–y plane has 2 × 3 cells, so the bulk area measures (3 × 7.5)x(2 × 7.5) = 337.5 mm^2. Even if SF specimens show the lowest strain at break, due to the low number of sample tested, there is no significant difference among the samples. Fillet radius does not appear to affect the elongation at break. A wide range of elongation at break can be found for the bulk material, as shown in Table 5 and Fig. 7. In the lattice specimens, the ratio between area and volume increases, increasing the chance to run into local surface defects that could be the cause of the elongation at break variability. Moreover, the position of the samples in the chamber could be another reason for the outcomes variability.

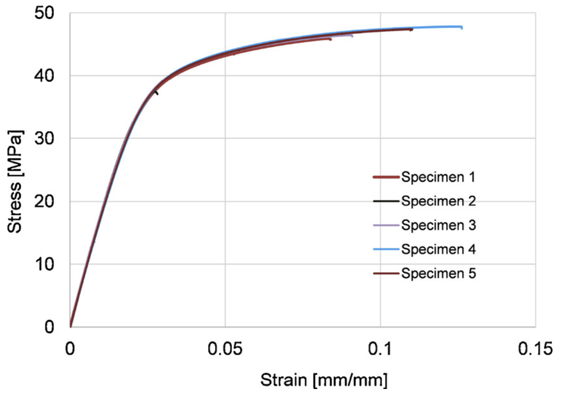

Fig. 7. Stress/Strain curves for ISO 527 specimens.

Table 5
Static tension test results according to ISO 527.

	Mean	Std Dev
E [MPa]	1869.8	43.3
UTS [MPa]	46.93	0.86
ε_{max}[mm/mm]	0.1028	0.0192

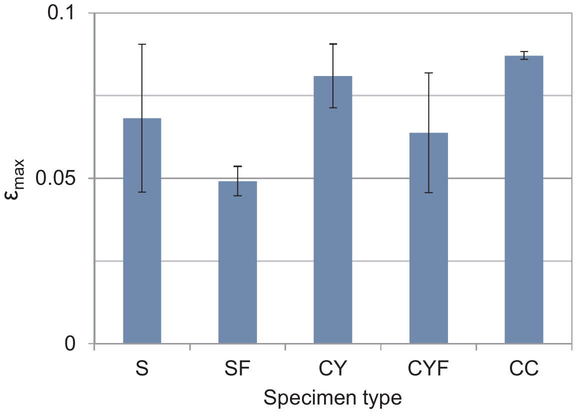

Fig. 8. Strain at break for lattice specimens.

S specimens show the lowest UTS*. Nevertheless, all the UTSs* range between 5 and 5.5 MPa, and there is no evidence of a significant difference among the samples. Fillets induce stiffness and consequently higher Young's Modulus that reaches the maximum value for the CC cell shape, due to the continuous variation in the struts section.

Fig. 10 shows the results of experimental fatigue tests together with the S – N curves for all the 5 types of specimen (S is the stress amplitude, N is the number of cycles to failure i.e. the fatigue life). Statistical analysis of data was executed according to ISO/DIS 12107 [61]. S–N curves were obtained by the model equation:

$$\log_{10}N = b_0 + b_1 \cdot \log_{10}S \qquad (2)$$

where b_0 and b_1 are the calculated fitting parameters reported in Table 6, together with the standard deviation SD and the correlation

Table 4
Mean mass for specimen types.

	Specimen type														
	S			SF			CY			CYF			CC		
	Nominal	Mean	SD	Nominal	Mean	SD	Nominal	Mean	SD	Nominal	Mean	SD	Nominal	Mean	SD
Mass [g]	17.946	19.373	0.109	18.133	19.511	0.165	17.919	19.270	0.139	18.036	19.428	0.108	18.270	19.664	0.152

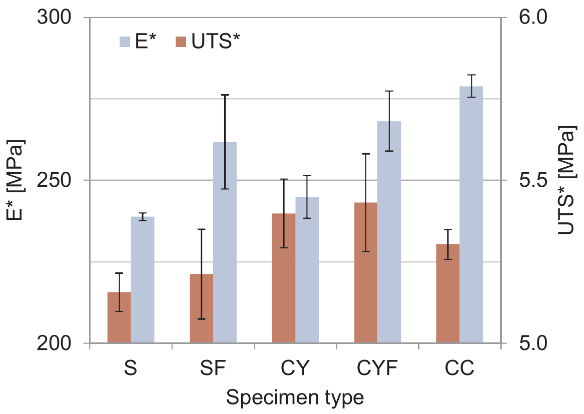

Fig. 9. Effective UTS and Young's Modulus for lattice specimens.

Table 6
Statistical parameters for S-N curve, according to ISO/DIS 12107.

Specimen type	b_0	b_1	SD	R^2
S	47.07	−28.89	0.35	0.86
SF	49.59	−30.00	0.35	0.89
CY	32.40	−18.55	0.47	0.60
CYF	51.58	−30.77	0.53	0.74
CC	39.48	−22.32	0.43	0.69

coefficient R^2.

The trend of the curves confirms that fillet edges increase the fatigue life compared to specimens with sharp edges. Sharp edges lead to stress concentrations that weaken the material and can be a preferential zone for crack initiation; all the specimens broke indeed near the node of the cell, i.e. where beams connect to each other. Catmull-Clark subdivision is the smoothest modeling approach and CC specimens resist up to one order of magnitude of cycles more than filleted specimens. Except for the CY, the curves have similar slopes. Statistical dispersion of data seems to be higher for high stress levels. The low values of R^2 show a considerable dispersion of the results that can be originated from the fabrication technology. Indeed SLS, as well as SLM and EBM, are complex processes and so will be most susceptible to imperfections due to the stacking-layered-fused nature [67] that influences surface roughness, dimensional and geometric accuracy, strut imperfections, microstructure inclusions, residual stress and overall stiffness and strength. This behavior is probably due to the presence of porosity and unmelted powder particles: cracks are more likely to initiate from inclusion [12], while pores and microvoids can delay fatigue failure [13]. Studies highlighted that selective laser sintered PA12 always presents a certain degree of porosity and inclusions, depending on process parameters used [68–71]. Specimen porosity, defects, and surface roughness can vary even in the same batch and this affects specimens fatigue life, leading to the dispersion of data. Using the same process parameters in the same batch and the same resistant area for all the specimens highlights the influence of the shape on fatigue life. Nevertheless, different shape variations could lead to different distributions of residual stresses and deformations. In our opinion, fillet radius and smooth shapes lead to locally more massive parts, therefore increasing residual stresses. On the other hand, sharp edges and different cross sections lead to a variation of the heat dissipation mechanisms during manufacture. We believe that these process issues are negligible compared to the effects of the modeling approach, which consists of small shape variation, and to the outcomes dispersion due to defects. Process simulation, curvature, and stress concertation integrated analyses could help to handle the intricate link between shape, process issues, and fatigue behavior. In other words, integrated simulations can help to distinguish individual effects of dependent variables. Anyhow, experimental results show that the modeling approach, based on subdivision surface, improve the fatigue life independently from other process dependent issues.

The results obtained through FEA are reported in Fig. 11 and 12. Fig. 11 shows the Von Mises stress for CC, CYF and SF cells adopting the nominal dimension of the specimens tested, on the surface and in the median section of cells, obtained applying a displacement inducing a mean stress in the beam equal to 10 MPa. The CC cell shows a smoother stress distribution, while CYF and SF show a concentration of stress at the transition between fillets and beam. This is closely related to the surface curvature; indeed a fillet introduces a discontinuity in surface curvature and consequently a stress concentration, while Catmull-Clark subdivision scheme produces a C^2 surface (i.e. a surface with continuity in curvature) [56], reducing K_t.

Fig. 12 shows the K_t behavior as the fillet radius changes for CYF and SF cells. CC cell has a smooth surface shape guaranteed by the modeling technique adopted and do not allow fillets, obtaining $K_t = 1.1$. Both the CYF and SF cells have a decreasing behavior as the fillet radius r increases. This is due to the beneficial effects that large fillet radii have on the peak stresses. As far as fillet radius increases, CYF and SF cells cannot reach the CC K_t value. These results are

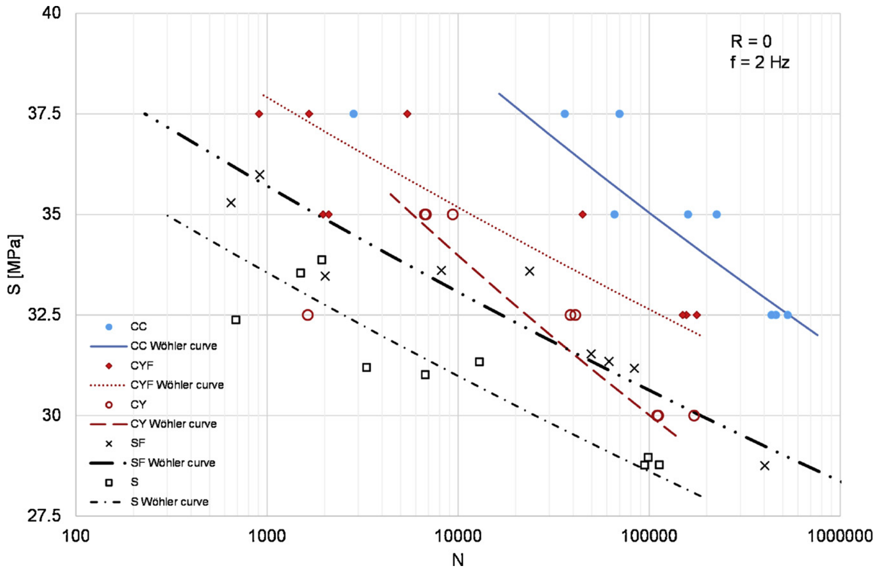

Fig. 10. S - N curves for lattice specimens, according to ISO/DIS 12107.

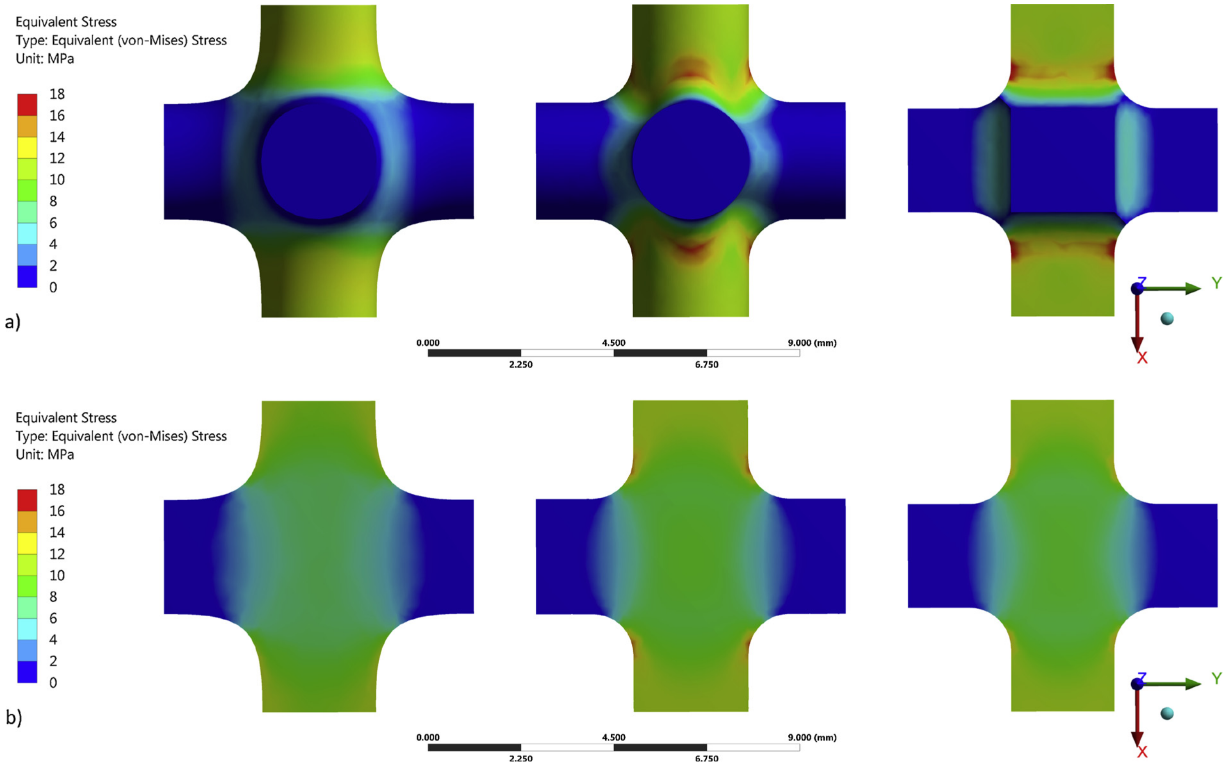

Fig. 11. Distribution of Von Mises stress for CC, CYF and SF cells a) on the surface and b) in the median section. Dimension as in Section 2.2.

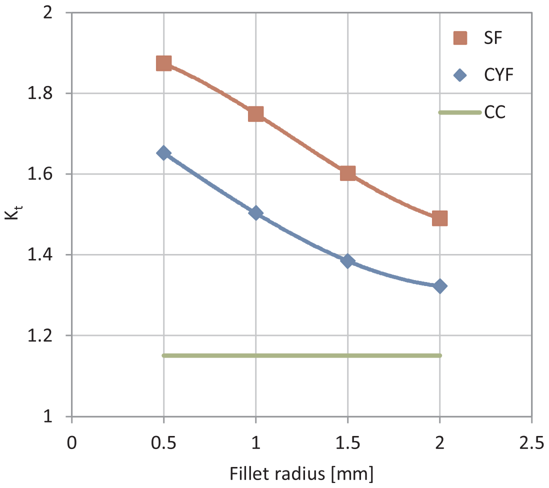

Fig. 12. K_t behavior depending on fillet radius for CYF, SF and CC cells. Other dimension as in Section 2.2.

consistent with the fatigue data obtained experimentally. The cell shape that proved to have the best fatigue behavior is the CC; this conclusion is confirmed by the smallest K_t values. In the same way, K_t proves the better fatigue resistance of the CYF cell with respect to the SF cell.

Over the improvement of fatigue life, the proposed approach brings several advantages in geometric modeling and data exchange for additive manufacturing. Besides being easy to implement and efficient [52], subdivision algorithms together with slicing tools are suitable for parallel computation, and some implementations at graphics processing unit (GPU) are available [72,73]. Moreover GPU developers had implemented subdivision algorisms in their hardware (e.g. NVIDIA). These opportunities will increase the potential of subdivision approaches, reducing computational time and file size [74]. The proposed approach could be extended to other cell types by identifying an adequate mesh topology [48]. Future work will be addressed in the comparison of mechanical properties of triply periodic minimal surfaces, whose advantages are described in literature [75], versus subdivided model.

4. Conclusions

In this work, SLS process was used to manufacture lattice specimens based on cubic cell, according to different geometric modeling approaches: a squared section with or without fillets, a circular section with or without fillets, and an original mesh modeling method based on Catmull-Clark subdivision surface. Static and fatigue tests were performed to study the behavior of these different types of specimen. Moreover, stress concentration factors were assessed by numerical analyses.

Results show that fillets increase structure stiffness and subdivided specimens show the highest Young's Modulus. Similarly, fillets improve fatigue life and subdivided specimens show the best fatigue behavior. Moreover, circular sections have a longer life than the squared section. Finally, numerical analyses show that increasing fillet radius, K_t decreases, but it is not able to reach the K_t of subdivided cell, whatever the radius is.

Over the mechanical properties improvements, the proposed approach shows several advantages in geometric modeling and data exchange for additive manufacturing. These results open new perspectives in the development of lattice structures for additive manufacturing technologies, improving fatigue life characteristics, meeting the design requirements in a number of industrial, biomedical and aerospace applications.

Declarations of interest

None.

Acknowledgements

The authors gratefully acknowledge generous in-kind support from

3Dfast srl and Andrea Sandi for fabricating test parts. This work was partially supported by the grants “FSE 2105-116-2216-2016” by Regione Veneto (Italy) and “BIRD175287/17” by University of Padua – Department of Civil, Environmental and Architectural Engineering ICEA (Italy).

References

[1] ISO/ASTM 52900:2015 Additive manufacturing – General principles – Terminology, 2015.

[2] T. Wohlers, Wohlers Report 2010: Additive Manufacturing State of the Industry Annual Worldwide Progress Report, Wohlers Associates, Inc., Color. USA, 2010.

[3] C.K. Chua, K.F. Leong, 3D PRINTING AND ADDITIVE MANUFACTURING: Principles and Applications (with Companion Media Pack) of Rapid Prototyping, World Scientific Publishing Co Inc, 2014.

[4] N. Lammens, M. Kersemans, I. De Baere, W. Van Paepegem, On the visco-elasto-plastic response of additively manufactured polyamide-12 (PA-12) through selective laser sintering, Polym. Test. 57 (2017) 149–155, https://doi.org/10.1016/j.polymertesting.2016.11.032.

[5] J.P. Singh, P.M. Pandey, Fitment study of porous polyamide scaffolds fabricated from selective laser sintering, Procedia Eng. 59 (2013) 59–71, https://doi.org/10.1016/j.proeng.2013.05.094.

[6] D. Bourell, M.C. Leu, D.W. Rosen (Eds.), Roadmap for Additive Manufacturing Identifying the Future of Freeform Processing, The University of Texas at Austin Laboratory for Freeform Fabrication Advanced Manufacturing Center, 2009.

[7] M. Blattmeier, G. Witt, J. Wortberg, J. Eggert, J. Toepker, Influence of surface characteristics on fatigue behaviour of laser sintered plastics, Rapid Prototyp. J. 18 (2012) 161–171, https://doi.org/10.1108/13552541211212140.

[8] J. Munguia, K. Dalgarno, Fatigue behaviour of laser-sintered PA12 specimens under four-point rotating bending, Rapid Prototyp. J. 20 (2014) 291–300, https://doi.org/10.1108/RPJ-07-2012-0064.

[9] G.V. Salmoria, J.L. Leite, L.F. Vieira, A.T.N. Pires, C.R.M. Roesler, Mechanical properties of PA6/PA12 blend specimens prepared by selective laser sintering, Polym. Test. 31 (2012) 411–416, https://doi.org/10.1016/j.polymertesting.2011.12.006.

[10] A. Salazar, A. Rico, J. Rodríguez, J. Segurado Escudero, R. Seltzer, F. Martin De La Escalera, Cutillas, Fatigue crack growth of SLS polyamide 12: effect of reinforcement and temperature, Compos. Part B Eng. 59 (2014) 285–292, https://doi.org/10.1016/j.compositesb.2013.12.017.

[11] A. Salazar, A. Rico, J. Rodríguez, J. Segurado Escudero, R. Seltzer, F. Martin De La Escalera, Cutillas, Monotonic loading and fatigue response of a bio-based polyamide PA11 and a petrol-based polyamide PA12 manufactured by selective laser sintering, Eur. Polym. J. 59 (2014) 36–45, https://doi.org/10.1016/j.eurpolymj.2014.07.016.

[12] B. Van Hooreweder, F. De Coninck, D. Moens, R. Boonen, P. Sas, Microstructural characterization of SLS-PA12 specimens under dynamic tension/compression excitation, Polym. Test. 29 (2010) 319–326, https://doi.org/10.1016/j.polymertesting.2009.12.006.

[13] B. Van Hooreweder, D. Moens, R. Boonen, J.P. Kruth, P. Sas, On the difference in material structure and fatigue properties of nylon specimens produced by injection molding and selective laser sintering, Polym. Test. 32 (2013) 972–981, https://doi.org/10.1016/j.polymertesting.2013.04.014.

[14] B. Van Hooreweder, J.P. Kruth, High cycle fatigue properties of selective laser sintered parts in polyamide 12, CIRP Ann. Manuf. Technol. 63 (2014) 241–244, https://doi.org/10.1016/j.cirp.2014.03.060.

[15] L.J. Gibson, M.F. Ashby, Cellular Solids, Cambridge University Press, Cambridge, 1997, https://doi.org/10.1017/CBO9781139878326.

[16] F. Tamburrino, S. Graziosi, M. Bordegoni, The design process of additively manufactured mesoscale lattice structures: a review, J. Comput. Inf. Sci. Eng. 18 (2018) 1–16, https://doi.org/10.1115/1.4040131.

[17] G. Savio, S. Rosso, R. Meneghello, G. Concheri, Geometric modeling of cellular materials for additive manufacturing in biomedical field: a review, Appl. Bionics Biomech. 2018 (2018) 1–14, https://doi.org/10.1155/2018/1654782.

[18] P. Moongkhamklang, V.S. Deshpande, H.N.G. Wadley, The compressive and shear response of titanium matrix composite lattice structures, Acta Mater. 58 (2010) 2822–2835, https://doi.org/10.1016/j.actamat.2010.01.004.

[19] M. Zupan, V.S. Deshpande, N.A. Fleck, The out-of-plane compressive behaviour of woven-core sandwich plates, Eur. J. Mech. A/Solids. 23 (2004) 411–421, https://doi.org/10.1016/j.euromechsol.2004.01.007.

[20] F. Côté, V.S. Deshpande, N.A. Fleck, A.G. Evans, The compressive and shear responses of corrugated and diamond lattice materials, Int. J. Solids Struct. 43 (2006) 6220–6242, https://doi.org/10.1016/j.ijsolstr.2005.07.045.

[21] V.S. Deshpande, N.A. Fleck, M.F. Ashby, Effective properties of the octet-truss lattice material, J. Mech. Phys. Solids 49 (2001) 1747–1769, https://doi.org/10.1016/S0022-5096(01)00010-2.

[22] M. Smith, Z. Guan, W.J. Cantwell, Finite element modelling of the compressive response of lattice structures manufactured using the selective laser melting technique, Int. J. Mech. Sci. 67 (2013) 28–41, https://doi.org/10.1016/j.ijmecsci.2012.12.004.

[23] S. Tsopanos, Ra.W. Mines, S. McKown, Y. Shen, W.J. Cantwell, W. Brooks, C.J. Sutcliffe, The influence of processing parameters on the mechanical properties of selectively laser melted stainless steel microlattice structures, J. Manuf. Sci. Eng. 132 (2010) 41011, https://doi.org/10.1115/1.4001743.

[24] M.H. Luxner, J. Stampfl, H.E. Pettermann, Finite element modeling concepts and linear analyses of 3D regular open cell structures, J. Mater. Sci. 40 (2005) 5859–5866, https://doi.org/10.1007/s10853-005-5020-y.

[25] J.C. Wallach, L.J. Gibson, Mechanical behavior of a three-dimensional truss material, Int. J. Solids Struct. 38 (2001) 7181–7196, https://doi.org/10.1016/S0020-7683(00)00400-5.

[26] E. Ptochos, G. Labeas, Shear modulus determination of cuboid metallic open-lattice cellular structures by analytical, numerical and homogenisation methods, Strain. 48 (2012) 415–429, https://doi.org/10.1111/j.1475-1305.2012.00837.x.

[27] G. Campoli, M.S. Borleffs, S. Amin Yavari, R. Wauthle, H. Weinans, A.A. Zadpoor, Mechanical properties of open-cell metallic biomaterials manufactured using additive manufacturing, Mater. Des. 49 (2013), https://doi.org/10.1016/j.matdes.2013.01.071.

[28] M. Dallago, M. Benedetti, V. Luchin, V. Fontanari, Orthotropic elastic constants of 2D cellular structures with variously arranged square cells: the effect of filleted wall junctions, Int. J. Mech. Sci. 122 (2017) 63–78, https://doi.org/10.1016/j.ijmecsci.2016.12.026.

[29] O. Al-Ketan, R. Rowshan, R.K. Abu Al-Rub, Topology-mechanical property relationship of 3D printed strut, skeletal, and sheet based periodic metallic cellular materials, Addit. Manuf. 19 (2018) 167–183, https://doi.org/10.1016/j.addma.2017.12.006.

[30] S. Josupeit, P. Delfs, D. Menge, H. Schmid, Manufacturability and mechanical characterization of laser sintered lattice structures, proc. 26th annu, Int. Solid Free. Fabr. Symp. (2016) 2077–2086.

[31] N. Sudarmadji, J.Y. Tan, K.F. Leong, C.K. Chua, Y.T. Loh, Investigation of the mechanical properties and porosity relationships in selective laser-sintered polyhedral for functionally graded scaffolds, Acta Biomater. 7 (2011) 530–537, https://doi.org/10.1016/j.actbio.2010.09.024.

[32] A. Cerardi, M. Caneri, R. Meneghello, G. Concheri, M. Ricotta, Mechanical characterization of polyamide cellular structures fabricated using selective laser sintering technologies, Mater. Des. 46 (2013) 910–915, https://doi.org/10.1016/j.matdes.2012.11.042.

[33] R. Rezaei, M. Karamooz Ravari, M. Badrossamay, M. Kadkhodaei, Mechanical characterization and finite element modeling of polylactic acid BCC-Z cellular lattice structures fabricated by fused deposition modeling, Proc. Inst. Mech. Eng. Part C J. Mech. Eng. Sci. 231 (2017) 1995–2004, https://doi.org/10.1177/0954406215626941.

[34] N. Lammens, D.I. Baere, V.W. Paepegem, Mechanical response of 3D-Printed lightweight Polyamide-12 lattice structures, Abstr. Atem Int. Conf. Adv. Technol. Exp. Mech. Asian Conf. Exp. Mech. (2017) 2–3 ICEM 17.

[35] I. Maskery, L. Sturm, A.O. Aremu, A. Panesar, C.B. Williams, C.J. Tuck, R.D. Wildman, I.A. Ashcroft, R.J.M. Hague, Insights into the mechanical properties of several triply periodic minimal surface lattice structures made by polymer additive manufacturing, Polymer (Guildf). 152 (2018) 62–71, https://doi.org/10.1016/j.polymer.2017.11.049.

[36] M. Vesenjak, L. Krstulović-Opara, Z. Ren, Ž. Domazet, Cell shape effect evaluation of polyamide cellular structures, Polym. Test. 29 (2010) 991–994, https://doi.org/10.1016/j.polymertesting.2010.09.001.

[37] A.M. Harte, N.A. Fleck, M.F. Ashby, Fatigue failure of an open cell and a closed cell aluminum alloy foam, Acta Mater. 47 (1999) 2511–2524, https://doi.org/10.1016/S1359-6454(99)00097-X.

[38] S. Amin Yavari, R. Wauthle, J. Van Der Stok, A.C. Riemslag, M. Janssen, M. Mulier, J.P. Kruth, J. Schrooten, H. Weinans, A.A. Zadpoor, Fatigue behavior of porous biomaterials manufactured using selective laser melting, Mater. Sci. Eng. C. 33 (2013) 4849–4858, https://doi.org/10.1016/j.msec.2013.08.006.

[39] S. Amin Yavari, S.M. Ahmadi, R. Wauthle, B. Pouran, J. Schrooten, H. Weinans, A.A. Zadpoor, Relationship between unit cell type and porosity and the fatigue behavior of selective laser melted meta-biomaterials, J. Mech. Behav. Biomed. Mater. 43 (2015) 91–100, https://doi.org/10.1016/j.jmbbm.2014.12.015.

[40] F. Li, J. Li, H. Kou, L. Zhou, Porous Ti6Al4V alloys with enhanced normalized fatigue strength for biomedical applications, Mater. Sci. Eng. C. 60 (2016) 485–488, https://doi.org/10.1016/j.msec.2015.11.074.

[41] B. Van Hooreweder, Y. Apers, K. Lietaert, J.P. Kruth, Improving the fatigue performance of porous metallic biomaterials produced by Selective Laser Melting, Acta Biomater. 47 (2017) 193–202, https://doi.org/10.1016/j.actbio.2016.10.005.

[42] P. Lipinski, A. Barbas, A.S. Bonnet, Fatigue behavior of thin-walled grade 2 titanium samples processed by selective laser melting. Application to life prediction of porous titanium implants, J. Mech. Behav. Biomed. Mater. 28 (2013) 274–290, https://doi.org/10.1016/j.jmbbm.2013.08.011.

[43] R. Hedayati, H. Hosseini-Toudeshky, M. Sadighi, M. Mohammadi-Aghdam, A.A. Zadpoor, Computational prediction of the fatigue behavior of additively manufactured porous metallic biomaterials, Int. J. Fatigue 84 (2016) 67–79, https://doi.org/10.1016/j.ijfatigue.2015.11.017.

[44] M. Jamshidinia, L. Wang, W. Tong, R. Ajlouni, R. Kovacevic, Fatigue properties of a dental implant produced by electron beam melting® (EBM), J. Mater. Process. Technol. 226 (2015) 255–263, https://doi.org/10.1016/j.jmatprotec.2015.07.013.

[45] A. Zargarian, M. Esfahanian, J. Kadkhodapour, S. Ziaei-Rad, Numerical simulation of the fatigue behavior of additive manufactured titanium porous lattice structures, Mater. Sci. Eng. C. 60 (2016) 339–347, https://doi.org/10.1016/j.msec.2015.11.054.

[46] N.W. Hrabe, P. Heinl, B. Flinn, C. Körner, R.K. Bordia, Compression-compression fatigue of selective electron beam melted cellular titanium (Ti-6Al-4V), J. Biomed. Mater. Res. - Part B Appl. Biomater. 99 B (2011) 313–320, https://doi.org/10.1002/jbm.b.31901.

[47] S.J. Li, L.E. Murr, X.Y. Cheng, Z.B. Zhang, Y.L. Hao, R. Yang, F. Medina, R.B. Wicker, Compression fatigue behavior of Ti-6Al-4V mesh arrays fabricated by electron beam melting, Acta Mater. 60 (2012) 793–802, https://doi.org/10.1016/j.

actamat.2011.10.051.
[48] G. Savio, R. Meneghello, G. Concheri, Geometric modeling of lattice structures for additive manufacturing, Rapid Prototyp. J. 24 (2018) 351–360, https://doi.org/10.1108/RPJ-07-2016-0122.
[49] A. Pasko, O. Fryazinov, T. Vilbrandt, P. Fayolle, V. Adzhiev, Procedural function-based modelling of volumetric microstructures, Graph. Models 73 (2011) 165–181, https://doi.org/10.1016/j.gmod.2011.03.001.
[50] E. Catmull, J. Clark, Recursively generated B-spline surfaces on arbitrary topological meshes, Comput. Des. 10 (1978) 350–355, https://doi.org/10.1016/0010-4485(78)90110-0.
[51] D. Doo, M. Sabin, Behaviour of recursive division surfaces near extraordinary points, Comput. Des. 10 (1978) 356–360, https://doi.org/10.1016/0010-4485(78)90111-2.
[52] D. Zorin, P. Schröder, Subdivision for Modeling and Animation, New York. 98, 2000, 1–203. http://en.scientificcommons.org/43038503.
[53] J. Peters, U. Reif, The simplest subdivision scheme for smoothing polyhedra, ACM Trans. Graph. 16 (1997) 420–431, https://doi.org/10.1145/263834.263851.
[54] N. Dyn, D. Levine, Ja. Gregory, A butterfly subdivision scheme for surface interpolation with tension control, ACM Trans. Graph. 9 (1990) 160–169, https://doi.org/10.1145/78956.78958.
[55] D. Zorin, P. Schröder, W. Sweldens, Interpolating Subdivision for meshes with arbitrary topology, Proc. 23rd Annu. Conf. Comput. Graph. Interact. Tech. - SIGGRAPH' 96 (1996) 189–192, https://doi.org/10.1145/237170.237254.
[56] D. Zorin, Subdivision zoo, Subdiv. Model. Animat. (2000) 65–104.
[57] A. Levin, Combined subdivision schemes for the design of surfaces satisfying boundary conditions, Comput. Aided Geom. Des. 16 (1999) 345–354, https://doi.org/10.1016/S0167-8396(98)00051-X.
[58] ISO 572-1:2012 Plastics – Determination of tensile properties – Part 1: General principles, 2012.
[59] PA 2200 Performance 1. 0, EOS GmbH - Electro Opt. Syst. (n.d.). https://eos.materialdatacenter.com/eo/ (accessed July 28, 2018).
[60] ISO 1926:2009 Rigid cellular plastics – Determination of tensile properties, 2009.
[61] ISO International Organization for Standardization, ISO/DIS 12107 – Metallic materials – Fatigue testing – Statistical planning and analysis of data, (2017).
[62] A. Amado-Becker, J. Ramos-Grez, M.J. Yañez, Y. Vargas, L. Gaete, Elastic tensor stiffness coefficients for SLS Nylon 12 under different degrees of densification as measured by ultrasonic technique, Rapid Prototyp. J. 14 (2008) 260–270, https://doi.org/10.1108/13552540810907929.
[63] L. Di Angelo, P. Di Stefano, A. Marzola, Surface quality prediction in FDM additive manufacturing, Int. J. Adv. Manuf. Technol. 93 (2017) 3655–3662, https://doi.org/10.1007/s00170-017-0763-6.
[64] M. Vetterli, M. Schmid, K. Wegener, Comprehensive investigation of surface characterization methods for laser sintered parts, DDMC 2014 Fraunhofer Direct Digit. Manuf. Conf. Proc. (2014), https://doi.org/10.3929/ethz-a-010357719.
[65] M. Launhardt, A. Wörz, A. Loderer, T. Laumer, D. Drummer, T. Hausotte, M. Schmidt, Detecting surface roughness on SLS parts with various measuring techniques, Polym. Test. 53 (2016) 217–226, https://doi.org/10.1016/j.polymertesting.2016.05.022.
[66] A. Sachdeva, S. Singh, V.S. Sharma, Investigating surface roughness of parts produced by SLS process, Int. J. Adv. Manuf. Technol. 64 (2013) 1505–1516, https://doi.org/10.1007/s00170-012-4118-z.
[67] M. Ashraf, I. Gibson, M.G. Rashed, Challenges and prospects of 3D printing in structural engineering, 13th Int. Conf. Steel, Sp. Compos. Struct. (2018) 1–10.
[68] H. Zarringhalam, N. Hopkinson, N.F. Kamperman, J.J. de Vlieger, Effects of processing on microstructure and properties of SLS Nylon 12, Mater. Sci. Eng. A. 435–436 (2006) 172–180, https://doi.org/10.1016/j.msea.2006.07.084.
[69] M. Pavan, T. Craeghs, P. Van Puyvelde, J. Kruth, W. Dewulf, Understanding the link between process parameters, microstructure and mechanical properties of laser sintered PA12 parts through X-ray computed tomography, Proc. 2nd Int. Conf. Prog. Addit. Manuf. (2016), pp. 569–574.
[70] S. Dadbakhsh, L. Verbelen, O. Verkinderen, D. Strobbe, P. Van Puyvelde, J.-P. Kruth, Effect of PA12 powder reuse on coalescence behaviour and microstructure of SLS parts, Eur. Polym. J. 92 (2017) 250–262, https://doi.org/10.1016/j.eurpolymj.2017.05.014.
[71] B. Caulfield, P.E. McHugh, S. Lohfeld, Dependence of mechanical properties of polyamide components on build parameters in the SLS process, J. Mater. Process. Technol. 182 (2007) 477–488, https://doi.org/10.1016/j.jmatprotec.2006.09.007.
[72] J. Konečný, Catmull-Clark Subdivision Surfaces on GPU, in: CESCG 2007, (2007) http://www.cescg.org/CESCG-2007/index.html.
[73] L.J. Shiue, I. Jones, J. Peters, A realtime GPU subdivision kernel, ACM SIGGRAPH 2005 Pap. - SIGGRAPH' 05, 2005. 10. doi:https://doi.org/10.1145/1186822.1073304.
[74] G. Savio, R. Meneghello, S. Rosso, G. Concheri, 3D model representation and data exchange for additive manufacturing, Adv. Mech. Des. Eng. Manuf. II. Lect. Notes Mech. Eng. (2019).
[75] F.S.L. Bobbert, K. Lietaert, A.A. Eftekhari, B. Pouran, S.M. Ahmadi, H. Weinans, A.A. Zadpoor, Additively manufactured metallic porous biomaterials based on minimal surfaces: a unique combination of topological, mechanical, and mass transport properties, Acta Biomater. 53 (2017) 572–584, https://doi.org/10.1016/j.actbio.2017.02.024.

International Journal on Interactive Design and Manufacturing (IJIDeM) (2019) 13:263–276
https://doi.org/10.1007/s12008-019-00543-0

ORIGINAL PAPER

Homogenization driven design of lightweight structures for additive manufacturing

Gianpaolo Savio[1] · **Andrea Curtarello**[1] · **Stefano Rosso**[1] · **Roberto Meneghello**[2] · **Gianmaria Concheri**[1]

Received: 26 October 2018 / Accepted: 9 January 2019 / Published online: 16 January 2019
© Springer-Verlag France SAS, part of Springer Nature 2019

Abstract

The diffusion of design tools suitable for regular lattice structures was recently stimulated by the spread of additive manufacturing technologies that enable the fabrication of complex geometries, exceeding the limits of traditional manufacturing methods. Fillet radii play a fundamental role in the design of lattice materials, reducing the stress concentration and improving fatigue life. However, only simplified beam and 2D models are available in the literature, which are unable to capture the actual stiffness and stress concentrations in the cell nodes of the 3-D beam based lattice structures with fillets. In this paper, four types of polyamide 12 cells, fabricated by selective laser sintering technology, based on cylindrical elements, are studied by finite element (FE) analysis, evaluating the influence of struts and fillet radii on the mechanical properties. In order to study a single cell, specific boundary conditions, simulating the presence of adjacent cells, were adopted in FE analysis. As a result, a model describing mechanical properties as a function of geometrical characteristics is obtained. By this model, it is possible to replace the complex shape of a lattice structure with its boundary, simplifying numerical analyses. This approach, called homogenization, is very useful in the design process of lightweight structures and can be adopted in optimization strategies. Numerical outcomes show that the effect of fillet radius is not negligible, especially in cells having a large number of struts. Moreover, experimental tests were also carried out showing a good agreement with the numerical analysis. Finally, an interactive design process for lattice structures based on experimental and numerical outcomes is proposed.

Keywords Lattice structures · Homogenization · Additive manufacturing · Polyamide 12 · Finite element analysis · Tensile tests

List of symbols

E	Young modulus
G	Shear modulus
ν	Poisson's ratio
R	Beam radius
r	Fillet radius
L	Cell dimension
Δ	Displacement
σ	Tensile stress
ε	Tensile strain
τ	Shear stress
γ	Shear strain
F	Force
ρ	Relative density or volume fraction
V	Actual cell volume
V_0	Volume occupied by the cell
$E_0, G_0, \nu_0, \sigma_0$	Mechanical properties of the bulk material
$E_{ef}, G_{ef}, \nu_{ef}, \sigma_{ef}, \tau_{ef}$	Effective mechanical properties of the virtual material of a cell
R^2	Coefficient of determination

Abbreviations

BCC	Body-centered cubic
BCCZ	Body-centered cubic with vertical pillars

✉ Gianpaolo Savio
gianpaolo.savio@unipd.it

[1] Laboratory of Design Tools and Methods in Industrial Engineering, Department of Civil, Environmental and Architectural Engineering, University of Padua, Via Venezia, 1, 35131 Padua, Italy

[2] Laboratory of Design Tools and Methods in Industrial Engineering, Department of Management and Engineering, University of Padua, Stradella S. Nicola, 3, 36100 Vicenza, Italy

SC	Simple cubic
RBCC	Reinforced body-centered cubic
GA	Modified Gibson–Ashby
OT	Octet-truss
FE	Finite element
AM	Additive manufacturing
PA 12	Polyamide 12
SLM	Selective laser melting
SLS	Selective laser sintering

1 Introduction

A cellular solid is a material made up of an interconnected network of solid struts, or plates which form the edges or faces of cells. These materials are characterized by light structures, high strength, and good energy absorption [1]. Due to their properties, many different application fields can be identified e.g. automotive, aerospace, biomedical, mechanical engineering, and industrial design [2–4]. Recently additive manufacturing (AM) technologies were widely adopted in the fabrication of cellular materials due to their capability of dealing with shape complexity, and several approaches in lattice structures design were reported [5–7]. At the same time, limits on simulation of complex shapes were highlighted in the literature [8]. The ability to assess the mechanical behavior of such materials is fundamental for their applicability. In literature, two different approaches can be found to achieve this goal by adopting micromechanical or continuum model [9]. The first method uses a detailed model of the base cell geometry and material, with the advantage of capturing the influence of both shape and material on the structural properties of the investigated part. On the other hand, this means high computational costs and thus it is difficult to apply as a standard tool for product design. The continuum approach uses a model in which the geometry is represented by the volume occupied by cells and material constants are calculated by means of the micromechanical model results. The process that allows obtaining the stiffness matrix of a lattice material starting from the base cell material and geometry to study the mechanical behavior of an equivalent continuum model is called homogenization. The main advantages of this approach are the reduced time and model complexity for the FE analysis and the possibility to investigate and predict the structural performances of many different parts from the mechanical characterization of the single cell that constitutes them. In this work, the homogenization process is adopted to characterize the mechanical behavior of four different lattice structures varying relative density and fillet radius. Previous researches investigated the effects of different relative densities on the longitudinal and tangential elastic moduli, Poisson ratio and the maximum stress of lattice structures. Vigliotti and Pasini [10, 11] studied the mechanical properties of open and closed cell lattices with arbitrary topology through a multiscale approach. Concli and Gilioli [12] studied a ductile damage model for an aluminum alloy A357 structure with Kagome cells. Arbenejad and Pasini [13] applied the asymptotic homogenization to lattice materials and compared the results with other homogenization methods. Freund et al. [9] proposed a computational homogenization method for planar cells and defined the effective elastic parameters. They concluded that these parameters do not depend on the cell shape. Homogenization methods are facilitated using base cells characterized by symmetry planes and thus by isotropic behavior. Xu et al. [14] developed two design methods for lattice structures with controlled anisotropy and proposed two different novel cell shapes. Moongkhamklang et al. [15], Zupan et al. [16], and Coté et al. [17] studied shear and compressive behavior of two cell geometry (diamond and square) realized in titanium matrix composite by means of static tests and analytical formulations. They underline how the buckling effects are not negligible in the failure mode. Even Deshpande et al. [18] described the compressive properties of aluminum alloy octet truss cell and obtained the behavior of E and ν as the density changes through analytical, experimental and numerical analysis. They concluded that the elastic buckling of the struts truncates the plastic collapse. Smith et al. [19] investigated the mechanical performance of body-centered cubic (BCC) and body-centered cubic with vertical pillars (BCCZ) cells realized by SLM technique and compared E and σ behaviors obtained through FE analysis with experimental results finding good agreement. Tsopanos et al. [20], analyzed stainless steel BCC cells mechanical properties; they defined E and σ parameters as the density changes by tensile and compression tests; a relation that occurs between process parameters and strength of the structures was proposed. By this relation, it is possible to assess the mechanical properties based on the combinations of laser power manufacturing parameters, laser exposure time and relative density. Relationships that relate the process parameters and the direction of component growth with the mechanical properties of the structure were also obtained by Caulfield et al. [21]. To assess the mechanical properties of cellular structures many researchers studied the effects of the AM process on the shape of the structure in terms of generated imperfections. Park et al. [22] studied the mechanical properties of lattice material subject to shape variations caused by the AM process by means of a two-step homogenization method. They constructed a voxel-based model to determine the effective structural element parameters (strut diameter and length). The numerical results, compared with the experimental ones, showed a smaller error than the direct implementation of the homogenization method. Moreover, the authors assessed the effects of geometric degradation caused by AM on lattice structures [23], confirming that the lattice structures are affected by the material extrusion process. Suard et al. [24] found significant size differences between designed and fabricated struts produced by EBM. Consequently, they studied the struts mechanical properties by FEM model using the actual diameter. De Formanoir et al. [25] showed that chemical etching post-treatment, of titanium lattice structures fabricated by EBM, decreases surface roughness and increases the stiffness-to-density ratio. Several researches propose formulations that correlate stiffness matrix constants E, G and ν with the base cell geometric characteristics. Luxner et al. [26] investigated the mechanical behavior of four open cell shapes by 3D FE analysis. The cells were analyzed as monodimensional beam element. A comparison between numerical and experimental results underlines how the FE accuracy depends on the geometry and on the governing deformation mechanisms. Wallach et al. [27] studied E and G for fully triangulated 3D truss structures; Ptochos et al. [28] analyzed the behavior of shear modulus in BBC metallic cell by means of analytical and numerical methods, suggesting relations for G in comparison with the base material longitudinal elastic modulus E_0. Campoli et al. [29] investigated strength properties of porous titanium produced by SLM or selective electron beam melting comparing them with FE and experimental results; they pointed out the influence of structural imperfections produced in the manufacturing process in the mechanical properties of porous biomaterials. The effects of geometry imperfections due to the AM process were underlined also by Dallago et al. [30]. They investigated the manufacturing defects by means of micro-X-ray computed tomography and optical methods and they showed how the Hot Isostatic Pressing treatment has not a clear effect on the fatigue resistance because it is affected by surface defects. Despite the recent developing of the mechanical properties assessment methods for lattice materials have notable growth, in literature there is still a lack of data on fillet radius effects on mechanical behavior. It affects stress concentrations in nodes of the struts. The fillet radius influences also the lattice fatigue life under cyclic loads. The work of Dallago et al. [31] is one among the few that pointed out the not negligible effects of fillet radius for 2D square cell cellular materials. The authors studied the influence of this parameter in the elastic properties of such structures with an analytical–numerical approach. Xiong et al. [32] investigated the effect of fillet radius on Poisson's ratio and stress concentration behaviour of structures fabricated by selective laser melting (SLM), and they concluded that as the fillet radius increases the investigated parameters decrease significantly.

In this work, a numerical model to estimate the mechanical properties of lattice structures as a function of the cell shape, dimension, beam diameter, and fillet radius was proposed. This model was obtained by fitting with a second-order polynomial the mechanical properties of four types of cell by FE analysis. An original approach was adopted to define boundary conditions using coupling equations, which allows accuracy and low processing times. Numerical results show a not negligible effect of the fillet radius on mechanical properties especially in cells with a large number of struts.

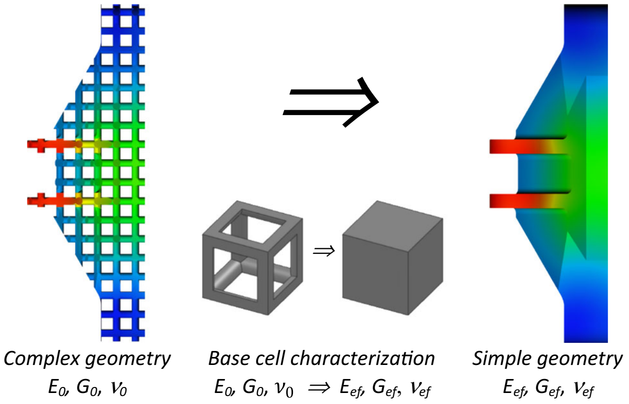
Complex geometry
E_0, G_0, ν_0
Base cell characterization
E_0, G_0, ν_0 ⇒ E_{ef}, G_{ef}, ν_{ef}
⇒
Simple geometry
E_{ef}, G_{ef}, ν_{ef}

Fig. 1 Homogenization process scheme: the analysis of the complex shape adopting the bulk material on the left is equivalent to the analysis of the simple shape adopting a virtual material on the right. Mechanical properties of this effective material were derived studying a single cell

Tensile tests were assessed on specimens fabricated by selective laser sintering (SLS) in polyamide 12, for both bulk material and four types of lattice structures. Numerical and experimental results show a good agreement within the technological and methodological limits.

Finally, a lattice structures design procedure was proposed, which is based on an iterative interaction between the designer and the proposed numerical model through a user interface.

2 Materials and methods

2.1 Homogenization process

The single cell behaves as a continuum cubic element made up of a virtual material called effective material. Specifically, the longitudinal E_{ef} and shear G_{ef} moduli, the Poisson's ratio ν_{ef} and relative density ρ are computed as a function of beam and fillet radii based on the cell material mechanical properties (E_0, G_0, ν_0) by FE analysis and experimental tests. This process, known in the literature as homogenization, is the basis for topology optimization [33] and allows to simplify the FE analysis of lattice structures. In other words, the complex geometry of a cellular solid is studied as a continuum domain consisting of the region occupied by cells using an equivalent material (Fig. 1).

2.2 Cells material, shape and dimensions

In this work, the mechanical behavior of four different cell shapes made of Polyamide 12 (PA2200 Performance 1.0

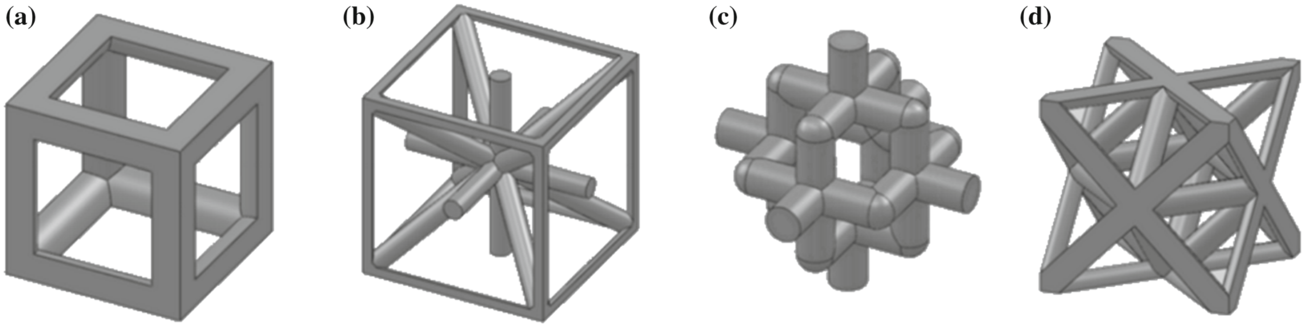

Fig. 2 Shape of the investigated cells: **a** simple cubic (SC); **b** reinforced body-centered cubic (RBCC); **c** modified Gibson–Ashby (GA); **d** octet truss (OT)

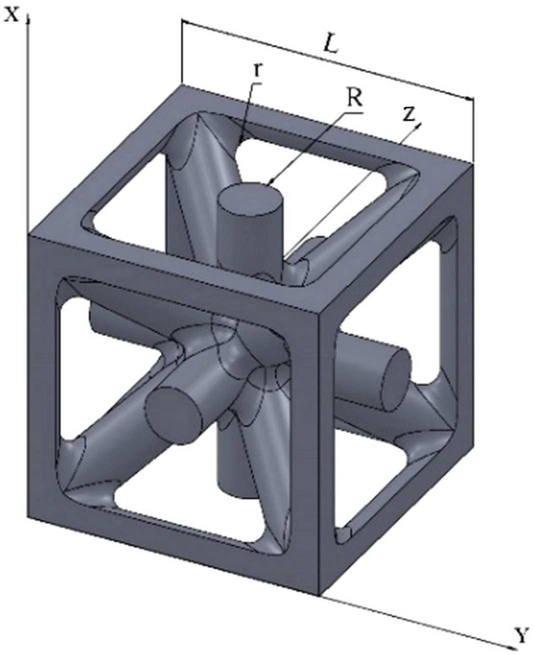

Fig. 3 Dimensional parameters of the cells: cell dimension L, struts radius R and fillets radius r

Table 1 Values of the dimensional parameters of the cells adopted in the numerical and experimental analysis

Relative density (%)	R/L			
	SC	RBCC	GA	OT
10[a]	0.110	0.053	0.071	0.047
20	0.162	0.078	0.104	0.068
30	0.206	0.099	0.133	0.087
40	0.245	0.118	0.160	0.104

Cell dimension: 7.5 mm

Fillet radii for numerical analysis: 0.1, 0.16, 0.25, 0.4, 0.63, 1 mm

For each relative density, 5 specimens were experimentally studied, adopting a 0.4 mm fillet radius

[a] Due to the too small section, no experimental tests were executed at ρ = 10%

[34]) fabricated by EOS was studied. Specimens were manufactured vertically oriented in the building chamber, and consequently, the growing direction matches the longitudinal direction of the samples. The cell shapes adopted for numerical and experimental analysis were (Fig. 2): simple cubic (SC) [20, 21], reinforced body-centred cubic (RBCC) [26], modified Gibson–Ashby (GA) [35], Octet-Truss (OT) [18]. The relative density is the ratio between the actual volume of the cell *V* and the volume of the region occupied by cell V_0. The relative density is a function of the geometric parameters that characterize the base cell:

$$\rho(R/L, r/L) = V/V_0 \quad (1)$$

where *L* is the cell dimension, *R* is the radius of the struts, *r* is the fillet radius (Fig. 3). Relative densities in the range from 10 to 40% were studied, adopting the cells dimensional parameters as in Table 1. In order to reduce the sample dimensions, the material consumption and to limit geometrical and dimensional errors, *L* was set to 7.5 mm.

2.3 Numerical approach

To explain the proposed approach some considerations concerning material, AM technology, and constraints modeling are needed. Amado-Becker et al. [36] showed that the process parameters significantly affect the mechanical properties of the material. Components realized by AM technique are built layer upon layer obtaining a transverse isotropic behavior that is fully characterized by 5 independent elastic constants, unlike isotropic materials which are defined by only 2 independent constants [18]. The effects of anisotropy and build orientation were underlined also by Stankovic et al. [37], Choy et al. [38] and Wauthle et al. [39]. However, increasing the laser energy density, the mass density of the material increases as well as the mechanical properties, so that the Young's and shear moduli referred to different planes converge to a certain value [36]. According to these results, it can be stated that a sintered material assumes isotropic behavior for certain values of energy density, which is a hypothesis of our work. Since the geometry of all the investigated cells consists of nine symmetry planes, the mechanical properties are described by 3 independent elastic constants: E, G, ν [18, 28]. These constants are computed by numerical analysis imposing tensile and shear displacements.

E_{ef} is calculated as follows:

- a displacement Δx is imposed on the nodes lying on a cell face parallel to the y–z plane and the constraint conditions are defined as explained in detail below;
- the longitudinal strain ε_x is calculated as:

$$\varepsilon_x = \Delta x/L \tag{2}$$

- the reaction force F_x along the load axis direction is calculated as the sum of the reaction force of all constrained nodes;
- the effective stress σ_{xef} of the cell is then computed:

$$\sigma_{xef} = F_x/L^2 \tag{3}$$

- E_{ef} is finally obtained:

$$E_{ef} = \sigma_{xef}/\varepsilon_x \tag{4}$$

Using the same loads and constraints conditions, the effective Poisson's ratioν_{ef} is also calculated:

- the contraction ε_y of a couple of lateral opposite faces (faces parallel to the x–z plane or to the x–y plane) is calculated as the ratio between the lateral displacement (Δy or Δz) and L:

$$\varepsilon_y = \Delta y/L = \varepsilon_z = \Delta z/L \tag{5}$$

- ν_{ef} is obtained by the equation:

$$\nu_{ef} = -\varepsilon_y/\varepsilon_x = -\Delta y/\Delta x \tag{6}$$

Shear modulus G_{ef} is computed as follows:

- a displacement Δy (y-axis is the shear direction) is imposed to a face of the cell parallel to the y–z plane and the y displacement is constrained for all the nodes in the opposite face;
- shear strain γ is calculated by the ratio:

$$\gamma = \Delta y/L \tag{7}$$

- the reaction force F_y along the y-axis is calculated as the sum of the reaction forces of all constrained nodes;
- the effective shear stresses τ_{ef} of the cell are computed as:

$$\tau_{ef} = F_y/L^2 \tag{8}$$

- finally, G_{ef} is calculated by the equation:

$$G_{ef} = \tau/\gamma \tag{9}$$

Linear elastic 3-D models analysis were performed by ANSYS® Release 14.5 software package, using APDL [40] and "8-nodes Solid185" 3-D brick elements. The input material parameters were experimentally obtained or taken from literature: $E_0 = 1529$ MPa was computed from tensile tests on PA 2200 specimens; $\nu_0 = 0.35$ was found in the literature [41]. Due to the assumption of an isotropic material, the shear $G_0 = 566$ MPa was calculated through the equation:

$$G_0 = E_0/(2(1 + \nu_0)) \tag{10}$$

In order to capture the effects of fillet radii as well as the actual nodes stiffness, 3-D elements instead of monodimensional beam elements were adopted. The constraints applied to the single cell model must take into account the behavior of the adjacent cells that constitute the actual lattice structure. As an example, the procedure followed to ensure these constraints for the computation of E_{ef} and ν_{ef} on an SC cell is reported. In other cases, the same approach was applied.

Imposing a uniform tensile load to the CS cell on a face parallel to the y–z plane, and constraining all degrees of freedom of the opposite face, the deformed model highlights the following issues (Fig. 4a):

1. the face in which the pressure is applied assumes a deformation which is not consistent with the presence of an adjacent cell;
2. the constraints are too restrictive as they prevent lateral contractions. These deformations are not compliant with the actual deformation of the surrounding cells;
3. due to boundary effects, lateral elements of the cell are bent internally.

The first issue can be solved by applying a displacement along the x-axis instead of a uniform tensile load. The second one was overcome increasing degrees of freedom, locking only the displacement along the x-axis of all the nodes lying on the constrained face and anchoring only a node. A similar method was adopted by Koizumi et al. [42]. The other issue can be approached in two ways. One is to study a structure consisting of an array of cells repeated along the Cartesian axes, and calculating the mechanical constants in the central cell, avoiding boundary effects. As the number of cells increases, the boundary effects are reduced, but time and

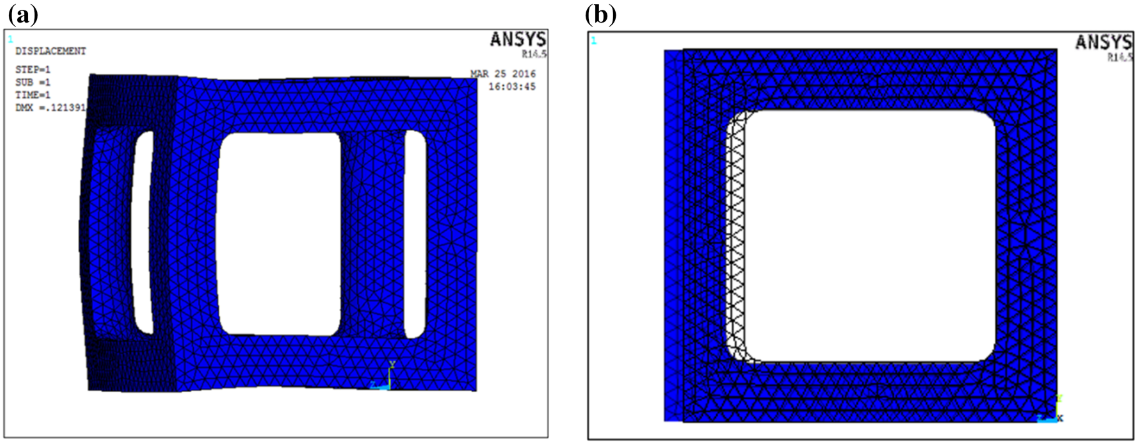

Fig. 4 Different approaches for analyzing a single cell: **a** deformation obtained by applying a uniformly distributed force on the face parallel to the y–z plane and constraining all degrees of freedom of the opposite one; **b** cell deformation obtained by applying the proposed constraining conditions

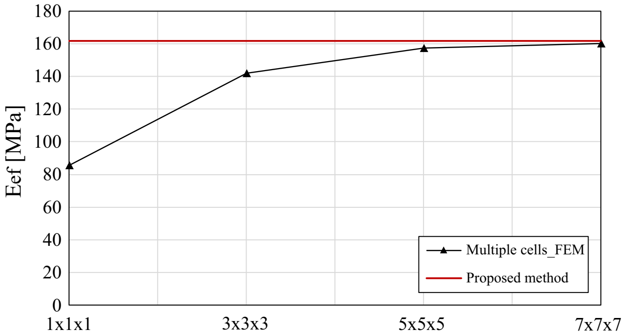

Fig. 5 Comparison of different FE analyses methods on CS Young's module

computational cost increases cubically, due to the geometric complexity. Alternatively, it is possible to model a single cell introducing a constraints scheme that takes into account the actual constraints generated by the adjacent cells, by applying coupling conditions [40, 43]. These conditions require to force one or more degrees of freedom to assume the same value, in terms of rotations or translations, ensuring the cell to contract without bending. In detail, the same translations and rotation are assigned to couples of parallel faces of the cell. This guarantees the cell maintains coherent surfaces with hypothetical adjacent cells. The effects of these boundaries conditions can be appreciated in Fig. 4b. Some preliminary simulations were conducted to investigate the effect of the proposed method. In Fig. 5 the E_{ef} behavior for a CS cell modeled with the proposed method and with multiple cells models is reported. It can be seen that as the number of cells increases, the solutions tend to a constant value due to the reduction of the boundary effects. This convergence value corresponds to the value obtained with the proposed method, which involves the simulation of the single cell. This method is able not only to compute accurate solutions but also to reduce calculation times and computational cost, and consequently has been adopted for all the other numerical analyses.

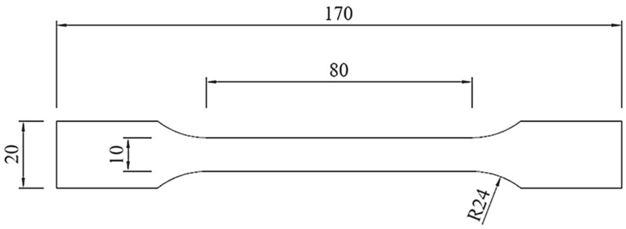

Fig. 6 Specimen geometry adopted in the tensile tests (thickness equal to 4 mm)

2.4 Experimental approach

Static properties of the bulk material were assessed by tensile tests on 5 specimens using Galdabini SUN2500 machine equipped with a 25 kN load cell. The test speed was 2.00 mm/min. Longitudinal displacement was measured by the extensometer MICRON 34187/9 with gauge length equal to 50 mm. The shape of specimens (Fig. 6) and tensile test procedures were selected according to ISO standards [44, 45]. To evaluate the mechanical properties of lattice structures, tensile tests were conducted with the same parameters adopted for the bulk material characterization with the exception of the gauge length, equal to 37.5 mm, equivalent to the length of 5 cells. Four cell shapes, 3 relative densities for each cell shape (20%, 30%, and 40%) and 5 specimens for each condition, for a total of 60 specimens were tested. Samples were characterized by a central lattice constitutes of $2 \times 3 \times 7$ cells, cell dimension 7.5 mm and fillet radius 0.4 mm, as shown in Fig. 7.

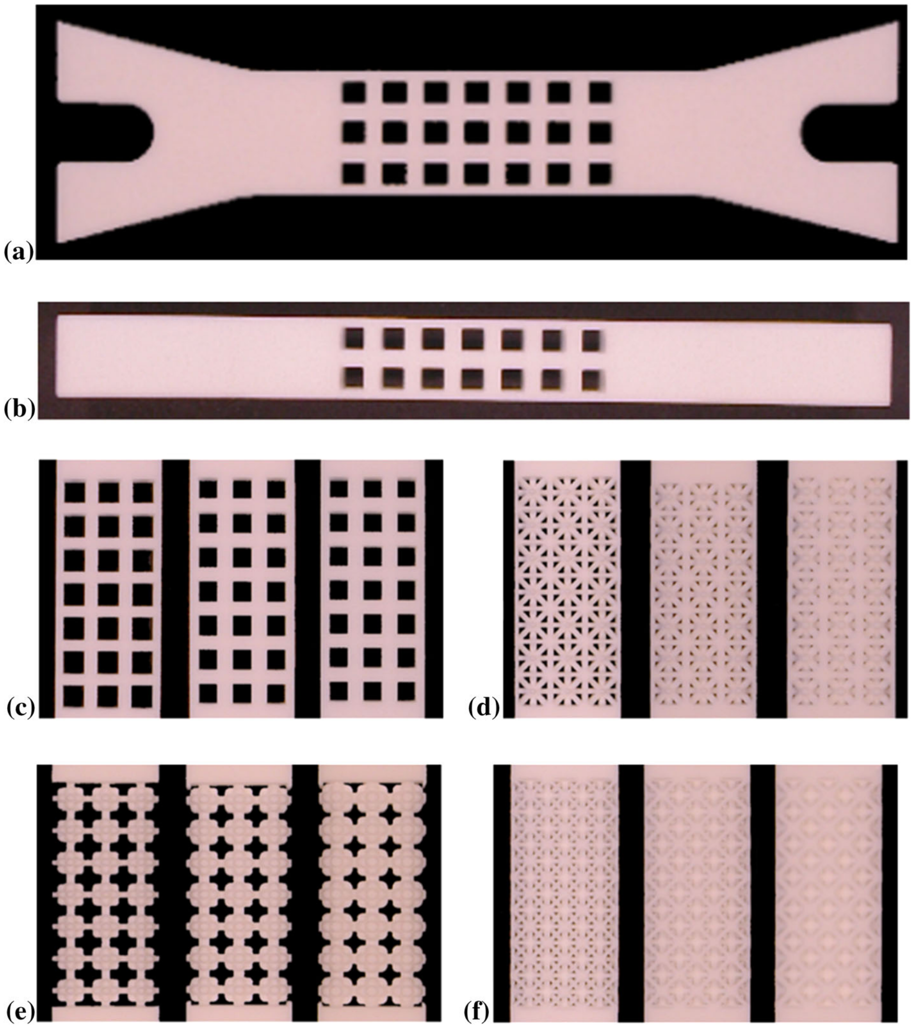

Fig. 7 Specimen: **a** front, **b** lateral view of a cubic cell sample. Lattice portion of the specimens with different relative densities (20%, 30%, 40%): **c** simple cubic (SC), **d** reinforced body center cubic (RBCC), **e** modified Gibson–Ashby (GA), **f** octet truss (OT)

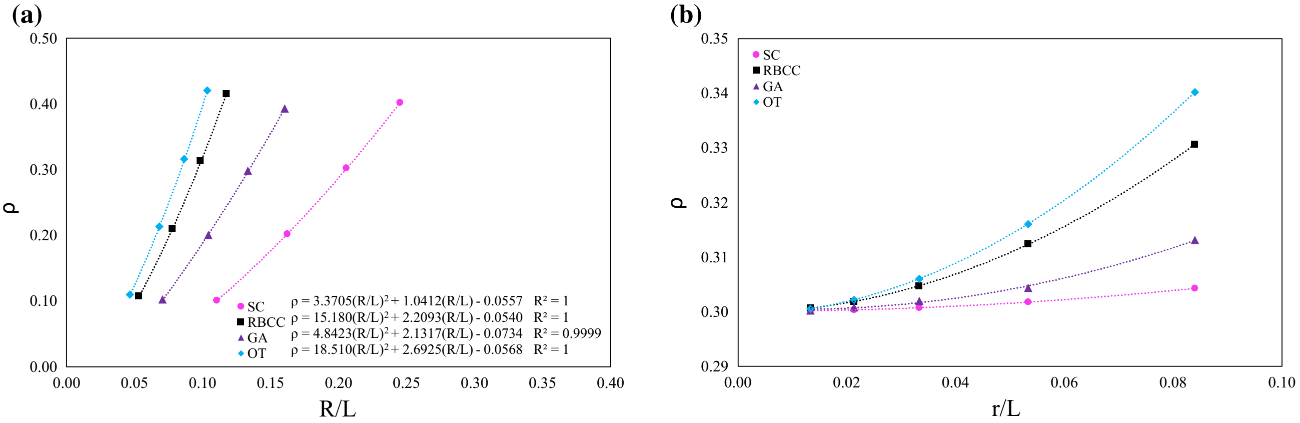

Fig. 8 Relative density behaviour with **a** R/L (r = 0.4 mm), **b** r/L (ρ = 30%)

3 Results and discussion

3.1 Numerical results

Due to the considerable number of numerical simulations performed (160 configurations), and the number of different parameters, only a few results are graphically shown while all outcomes are summarized by fitting equations.

Figure 8 shows the ρ behavior as a function of R/L assuming r = 0.4 mm and r/L for ρ = 0.3, including fitting equations and coefficient of determination (R^2). It is possible to observe that the relative density increases as the R/L and r/L increase.

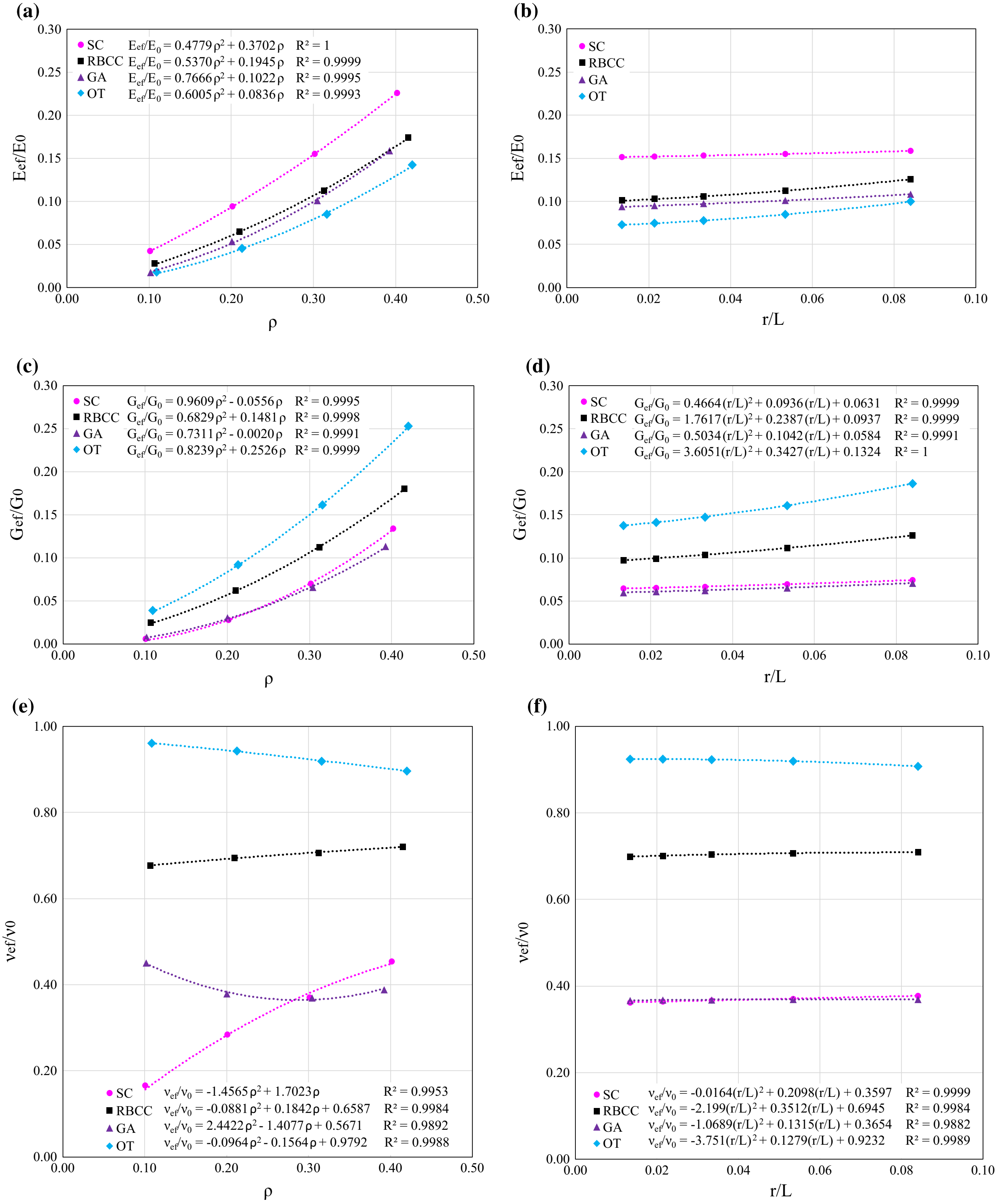

Fig. 9 Mechanical properties of different cell types as a function of ρ and r/L: **a** E/E_0 with r = 0.4 mm; **b** E/E_0 with ρ = 0.3; **c** G/G_0 with r = 0.4 mm; **d** G/G_0 with ρ = 0.3; **e** ν/ν_0 with r = 0.4 mm; **f** ν/ν_0 with ρ = 0.3

Table 2 Fitting coefficients a_i of the second-order polynomial representing E_{ef}/E_0, G_{ef}/G_0, ν_{ef}/ν_0 and ρ as a function of r/L and R/L

Cell shape	M (x, y)	a0	a1	a2	a3	a4	a5	a6	a7	a8	ε_{max} (%)
SC	E_{ef}/E_0	5.16	0.58	2.13	− 0.14	4.32	− 0.03	− 0.21	0.01	0.01	0.30
	ν_{ef}/ν_0	− 1.50	4.72	3.46	− 0.09	− 1.46	− 0.93	2.57	0.08	− 0.11	0.90
	G_{ef}/G_0	13.95	− 0.70	5.60	− 0.85	6.32	− 0.03	− 1.38	0.04	0.08	6.60
	ρ	− 0.38	2.98	− 0.13	0.06	3.38	0.00	1.03	− 0.01	− 0.06	0.42
RBCC	E_{ef}/E_0	127.45	18.64	51.20	− 5.22	16.92	− 0.88	− 0.93	0.17	0.03	1.23
	ν_{ef}/ν_0	3018.77	− 556.25	− 129.21	28.86	− 0.49	20.83	0.51	− 1.09	0.65	0.10
	G_{ef}/G_0	1323.30	− 152.25	− 5.24	4.49	20.91	3.93	− 1.57	− 0.14	0.05	1.80
	ρ	− 749.60	176.98	69.23	− 12.46	13.59	− 5.90	2.36	0.55	− 0.07	0.46
GA	E_{ef}/E_0	1041.90	− 88.31	60.45	− 5.05	21.75	2.25	− 1.51	0.13	0.04	2.40
	ν_{ef}/ν_0	1581.95	− 276.11	− 48.51	8.81	− 8.82	7.29	0.22	− 0.19	0.97	0.14
	G_{ef}/G_0	989.10	− 49.88	108.74	− 8.44	30.32	1.15	− 1.51	0.22	0.04	1.00
	ρ	− 1006.85	235.53	58.67	− 10.09	17.98	− 6.32	2.60	0.38	− 0.06	0.49
OT	E_{ef}/E_0	− 88.41	18.90	9.00	0.00	8.83	− 0.97	− 0.57	0.03	0.01	2.40
	ν_{ef}/ν_0	− 641.86	155.82	18.29	− 1.50	25.15	− 10.14	− 6.64	− 0.02	0.80	0.76
	G_{ef}/G_0	− 97.06	19.49	12.09	− 0.75	8.75	− 0.94	− 0.95	0.03	0.03	0.92
	ρ	381.47	− 83.67	− 16.78	4.67	5.04	5.22	2.03	− 0.25	− 0.07	0.85

This trend can be well represented by quadratic relations, as R^2 is close to 1. For the same relative density, it can be observed that cells with fewer struts (e.g. SC) have a greater R/L ratio than the cells consisting of many struts (e.g. OT). Moreover, on constant R/L, increasing r/L, the ρ variation is more affected by cells consisting of many struts due to the greater number of joints (e.g. OT).

Figure 9 shows E_{ef}/E_0, G_{ef}/G_0 and ν_{ef}/ν_0 behaviors as a function of ρ ($r = 0.4$ mm) and as a function of r/L ($\rho = 0.3$), which are well described by quadratic curves. On equal ρ, SC cell shows the higher E_{ef}/E_0 while the OT has the lower longitudinal stiffness (Fig. 9a). The SC trend can be explained because of the presence of struts parallel to the loading axis that increases the longitudinal stiffness. Instead, OT slanting struts make the structure more flexible in the longitudinal direction. This geometrical configuration explains the stiffer behavior of OT in the transverse direction (G_{ef}/G_0 in Fig. 9c). With shear stress, the SC cell is the most compliant, while the other cells show an intermediate behavior. ν_{ef}/ν_0 is close to 1 for the OT cell, meaning a quasi-isotropic behavior (Fig. 9e). The SC cell shows a moderate contraction due to struts parallel to the loading axis; for this cell ν_{ef}/ν_0 grows significantly together with ρ. E_{ef}/E_0 and G_{ef}/G_0 of RBCC and OT cells significantly change as the r/L ratio increases, due to the greater number of the joints that generate a greater stiffness (Fig. 9b, d). Conversely, the effect of r/L on ν is less evident (Fig. 9f).

All numerical results were summarized by a second-order polynomial as a function of $x = r/L$ and $y = R/L$:

$$\begin{aligned} M(x, y) = {} & a_0x^2y^2 + a_1x^2y + a_2xy^2 + a_3xy \\ & + a_4y^2 + a_5x^2 + a_6y + a_7x + a_8 \end{aligned} \tag{11}$$

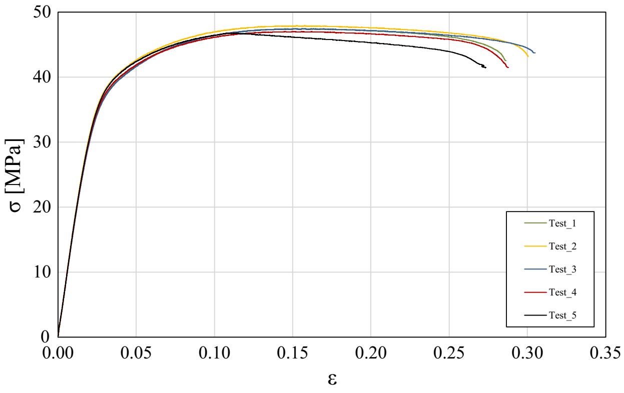

Fig. 10 Bulk material stress–strain curves

where M represents E_{ef}/E_0, G_{ef}/G_0, ν_{ef}/ν_0 and ρ, and a_i are the coefficients reported in Table 2 obtained by least squares fitting. The maximum differences between the proposed model and the numerical results are also reported in Table 2.

3.2 Experimental results

Figure 10 shows the stress–strain curves obtained by tensile tests on bulk material. The average Young's modulus, calculated in the strain range between 0.05 and 0.25%, as suggested by the ISO standards [44], is equal to $E_0 = 1529 \pm 14$ MPa. The average maximum stress is 47.29 ± 0.43 MPa and the corresponding strain is $14.56 \pm 1.95\%$. The average ultimate stress is 42.47 ± 1.01 MPa and the corresponding strain is $29.06 \pm 1.27\%$.

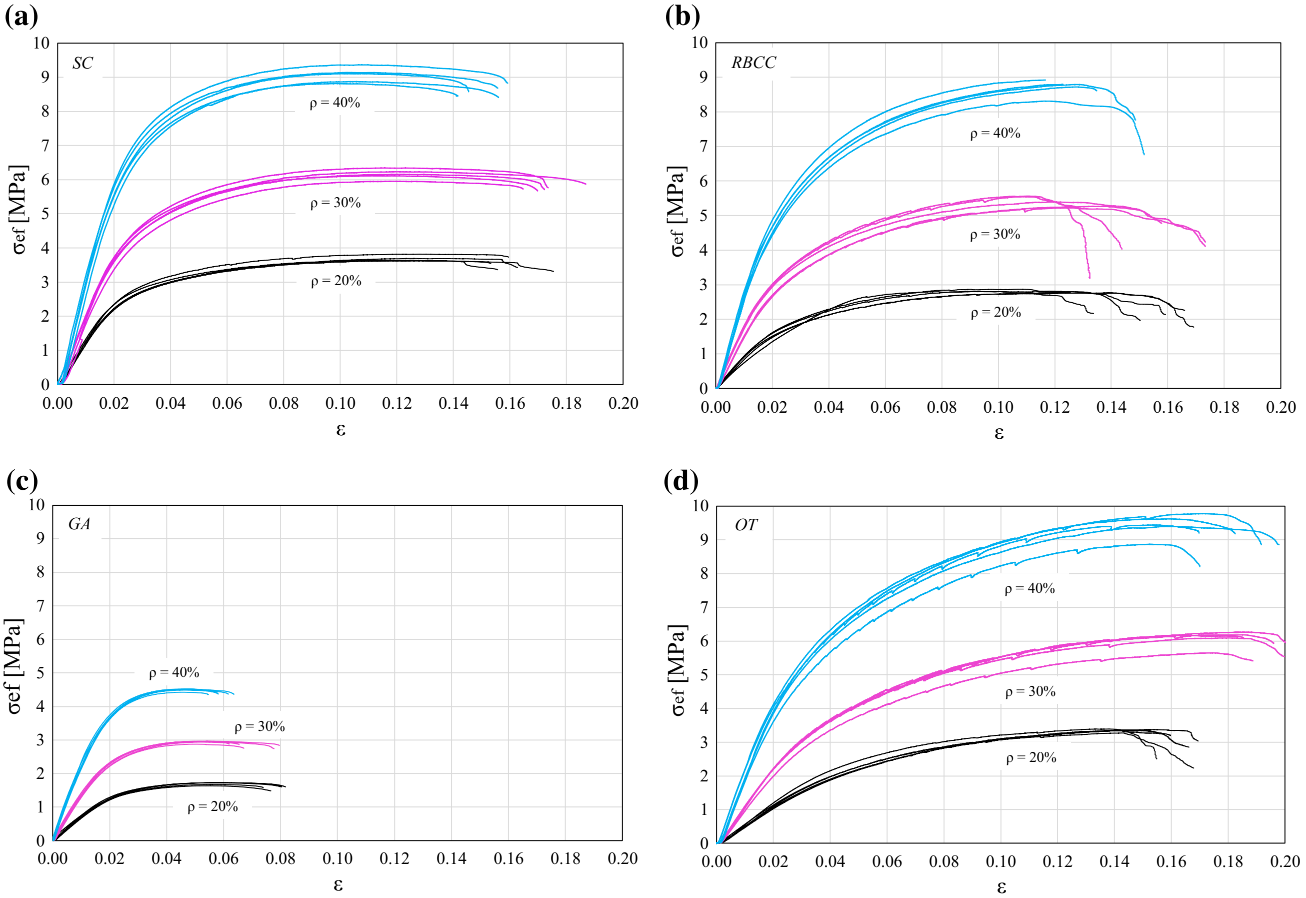

Fig. 11 Lattice material stress–strain curves at three different relative densities: **a** SC; **b** RBCC; **c** GA; **d** OT

In Fig. 11 the stress–strain curves obtained by tensile tests on lattice specimens are reported. The effective stress σ_{ef} is calculated referring to an equivalent resistant section equal to $22.5 \times 15\ \mathrm{mm}^2$ (total width and thickness of the specimen). The average characteristic parameters, dimensionless compared to the corresponding bulk material parameters, are summarized in Table 3. Experimental results show that OT cell guarantees the best performance in terms of maximum and ultimate stresses and strains, followed with similar results by SC and RBCC, instead, GA reaches significantly lower values. Moreover, it should be noted that the maximum strains are reached by the OT confirming that this geometry, subjected to tension loads, has good energy absorption properties (surface area subtended by the curve). On the contrary, the GA and SC, with lower maximum strains, confirm they are the cells less able to absorb energy.

3.3 Results overview

In Fig. 12 the experimental and numerical results of E_{ef}/E_0 are reported together as a function of the relative density for the 4 cells, finding a good agreement. Differences between experimental and numerical results can be explained considering that FE analyses are provided for a lattice of unlimited size and not considering boundary effects due to the limited dimensions of the specimens. The accuracy of the SLS process [46] also affects the experimental results. Moreover, due to the absence of post-processing such as sanding, the actual dimension of the beams is greater than the nominal.

As described in the literature, the structural behavior is strongly influenced by cell geometry and two structure classes can be identified. Those called “bending dominated” and those defined “stretching dominated”. The first is characterized by elements mostly subjected to bending loads, the latter by axial loads. The first are more flexible, the second are more stiff. A structure such as the one that constitutes the SC cell, has to do with bending dominated structures unless it is subjected to longitudinal loads [31]. The works of Deshpande et al. [47] and Fleck et al. [48] show that for 2D cells, a condition for having a rigid structural behavior is to have a number of converging struts at each node at least equal to 4. In the present work, it must be observed that under shear loads, the stiffer cells proved to be the OT and RBCC, because they have the major numbers of struts converging at each node.

Table 3 Average values and standard deviation (SD) of the mechanical properties assessed by tensile tests on lattice samples

Base cell	ρ (%)	E_{ef}/E_0	SD	σ_{ef}, max (MPa)	SD	ε (σ_{ef}, max, %)	SD (%)	σ_{ef}, R (MPa)	SD	ε (σ_{ef}, R, %)	SD (%)
SC	20	0.0900	0.00428	3.52	0.08	12.30	0.58	3.32	0.17	16.01	0.87
	30	0.1395	0.00668	5.89	0.10	11.71	0.31	5.48	0.12	17.16	0.82
	40	0.2200	0.01379	8.57	0.35	10.21	0.38	8.11	0.29	14.14	0.72
RBCC	20	0.0637	0.00597	2.73	0.04	11.27	1.90	1.99	0.18	15.78	1.04
	30	0.1179	0.01646	5.22	0.14	11.85	1.12	3.56	0.52	15.96	2.06
	40	0.1861	0.01449	8.53	0.21	12.19	0.52	7.13	0.36	14.99	0.15
GA	20	0.0615	0.00212	1.65	0.06	4.61	0.16	1.52	0.07	6.51	0.26
	30	0.1167	0.00318	2.89	0.04	4.34	0.15	2.76	0.07	5.84	0.67
	40	0.1938	0.00649	4.39	0.07	3.83	0.15	4.27	0.04	4.92	0.27
OT	20	0.0366	0.00171	3.25	0.04	14.06	0.71	2.67	0.38	16.15	0.64
	30	0.0777	0.00367	5.95	0.24	17.62	0.82	5.65	0.30	19.39	0.61
	40	0.1485	0.01212	9.23	0.36	15.76	0.76	8.65	0.40	18.15	1.30

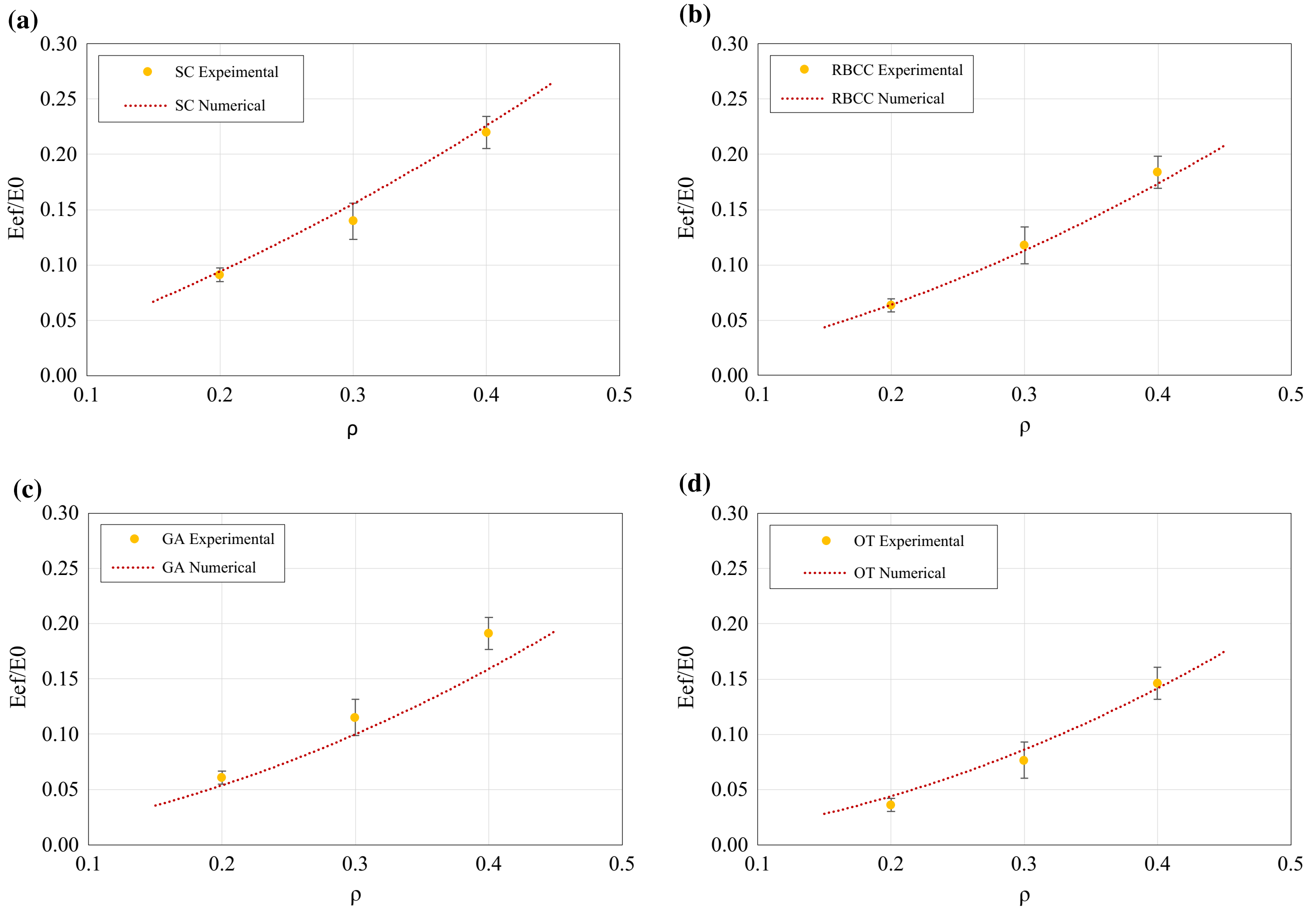

Fig. 12 Numerical and experimental E_{ef}/E_0 behavior (0.4 mm fillet radius): **a** SC; **b** RBCC; **c** GA; **d** OT

4 Integration of the model in a virtual environment for interactive lattice design

Interactive design can be defined as the practice of data exchange/processing between people and technology, characterized by 3 elements, input, process, and output, which is equivalent to listen, think, and speak in the human interaction [49]. Our work is put in this context by defining a structured method useful for lattice design and integrating the proposed numerical model (this model is equivalent to the

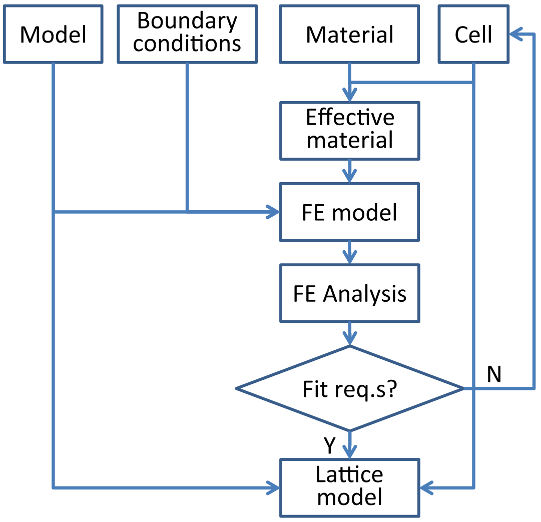

Fig. 13 Procedure for the design of lattice structures

process in an interactive design context) with a user interface (input/output).

By the results achieved it is possible to define an iterative procedure for the design of lattice structures (Fig. 13). Starting from the bulk material properties, the cell properties (shape, dimension, struts diameter, fillet radius), and the fitting equations (e.g. Eq. 11), it is possible to obtain the mechanical properties of the effective material. This procedure can be easily implemented in a CAD/CAE software, providing the input parameters by a user interface as shown in Fig. 14, obtaining the mechanical properties of the effective material in real-time. Fitting coefficients of equations for effective material properties computation (e.g. coefficients in Table 2), as well as bulk materials properties, can be stored in a text file. In this way, the model can be easily updated with other cell types and materials.

Considering the model shape, the boundary conditions and the effective material, it is possible to define and analyze an FE model (Fig. 13). The cell characteristics can be cyclically changed by the user, until the results of the FE analysis, e.g. maximum displacement, fit the functional requirements. When the cell characteristics are established, it is possible to generate the lattice structure iterating the cell in the model space.

5 Conclusion

In this work, a model to estimate the mechanical properties of lattice structures as a function of the cell shape, dimension, beam diameter, and fillet radius was proposed. This model is an effective tool suitable to support an interactive design process of lightweight structures.

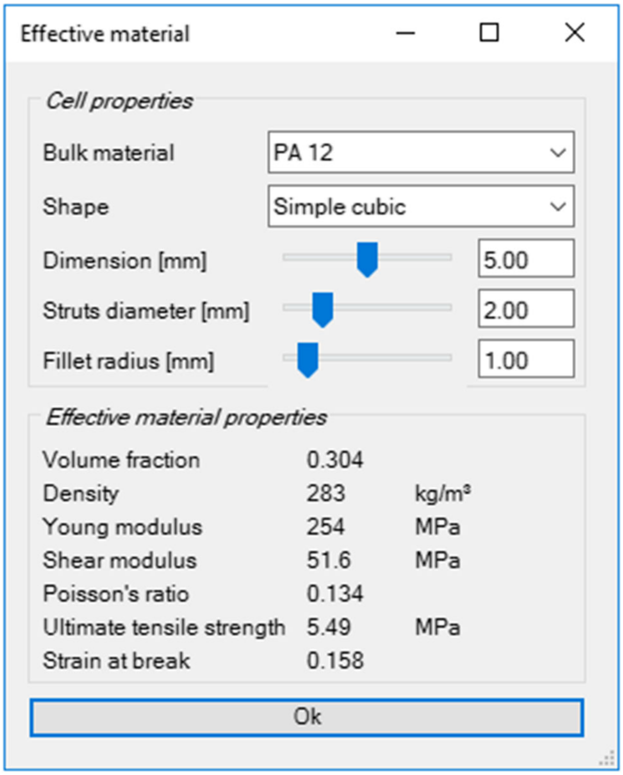

Cell properties

Bulk material	PA 12
Shape	Simple cubic
Dimension [mm]	5.00
Struts diameter [mm]	2.00
Fillet radius [mm]	1.00

Effective material properties

Volume fraction	0.304	
Density	283	kg/m³
Young modulus	254	MPa
Shear modulus	51.6	MPa
Poisson's ratio	0.134	
Ultimate tensile strength	5.49	MPa
Strain at break	0.158	

Fig. 14 User interface for the computation of the effective material properties

Bulk material and lattice samples manufactured in polyamide 12 by SLS technology were also experimentally characterized varying the cell shape and relative density. Numerical and experimental results show a good agreement within the technological and methods limits.

The main original contributions are related to the numerical approach, which allows to study a single cell as it is surrounded by others, thanks to the specific boundary conditions and to the coupling equations, and which allows the assessment of the mechanical properties as a function of the fillet radius, covering a lack in the literature. Numerical results show that the proposed approach is suitable for both accuracy and low processing times and that the fillet radius is not negligible, especially in cells having a large number of struts.

Future works will be addressed to experimentally evaluate the influence of the fillet radii, in order to confirm numerical results, and to validate the use of filleted lattice in real industrial parts.

Acknowledgements The authors gratefully acknowledge generous in-kind support from 3Dfast Srl and Andrea Sandi for fabricating test parts and Mario Saraceni of Enginlab Srl for the tensile test machine. This work was partially supported by the Grants “FSE 2105-116-2216-2016” by Regione Veneto and “BIRD175287/17” by Department of Civil, Environmental and Architectural Engineering ICEA—University of Padua.

References

1. Gibson, L.J., Ashby, M.F.: Cellular Solid. Cambridge University Press, Cambridge (1999)
2. Rashed, M.G., Ashraf, M., Mines, R.A.W., Hazell, P.J.: Metallic microlattice materials: a current state of the art on manufacturing, mechanical properties and applications. Mater. Des. **95**, 518–533 (2016). https://doi.org/10.1016/j.matdes.2016.01.146
3. Sun, W., Starly, B., Nam, J., Darling, A.: Bio-CAD modeling and its applications in computer-aided tissue engineering. Comput. Des. **37**, 1097–1114 (2005). https://doi.org/10.1016/j.cad.2005.02.002
4. Tao, W., Leu, M.C.: Design of lattice structures for additive manufacturing. In: 2016 International Symposium Flexible Automation, pp. 1–3 (2016)
5. Tamburrino, F., Graziosi, S., Bordegoni, M.: The design process of additively manufactured mesoscale lattice structures: a review. J. Comput. Inf. Sci. Eng. **18**, 1–16 (2018). https://doi.org/10.1115/1.4040131
6. Savio, G., Rosso, S., Meneghello, R., Concheri, G.: Geometric modeling of cellular materials for additive manufacturing in biomedical field: a review. Appl. Bionics Biomech. **2018**, 1–14 (2018). https://doi.org/10.1155/2018/1654782
7. Ceruti, A., Ferrari, R., Liverani, A.: Design for additive manufacturing using LSWM: a CAD tool for the modelling of lightweight and lattice structures. In: Campana, G., Howlett, R.J., Setchi, R., Cimatti, B. (eds.) Sustainable Design and Manufacturing 2017. Smart Innovation, Systems and Technologies, pp. 756–765. Springer, Cham (2017)
8. Zeinalabedini, H., Yildiz, Y.O., Zhang, P., Laux, K., Kirca, M., To, A.C.: Homogenization of additive manufactured polymeric foams with spherical cells. Addit. Manuf. **12**, 274–281 (2016). https://doi.org/10.1016/j.addma.2016.04.008
9. Freund, J., Karakoç, A., Sjölund, J.: Computational homogenization of regular cellular material according to classical elasticity. Mech. Mater. **78**, 56–65 (2014). https://doi.org/10.1016/j.mechmat.2014.07.018
10. Vigliotti, A., Pasini, D.: Linear multiscale analysis and finite element validation of stretching and bending dominated lattice materials. Mech. Mater. **46**, 57–68 (2012). https://doi.org/10.1016/j.mechmat.2011.11.009
11. Vigliotti, A., Pasini, D.: Stiffness and strength of tridimensional periodic lattices. Comput. Methods Appl. Mech. Eng. **229–232**, 27–43 (2012). https://doi.org/10.1016/j.cma.2012.03.018
12. Concli, F., Gilioli, A.: Numerical and experimental assessment of the static behavior of 3D printed reticular Al structures produced by selective laser melting: progressive damage and failure. Proc. Struct. Integr. **12**, 204–212 (2018). https://doi.org/10.1016/j.prostr.2018.11.094
13. Arabnejad, S., Pasini, D.: Mechanical properties of lattice materials via asymptotic homogenization and comparison with alternative homogenization methods. Int. J. Mech. Sci. **77**, 249–262 (2013). https://doi.org/10.1016/j.ijmecsci.2013.10.003
14. Xu, S., Shen, J., Zhou, S., Huang, X., Xie, Y.M.: Design of lattice structures with controlled anisotropy. Mater. Des. **93**, 443–447 (2016). https://doi.org/10.1016/j.matdes.2016.01.007
15. Moongkhamklang, P., Deshpande, V.S., Wadley, H.N.G.: The compressive and shear response of titanium matrix composite lattice structures. Acta Mater. **58**, 2822–2835 (2010). https://doi.org/10.1016/j.actamat.2010.01.004
16. Zupan, M., Deshpande, V.S., Fleck, N.A.: The out-of-plane compressive behaviour of woven-core sandwich plates. Eur. J. Mech. A/Solids **23**, 411–421 (2004). https://doi.org/10.1016/j.euromechsol.2004.01.007
17. Côté, F., Deshpande, V.S., Fleck, N.A., Evans, A.G.: The compressive and shear responses of corrugated and diamond lattice materials. Int. J. Solids Struct. **43**, 6220–6242 (2006). https://doi.org/10.1016/j.ijsolstr.2005.07.045
18. Deshpande, V.S., Fleck, N.A., Ashby, M.F.: Effective properties of the octet-truss lattice material. J. Mech. Phys. Solids **49**, 1747–1769 (2001). https://doi.org/10.1016/S0022-5096(01)00010-2
19. Smith, M., Guan, Z., Cantwell, W.J.: Finite element modelling of the compressive response of lattice structures manufactured using the selective laser melting technique. Int. J. Mech. Sci. **67**, 28–41 (2013). https://doi.org/10.1016/j.ijmecsci.2012.12.004
20. Tsopanos, S., Mines, R.A.W., McKown, S., Shen, Y., Cantwell, W.J., Brooks, W., Sutcliffe, C.J.: The influence of processing parameters on the mechanical properties of selectively laser melted stainless steel microlattice structures. J. Manuf. Sci. Eng. **132**, 41011 (2010). https://doi.org/10.1115/1.4001743
21. Caulfield, B., McHugh, P.E., Lohfeld, S.: Dependence of mechanical properties of polyamide components on build parameters in the SLS process. J. Mater. Process. Technol. **182**, 477–488 (2007). https://doi.org/10.1016/j.jmatprotec.2006.09.007
22. Park, S.I., Rosen, D.W., Choi, S.K., Duty, C.E.: Effective mechanical properties of lattice material fabricated by material extrusion additive manufacturing. Addit. Manuf. **1**, 12–23 (2014). https://doi.org/10.1016/j.addma.2014.07.002
23. Park, S., Rosen, D.W.: Quantifying effects of material extrusion additive manufacturing process on mechanical properties of lattice structures using as-fabricated voxel modeling. Addit. Manuf. **12**, 265–273 (2016). https://doi.org/10.1016/j.addma.2016.05.006
24. Suard, M., Martin, G., Lhuissier, P., Dendievel, R., Vignat, F., Blandin, J.J., Villeneuve, F.: Mechanical equivalent diameter of single struts for the stiffness prediction of lattice structures produced by electron beam melting. Addit. Manuf. **8**, 124–131 (2015). https://doi.org/10.1016/j.addma.2015.10.002
25. de Formanoir, C., Suard, M., Dendievel, R., Martin, G., Godet, S.: Improving the mechanical efficiency of electron beam melted titanium lattice structures by chemical etching. Addit. Manuf. **11**, 71–76 (2016). https://doi.org/10.1016/j.addma.2016.05.001
26. Luxner, M.H., Stampfl, J., Pettermann, H.E.: Finite element modeling concepts and linear analyses of 3D regular open cell structures. J. Mater. Sci. **40**, 5859–5866 (2005). https://doi.org/10.1007/s10853-005-5020-y
27. Wallach, J.C., Gibson, L.J.: Mechanical behavior of a three-dimensional truss material. Int. J. Solids Struct. **38**, 7181–7196 (2001). https://doi.org/10.1016/S0020-7683(00)00400-5
28. Ptochos, E., Labeas, G.: Shear modulus determination of cuboid metallic open-lattice cellular structures by analytical, numerical and homogenisation methods. Strain **48**, 415–429 (2012). https://doi.org/10.1111/j.1475-1305.2012.00837.x
29. Campoli, G., Borleffs, M.S., Amin Yavari, S., Wauthle, R., Weinans, H., Zadpoor, A.A.: Mechanical properties of open-cell metallic biomaterials manufactured using additive manufacturing. Mater. Des. (2013). https://doi.org/10.1016/j.matdes.2013.01.071
30. Dallago, M., Fontanari, V., Winiarski, B., Zanini, F., Carmignato, S., Benedetti, M.: Fatigue properties of Ti6Al4V cellular specimens fabricated via SLM: CAD vs real geometry. Proc. Struct. Integr. **7**, 116–123 (2017). https://doi.org/10.1016/j.prostr.2017.11.068
31. Dallago, M., Benedetti, M., Luchin, V., Fontanari, V.: Orthotropic elastic constants of 2D cellular structures with variously arranged square cells: the effect of filleted wall junctions. Int. J. Mech. Sci. **122**, 63–78 (2017). https://doi.org/10.1016/j.ijmecsci.2016.12.026
32. Xiong, J., Gu, D., Chen, H., Dai, D., Shi, Q.: Structural optimization of re-entrant negative Poisson's ratio structure fabricated by selective laser melting. Mater. Des. **120**, 307–316 (2017). https://doi.org/10.1016/j.matdes.2017.02.022
33. Bendsøe, M.P., Sigmund, O.: Topology Optimization. Springer, Berlin (2004)
34. PA 2200 Performance 1.0 | PA12. https://eos.materialdatacenter.com/eo/

35. Roberts, A.P., Garboczi, E.J.: Elastic moduli of model random three-dimensional closed-cell cellular solids. Acta Mater. **49**, 189–197 (2001). https://doi.org/10.1016/S1359-6454(00)00314-1
36. Amado-Becker, A., Ramos-Grez, J., Yañez, M.J., Vargas, Y., Gaete, L.: Elastic tensor stiffness coefficients for SLS Nylon 12 under different degrees of densification as measured by ultrasonic technique. Rapid Prototyp. J. **14**, 260–270 (2008). https://doi.org/10.1108/13552540810907929
37. Stanković, T., Mueller, J., Shea, K.: The effect of anisotropy on the optimization of additively manufactured lattice structures. Addit. Manuf. **17**, 67–76 (2017). https://doi.org/10.1016/j.addma.2017.07.004
38. Choy, S.Y., Sun, C.-N., Leong, K.F., Wei, J.: Compressive properties of Ti–6Al–4V lattice structures fabricated by selective laser melting: design, orientation and density. Addit. Manuf. **16**, 213–224 (2017). https://doi.org/10.1016/j.addma.2017.06.012
39. Wauthle, R., Vrancken, B., Beynaerts, B., Jorissen, K., Schrooten, J., Kruth, J.P., Van Humbeeck, J.: Effects of build orientation and heat treatment on the microstructure and mechanical properties of selective laser melted Ti6Al4V lattice structures. Addit. Manuf. **5**, 77–84 (2015). https://doi.org/10.1016/j.addma.2014.12.008
40. ANSYS Mechanical APDL Command Reference. ANSYS, Inc. SAS IP, Inc., Southpointe 275 Technology Drive Canonsburg (2013)
41. Cerardi, A., Caneri, M., Meneghello, R., Concheri, G., Ricotta, M.: Mechanical characterization of polyamide cellular structures fabricated using selective laser sintering technologies. Mater. Des. **46**, 910–915 (2013). https://doi.org/10.1016/j.matdes.2012.11.042
42. Koizumi, Y., Okazaki, A., Chiba, A., Kato, T., Takezawa, A.: Cellular lattices of biomedical Co–Cr–Mo-alloy fabricated by electron beam melting with the aid of shape optimization. Addit. Manuf. **12**, 305–313 (2016). https://doi.org/10.1016/j.addma.2016.06.001
43. Kohnke, P. (ed.): ANSYS Theory Reference, Release 5.6. ANSYS, Inc. SAS IP, Inc., Southpointe 275 Technology Drive Canonsburg (1999)
44. ISO 527-1: Determination of tensile properties. Part 1: general principles (2012)
45. ISO 527-2: Determination of tensile properties. Part 2: test conditions for moulding and extrusion plastics (2012)
46. Fahad, M., Hopkinson, N.: Evaluation and comparison of geometrical accuracy of parts produced by sintering-based additive manufacturing processes. Int. J. Adv. Manuf. Technol. **88**, 3389–3394 (2017). https://doi.org/10.1007/s00170-016-9036-z
47. Deshpande, V.S., Ashby, M.F., Fleck, N.A.: Foam topology: bending versus stretching dominated architectures. Acta Mater. **49**, 1035–1040 (2001). https://doi.org/10.1016/S1359-6454(00)00379-7
48. Fleck, N.A., Deshpande, V.S., Ashby, M.F.: Micro-architectured materials: past, present and future. Proc. R. Soc. A Math. Phys. Eng. Sci. **466**, 2495–2516 (2010). https://doi.org/10.1098/rspa.2010.0215
49. Crawford, C.: The Art of Interactive Design: A Euphonious and Illuminating Guide to Building Successful Software. No Starch Press Inc., San Francisco (2003)

Publisher's Note Nature remains neutral with regard to jurisdictional claims in published maps and institutional affiliations.